EMPLOYING BIOMATERIALS TO FURTHER BASIC UNDERSTANDING OF IMMUNOBIOLOGY

EDITED BY: Evan Alexander Scott, Lonnie Shea, Ankur Singh and Li Tang
PUBLISHED IN: Frontiers in Immunology and Frontiers in Oncology

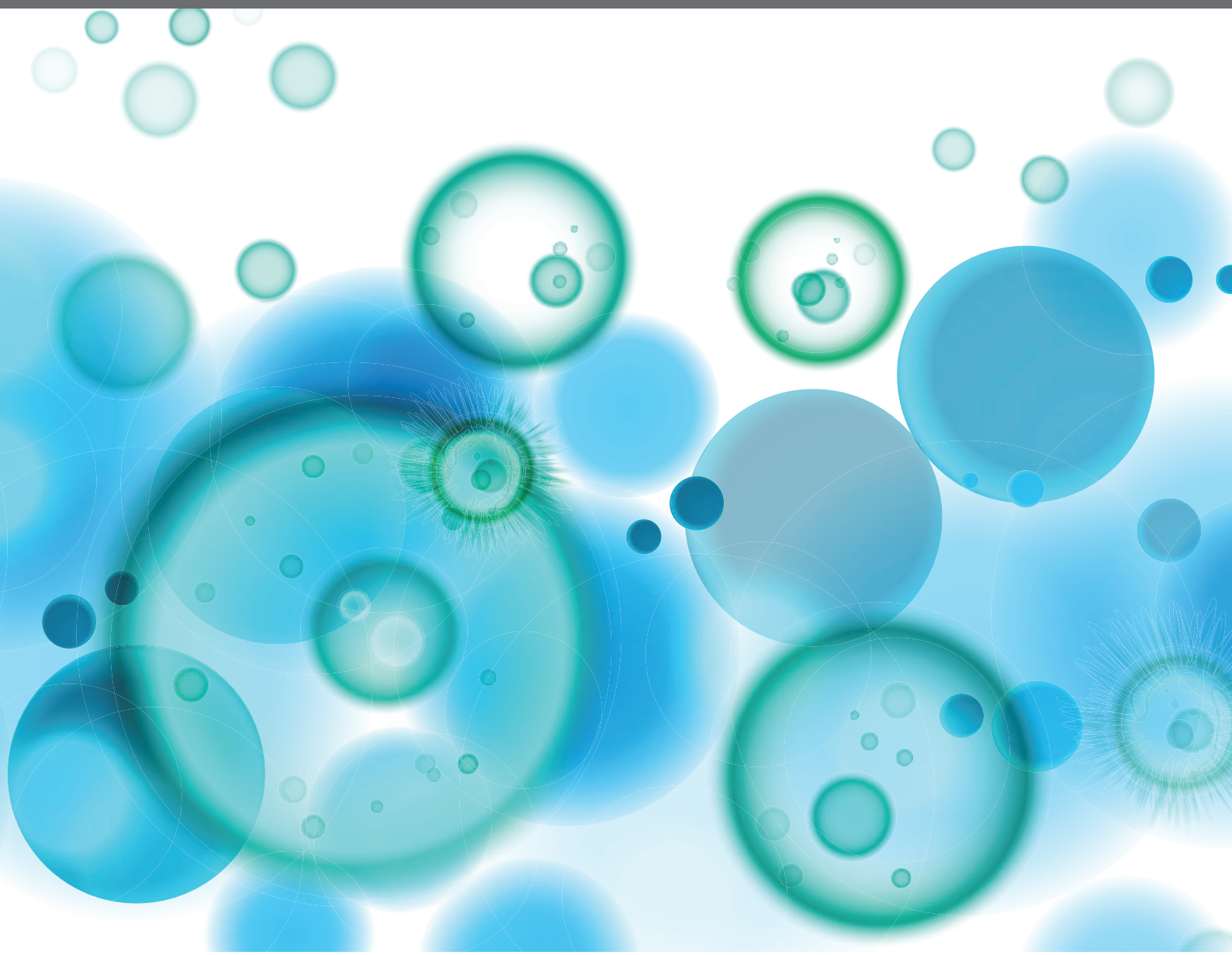

frontiers Research Topics

frontiers

ISSN 1664-8714
ISBN 978-2-88971-886-3
DOI 10.3389/978-2-88971-886-3

About Frontiers

Frontiers is more than just an open-access publisher of scholarly articles: it is a pioneering approach to the world of academia, radically improving the way scholarly research is managed. The grand vision of Frontiers is a world where all people have an equal opportunity to seek, share and generate knowledge. Frontiers provides immediate and permanent online open access to all its publications, but this alone is not enough to realize our grand goals.

Frontiers Journal Series

The Frontiers Journal Series is a multi-tier and interdisciplinary set of open-access, online journals, promising a paradigm shift from the current review, selection and dissemination processes in academic publishing. All Frontiers journals are driven by researchers for researchers; therefore, they constitute a service to the scholarly community. At the same time, the Frontiers Journal Series operates on a revolutionary invention, the tiered publishing system, initially addressing specific communities of scholars, and gradually climbing up to broader public understanding, thus serving the interests of the lay society, too.

Dedication to Quality

Each Frontiers article is a landmark of the highest quality, thanks to genuinely collaborative interactions between authors and review editors, who include some of the world's best academicians. Research must be certified by peers before entering a stream of knowledge that may eventually reach the public - and shape society; therefore, Frontiers only applies the most rigorous and unbiased reviews.
Frontiers revolutionizes research publishing by freely delivering the most outstanding research, evaluated with no bias from both the academic and social point of view. By applying the most advanced information technologies, Frontiers is catapulting scholarly publishing into a new generation.

What are Frontiers Research Topics?

Frontiers Research Topics are very popular trademarks of the Frontiers Journals Series: they are collections of at least ten articles, all centered on a particular subject. With their unique mix of varied contributions from Original Research to Review Articles, Frontiers Research Topics unify the most influential researchers, the latest key findings and historical advances in a hot research area! Find out more on how to host your own Frontiers Research Topic or contribute to one as an author by contacting the Frontiers Editorial Office: frontiersin.org/about/contact

EMPLOYING BIOMATERIALS TO FURTHER BASIC UNDERSTANDING OF IMMUNOBIOLOGY

Topic Editors:
Evan Alexander Scott, Northwestern University, United States
Lonnie Shea, University of Michigan, United States
Ankur Singh, Georgia Institute of Technology, United States
Li Tang, Swiss Federal Institute of Technology Lausanne, Switzerland

Citation: Scott, E. A., Shea, L., Singh, A., Tang, L., eds. (2021). Employing Biomaterials to Further Basic Understanding of Immunobiology. Lausanne: Frontiers Media SA. doi: 10.3389/978-2-88971-886-3

Table of Contents

frontiers in Immunology

ORIGINAL RESEARCH
published: 22 April 2020
doi: 10.3389/fimmu.2020.00560

Lipid-Mediated Insertion of Toll-Like Receptor (TLR) Ligands for Facile Immune Cell Engineering

Michael H. Zhang[1,2], *Emily M. Slaby*[1], *Georgina Stephanie*[1], *Chunsong Yu*[3], *Darcy M. Watts*[1], *Haipeng Liu*[3] *and Gregory L. Szeto*[1,2,4,5*†]

[1] *Chemical, Biochemical, and Environmental Engineering, University of Maryland Baltimore County, Baltimore, MD, United States,* [2] *Marlene and Stewart Greenebaum Comprehensive Cancer Center, University of Maryland, Baltimore, MD, United States,* [3] *Department of Chemical Engineering and Materials Science, Wayne State University, Detroit, MI, United States,* [4] *Center for Biomedical Engineering and Technology, University of Maryland School of Medicine, Baltimore, MD, United States,* [5] *Translational Center for Age-Related Disease and Disparities, University of Maryland Baltimore County, Baltimore, MD, United States*

Cell-based immunotherapies have tremendous potential to treat many diseases, such as activating immunity in cancer or suppressing it in autoimmune diseases. Most cell-based cancer immunotherapies in the clinic provide adjuvant signals through genetic engineering to enhance T cell functions. However, genetically encoded signals have minimal control over dosing and persist for the life of a cell lineage. These properties make it difficult to balance increasing therapeutic efficacy with reducing toxicities. Here, we demonstrated the potential of phospholipid-coupled ligands as a non-genetic system for immune cell engineering. This system provides simple, controlled, non-genetic adjuvant delivery to immune cells via lipid-mediated insertion into plasma membranes. Lipid-mediated insertion (termed depoting) successfully delivered Toll-like receptor (TLR) ligands intracellularly and onto cell surfaces of diverse immune cells. These ligands depoted into immune cells in a dose-controlled fashion and did not compete during multiplex pairwise loading. Immune cell activation could be enhanced by autocrine and paracrine mechanisms depending on the biology of the TLR ligand tested. Depoted ligands functionally persisted on plasma membranes for up to 4 days in naïve and activated T cells, enhancing their activation, proliferation, and skewing cytokine secretion. Our data showed that depoted ligands provided a persistent yet non-permanent adjuvant signal to immune cells that may minimize the intensity and duration of toxicities compared to permanent genetic delivery. Altogether, these findings demonstrate potential for lipid-mediated depoting as a universal cell engineering approach with unique, complementary advantages to other cell engineering methods.

Keywords: membrane insertion, drug delivery, immunotherapy, adjuvants, Toll-like receptors, cell engineering, T cells, B cells

OPEN ACCESS

Edited by:
Ankur Singh,
Georgia Institute of Technology, United States

Reviewed by:
Christopher M. Jewell,
University of Maryland, United States
Raffaele De Palma,
University of Genoa, Italy

****Correspondence:***
Gregory L. Szeto
gszeto@umbc.edu;
greg.szeto@alleninstitute.org

†Present address:
Gregory L. Szeto,
Allen Institute for Immunology, Seattle, WA, United States

Specialty section:
This article was submitted to T Cell Biology, a section of the journal Frontiers in Immunology

Received: *20 November 2019*
Accepted: *11 March 2020*
Published: *22 April 2020*

Citation:
Zhang MH, Slaby EM, Stephanie G, Yu C, Watts DM, Liu H and Szeto GL (2020) Lipid-Mediated Insertion of Toll-Like Receptor (TLR) Ligands for Facile Immune Cell Engineering. Front. Immunol. 11:560. doi: 10.3389/fimmu.2020.00560

INTRODUCTION

Advances in drug delivery have enhanced our understanding of basic biology and generated novel therapies. In cell-based immunotherapy, drugs are administered systemically to target immune cells *in vivo*, or carried by *ex vivo*-primed autologous immune cells that are reinfused into patients. Strategies to engineer cells as drug-carriers *ex vivo* include genome editing, conjugating

biomaterial-based carriers to cell surfaces, and binding of the plasma membrane for passive diffusion of immunostimulatory ligands (1, 2). Despite successful implementation in the clinic, cell-based immunotherapies still face challenges of implementing simple and efficient delivery that improve therapeutic responses. For example, genome editing can decrease cell viability and has low efficiency in some cell types of interest, particularly T cells (3–5). Biomaterial-based drug carriers with defined size, shape, cargo loading, composition, and physiochemical parameters can enable controlled delivery to intracellular cell compartments for autocrine signaling or to surrounding cell surface receptors for paracrine signaling (2). However, optimization of nanoparticle design parameters is complex, and often requires empirical testing due to the variability associated with formulations for each drug-particle combination, causing inconsistent cell loading or uptake (6). Here, we propose a simplified delivery platform that couples diverse biomolecular cargo to phospholipids that directly insert into plasma membranes for universal loading into plasma membranes of cells without the need for gene editing or complex biomaterial design.

Biomolecules have been previously conjugated to phospholipids for cell loading by plasma membrane interactions. Our previous study generated potent vaccines by exploiting the affinity of lipids to bind albumin and deliver antigen and adjuvant conjugates to lymphoid organs (7). *Ex vivo* modification with lipid conjugated immunostimulatory ligands has also been investigated for some adjuvants. In cancer, lipid-mediated delivery of T-cell adjuvants elicit tumor regression in multiple preclinical models of cancer (8, 9). Lipid conjugated adjuvants also strongly associate with plasma membranes of dendritic cells and tumor cells (10, 11). However, previous studies have not fully characterized the efficiency of lipid-mediated insertion into plasma membranes, or expanded this delivery approach to diverse immunostimulatory cargoes.

Toll-like receptors (TLRs) are one family of molecules that are heavily used to enhance immune responses. TLRs are a major contributor to innate immune sensing, and also directly implicated in adaptive immunity during many diseases (12–15). For example, TLR2 is a cell surface receptor that senses molecules from microbial cell-walls. TLR2 activation results in increased pro-inflammatory cytokine secretion, suppression of regulatory T cells, and enhanced sensitivity of cytotoxic T cells (3, 13, 16). TLR9 is an intracellular receptor that senses unmethylated CpG DNA from viruses and bacteria. TLR9 ligands are frequently used as vaccine adjuvants (17, 18), and can directly enhance proliferation and survival of T cells (19, 20). Successful delivery of both TLR2 and TLR9 ligands has demonstrated promising therapeutic responses, particularly in cancer (13, 21–23). However, improved delivery approaches are needed to more easily deliver cell surface and intracellular ligands to diverse immune cells.

We report that lipid-conjugated TLR2 and TLR9 ligands can rapidly and simply insert into immune cell plasma membranes (hereafter termed depoting), delivering ligands to both cell surface and intracellular receptors. We analyzed ligand loading, dynamics of ligand persistence, and activation of mouse immune cells to demonstrate the feasibility of depoting to provide paracrine and autocrine signals that can enhance immune cell function. This study provides proof-of-concept that depoting immunostimulatory ligands into plasma membranes can enhance cell function, highlights key features of this platform including dynamics of single and multiplex ligand loading and turnover, and provides a new method for engineering cell-based therapies that can complement existing methods.

METHODS

TLR2 and TLR9 Ligands

Synthetic ligands for TLR2, Pam2CSK4 and Pam3CSK4, and their biotinylated variants were purchased from Tocris Bioscience and InvivoGen. TLR9 ligand, CpG oligonucleotide 1826 (5′-tccatgacgttcctgacgtt-3′ with a phosphorothioated backbone) (CpG) and fluorescein (FAM)-labeled CpG, were commercially synthesized (Integrated DNA Technologies). Diacyl stearoyl (C18) lipid conjugated CpG (lipid-CpG) and FAM-labeled lipid-CpG were made as previously described by synthesizing diacyl C18 lipid phosphoramidite and conjugating to either CpG or CpG-FAM on a ABI 394 synthesizer on 1.0 micromole scale (11). Lipid-CpG was purified by reverse phase HPLC with a C4 column (BioBasic4, 200 mm × 4.6 mm, Thermo Scientific). A gradient eluent (Sigma-Aldrich) was implemented with 100 mM triethylamine-acetic acid buffer (pH 7.5) and acetonitrile (0–30 min, 10–100%).

Isolation of Naïve and Primed Mouse Immune Cells

All procedures with animals and animal-derived materials were approved by the UMBC Institutional Animal Care and Use Committee (OLAW Animal Welfare Assurance D16-00462). C57BL/6 mice and CD45.1$^+$ (B6.SJL-Ptprca Pepcb/Boy) congenic mice from Jackson Laboratory were bred in the UMBC animal facility and used for all experiments. Spleens from 12–52 week old C57BL/6 mice were mashed through a 40-μm cell strainer treated with ACK lysis buffer (1 mL per spleen, ThermoFisher) for 5 min at 25°C to lyse red blood cells. Naïve CD4$^+$ and CD8$^+$ T cells were isolated using a negative selection cocktail containing the following biotinylated mouse antibodies (Biolegend): TCR γ/δ (clone GL3), CD24 (clone M1/69), TER-119 (clone TER-119), CD49b (clone HMα2), CD45R/B220 (clone RA3-6B2), CD19 (clone 6D5), CD11c (clone N418), and CD11b (clone M1/70). B cells were isolated from splenocytes using a negative selection cocktail containing the following biotinylated mouse antibodies: CD43 (clone 1B11), CD90.2 (clone 30-H12), Gr-1 (clone RB6-8C5), TER-119 (clone TER-119), CD49b (clone HMα2), CD11b (clone M1/70), CD8 (clone 53-6.7), and CD4 (clone H129.19). Antibody-bound cells were depleted with Rapidsphere streptavidin magnetic beads according to the manufacturer's instructions (STEMCELL Technologies). Cells with >90% purity were used for experiments.

Primed T cells were obtained by culturing splenocytes in complete RPMI 1640 media supplemented with 10% fetal bovine serum (FBS; ThermoFisher), Concanavalin A (2 μg/mL; Sigma-Aldrich), and IL-7 (2 ng/mL, Biolegend) at 37°C for 2 days. Ficoll-Paque Plus (GE Healthcare Life Sciences) gradient

separation was used for dead cell removal by centrifugation at 500 × g for 20 min with no brake. Primed T cells were isolated with the negative selection cocktail described above.

Lipid-Mediated Insertion (Depoting) of Lipid-Conjugated Ligands

Unless specified otherwise (in **Figure 2**), splenocytes, isolated B cells, or isolated T cells were incubated with CpG (5 μM), lipid-CpG (5 μM), Pam2CSK4 (10 μg/mL), or Pam3CSK4 (10 μg/mL) for 1 h in complete RPMI 1640 media supplemented with 10% fetal bovine serum. Splenocytes or T cells were then washed 3 times with PBS plus 1% bovine serum albumin to remove unbound ligand.

Cells were incubated with αCD16/32 antibody (clone 93; Biolegend) to block non-specific antibody binding by Fc receptors for 5 min at 25°C. Cells were stained with the following antibodies: CD4 (clone GK1.5; PerCP/Cyanine5.5), CD8a (clone 53-6.7; APC), and B220 (clone RA3-6B2; PE/Cy7) 15 min at 25°C. PE-conjugated streptavidin was used to bind depoted biotinylated Pam2CSK4. Cell viability was determined by LIVE/DEAD^{TM} exclusion staining per manufacturer's instructions (ThermoFisher).

TLR2 Ligand Persistence and Bystander Cell Activation Assays

Naïve or primed T cells were rested in complete RPMI 1640 media and supplemented with 10% FBS after depoting with Pam2CSK4 or Pam3CSK4 as described above. At selected time-points (0, 1, 2, 5, or 8 days post-depoting), T cells were washed and fixed with 4% paraformaldehyde (Sigma) for 15 min at 25°C. After washing 5 times with PBS + 1% BSA, at 1,000 × g for 5 min, T cells were cultured in complete RPMI 1640 media and supplemented with 10% FBS. Bystander B cells were added in co-cultures at a 1:1 B cell:T cell ratio. Naïve T cells without fixation were immediately cultured with bystander B cells. After 2 days of incubation at 37°C and 5% CO_2, B-cell activation was measured by fluorescent staining for MHCII (clone M5/114.15.2; FITC) and CD69 (clone H1.2F3; PerCP/Cy5.5).

Lipid-Conjugated TLR9 Ligand B-Cell Activation Assay

Isolated B cells from C57/BL6 mice were cultured in complete RPMI 1640 media supplemented with 10% FBS after depoting with lipid-CpG and combined with an equal number (50,000 cells) of isolated CD45.1^{+} B cells. After 2 days of co-culture at 37°C and 5% CO_2, B cells were identified by B220 (clone RA3-6B2; PE-Cy7) CD45.1 (clone A20; PE) antibody, and B-cell activation was measured by MHCII (clone M5/114.15.2; FITC) and CD69 (clone H1.2F3; PerCP/Cy5.5).

T-Cell Activation Assays

Naïve T cells were labeled with 5 μM of carboxyfluorescein succinimidyl ester (CFSE, ThermoFisher). Labeled cells were cultured in RPMI 1640 media and supplemented with 10% FBS as well as αCD3/CD28 coated Dynabeads^{TM} (Thermo) at a 1:5 bead to T cell ratio after depoting of lipid-CpG, Pam2CSK4, and/or Pam3CSK4 ligands. Non-depoted T cells were treated with soluble lipid-CpG (5 μM), Pam2CSK4 (10 μg/mL), and/or Pam3CSK4 (10 μg/mL). Cell proliferation was measured by CFSE dilution after 3 days, and cell activation was measured by fluorescent staining for CD25 (clone PC61; PE). Cell proliferation index and division index were calculated using FlowJo LLC software. Proliferation index is defined as the total number of cell divisions divided by the number of divided cells, whereas division index is the total number of cell divisions divided by the number of total original cells (24). Paracrine-enhanced proliferation of bystander T cells was measured as described above, with αCD3/CD28 beads added at a 2:5 bead to T-cell ratio.

Flow Cytometry and Microscopy Analyses

Fluorescently labeled cells were analyzed on a BD LSRII or Beckman Coulter CyAn ADP flow cytometer. The LSRII flow cytometer consisted of 405, 488, 561, and 640 nm excitation laser lines. The CyAn ADP flow cytometer consists of 405, 488, and 635 nm excitation laser lines. Data were analyzed using FlowJo LLC software v10 (Tree Star Inc.).

Cells loaded with FAM-labeled lipid-CpG were prepared for confocal analysis by blocking with normal goat serum and labeling with early endosome marker-1 (EEA1) (clone C45B10; Cell Signaling Technologies) for 12 h at 4°C. Cells were fluorescently labeled with AF647 anti-rabbit IgG (Invitrogen) and DAPI for 60 min at 25°C. Confocal anaylsis was performed on a TCS SP5 microscope (Leica Microsystems). The excitation laser lines used were 405, 488, and 633 nm. Lipid-CpG and EEA1 pixel intensities were obtained from 8-bit images, and pixels were binned in 2 × 2 matrices after noise subtraction (removing pixels $=< 5$ and pixels $= 255$). All imaging analysis was performed using Matlab.

Enzyme-Linked Immunosorbent Assays (ELISAs) for Lipid-Conjugated Ligand Detection and Cytokine Quantification

One million purified T cells were depoted with FAM-labeled lipid-CpG, biotinylated Pam2CSK4, or biotinylated Pam3CSK4 as described above, and then lysed with Glo lysis buffer (Promega) for 10 min at 25°C. Lysates were collected and plated onto Nunc MaxiSorp ELISA plates (Thermo). After 2 h of incubation at 25°C, FAM-labeled lipid-CpG was excited at 488 nm, and fluorescent emission at 520 nm was quantified by a microplate fluorescence reader. For Pam2CSK4 and Pam3CSK4 samples, horseradish peroxidase (HRP)-labeled streptavidin was added for 2 h incubation at 25°C, and then TMB substrate (Thermo) was added to observe changes in absorbance at 450 nm with a microplate spectrophotometer (BioTek).

T-cell activation was analyzed by collecting supernatants on day 2 post-activation for IL-2, IL-4, and IFNγ quantification by ELISA per manufacturer's instructions (BioLegend).

Regression and Statistical Analyses

For regression models, a least-squares two-phase decay model was fit to the median fluorescence intensity (MFI) data from the TLR2 ligand persistence assay. Effective half-life, the fast half-life

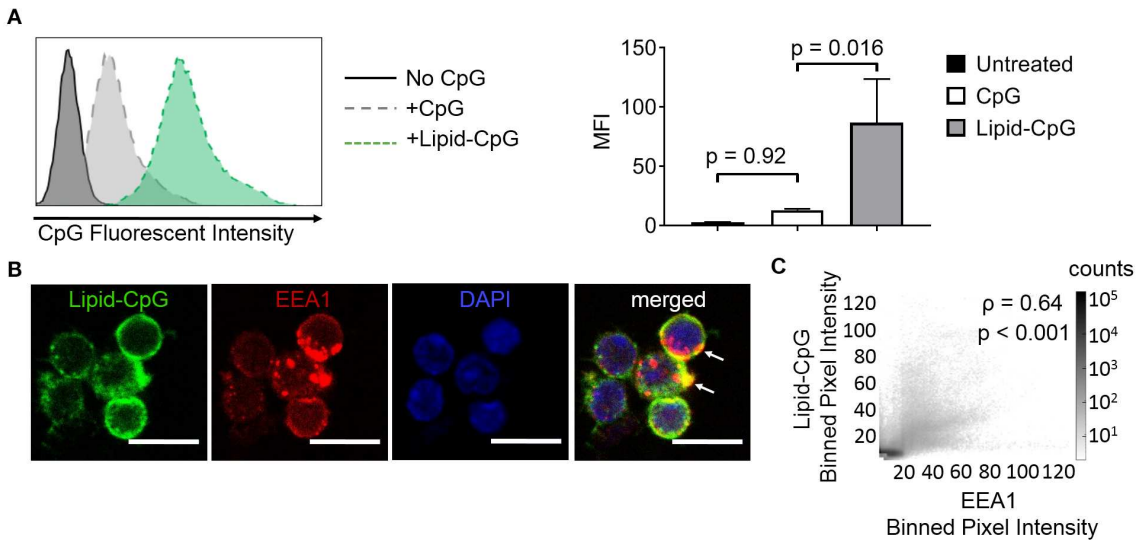

FIGURE 1 | Insertion of TLR9 ligand into murine immune cells is enhanced by lipid tail. Fluorescein (FAM) labeled CpG ODN or diacyl lipid conjugated CpG ODN (lipid-CpG) were incubated with splenic immune cells at 5 μM for 1 h at 37°C in supplemented RPMI media. **(A)** Representative fluorescent intensity as measured by flow cytometry (left), and quantification of fluorescent intensity (right). *p*-values between indicated conditions were determined by one-way ANOVA with Sidak's method for multiple comparisons correction. Data showed m ± s.d. ($n = 3$ independent samples). **(B)** Confocal micrographs showed lipid-CpG delivery to cell plasma membranes and associated with early endosome marker-1 (EEA1) (white arrows). Lipid-CpG (green), EEA1 (red), DAPI (blue). Scale bar = 10 μm. **(C)** Bivariate scatter plot showed binned (2x2) pixel intensities between lipid-CpG and EEA1. Pearson's correlation coefficient was determined as $\rho = 0.64$ ($p < 0.001$). Data compiled from $n = 52$ cells from 3 independent samples.

of the two-phase decay, is computed as followed:

$$t_{1/2} = \ln(\frac{2}{\textit{fast rate constant}})$$

Colocalization analysis was performed on confocal micrographs using Pearson's correlation coefficient, ρ, computed as followed:

$$\rho = \frac{\Sigma_i (x_i - \bar{x})(y_i - \bar{y})}{\sqrt{\Sigma_i (x_i - x)^2 \Sigma_i (y_i - y)^2}}$$

where x and y are the pixel values of respective lipid-CpG and EEA1 fluorescence intensities from spatial location denoted by i. $\bar{x}$ and $\bar{y}$ are mean pixel intensities of lipid-CpG and EEA1 fluorescence intensities over i, respectively. Analysis was performed with Matlab.

One-way, repeated measures (RM) one-way, and two-way analyses of variance (ANOVAs) were performed followed by comparisons using Sidak's correction methods. Comparisons to soluble controls were also performed using one-tailed ratio-paired *t*-tests. All statistical analysis and regression models were performed with Prism software (GraphPad).

RESULTS

Lipid-Conjugated TLR Ligands Efficiently Inserted Into Plasma Membranes

The ability of lipids to insert into plasma membranes can be exploited for stable anchoring of lipid-conjugated immunostimulatory TLR ligands into cells. This phenomenon is similar to the natural membrane insertion of GPI-anchored proteins. We have previously conjugated the intracellular TLR9 ligand CpG DNA to a diacyl stearoyl (C18) lipid, termed lipid-CpG, and demonstrated strong association with plasma membranes of cancer cells (10). Here, we tested whether lipid-CpG can also depot into plasma membranes of immune cells. Lipid-CpG incubated for 1 h with resting splenocytes (B cells, $CD4^+$ T cells, $CD8^+$ T cells) showed increased ligand loading by 6.7-fold compared to free CpG (**Figure 1A**). Confocal microscopy analysis suggested lipid-CpG associated with early endosomal marker-1 (EEA1) within immune cells (**Figure 1B**). A bivariate scatter plot showed counts of lipid-CpG and EEA1 pixels from multiple confocal micrographs; colocalization analysis between lipid-CpG and EEA1 pixel intensities demonstrated a Pearson correlation coefficient of $\rho = 0.64$ ($p < 0.001$), supporting partial colocalization and uptake by endocytosis (**Figure 1C**) (25). These data demonstrated lipid-mediated cell loading can deliver cargo to cell surface and intracellular compartments, overcoming the challenges of low non-specific uptake generally associated with resting lymphocytes (26). We termed this lipid-mediated insertion "depoting," reflecting the likely rapid partitioning of lipid moieties into the lipid bilayer of plasma membranes (27, 28).

We next investigated whether a cell surface TLR ligand, Pam2CSK4, can also be depoted into splenic immune cells given differences in its diacyl palmitoyl (C16) lipid tail. We also tested depoting of Pam2CSK4 in parallel with lipid-CpG to determine if multiple lipid-tailed ligands can be depoted

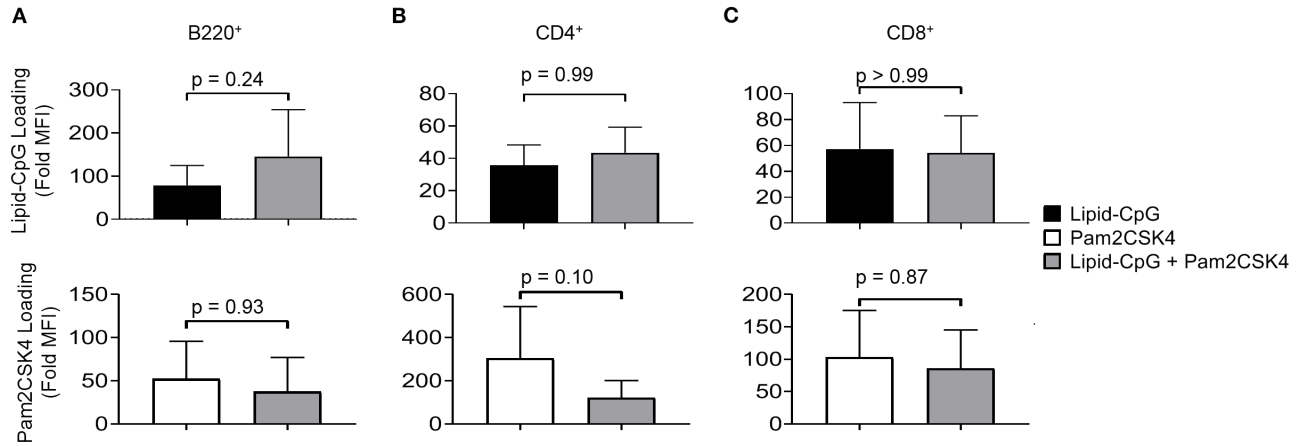

FIGURE 2 | Lipid-tailed ligands efficiently depot alone and together into resting B and T cells. Fluorescently labeled lipid-CpG or biotinylated Pam2CSK4 was incubated either separately or together with splenic immune cells at 5 μM or 10 μg/mL, respectively, for 1 h at 37°C. Splenic immune cells were gated by lineage markers to analyze lipid-CpG (*top row*) and Pam2CSK4 (*bottom row*) depoting in 3 cell types: **(A)** B220$^+$ B cells, **(B)** CD4$^+$ T cells, and **(C)** CD8$^+$ T cells. Loading was calculated as the fold increase of sample median fluorescent intensity (MFI) normalized to non-depoted cells for each ligand. *p*-values between indicated conditions for each panel (top and bottom) were determined by one-way ANOVA with Sidak's method for multiple comparisons correction. Data showed m ± s.d. ($n = 4$ independent samples).

into cells without membrane saturation. We analyzed lipid-CpG and Pam2CSK4 depoting individually and together in B220$^+$ B cells (**Figure 2A**), CD4$^+$ T cells (**Figure 2B**), and CD8$^+$ T cells (**Figure 2C**). Depoting lipid-CpG and Pam2CSK4 together did not decrease ligand levels compared to ligands depoted alone. These data suggested that delivery of TLR2 and TLR9 ligands can be mediated by C16 or C18 lipid tails, respectively, and that depoting 2 ligands was feasible without loading saturation under tested conditions. Depoting also had no effect on cell viability compared to untreated cells (**Figure S1**). Overall, our data showed that B and T cells have a high capacity for rapid depoting with multiple lipid-conjugated TLR ligands, and that depoting achieved delivery of ligands into plasma membranes without toxicity to cells.

Next, we optimized depoting conditions to more precisely control the abundance of ligands. Enzyme-linked immunosorbent assays (ELISAs) were used to quantify depoted lipid conjugates in purified mouse T cells. Conjugate concentration during depoting was tested over a 100-fold range and depoting times were tested ranging from 5 to 60 min. Cells were lysed after depoting to detect the average number of ligands per T cell. Depoting 5 μM of lipid-CpG for 60 min resulted in 25-fold more molecules per T cell when compared to depoting 0.05 μM of lipid-CpG (**Figure 3A**).

We then quantified depoting of TLR2 ligands. Increasing depoting concentration of Pam2CSK4 from 0.1 to 10 μg/mL resulted in a 130-fold increase in the number of depoted molecules per T cell (**Figure 3B**, left). Both lipid-CpG and Pam2CSK4 depoting plateaued after 1 h. Increasing depoting concentration did not change preferential insertion into CD4$^+$ or CD8$^+$ T cells (**Figures S2A,B**). Pam3CSK4, a synthetic lipid-peptide with a triacyl palmitoyl lipid, is another well-defined TLR2 ligand (16, 29). We used this ligand to test if the third hydrophobic lipid tail altered depoting in T cells. Pam3CSK4 depoting increased with time, but increasing the depoting concentration of Pam3CSK4 from 0.1 μg/mL to 10 μg/mL resulted in a smaller 2.2-fold increase in number of depoted molecules per T cell (**Figure 3B**, right) when compared to Pam2CSK4. The diacyl and triacyl TLR2 ligands depoted into T-cell plasma membranes in a dose-dependent manner, suggesting that depoting is largely independent of tail number. We depoted cells in subsequent experiments for 1 h at the highest ligand concentrations above to maximize depoting.

Depoted Cell-Surface Ligands Induced Paracrine Cell Activation

TLR2 ligation has successfully enhanced cellular immunity by direct signaling on effector cells (e.g., T cells) and antigen-presenting cells (APCs) (16, 22). We hypothesized that TLR2 depoting can enhance bystander APC functions. To test this, we first validated that TLR2 ligands on T cells can engage its receptor on bystander cells using TLR2$^+$ APCs. B cells were chosen as bystander APCs due to their dose-dependent sensitivity to Pam2CSK4 and Pam3CSK4 (**Figures S3A,B**). T cells depoted with Pam2CSK4 activated B cells after 2 days of co-culture, upregulating MHC II (19-fold) and CD69 (3.8-fold) (**Figure 4A**) (24). T cells depoted with Pam3CSK4 also activated B cells in co-culture, upregulating MHC II (21-fold) and CD69 (4.4-fold) (**Figure 4B**). MHC II and CD69 expression levels activated by Pam2CSK4 and Pam3CSK4-depoted T cells were similar to 10 μg/mL of soluble ligand. In fact, depoted Pam3CSK4 induced 1.5-fold higher MHC II expression than 10 μg/mL of soluble Pam3CSK4. This high dose of soluble ligand was 1,000-5,000-fold more concentrated than the estimated dose on depoted T cells (**Table S1**).

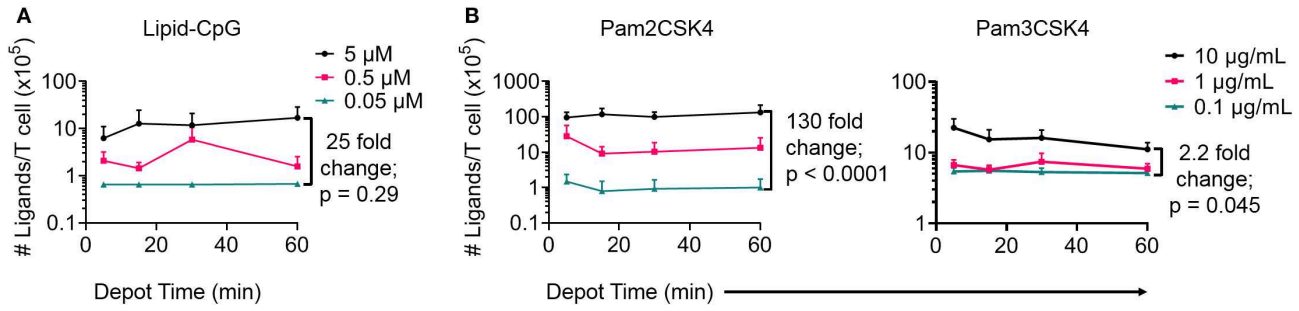

FIGURE 3 | Depoting of TLR ligands provides dose control. Depoted lipid-tailed TLR ligands into polyclonal T cells was dependent on input concentration for **(A)** lipid-CpG; and **(B)** Pam2CSK4 or Pam3CSK4 polypeptides. The fold increase in average ligand per T cell is indicated per ELISA analysis. *p*-values between indicated comparisons as determined by two-way ANOVA with Sidak's tests. Data showed mean ± s.d. ($n = 3$–4 independent samples).

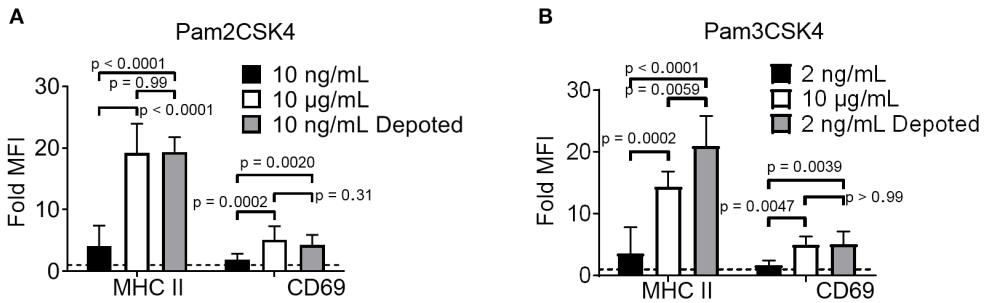

FIGURE 4 | Depoted TLR ligands activate cells through paracrine signaling. Polyclonal T cells were incubated with **(A)** Pam2CSK4 or **(B)** Pam3CSK4 for 1 h under indicated conditions, and then co-cultured with B cells for 2 days. B-cell activation was determined by fold MFI of activation markers, MHC II and CD69, as measured by flow cytometry. Sample MFIs were normalized to unstimulated B cell controls. Dashed line represents theoretical no activation (MFI = 1). *p*-values between indicated conditions were determined by RM one-way ANOVA with Sidak's method for multiple comparisons correction. Data showed m ± s.d. ($n = 5$–6 independent experiments).

We next tested whether depoting can enhance cell sensitivity to TLR2 signaling per dose of ligand compared to soluble delivery. These doses (10 ng/mL for Pam2CSK4 and 2 ng/mL for Pam3CSK4) were matched to the respective amount of ligand quantified in depoted cells as determined by ELISA (**Figures 3B,C**, **Table S1**). T cells depoted with Pam2CSK4 induced higher expression of MHC II (5.3-fold) and CD69 (2.2-fold) when compared to the same dose of soluble Pam2CSK4 (**Figure 4A**). Depoted Pam3CSK4 induced higher expression of MHC II (6.1-fold) and CD69 (2.8-fold) when compared to the same dose of soluble Pam3CSK4 (**Figure 4B**). Consistent with our hypothesis, none of the dose-matched soluble Pam2CSK4 and Pam3CSK4 activated B cells. These studies demonstrated that depoted TLR2 ligands were presented to bystander cells, and that cell surface-bound presentation of TLR2 ligands provided stronger signaling than the equivalent ligand dose in solution.

Intracellular Ligands Activated Depoted Immune Cells but Not Bystanders

Bystander cells can be activated by paracrine interactions with depoted cells, as well as from release of depoted ligands over time into solution. We used lipid-CpG, a TLR9 ligand that must be internalized for signaling, to test whether release of depoted ligand over time contributed to paracrine cell activation. A co-culture assay was used with B cells as both depoted cells and bystander cells given their sensitivity to CpG stimulation (30). Lipid-CpG was depoted into B cells from wild-type mice, and then cocultured with congenic CD45.1$^+$ bystander B cells for 2 days. Lipid-CpG depoted B cells showed increased expression of MHC II (19-fold) and CD69 (3.3-fold) when normalized to unstimulated B cells (**Figure 5**). Levels of MHC II and CD69 were similar to those induced by a high dose of free CpG (5 μM) in solution. This confirmed that depoted ligand can be internalized to provide autocrine stimulation. We then analyzed activation of bystander cells to determine whether paracrine signaling occurred through soluble ligand release. Bystander CD45.1$^+$ B cells were not activated, with activation marker levels comparable to unstimulated controls (**Figure 5**). We analyzed whether ligand can spontaneously transfer from plasma membranes of depoted cells to undepoted bystanders. The presence of bystander B cells did not decrease activation of depoted B cells since MHC II and CD69 expression levels in co-cultures were comparable to expression on depoted cells cultured alone. These data demonstrated that depoted ligand remained stably compartmentalized in depoted cells, and that lipid-CpG was not released at functional levels into solution or transferred to plasma membranes of bystander cells.

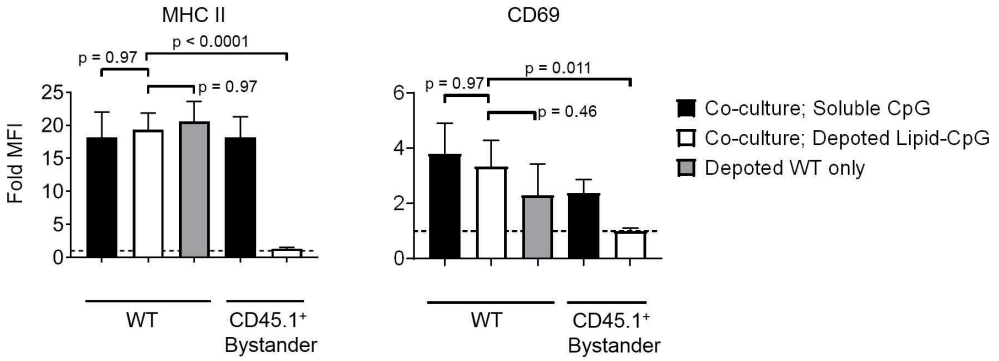

FIGURE 5 | Depoted TLR ligands activate cells through autocrine signaling. Wildtype (WT) B cells were depoted with 5 μM of lipid-CpG and co-cultured with CD45.1$^+$ bystander B cells. MHCII and CD69 on both depoted (WT) and bystander (CD45.1$^+$) B cells were measured after 2 days of co-culture by flow cytometry and normalized to respective unstimulated B cells. Dashed line represents theoretical no activation (MFI = 1). Indicated *p*-values were determined by RM one-way ANOVA with Sidak's method for multiple comparisons correction. Data showed m ± s.d. ($n = 4$ independent samples).

Surface Presentation of Depoted TLR2 Ligands Was Non-permanent

Depoting is a non-permanent cell modification, so we next characterized the persistence of depoted ligands on immune cell surfaces. Purified T cells were depoted with TLR2 ligands, and then rested for up to 8 days in IL-7. After resting, cells were fixed in 4% paraformaldehyde to preserve persisting surface TLR2 ligands. The persistence of surface TLR2 ligands was determined by co-culturing fixed T cells with bystander B cells. Low level IL-7 supplementation was used to sustain T-cell viability without eliciting cell proliferation over the 8-day rest period (**Figure S4**). We analyzed MHC II and CD69 levels on B cells induced by T cells fixed immediately after depoting (0-day) and determined levels were comparable to levels observed in **Figure 3**. This verified that fixation did not alter the recognition of TLR2 ligand. Levels of surface-bound ligand decayed over time, with the shortest effective fast half-life of 0.49 days for Pam3CSK4 induction of CD69 (**Figure 6A**). Overall, bystander cell activation showed that surface-presented ligand functionally persisted between 2 and 4 days post-depoting.

Depoted ligands are not permanently persistent on cell surfaces, so their efficacy could be diluted as T cells divide. We used proliferating T cells to determine whether cell division causes faster decay of depoted ligands. Naïve T cells were primed for 2 days with concanavalin A and IL-7 before depoting. Primed cells were depoted with Pam2CSK4 or Pam3CSK4 and rested for up to 8 days. Primed T cells retained viability for 8 days in IL-7, similar to naïve T cells (**Figure S4A**, right). Depoted Pam2CSK4 and Pam3CSK4 decayed at a similar rate on primed T cells compared to naïve T cells, activating B cell bystanders as determined by MHC II and CD69 expression (**Figure 6B**). The shortest effective fast half-life of 0.17 days was observed for MHC II levels stimulated by Pam3CSK4. Altogether, our data demonstrated that depoted TLR2 ligands persisted on plasma membranes of both naïve and primed T cells, providing functional paracrine signaling to bystander cells for multiple days. Proliferation of primed T cells did not further increase the surface decay rate for depoted ligands.

Depoted Lipid-Conjugated TLR2 Enhanced T Cell Activation

T cells do not constitutively express abundant levels of TLR2 or TLR9, but activated T cells rapidly increase TLR expression (31). Previous studies demonstrate TLR ligands can enhance T cell activation (16, 17, 32). Here, we tested whether depoting TLR ligands in T cells can enhance activation by increased proliferation. We added TLR ligands in solution or depoted into pan CD4$^+$ and CD8$^+$ T cells from wild-type C57BL/6J mice. T cells were stimulated with αCD3/CD28-coated beads for 3 days, then analyzed for proliferation by flow cytometry. Depoting of TLR2 ligands induced more CD4$^+$ T-cell proliferation compared to dose-matched soluble ligands (**Figure 7A**). Depoting of Pam3CSK4 alone increased CD4$^+$ and CD8$^+$ T-cell division indices by 1.9- and 2.9-fold, respectively, compared to soluble Pam3CSK4 (**Figures 7B,C**). Depoting both TLR2 ligands increased CD4$^+$ and CD8$^+$ T-cell division indices by 2.2-fold and 3.3-fold, respectively, compared to soluble ligands. No lipid-conjugated ligands enhanced CD4$^+$ T-cell proliferation index by depoting, but depoted Pam3CSK4 did enhance CD8$^+$ T-cell proliferation index (**Figure S5**). Altogether, these data demonstrated that Pam3CSK4, alone and in combination with other lipid-conjugated ligands, provided co-stimulation during T-cell division.

Depoted TLR2 Ligands Enhanced T-Cell Activation by Paracrine Signaling

We tested whether depoting with TLR9 ligand can enhance T-cell activation and functions. Lipid-CpG did not increase proliferation of CD4$^+$ or CD8$^+$ T cells above levels compared to those without ligand. Combining lipid-CpG with Pam2CSK4 or Pam3CSK4 did not enhance CD4$^+$ T-cell proliferation. CD8$^+$ T-cell proliferation did increase with depoted lipid-CpG and Pam3CSK4 (**Figure S6**), but these levels were lower than T cells depoted with Pam3CSK4 alone, as shown in **Figure 7C** or **Figure S5B**. We determined how depoting with TLR2 and TLR9 ligands affected cytokine secretion by

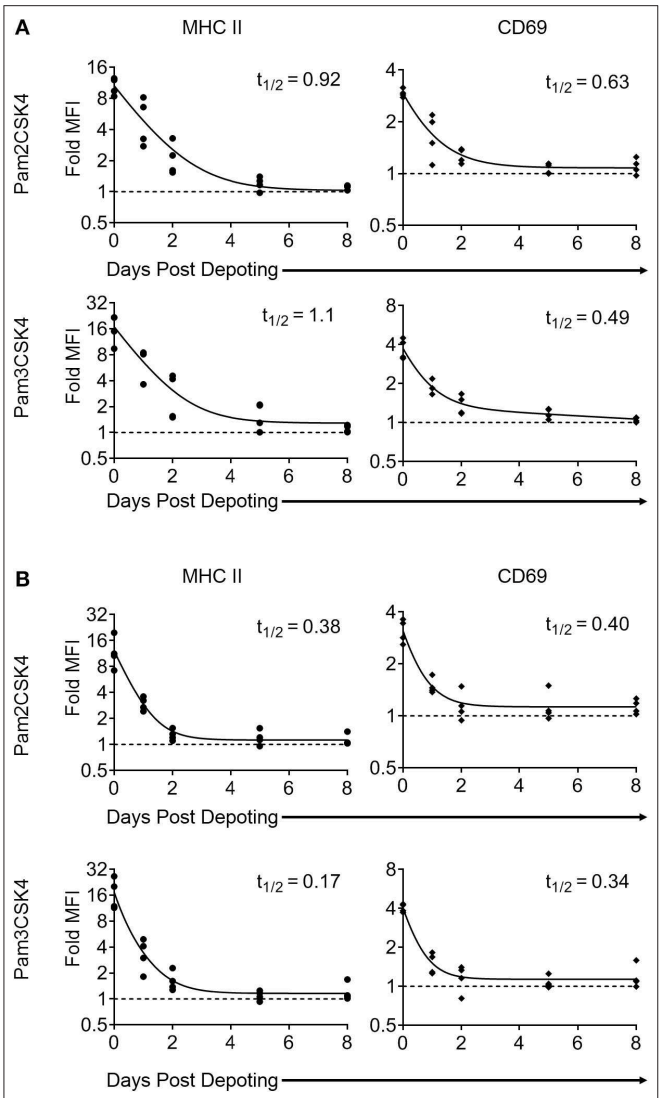

FIGURE 6 | Surface presentation of depoted TLR2 ligands on T cells is non-permanent. Splenocytes were cultured either **(A)** (as naïve T cells) in absence of, or **(B)** (as primed T cells) in presence of 2 μg/mL of Concanavalin A and 10 ng/mL of IL-7 for 2 days. Purified T cells were then depoted with either Pam2CSK4 or Pam3CSK4 for 1 h at 37°C in supplemented RPMI media. T cells were then rested in IL-7 for 0, 1, 2, 5, or 8 days. At each time-point, cells were fixed and co-cultured for 2 days with purified B cells. B-cell activation was determined by fold MFI of MHC II (circle) and CD69 (diamond) with respect to unstimulated controls. Dashed line represents theoretical no activation (MFI = 1). Solid lines are two-phase decay non-linear regression curves as determined by independent samples shown. Effective fast half-life in days ($t_{1/2}$) as shown. n = 3–4 independent samples.

analyzing IL-2 and IL-4 levels as signature Th1 and Th2 cytokines, respectively. Soluble TLR9 ligand elicited detectable IL-4 production, while depoted TLR9 ligand decreased IL-4 levels below the limit of detection (**Figure S7A**). Soluble and depoted TLR2 ligands resulted in IL-4 levels below the limit of detection. Depoting of TLR2 and TLR9 ligands resulted in higher IL-2 levels compared to dose-matched soluble ligands (**Figure S7B**). These data suggested that co-stimulation of T cells by depoted TLR ligands elicited a more pro-inflammatory Th1-like phenotype.

While depoting increased T-cell proliferation, we next analyzed whether depoted TLR2 ligands provide autocrine co-stimulation or paracrine co-stimulation to bystander T cells. Depoted T cells were mixed with non-depoted bystander T cells, and co-cultures were stimulated with αCD3/CD28 beads for 3 days. $CD4^+$ and $CD8^+$ T-cell division indices of Pam3CSK4-depoted cells increased 1.6-fold compared to respective soluble ligand (**Figure 8A**). *Cis*-depoted Pam2CSK4 and Pam3CSK4 (depoted onto the same cell) increased division indices of depoted cells: 1.8-fold for $CD4^+$ T cells and 1.7-fold for $CD8^+$ T cells compared to soluble ligands. No changes were observed in proliferation indices (**Figure S8**). Pam3CSK4-depoted T cells also increased bystander $CD4^+$ and $CD8^+$ T-cell division indices by 1.3-fold compared to soluble ligand. *Cis*-depoted Pam2CSK4 and Pam3CSK4 increased division indices of bystander cells by 1.4-fold for $CD4^+$ T cells and 1.3-fold for $CD8^+$ T cells compared to soluble ligands. These data demonstrated that TLR2 ligand depoted T cells can engage in autocrine and paracrine enhancement of proliferation, activating themselves as well as bystander T cells. We analyzed whether depoted T cells can enhance cytokine secretion by paracrine engagement of bystander T cells. No differences in secretion of Th1 cytokines, IFNγ or IL-2, were observed with addition of bystander T cells to depoted T cells (**Figure 8B**, **Figure S9A**). These data showed that depoted TLR2 ligands enhanced bystander T-cell proliferation but not Th1 cytokine secretion.

However, depoting of TLR2 ligands increased IFNγ and IL-2 secretion levels when compared to dose-matched soluble ligands. Depoting TLR2 ligands did not increase IFNγ levels (**Figure S9A**), but did increase IL-2 levels and expression levels of the IL-2 receptor, CD25 (**Figure 8B**, **Figure S9B**). Depoting with Pam2CSK4 induced a 2.7-fold increase IL-2 levels compared to soluble ligand (**Figure 8B**). Depoting with Pam3CSK4 induced a 3.4-fold increase in IL-2 levels compared to soluble ligand. *Cis*-depoted Pam2CSK4 and Pam3CSK4 induced a 3.4-fold increase in IL-2 levels compared to soluble ligands. These data again demonstrated that surface-bound presentation of depoted TLR2 ligands provided stronger signaling than dose-matched soluble ligands through enhanced IL-2 secretion.

DISCUSSION

In this study, we characterized depoting of lipid conjugates as a novel method for simple, non-genetic engineering of immune cells. Our data showed diacyl C16 and C18, and triacyl C16 lipid tails conjugated to DNA and protein cargoes, and depoted into plasma membranes in a concentration-dependent manner. We demonstrated the potential to engineer cells with TLR2 and TLR9 ligands targeting surface and intracellular receptors, respectively. Depoted TLR2 ligands enhanced bystander B- and T-cell activation when compared to dose-matched soluble ligands. Depoted TLR9 ligands showed autocrine activation of depoted B cells with minimal

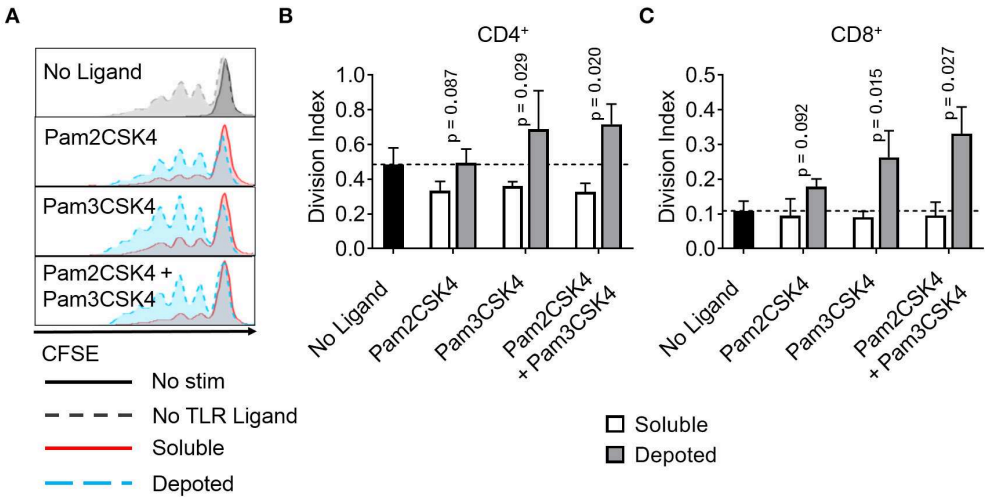

FIGURE 7 | Depoted TLR2 ligands enhance proliferation of activated murine T cells. Purified polyclonal T cells were stained with 5 μM of carboxyfluorescein succinimidyl ester (CFSE). Different combinations of cell surface ligands (Pam2CSK4 and Pam3CSK4) were either directly added in solution (soluble) or depoted into polyclonal T cells for 1 h at 37°C and cultured with αCD3/CD28 beads for 3 days. **(A)** Representative histograms of $CD4^+$ T-cell proliferation from delivery of lipid-TLR2 ligand as measured by CFSE dilution. Quantification of division index of **(B)** $CD4^+$ and **(C)** $CD8^+$ T cells in bulk polyclonal T cells. Dashed lines represent respective averages (mean) of "No Ligand" conditions. *p*-values by between soluble vs. depoted ligands as determined by one-tailed ratio paired *t*-test. Data showed m ± s.d. ($n = 3$ independent samples).

paracrine activation of bystanders, demonstrating delivery of depoted ligands with minimal release into solution or transfer between plasma membranes. Depoting stored detectable levels of surface-bound ligands on resting and proliferating T cells for bystander cell activation for similar durations, up to 4 days of *in vitro* co-culture. We also demonstrated multiplex loading of 2 distinct ligands onto the same plasma membranes without reaching loading saturation or decreasing cell viability. Altogether, our results demonstrated lipid-mediated depoting is a facile, modular drug delivery platform for diverse ligands that target receptors in distinct subcellular spaces.

Depoting TLR ligands can provide precise control over ligand dose by changing input ligand concentration. Varying the depoting concentration of lipid-CpG and Pam2CSK4 over a 100-fold range resulted in 25- and 130-fold increases, respectively, of detected ligand on cells. This suggests that changing depoting concentrations can precisely control drug dosing, a feature that can dictate whether a drug induces immunogenic or tolerogenic responses (33, 34). We determined that cells can be loaded by multiplexing with 2 depoted ligands and have no detectable loading saturation. However, differential loading levels on B and T cells in **Figure 2** suggest that lymphocyte subsets have distinct plasma membrane compositions, including TLR9 ligand-internalization receptors that may skew immune cell surface binding and alter total depoting capacity in a ligand- and cell-dependent manner (35, 36). Here, we demonstrated depoting of >1 million molecules per cell for some ligands, which is classified as very abundant based on recent estimates (37). This suggests that depoting loads a high absolute amount of cargoes onto plasma membranes beyond the likely capacity of just surface receptor binding.

We also demonstrated that the lipids we used (i.e., diacyl/triacyl C16 and diacyl C18 tails) effectively delivered ligands to plasma membranes. Our previous study showed that a single acyl lipid tail is inefficient at TLR ligand delivery (7, 10). Here, our results demonstrated that two and three-tailed lipids depoted efficiently. Thus, multiple lipid tails are a key design parameter for membrane delivery, and may be a simple way to enhance delivery of cargo to plasma membranes. One explanation of lipid-mediated insertion of TLR2 lipid-ligands, i.e., Pam2CSK4 and Pam3CSK4, into plasma membranes is the spontaneous formation of micelles when delivered at a high ligand concentration. This may result in particulate-mediated fusion with plasma membranes. However, the critical micelle concentrations of Pam2CSK4 and Pam3CSK4 are much higher than our input concentrations of 10 μg/mL (38). Our hypothesis of lipid-ligand "depoting" is a likely explanation that is supported by lipid-mediated partitioning of plasma membranes (27, 28) and the natural membrane insertion of GPI-anchored proteins. Altogether, depoting is advantageous not only for delivering synthetic TLR2 and TLR9 ligands as shown in our study, but may also apply to other potent immunostimulatory TLR ligands with greater than three lipid tails, including TLR4 ligands.

The controlled delivery of autocrine or paracrine signaling is critical to the further understanding of immunological signaling and enhancing cell-based therapies. Depoted Pam3CSK4 induced higher levels of MHC II on APCs than a soluble dose that was 5,000-fold larger, suggesting the depoted cells may increase antigen presentation by bystander APCs. This increase in cell activation highlights the enhanced potency of surface presented TLR2 ligands compared to the same dose of ligand delivered in solution. We also demonstrated that depoting of a cell surface ligand enhanced other lymphocyte functions; depoting TLR2

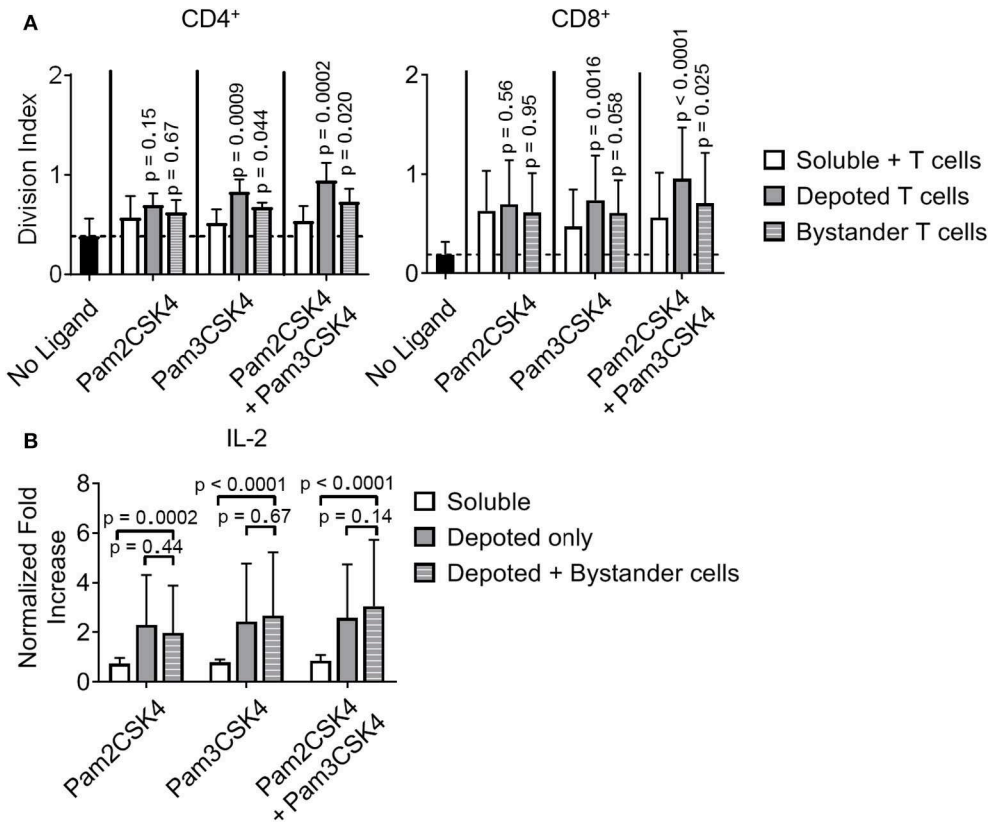

FIGURE 8 | Depoted TLR2 ligands enhance murine T-cell activation by increased cell division and inflammatory IL-2 secretion. **(A)** Purified polyclonal T cells were stained with 5 μM of carboxyfluorescein succinimidyl ester (CFSE). Different combinations of cell surface ligands (Pam2CSK4 and Pam3CSK4) were either directly added in solution (soluble) or depoted into polyclonal T cells, and co-cultured with non-depoted T cells and αCD3/CD28 beads for 3 days. Quantification of division index of $CD4^+$ and $CD8^+$ T cells in bulk polyclonal T cells. Dashed lines represent respective averages (mean) of "No Ligand" conditions. *p*-values within each group were determined by comparing with respective soluble ligand as determined by RM one-way ANOVA with Sidak's method for multiple comparisons correction. Data showed m ± s.d. ($n = 5$ independent samples). **(B)** IL-2 from cell supernatants was measured by ELISA on day 2. Concentrations were normalized to αCD3/CD28 bead-stimulated T cells in the absence of TLR2 ligand. *p*-values between indicated pairwise comparisons were determined by two-way ANOVA with Sidak's method for multiple comparisons correction. Data showed m ± s.d. ($n = 5$ independent samples).

ligands increased $CD4^+$ and $CD8^+$ T-cell division, and promoted inflammatory responses of bystander T cells. This simple method of delivery can be leveraged in the clinic to activate TLR2 in cytotoxic cells, including T cells and NK cells (22, 39).

In cancer, prolonging the persistence of infused T cells while also eliciting inflammatory responses by promoting endogenous anti-tumor immune cell functions can enhance therapeutic efficacy. However, paracrine signaling of delivered adjuvants is not always desirable for promoting anti-tumor responses (40, 41). Our delivery platform also demonstrated exclusive autocrine signaling with an intracellular ligand by targeting cell endosomes while avoiding paracrine and bystander activation. Analysis of the correlation between lipid-CpG and EEA1 fluorescent intensities showed a positive Pearson's correlation coefficient ($\rho = 0.64$), suggesting partial colocalization between lipid-ligand and endosomes after uptake (25). Since the correlation of lipid-ligand is not perfect with early endosomes, lipid-mediated depoting likely traffics to multiple intracellular compartments, which may provide unique opportunities for drug delivery. Extensive studies have demonstrated engineered systems to deliver drugs, including vaccines, genomic DNA, and anti-cancer cargoes to intracellular compartments (42–46). Lipid-mediated delivery has the potential to deliver cargoes to multiple compartments due to the natural partitioning of membrane lipids. For example, lipid-conjugated vaccine antigen and adjuvant demonstrated increased therapeutic efficacy in treating tumor models (7, 47). This may partially be due to the increased efficiency of antigen delivery to MHC class I and II pathways to prime $CD4^+$ and $CD8^+$ T cells. The ability to deliver antigen to these pathways for any cell type may reveal new opportunities for antigen-specific immunotherapy development, such as use of non-traditional APCs.

The use of genetically modified cells for cell-based immunotherapies has been one of the most promising, fastest-developing therapeutic approaches in recent years. However, there is a critical need to improve efficacy while reducing toxicity (48, 49). In 2017, the FDA approved 2 adoptive T-cell immunotherapies using chimeric antigen receptors

(CARs) for treating cancer, with hundreds of other T-cell therapies currently in clinical trials in cancer and other chronic diseases (50). The addition of more co-stimulatory signals, other adjuvants, or signaling domains to CARs by genetic additions has become an increasing trend in the field (51–53). However, the uncontrolled release of genetically encoded inflammatory cytokines or other adjuvants from perpetually activated CAR T cells presents a new challenge for toxicity management: lack of dose control (49, 54). New CAR technologies will likely entail even more genetic additions, which invariably will carry genetically-related adverse responses and toxicities. These genetic encodings prolong this adverse risks over the lifetime of the cell (55, 56). Expanding genetic modifications to future therapeutic genes is also limited by the packaging capacity of viral vectors (57). We propose that depoting can address these challenges by complementing genetic engineering and providing non-permanent delivery of co-stimulatory signals for 2–4 days. While depoted cargoes are inherently transient, this time window can be critical for therapeutic efficacy. For example, CAR T cells can initially kill a large proportion of target cells within 2-3 days post-infusion (58, 59). Further, Pam3CSK4 can reactivate latently infected HIV reservoirs in patients to enhance recognition and eradication of infected cells (60). TLR2 surface presentation by depoted T cells may enhance this "shock and kill" response by localizing ligand activity and enhancing ligand potency of cytotoxic T cells to reactivate the latent reservoir. Rational selection and combination of depoted vs. genetically engineered features can improve CAR T-cell persistence and efficacy *in vivo* while minimizing toxicities that may constrain clinical efficacy.

Drug delivery strategies for cellular engineering, from gene editing to nanoparticle and lipid carriers, are under continuous and rapid development (1, 2, 61). For example, nanoparticles have been used in multiple formulations to boost cellular therapies by delivering drugs with immune cells *in vivo* (62–64). Previous studies have shown palmitoyl lipid-tailed conjugates of CD28 ligand or IL-2 cytokine can be "painted" onto T cell surfaces without nanoparticles to enhance cell function (8, 9). Our study significantly expands upon these results by demonstrating the modularity of lipid-mediated delivery for different tail lengths and numbers, and showing that delivery of lipid-ligands can be achieved to cell surface and intracellular receptors. A current limitation of lipid-mediated depoting is the transient nature of the ligand on the cell surface, which will limit duration of ligand signaling on therapeutic cells against chronic diseases such as cancer. Future studies should focus on testing this cell engineering system in applications *in vivo*, as well as on determining design criteria to effectively depot other ligand combinations with longer persistence or higher abundance to optimize immunogenic or immunosuppressive effects in disease models.

Our data prove that depoting can engineer diverse immune cell types and expand existing knowledge on lipid dynamics that can be used for designing future drug delivery approaches. We used two innate TLRs targeted to directly enhance T-cell immunotherapies, and showed enhanced T-cell responses with depoted lipid-TLR ligands. This enables re-examination of pathways for T-cell activation that have been previously understudied due to delivery barriers. Rational selection of more clinically potent ligands for autocrine or paracrine signaling will illustrate the utility of depoting in a broad array of cell-based therapies.

DATA AVAILABILITY STATEMENT

The datasets generated for this study are available on request to the corresponding author.

ETHICS STATEMENT

The animal study was reviewed and approved by UMBC Institutional Animal Care and Use Committee (OLAW Animal Welfare Assurance D16-00462).

AUTHOR CONTRIBUTIONS

MZ and GLS conceptualized the study, analyzed the data, and wrote the manuscript. MZ, ES, GS, and GLS designed the experiments. MZ, ES, GS, and DW performed the experiments. CY and HL contributed experimental resources and methods. All authors participated in reviewing and editing the manuscript.

FUNDING

This work was supported by a grant from the Elsa U Pardee Foundation (to GLS), UMBC's Undergraduate Research Awards (to ES and GS), UMBC Summer Faculty Fellowship (to GLS), a Supplement for Undergraduate Research Experiences (to GLS and ES), and the Commercialization & ENTR REsearch (CENTER) Funding Initiative of the Alex Brown Center for Entrepreneurship at UMBC (to GLS). GLS is funded in part by the UMGCC P30 grant under award number P30 CA134274 from the National Cancer Institute, NIH. ES was supported in part by the Nathan Schnaper Intern Program in Translational Cancer Research (NIH R25CA186872).

ACKNOWLEDGMENTS

Flow cytometry analyses were performed at the University of Maryland School of Medicine Center for Innovative Biomedical Resources, Flow Cytometry Shared Service—Baltimore, Maryland. Confocal analyses were performed at the Keith Porter Imaging Facility. We thank Dr. Darrell Irvine and Debra Van Egeren for critical discussions for the manuscript. We thank Yun Jiao, Drs. Ryan Pearson and Jennie Leach for critical reading and feedback on the manuscript. This manuscript has been released as a preprint at bioRxiv (65).

SUPPLEMENTARY MATERIAL

The Supplementary Material for this article can be found online at: https://www.frontiersin.org/articles/10.3389/fimmu.2020.00560/full#supplementary-material

Figure S1 | Viability of murine immune cells is not decreased after TLR ligand loading. Cell viability of each treatment group was measured by LIVE/DEAD™ exclusion staining. *p*-values when compared to "Untreated" condition were determined by one-way ANOVA and Sidak's method for multiple comparisons correction. Data showed m ± s.d. ($n = 3$ independent samples).

Figure S2 | Depoting concentration does not preferentially affect loading into T cells. Increasing concentration of lipid-tailed TLR ligands does not change $CD4^+$ or $CD8^+$ T-cell depoting ratio for **(A)** lipid-CpG, and **(B)** Pam2CSK4. Median fluorescent intensity (MFI) ratio was determined by dividing the MFI of fluorescent ligand on $CD4^+$ T cells by that of $CD8^+$ T cells. Data represented mean ± s.d. ($n = 3$ independent samples).

Figure S3 | B cells activate in presence of soluble TLR2 ligand in a dose-dependent manner. **(A)** Dose response of Pam2CSK4 and Pam3CSK4 in B-cell culture for 2 days was measured by fold MFI of B cells. Data represented mean ± s.d. ($n = 3$ independent samples). **(B)** Dose response of Pam2CSK4 and Pam3CSK4 in B- and T-cell culture for 2 days was measured by fold MFI of B cells. Data represented mean ± s.d. ($n = 2$ independent samples).

Figure S4 | Viability of purified T cells is unchanged after addition of IL-7. Cell viability of T cells that were **(A)** in absence of (naïve T cells, left), or in presence of (primed T cells, right) 2 μg/mL of Concanavalin A and 10 ng/mL of IL-7 for 2 days and then resting in 10 ng/mL of IL-7 for up to 8 days. **(B)** Cell viability of T cells that were without IL-7. Data showed m ± s.d ($n = 1$–2 independent samples).

Figure S5 | Depoted TLR2 ligands do not enhance proliferation indices of activated $CD4^+$ T cells, but do of $CD8^+$ T cells. Purified polyclonal T cells were stained with 5 μM of carboxyfluorescein succinimidyl ester (CFSE). Different combinations of cell surface ligands (Pam2CSK4 and Pam3CSK4) were either directly added in solution (soluble) or depoted into polyclonal T cells for 1 h and cultured with αCD3/CD28 beads for 3 days. Quantification of proliferation indices of **(A)** $CD4^+$ and **(B)** $CD8^+$ T cells in bulk polyclonal T cells as measured by CFSE dilution. Dashed lines represent respective averages (mean) of "No Ligand" controls. *p*-values by between soluble vs. depoted ligands as determined by one-tailed ratio paired *t*-test. Data showed m ± s.d. ($n = 3$ independent samples).

Figure S6 | Depoted lipid-TLR9 ligand does not enhance proliferation of activated T cells. Purified polyclonal T cells were stained with 5 μM of carboxyfluorescein succinimidyl ester (CFSE). Different combinations of TLR2 ligands (Pam2CSK4 and Pam3CSK4) and TLR9 ligand (lipid-CpG) were either directly added in bulk solution (soluble) or depoted into polyclonal T cells for 1 h and cultured with αCD3/CD28 beads for 3 days. **(A)** Representative histograms of $CD4^+$ T-cell proliferation from delivery of lipid-TLR ligand as measured by CFSE dilution. Quantification of division and proliferation indices of **(B)** $CD4^+$ and **(C)** $CD8^+$ T cells in bulk polyclonal T cells as measured by CFSE dilution. Dashed lines represent respective averages (mean) of "No Ligand" controls. *p*-values by between soluble vs. depoted ligands were determined by one-tailed ratio paired *t*-test. Data showed m ± s.d. ($n = 3$ independent samples).

Figure S7 | Depoted TLR ligands promote Th1-based T-cell response. Different combinations of TLR2 ligands (Pam2CSK4 and Pam3CSK4) and TLR9 ligand (lipid-CpG) were either directly added in solution (soluble) or depoted into polyclonal T cells for 1 h and cultured with αCD3/CD28 beads for 3 days. Quantification of **(A)** IL-4 and **(B)** IL-2 levels in T-cell supernatents as measured by ELISA. Dashed lines represent limit of detection for respective cytokine detection. ($n = 1$–3 independent samples).

Figure S8 | Depoted TLR2 ligands do not enhance cell proliferation indices. Purified polyclonal T cells were stained with 5 μM of carboxyfluorescein succinimidyl ester (CFSE). Different combinations of TLR2 ligands (Pam2CSK4 and Pam3CSK4) were either directly added in bulk solution (soluble) or depoted into stained T cells for 1 h and cultured with non-depoted, stained T cells and αCD3/CD28 beads for 3 days. Quantification of proliferation index of $CD4^+$ and $CD8^+$ T cells in bulk polyclonal T cells as measured by CFSE dilution. Dashed lines represent respective averages (mean) of "No Ligand" controls. *p*-values within each group is determined by comparing with respective soluble ligand were determined by one-way ANOVA with Sidak's method for multiple comparisons correction. Data showed m ± s.d. ($n = 5$ independent samples).

Figure S9 | Depoted TLR2 ligands increase CD25 expression on activated T cells. Purified polyclonal T cells were stained with 5 μM of carboxyfluorescein succinimidyl ester (CFSE). Different combinations of TLR2 ligands (Pam2CSK4 and Pam3CSK4) and TLR9 ligand (lipid-CpG) were either directly added in bulk solution (soluble) or depoted into polyclonal T cells and cultured with αCD3/CD28 beads for 3 days. **(A)** IFNγ from cell supernatants were measured by ELISA on day 2. Concentrations were normalized to αCD3/CD28 bead-stimulated T cells in the absence of TLR2 ligand. *p*-values between indicated comparisons were determined by two-way ANOVA with Sidak's tests; Data depict m ± s.d. ($n = 4$ independent samples). **(B)** CD25 expression as measured by MFI. *p*-values between corresponding soluble vs. depoted ligands as determined by two-way ANOVA with Sidak's multiple comparisons test; Data showed m ± s.d. ($n = 3$ independent samples).

Table S1 | Quantitation of cell surface TLR2 ligands.

REFERENCES

1. Csizmar CM, Petersburg JR, Wagner CR. Programming cell-cell interactions through non-genetic membrane engineering. *Cell Chem Biol*. (2018) 25:931–40. doi: 10.1016/j.chembiol.2018.05.009
2. Stewart MP, Langer R, Jensen KF. Intracellular delivery by membrane disruption: mechanisms, strategies, and concepts. *Chem Rev*. (2018) 118:7409–531. doi: 10.1021/acs.chemrev.7b00678
3. Kunath K, von Harpe A, Fischer D, Peteren H, Bickel U, Voigt K, et al. Low-molecular-weight polyethylenimine as a non-viral vector for DNA delivery: comparison of physicochemical properties, transfection efficiency and *in vivo* distribution with high-molecular-weight polyethylenimine. *J Control Release*. (2003) 89:113–25. doi: 10.1016/S0168-3659(03)00076-2
4. Olden BR, Cheng Y, Yu JL, Pun SH. Cationic polymers for non-viral gene delivery to human T cells. *J Control Release*. (2018) 282:140–7. doi: 10.1016/j.jconrel.2018.02.043
5. Nayerossadat N, Maedeh T, Ali PA. Viral and nonviral delivery systems for gene delivery. *Adv Biomed Res*. (2012) 1:27. doi: 10.4103/2277-9175.98152
6. Park K. Facing the truth about nanotechnology in drug delivery. *ACS Nano*. (2013) 7:7442–7. doi: 10.1021/nn404501g
7. Liu H, Moynihan KD, Zheng Y, Szeto GL, Li AV, Huang B, et al. Structure-based programming of lymph-node targeting in molecular vaccines. *Nature*. (2014) 507:519–22. doi: 10.1038/nature12978
8. Zheng G, Liu S, Wang P, Xu Y, Chen A. Arming tumor-reactive T cells with costimulator B7–1 enhances therapeutic efficacy of the T cells. *Cancer Res*. (2006) 66:6793–9. doi: 10.1158/0008-5472.CAN-06-0435
9. Chou SH, Shetty AV, Geng Y, Xu L, Munirathinam G, Pipathsouk IT, et al. Palmitate-derivatized human IL-2: a potential anticancer immunotherapeutic of low systemic toxicity. *Cancer Immunol Immunother*. (2013) 62:597–603. doi: 10.1007/s00262-012-1364-8
10. Liu H, Kwong B, Irvine DJ. Membrane anchored immunostimulatory oligonucleotides for *in vivo* cell modification and localized immunotherapy. *Angew Chem Int Ed Engl*. (2011) 50:7052–5. doi: 10.1002/anie.201101266
11. Yu C, An M, Li M, Liu H. Immunostimulatory properties of lipid modified CpG oligonucleotides. *Mol Pharm*. (2017) 14:2815–23. doi: 10.1021/acs.molpharmaceut.7b00335
12. Adams S. Toll-like receptor agonists in cancer therapy. *Immunotherapy*. (2009) 1:949–64. doi: 10.2217/imt.09.70
13. Zhang Y, Luo F, Cai Y, Liu N, Wang L, Xu D, et al. TLR1/TLR2 agonist induces tumor regression by reciprocal modulation of effector and regulatory T cells. *J Immunol*. (2011) 186:1963–9. doi: 10.4049/jimmunol.1002320

14. Uehori J, Matsumoto M, Tsuji S, Akazawa T, Takeuchi O, Akira S, et al. Simultaneous blocking of human Toll-like receptors 2 and 4 suppresses myeloid dendritic cell activation induced by *Mycobacterium bovis* bacillus Calmette-Guerin peptidoglycan. *Infect Immun*. (2003) 71:4238–49. doi: 10.1128/IAI.71.8.4238-4249.2003
15. Lamm DL, Blumenstein BA, Crawford ED, Montie JE, Scardino P, Grossman HB, et al. A randomized trial of intravesical doxorubicin and immunotherapy with bacille Calmette-Guerin for transitional-cell carcinoma of the bladder. *N Engl J Med*. (1991) 325:1205–9. doi: 10.1056/NEJM199110243251703
16. Geng D, Zheng L, Srivastava R, Velasco-Gonzalez C, Riker A, Markovic SN, et al. Amplifying TLR-MyD88 signals within tumor-specific T cells enhances antitumor activity to suboptimal levels of weakly immunogenic tumor antigens. *Cancer Res*. (2010) 70:7442–54. doi: 10.1158/0008-5472.CAN-10-0247
17. Wong RM, Smith KA, Tam VL, Pagarigan RR, Meisenburg BL, Quach AM, et al. TLR-9 signaling and TCR stimulation co-regulate CD8(+) T cell-associated PD-1 expression. *Immunol Lett*. (2009) 127:60–7. doi: 10.1016/j.imlet.2009.09.002
18. Nierkens S, den Brok MH, Roelofsen T, Wagenaars JA, Figdor CG, Ruers TJ, et al. Route of administration of the TLR9 agonist CpG critically determines the efficacy of cancer immunotherapy in mice. *PLoS ONE*. (2009) 4:e8368. doi: 10.1371/journal.pone.0008368
19. Bendigs S, Salzer U, Lipford GB, Wagner H. CpG-oligodeoxynucleotides co-stimulate primary T cells in the absence of antigen-presenting cells. *Eur J Immunol*. (1999) 29:1209–18. doi: 10.1002/(SICI)1521-4141(199904)29:04<1209::AID-IMMU1209>3.0.CO;2-J
20. Davila E, Velez MG, Heppelmann CJ, Celis E. Creating space: an antigen-independent, CpG-induced peripheral expansion of naive and memory T lymphocytes in a full T-cell compartment. *Blood*. (2002) 100:2537–45. doi: 10.1182/blood-2002-02-0401
21. Ribas A, Medina T, Kummar S, Amin A, Kalbasi A, Drabick JJ, et al. SD-101 in Combination with pembrolizumab in advanced melanoma: results of a phase Ib, multicenter study. *Cancer Discov*. (2018) 8:1250–7. doi: 10.1158/2159-8290.CD-18-0280
22. Lu H, Yang Y, Gad E, Inatsuka C, Wenner CA, Disis ML, et al. TLR2 agonist PSK activates human NK cells and enhances the antitumor effect of HER2-targeted monoclonal antibody therapy. *Clin Cancer Res*. (2011) 17:6742–53. doi: 10.1158/1078-0432.CCR-11-1142
23. Thomas M, Ponce-Aix S, Navarro A, Riera-Knorrenschild J, Schmidt M, Wiegert E, et al. Immunotherapeutic maintenance treatment with toll-like receptor 9 agonist lefitolimod in patients with extensive-stage small-cell lung cancer: results from the exploratory, controlled, randomized, international phase II IMPULSE study. *Ann Oncol*. (2018) 29:2076–84. doi: 10.1093/annonc/mdy326
24. Szeto GL, Van Egeren D, Worku H, Sharei A, Alejandro B, Park C, et al. Microfluidic squeezing for intracellular antigen loading in polyclonal B-cells as cellular vaccines. *Sci Rep*. (2015) 5:10276. doi: 10.1038/srep10276
25. Dunn KW, Kamocka MM, McDonald JH. A practical guide to evaluating colocalization in biological microscopy. *Am J Physiol Cell Physiol*. (2011) 300:C723–42. doi: 10.1152/ajpcell.00462.2010
26. Avalos AM, Ploegh HL. Early BCR events and antigen capture, processing, and loading on MHC class II on B cells. *Front Immunol*. (2014) 5:92. doi: 10.3389/fimmu.2014.00092
27. Ong S, Liu H, Qiu X, Bhat G, Pidgeon C. Membrane partition coefficients chromatographically measured using immobilized artificial membrane surfaces. *Anal Chem*. (1995) 67:755–62. doi: 10.1021/ac00100a011
28. Jacobs RE, White SH. The nature of the hydrophobic binding of small peptides at the bilayer interface: implications for the insertion of transbilayer helices. *Biochemistry*. (1989) 28:3421–37. doi: 10.1021/bi00434a042
29. Krishnegowda G, Hajjar AM, Zhu J, Douglass EJ, Uematsu S, Akira S, et al. Induction of proinflammatory responses in macrophages by the glycosylphosphatidylinositols of Plasmodium falciparum: cell signaling receptors, glycosylphosphatidylinositol (GPI) structural requirement, and regulation of GPI activity. *J Biol Chem*. (2005) 280:8606–16. doi: 10.1074/jbc.M413541200
30. Krieg AM, Yi AK, Matson S, Waldschmidt TJ, Bishop GA, Teasdale R, et al. CpG motifs in bacterial DNA trigger direct B-cell activation. *Nature*. (1995) 374:546–9. doi: 10.1038/374546a0
31. Hornung V, Rothenfusser S, Britsch S, Krug A, Jahrsdörfer B, Giese T, et al. Quantitative expression of toll-like receptor 1-10 mRNA in cellular subsets of human peripheral blood mononuclear cells and sensitivity to CpG oligodeoxynucleotides. *J Immunol*. (2002) 168:4531–7. doi: 10.4049/jimmunol.168.9.4531
32. Komai-Koma M, Jones L, Ogg GS, Xu D, Liew FY. TLR2 is expressed on activated T cells as a costimulatory receptor. *Proc Natl Acad Sci USA*. (2004) 101:3029–34. doi: 10.1073/pnas.0400171101
33. Ray A, Chakraborty K, Ray P. Immunosuppressive MDSCs induced by TLR signaling during infection and role in resolution of inflammation. *Front Cell Infect Microbiol*. (2013) 3:52. doi: 10.3389/fcimb.2013.00052
34. Volpi C, Fallarino F, Pallotta MT, Bianchi R, Vacca C, Belladonna ML, et al. High doses of CpG oligodeoxynucleotides stimulate a tolerogenic TLR9-TRIF pathway. *Nat Commun*. (2013) 4:1852. doi: 10.1038/ncomms2874
35. Lahoud MH, Ahmet F, Zhang J, Meuter S, Policheni AN, Kitsoulis S, et al. DEC-205 is a cell surface receptor for CpG oligonucleotides. *Proc Natl Acad Sci USA*. (2012) 109:16270–5. doi: 10.1073/pnas.1208796109
36. Häcker H, Mischak H, Miethke T, Liptay S, Schmid R, Sparwasser T, et al. CpG-DNA-specific activation of antigen-presenting cells requires stress kinase activity and is preceded by non-specific endocytosis and endosomal maturation. *EMBO J*. (1998) 17:6230–40. doi: 10.1093/emboj/17.21.6230
37. Wiśniewski JR, Hein MY, Cox J, Mann M. A "proteomic ruler" for protein copy number and concentration estimation without spike-in standards. *Mol Cell Proteomics*. (2014) 13:3497–506. doi: 10.1074/mcp.M113.037309
38. Hamley IW, Kirkham S, Dehsorkhi A, Castelletto V, Reza M, Ruokolainen J. Toll-like receptor agonist lipopeptides self-assemble into distinct nanostructures. *Chem Commun*. (2014) 50:15948–51. doi: 10.1039/C4CC07511K
39. Lu H, Yang Y, Gad E, Wenner CA, Chang A, Larson ER, et al. Polysaccharide krestin is a novel TLR2 agonist that mediates inhibition of tumor growth via stimulation of CD8 T cells and NK cells. *Clin Cancer Res*. (2011) 17:67–76. doi: 10.1158/1078-0432.CCR-10-1763
40. Akkaya M, Akkaya B, Kim AS, Miozzo P, Sohn H, Pena M, et al. Toll-like receptor 9 antagonizes antibody affinity maturation. *Nat Immunol*. (2018) 19:255–66. doi: 10.1038/s41590-018-0052-z
41. Moseman EA, Liang X, Dawson AJ, Panoskaltsis-Mortari A, Krieg AM, Liu Y, et al. Human plasmacytoid dendritic cells activated by CpG oligodeoxynucleotides induce the generation of CD4+CD25+ regulatory T cells. *J Immunol*. (2004) 173:4433–42. doi: 10.4049/jimmunol.173.7.4433
42. Yoshikawa T, Okada N, Oda A, Matsuo K, Matsuo K, Mukai Y, et al. Development of amphiphilic gamma-PGA-nanoparticle based tumor vaccine: potential of the nanoparticulate cytosolic protein delivery carrier. *Biochem Biophys Res Commun*. (2008) 366:408–13. doi: 10.1016/j.bbrc.2007.11.153
43. Liu X, Xu Y, Yu T, Clifford C, Liu Y, Yan H, et al. A DNA nanostructure platform for directed assembly of synthetic vaccines. *Nano Lett*. (2012) 12:4254–9. doi: 10.1021/nl301877k
44. Maniganda S, Sankar V, Nair JB, Raghu KG, Maiti KK. A lysosome-targeted drug delivery system based on sorbitol backbone towards efficient cancer therapy. *Org Biomol Chem*. (2014) 12:6564–9. doi: 10.1039/C4OB01153H
45. Schröder T, Niemeier N, Afonin S, Ulrich AS, Krug HF, Bräse S. Peptoidic amino- and guanidinium-carrier systems: targeted drug delivery into the cell cytosol or the nucleus. *J Med Chem*. (2008) 51:376–9. doi: 10.1021/jm070603m
46. Yuan Y, Zhang CJ, Liu B. A Photoactivatable AIE polymer for light-controlled gene delivery: concurrent endo/lysosomal escape and DNA unpacking. *Angew Chem Int Ed Engl*. (2015) 54:11419–23. doi: 10.1002/anie.201503640
47. Moynihan KD, Opel CF, Szeto GL, Tzeng A, Zhu EF, Engreitz JM, et al. Eradication of large established tumors in mice by combination immunotherapy that engages innate and adaptive immune responses. *Nat Med*. (2016) 22:1402–10. doi: 10.1038/nm.4200
48. Rosenberg SA, Restifo NP. Adoptive cell transfer as personalized immunotherapy for human cancer. *Science*. (2015) 348:62–8. doi: 10.1126/science.aaa4967
49. Bonifant CL, Jackson HJ, Brentjens RJ, Curran KJ. Toxicity and management in CAR T-cell therapy. *Mol Ther Oncolytics*. (2016) 3:16011. doi: 10.1038/mto.2016.11

50. Home - ClinicalTrials.gov (2019). Available online at: www.ClinicalTrials.gov/
51. Rafiq S, Yeku OO, Jackson HJ, Purdon TJ, van Leeuwen DG, Drakes DJ, et al. Targeted delivery of a PD-1-blocking scFv by CAR-T cells enhances anti-tumor efficacy *in vivo*. *Nat Biotechnol*. (2018) 36:847–56. doi: 10.1038/nbt.4195
52. Zhao Z, Condomines M, van der Stegen S, Perna F, Kloss CC, Gunset G, et al. Structural design of engineered costimulation determines tumor rejection kinetics and persistence of CAR T cells. *Cancer Cell*. (2015) 28:415–28. doi: 10.1016/j.ccell.2015.09.004
53. Schubert ML, Hoffmann J, Dreger P, Müller-Tidow C, Schmitt M. Chimeric antigen receptor transduced T cells: Tuning up for the next generation. *Int J Cancer*. (2018) 142:1738–47. doi: 10.1002/ijc.31147
54. Neelapu SS, Tummala S, Kebriaei P, Wierda W, Locke FL, Lin Y, et al. Toxicity management after chimeric antigen receptor T cell therapy: one size does not fit 'ALL'. *Nat Rev Clin Oncol*. (2018) 15:218. doi: 10.1038/nrclinonc.2018.20
55. Essand M, Loskog AS. Genetically engineered T cells for the treatment of cancer. *J Intern Med*. (2013) 273:166–81. doi: 10.1111/joim.12020
56. Ruella M, Xu J, Melenhorst J. Induction of resistance to chimeric antigen receptor T cell therapy by transduction of a single leukemic B cell. *Nat Med*. (2018) 24:1499–503. doi: 10.1038/s41591-018-0201-9
57. Wang X, Riviere I. Clinical manufacturing of CAR T cells: foundation of a promising therapy. *Mol Ther Oncolytics*. (2016) 3:16015. doi: 10.1038/mto.2016.15
58. Herzig E, Kim KC, Packard TA, Vardi N, Schwarzer R, Gramatica A, et al. Attacking latent HIV with convertibleCAR-T cells, a highly adaptable killing platform. *Cell*. (2019) 179:880–94.e10. doi: 10.1016/j.cell.2019.10.002
59. Anurathapan U, Chan RC, Hindi HF, Mucharla R, Bajgain P, Hayes BC, et al. Kinetics of tumor destruction by chimeric antigen receptor-modified T cells. *Mol Ther*. (2014) 22:623–33. doi: 10.1038/mt.2013.262
60. Novis CL, Archin NM, Buzon MJ, Verdin E, Round JL, Lichterfeld M, et al. Reactivation of latent HIV-1 in central memory CD4(+) T cells through TLR-1/2 stimulation. *Retrovirology*. (2013) 10:119. doi: 10.1186/1742-4690-10-119
61. Neelapu SS, Tummala S, Kebriaei P, Wierda W, Gutierrez C, Locke FL, et al. Chimeric antigen receptor T-cell therapy - assessment and management of toxicities. *Nat Rev Clin Oncol*. (2018) 15:47–62. doi: 10.1038/nrclinonc.2017.148
62. Bourquin C, Anz D, Zwiorek K, Lanz A, Fuchs S, Weigel S, et al. Targeting CpG oligonucleotides to the lymph node by nanoparticles elicits efficient antitumoral immunity. *J Immunol*. (2008) 181:2990–8. doi: 10.4049/jimmunol.181.5.2990
63. McHugh MD, Park J, Uhrich R, Gao W, Horwitz DA, Fahmy TM. Paracrine co-delivery of TGF- β and IL-2 using CD4-targeted nanoparticles for induction and maintenance of regulatory T cells. *Biomaterials*. (2015) 59:172–81. doi: 10.1016/j.biomaterials.2015.04.003
64. Kwong B, Liu H, Irvine DJ. Induction of potent anti-tumor responses while eliminating systemic side effects via liposome-anchored combinatorial immunotherapy. *Biomaterials*. (2011) 32:5134–47. doi: 10.1016/j.biomaterials.2011.03.067
65. Zhang MH, Slaby EM, Stephanie G, Yu C, Watts DM, Liu H, et al. Lipid-mediated insertion of Toll-like receptor (TLR) ligands for facile immune cell engineering. *bioRxiv [Preprint]*. (2019) 840876. doi: 10.1101/840876

Conflict of Interest: GLS, MZ, and ES are inventors on a pending US patent application 62/542,842 submitted by University of Maryland, Baltimore County, describing cell engineering by lipid-mediated depoting, which are described in this manuscript.

The remaining authors declare that the research was conducted in the absence of any commercial or financial relationships that could be construed as a potential conflict of interest.

frontiers in Immunology

ORIGINAL RESEARCH
published: 07 July 2020
doi: 10.3389/fimmu.2020.01412

Arginine-Based Poly(I:C)-Loaded Nanocomplexes for the Polarization of Macrophages Toward M1-Antitumoral Effectors

Tamara G. Dacoba[1,2†], Clément Anfray[3†], Francesco Mainini[3], Paola Allavena[3], María José Alonso[1,2], Fernando Torres Andón[1,3†] and José Crecente-Campo[1,2*†]*

[1] Center for Research in Molecular Medicine and Chronic Diseases (CIMUS), IDIS Research Institute, Universidade de Santiago de Compostela, Santiago de Compostela, Spain, [2] Department of Pharmacology, Pharmacy and Pharmaceutical Technology, School of Pharmacy, Universidade de Santiago de Compostela, Santiago de Compostela, Spain, [3] Laboratory of Cellular Immunology, Humanitas Clinical and Research Center IRCCS, Milan, Italy

OPEN ACCESS

Edited by:
Ankur Singh,
Georgia Institute of Technology,
United States

Reviewed by:
Bozena Kaminska,
Nencki Institute of Experimental Biology (PAS), Poland
Ryan M. Pearson,
University of Maryland, Baltimore, United States
Yizhou Dong,
The Ohio State University, United States

***Correspondence:**
Fernando Torres Andón
fernando.torres.andon@usc.es
José Crecente-Campo
jose.crecente@usc.es

[†] These authors have contributed equally to this work

Specialty section:
This article was submitted to Cancer Immunity and Immunotherapy, a section of the journal Frontiers in Immunology

Received: 05 February 2020
Accepted: 02 June 2020
Published: 07 July 2020

Citation:
Dacoba TG, Anfray C, Mainini F, Allavena P, Alonso MJ, Torres Andón F and Crecente-Campo J (2020) Arginine-Based Poly(I:C)-Loaded Nanocomplexes for the Polarization of Macrophages Toward M1-Antitumoral Effectors. Front. Immunol. 11:1412. doi: 10.3389/fimmu.2020.01412

Background: Tumor-associated macrophages (TAMs), with M2-like immunosuppressive profiles, are key players in the development and dissemination of tumors. Hence, the induction of M1 pro-inflammatory and anti-tumoral states is critical to fight against cancer cells. The activation of the endosomal toll-like receptor 3 by its agonist poly(I:C) has shown to efficiently drive this polarization process. Unfortunately, poly(I:C) presents significant systemic toxicity, and its clinical use is restricted to a local administration. Therefore, the objective of this work has been to facilitate the delivery of poly(I:C) to macrophages through the use of nanotechnology, that will ultimately drive their phenotype toward pro-inflammatory states.

Methods: Poly(I:C) was complexed to arginine-rich polypeptides, and then further enveloped with an anionic polymeric layer either by film hydration or incubation. Physicochemical characterization of the nanocomplexes was conducted by dynamic light scattering and transmission electron microscopy, and poly(I:C) association efficiency by gel electrophoresis. Primary human-derived macrophages were used as relevant *in vitro* cell model. Alamar Blue assay, ELISA, PCR and flow cytometry were used to determine macrophage viability, polarization, chemokine secretion and uptake of nanocomplexes. The cytotoxic activity of pre-treated macrophages against PANC-1 cancer cells was assessed by flow cytometry.

Results: The final poly(I:C) nanocomplexes presented sizes lower than 200 nm, with surface charges ranging from +40 to −20 mV, depending on the envelopment. They all presented high poly(I:C) loading values, from 12 to 50%, and great stability in cell culture media. *In vitro*, poly(I:C) nanocomplexes were highly taken up by macrophages, in comparison to the free molecule. Macrophage treatment with these nanocomplexes did not reduce their viability and efficiently stimulated the secretion of the T-cell recruiter chemokines CXCL10 and CCL5, of great importance for an effective anti-tumor immune response. Finally, poly(I:C) nanocomplexes significantly increased the ability of treated macrophages to directly kill cancer cells.

Conclusion: Overall, these enveloped poly(I:C) nanocomplexes might represent a therapeutic option to fight cancer through the induction of cytotoxic M1-polarized macrophages.

Keywords: poly(I:C), toll-like receptor (TLR) 3, tumor-associated macrophages (TAMs), arginine-rich peptides, nanocomplexes, cancer immunotherapy

INTRODUCTION

The discovery of the capacity of the immune system to fight and eliminate tumors has represented a major paradigmatic change in the treatment of cancer, classically addressed with cytotoxic drugs (1, 2). Despite the inherent anti-tumoral capacity of immunocompetent cells, tumors produce immunosuppressive signals that lead to tumor immune tolerance, thus facilitating tumor progression (3–5). Among the different cells involved in this process, tumor-associated macrophages (TAMs) are key players with the capacity to promote the proliferation of cancer cells, angiogenesis and metastasis (5–8). TAMs present anti-inflammatory and tolerogenic features, that are similar to M2-like macrophages (9). Importantly, recent investigations have proposed the possibility to reprogram TAMs toward pro-inflammatory and anti-tumoral M1 states as a promising approach to re-activate the immune response against tumors (8, 10–13).

An important strategy to re-educate TAMs toward M1-like phenotypes (14, 15), has relied on the use of agents that activate the toll-like receptors (TLRs) (13, 16). Upon interaction with their corresponding agonists, TLRs activate MyD88 and TRIF pathways, thereby triggering innate and adaptive immune responses (17, 18). Indeed, some of these agonists are already marketed, or under clinical trials, for vaccination and/or cancer applications (18). Among the different TLR agonists, poly(I:C), a double-stranded (ds)RNA that activates the TLR3, has shown the capacity to polarize TAMs toward M1-like anti-tumoral phenotypes (19). Nevertheless, the clinical potential of poly(I:C) has been undermined by its indiscriminate biodistribution, that leads to an unrestrained immune activation and systemic inflammation, with serious toxic effects (20–24). Another major issue for the use of poly(I:C) in the clinic is related to its systemic degradation (21). In this sense, the association of poly(I:C) into a nano-delivery system could protect the drug and improve its transport to the tumor site and, consequently, ameliorate its safety profile (21, 25–30).

Synthetic nanosystems for polynucleotide delivery are mainly based on their complexation with positively charged lipids or polymers (31–33). For example, it has been reported that the complexation of poly(I:C) with cationic polymers, i.e., polyethyleneimine (PEI), leads to positive *in vivo* results in different cancer models (34), and is currently in a phase I clinical trial (35). Unfortunately, PEI itself is not absent of systemic toxicity (36). In our research group, alternative nanocarriers for the delivery of polynucleotides have already been explored. Based on the known capacity of cell penetrating peptides (CPPs) to efficiently condense nucleic acids and facilitate their transport across biological barriers (37), we have developed polyarginine- (pArg) and protamine-based nanosystems, which have shown the capacity to efficiently deliver different polynucleotides (38–40). Indeed, we have recently reported the formation of nanocomplexes of polynucleotides with cationic molecules, and their posterior envelopment with an hydrophilic anionic polymer, named as enveloped nanocomplexes (ENCPs), as a way to facilitate the delivery of miRNA to the brain (40).

As a whole, despite the potential of poly(I:C) for polarizing macrophages toward an anti-tumoral M1-like phenotype with the capacity to fight tumors, the *in vivo* administration of this TLR3 agonist presents significant side effects. Therefore, here we aimed at engineering a nanocomplex to improve the capacity of poly(I:C) to polarize macrophages toward M1-like phenotypes. After an optimization process, we evaluated the *in vitro* capacity of the developed poly(I:C) nanocomplexes to polarize primary human monocyte-derived macrophages toward pro-inflammatory M1-like anti-tumoral phenotypes.

MATERIALS AND METHODS

Materials

n-Butyl-poly(L-arginine) hydrochloride (pArg) (150 arginine residues, MW 24 kDa) and the different pegylated-poly(L-glutamic acid) (PEG–PGA) polymers were purchased from Polypeptide Therapeutic Solutions (PTS, Valencia, Spain). For the PEG–PGA, three types of branched conformations were acquired: PGA, either 10 or 30 units, with a molar substitution degree of 10 or 30% of PEG (5 kDa), referred as: PEG_{5k}10–PGA10, PEG_{5k}10–PGA30, and PEG_{5k}30–PGA10. Also, two conformation of the diblock PEG-PGA were purchased: 10 units of PGA and a 20 kDa PEG tail; and 30 units of PGA with a 5 kDa PEG tail, named as diblock PEG_{20k}-PGA10 and diblock PEG_{5k}-PGA30, respectively.

Octa-D-arginine (r8) and laurate octa-D-arginine (C12r8) were obtained from ChinaPeptides (Shanghai, China). Sodium hyaluronate (HA) (MW 57 kDa) was purchased from Lifecore Biomedical (MN, USA). HMW poly(I:C) and HMW poly(I:C)-rhodamine were acquired from InvivoGen (CA, USA). Endotoxin-free water was used for all the *in vitro* experiments.

Preparation of the Nanocomplexes

Screening of Arginine-Rich Polymers

To 400 μL of arginine-rich polymer solution (0.5, 1, or 2 mg/mL), 200 μL of poly(I:C) (at 1 or 0.5 mg/mL) were added under mild magnetic stirring. Weight ratios polymer to poly(I:C)

Abbreviations: C12r8, laurate octaarginine; CPP, cell penetrating peptide; ENCP, enveloped nanocomplex; HA, hyaluronic acid; pArg, polyarginine; PEG–PGA, pegylated polyglutamic acid; TAM, Tumor-associated macrophage.

1:1, 2:1 and 4:1 were tested (**Supplementary Table 1**). After 1–5 min of stirring, the resulting nanocomplexes were allowed to stabilize for at least 3 min before further characterization or envelopment.

Envelopment With PEG–PGA Polymers

A volume of 400 μL of a PEG–PGA aqueous solution at 1 mg/mL was added to a round bottom flask, and the water was evaporated in a rotavapor (Heidolph Hei–VAP Advantage, Schwabach, Germany) for 10 min, at 37°C, under vacuum and mild rotary speed, until a thin film was formed. Then, the same volume of nanocomplexes (with a poly(I:C) concentration of 0.33 or 0.17 mg/mL) (**Supplementary Table 2**), was added to the round bottom flask, in order to achieve their envelopment by PEG–PGA. The same the same rotary speed was maintained for 10 min, at room temperature and atmospheric pressure.

Envelopment With HA

To 250 μL of the nanocomplexes with a poly(I:C) concentration of 0.33 or 0.17 mg/mL, the same volume of an HA solution of concentrations ranging from 0.25 to 2.00 mg/mL, was added under mild magnetic stirring, for a final poly(I:C) to HA weight ratio of 1:1.5, 1:3, or 1:6 (**Supplementary Table 3**). The ENCPs were allowed to be formed for 5 min under stirring, and to be stabilized during other 5 min prior to their characterization.

Nanoparticle Characterization by Dynamic Light Scattering (DLS)

The mean particle size (Z-average) and polydispersity index (PDI) of the non-diluted samples were characterized by DLS. The zeta potential values were determined by Laser Doppler Anemometry (LDA), measuring the mean electrophoretic mobility after a 20-times dilution of the ENCPs in ultrapure water. These properties were measured using a Zetasizer® NanoZS, with the software Zetasizer v7.13 (Malvern Panalytical Ltd., Malvern, UK), and were performed at 25°C with a detection angle degree of 173.

Electron Microscopy

Field emission scanning electron microscopy (FESEM) (Zeiss Gemini Ultra Plus, Oberkochen, Germany) was used to evaluate the particle size and morphology. ENCPs were diluted in a ratio between 1:100 and 1:1,000 in water, and then 1:1 with phosphotungstic acid (2% in water). A sample volume of 1 μL was placed on a copper grid with carbon films and, once dried, it was washed with 1 mL of ultrapure water. Dried samples were analyzed under the microscope using the InLens detector. Images with 50,000x magnification were taken for all the prototypes.

Nanocomplex Stability in Cell Culture Media

The colloidal stability of the different ENCPs in cell culture media (RPMI + 10% FBS + 2% penicillin/streptomycin) was assessed at 37°C for up to 24 h. For this purpose, ENCPs were diluted 5 times in pre-warmed media, or water as the control, and particle size and PDI measured at 0, 4, and 24 h of incubation.

Agarose Gel Retardation Assay

To qualitatively determine the amount of poly(I:C) within the ENCPs, samples were loaded in an agarose gel at 1% w/v in Tris Acetate-EDTA buffer (Sigma-Aldrich, MO, USA) before and after the incubation with an excess of heparin for poly(I:C) displacement. Each lane was loaded with 2.5 μg of poly(I:C) and with 1x SYBR®Gold nucleic acid stain (Invitrogen, CA, USA). For the displacement with heparin, 20:1 and 500:1 weight ratios of heparin (Sigma-Aldrich, MO, USA) to poly(I:C) were added for the C12r8 or pArg ENCPs, respectively, and incubated for 30 min at 37°C. Control lanes included a DNA 1 kb ladder (Invitrogen, CA, USA), and free poly(I:C) in the same conditions as the ENCPs. Gels were run for 30 min at 90 V in a Sub-Cell GT cell 96/192 (Bio-Rad Laboratories, CA, USA), evaluated with an UV transilluminator (Molecular Imager® Gel Doc™ XR, Bio-Rad Laboratories, CA, USA) and analyzed with Image Lab™ Software (Bio-Rad Laboratories, CA, USA).

For the release of poly(I:C), ENCPs were incubated in cell culture media, in a 1:1 (v/v) ratio, for 4 or 24 h, prior to been processed as described above. Free poly(I:C) exposed to the same conditions was used as the control.

Human Primary Macrophage Differentiation

Human primary monocytes from blood of healthy donors were purified through density gradients, as previously reported (12, 41). M0 macrophages were obtained by culturing 1×10^6 cells/mL human monocytes for 5 days in 5% FBS/RPMI supplemented with 25 ng/mL of recombinant human M-CSF (rhM-CSF; PeproTech, London, UK). M1 macrophages were polarized by stimulating M0 macrophages with LPS (100 ng/mL) (PeproTech, London, UK) and IFN-γ (50 ng/mL) (PeproTech, London, UK) for 24 h, and M2 macrophages were obtained by polarizing M0 macrophages with IL-4 (20 ng/mL) (PeproTech, London, UK) for 24 h. These cells were seeded in multiwell plates as indicated below for each experiment, and incubated at 37°C and 5% CO_2. In all experiments, the final poly(I:C) dose employed was 5 μg/mL, with the exception of cell viability studies, where the specific doses are indicated.

Cell Viability Studies

M0 and M2 human-derived macrophages were isolated and differentiated, and then seeded in 96-well plates at a density of 1×10^5 cells/well. Cells were treated with poly(I:C), in solution or nanocomplexed, at poly(I:C) concentrations of 1, 5, 10, and 20 μg/mL. Macrophages were incubated with the nanosystems at indicated times, and cell viability was determined by Alamar Blue assay (Invitrogen, CA, USA), following manufacturer's protocol. Fluorescence intensity was measured in a plate reader (Synergy H4, BioTek, VT, USA), setting the λ_{abs} at 560 nm and the λ_{em} at 590 nm. Non-treated macrophages were used as controls and considered as 100% cell viability. Cell viability was calculated according to Equation (1).

$$\%\ Cell\ viability = \left(1 - \frac{Fluorescence}{Control\ fluorescence}\right) \times 100 \quad (1)$$

Uptake Studies

Human monocytes were purified and polarized toward M0 macrophages as described in section Human Primary Macrophage Differentiation. These cells were seeded at a density of 1×10^6 cells/well in low-attachment 24-well plates (Corning, ME, USA), and 0.5 mL of fresh RPMI media containing poly(I:C), either free or nanocomplexed, were added to them. The final poly(I:C) dose per well was of 5 μg/mL of poly(I:C), of which 0.25 μg/mL were poly(I:C)-rhodamine. After 24 h of incubation, cells were detached from the wells with trypsin-EDTA. Cells were then washed one time with FACS buffer (PBS 1% BSA) and fixed in FACS Fix (PBS 1% PFA) for 20 min at 4°C. Cell suspensions were centrifuged at 1,750 rpm for 10 min and 4°C. The supernatants were then discarded, and cells re-suspended in 300 μL of FACS buffer (PBS 1% BSA). Treated macrophages were analyzed by flow cytometry using a BD LSR Fortessa™ (BD Biosciences, CA, USA), and the resulting data analyzed by FACS Diva software (BD Biosciences, CA, USA), determining the mean fluorescence intensity (MFI) of rhodamine-positive cells. Results were expressed as fold change in comparison to the free poly(I:C)-rhodamine.

Co-localization Studies

Purified human monocytes were seeded in 24-well plates with a round glass coverslip at the bottom, at a density of 1×10^6 cells/well in 1 mL of complete RPMI supplemented with M-CSF (25 ng/ml) to differentiate them to M0 macrophages. At day 5, 10 μL/well of CellLight® lysosome-GFP, BacMam 2.0 (Molecular Probes, OR, USA) were added. At day 6, coverslips were washed and poly(I:C), free or in pArg:pIC ENCPs, was added in 500 μL of fresh complete RPMI for 2 or 8 h. The final poly(I:C) dose per well was 5 μg/mL, of which 0.25 μg/mL were poly(I:C)-rhodamine. After incubation, cells were washed one time with PBS, nuclei were stained with DAPI and cells were fixed in 4% PFA (in PBS) for 10 min at room temperature. The glass coverslip was then recovered, mounted and analyzed with a Leica TCS SP8 3X SMD confocal microscope (Leica Microsystems, Wetzla, Germany). Signal co-localization was quantified with IMARIS software (Oxford Instruments, Abingdon, UK).

Macrophage Surface Marker Expression

M0 or M2 human-derived macrophages were seeded in 24-well low-attachment plates at a density of 1×10^6 cells/well and incubated in 5% FBS supplemented RPMI for 48 h at 37°C. Macrophages were then incubated with 5 μg/mL of poly(I:C), either in solution or nanocomplexed. M1 macrophages were also used as control, and M2 macrophages were polarized toward M1 phenotypes upon incubation with LPS/IFN-γ. Prior to their staining, cells were washed, collected and resuspended in FACS buffer (PBS 1% BSA). They were then stained with APC-mouse anti-human HLA-DR (552764, BD Biosciences, CA, USA), FITC-mouse anti-human mannose receptor CD206 (551135), anti-human CD163-BV421 (562643), CD80 APC-H7-mouse anti-Human CD80 (Clone L307.4; 561134) and anti-human CD68-PE (556078) (all from BD Biosciences, CA, USA). Cells were analyzed by flow cytometry on FACS Canto II Instrument (BD Biosciences, CA, USA) and the generated data by FACS Diva software. The gated cells were plotted on APC (CD80), PerCP (MHC II), Pacific Blue (CD163) or FITC (CD206) and analyzed for mean fluorescent intensity (MFI). Results were expressed as fold change in comparison to untreated M0 macrophages.

Secretion of Chemokines

The levels of the chemokines CXCL10 and CCL5 were measured by commercially available ELISA kits following the manufacturer's instructions (R&D Systems, MN, USA). The supernatants were collected after 24 h of treatments.

PCR

Total RNA was collected from macrophages with PureZOL™ RNA Isolation Reagent (Bio-Rad, CA, USA) and purified with Direct-zol RNA Miniprep kit (Zymo Research, CA, USA). From 1 μg total RNA, cDNA was synthesized by random priming with the High-Capacity cDNA Reverse Transcription kit (Applied Biosystems, CA, USA) according to the manufacturer's instructions. SYBR™ Green PCR Master Mix (Applied Biosystems, CA, USA) was used for Real-Time PCR on a QuantStudio 7 Flex Real Time PCR Systems (Applied Biosystems, CA, USA) according to the manufacturer instructions. The sequences of primer pairs were as follows: hGAPDH; 5′-AGA TCA TCA GCA ATG CCT CCT G-3′ and 5′-ATG GCA TGG ACT GTG GTC ATG-3′, hCCL5; 5′-TGC ATC TGC CTC CCC ATA TT-3′ and 5′- GAC CTT GCC ACT GGT GTA GAA A-3′, hIRF7; 5′- CCA CGC TAT ACC ATC TAC CTG G—3′ and 5′- GCT GCT ATC CAG GGA AGA CAC A—3′, hCD206; 5′-GGA GTG ATG GTT CTC CTG TTT-3′ and 5′- CCT TTC AGC TCA CCA CAG TAT T-3′. Cycling conditions: 10 min at 95°C, 40 cycles of 15 s at 95°C, and 1 min at 60°C. Data were normalized to *GAPDH* mRNA by subtraction of the cycle threshold (Ct) value of *GAPDH* mRNA from the Ct value of the gene (ΔCt). Fold difference was calculated by comparing the ΔCt with the ΔCt of untreated M0 macrophages (ΔΔCt).

Cytotoxicity of Pre-treated Macrophages Toward PANC-1 Tumor Cell Line

The cytotoxicity of the pre-treated macrophages toward cancer cells was performed as described in a recent publication (12). Briefly, primary monocytes isolated from human healthy donors were stimulated with M-CSF in 5% FBS supplemented RMPI medium for 5 days. Then, macrophages were treated with the different ENCPs or free poly(I:C) in a dose of 5 μg/mL for 24 h. Alternatively, macrophages were treated with LPS/IFN-γ or IL-4 to polarize them toward M1 or M2 phenotypes. Macrophages were then washed and co-incubated for 2 days with 25,000 cells of a pancreatic cancer cell line (PANC-1), that were previously stained with Cell Trace Far Red (Invitrogen, CA, USA). The cells were trypsinized and fixed in FACS Fix for 20 min at 4°C for flow cytometry analysis using FACS Canto II Instrument (BD Biosciences, CA, USA). For the flow cytometry analysis, acquisition was set to 45 s and the number of high fluorescence intensity events (corresponding only to proliferating PANC-1 cells) were counted for each sample and normalized to the non-treated (M0) macrophages.

Statistical Analysis

Data analysis was performed with GraphPad Prism version 7.0 (GraphPad Inc.). Statistical comparison was done using a two-way ANOVA followed by a Tukey's multiple comparison test; an ordinary one-way ANOVA followed by a Tukey's multiple comparison test; or a paired *t*-test when comparing only two sets of data. Data are expressed as the mean ± standard deviation (SD). *p*-values of 0.05 or less were considered statistically significant. In the *in vitro* experiments "*n*" represents the number of each macrophage population obtained from each blood donor. For the PCR results "*N*" represents the number of experimental replicates.

RESULTS AND DISCUSSION

The main objective of this study has been to develop a delivery carrier for poly(I:C) that would promote the polarization of macrophages toward an anti-tumoral M1-like phenotype. With this idea in mind, we selected different arginine-rich polymers and oligomers for the complexation of poly(I:C) and, then, we enveloped these positively charged nanocomplexes with pegylated polyglutamic acid (PEG–PGA) or hyaluronic acid (HA) to produce ENCPs. Following a rigorous characterization in terms of particle size, zeta potential and drug loading capacity, these ENCPs were evaluated *in vitro* for their biocompatibility, capacity to be internalized and ability to revert the polarization of human primary macrophages toward M1-like anti-tumoral phenotypes. Finally, the capacity of the macrophages treated with nanoformulated poly(I:C) to secrete T-cell attracting chemokines and to directly kill cancer cells was also assessed.

Design and Development of Poly(I:C) Nanocomplexes

In the last decades, the formulation of anti-cancer drugs in nanosystems has been extensively studied with the aim of improving their accumulation in the tumor site, hence decreasing their off-target effects (42, 43). This research has led to a significant number of marketed nanoparticle-based anti-cancer drugs with an improved safety profile (42). In parallel, although at early stages, the development of nanosystems associating immunomodulators is already showing promising results at the preclinical level (44). At the same time, the formulation of polynucleotides within nanosystems is able to protect them from degradation (45). Bearing all this in mind, we have formulated poly(I:C) in the form of nanocomplexes enveloped with two biodegradable and stabilizing polymers (PEG–PGA and HA), known to facilitate the arrival to the tumor site (40, 46–53). Once in the tumor, a preferential uptake of the nanosystems by macrophages could be anticipated due to their high phagocytic capacity, as already described for both, targeted and non-targeted nanosystems (15, 54, 55). Considering our own previous results and also relevant literature in the field (46, 53), the targeted nanocomplexes should present particle sizes lower than 200 nm, with a pegylated or negative surface, and a high stability in relevant media.

Screening of Different Arginine-Rich Polymers

As the first step in the development of a poly(I:C)-loaded nanoformulation and, based on a nanosystem recently reported by our group showing the capacity of modified octaarginine to complex polynucleotides (40), different positively-charged arginine-rich polymers were selected for poly(I:C) complexation. Oligo-arginines have been extensively employed for the delivery of different nucleic acids due to their CPP nature, which increases their uptake and, as a result, improves their therapeutic performance (37, 40, 56). For this purpose, and taking as a reference our previous work (40) and additional reports (57), two oligopeptides were selected: octaarginine (r8) and a hydrophobically-modified r8, that contains a laurate chain (C12r8). As a comparison, a higher MW arginine polymer, polyarginine (pArg), was also selected. Weight ratios arginine-rich polymer/oligomer to poly(I:C) ranging from 1:1 to 4:1 were evaluated in terms of their capacity to form nanocomplexes (**Figure 1**). In the case of the unmodified r8, despite previous works making use of this biomaterial, no stable nanosystems were obtained at the different ratios and thus, its use was discarded. On the contrary, the hydrophobized r8 could form stable nanocomplexes at ratios 2:1 and 4:1, a fact that indicates that the hydrophobic tail of C12r8 is critical for improving the stability of the resulting complexes (58, 59). In the case of the pArg-based nanocomplexes, all ratios yielded particles with sizes increasing from 150 to 300 nm, as the amount of pArg increased (**Figure 1A**). Positive surface charge values incremented following the same trend (**Figure 1B**).

In order to evaluate their suitability for *in vitro* testing, the nanocomplexes were incubated in cell culture media at 37°C, to determine their stability. In the case of C12r8, the particle size of the nanocomplexes increased upon incubation in cell culture media (**Supplementary Figure 1A**). On the contrary, pArg-based nanosystems (ratio 1:1) maintain their particle size under the same conditions (**Supplementary Figure 1B**). We hypothesized that the different stability of the nanocomplexes could be due to their different MWs, since the long positive chains of the pArg would offer a higher number of positive sites for binding the dsRNA, in comparison to the smaller chains of the C12r8 (60).

PEG–PGA-Enveloped Nanocomplexes

In order to improve the nanocomplexes stability, we applied the technology previously described by our group (40, 61), using different pegylated polyglutamic acid (PEG–PGA) copolymers for the envelopment of the nanocomplexes. The presence of PEG as the external layer of the system was intended to provide steric protection and increase its colloidal stability (62). Additionally, the combination of PEG and PGA as the outer layer of polymeric nanocapsules has already been shown to facilitate their access to the tumor site in a passive manner (46, 47), and to improve the stability of C12r8-based nanocomplexes in biologically relevant media (61, 63).

It has been extensively reported that both, the PEG layer density and its conformation, are two key aspects in determining the fate and stability of the nanosystems (48, 49). In this work, we investigated different parameters of the copolymers with the idea to optimize the enveloping process, namely (i) a branched

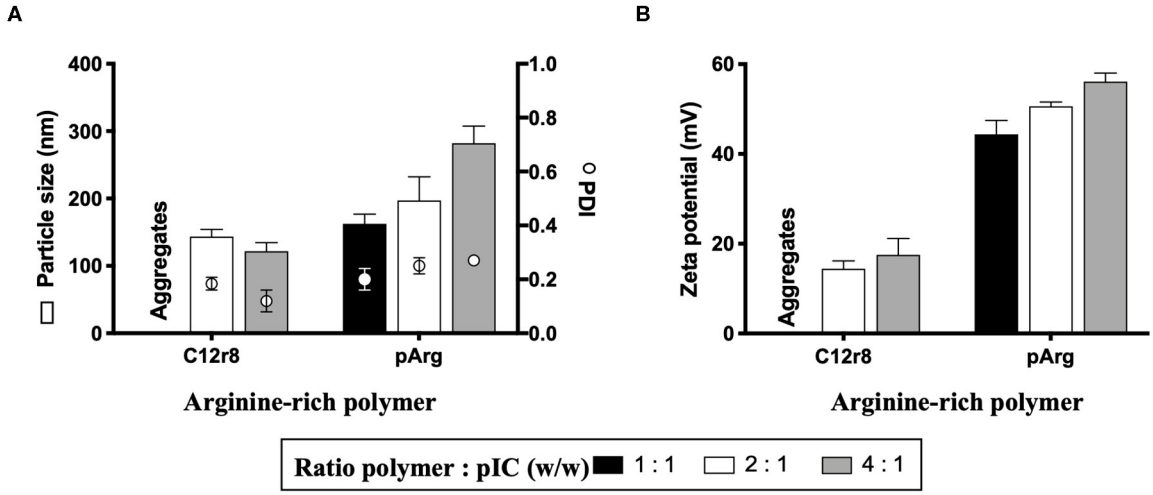

FIGURE 1 | Screening of different arginine-rich polymers to form nanocomplexes with poly(I:C). Values of **(A)** particle size, PDI and **(B)** zeta potential of the nanocomplexes obtained for the different ratios tested. Values represent mean ± SD ($n \geq 3$). C12r8, laurate-octaarginine; pArg, polyarginine; PDI, polydispersity index; pIC, poly(I:C); w/w, weight/weight.

or diblock conformation, (ii) the length of the PGA chain, and (iii) the PEG density. For this purpose, branched copolymers with two PGA lengths (10 and 30 units) and different PEG substitution degrees (10 and 30%) were studied. At the same time, two diblock copolymer conformations with PGA lengths of 10 and 30 units, and a PEG tail of 20 and 5 kDa MW, were also evaluated (**Supplementary Figure 2**).

For the enveloping process, we searched for the optimal amount of PEG–PGA for an efficient coating. For this, we evaluated two different amounts of PEG–PGA polymer over the C12r8:pIC. For a weight ratio C12r8:pIC:PEG–PGA 4:1:6, narrow particle sizes were obtained and, although surface charge was decreased, only the diblock PEG_{5k}-PGA30 generated a zeta-potential inversion (**Supplementary Figures 3A,B**). Similarly, a lower amount of PEG—PGA (4:1:3) caused a slight particle size increase, and a moderate decrease in the surface charge, with no charge inversion for any of the conditions (**Supplementary Figures 3A,B**). It is interesting to mention that the branched PEG_{5k}30–PGA10 did not produce an important change in the surface charge of any of the ENCPs (**Supplementary Figure 3B**), behavior already reported for similar systems (61). In this regard, we can speculate that the small size of the PGA chain, and the high number of PEG tails, might hinder the adequate interaction of the polymer with the systems, making this copolymer inadequate for an efficient coating of these nanocarriers.

To determine the efficiency of PEG–PGA envelopments in improving the ENCPs stability, the variation of their physicochemical properties in cell culture media was monitored (**Supplementary Figures 4A,B**). The results showed that both diblock copolymers were able to stabilize the nanocomplexes in a weight ratio C12r8:pIC:PEG–PGA 4:1:3 (**Supplementary Figure 4B**). Nevertheless, the ENCPs with the diblock PEG_{5k}-PGA30 did not present as good short-term stability in storage conditions as the PEG_{20k}-PGA10 (data not shown), which led us to discard the use of that copolymer. Similar C12r8 nanosystems enveloped with this PEG–PGA arrangement were also significantly stabilized (40, 63), which confirms that this diblock combination of a low number of PGA units (10) with a long PEG tail (20 kDa) provides good steric protection to a nanosystem.

Based on these results, the diblock PEG_{20k}-PGA10 polymer was used for enveloping the pArg nanocomplexes, maintaining the pIC:PEG–PGA ratio, so that a more systematic comparison between the different nanocomplexes could be conducted. These ENCPs (weight ratio pArg:pIC:PEG–PGA 1:1:3) presented a particle size of 190 ± 15 nm, and a lower positive surface charge, when compared with the non-enveloped nanocomplexes (**Supplementary Figures 3C,D**). Furthermore, the colloidal stability in cell culture media showed that all ENCPs properties were maintained after 24 h of incubation (**Supplementary Figure 4C**), concluding that PEG_{20k}-PGA10 has highly interesting properties for increasing the stability of nanosystems.

HA-Enveloped Nanocomplexes

Hyaluronic acid (HA) was also evaluated for the envelopment of the nanocomplexes, based on its anionic character and stabilization properties (50–52). Indeed, a recent report has claimed that HA coatings are able to decrease the adsorption of immunogenic proteins in comparison to other anionic coatings (64). Furthermore, HA-coated nanocapsules recently developed by our group showed an improved tumor accumulation after systemic administration (53). All these characteristics were expected to confer stability to the ENCPs, together with longer circulation times.

In line with this, several weight ratios of HA were evaluated to envelop the C12r8 and the pArg nanocomplexes. In the case of C12r8, the lowest amounts of HA led to aggregation, probably because the surface charges of the ENCPs were close to neutrality.

For the other ratios, the ENCPs presented sizes of 150–200 nm and negative surface charges (**Supplementary Figure 5**).

When evaluating the stability in cell culture media, none of the C12r8 ENCPs were sufficiently stable after the envelopment with HA, reason why they were discontinued for the following experiments (**Supplementary Figure 6A**). Oppositely, for HA-enveloped pArg nanosystems, all ENCPs were stable after incubation in cell culture media (**Supplementary Figure 6B**). Among them, the weight ratio pArg:pIC:HA 1:1:1.5 showed the best properties in terms of its short-term stability (data not shown), and, therefore, was selected for further evaluation. Regarding the different stability of the HA-enveloped nanosystems, it is known that the presence of salts and the high ionic strength of the cell culture media can potentially disturb the ionic interactions governing the stability of some colloidal systems (65). Additionally, we hypothesized that the different MW of pArg and the C12r8 can cause a more tightly attachment of the HA coating in the case of the longer chains of the pArg, increasing their stability in cell culture media.

Overall, the conclusion from these envelopment tests is that the polymeric coating can significantly increase the stability of the nanocomplexes, but the process needs to be optimized in a case-by-case basis, being mainly determined by the nanocomplexes composition and the nature of the enveloping polymer.

Association Capacity of Poly(I:C) to the Enveloped Nanocomplexes (ENCPs)

After the screenings described in the precedent sections, a total of four ENCPs were selected to investigate their capacity to polarize macrophages: non-enveloped, diblock PEG_{20k}-PGA10 enveloped and HA-enveloped pArg nanocomplexes (pArg:pIC ENCPs; pArg:pIC/PEG–PGA ENCPs and pArg:pIC/HA ENCPs, respectively) and diblock PEG_{20k}-PGA10 enveloped C12r8 nanocomplexes (C12r8:pIC/PEG–PGA ENCPs). Their main physicochemical properties are summarized in **Table 1**. All ENCPs presented particle sizes between 150 and 200 nm, with low PDIs and surface charges ranging from highly positive (pArg:pIC), through neutral (C12r8:pIC/PEG–PGA) to negatively charged (pArg:pIC/HA). Remarkably, high loading values of poly(I:C) were obtained for the different systems (**Table 1**). Electron microscopy confirmed the size, homogeneity and spherical shape of the ENCPs (**Figure 2A**).

Secondly, the efficacy of the ENCPs to associate poly(I:C) was qualitatively evaluated. An agarose gel retardation assay confirmed that all nanosystems efficiently interacted with poly(I:C), with no free poly(I:C) detected, and the incubation with the competitor polyanion heparin was able to partially displace the cargo (**Figure 2B**). Moreover, the incubation of the nanocomplexed poly(I:C) in cell culture media during 4 or 24 h did not disrupt the interaction between poly(I:C) and pArg (**Figure 2C** and **Supplementary Figure 7A**, lanes 2–7). Instead, free poly(I:C) suffered a degradation when exposed to the cell culture media, as noted by the decrease in the MW (**Figure 2C** and **Supplementary Figure 7A**, lane 2). This degradation was probably caused by the RNases present in the media, since this degradation did not happen in water in the same conditions (**Supplementary Figure 7B**).

TABLE 1 | Summary of the main physicochemical properties of the four enveloped nanocomplexes used in the *in vitro* experiments.

Formulation	Ratio (w/w)	Particle size (nm)	PDI	ζ-Potential (mV)	Poly(I:C) loading (%)
pArg:pIC	1:1	163 ± 14	0.20	+44 ± 3	50
pArg:pIC /PEG–PGA	1:1 :3	190 ± 14	0.18	+26 ± 8	20
pArg:pIC /HA	1:1 :1.5	157 ± 10	0.16	−15 ± 7	29
C12r8:pIC /PEG–PGA	4:1 :3	165 ± 14	0.07	+5 ± 1	12.5

Mean ± SD, n ≥ 12. C12r8, laurate octa-arginine; HA, hyaluronic acid; pArg, polyarginine; PDI, polydispersity index; PEG–PGA, pegylated polyglutamic acid; pIC, poly(I:C); w/w: weight/weight.

In the case of the C12r8:pIC/PEG–PGA ENCPs, poly(I:C) was not released upon incubation in cell culture medium, but after the displacement with heparin some degradation could be observed at 4 and 24 h (**Figure 2C** and **Supplementary Figure 7A**, lanes 9–10). We hypothesized that this degradation could be due to the interaction of the displaced poly(I:C) with the enzymes of the media (**Supplementary Figure 7B**), since the poly(I:C) inside the nanocomplexes is expected to be protected from enzymes. Therefore, these results demonstrate the capacity of the ENCPs to protect and prevent the premature release of poly(I:C).

In vitro Toxicity of the Nanocomplexes

Considering that the target cells of the developed ENCPs are immune cells of the myeloid lineage, primary human monocyte-derived macrophages were used to evaluate the *in vitro* biocompatibility of the nanosystems. M0 or M2 macrophages were incubated with the selected ENCPs for different times. When M0 macrophages were exposed to different concentrations of free or nanocomplexed poly(I:C) for 24 h, minor toxicity values were observed for the lowest doses (1 and 5 μg/mL), with no significant differences among ENCPs (**Figure 3A**). At higher doses (10 μg/mL), the poly(I:C) nanocomplexed with C12r8 showed higher toxicity than the free dsRNA (**Figure 3A**). This increased toxicity could be caused by the higher amount of the polypeptide C12r8 in comparison to pArg for the same dose of poly(I:C) (weight ratio 4:1 and 1:1, respectively), and due to the intrinsic toxicity of CPPs (66). A similar tendency was observed for M2 macrophages, showing similar toxicities for all the ENCPs at 10 μg/mL of poly(I:C), while the lower doses were much better tolerated (**Figure 3B**). As expected, shorter incubation times produced negligible toxicities (**Supplementary Figures 8A,C**), while longer incubation times decreased cell viability (**Supplementary Figures 8B,D**).

Overall, a similar toxicity of ENCPs vs. the free poly(I:C) at 5 μg/mL toward macrophages cultured *in vitro* was observed. Only a higher toxicity was found for some ENCPs at higher concentrations and longer time points (48 h), which could be expected, due to a higher uptake of the nanocomplexes vs. the free drug, as described in the next results section (**Figures 3C–E**).

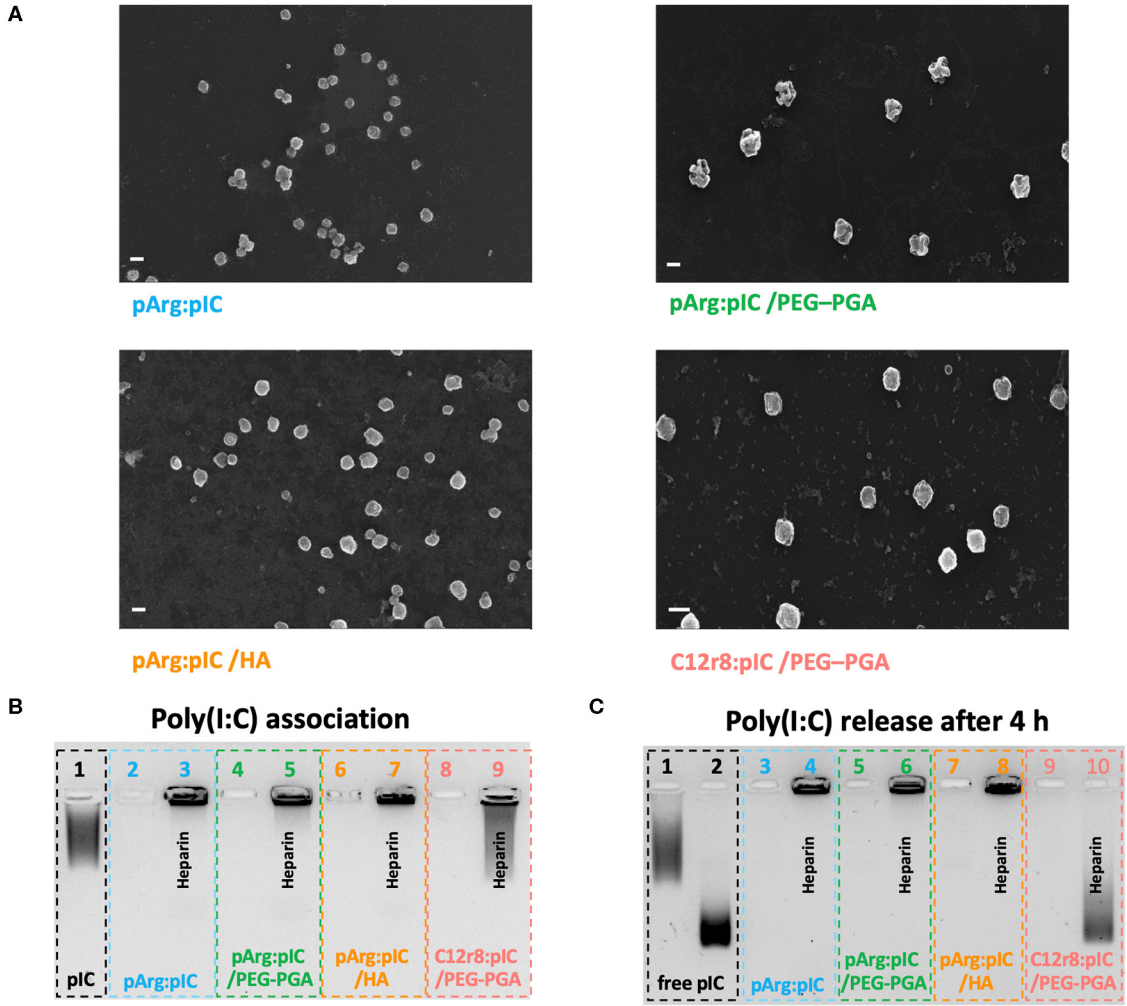

FIGURE 2 | Physicochemical properties and poly(I:C) binding affinity of the selected nanocomplexes. **(A)** FESEM images of each of the four developed nanosystems. Values represent mean ± SD ($n \geq 12$). Size bars represent 200 nm, and all images present a 50 K magnification. **(B)** Agarose gel retardation assay to evaluate the poly(I:C) binding capacity of the nanocomplexes. Lanes: (1) free poly(I:C), (2,4,6,8) are pArg:pIC, pArg:pIC/PEG–PGA, pArg:pIC/HA and C12r8:pIC/PEG–PGA nanocomplexes, respectively; and (3,5,7,9) are the corresponding nanocomplexes incubated with heparin. **(C)** Agarose gel retardation assay to evaluate the release and integrity of poly(I:C) after 4 h of incubation in cell culture media at 37°C. Lanes: (1) free poly(I:C) in solution and (2) in cell culture media; (3,5,7,9) are pArg:pIC, pArg:pIC/PEG–PGA, pArg:pIC/HA and C12r8:pIC/PEG–PGA nanocomplexes in cell culture media; and (4,6,8,10) are the same conditions incubated with heparin. C12r8, laurate-octaarginine; FESEM, field emission scanning electron microscopy; HA, hyaluronic acid; pArg, poly-arginine; PEG–PGA, pegylated polyglutamic acid; PDI, polydispersity index; pIC, poly(I:C); w/w, weight/weight.

Thus, a non-toxic dose of 5 μg/mL of poly(I:C) was selected for the following experiments, finding a compromise between biocompatibility and an effective dose.

Uptake and Cellular Internalization of the Nanocomplexes by Macrophages

In order to bind to its intracellular receptor (TLR3), poly(I:C) must be internalized by the macrophages. Thus, we evaluated if the uptake of poly(I:C) was improved when included into the ENCPs. Using rhodamine-labeled poly(I:C), the ability of macrophages to internalize free and nanocomplexed poly(I:C), together with its localization inside the cells, were studied (**Figures 3C–E**). When complexed only with pArg, the uptake of poly(I:C) was highly improved at 4 h, and even more at 24 h. This effect could be related to the high positive surface charge of the ENCPs vs. free poly(I:C) (**Figure 3C**). Similarly, a higher uptake was also observed for the HA-ENCPs, probably associated to the affinity of HA to the CD44 receptor on the surface of macrophages (67). In the case of the two PEG–PGA ENCPs, the uptake was only slightly better than the free dsRNA (**Figure 3C**). These results could be caused by the effect of the PEG chains, which might decrease the interaction of the ENCPs with the cell membrane, thus reducing their uptake by macrophages, as reported before for other nanoparticles (63, 68).

The ultimate target of the developed poly(I:C) ENCPs is the intracellular endosomal receptor TLR3. In order

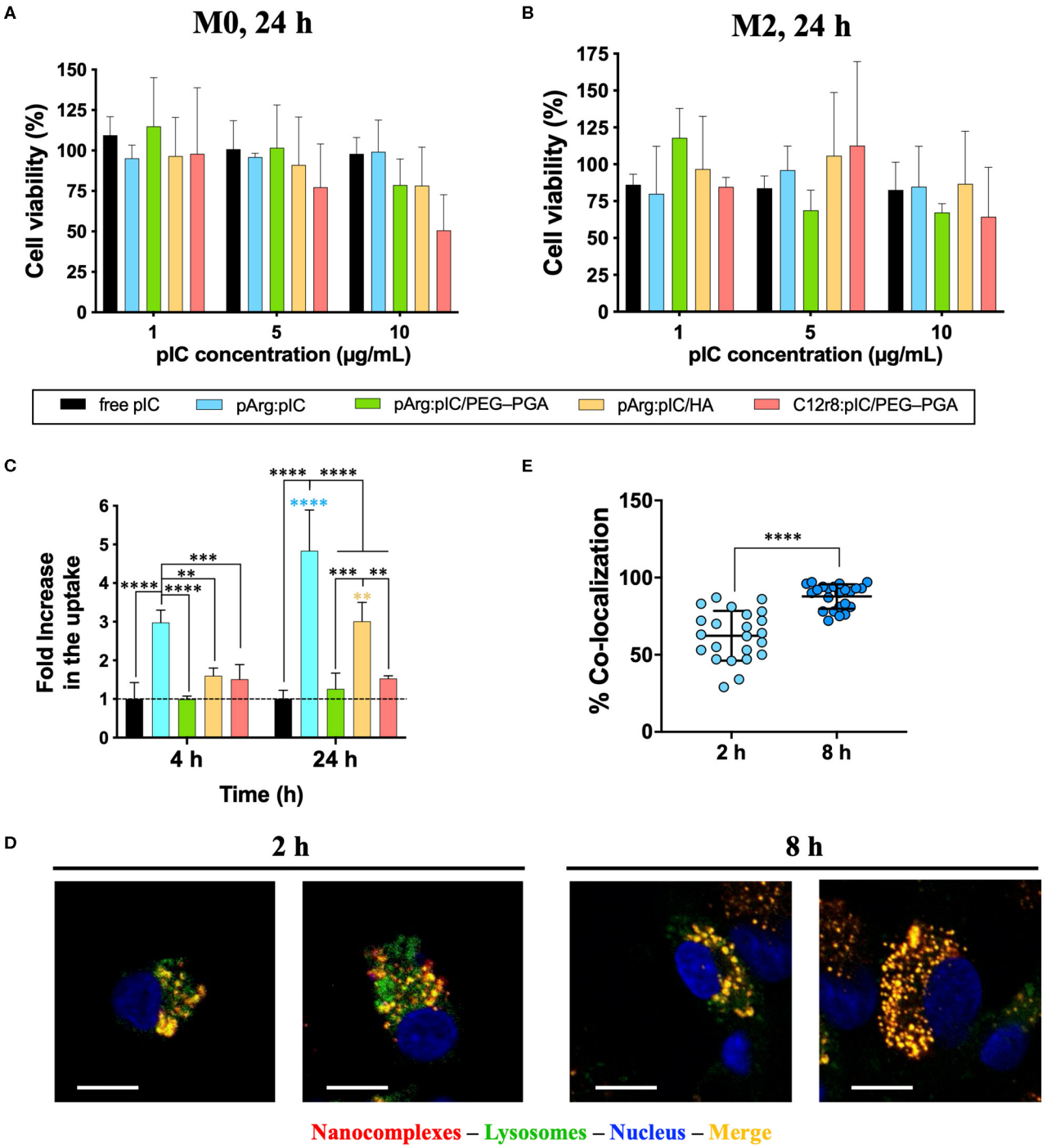

FIGURE 3 | Toxicity, uptake and cellular localization of poly(I:C) and nanocomplexes. Toxicity toward **(A)** M0 and **(B)** M2 primary human monocyte-derived macrophages after 24 h of incubation. **(C)** FACS evaluation of rhodamine-labeled-poly(I:C) uptake by primary human monocyte-derived macrophages when included in the different nanocomplexes after 4 and 24 h of incubation, expressed as the fold increase in comparison to free poly(I:C), for a final poly(I:C) dose of 5 μg/mL. **(D)** Co-localization with the endosome of rhodamine-labeled pArg:pIC nanocomplexes after 2 and 8 h of incubation (100x magnification, size bars of 10 μm) evaluated by confocal microscopy. **(E)** Quantification of the co-localization of rhodamine-labeled pArg:pIC nanocomplexes with the endosome after 2 and 8 h of incubation, with a poly(I:C) dose of 5 μg/mL. Values represent mean ± SD ($n \geq 3$). Statistical comparison was done using a two-way ANOVA followed by a Tukey's multiple comparison test. Statistically significant differences are represented as $^{**}p < 0.01$, $^{***}p < 0.005$, and $^{****}p < 0.001$. C12r8, laurate-octaarginine; HA, hyaluronic acid; pArg, poly-arginine; PEG–PGA, pegylated polyglutamic acid; pIC, poly(I:C).

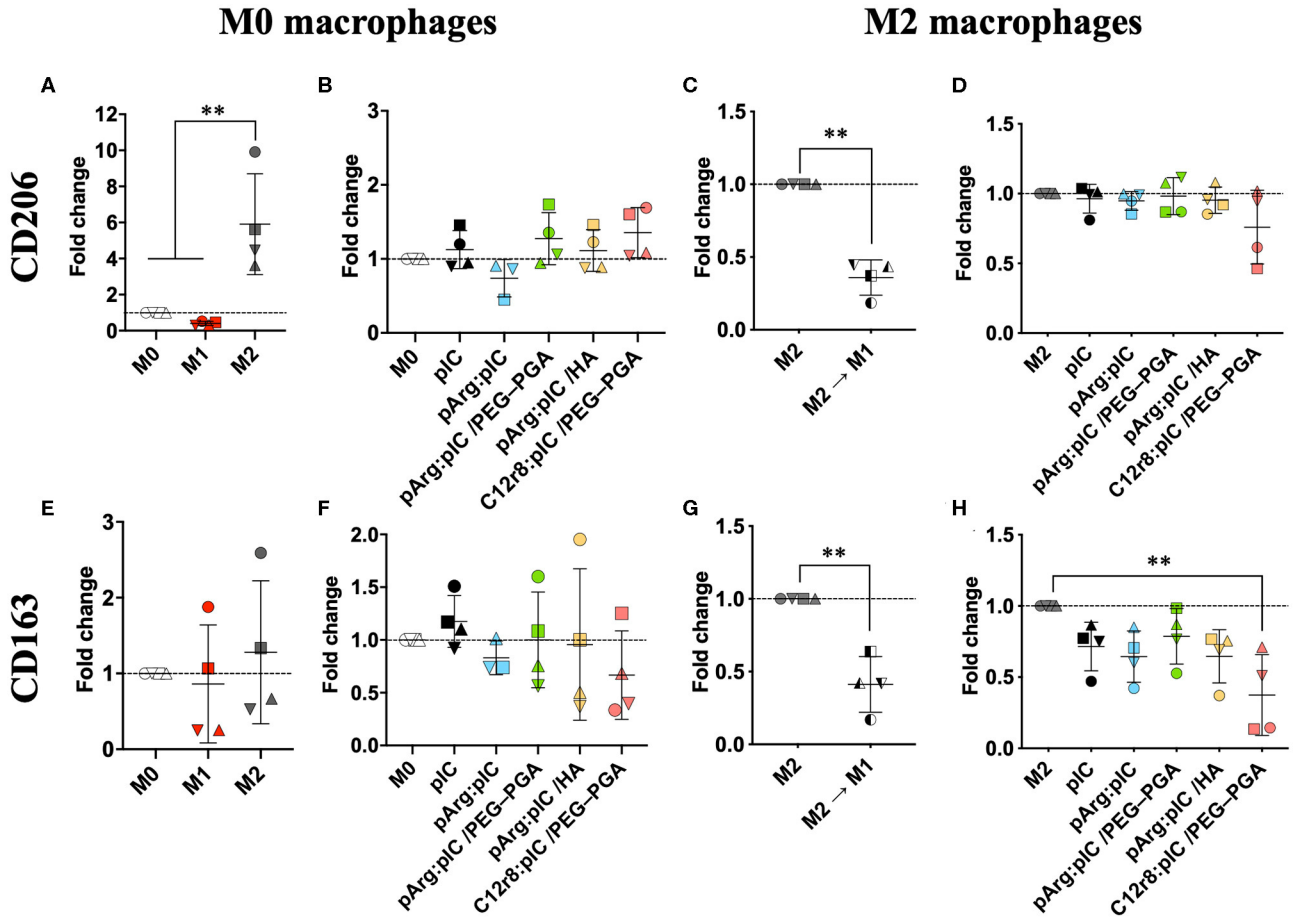

FIGURE 4 | Polarization of M0 and M2 macrophages after treatment with free and nanocomplexed poly(I:C). Expression of the M2 markers **(A–D)** CD206 and **(E–H)** CD163 in ENCP-treated M0 and M2 macrophages, in comparison to the prototypic phenotypes evaluated by FACS. M2 M1 represents M2 macrophages that were treated with LPS + IFN-γ for their M1 polarization. Macrophages were incubated with the treatments for 48 h, and the poly(I:C) dose used was 5 μg/mL. Each symbol shape represents a different donor. Values are shown as mean ± SD ($n \geq 3$). Statistical comparison was done using an ordinary one-way ANOVA followed by a Tukey's comparison test between groups; or a paired *t*-test for **(C,G)**. Statistically significant differences are represented as $^{**}p < 0.01$. C12r8, laurate-octaarginine; HA, hyaluronic acid; pArg, poly-arginine; PEG–PGA, pegylated polyglutamic acid; pIC, poly(I:C).

to confirm that the nanocomplexed poly(I:C) was able to reach this receptor, we studied the localization of the free and nanocomplexed poly(I:C) once inside the cells, as a proof-of-concept. For this, pArg:pIC ENCPs containing rhodamine-labeled poly(I:C), and CellLight® were used to track the cargo and the endosomes, respectively. Confocal experiments demonstrated the presence of poly(I:C) (in red) inside the endosome (in green) after 2 and 8 h of incubation, confirming the co-localization of the drug and its target (**Figures 3D,E**).

With this set of experiments, we can conclude that the inclusion of poly(I:C) into ENCPs improves its uptake and internalization, allowing the drug to efficiently reach its endosomal target inside macrophages. The functional studies described below were taken as additional validation of the adequate interaction of poly(I:C) with its target receptor.

Macrophage Polarization Toward a Pro-inflammatory Phenotype

The interaction of poly(I:C) with the endosomal TLR3 triggers an immune response through the TRIF pathway, and the subsequent activation of type I IFN genes (69). This should lead to a decreased expression of the M2-like features (e.g., CD206 and CD163); while M1 pro-inflammatory markers such as CD80 and MHCII should be increased (**Figure 4** and **Supplementary Figure 9**). Therefore, we analyzed the presence of both M1 and M2 markers on the surface of macrophages 48 h after exposure to nanocomplexed poly(I:C) (5 μg/mL) (9, 11). As controls, M0 or M2 macrophages were polarized toward the M1 prototypic phenotype by treatment for 48 h with LPS and IFN-γ; or with IL-4 for inducing the prototypic M2 phenotype. No significant changes were detected in the mannose receptor CD206 upon treatment with free poly(I:C) or the ENCPs, in comparison to the

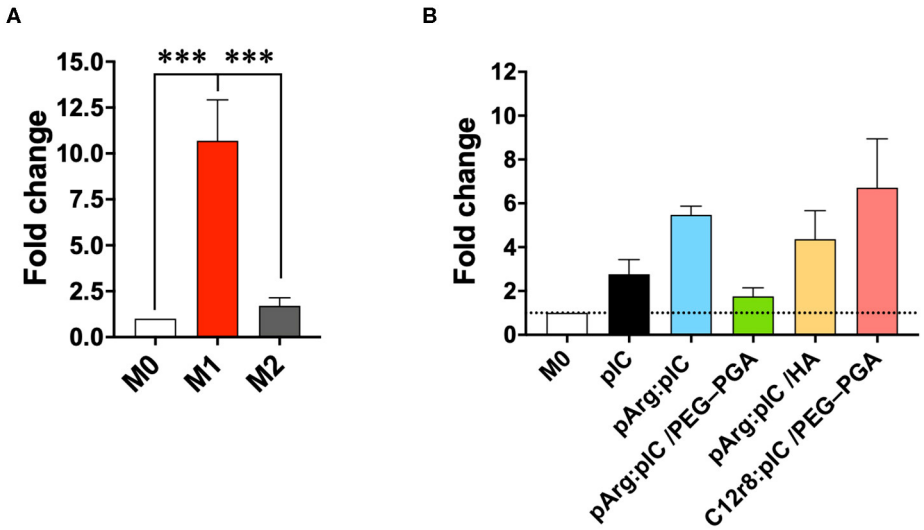

FIGURE 5 | mRNA production of different M1/M2 associated factors. Fold change in the mRNA levels of *IRF7* in **(A)** prototypic M1/M2 macrophages and in **(B)** M0 macrophages treated with the different nanocomplexes after 8 h of incubation. The dose of poly(I:C) was 5 μg/mL. Values represent mean ± SD ($N = 4$). Statistical comparison was done using an ordinary one-way ANOVA followed by a Tukey's comparison test between groups. Statistically significant differences are represented as ***$p < 0.005$. C12r8, laurate-octaarginine; HA, hyaluronic acid; pArg, poly-arginine; PEG–PGA, pegylated polyglutamic acid; pIC, poly(I:C).

untreated cells (**Figures 4B,D**); while it was overexpressed in the case of prototypic M2 macrophages (**Figures 4A,C**). Nevertheless, PCR analysis showed that the *CD206* mRNA levels for M0 macrophages exposed for 8 h to any of the ENCPs were indeed decreased (**Supplementary Figures 10A,B**). The difference observed between flow cytometry and PCR analysis might be due to the fact that protein receptors stay for long times in the membrane, therefore, the presence of CD206 receptor on the surface of macrophages could not be representative of the gene downregulation induced by the drug at the times of analysis. Meanwhile, this change could be already be seen in the *CD206* mRNA levels, as already reported for similar cases (12).

In the case of the scavenger receptor CD163, its presence on the surface of macrophages was lower upon treatment with any of the ENCPs, with significant differences in M2 macrophages treated with C12r8:pIC/PEG–PGA ENCPs (**Figures 4E–H**). This slight decrease of CD163 in macrophages exposed to ENCPs could be related to the polarization of macrophages toward the M1 phenotype, although we cannot discard that it might also be related to an involvement of this scavenger receptor in the uptake of the ENCPs. Further experiments would be required to fully understand the interaction of CD163 with the ENCPs.

Overall, no significant changes in CD80 and MHCII were observed in the surface of M0 or M2 macrophages upon treatment with free or nanocomplexed poly(I:C) (**Supplementary Figures 9B,D,F,H**). Only a slight increase for the M1 markers CD80 and MHCII, was observed in macrophages exposed to C12r8:pIC/PEG–PGA ENCPs, but with no significant differences (**Supplementary Figures 9B,D,F,H**). A similar tendency was observed in the M1 controls (**Supplementary Figures 9A,C,E,G**). Furthermore, we also analyzed the levels of *IRF7* mRNA by PCR, a key molecule in the TRIF signaling pathway, which is triggered downstream of TLR3 activation (70). These experiments showed a higher level of *IRF7* mRNA in macrophages treated either with free or nanocomplexed poly(I:C) vs. M0 and M2 prototypic macrophages (**Figure 5**). In fact, these results correlated with the ones of the ENCPs uptake (**Figure 3C**).

As a whole, these results show a limited ability of free or nanocomplexed poly(I:C) to modulate the ratio of M1/M2 receptors on the surface of prototypical M0 or M2 macrophages, confirming the results recently published regarding the polarization capacity of poly(I:C) and imiquimod *in vitro* (12). The dynamic turnover of all these receptors probably hampers their precise quantification to assess the M1/M2 phenotypes *in vitro*. On the basis of these data, and being conscious that the ability of poly(I:C) to polarize macrophages toward M1-like anti-tumoral phenotypes can be better evaluated by conducting functional assays, we decided to test the ability of macrophages to secrete chemokines involved in the recruitment of T cells and the cytotoxic potential of pre-treated macrophages toward cancer cells.

Improved T Cell Recruitment Capacity

Cytotoxic T cells (CTLs) are also important players in the anti-tumoral immune response (71, 72). CXCL10 and CCL5 are two key chemokines implicated in the recruitment of these CTLs by macrophages in order to fight against the cancer cells. Thus, we have evaluated the secretion of these chemokines by macrophages exposed to the ENCPs. We found a higher production of CXCL10 and CCL5 by macrophages treated with ENCPs vs. free poly(I:C) and the control (non-treated M0 macrophages) (**Figure 6** and **Supplementary Figure 11**). Importantly, the levels of

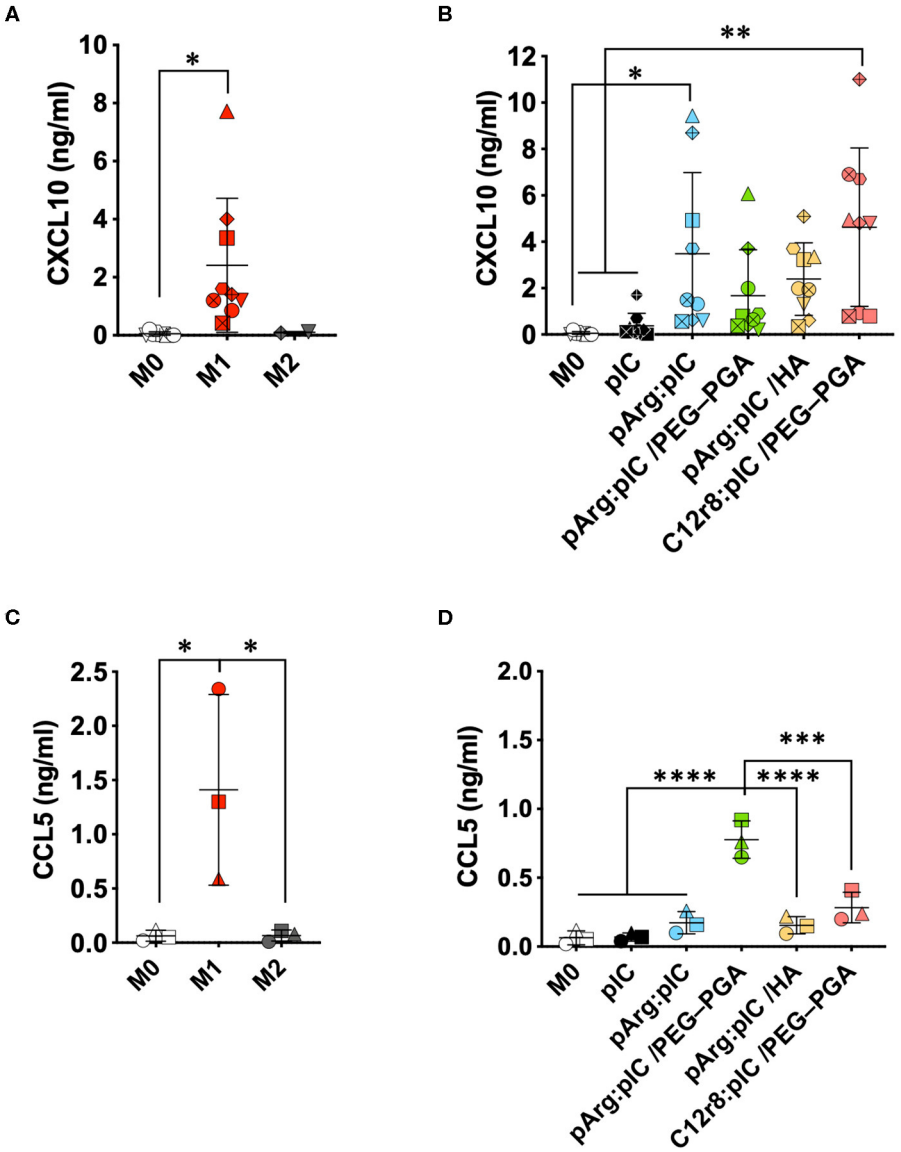

FIGURE 6 | Secretion of the T cell attracting chemokines upon treatment with the poly(I:C) nanocomplexes. **(A,B)** CXCL10 secretion in **(A)** prototypic macrophages and in **(B)** M0 macrophages treated with the different nanocomplexes after 24 h of incubation. **(C,D)** CCL5 secretion in **(C)** prototypic macrophages and in **(D)** M0 macrophages treated with the different nanocomplexes after 24 h of incubation. Poly(I:C) was used at the final dose of 5 μg/mL. Each symbol shape represents a different donor. Values represent mean ± SD ($n \geq 3$). Statistical comparison was done using an ordinary one-way ANOVA followed by a Tukey's comparison test between groups. Statistically significant differences are represented as $^{*}p < 0.05$, $^{**}p < 0.01$, $^{***}p < 0.005$, and $^{****}p < 0.001$. C12r8, laurate-octaarginine; HA, hyaluronic acid; pArg, poly-arginine; PEG–PGA, pegylated polyglutamic acid; pIC, poly(I:C).

CXCL10 stimulated by the ENCPs were similar to the ones observed for M1 macrophages at 24 h, or even higher, in the case of the pArg:pIC and C12r8:pIC/PEG–PGA ENCPs (**Figures 6A,B**). Regarding CCL5, a minor increase in the secretion of this chemokine was observed after treatment with the ENCPs, which was only significantly higher for the pArg:pIC/PEG–PGA ENCPs (**Figures 6C,D**). In addition, *CCL5* mRNA levels further confirmed the stimulation of CCL5 production upon treatment with ENCPs, vs. the free poly(I:C) (**Supplementary Figures 10C,D**).

Altogether, these results indicate that, even though nanocomplexed poly(I:C) does not provoke an important change in the surface marker expression of macrophages, other anti-tumoral features such as the secretion of T cell-recruiting chemokines, was greatly improved.

Increased Ability of Pre-treated Macrophages to Kill Tumor Cells

Besides their role in activating the immune system to fight cancer, anti-tumoral macrophages have also the capacity to

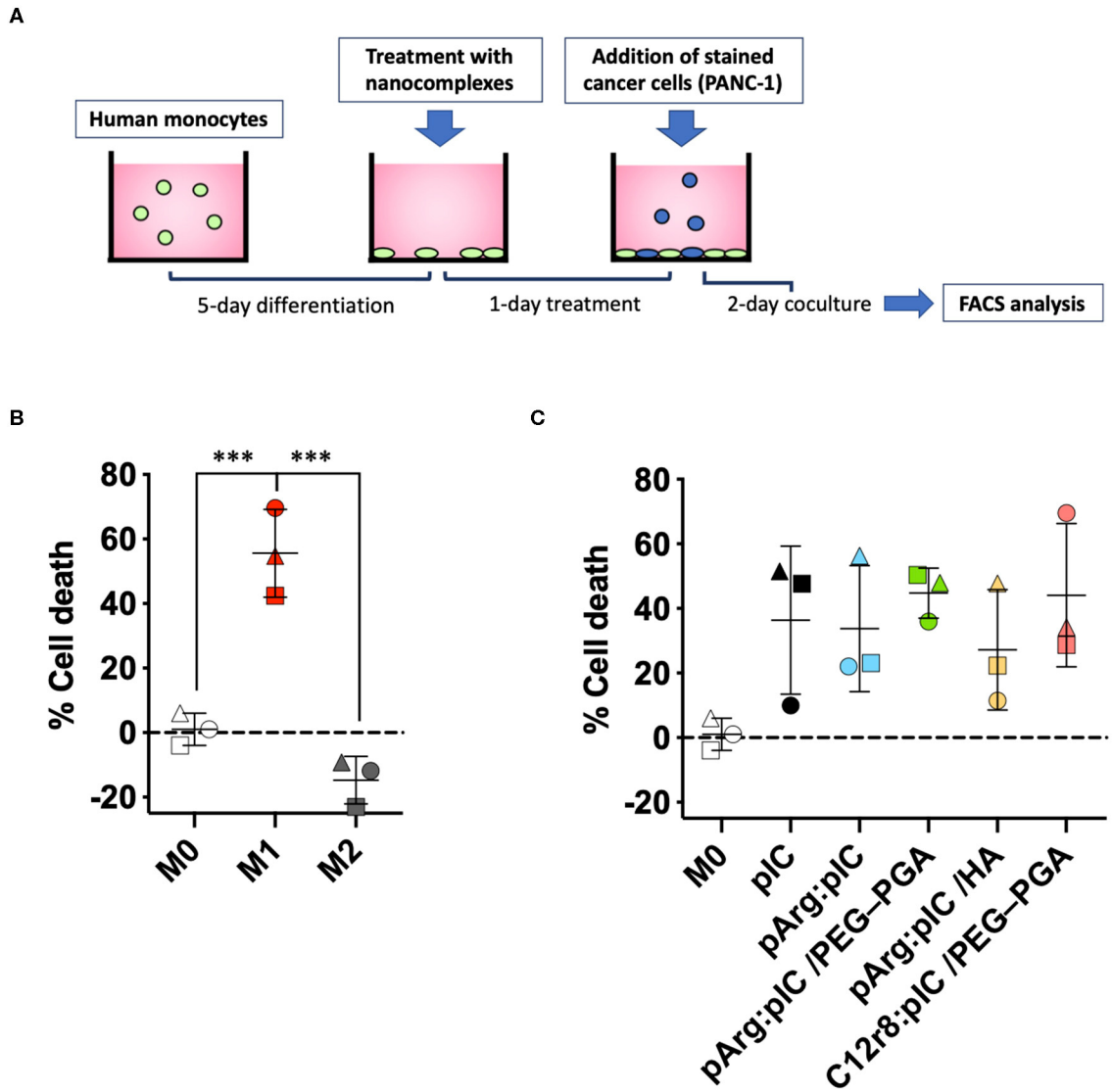

FIGURE 7 | Macrophage cytotoxicity toward PANC-1 cancer cells after pre-treatment with the different nanocomplexes. **(A)** Schematic representation of the *in vitro* model for the determination of the killing capacity of pre-treated macrophages. **(B,C)** % of cancer cell death caused by **(B)** the prototypic macrophages or **(C)** M0 macrophages pre-treated with free or nanocomplexed poly(I:C). Poly(I:C) was used at the final dose of 5 μg/mL. Each symbol shape represents a different donor. Values represent mean ± SD ($n \geq 3$). Statistical comparison was done using an ordinary one-way ANOVA followed by a Tukey's multiple comparison test between groups. Statistically significant differences are represented as ***$p < 0.005$. C12r8, laurate-octaarginine; HA, hyaluronic acid; pArg, poly-arginine; PANC-1, pancreatic cancer cells; PEG–PGA, pegylated polyglutamic acid; pIC, poly(I:C).

directly kill tumor cells (73). To assess the potential of the poly(I:C) ENCPs to polarize macrophages toward M1-like anti-tumoral phenotypes, we performed a functional assay to evaluate their ability to kill tumor cells (**Figure 7A**). For this, M0 macrophages were treated with the different ENCPs during 24 h, or were differentiated to prototypical M1 or M2 phenotypes used as controls. These pre-treated macrophages were then co-cultured with stained pancreatic cancer cells (PANC-1) for 48 h. As expected, PANC-1 cells proliferated 15% more in co-culture with M2 macrophages, compared to non-polarized M0 macrophages (**Figure 7B**). On the other side, as a positive control, M1 macrophages presented a 60% increased ability to kill the cancer cells, when compared to M0 macrophages (**Figure 7B**). In the case of macrophages pre-treated with free and nanocomplexed poly(I:C), a 30–40% increase in their cytotoxicity toward cancer cells was observed vs. the untreated macrophages (**Figure 7C**). Considering that nanocomplexed poly(I:C) performed as well as the free drug, we can confirm that the dsRNA inside the nanocomplexes remained active.

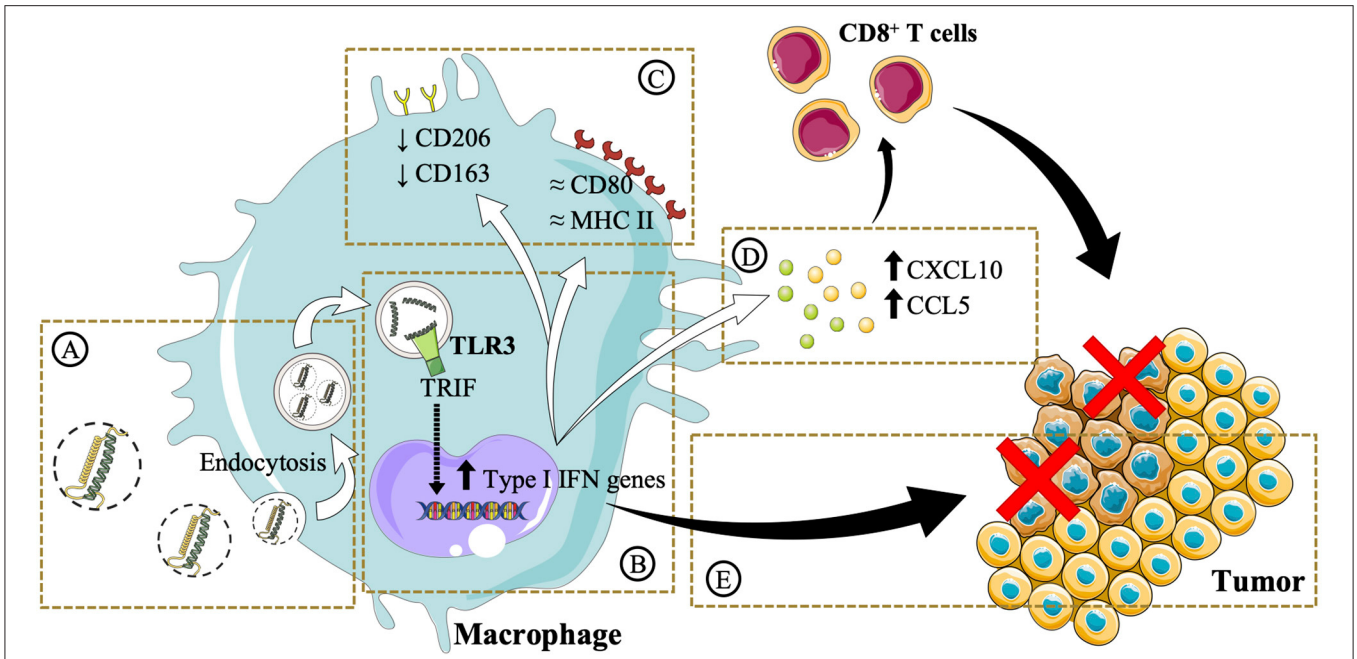

FIGURE 8 | Schematic illustration of the *in vitro* effects of the poly(I:C) ENCPs developed in this study. **(A)** Upon interaction with macrophages, poly(I:C) nanocomplexes are taken up. **(B)** This process allows poly(I:C) to reach its target receptor TLR3, found in the endosomes. It is expected that this interaction activates the TLR3 and the TRIF pathway, stimulating the upregulation of type I IFN genes. **(C)** The expression of M2 (CD206 and CD163) surface markers was slightly decreased, while M1 (CD80 and MHC II) markers are not substantially modified. Nevertheless, **(D)** CXCL10 and CCL5 chemokines, involved in the attraction of CD8 T cells to the tumor microenvironment, are secreted. **(E)** The direct cytotoxicity of macrophages toward cancer cells is also enhanced. Images were reproduced from Servier Medical Art under a Creative Commons Attribution 3.0 Unported License https://creativecommons.org/licenses/by/3.0.

CONCLUSIONS

This work highlights the importance of a rational design in the development of poly(I:C) nanocomplexes to maintain the efficacy of the free drug while increasing its stability for *in vivo* administration. The complexation of poly(I:C) with arginine-rich polymers and their subsequent envelopment with either PEG–PGA or HA resulted in the formation of ENCPs with adequate physicochemical and stability properties. This delivery strategy facilitated the accumulation of poly(I:C) in the endosomal compartments, where the TLR3 is localized (**Figures 8A,B**). Minor changes in surface marker expression were detected, probably due to the dynamic turnover of these surface receptors (**Figure 8C**). However, in agreement with an improved poly(I:C) delivery, macrophages pre-treated with nanocomplexed poly(I:C) presented an enhanced secretion of T-cell attracting chemokines, which are critical for triggering effective anti-tumoral immune responses (**Figure 8D**). Moreover, macrophages pre-treated with either free or nanocomplexed poly(I:C) presented an improved capacity to directly kill cancer cells (**Figure 8E**). Altogether, these results provide evidence of arginine-based poly(I:C) nanocomplexes as a potential strategy for the M1-polarization of macrophages, that could be of advantage in the setting of cancer immunotherapy. Further *in vivo* biodistribution and anti-tumoral efficacy studies will help to elucidate whether these *in vitro* results are translatable, and if the systemic toxicity of the free dsRNA is indeed decreased.

DATA AVAILABILITY STATEMENT

The datasets generated for this study are available on request to the corresponding author.

AUTHOR CONTRIBUTIONS

TD, CA, and FT have contributed to the design, acquisition, analysis, interpretation of data, and the drafting and the revision of the work. FM has contributed to the design, acquisition, analysis, and interpretation of data. PA, MA, and JC-C have contributed to the design, the drafting, and the revision of the work. All authors contributed to the article and approved the submitted version.

FUNDING

This work was supported by the 2-INTRATARGET project (PCIN-2017-129/AEI) funded by MINECO-PCIN-2017-129/AEI, under the frame of EuroNanoMed III; by FEDER/Spanish Ministry of Science, Innovation and Universities (Ref.: SAF2017-86634-R); and by *Xunta de Galicia*'s *Grupos de referencia competitiva* (grant number ED431C 2017/09). TD acknowledges a predoctoral FPU grant from the Spanish Ministry of Education, Culture and Sports (grant number FPU14/05866). FT was the recipient of a grant by the AECC (*Asociación Española Contra el Cáncer*, Spain).

ACKNOWLEDGMENTS

Authors would like to thank the RIAIDT-USC analytical facilities, for the microscopy imaging.

SUPPLEMENTARY MATERIAL

The Supplementary Material for this article can be found online at: https://www.frontiersin.org/articles/10.3389/fimmu.2020.01412/full#supplementary-material

REFERENCES

1. Schreiber RD, Old LJ, Smyth MJ. Cancer immunoediting: integrating immunity's roles in cancer suppression and promotion. *Science.* (2011) 331:1565–70. doi: 10.1126/science.1203486
2. Couzin-Frankel J. Cancer immunotherapy. *Science.* (2013) 342:1432–3. doi: 10.1126/science.342.6165.1432
3. Zou W. Immunosuppressive networks in the tumour environment and their therapeutic relevance. *Nat Rev Cancer.* (2005) 5:263–74. doi: 10.1038/nrc1586
4. Balkwill F. Cancer and the chemokine network. *Nat Rev Cancer.* (2004) 4:540–50. doi: 10.1038/nrc1388
5. Mantovani A, Sica A. Macrophages, innate immunity and cancer: balance, tolerance, and diversity. *Curr Opin Immunol.* (2010) 22:231–7. doi: 10.1016/j.coi.2010.01.009
6. Vlaicu P, Mertins P, Mayr T, Widschwendter P, Ataseven B, Högel B, et al. Monocytes/macrophages support mammary tumor invasivity by co-secreting lineage-specific EGFR ligands and a STAT3 activator. *BMC Cancer.* (2013) 13:197. doi: 10.1186/1471-2407-13-197
7. Noy R, Pollard JW. Tumor-associated macrophages: from mechanisms to therapy. *Immunity.* (2014) 41:49–61. doi: 10.1016/j.immuni.2014.06.010
8. Mantovani A, Marchesi F, Malesci A, Laghi L, Allavena P. Tumour-associated macrophages as treatment targets in oncology. *Nat Rev Clin Oncol.* (2017) 14:399–416. doi: 10.1038/nrclinonc.2016.217
9. Mantovani A, Sozzani S, Locati M, Allavena P, Sica A. Macrophage polarization: tumor-associated macrophages as a paradigm for polarized M2 mononuclear phagocytes. *Trends Immunol.* (2002) 23:549–55. doi: 10.1016/S1471-4906(02)02302-5
10. Ovais M, Guo M, Chen C. Tailoring nanomaterials for targeting tumor-associated macrophages. *Adv Mater.* (2019) 31:1808303. doi: 10.1002/adma.201808303
11. Aras S, Zaidi MR. TAMeless traitors: macrophages in cancer progression and metastasis. *Br J Cancer.* (2017) 117:1583–91. doi: 10.1038/bjc.2017.356
12. Maeda A, Digifico E, Andon FT, Mantovani A, Allavena P. Poly(I:C) stimulation is superior than imiquimod to induce the antitumoral functional profile of tumor-conditioned macrophages. *Eur J Immunol.* (2019) 49:801–11. doi: 10.1002/eji.201847888
13. Anfray C, Ummarino A, Torres-Andón F, Allavena P. Current strategies to target tumor-associated-macrophages to improve anti-tumor immune responses. *Cells.* (2019) 9:46. doi: 10.3390/cells9010046
14. Song W, Musetti SN, Huang L. Nanomaterials for cancer immunotherapy. *Biomaterials.* (2017) 148:16–30. doi: 10.1016/j.biomaterials.2017.09.017
15. Andón FT, Digifico E, Maeda A, Erreni M, Mantovani A, Alonso MJ, et al. Targeting tumor associated macrophages: the new challenge for nanomedicine. *Semin Immunol.* (2017) 34:103–13. doi: 10.1016/j.smim.2017.09.004
16. Zeng Q, Jewell CM. Directing toll-like receptor signaling in macrophages to enhance tumor immunotherapy. *Curr Opin Biotechnol.* (2019) 60:138–45. doi: 10.1016/j.copbio.2019.01.010
17. Cen X, Liu S, Cheng K. The role of Toll-like receptor in inflammation and tumor immunity. *Front Pharmacol.* (2018) 9:1–8. doi: 10.3389/fphar.2018.00878
18. Iribarren K, Bloy N, Buqué A, Cremer I, Eggermont A, Fridman WH, et al. Trial watch: immunostimulation with Toll-like receptor agonists in cancer therapy. *Oncoimmunology.* (2016) 5:e1088631. doi: 10.1080/2162402X.2015.1088631
19. Shime H, Matsumoto M, Oshiumi H, Tanaka S, Nakane A, Iwakura Y, et al. Toll-like receptor 3 signaling converts tumor-supporting myeloid cells to tumoricidal effectors. *Proc Natl Acad Sci USA.* (2012) 109:2066–71. doi: 10.1073/pnas.1113099109
20. Engel AL, Holt GE, Lu H. The pharmacokinetics of Toll-like receptor agonists and the impact on the immune system. *Expert Rev Clin Pharmacol.* (2011) 4:275–89. doi: 10.1586/ecp.11.5
21. Hafner AM, Corthésy B, Merkle HP. Particulate formulations for the delivery of poly(I:C) as vaccine adjuvant. *Adv Drug Deliv Rev.* (2013) 65:1386–99. doi: 10.1016/j.addr.2013.05.013
22. Milling L, Zhang Y, Irvine DJ. Delivering safer immunotherapies for cancer. *Adv Drug Deliv Rev.* (2017) 114:79–101. doi: 10.1016/j.addr.2017.05.011
23. Kroschinsky F, Stölzel F, von Bonin S, Beutel G, Kochanek M, Kiehl M, et al. New drugs, new toxicities: severe side effects of modern targeted and immunotherapy of cancer and their management. *Crit Care.* (2017) 21:89. doi: 10.1186/s13054-017-1678-1
24. Dajon M, Iribarren K, Cremer I. Toll-like receptor stimulation in cancer: a pro- and anti-tumor double-edged sword. *Immunobiology.* (2017) 222:89–100. doi: 10.1016/j.imbio.2016.06.009
25. Riley RS, June CH, Langer R, Mitchell MJ. Delivery technologies for cancer immunotherapy. *Nat Rev Drug Discov.* (2019) 18:175–96. doi: 10.1038/s41573-018-0006-z
26. Nordly P, Rose F, Christensen D, Nielsen HM, Andersen P, Agger EM, et al. Immunity by formulation design: induction of high CD8+ T-cell responses by poly(I:C) incorporated into the CAF01 adjuvant via a double emulsion method. *J Control Release.* (2011) 150:307–17. doi: 10.1016/j.jconrel.2010.11.021
27. Correia-Pinto JF, Csaba N, Schiller J, Alonso MJ. Chitosan-poly (I:C)-PADRE based nanoparticles as delivery vehicles for synthetic peptide vaccines. *Vaccines.* (2015) 3:730–50. doi: 10.3390/vaccines3030730
28. Han HD, Byeon Y, Jang J-H, Jeon HN, Kim GH, Kim MG, et al. *In vivo* stepwise immunomodulation using chitosan nanoparticles as a platform nanotechnology for cancer immunotherapy. *Sci Rep.* (2016) 6:38348. doi: 10.1038/srep38348
29. Cobaleda-Siles M, Henriksen-Lacey M, de Angulo AR, Bernecker A, Vallejo VG, Szczupak B, et al. An iron oxide nanocarrier for dsRNA to target lymph nodes and strongly activate cells of the immune system. *Small.* (2014) 10:5054–67. doi: 10.1002/smll.201470156
30. Schau I, Michen S, Hagstotz A, Janke A, Schackert G, Appelhans D, et al. Targeted delivery of TLR3 agonist to tumor cells with single chain antibody fragment-conjugated nanoparticles induces type I-interferon response and apoptosis. *Sci Rep.* (2019) 9:1–5. doi: 10.1038/s41598-019-40032-8
31. Kauffman KJ, Webber MJ, Anderson DG. Materials for non-viral intracellular delivery of messenger RNA therapeutics. *J Control Release.* (2016) 240:227–34. doi: 10.1016/j.jconrel.2015.12.032
32. Buck J, Grossen P, Cullis PR, Huwyler J, Witzigmann D. Lipid-based DNA therapeutics: hallmarks of non-viral gene delivery. *ACS Nano.* (2019) 13:3754–82. doi: 10.1021/acsnano.8b07858
33. Xiong Q, Lee GY, Ding J, Li W, Shi J. Biomedical applications of mRNA nanomedicine. *Nano Res.* (2018) 11:5281–309. doi: 10.1007/s12274-018-2146-1
34. Aznar MA, Planelles L, Perez-Olivares M, Molina C, Garasa S, Etxeberría I, et al. Immunotherapeutic effects of intratumoral nanoplexed poly I:C. *J Immunother Cancer.* (2019) 7:116. doi: 10.1186/s40425-019-0568-2
35. *Exploratory Study of BO-112 in Adult Patients With Aggressive Solid Tumors*. (2016). Available online at: https://clinicaltrials.gov/ct2/show/NCT02828098 (accessed January 9, 2020).
36. Chollet P, Favrot MC, Hurbin A, Coll J-L. Side-effects of a systemic injection of linear polyethylenimine-DNA complexes. *J Gene Med.* (2002) 4:84–91. doi: 10.1002/jgm.237

37. Torchilin VP. Cell penetrating peptide-modified pharmaceutical nanocarriers for intracellular drug and gene delivery. *Biopolymers.* (2008) 90:604–10. doi: 10.1002/bip.20989
38. Reimondez-Troitiño S, González-Aramundiz J V., Ruiz-Bañobre J, López-López R, Alonso MJ, Csaba N, et al. Versatile protamine nanocapsules to restore miR-145 levels and interfere tumor growth in colorectal cancer cells. *Eur J Pharm Biopharm.* (2019) 142:449–59. doi: 10.1016/j.ejpb.2019.07.016
39. Ledo AM, Sasso MS, Bronte V, Marigo I, Boyd BJ, Garcia-Fuentes M, et al. Co-delivery of RNAi and chemokine by polyarginine nanocapsules enables the modulation of myeloid-derived suppressor cells. *J Control Release.* (2019) 295:60–73. doi: 10.1016/j.jconrel.2018.12.041
40. Samaridou E, Walgrave H, Salta E, Álvarez DM, Castro-López V, Loza M, Alonso MJ. Nose-to-brain delivery of enveloped RNA - cell permeating peptide nanocomplexes for the treatment of neurodegenerative diseases. *Biomaterials.* (2020) 230:119657. doi: 10.1016/j.biomaterials.2019.119657
41. Kawai T, Akira S. The role of pattern-recognition receptors in innate immunity: update on Toll-like receptors. *Nat Immunol.* (2010) 11:373–84. doi: 10.1038/ni.1863
42. Tran S, DeGiovanni P-J, Piel B, Rai P. Cancer nanomedicine: a review of recent success in drug delivery. *Clin Transl Med.* (2017) 6:44. doi: 10.1186/s40169-017-0175-0
43. Sindhwani S, Syed AM, Ngai J, Kingston BR, Maiorino L, Rothschild J, et al. The entry of nanoparticles into solid tumours. *Nat Mater.* (2020) 19:566–75. doi: 10.1038/s41563-019-0566-2
44. Goldberg MS. Improving cancer immunotherapy through nanotechnology. *Nat Rev Cancer.* (2019) 19:587–602. doi: 10.1038/s41568-019-0186-9
45. Lächelt U, Wagner E. Nucleic acid therapeutics using polyplexes: a journey of 50 years (and beyond). *Chem Rev.* (2015) 115:11043–78. doi: 10.1021/cr5006793
46. Borrajo E, Abellan-Pose R, Soto A, Garcia-Fuentes M, Csaba N, Alonso MJ, et al. Docetaxel-loaded polyglutamic acid-PEG nanocapsules for the treatment of metastatic cancer. *J Control Release.* (2016) 238:263–71. doi: 10.1016/j.jconrel.2016.07.048
47. Abellan-Pose R, Rodríguez-Évora M, Vicente S, Csaba N, Évora C, Alonso MJ, Delgado A. Biodistribution of radiolabeled polyglutamic acid and PEG-polyglutamic acid nanocapsules. *Eur J Pharm Biopharm.* (2017) 112:155–63. doi: 10.1016/j.ejpb.2016.11.015
48. Perry JL, Reuter KG, Kai MP, Herlihy KP, Jones SW, Luft JC, et al. PEGylated PRINT nanoparticles: the impact of PEG density on protein binding, macrophage association, biodistribution, and pharmacokinetics. *Nano Lett.* (2012) 12:5304–10. doi: 10.1021/nl302638g
49. Bertrand N, Grenier P, Mahmoudi M, Lima EM, Appel EA, Dormont F, et al. Mechanistic understanding of *in vivo* protein corona formation on polymeric nanoparticles and impact on pharmacokinetics. *Nat Commun.* (2017) 8:777. doi: 10.1038/s41467-017-00600-w
50. Peer D, Margalit R. Loading mitomycin C inside long circulating hyaluronan targeted nano-liposomes increases its antitumor activity in three mice tumor models. *Int J Cancer.* (2004) 108:780–89. doi: 10.1002/ijc.11615
51. Choi KY, Min KH, Na JH, Choi K, Kim K, Park JH, et al. Self-assembled hyaluronic acid nanoparticles as a potential drug carrier for cancer therapy: synthesis, characterization, and *in vivo* biodistribution. *J Mater Chem.* (2009) 19:4102. doi: 10.1039/b900456d
52. Yang X, Li Y, Li M, Zhang L, Feng L, Zhang N. Hyaluronic acid-coated nanostructured lipid carriers for targeting paclitaxel to cancer. *Cancer Lett.* (2013) 334:338–45. doi: 10.1016/j.canlet.2012.07.002
53. Teijeiro-Valiño C, Novoa-Carballal R, Borrajo E, Vidal A, Alonso-Nocelo M, de la Fuente Freire M, et al. A multifunctional drug nanocarrier for efficient anticancer therapy. *J Control Release.* (2019) 294:154–64. doi: 10.1016/j.jconrel.2018.12.002
54. Miller MA, Zheng Y-R, Gadde S, Pfirschke C, Zope H, Engblom C, et al. Tumour-associated macrophages act as a slow-release reservoir of nano-therapeutic Pt(IV) pro-drug. *Nat Commun.* (2015) 6:8692. doi: 10.1038/ncomms9692
55. Dai Q, Wilhelm S, Ding D, Syed AM, Sindhwani S, Zhang Y, et al. Quantifying the ligand-coated nanoparticle delivery to cancer cells in solid tumors. *ACS Nano.* (2018) 12:8423–35. doi: 10.1021/acsnano.8b03900
56. Endoh T, Ohtsuki T. Cellular siRNA delivery using cell-penetrating peptides modified for endosomal escape. *Adv Drug Deliv Rev.* (2009) 61:704–9. doi: 10.1016/j.addr.2009.04.005
57. Li Y, Li Y, Wang X, Lee RJ, Teng L. Fatty acid modified octa-arginine for delivery of siRNA. *Int J Pharm.* (2015) 495:527–35. doi: 10.1016/j.ijpharm.2015.09.006
58. Sun C, Tang T, Uludag H. A molecular dynamics simulation study on the effect of lipid substitution on polyethylenimine mediated siRNA complexation. *Biomaterials.* (2013) 34:2822–33. doi: 10.1016/j.biomaterials.2013.01.011
59. Pärnaste L, Arukuusk P, Langel K, Tenson T, Langel Ü. The formation of nanoparticles between small interfering RNA and amphipathic cell-penetrating peptides. *Mol Ther Nucleic Acids.* (2017) 7:1–10. doi: 10.1016/j.omtn.2017.02.003
60. Gary DJ, Puri N, Won Y-Y. Polymer-based siRNA delivery: perspectives on the fundamental and phenomenological distinctions from polymer-based DNA delivery. *J Control Release.* (2007) 121:64–73. doi: 10.1016/j.jconrel.2007.05.021
61. Samaridou E, Kalamidas N, Santalices I, Crecente-Campo J, Alonso MJ. Tuning the PEG surface density of the PEG-PGA enveloped octaarginine-peptide nanocomplexes. *Drug Deliv Transl Res.* (2020) 10:241–58. doi: 10.1007/s13346-019-00678-3
62. Santander-Ortega MJ, Jódar-Reyes AB, Csaba N, Bastos-González D, Ortega-Vinuesa JL. Colloidal stability of pluronic F68-coated PLGA nanoparticles: a variety of stabilisation mechanisms. *J Colloid Interface Sci.* (2006) 302:522–9. doi: 10.1016/j.jcis.2006.07.031
63. Niu Z, Samaridou E, Jaumain E, Coëne J, Ullio G, Shrestha N, et al. PEG-PGA enveloped octaarginine-peptide nanocomplexes: an oral peptide delivery strategy. *J Control Release.* (2018) 276:125–39. doi: 10.1016/j.jconrel.2018.03.004
64. Almalik A, Benabdelkamel H, Masood A, Alanazi IO, Alradwan I, Majrashi MA, et al. Hyaluronic acid coated chitosan nanoparticles reduced the immunogenicity of the formed protein corona. *Sci Rep.* (2017) 7:1–9. doi: 10.1038/s41598-017-10836-7
65. Correa S, Boehnke N, Deiss-Yehiely E, Hammond PT. Solution conditions tune and optimize Loading of therapeutic polyelectrolytes into layer-by-layer functionalized liposomes. *ACS Nano.* (2019) 13:5623–34. doi: 10.1021/acsnano.9b00792
66. Verdurmen WPR, Brock R. Biological responses towards cationic peptides and drug carriers. *Trends Pharmacol Sci.* (2011) 32:116–24. doi: 10.1016/j.tips.2010.11.005
67. Dacoba TG, Olivera A, Torres D, Crecente-Campo J, Alonso MJ. Modulating the immune system through nanotechnology. *Semin Immunol.* (2017) 34:78–102. doi: 10.1016/j.smim.2017.09.007
68. Qie Y, Yuan H, von Roemeling CA, Chen Y, Liu X, Shih KD, et al. Surface modification of nanoparticles enables selective evasion of phagocytic clearance by distinct macrophage phenotypes. *Sci Rep.* (2016) 6:26269. doi: 10.1038/srep26269
69. Liu B, Liu Q, Yang L, Palaniappan SK, Bahar I, Thiagarajan PS, et al. Innate immune memory and homeostasis may be conferred through crosstalk between the TLR3 and TLR7 pathways. *Sci Signal.* (2016) 9:ra70. doi: 10.1126/scisignal.aac9340
70. Ning S, Pagano JS, Barber GN. IRF7: activation, regulation, modification and function. *Genes Immun.* (2011) 12:399–414. doi: 10.1038/gene.2011.21
71. Franciszkiewicz K, Boissonnas A, Boutet M, Combadiere C, Mami-Chouaib F. Role of chemokines and chemokine receptors in shaping the effector phase of the antitumor immune response. *Cancer Res.* (2012) 72:6325–32. doi: 10.1158/0008-5472.CAN-12-2027
72. Arango Duque G, Descoteaux A. Macrophage cytokines: involvement in immunity and infectious diseases. *Front Immunol.* (2014) 5:1–12. doi: 10.3389/fimmu.2014.00491

73. Singh M, Khong H, Dai Z, Huang X-F, Wargo JA, Cooper ZA, et al. Effective innate and adaptive antimelanoma immunity through localized TLR7/8 activation. *J Immunol.* (2014) 193:4722–31. doi: 10.4049/jimmunol.1401160

Conflict of Interest: The authors declare that the research was conducted in the absence of any commercial or financial relationships that could be construed as a potential conflict of interest.

frontiers in Immunology

ORIGINAL RESEARCH
published: 21 July 2020
doi: 10.3389/fimmu.2020.01547

Rational Design of Antigen Incorporation Into Subunit Vaccine Biomaterials Can Enhance Antigen-Specific Immune Responses

*Alexandra N. Tsoras, Kong M. Wong, Anant K. Paravastu and Julie A. Champion**

School of Chemical & Biomolecular Engineering, Atlanta, GA, United States

Peptide subunit vaccines increase safety by reducing the risk of off-target responses and improving the specificity of the induced adaptive immune response. The immunogenicity of most soluble peptides, however, is often insufficient to produce robust and lasting immunity. Many biomaterials and delivery vehicles have been developed for peptide antigens to improve immune response while maintaining specificity. Peptide nanoclusters (PNC) are a subunit peptide vaccine material that has shown potential to increase immunogenicity of peptide antigens. PNC are comprised only of crosslinked peptide antigen and have been synthesized from several peptide antigens as small as 8 amino acids in length. However, as with many peptide vaccine biomaterials, synthesis requires adding residues to the peptide and/or engaging amino acids within the antigen epitope covalently to form a stable material. The impact of antigen modifications made to enable biomaterial incorporation or formation is rarely investigated, since the goal of most studies is to compare the soluble antigen with biomaterial form of antigen. This study investigates PNC as a platform vaccine biomaterial to evaluate how peptide modification and biomaterial formation with different crosslinking chemistries affect epitope-specific immune cell presentation and activation. Several types of PNC were synthesized by desolvation from the model peptide epitope SIINFEKL, which is derived from the immunogenic protein ovalbumin. SIINFEKL was altered to include extra residues on each end, strategically chosen to enable multiple conjugation chemistry options for incorporation into PNC. Several crosslinking methods were used to control which functional groups were used to stabilize the PNC, as well as the reducibility of the crosslinking. These variations were evaluated for immune responses and biodistribution following *in vivo* immunization. All modified antigen formulations still induced comparable immune responses when incorporated into PNC compared to unmodified soluble antigen alone. However, some crosslinking methods led to a significant increase in desirable immune responses while others did not, suggesting that not all PNC were processed the same. These results help guide future peptide vaccine biomaterial design, including PNC and a wide variety of conjugated and self-assembled peptide antigen materials, to maximize and tune the desired immune response.

Keywords: peptides, nanoparticles, crosslinking, biomaterials, subunit vaccines, immune cell processing, T cell activation

OPEN ACCESS

Edited by:
Li Tang,
École Polytechnique Fédérale de Lausanne, Switzerland

Reviewed by:
Haijun Yu,
Chinese Academy of Sciences, China
Carole Bourquin,
Université de Genève, Switzerland

****Correspondence:***
Julie A. Champion
julie.champion@chbe.gatech.edu

Specialty section:
This article was submitted to Cancer Immunity and Immunotherapy, a section of the journal Frontiers in Immunology

Received: *01 April 2020*
Accepted: *11 June 2020*
Published: *21 July 2020*

Citation:
Tsoras AN, Wong KM, Paravastu AK and Champion JA (2020) Rational Design of Antigen Incorporation Into Subunit Vaccine Biomaterials Can Enhance Antigen-Specific Immune Responses. Front. Immunol. 11:1547. doi: 10.3389/fimmu.2020.01547

INTRODUCTION

There are many challenges associated with currently available vaccines, including safety concerns, lack of specificity, and absence of protection against heterogenous pathogenic strains (1, 2). Subunit vaccines are a promising solution that address many of these issues. However, they tend to lack comparable immunogenicity to whole pathogen vaccines and often require multiple boosts and adjuvants (3, 4). Peptides are among the smallest antigenic subunits that can be used as vaccines. Specific sequences in an antigenic protein capable of binding immune cell receptors, known as peptide epitopes, can be identified using a variety of advanced analytical techniques (5–10). These peptides can be administered as vaccines to induce proliferation and differentiation of antigen-specific immune cells for future protection against pathogens containing this antigenic peptide sequence (10).

To increase the immunogenic response to small proteins and peptides, they are often conjugated to or incorporated into other proteins and/or biomaterials (11). Although there are some biomaterials that can encapsulate or adsorb unmodified proteins and peptides (12–14), they can also induce immune responses to the material itself (15–19), or induce tolerance to antigens if a delivery material is used multiple times (20). Therefore, it is beneficial for vaccine formulations to minimize delivery of material that is not the target antigen. Vaccine biomaterials in development must balance the minimization of non-target antigen delivery with antigen modifications necessary to incorporate or form into a biomaterial. Many materials address this challenge by utilizing engineering design to induce structurally ordered, hydrophobically assembled, or electrostatically assembled materials made of mostly a target antigen or an altered variant of it (21–27). Covalent or sequence modification of the antigen is often required to enable its stable incorporation into a material. For large protein antigens, modification may have little effect on specific antigenic epitopes. However, for smaller peptides, modification is more likely to affect the characteristics of the peptide, both physicochemical and antigenic.

Non-biodegradable conjugation or sequence modifications are a potential concern regarding the processing and presentation of the peptides by antigen presenting cells (APCs). Peptide antigens are usually the minimum length that APCs can present to other immune cells on surface-presenting proteins, major histocompatibility complex I, or II (MHC I or MHC II) (28, 29). MHC I proteins present intracellular antigens, and are more restrictive in what length of peptides they are able to present. MHC II proteins present extracellular antigens, and, while less restrictive, still have limits in the length of peptide that can be presented (30). Similarly, peptide length is likely to affect the affinity and specificity of attachment to a T or B cell receptor and, ultimately, activation and proliferation of those cells (31, 32). If modified peptide antigens are cleaved to remove part of the epitope sequence while the modifications remain, or residues are altered to the point that the peptide cannot attach to MHC molecules, the peptides will not be able to activate antigen-specific immune cells or induce protection (31, 33). Similarly, if covalent conjugation chemistry disables the ability of APCs to break down peptides into presentable minimal epitopes, the peptides will not be presented.

Peptide nanoclusters (PNC) are vaccine biomaterials designed to completely eliminate carrier materials or self-assembly sequences and, therefore, avoid off target immune responses. PNC are formed by desolvation of peptide antigens and crosslinking into stabilized clusters in suspension (27). This process can be tuned for many different peptides with different characteristics by choosing optimal desolvation conditions for each peptide to yield nanoclusters in a desired size range. Protein nanoclusters are synthesized the same way, but with larger proteins, and have demonstrated the ability to increase the potency and breadth of immune responses (34, 35). PNC allow for comparatively more specific target antigen delivery. However, their small size and limited amino acid diversity lead to the aforementioned antigen incorporation challenges. A key factor that affects PNC formation and stability is the availability of residues with reactive groups that can be used for crosslinking. While residues in the minimal epitope sequence could be used, crosslinking these residues could compromise peptide processing and presentation by APCs or recognition by T or B cell receptors. Furthermore, every peptide epitope has a different sequence, and each new antigen may require different crosslinking mechanisms depending on the available amino acids. Some epitopes may have too few or no reactive groups that could be used for crosslinking. It would be beneficial to be able to apply a standard modification to each antigen that eliminates the dependence on the antigen sequence for reactive groups to crosslink. Such a modification would provide available reactive groups outside of the minimal epitope, ideally orthogonal from those inside the minimal epitope, that can be used to crosslink and stabilize PNC. There are also different types of crosslinking mechanisms that may affect cellular breakdown of particles, which could affect processing and presentation.

To our knowledge, a systematic evaluation of how peptide modifications and crosslinking chemistry for biomaterial synthesis affect immune cell responses to the desired antigen has not been performed. To address this gap, a model epitope, SIINFEKL, derived from the model protein antigen, ovalbumin, was modified for incorporation into PNC. PNC were synthesized by desolvation using several crosslinking methods for different modes of biomaterial incorporation. With multiple formulations of PNC containing the SIINFEKL epitope, we evaluated how the peptide modifications and different PNC crosslinking schemes affected the strength and type of immune response to SIINFEKL. Differences in dendritic cell maturation and antigen presentation, T cell activation, and biodistribution of PNC were observed.

MATERIALS AND METHODS

Materials and Animals

Peptides (SFK: SIINFEKL, SLS: GKCSIINFEKLCKG) were purchased from Genscript at >95% purity. Tetramethylrhodamine (TAMRA)-labeled versions of the

above peptides were purchased from Biomatik at >99% purity with TAMRA conjugated to an additional C-terminal lysine. Trimethylolpropane tris(3-mercaptopropionate) (tri-thiol) crosslinker was purchased from Sigma. Tris(2-maleimidoethyl)amine (tri-maleimide) and tris-(succinimidyl)aminotriacetate (tri-NHS) were purchased from ThermoFisher.

Six to eight week old C57BL/6 mice were purchased from Jackson Laboratories and kept in the Physiological Research Laboratory at Georgia Institute of Technology. Mice were fed a standard diet during all studies except for biodistribution studies, in which they were given an alfalfa-free diet to reduce background fluorescence during imaging. All procedures and care were carried out according to regulations and guidelines approved by the Georgia Institute of Technology Institutional Animal Care and Use Committee (Protocol A100259).

Nanocluster Synthesis

All PNC were synthesized using desolvation with conditions tuned for the characteristics of each peptide and crosslinker combination. The general process remained the same for all variations, and conditions specific to each PNC variation are described in the (**Supplementary Table 1**). All peptides were solubilized in hexafluoroisopropanol (HFIP) at 2.5 mg/ml, and 100 μl was added to a 6 ml glass vial. Safety note: HFIP is a hazardous chemical with acute oral, dermal, and vapor inhalation toxicity. All handling was conducted with proper personal protective equipment. Under constant stirring at 400 rpm with a 1 cm stir bar, the desired crosslinker was added at the indicated amount. A specific volume of diethyl ether (DEE) was then added at a rate of 1 ml/min with a syringe pump. The solution reacted under constant mixing for the indicated amount of time for crosslinking stabilization to occur. The solution was then transferred to a centrifuge tube and centrifuged at 18,000 g for 7 min. The supernatant was removed, and the pellet resuspended in water at 1 mg/ml. To ensure full resuspension, the solutions were sonicated with a probe 3–4 times for 1 s on/1 s off at 60% strength. For fluorescent versions of each particle type, 10% TAMRA-labeled SLS was added to the initial peptide solution.

Nanoparticle Characterization

The size and polydispersity (PDI) of PNC were determined by dynamic light scattering (DLS) (Malvern Zetasizer Nano ZS). To ensure stability during storage in Milli-Q® (MQ) water at 4°C, multiple measurements were taken over several days starting at Day 0 immediately after synthesis. Measurement settings are listed in (**Supplementary Table 2**). At least 10 batches for each PNC type were synthesized and size and PDI measured to ensure reproducibility.

Yield of PNC synthesis batches were measured with quantitative 1D ^{1}H nuclear magnetic resonance (NMR) spectra of resuspended PNC. Particles from each synthesis batch were centrifuged as previously described, and the pellet was allowed to dry overnight in a fume-hood to ensure complete removal of HFIP and DEE. Dried PNC were resuspended in a 200 μl solution of deuterated DMSO (Cambridge Isotope Libraries, Inc.) and 10 mM maleic acid (Alfa Aesar). Maleic acid served as an internal standard for ^{1}H NMR intensity. All ^{1}H spectra were collected on an 18.8 T Bruker Avance III HD NMR with a 3 mm HCN CryoProbe. The relaxation delay (d1) was set to 20 s to ensure complete spin relaxation, and the pulse width was programmed for 30° pulses (36, 37). Peaks in ^{1}H NMR spectra were fit using custom code in Wolfram Mathematica and compared to standard solutions to determine the amount of peptide within PNC batches.

In vivo Immunization and Immunological Assays

For immune response study, 6–8 week old C57/BL16 mice (N = 6, 50% female, 50% male) were injected intradermally in each forearm with 30 μl (60 μl total) of 1 mM soluble SIINFEKL, soluble SIINFEKL + 10 mM Poly(I:C) low molecular weight (LMW) adjuvant (Invitrogen), SLS-T PNC, SLS-M PNC, or SLS-N PNC. Three additional mice (2 female, 1 male) were injected with saline as a control. Mice in each group were then boosted with a half dose (15 μl in each forearm) on Day 7 and Day 14. On Day 16, mice were sacrificed and axillary and brachial lymph nodes on both sides and spleens were harvested.

Lymphocytes and splenocytes were obtained by gently breaking up tissues in PBS and straining through a 70 μm cell strainer. Pooled lymph node or spleen cells were washed with 15–20 ml PBS and centrifuged at 4°C, 350 g for 5 min. Spleen cells were resuspended in 1 ml 1X RBC lysis buffer (150 mM ammonium chloride, 10 mM sodium bicarbonate, 1.27 mM EDTA) and incubated for 5–10 min on ice. Lysis was then quenched with 10 ml PBS and spleen cells were centrifuged again at 4°C, 350 g for 5 min. All cells were suspended in PBS and divided for surface marker staining or re-stimulation. Cells used for re-stimulation were centrifuged in a round-bottom 96 well-plate at 4°C, 350 g for 5 min and resuspended in 100 μl culture media (RPMI 1640 + L-glutamine + 25 mM 4-(2-hydroxyethyl)-1-piperazineethanesulfonic acid (HEPES) supplemented with 10% heat inactivated fetal bovine serum and 1% penicillin/streptomycin) with 10^6 cells/well. Media was also supplemented with 1 mg/ml SIINFEKL for 6 h for re-stimulation. For the last 3 h of culture, 1X brefeldin A (Biolegend) was added to the wells. After re-stimulation, cells were stained according to the procedures below.

Cells were stained for DC surface markers, T cell surface markers, or intracellular cytokines according to the following protocol. Cells in a round-bottom 96 well-plate, either in PBS from original organ harvest or culture medium from re-stimulation culture, were centrifuged at 4°C, 350 g for 5 min and resuspended in 100 μl PBS premixed with 5 μl/ml Trustain FcX blocking solution (Biolegend). Cells were incubated for 10 min on ice. Cells were centrifuged again and stained with Zombie Violet or Zombie Aqua Fixable Viability Kit (Biolegend) for 30 min according to manufacturer protocols. Cells were centrifuged and washed with 100 μl sterile 1% bovine serum albumin (BSA) in PBS. Cells were centrifuged and suspended in staining solution for 30 min on ice. Cell staining solution was made for each staining panel by adding all antibody stains to 1% BSA in PBS and then adding directly to wells at 100

μl/well. DCs were stained for CD11c (APC/Cy7, 2.5 μl/well), H-2Kb-SIINFEKL (APC, 1 μl/well), CD86 (PE, 2.5 μl/well) (Biolegend), and MHC II (FITC, 0.5 μl/well) (eBioscience). T cells were stained for CD3 (PerCP, 1 μl/well), CD8 (FITC, 0.313 μl/well), CD4 (APC/Cy7, 0.156 μl/well) (Biolegend), and CD69 (APC, 2 μl/well) (Southern Biotech). After staining, cells were washed with 1% BSA in PBS, centrifuged, and fixed with 100 μl 3.7% formaldehyde in PBS for 45 min on ice. Surface-stained T cells and DCs were centrifuged and resuspended in 200 μl 1% BSA in PBS and stored at 4°C until flow cytometry analysis. If intracellular cytokine staining was performed, cells were centrifuged after fixation in the plate and resuspended in 100 μl permeabilization buffer (eBioscience) with intracellular cytokine staining antibodies anti-IFN-γ (PE, 1.5 μl/well) and anti-TNF-α (PE/Cy7, 1.5 μl/well) (Biolegend), and incubated for 45 min on ice. These cells were then centrifuged in the plate, washed with 100 μl 1% BSA in PBS, and resuspended in 200 μl 1% BSA in PBS for storage at 4°C until flow cytometry analysis. Flow cytometry was performed with a BD LSR Fortessa, with up to 3,000,000 lymphocyte events collected (ensuring all data was collected from 150 μl volume run). Data was analyzed with Flow Jo using the gating strategies shown in **Supplementary Figures 1–3**.

Biodistribution

Six to eight week old mice were injected intradermally in each forearm with 30 μl (60 μl total) of 1 mM soluble SIINFEKL (10% TAMRA-labeled) or SLS-T (10% TAMRA-labeled). Mice were split into three end point groups: 4, 24, or 72 h ($N = 4$, 50% female, 50% male). For each group, mice were fluorescently imaged (IVIS Spectrum CT) under anesthesia, and then sacrificed at the indicated time point. Two additional mice were injected with 30 μl saline in each forearm (60 μl total) and sacrificed at 4 h to serve as controls. After sacrifice, axillary and brachial lymph nodes and spleens were harvested, imaged in IVIS Spectrum CT, and then placed into vials with 1.4 mm acid washed zirconium grinding beads (VWR). Lymph nodes were pooled into the same vial with 200 μl PBS, and spleens were placed in vial with 500 μl PBS. Organs were homogenized for 1 min in a FastPrep-24 Automated Homogenizer (MP Biomedicals) 0.150 μl of homogenate in PBS from each mouse's pooled lymph nodes or spleens were added to a 96-well-plate and analyzed for fluorescence using 557/583 nm excitation and emission reading on a plate reader (BioTek Synergy H4 Microplate Reader).

Statistical Methods

All statistical comparisons made between groups in this manuscript were performed using an unmatched ordinary one-way ANOVA comparison. Tukey's *post-hoc* multiple comparison analysis was performed to compare differences between each group. This analysis was performed using Graphpad Prism software (V8.4). Each group comparison with a $p < 0.05$ were considered significantly different from one another. Statistical differences exist between groups labeled with different letters. Groups that share the same letter are not statistically different from each other.

RESULTS

SIINFEKL Modification and Nanocluster Synthesis

Protein and peptide nanocluster synthesis via desolvation and crosslinking has been demonstrated for a number of different antigens (34, 38–40). In this study, a strategic peptide modification was applied to the model epitope SIINFEKL, a well-studied MHC I epitope derived from the protein antigen ovalbumin. The new peptide, named strategically lengthened SIINFEKL (SLS), contains the SIINFEKL sequence with the addition of Gly-Lys-Cys to the N-terminus and Cys-Lys-Gly to the C-terminus (GKCSIINFEKLCKG). This design keeps the minimal epitope in the middle of the sequence, releasable by proteolytic cleavage at the cysteines, while enabling PNC crosslinking via multiple cysteines or lysines using thiol-reactive or amine-reactive crosslinkers. Lysines and cysteines were chosen as flanking residues to enable several forms of crosslinking for stabilization without dependence on minimal epitope residues. In this study, SIINFKEL represented a case where one of the flanking modifications (cysteine) had orthogonal reactivity to the epitope, and one (lysine) did not. The glycines were added as non-reactive, water-soluble residues to increase the length and decrease the likelihood that SLS could be loaded onto MHC I without proteolytic cleavage. Peptides larger than 10 amino acids do not bind to the MHC I loading pocket well (30, 32). To evaluate potential differences in how PNC are processed into minimum peptide epitopes, three different crosslinking mechanisms were used to stabilize PNC after desolvation. Trimethylolpropane tris-3(mercaptopropionate) (tri-thiol) is a homo-trifunctional crosslinker that reacts with thiols to create disulfide bonds. Tris(2-maleimidoethyl)amine (tri-maleimide) also reacts with thiols, creating thioether bonds. Tri-thiol is reducibly reversible and tri-maleimide is not (41, 42). However, both crosslinkers react with cysteines in SLS outside of the minimum epitope, ensuring that any crosslinked residues would be removed after proteolytic cleavage into the minimal SIINFEKL epitope. Tris-(succinimidyl)aminotriacetate (tri-NHS) is a tri-functional amine-reactive crosslinker, and forms non-reducible amide bonds with lysines and the terminal amine in SLS. Tri-NHS can also react with the lysine within SIINFEKL, which could hinder the ability of the peptide to be presented or to bind T cell receptors. However, lysine has been shown not to be an important anchor residue in binding MHC I for effective SIINFEKL presentation (30, 33) and since Tri-NHS forms an amide bond, it is possible for it to be cleaved proteolytically (43). Trifunctional crosslinkers were chosen instead of bifunctional to maximize the amount of crosslinking and increase the likelihood of a fully entangled and stabilized nanocluster.

SLS PNC were synthesized by desolvation using tri-thiol (SLS-T), tri-maleimide (SLS-M), and tri-NHS (SLS-N) crosslinkers. Although each of these PNC were formed from the same modified SIINFEKL peptide antigen, utilizing different crosslinkers required slight alteration of desolvation conditions to achieve comparable size, PDI, and stability. **Table 1** reports particle size and polydispersity index (PDI), which ranged from 184 to 233 nm and 0.189–0.232, respectively (*n*

= 10 per PNC type). PNC stability in water at 4°C was evaluated by measuring size over time. Size and PDI remained consistent over several days to weeks as demonstrated by DLS size distributions in **Figure 1**, so it was expected that changes in size or structure would mainly be due to changing conditions *in vivo*, such as interactions with extracellular proteins or intracellular processing. Size was confirmed and roughly spherical morphology of PNC was observed by Transmission Electron Microscopy (TEM) (**Supplementary Figure 4**).

Based on the design of each PNC, SLS-N, and SLS-M particles would likely need to be broken up inside cells proteolytically, whereas the reducing environments inside endo/lysosomes may break up SLS-T PNC. Upon incubating PNC with reducing agents β-mercaptoethanol and DTT, however, it was observed that SLS-T PNC only began to show instability after 24 h incubation with DTT at 37°C (**Supplementary Figure 5**). Incubation with β-mercaptoethanol for the same time period and temperature did not induce particle instability nor did room temperature incubation with DTT. These results imply that SLS-T PNC are highly crosslinked with disulfide bonds that may have limited accessibility that only allows gradual reducibility. Additionally, SLS-M PNC also showed signs of slight instability with 37°C incubation with DTT. Although thioether bonds are considered non-reducible, maleimide reactions have shown reversibility in some cases (44, 45). SLS-N PNC were unaffected by reducing agents in any conditions and remained stable in size and PDI. This result confirmed that SLS-N PNC were the most likely to require proteolytic cleavage to enable breakup into the minimal epitope.

The yield of SLS peptide incorporated into PNC during the desolvation process was determined to be ∼79% for SLS-T, SLS-M, and SLS-N PNC synthesis from measuring three different batches of each PNC (**Table 1**). These results highlight the consistency of PNC produced by desolvation independent of crosslinking chemistry. Yields were determined by NMR peak integration of ^{1}H NMR spectra of PNC resuspended in deuterated DMSO. Peaks around 7.2 ppm were uniquely assigned to the aromatic protons of the phenylalanine sidechain in the SLS peptide (46). By comparing the peak areas in resuspended PNC solutions to a standard solution of unassembled SLS peptide, the total mass of peptide was calculated. The synthesis yield was determined based on comparison to the amount of soluble peptide in the solvent before desolvation. Peak shapes of aromatic protons of the phenylalanine sidechain in all three types of SLS PNC matched those of the unassembled SLS peptide (**Supplementary Figure 6**). This alignment suggests the crosslinked peptide was well-solvated in DMSO, preventing spin relaxation effects. We also note that large macromolecular assemblies typically exhibit increased peak linewidths due to slower tumbling, complicating quantitative analysis of chemical shift peak areas (47). However, swelling of SLS PNC in DMSO, as indicated by the increase in particle size measured by DLS (**Supplementary Figure 7**), likely enhanced the mobility of the amino acid sidechains. This solvation of the peptide particles is consistent with a prior molecular dynamics study of α-helical transmembrane peptides where DMSO solvated both hydrophilic and hydrophobic residue sidechains (48). Similar high-resolution quantitative NMR measurements are commonly performed on swollen polymer systems and microplastic particles (49–52). Standard methods of peptide quantification including absorbance and mass spectrometry required large amounts of processing including separation and solvent exchange, which proved challenging and increased measurement error. ^{1}H NMR spectroscopy quantified peptide incorporation yields accurately and quickly without the need for separation or extensive processing steps.

TABLE 1 | Size, polydispersity, and yield of different SLS PNC formulations.

PNC	Diameter size (nm)	Polydispersity index (PDI)	Yield (%)
SLS-T	233 ± 14	0.232 ± 0.035	78.9 ± 9.9
SLS-M	184 ± 15	0.189 ± 0.040	79.3 ± 3.2
SLS-N	205 ± 20	0.225 ± 0.030	78.8 ± 8.3

n = 10 for size and polydispersity measurements, n = 3 for yield measurements.

In vivo Immune Responses

To assess how peptide antigen modification and biomaterial formulation affected immune responses, SLS-T, SLS-M, and SLS-N PNC formulations were injected intradermally into mice and compared to soluble SIINFEKL antigen and SIINFEKL

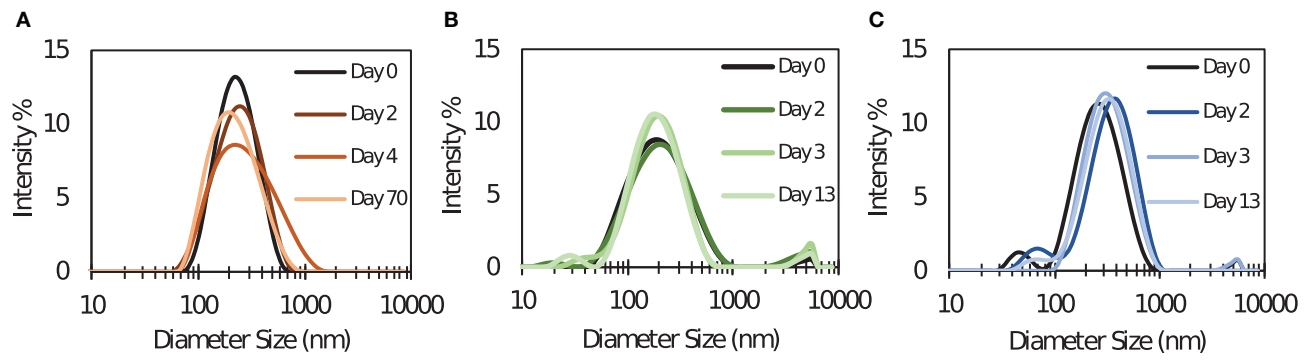

FIGURE 1 | Dynamic light scattering size distribution measurements of **(A)** SLS-T, **(B)** SLS-M, and **(C)** SLS-N PNC taken at several times after synthesis. Distributions over time shown are from one batch, representative of five repeated experiments with different batches of PNC.

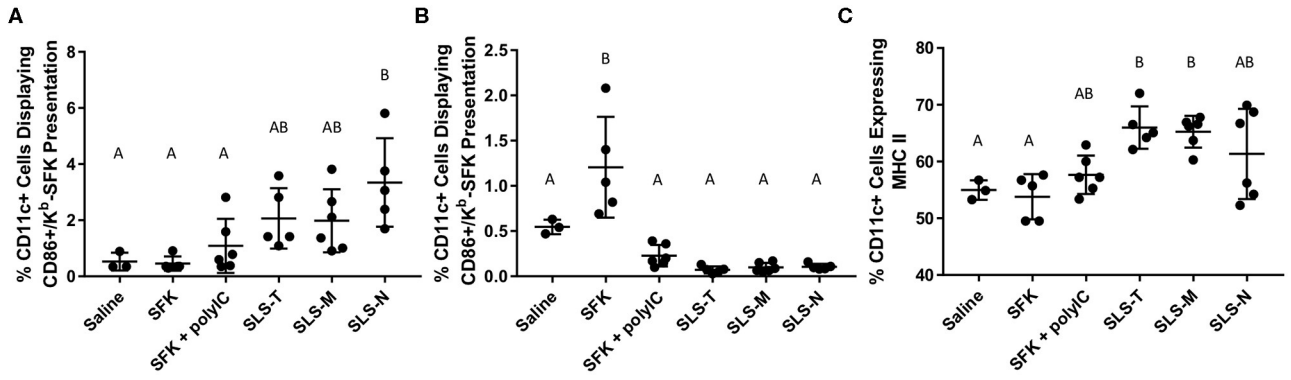

FIGURE 2 | Percent of CD11c+ cells in **(A)** draining lymph nodes and **(B)** spleen co-expressing CD86 and K^b-SFK. **(C)** Percent of CD11c+ cells in draining lymph nodes expressing MHC II. $N = 5$–6. Differences between letters show significant differences between samples ($p < 0.05$). Samples that share the same letter are not statistically different from each other.

+ poly(I:C) adjuvant injections and a saline control injection. Animals were administered 60 nmol of antigen formulation split into two 30 μl injections; one in each forearm. Intradermal vaccination was chosen because of the significant level of tissue-resident DCs in the skin. This makes the skin a potent target for vaccine delivery compared to muscular or subcutaneous tissue, which do not contain as many DCs (53). Animals were given two half-dose boost injections over 2 weeks and sacrificed on day 16 to harvest draining axillary and brachial lymph nodes and spleens for DC and T cell analysis. Prior to *in vivo* work, cytotoxicity of PNC and SLS peptide in both DC and T cell hybridoma cell lines was evaluated to assess potential toxic side effects *in vivo* (**Supplementary Figure 8**). Results indicated toxic side effects were not likely based on minimal to no observed cytotoxicity in either cell line.

Dendritic Cell Processing

Cellular responses induced by immunization with different antigen formulations varied in several ways. To assess APC processing, CD11c+ DCs in the lymph nodes and spleen were evaluated for MHC I presentation of SIINFEKL and coinciding maturation markers. **Figure 2A** illustrates that only SLS-N PNC induced a significant increase in co-expression of MHC I presenting SIINFEKL and CD86 in lymph node DCs. Nanoparticles have been shown to have "self-adjuvanting" properties due to their nanoparticulate nature (54–56). This benefit of PNC may explain the increased maturation specifically of SIINFEKL-presenting DCs in mice administered PNC compared to soluble groups, which displayed low levels of maturation. **Supplementary Figure 9A** shows that of the DCs presenting SIINFEKL, only those in PNC groups have significant surface expression of CD86. It was expected that particles of similar size would have similar DC internalization mechanisms (39, 57). While SLS-T and SLS-M should have similar self-adjuvancy to SLS-N, less efficient, or effective processing of the PNC may have occurred, as they did not induce significantly more co-expression of MHC I presenting SIINFEKL and CD86 than soluble controls (**Figure 2A**). This suggests that the SLS-N formulation was able to be broken down and processed sufficiently to induce significant levels of DC presentation and maturation. Proteases in endolysosomes and the proteasome in cytosol upon endosomal escape, cleave proteins into minimal epitopes using several mechanisms of amide bond breakage, so it is possible that the amide bonds that form SLS-N PNC are broken down more efficiently by these mechanisms (58, 59) SLS-M is stabilized with thioether bonds, which are commonly used to increase metabolic stability (60–62). Although SLS-T PNC are crosslinked with reversible disulfide bonds, these bonds were shown to be difficult to fully reduce (**Supplementary Figure 5**) and may lead to decreased ability of DCs to break-up SLS-T PNC. Reduction of these bonds required extended reducing time, indicating slow kinetics, which is also likely due to the fact that disulfide reduction is reversible. The need for exposure to a reducing environment for extended periods demonstrated in **Supplementary Figure 5** may not be met in the DC intracellular trafficking process and may lead to decreased ability to break-up SLS-T PNC.

While PNC essentially serve as the antigen and adjuvant, co-administration of adjuvants is common, and we included the SIINFEKL + poly(I:C) group as a positive control, and also to compare intrinsic vs. extrinsic adjuvant approaches. Poly(I:C) is a synthetic dsRNA analog commonly used as a pathogen-associated molecular pattern (PAMP) adjuvant to non-specifically induce elements of host defense mechanisms associated with viral infection (63). It induces immune signaling associated with cytotoxic T lymphocyte (CTL) responses for intracellular antigens, but also induces innate immune responses similar to many non-specific PAMPs. Poly(I:C) has previously been evaluated with SIINFEKL as a standard method for improving SIINFEKL-specific immune responses since SIINFEKL is an MHC I epitope (21). APCs receive both the antigen and "adjuvant" signal simultaneously from PNC, unlike co-administration of soluble SIINFEKL and poly(I:C), which do not necessarily reach the same cells (64–66). **Supplementary Figure 9** corroborates this phenomenon, as significantly more lymphatic DCs that received PNC and upregulated CD86 also presented SIINFEKL and significantly more lymphatic DCs that received PNC and presented SIINFEKL

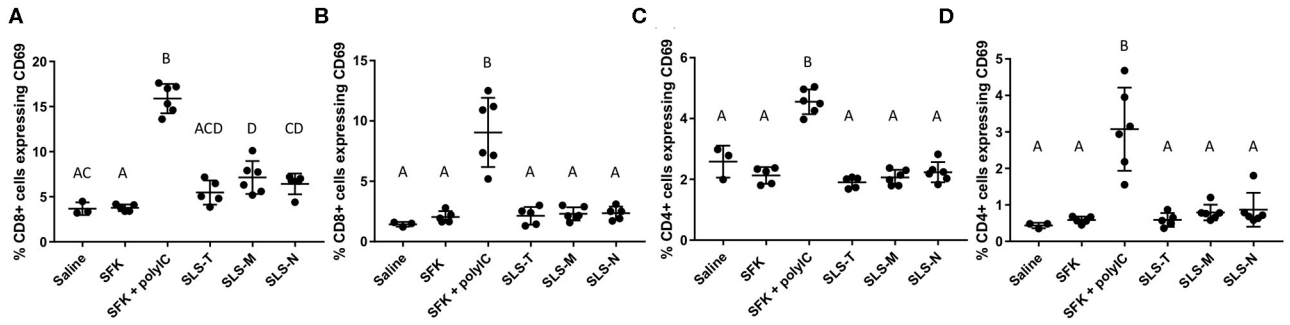

FIGURE 3 | Percent of **(A,B)** CD8+ and **(C,D)** CD4+ T cells in **(A,C)** draining lymph nodes and **(B,D)** spleen expressing early activation marker CD69. $N = 5–6$. Differences between letters show significant differences between samples ($p < 0.05$). Samples that share the same letter are not statistically different from each other.

also upregulated CD86. Neither of these combinations was seen for SIINFEKL + Poly(I:C). Furthermore, significantly more lymphatic DCs with CD86 upregulation that received SIINFEKL + Poly(I:C) did not present SIINFEKL, supporting the disconnection between soluble mixtures of SIINFEKL and Poly(I:C).

Contrary to lymph node DCs, splenic DCs only showed significant maturation and MHC I-SIINFEKL presentation when administered soluble SIINFEKL alone (**Figure 2B**). This could be due to the different trafficking properties of PNC and soluble peptide observed in the biodistribution study discussed below. Antigen in PNC form diffused slower and was trafficked to draining lymph nodes, likely by DCs. Soluble SIINFEKL passively diffused in limited amounts to the spleen, where it may have directly attached to MHC I on DC surfaces without being internalized and presented (67, 68). While MHC I/SIINFEKL and CD86 co-expression is high in the spleen for this soluble group, the low levels of T cell activation in the spleen shown in **Figure 3B** suggest that DC presentation and signaling were still ineffective at inducing antigen-specific T cell responses. The addition of adjuvant in the SIINFEKL + poly(I:C) group may also affect DC trafficking, resulting in less localization in the spleen. Poly(I:C) is negatively charged, and like other nucleic acid adjuvants, may have the propensity to aggregate (69, 70). Evidence of small aggregates in the soluble SIINFEKL + poly(I:C) were seen after combining adjuvant with antigen. This observation supports that SIINFEKL + poly(I:C) may not represent a completely soluble antigen formulation, resulting in different trafficking properties than those of soluble peptide alone observed in the biodistribution study. Furthermore, adjuvants can cause inflammation which increases lymphatic drainage and affects overall antigen diffusion and transport (71).

MHC II is another DC maturation marker, which presents exogenous antigen for CD4+ T cell activation (30). Lymph node DCs from mice administered SLS-T and SLS-M PNC, though not SLS-N PNC, showed upregulation of MHC II compared to soluble SIINFEKL or and saline (**Figure 2C**). Upregulation of MHC II in SLS-T and SLS-M groups did not occur at levels that resulted in increased CD4+ activation (**Figure 3C**). Additionally, upregulation of MHC II is also associated with a reduction in antigen processing, which may have contributed to reduced SIINFEKL presentation in the SLS-T and SLS-M groups (72). No groups displayed significant MHC II expression in the spleen (**Supplementary Figure 11**). While general DC maturation can be beneficial, MHC II upregulation does not indicate antigen-specific presentation or maturation due to intracellular signaling of an endogenous MHC I antigen such as SIINFEKL. The differences in MHC II upregulation between different PNC types may indicate different signaling in DCs due to different interactions between the PNC and DCs. Different levels of internalization different mechanisms of internalization can affect DC presentation and maturation profiles and overall immune cell response (73). *In vitro* internalization studies demonstrate that all peptide and PNC formulations are internalized by DCs in significant amounts (**Supplementary Figure 10**). However, the mechanism of internalization may be different for different formulations (39). Several nanoparticle characteristics, including size, shape, surface charge, and hydrophobicity, have been shown to affect mechanisms of internalization, processing, and maturation in DCs (73). SLS-T, SLS-M, and SLS-N PNC are formed via different crosslinking chemistries, and, therefore, differences in surface chemistry and degradability could affect the mechanisms of DC antigen processing and maturation.

T Cell Activation

In analyzing the next step in the adaptive immune response process, differences in T cell activation were also observed. CD8+ and CD4+ T cells harvested from lymph nodes and spleens were analyzed for upregulation of CD69, an early activation marker indicatory of T cell proliferation and retention of lymphocytes in antigen-resident tissues (74). **Figures 3A,B** shows that small, but statistically significant, increases in CD8+/CD69+ T cells were seen only in lymph nodes of mice given SLS-M and SLS-N PNC compared to soluble SIINFEKL. The modest upregulation of CD69 seen only in the lymph nodes for PNC groups correlated with the enhancement of DC presentation of SIINFEKL and maturation in the lymph nodes. In contrast, CD69 expression in CD8+ T cells increased considerably in both the draining lymph nodes and spleen of mice that received SIINFEKL + poly(I:C) adjuvant, despite low maturation levels in SIINFEKL-presenting DCs. Furthermore, CD4+ upregulation of CD69 was observed

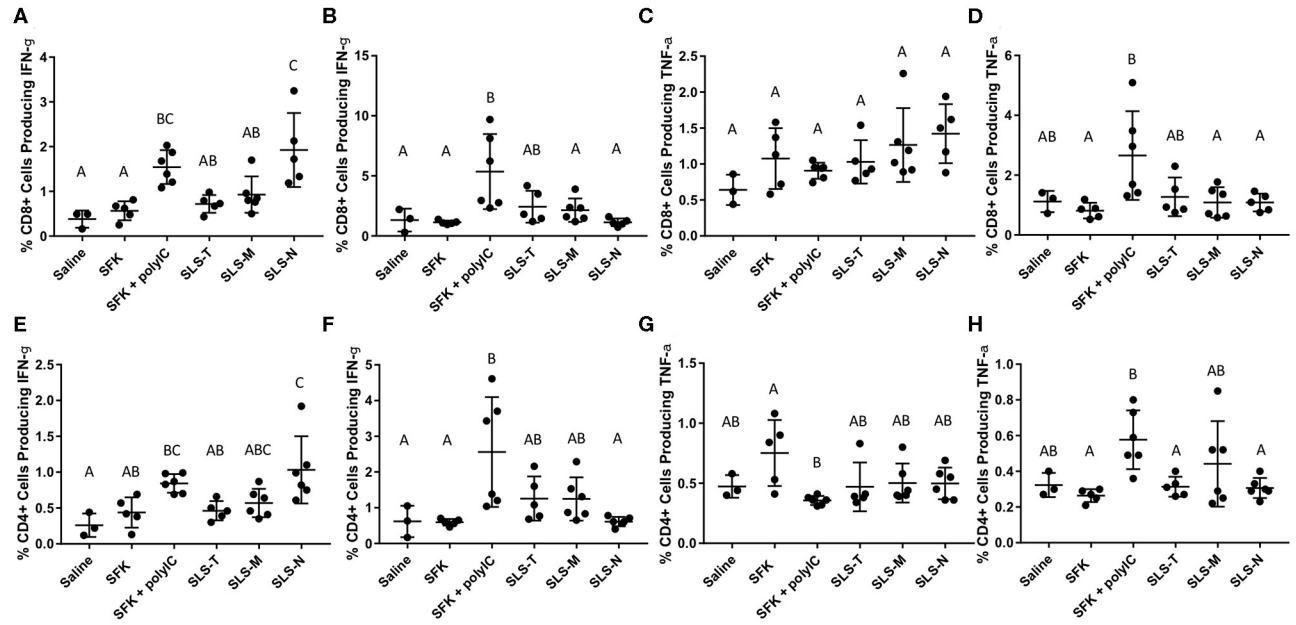

FIGURE 4 | (A–D) Percent CD8+ T cells producing **(A,B)** IFN-g and **(C,D)** TNF-a in **(A,C)** axillary/brachial lymph nodes and **(B,D)** spleens when re-stimulated with 1 mg/ml SIINFEKL. **(E–H)** Percent CD4+ T cells producing **(E,F)** IFN-g and **(G,H)** TNF-a in **(E,G)** axillary/brachial lymph nodes and **(F,H)** spleens when re-stimulated with 1 mg/ml SIINFEKL. $N = 5$–6. Differences between letters show significant differences between samples ($p < 0.05$). Samples that share the same letter are not statistically different from each other.

in lymph nodes and spleen only in the SIINFEKL + poly(I:C) group (**Figures 3C,D**). These results suggest that non-specific T cell activation occurred in this group due to the uncoupled co-administration of antigen and adjuvant, the nature of poly(I:C) function, or both.

To more directly evaluate SIINFEKL-specific T cell activation, lymphocytes harvested from draining lymph nodes and spleens were re-stimulated *ex vivo* with SIINFEKL peptide and assessed for intracellular cytokines IFN-γ and TNF-α. The intracellular IFN-γ results for CD8+ T cells corroborate the DC and CD69 data that SLS-N PNC have the best conversion of DC presentation into activated, antigen-specific T cells. **Figure 4A** shows that significantly more CD8+ T cells from mice that received SLS-N PNC produced IFN-γ when re-stimulated with SIINFEKL than those that received soluble SIINFEKL, SLS-T, or SLS-M PNC. Despite the differences between the SLS PNC groups, all three SLS PNC groups without adjuvant displayed statistically similar IFN-γ levels as the SIINFEKL + poly(I:C) group. While the CD69 measurement was not connected to antigen specificity, cytokine production was measured after re-stimulation with SIINFEKL. CD69 upregulation in the SIINFEKL + poly(I:C) group was much greater than PNC groups, but the IFN-γ response was similar to PNC, indicating that cytokine production may have been residual from non-specific activation rather than stimulated by SIINFEKL. Therefore, one conclusion is that despite the lower overall immune cell responses to PNC relative to SIINFEKL + poly(I:C), comparable levels of antigen-specific activation occurred. This may be a more desirable outcome in an effort to maintain balance between a strong enough immune response to induce memory cell formation and pathogen protection and overstimulation that causes allergic reaction or other unwanted side effects commonly associated with adjuvants (75–77). IFN-γ is associated with the increase of MHC I expression and APC recruitment, which ultimately improves the specificity of the adaptive immune response by enabling higher antigen presentation levels and increasing the amount of CD8+ T cell activation and proliferation (30). Consistent with other analyses of spleen-resident DCs and T cells, **Figures 4B,F** demonstrates that there was no IFN-γ production evident in groups that were administered PNC. A significant amount of splenic T cells from the poly(I:C) adjuvanted group, however, did produce IFN-γ when re-stimulated with SIINFEKL. This correlates with the general activation of T cells in the spleen as shown by CD69 upregulation and may be at least partially due to non-specific adjuvant-related activation. CD4+ T cell production of IFN-γ in all groups and locations displayed the same trends as CD8+ production (**Figures 4A,B,E,F**). CD4+ T cells cannot have a specific immunological response to the SIINFEKL epitope. CD4+ CD69 upregulation, however, did not align with CD8+ T cell trends; only CD8+ T cells showed upregulation of CD69 in PNC groups. This result suggests that bystander CD4+ activation may have occurred, but only in limited occasions when strong signaling from an antigen-specific response (CD8+ activation/IFN-γ production after re-stimulation with SIINFEKL) was present, such as in the wells *ex vivo*. It has been observed that non-specific, naïve CD4+ T cell activation can occur as a result of strong antigen-specific T cell activation (78, 79). This phenomenon involves the phenotypic changes related to effector T cell function, such as cytokine production, without the necessity for TCR signaling, which could

explain the observed IFN-γ production in this study despite the lack of a CD4 epitope (80).

TNF-α production was also measured upon re-stimulation of lymphatic and splenic CD8+ and CD4+ T cells with SIINFEKL (**Figures 4C,D,G,H**). No groups displayed significant TNF-α production except for splenic CD8+ and CD4+ T cells in the SIINFEKL + poly(I:C) group. While TNF-α production is important for the enhancement of immune responses, it is more often associated with innate immune responses, including increased inflammation (30, 71). Inflammation is valuable in recruiting tissue resident lymphocytes to potentially infected areas. However, systemic production results in dangerous side effects, including shock. TNF-α production in the spleen, therefore, may not necessarily be considered an indicator of strong specific immunity, but rather, evidence of strong, non-specific T cell activation induced by poly(I:C) adjuvant, which may not be beneficial. It is notable that despite comparable levels of lymphatic IFN-γ production in SLS PNC and poly(I:C) groups, TNF-α remained low in lymphatic and splenic tissues evaluated from mice administered PNC.

Biodistribution

To help explain the differences in immune responses observed between PNC and soluble groups and validate expected nanoparticle transport behavior that may contribute to those differences, peptide localization in the lymph nodes and spleen was assessed. Fluorescent-labeled SLS peptide in soluble and SLS-N PNC form were injected the same way as for the immune response study. It was expected that the modified SIINFEKL peptide, SLS, would have very similar diffusion properties to SIINFEKL because of its similar size. TAMRA-labeled SIINFEKL was highly insoluble in aqueous solutions, and the increased number of hydrophilic residues in SLS increased solubility in aqueous solution when fluorescently-labeled. Therefore, TAMRA-labeled SLS peptide was used as a minimally modified representative soluble peptide that ensured the soluble peptide group did not contain peptide aggregates and eliminated the need for additives to increase solubility of TAMRA-labeled SIINFEKL. Similarly, SLS-N PNC were used as a representative PNC group to evaluate biodistribution because PNC of similar size and morphology were expected to have similar biodistribution. Although several physicochemical characteristics can affect trafficking, such as surface charge, many are often correlated with a potential effect on particle size, which is the most well-studied factor in optimizing lymph node trafficking (81–87). Nanoparticles 20–200 nm are reported to be able to passively diffuse to regional lymph nodes whereas 200–2,000 nm particles require active APC transport to lymph nodes (83). The SLS PNC fall between these two size ranges, so both passive and active trafficking could have occurred. PNC have been shown to have different diffusion rates in tissue than soluble peptide (27). While we previously observed longer injection site retention of PNC, which could increase interactions with tissue resident DCs, it is also important that PNC are trafficked into the lymphatic system where they are more likely to initiate T cell activation.

Peptide localization in axillary and brachial draining lymph nodes and the spleen were evaluated at 4, 24, and 72 h after forearm injections. **Figures 5A–C** illustrates that soluble fluorescent peptide accumulated in lymph nodes at almost undetectable levels over 72 h. However, as shown in **Figures 5D–F**, peptide administered in PNC form reached lymph nodes at moderate levels after 4 h and continued to accumulate up to 24 h after injection. After 72 h, low levels of peptide were still detected in some lymph nodes in the SLS-N PNC group. Quantitation of fluorescence in homogenized organs confirmed that a significant amount of peptide was retained in lymph nodes at both 4 and 24 h after injection only in mice that received SLS-N PNC (**Figure 6**). These results validate several immune response observations. The increased amount of PNC peptide trafficking to draining lymph nodes combined with retention of PNC peptide in the nodes for at least 20 h align with improved DC presentation and maturation as well as T cell activation in these tissues. This correlation between improved immune response due to these trafficking and retention properties is corroborated by several other studies that evaluate biomaterials for increased immunogenicity of subunit vaccines (16, 88, 89).

Although undetectable in fluorescent images, quantitation of peptide in homogenized spleens revealed that significant splenic accumulation of soluble peptide occurred 4 h after injection, but no soluble peptide was detected in the spleen at 24 or 72 h (**Figure 6B**). These results illustrate that although there is limited passive diffusion or trafficking of soluble antigen through the lymphatic system, this process occurs more quickly and transiently than for PNC. The insufficient residence time of soluble peptide aligned with the similarly limited immune responses observed with soluble peptide administration *in vivo*. There was some evidence of DC presentation and maturation in the spleen, in agreement with low levels of peptide present there, but this ultimately did not result in CD8+ T cell activation. Similarly, soluble peptide that was administered with adjuvant also displayed evidence of immune cell activation in splenic cells. The ability to quantify soluble peptide in the spleen, although transiently, implies that the limited presence of peptide in the lymphatic system can still induce a response when there is significant activation signaling provided by an adjuvant, which was observed in our immune response studies. This observation supports the many instances of increased immune responses with peptide/adjuvant co-administration seen in vaccine formulations (24, 63, 90) It should be noted, however, that while some aspects of adjuvant driven immune responses are beneficial, there are several drawbacks for vaccine safety and control over the immune response (91, 92). These challenges highlight the value of development of biomaterials, such as PNC, which enhance only certain aspects of immune cell activation more associated with antigen-specific adaptive immunity and may be more desirable from a safety standpoint.

CONCLUSION

While modifying peptide antigens for biomaterial incorporation has the potential to reduce specificity and the ability of the

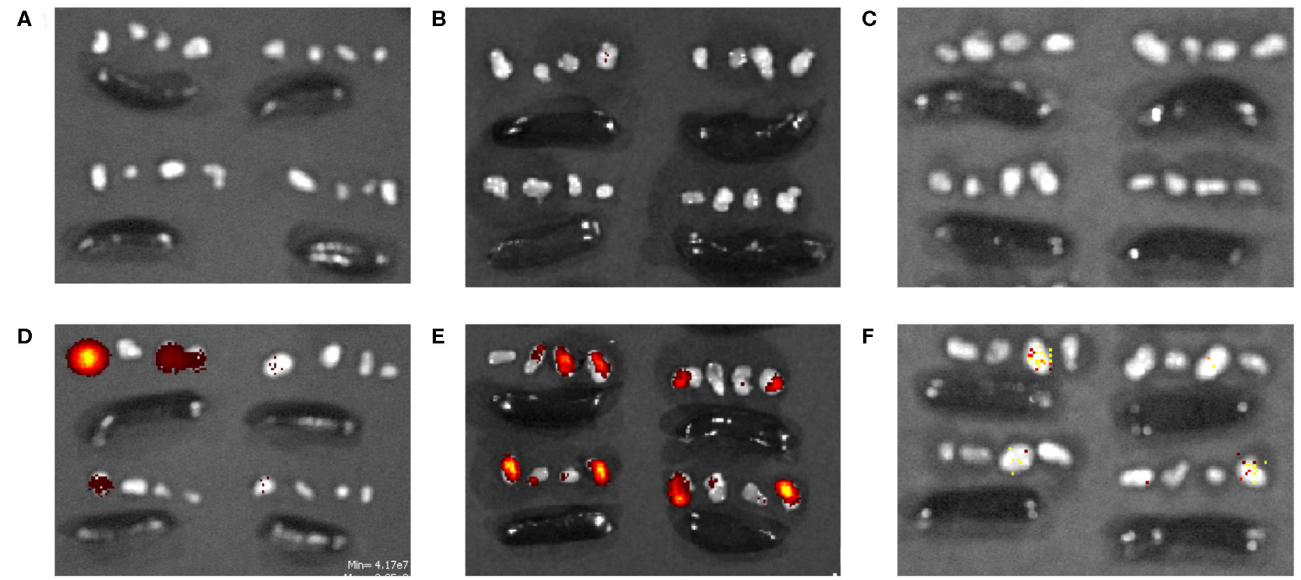

FIGURE 5 | TAMRA-labeled **(A–C)** soluble SLS and **(D–F)** SLS-N PNC in axillary/brachial lymph nodes (groups of 4 small organs) and spleens (large, oblong organs) **(A,D)** 4, **(B,E)** 24, and **(C,F)** 72 h after injection.

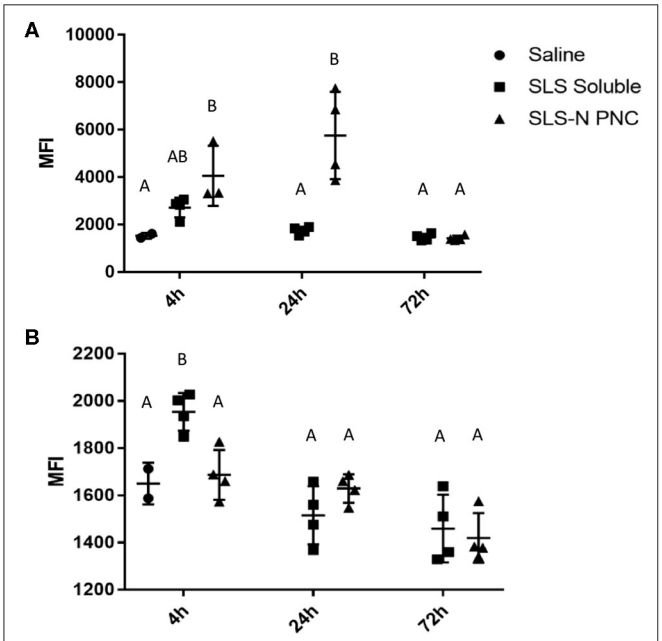

FIGURE 6 | Fluorescent peptide localized in **(A)** draining lymph nodes and **(B)** spleen 4, 24, and 72 h after i.d. injection in both forearms of 10% TAMRA-labeled SLS peptide in soluble or SLS-N PNC form. MFI, Mean Fluorescence Intensity. $N = 4$. Differences between letters show significant differences between samples ($p < 0.05$). Samples that share the same letter are not statistically different from each other.

antigen to interact with immune cells effectively, observations in this work suggest that limited, strategic modifications when combined with biomaterial formation offer benefits that afford similar or better levels of activation against the target antigen. Importantly, the method of incorporation into biomaterials in PNC affected the ability of the material to induce improved immunogenicity at several stages of activation. DC presentation and maturation were significantly improved over soluble antigen for PNC stabilized by amide bonds. This improved antigen-specific response carried through to T cell activation, where antigen-specific CD8+ responses were observed in all SLS PNC at comparable levels to antigen with adjuvant. These results suggest that utilizing design tools to alter antigens in a way that allows several routes of biomaterial incorporation may be highly beneficial so that a method that maximizes the desired response can be identified. More specifically, SLS-N PNC demonstrate the importance of understanding the likely mechanism of material processing and ultimate intracellular fate. Utilizing this amide bond crosslinking formulation, which mimicked foreign antigens in that it was proteolytically cleavable but stable in most other environments, proved to be highly beneficial in achieving the desired increased immune cell response. Additionally, the ability to improve specific responses to a target antigen with comparable levels of activation to an adjuvanted antigen formulation, while maintaining low levels of non-specific activation markers, demonstrates a unique level of control provided by PNC.

More work is needed to further characterize the various modifications and conjugation mechanisms that may be used for different methods of biomaterial incorporation of antigens. However, the knowledge developed in this study provides insight into the immune cell activation processes triggered by biomaterials depending on their formulation. These results offer a guide both for future PNC synthesis and antigen incorporation methods into a variety engineered peptide biomaterial subunit vaccines, as

they demonstrate potential approaches to systematically design biomaterials to control and maximize the specific immune cell responses desired.

DATA AVAILABILITY STATEMENT

The raw data supporting the conclusions of this article will be made available by the authors, without undue reservation.

ETHICS STATEMENT

The animal studies were reviewed and approved by Georgia Institute of Technology Institutional Animal Care and Use Committee.

AUTHOR CONTRIBUTIONS

AT and JC contributed conception and design of the study. AT conducted experiments, organized results, and performed statistical analyses. KW and AP contributed design of yield characterization. KW performed experiments and analysis and contributed manuscript text for NMR yield characterization. AT drafted the manuscript. JC and AP edited the manuscript. All authors contributed to manuscript revision, read, and approved the submitted version.

FUNDING

This research was financially supported by the National Institutes of Health, Award number 1R01AI143844-01 from the National Institute of Allergy and Infectious Disease, and by M. T. Campagna.

ACKNOWLEDGMENTS

The authors gratefully acknowledge David Francis for consultation on the design of *in vivo* experiments and cellular analysis protocols. The authors also wish to acknowledge the core facilities at the Parker H. Petit Institute for Bioengineering and Bioscience at the Georgia Institute of Technology for the use of their shared equipment, services, and expertise.

SUPPLEMENTARY MATERIAL

The Supplementary Material for this article can be found online at: https://www.frontiersin.org/articles/10.3389/fimmu.2020.01547/full#supplementary-material

REFERENCES

1. Pica N, Palese P. Toward a universal influenza virus vaccine: prospects and challenges. *Ann Rev Med.* (2013) 64:189–202. doi: 10.1146/annurev-med-120611-145115
2. Moyle PM, Toth I. Self-adjuvanting lipopeptide vaccines. *Curr Med Chem.* (2008) 15:506–16. doi: 10.2174/092986708783503249
3. Moyle PM, Toth I. Modern subunit vaccines: development, components, research opportunities. *ChemMedChem.* (2013) 8:360–76. doi: 10.1002/cmdc.201200487
4. Pulendran B, Ahmed R. Immunological mechanisms of vaccination. *Nat Immunol.* (2011) 12:509. doi: 10.1038/ni.2039
5. Timmerman P, Puijk W, Boshuizen R, Dijken PV, Slootstra J, Beurskens F, et al. Functional reconstruction of structurally complex epitopes using CLIPS^{TM} technology. *Open Vaccine J.* (2009) 2:56–7. doi: 10.2174/1875035400902010056
6. Mayrose I, Penn O, Erez E, Rubinstein ND, Shlomi T, Freund NT, et al. Pepitope: epitope mapping from affinity-selected peptides. *Bioinformatics.* (2007) 23:3244–6. doi: 10.1093/bioinformatics/btm493
7. Anthony DD, Lehmann PV. T-cell epitope mapping using the ELISPOT approach. *Methods.* (2003) 29:260–9. doi: 10.1016/S1046-2023(02)00348-1
8. Newell EW, Sigal N, Nair N, Kidd BA, Greenberg HB, Davis MM. Combinatorial tetramer staining and mass cytometry analysis facilitate T-cell epitope mapping and characterization. *Nat Biotechnol.* (2013) 31:623. doi: 10.1038/nbt.2593
9. Kern F, Surel IP, Brock C, Freistedt B, Radtke H, Scheffold A, et al. T-cell epitope mapping by flow cytometry. *Nat Med.* (1998) 4:975–8. doi: 10.1038/nm0898-975
10. Nandy A, Basak SC. A brief review of computer-assisted approaches to rational design of peptide vaccines. *Int J Mol Sci.* (2016) 17:666. doi: 10.3390/ijms17050666
11. Tsoras AN, Champion JA. Protein and peptide biomaterials for engineered subunit vaccines and immunotherapeutic applications. *Ann Rev Chem Biomol Eng.* (2019) 10:337–59. doi: 10.1146/annurev-chembioeng-060718-030347
12. Wu Y, Yang H, Shin HJ. Viruses as self-assembled nanocontainers for encapsulation of functional cargoes. *Korean J Chem Eng.* (2013) 30:1359–67. doi: 10.1007/s11814-013-0083-y
13. Jabbal-Gill I, Lin W, Jenkins P, Watts P, Jimenez M, Illum L, et al. Potential of polymeric lamellar substrate particles (PLSP) as adjuvants for vaccines. *Vaccine.* (1999) 18:238–50. doi: 10.1016/S0264-410X(99)00195-4
14. Jiang W, Gupta RK, Deshpande MC, Schwendeman SP. Biodegradable poly (lactic-co-glycolic acid) microparticles for injectable delivery of vaccine antigens. *Adv Drug Deliv Rev.* (2005) 57:391–410. doi: 10.1016/j.addr.2004.09.003
15. Polonskaya Z, Deng S, Sarkar A, Kain L, Comellas-Aragones M, McKay CS, et al. T cells control the generation of nanomolar-affinity anti-glycan antibodies. *J Clin Invest.* (2017) 127:1491–504. doi: 10.1172/JCI91192
16. Shukla S, Myers JT, Woods SE, Gong X, Czapar AE, Commandeur U, et al. Plant viral nanoparticles-based HER2 vaccine: immune response influenced by differential transport, localization and cellular interactions of particulate carriers. *Biomaterials.* (2017) 121:15–27. doi: 10.1016/j.biomaterials.2016.12.030
17. Champion CI, Kickhoefer VA, Liu G, Moniz RJ, Freed AS, Bergmann LL, et al. A vault nanoparticle vaccine induces protective mucosal immunity. *PLoS ONE.* (2009) 4:e5409. doi: 10.1371/journal.pone.0005409
18. Zhang P, Sun F, Liu S, Jiang S. Anti-PEG antibodies in the clinic: current issues and beyond PEGylation. *J Control Release.* (2016) 244:184–93. doi: 10.1016/j.jconrel.2016.06.040
19. Wong-Baeza C, Reséndiz-Mora A, Donis-Maturano L, Wong-Baeza I, Zárate-Neira L, Yam-Puc JC, et al. Anti-lipid IgG antibodies are produced via germinal centers in a murine model resembling human lupus. *Front immunol.* (2016) 7:396. doi: 10.3389/fimmu.2016.00396
20. Da Silva DM, Pastrana DV, Schiller JT, Kast WM. Effect of preexisting neutralizing antibodies on the anti-tumor immune response induced by chimeric human papillomavirus virus-like particle vaccines. *Virology.* (2001) 290:350–60. doi: 10.1006/viro.2001.1179
21. Chiu, YC, Gammon JM, Andorko JI, Tostanoski LH, Jewell CM. Assembly and immunological processing of polyelectrolyte multilayers composed of antigens and adjuvants. *ACS Appl. Mater Interfaces.* (2016) 8:18722–31. doi: 10.1021/acsami.6b06275

22. Hess KL, Andorko JI, Tostanoski LH, Jewell CM. Polyplexes assembled from self-peptides and regulatory nucleic acids blunt toll-like receptor signaling to combat autoimmunity. *Biomaterials.* (2017) 118:51–62. doi: 10.1016/j.biomaterials.2016.11.052
23. Hussein WM, Liu TY, Jia Z, McMillan NA, Monteiro MJ, Toth, I, et al. Multiantigenic peptide–polymer conjugates as therapeutic vaccines against cervical cancer. *Bioorg Med Chem.* (2016) 24:4372–80. doi: 10.1016/j.bmc.2016.07.036
24. Kuai R, Ochyl LJ, Bahjat KS, Schwendeman A, Moon JJ. Designer vaccine nanodiscs for personalized cancer immunotherapy. *Nat Mater.* (2017) 16:489. doi: 10.1038/nmat4822
25. Moura APV, Santos LC, Brito CRN, Valencia E, Junqueira C, Filho AA, et al. Virus-like particle display of the α-Gal carbohydrate for vaccination against leishmania infection. *ACS Central Sci.* (2017) 3:1026–31. doi: 10.1021/acscentsci.7b00311
26. Ramirez A, Morris S, Maucourant S, D'Ascanio I, Crescente V, Lu IN, et al. A virus-like particle vaccine candidate for influenza A virus based on multiple conserved antigens presented on hepatitis B tandem core particles. *Vaccine.* (2018) 36:873–80. doi: 10.1016/j.vaccine.2017.12.053
27. Tsoras AN, Champion JA. Cross-linked peptide nanoclusters for delivery of oncofetal antigen as a cancer vaccine. *Bioconjug Chem.* (2018) 29:776–85. doi: 10.1021/acs.bioconjchem.8b00079
28. Williams A, Peh CA, Elliott T. The cell biology of MHC class I antigen presentation. *Tissue Antigens.* (2002) 59:3–17. doi: 10.1034/j.1399-0039.2002.590103.x
29. Almani M, Raffaeli S, Vider-Shalit T, Tsaban L, Fishbain V, Louzoun Y. Human self-protein CD8+ T-cell epitopes are both positively and negatively selected. *Eur J Immunol.* (2009) 39:1056–65. doi: 10.1002/eji.200838353
30. Murphy K, Weaver C. *Janeway's Immunobiology.* New York, NY: Garland Science. (2016). doi: 10.1201/9781315533247
31. Shastri N, Gonzalez F. Endogenous generation and presentation of the ovalbumin peptide/Kb complex to T cells. *J Immunol.* (1993) 150:2724–36.
32. York IA, Bhutani N, Zendzian S, Goldberg AL, Rock KL. Tripeptidyl peptidase II is the major peptidase needed to trim long antigenic precursors, but is not required for most MHC class I antigen presentation. *J Immunol.* (2006) 177:1434–43. doi: 10.4049/jimmunol.177.3.1434
33. Saito Y, Peterson PA, Matsumura M. Quantitation of peptide anchor residue contributions to class I major histocompatibility complex molecule binding. *J Biol Chem.* (1993) 268:21309–17.
34. Deng L, Mohan T, Chang TZ, Gonzalez GX, Wang Y, Kwon YM, et al. Double-layered protein nanoparticles induce broad protection against divergent influenza A viruses. *Nat Commun.* (2018) 9:1–12. doi: 10.1038/s41467-017-02725-4
35. Wang L, Hess A, Chang TZ, Wang YC, Champion JA, Compans RW, et al. Nanoclusters self-assembled from conformation-stabilized influenza M2e as broadly cross-protective influenza vaccines. *Nanomedicine.* (2014) 10:473–82. doi: 10.1016/j.nano.2013.08.005
36. Bharti SK, Roy R. Quantitative 1H NMR spectroscopy. *TrAC Trends Anal Chem.* (2012) 35:5–26. doi: 10.1016/j.trac.2012.02.007
37. Pauli GF, Jaki BU, Lankin DC. Quantitative 1H NMR: development and potential of a method for natural products analysis. *J Nat Prod.* (2005) 68:133–49. doi: 10.1021/np0497301
38. Chang TZ, Diambou I, Kim JR, Wang B, Champion JA. Host-and pathogen-derived adjuvant coatings on protein nanoparticle vaccines. *Bioeng Transl Med.* (2017) 2:120–30. doi: 10.1002/btm2.10052
39. Chang TZ, Stadmiller SS, Staskevicius E, Champion JA. Effects of ovalbumin protein nanoparticle vaccine size and coating on dendritic cell processing. *Biomater Sci.* (2017) 5:223–33. doi: 10.1039/C6BM00500D
40. Wang L, Chang TZ, He Y, Kim JR, Wang S, Mohan T, et al. Coated protein nanoclusters from influenza H7N9 HA are highly immunogenic and induce robust protective immunity. *Nanomedicine.* (2017) 13:253–62. doi: 10.1016/j.nano.2016.09.001
41. Zhang Q, Schenauer MR, McCarter JD, Flynn GC. IgG1 thioether bond formation *in vivo*. *J Biol Chem.* (2013) 288:16371–82. doi: 10.1074/jbc.M113.468397
42. Hermanson GT. *Bioconjugate Techniques.* Cambridge, MA: Academic Press (2013).
43. Bender ML, Kezdy FJ. Mechanism of action of proteolytic enzymes. *Ann Rev Biochem.* (1965) 34:49–76. doi: 10.1146/annurev.bi.34.070165.000405
44. Alley SC, Benjamin DR, Jeffrey SC, Okeley NM, Meyer DL, Sanderson RJ, et al. Contribution of linker stability to the activities of anticancer immunoconjugates. *Bioconjug Chem.* (2008) 19:759–65. doi: 10.1021/bc7004329
45. Smith NJ, Rohlfing K, Sawicki LA, Kharkar PM, Boyd SJ, Kloxin AM, et al. Fast, irreversible modification of cysteines through strain releasing conjugate additions of cyclopropenyl ketones. *Org Biomol Chem.* (2018) 16:2164–9. doi: 10.1039/C8OB00166A
46. Ulrich EL, Akutsu H, Doreleijers JF, Harano Y, Ioannidis YE, Lin J, et al. BioMagResBank. *Nucleic Acids Res.* (2007) 36(suppl_1):D402–8. doi: 10.1093/nar/gkm957
47. Foster MP, McElroy CA, Amero CD. Solution NMR of large molecules and assemblies. *Biochemistry*. (2007) 46:331–40. doi: 10.1021/bi0621314
48. Duarte AM, Van Mierlo CP, Hemminga MA. Molecular dynamics study of the solvation of an r-Helical transmembrane peptide by DMSO. *J Phys Chem B.* (2007) 112:8664–71. doi: 10.1021/jp076678j
49. O'Connor P, Cutie S, Smith P, Martin S, Sammler R, Harris W, et al. H NMR characterization of swelling in cross-linked polymer systems. *Macromolecules.* (1996) 29:7872–84. doi: 10.1021/ma960650g
50. Baumgartner S, Lahajnar G, Sepe A, Kristl J. Quantitative evaluation of polymer concentration profile during swelling of hydrophilic matrix tablets using 1H NMR and MRI methods. *Eur J Pharm Biopharm.* (2005) 59:299–306. doi: 10.1016/j.ejpb.2004.08.010
51. Zhang R, Yan T, Lechner BD, Schröter K, Liang Y, Li, B, et al. Heterogeneity, segmental and hydrogen bond dynamics, and aging of supramolecular self-healing rubber. *Macromolecules*. (2013) 46:1841–50. doi: 10.1021/ma400019m
52. Peez N, Janiska MC, Imhof W. The first application of quantitative 1 H NMR spectroscopy as a simple and fast method of identification and quantification of microplastic particles (PE, PET. and PS). *Anal Bioanal Chem.* (2019) 411:823–33. doi: 10.1007/s00216-018-1510-z
53. Hickling J, Jones R. *Intradermal Delivery of Vaccines: A Review of the Literature and Potential for Development for Use in Low- and Middle-Income Countries.* Ferney-Voltaire: PATH (2009).
54. Chen J, Pompano RR, Santiago FW, Maillat L, Sciammas R, Sun T, et al. The use of self-adjuvanting nanofiber vaccines to elicit high-affinity B cell responses to peptide antigens without inflammation. *Biomaterials.* (2013) 34:8776–85. doi: 10.1016/j.biomaterials.2013.07.063
55. Hussein WM, Mukaida S, Azmi F, Bartlett S, Olivier C, Batzloff MR, et al. Comparison of fluorinated and nonfluorinated lipids in self-adjuvanting delivery systems for peptide-based vaccines. *ACS Med Chem Lett.* (2017) 8:227–32. doi: 10.1021/acsmedchemlett.6b00453
56. DasSarma S, DasSarma P. Gas vesicle nanoparticles for antigen display. *Vaccines*. (2015) 3:686–702. doi: 10.3390/vaccines3030686
57. Shang L, Nienhaus K, Nienhaus GU. Engineered nanoparticles interacting with cells: size matters. *J Nanobiotechnol.* (2014) 12:5. doi: 10.1186/1477-3155-12-5
58. Hedstrom L. Serine protease mechanism and specificity. *Chem Rev.* (2002) 102:4501–24. doi: 10.1021/cr000033x
59. Kisselev AF, Songyang Z, Goldberg AL. Why does threonine, not serine. function as the active site nucleophile in proteasomes? *J Biol Chem.* (2000) 275:14831–7. doi: 10.1074/jbc.275.20.14831
60. Nilsson A, Lindgren J, Karlström EA. Intramolecular thioether crosslinking to increase the proteolytic stability of affibody molecules. *ChemBioChem*. (2017) 18:2056–62. doi: 10.1002/cbic.201700350
61. Gerona-Navarro G, Mujtaba S, Frasca A, Patel J, Zeng L, Plotnikov AN, et al. Rational design of cyclic peptide modulators of the transcriptional coactivator CBP: a new class of p53 inhibitors. *J Am Chem Soc.* (2011) 133:2040–3. doi: 10.1021/ja107761h
62. Fairlie DP, de Araujo AD. Stapling peptides using cysteine crosslinking. *Biopolymers*. (2016) 106:843–52. doi: 10.1002/bip.22877
63. Martins KA, Bavari S, Salazar AM. Vaccine adjuvant uses of poly-IC and derivatives. *Expert Rev Vaccines.* (2015) 14:447–59. doi: 10.1586/14760584.2015.966085
64. Tostanoski LH, Chiu YC, Andorko JI, Guo M, Zeng X, Zhang, P, et al. Design of polyelectrolyte multilayers to promote immunological tolerance. *ACS Nano.* (2016) 10:9334–45. doi: 10.1021/acsnano.6b04001

65. Blander JM, Medzhitov R. Toll-dependent selection of microbial antigens for presentation by dendritic cells. *Nature*. (2006) 440:808. doi: 10.1038/nature04596
66. Liu Y, Janeway CA. Cells that present both specific ligand and costimulatory activity are the most efficient inducers of clonal expansion of normal CD4 T cells. *Proc Natl Acad Sci USA*. (1992) 89:3845–9. doi: 10.1073/pnas.89.9.3845
67. Wang P, Dong S, Zhao P, He X, Chen M. Direct loading of CTL epitopes onto MHC class I complexes on dendritic cell surface *in vivo*. *Biomaterials*. (2018) 182:92–103. doi: 10.1016/j.biomaterials.2018.08.008
68. Dong S, Wang P, Zhao P, Chen M. Direct loading of iTEP-delivered CTL epitope onto MHC class I complexes on the dendritic cell surface. *Mol Pharm*. (2017) 14:3312–21. doi: 10.1021/acs.molpharmaceut.7b00367
69. Nordly P, Rose F, Christensen D, Nielsen HM, Andersen P, Agger EM, et al. Immunity by formulation design: induction of high CD8+ T-cell responses by poly (I: C) incorporated into the CAF01 adjuvant via a double emulsion method. *J Control Release*. (2011) 150:307–17. doi: 10.1016/j.jconrel.2010.11.021
70. Gungor B, Yagci FC, Tincer G, Bayyurt B, Alpdundar E, Yildiz S, et al. CpG ODN nanorings induce IFNα from plasmacytoid dendritic cells and demonstrate potent vaccine adjuvant activity. *Sci Transl Med*. (2014) 6:235ra261. doi: 10.1126/scitranslmed.3007909
71. Stowell NC, Seideman J, Raymond HA, Smalley KA, Lamb RJ, Egenolf DD, et al. Long-term activation of TLR3 by poly (I: C) induces inflammation and impairs lung function in mice. *Respir Res*. (2009) 10:43. doi: 10.1186/1465-9921-10-43
72. Bernhard H, Huseby ES, Hand SL, Lohmann M, Batten WY, Disis ML, et al. Dendritic cells lose ability to present protein antigen after stimulating antigen-specific T cell responses, despite upregulation of MHC class II expression. *Immunobiology*. (2000) 201:568–82. doi: 10.1016/S0171-2985(00)80075-3
73. Jia J, Zhang Y, Xin Y, Jiang C, Yan B, Zhai S. Interactions between nanoparticles and dendritic cells: from the perspective of cancer immunotherapy. *Front Oncol*. (2018) 8:404. doi: 10.3389/fonc.2018.00404
74. Cibrián D, Sánchez-Madrid F. CD69: from activation marker to metabolic gatekeeper. *Eur J Immunol*. (2017) 47:946–53. doi: 10.1002/eji.201646837
75. Kuroda Y, Nacionales DC, Akaogi J, Reeves WH, Satoh M. Autoimmunity induced by adjuvant hydrocarbon oil components of vaccine. *Biomed Pharmacother*. (2004) 58:325–37. doi: 10.1016/j.biopha.2004.04.009
76. Perrie Y, Mohammed AR, Kirby DJ, McNeil SE, Bramwell VW. Vaccine adjuvant systems: enhancing the efficacy of sub-unit protein antigens. *Int J Pharm*. (2008) 364:272–80. doi: 10.1016/j.ijpharm.2008.04.036
77. Petrovsky N, Aguilar JC. Vaccine adjuvants: current state and future trends. *Immunol Cell Biol*. (2004) 82:488–96. doi: 10.1111/j.0818-9641.2004.01272.x
78. van Aalst S, Ludwig IS, van der Zee R, van Eden W, Broere F. Bystander activation of irrelevant CD4+ T cells following antigen-specific vaccination occurs in the presence and absence of adjuvant. *PLoS ONE*. (2017) 12:e177365. doi: 10.1371/journal.pone.0177365
79. Polley R, Zubairi S, Kaye PM. The fate of heterologous CD4+ T cells during leishmania donovani infection. *Eur J Immunol*. (2005) 35:498–504. doi: 10.1002/eji.200425436
80. Bangs SC, McMichael AJ, Xu XN. Bystander T cell activation–implications for HIV infection and other diseases. *Trends Immunol*. (2006) 27:518–24. doi: 10.1016/j.it.2006.09.006
81. Zeng Q, Li H, Jiang H, Yu J, Wang Y, Ke H, et al. Tailoring polymeric hybrid micelles with lymph node targeting ability to improve the potency of cancer vaccines. *Biomaterials*. (2017) 122:105–13. doi: 10.1016/j.biomaterials.2017.01.010
82. Foged C, Brodin B, Frokjaer S, Sundblad A. Particle size and surface charge affect particle uptake by human dendritic cells in an *in vitro* model. *Int J Pharm*. (2005) 298:315–22. doi: 10.1016/j.ijpharm.2005.03.035
83. Manolova V, Flace A, Bauer M, Schwarz K, Saudan P, Bachmann MF. Nanoparticles target distinct dendritic cell populationsaccording to their size. *Eur J Immunol*. (2008) 38:1404–13. doi: 10.1002/eji.200737984
84. Blank F, Stumbles PA, Seydoux E, Holt PG, Fink A, Rothen-Rutishauser B, et al. Size-dependent uptake of particles by pulmonary antigen-presenting cell populations and trafficking to regional lymph nodes. *Am J Respir Cell Mol Biol*. (2013) 49:67–77. doi: 10.1165/rcmb.2012-0387OC
85. Hickey JW, Santos JL, Williford JM, Mao HQ. Control of polymeric nanoparticle size to improve therapeutic delivery. *J Control Release*. (2015) 219:536–47. doi: 10.1016/j.jconrel.2015.10.006
86. Jiang H, Wang Q, Sun X. Lymph node targeting strategies to improve vaccination efficacy. *J Control Release*. (2017) 267:47–56. doi: 10.1016/j.jconrel.2017.08.009
87. Howard GP, Verma G, Ke X, Thayer WM, Hamerly T, Baxter VK, et al. Critical size limit of biodegradable nanoparticles for enhanced lymph node trafficking and paracortex penetration. *Nano Res*. (2019) 12:837–44. doi: 10.1007/s12274-019-2301-3
88. Zhang R, Smith JD, Allen BN, Kramer JS, Schauflinger M, Ulery BD. Peptide amphiphile micelle vaccine size and charge influence the host antibody response. *ACS Biomater Sci Eng*. (2018) 4:2463–72. doi: 10.1021/acsbiomaterials.8b00511
89. Kuai R, Sun X, Yuan W, Xu Y, Schwendeman A, Moon JJ. Subcutaneous nanodisc vaccination with neoantigens for combination cancer immunotherapy. *Bioconjug Chem*. (2018) 29:771–5. doi: 10.1021/acs.bioconjchem.7b00761
90. Speiser DE, Liénard D, Rufer N, Rubio-Godoy V, Rimoldi D, Lejeune F, et al. Rapid and strong human CD8+ T cell responses to vaccination with peptide, IFA, and CpG oligodeoxynucleotide 7909. *J Clin Invest*. (2005) 115:739–46. doi: 10.1172/JCI23373
91. Dekker CL, Gordon L, Klein J. *Dose Optimization Strategies for Vaccines: The Role of Adjuvants and New Technologies*. Washington, DC: Vaccine Development and Supply Subcommittee of the National Vaccine Advisory Committee (2008).
92. Reed SG, Bertholet S, Coler RN, Friede M. New horizons in adjuvants for vaccine development. *Trends Immunol*. (2009) 30:23–32. doi: 10.1016/j.it.2008.09.006

Conflict of Interest: The authors declare that the research was conducted in the absence of any commercial or financial relationships that could be construed as a potential conflict of interest.

frontiers in Immunology

REVIEW
published: 04 August 2020
doi: 10.3389/fimmu.2020.01726

Biomaterial-Driven Immunomodulation: Cell Biology-Based Strategies to Mitigate Severe Inflammation and Sepsis

Jackline Joy Martín Lasola[1], *Henry Kamdem*[2], *Michael W. McDaniel*[2] *and Ryan M. Pearson*[1,2,3]*

[1] Department of Microbiology and Immunology, University of Maryland School of Medicine, Baltimore, MD, United States, [2] Department of Pharmaceutical Sciences, University of Maryland School of Pharmacy, Baltimore, MD, United States, [3] Marlene and Stewart Greenebaum Comprehensive Cancer Center, University of Maryland School of Medicine, Baltimore, MD, United States

OPEN ACCESS

Edited by:
Evan Alexander Scott, Northwestern University, United States

Reviewed by:
Anthony George Tsolaki, Brunel University London, United Kingdom
Xiuling Lu, University of Connecticut, United States

***Correspondence:**
Ryan M. Pearson
rpearson@rx.umaryland.edu

Specialty section:
This article was submitted to Molecular Innate Immunity, a section of the journal Frontiers in Immunology

Received: *13 March 2020*
Accepted: *29 June 2020*
Published: *04 August 2020*

Citation:
Lasola JJM, Kamdem H, McDaniel MW and Pearson RM (2020) Biomaterial-Driven Immunomodulation: Cell Biology-Based Strategies to Mitigate Severe Inflammation and Sepsis. Front. Immunol. 11:1726. doi: 10.3389/fimmu.2020.01726

Inflammation is an essential component of a wide variety of disease processes and oftentimes can increase the deleterious effects of a disease. Finding ways to modulate this essential immune process is the basis for many therapeutics under development and is a burgeoning area of research for both basic and translational immunology. In addition to developing therapeutics for cellular and molecular targets, the use of biomaterials to modify innate and adaptive immune responses is an area that has recently sparked significant interest. In particular, immunomodulatory activity can be engineered into biomaterials to elicit heightened or dampened immune responses for use in vaccines, immune tolerance, or anti-inflammatory applications. Importantly, the inherent physicochemical properties of the biomaterials play a significant role in determining the observed effects. Properties including composition, molecular weight, size, surface charge, and others affect interactions with immune cells (i.e., nano-bio interactions) and allow for differential biological responses such as activation or inhibition of inflammatory signaling pathways, surface molecule expression, and antigen presentation to be encoded. Numerous opportunities to open new avenues of research to understand the ways in which immune cells interact with and integrate information from their environment may provide critical solutions needed to treat a variety of disorders and diseases where immune dysregulation is a key inciting event. However, to elicit predictable immune responses there is a great need for a thorough understanding of how the biomaterial properties can be tuned to harness a designed immunological outcome. This review aims to systematically describe the biological effects of nanoparticle properties—separate from additional small molecule or biologic delivery—on modulating innate immune cell responses in the context of severe inflammation and sepsis. We propose that nanoparticles represent a potential polypharmacological strategy to

simultaneously modify multiple aspects of dysregulated immune responses where single target therapies have fallen short for these applications. This review intends to serve as a resource for immunology labs and other associated fields that would like to apply the growing field of rationally designed biomaterials into their work.

Keywords: nanoparticles, microparticles, biomaterials, innate immunity, macrophage, neutrophil, sepsis, inflammation

INTRODUCTION

Inflammation is a complex and essential homeostatic response to extrinsic and intrinsic damage. This process is responsible for everything from recognition of microbial breeches into sterile sites and tissue damage to clearance of the insulting microbe and resolution of the immune response. Host defense mechanisms act to mobilize immune cells and molecules into vascularized tissues with the objective to eliminate the source of cell injury. Acute inflammation has been noted since antiquity by the cardinal signs of *rubor* (redness), *tumor* (swelling), *calor* (heat), *dolor* (pain), and *functio laesa* (loss of function) (1). These cardinal signs may also be accompanied by systemic features triggered by cytokine release, such as fever, changes in the peripheral white blood cell count, and increases in clinically detectable acute phase reactants in the blood stream (2). Given the vast coordination of tissue sites and organ systems, inflammation requires a finely tuned, highly regulated physiologic process where a concerted regulatory network of cellular and chemical mediators exists to limit the extent, severity, and spread of inflammation. Failure to effectively and efficiently resolve this process leads to a state of chronic inflammation that can exacerbate disease and pathologic processes. As the role of inflammation becomes further appreciated as a major driver of pathogenesis in many diseases, the need for technologies capable of modulating vascular and immune responses during uncontrolled inflammation will become increasingly necessary.

In this review, we will facilitate our discussion of dysregulated inflammatory responses within the context of severe inflammation and sepsis. These serve as fitting models for understanding the inflammatory response and what occurs when it fails to resolve as expected (3, 4). Unfortunately, there are currently very few nanotechnology platforms that specifically investigate their utility for this indication. As such, we will address what is known about the physiologic pathways and mechanisms at play during inflammation through discussions of emerging technological developments to modulate inflammation in a variety of diseases. This will serve as a starting point to consider future nanotechnology prospects to improve patient health for those suffering from sepsis.

Here, we will specifically focus on technologies where the immune responses can be attributed to the inherent physicochemical properties of the engineered biomaterial itself (i.e., in the absence of any immunomodulatory small molecule or biologic). Although the immune response has previously been treated as something that must be overcome in the development of nanoparticles and microparticles (henceforth, referred to collectively as nanoparticles) for clinical usage, the rise of immunotherapy for vaccine and immune tolerance applications has shed new light on the ways nanoparticle physicochemical properties can be used for similar purposes to modify existing immune responses (5–8), especially for indications where dysfunctional or exaggerated inflammation and immunological processes are contributing factors. Lastly, these nanotechnology-based approaches will be discussed in the context of what is known about the biological processes during inflammation as appreciation of nano-bio interactions (9, 10) allows for development of design strategies for future biomaterial approaches. Our objective is to highlight emerging patterns in biomaterial designs for a variety of nanoparticle platforms and how they have been shown to regulate multifactorial immune responses by acting at various points in the inflammatory cascade. Given that inflammation is exceptionally complex, we propose nanoparticles as a polypharmacological approach to shift how we think about therapeutics for severe inflammation and sepsis.

THE PERSISTENCE OF SYSTEMIC INFLAMMATION AND LIMITATIONS OF SEPSIS THERAPEUTIC DEVELOPMENT

Inflammation is a powerful, multifactorial host defense mechanism intended to protect the host from microbial insult and tissue damage (11). As such, it is not only essential to the maintenance of homeostasis and protection but also can be deleterious on its own when regulatory mechanisms go awry. Examples of conditions characterized by dysregulated inflammatory responses include chronic inflammation, inappropriate fibrosis and scarring, and sepsis syndrome. These conditions demonstrate the delicate balance between damage and repair by which inflammation drives much of the pathology of common diseases including atherosclerosis, diabetes, neurodegenerative disorders, and others. Although situations of chronic inflammation and inappropriate wound healing are outside the scope of this review, sepsis syndrome provides a highly informative case study of what happens when acute inflammation continues unabated. When left unchecked, continuous inflammation leads to its own set of deleterious, systemic acute phase responses, and ineffectual regulatory responses.

Sepsis is a life-threatening condition of complex pathophysiological origin that develops due to an uncontrolled immune response during infection (12–14). Hallmark features of sepsis include profound acute pro-inflammatory cytokine responses, vascular endothelial leakage, and multi-organ

failure (15). Concomitantly, a compensatory anti-inflammatory response develops in an attempt to resolve inflammation and promote tissue repair. This is accompanied by immune paralysis whereby antigen presenting cells (APCs) such as macrophages and dendritic cells lose their responsiveness to subsequent inflammatory challenge and significant alterations in immune cell apoptotic programming results in immunosuppression occurring with immune-mediated organ dysfunction (16–19). Beyond the dramatic physiologic changes, the human toll of sepsis and septic shock remains quite dramatic and accounted for over 2.5 million cases and $52 billion in aggregate costs between January 2010 and September 2016 alone (20). The global burden of sepsis is even greater with conservative estimates indicating that it is the leading cause of mortality and critical illness worldwide (13, 21). In 2017, it was estimated that 19.7% of all global deaths could be attributed to sepsis or sepsis-related causes (12). Because of this acute burden and the long-term physical, psychological, and cognitive disabilities for those who survive sepsis (22) efforts to improve treatment strategies and therapeutic approaches for those with and at risk of sepsis have been ongoing. While mainstays of treatment remain early administration of broad-spectrum antibiotics and intravenous fluids along with resuscitation, additional successful attempts to improve patient management for those with sepsis remain limited (23, 24).

Since the 1980's, over 100 therapeutic clinical trials have been conducted for sepsis and septic shock with little to no improved prospects for those affected. The general strategy for research and drug development within this space has been the generation of highly targeted agents that can be classified into categories based on known mechanisms at play in inflammation. These include as disparate and broad categories as anti-cytokines, anti-virulence factors, coagulopathy agents, anti-inflammatory agents, and even immune stimulators [reviewed nicely in (23–26)] with some of these examples being described in what follows. Of all the clinical trials, only activated protein C (drotrecogin alfa-activated), whose mechanism of action is an antithrombotic effect due to inhibition of factors Va and VIIIa in the coagulation cascade, was successfully licensed following a highly publicized clinical trial (27, 28). Yet, it was removed from the market a decade later due to further work showing not only a lack of a survival benefit for sepsis patients but also increased bleeding risks (29–32). With the inconclusive clinical trial data and controversial marketing strategies for drotrecogin alfa-activated, the example of activated protein C therapies and other failed clinical trials for targeted therapeutics raises the question, what are we missing in our strategies to treat sepsis? Various researchers have attempted to answer this question and have identified a few major themes (24–26): (1) preclinical models poorly recapitulate the complex physiological and molecular changes of sepsis syndrome; (2) patients with sepsis are plagued by a variety of initiating microbial infections and modes of entry; and, (3) patients are themselves very demographically complex based on age, sex, comorbidities, genetics, and infection site. However, one factor that remains underappreciated is the complex and redundant mechanisms at play to initiate the underlying bout of severe inflammation and the resultant sepsis. As such, any attempts to resolve the underlying dysregulated inflammation that triggers sepsis requires an approach that can address the redundancies of this highly coordinated defense mechanism. Elucidation of this multifactorial process requires ongoing work in preclinical models despite current recommendations to move away from such investigations (33).

Collectively, the efficacy of these single-agent, single-target therapeutics has not been as successful as preclinical models has suggested and when shown to be of some benefit, responses are highly dependent on their administration during a narrow treatment window with the associated immunosuppression rarely being addressed along with the vast pro-inflammatory response (24, 34). As such, safe and effective multi-targeted therapeutics for sepsis are critically needed to overcome the considerable heterogeneity of deficiencies at the cellular and molecular level that accumulate to result in deleterious tissue and multiorgan damage in sepsis. Modification of these vascular and immune cell responses using engineered nanoparticles is the basis for new therapies aimed to suppress inflammatory responses and functionally reprogram dysregulated cells and molecular pathways (7, 35, 36). In the following sections, we will describe approaches to treating severe inflammation and sepsis using nanoparticle strategies informed by the known cellular and molecular pathophysiology of inflammatory processes.

NANOPARTICLE MODULATORS OF INTEGRATED VASCULAR AND IMMUNE INFLAMMATORY RESPONSES

As a highly regulated process, deficient and/or overexaggerated responses at any step in the inflammatory cascade can result in serious deterioration in the health status of an individual. The inflammatory response can be characterized by the following processes: (1) recognition of the injurious agent, (2) regulation of the response (control), (3) recruitment of leukocytes, (4) removal of the agent, and (5) resolution (repair) (11). Throughout this process, microvascular tissue, innate immune cells, and circulating soluble mediators act to respond. Further, deficits in the adaptive immune system can contribute to the body's inability to control the infection and repair. Within each step of this response, points for intervention exist for therapeutics to alter the progression of inflammation and modulate the systemic responses (**Figure 1**). For decades, researchers have focused on developing single molecule or single pathway targeted therapeutics to modify highly specific regulatory nodes of the inflammatory response. As our discussion progresses, a number of these approaches will be discussed to compare and contrast with newer nanotechnologies driven by current biological understanding of inflammation. By evaluating the numerous approaches, the intention is to suggest future paths of therapeutic research and development to alter outcomes for those with severe inflammation and sepsis.

Halting Inflammation Before It Starts: Strategies to Sequester the Initiating Warning Signals of Inflammation

Initiation of inflammation requires recognition of the infectious microbe or products of cell and tissue damage. This work

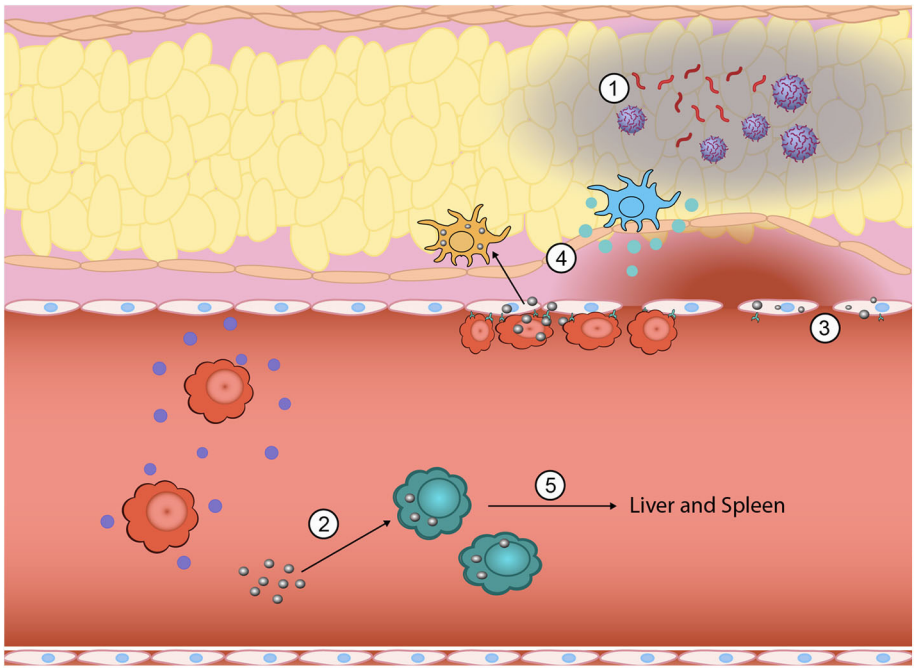

FIGURE 1 | Inflammation is a highly complex, multistep process where nanoparticles can be engineered to intervene to tune the response at multiple points. During the initial generation of PAMPs and DAMPs, biomimetic nanoparticles have been used to sequester PAMPs and DAMPs from immune cell recognition (1). Innate immune cells that have taken up nanoparticles can be functionally reprogrammed from a pro-inflammatory phenotype (i.e., TNF-α, IL-1β, and IL-6 secreting) to an anti-inflammatory phenotype (2). The vascular endothelium also plays a key role in promoting inflammation and nanoparticles can be used to downregulate attachment of circulating immune cells and subsequent exudation (3). Nano-bio interactions can also alter direct homing to inflamed tissue sites by either eliminating chemokine production at the site (4) or redirecting inflammatory cells away from the inflamed site to the liver and spleen for elimination (5).

is accomplished by tissue macrophages, dendritic cells, and mast cells of the innate immune system, in addition to other sentinel cells resident in tissues that contain pattern recognition receptors (PRRs). These PRRs are unique in that they can recognize pathogen-associated and damage-associated molecular patterns (PAMPs and DAMPs, respectively) in a manner that triggers general molecular warning programs to initiate protective processes against the inciting insults (37, 38). These receptors include Toll-like receptors (TLRs) on the plasma and endosomal membranes, C-type lectin receptors (CLRs) on the plasma membrane, NOD-like receptors (NLRs) on the plasma and endosomal membranes and in the cytoplasm, RIG-I-like receptors (RLRs) in the cytoplasm, and AIM2-like receptors (ALRs) in the cytoplasm and nucleus (39). These receptors are unique in that they recognize cellular products exclusively produced by microbes, such as lipopolysaccharide (LPS) from Gram-negative bacteria or double-stranded RNA from specific viral classes, or cellular components that are only released by the host during times of tissue and cellular damage like high mobility group box 1 (HMGB1) (40, 41). These cellular responses are complemented with circulating proteins that serve as complementary humoral responses. Antibodies, complement proteins (42), and collectins (43–45) also recognize microbes, opsonize them, and target them for ingestion by phagocytes and activation of other immune cells via Fc receptors.

Given that inflammation starts with recognition of these PAMPs, DAMPs, and microbes, at the nascent site of inflammation, limiting the initiation of this process serves as a potential strategy by which to limit the severity of inflammation and halt progression to systemic inflammation. Traditional strategies to halt these initial stages of the inflammatory cascade have focused on neutralizing microbes, such as continuing antibiotic development or even utilization of human antiserum against microbes, such as against *Escherichia coli* (46). Newer approaches aim to bind and neutralize PAMPs, such as the development of monoclonal antibodies targeting the lipid A moiety of LPS (47–50) or direct antagonizing of the PRRs like trials conducted with eritoran, a TLR4 antagonist derived from lipid A (51, 52), or small molecule inhibitors of TLR signaling like TAK-242 (53).

More recent biomaterial strategies to prevent this initial recognition of microbial products and their ensuing damage are notable for biomimetic approaches (**Figure 2** and **Table 1**) to sequester these initiators of inflammation and halt the cascade before it begins. Kunz et al. (55) developed cell-derived nanoparticles (CDNPs) to limit inflammation and showed that the CDNP platform was able to limit bacterial growth *in vitro*. CDNPs were generated via high-speed centrifugation of fibroblast cytoplasmic contents to isolate the desired exosomes. These exosomes were largely composed of proteins such as annexin A5, heat shock proteins, peroxiredoxines, with small

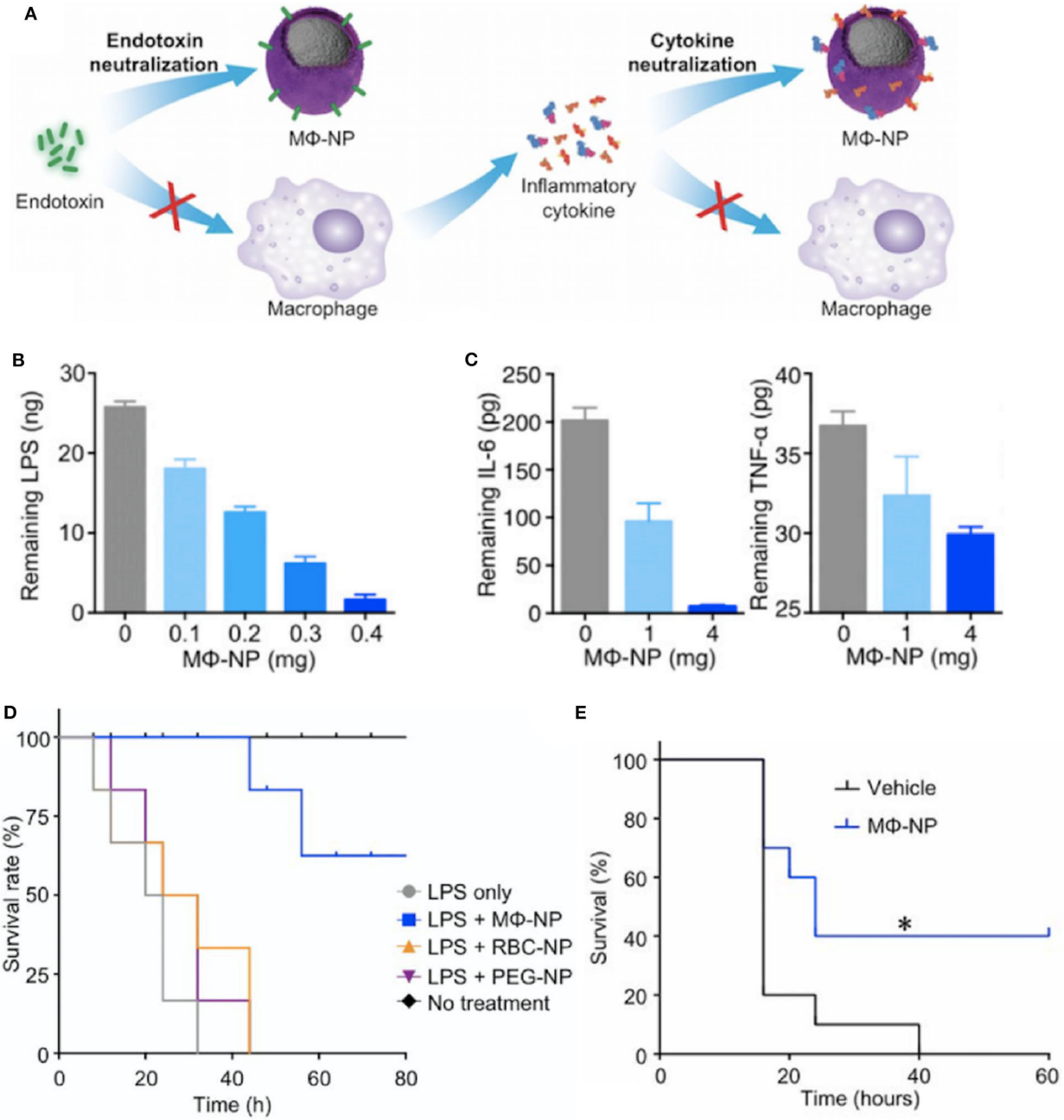

FIGURE 2 | Macrophage mimicking nanoparticles (MΦ-NP) sequester bacteria derived endotoxin and subsequent inflammatory cytokines to limit inflammation associated damage **(A)**. This results in a dose-dependent ability of the MΦ-NP to reduce free LPS **(B)** and pro-inflammatory cytokines such as IL-6 and TNF-α **(C)** *in vitro*. LPS-induced endotoxemia **(D)** and *E. coli* bacteremia **(E)** show a survival benefit specific to the biomimetic MΦ-NP, where $^{*}P < 0.05$. Adapted from (54). Copyright (2017) National Academy of Science.

traces of DNA and RNA, that showed preferential uptake by neutrophils, inflammatory monocytes, and macrophages, all key cells for the initiation of inflammation. This was correlated with decreased IL-6 levels in the peritoneum of mice with cecal ligation and puncture (CLP)-induced polymicrobial sepsis. Additional work showed that in an *in vitro* system, coincubation of these CDNPs with *Pseudomonas aeruginosa* resulted in direct decreases in bacterial colony-forming units, suggesting an additional bactericidal effect of the CDNPs. To contrast, a separate strategy by Thamphiwatana et al. (54) used a similar strategy of isolating immune cell components to drive protective responses against inflammation. The authors used poly(lactic-*co*-glycolic acid) (PLGA) as the core polymer for the particles and coated these particles with

TABLE 1 | Strategies to sequester the initiating warning signals of inflammation.

Biological effect	Physicochemical properties				Biological models		References
	Materials	Size	Zeta potential/ charge	Surface coating	Cell type	Animal models	
BIOMIMETIC STRATEGIES TO HALT INITIATION OF INFLAMMATION							
Decreased bacterial growth leading to decreased PAMP/DAMP availability	MC3T3-E1 fibroblast-derived annexins (abundant annexin A5), actin, histones, heath shock proteins, myosin, peroxiredoxines, vimentin; small traces of nucleic acids	50–200 nm			Neutrophils, inflammatory monocytes, macrophages	Mice	(55)
Sequestration of LPS and inflammatory cytokines	Poly(lactic-*co*-glycolic acid)	100–105 nm	−30 to −23 mV	Macrophage cell membrane	J774 macrophages, human umbilical vein endothelial cells	Mice (C57Bl/6, BALB/c)	(54)
SEQUESTRATION OF COMPLEMENT PROTEINS							
Sequestration of circulating complement proteins triggering opsonization	Poly(lactic-*co*-glycolic acid)	40–50 nm	−70 to −50 mV	Poly(ethylene glycol) (PEG_{550} and PEG_{2000})	J774 macrophages		(56)
Sequestration of circulating complement proteins triggering opsonization	Multi-walled carbon nanotubes	0.4–4.2 nm (length), 12–34 nm (diameter)		Carboxylmethyl cellulose	U937 monocytes, human peripheral blood monocytes		(56)
Sequestration of complement proteins triggering opsonization	Multi-walled carbon nanotubes	0.4–4.2 nm (length), 12–34 nm (diameter)		RNA	U937 monocytes, human peripheral blood monocytes		(56)

macrophage-derived cell membranes to prepare macrophage mimicking nanoparticles. As described in **Figure 2**, the authors show using both macrophages and endothelial cells (HUVECs), the ability of these macrophage mimicking nanoparticles to sequester LPS away from the PRRs of cells necessary to initiate the inflammatory cascade with an additional effect of also sequestering away inflammatory cytokines to prevent further inflammatory activation of macrophages and HUVECs. Using LPS-induced endotoxemia and *E. coli*-induced bacteremia murine models, these particles were shown to have a survival benefit specifically linked to the inclusion of the macrophage membranes in the particle formulation.

As noted above, in addition to direct cellular recognition of PAMPs and DAMPs, circulating proteins of the innate immune response can trigger activation of inflammatory pathways. Of particular note are those within the complement pathway where C3a, C4a, and C5a, serve as triggers of anaphylaxis and chemotaxis. Because of their key role as humoral mediators of inflammation, the interaction between biomaterials and the complement pathway are of great interest. In one study, PLGA particles were shown to trigger differential levels of complement activation based on the molecular weights of the poly(ethylene glycol) surface coating. By combining PEG_{550} with PEG_{2000} as the surface coating of PLGA particles, Pannuzzo et al. were able to limit generation of C5a and downstream complement components without altering particle uptake by macrophages (56). Another platform showed that multi-walled carbon nanotubes (CNTs) surface modified with carboxymethyl cellulose (CMC-CNT) or RNA (RNA-CNT) appear to serve as a type of sink for deposition of complement pathway proteins. This has the net effect of modifying the inherent pro-inflammatory responses of CNTs through analysis of dampened transcription of TNF-α and IL-1β in macrophages (57). In contrast, a study of CNTs showed that in combination with LPS activation, the pro-inflammatory effects of CNTs were mediated through inflammasome activation (58). This emphasizes the tunability of the immune response to CNTs in a manner dependent on their physicochemical properties. These varying responses to CNTs, with a particular emphasis on their effects on complement are described in a recent review (59).

Regulating the Regulators: Altering Production of Molecular Mediators of Inflammation

Due to its destructive potential, tight regulation of the initiation and progression of inflammation by its mediators is essential to limit deleterious effects beyond those necessary for eliminating the initial offending agent. As such, these mediators—including histamine, prostaglandins and leukotrienes, and cytokines and chemokines—are often targeted therapeutically to limit inflammation during disease processes (60, 61).

The vasoactive amine histamine is stored preformed in cells and is released upon mast cell degranulation (also blood

basophils and platelets). This release allows for binding to the H_1 receptor of microvascular endothelial cells to trigger arteriole dilation and increased venule vascular permeability. Due to histamine activity, it commonly serves as an anti-inflammatory target, particularly for allergy, and H_1 receptor antagonists like diphenhydramine, loratadine, and cetirizine, are some of the most commonly used drugs for managing allergic reactions and acute inflammatory processes (62).

Arachidonic acid (AA) is found in membrane phospholipids and can be released from the membrane phospholipids (particularly from phospholipase A_2, PLA_2) upon activation to produce interesting classes of inflammation mediators, prostaglandins (PGs) and leukotrienes. Cyclooxygenases (COX-1 and COX-2) in mast cells, macrophages, and endothelial cells produce PGs to trigger vascular and systemic signs and symptoms of inflammation (63). PGE_2 and PGD_2 (mast cells) trigger vasodilation and increases permeability of postcapillary venules to allow for edema formation, whereas PGF_{2a} stimulates uterine, bronchial, and small arteriole smooth muscle contraction. Prostacyclin (PGI_2) is produced in vascular endothelium and serves as a vasodilator and potent inhibitor of platelet aggregator, in addition to serving as a potentiator of other mediators that increase vascular permeability and chemotaxis to sites of injury. Thromboxane (TxA_2), produced in platelets, opposes the effects of prostacyclin in that it is a vasoconstrictor and a potent inducer of platelet aggregation. In addition to these local effects, prostaglandins are implicated in promoting the systemic symptoms of inflammation, namely pain and fever. In contrast, leukotrienes are produced in leukocytes and mast cells by lipoxygenases where LTB_4 serves as a potent chemoattractant while LTC_4, LTD_4, and LTE_4, serve to induce vasoconstriction, bronchospasm, and increased permeability of venules in a manner more potent than the initial histamine release from mast cell degranulation (64).

Given the central role of AA metabolites in inflammation, pharmacologic inhibitors of AA metabolism are widespread in the pharmacopeia. Corticosteroids are an essential class of drugs that can prevent the initial release of AA by phospholipase activity in addition to a series of other proposed mechanisms of action. Non-steroidal anti-inflammatory drugs (NSAIDs) like naproxen and ibuprofen are common over the counter and prescription medication that serve as COX inhibitors to limit inflammation, while lipoxygenase inhibitors and leukotriene receptor antagonists serve as therapeutic strategies in asthma management due to their specific induction of bronchial smooth muscle contraction (63).

In contrast to the non-specific, broad activities of corticosteroids or the highly specific COX inhibitors utilized for asthma management, the applicability of these strategies for severe inflammation and sepsis have been of limited utility. A variety of clinical trials using corticosteroids have shown inconclusive results ranging from benefit with hydrocortisone and fludrocortisone (65) to no overall effect with hydrocortisone (66–70), methylprednisolone, or dexamethasone (71) with some clinical studies concluding corticosteroid strategies with methylprednisolone to actually be a detriment to survival (72). Similarly, a trial for ibuprofen, a common NSAID that serves as an unselective COX inhibitor, showed no effect on mortality in severe sepsis (73).

The limited successes in utilizing these anti-inflammatory strategies in sepsis, has left open the opportunity for biomaterials to serve a role in modifying these immune mediators. Often, due to the inherent capability of materials to be easily altered to better bind a broad variety of metabolites in the bloodstream. An interesting approach is one taken by O'Brien et al. (74, 75) where poly(*N*-isopropylacrylamide) (NIPAm) particles generated in combination with other acrylamide moieties were synthesized to alter the affinity of the protein corona for a variety of plasma components (**Figure 3**). This desire to "tune" the corona for high affinity and selectivity to a variety of biomacromolecules showed that although NIPAm-based particles showed little affinity for plasma proteins, the hydrophobicity of NIPAm-based particles allowed for them to interact favorably with lipophilic molecules. This later was used to show that they could be used for lipid-bound toxin sequestration and neutralization, such as whole honey-bee venom containing a significant amount of venomous PLA_2. It would be interesting to see this work expanded to see if this sequestration and neutralization strategy via protein corona tuning could be applied to neutralizing endogenous lipid species released during inflammation such as the AA metabolites described above that are produced upon vascular endothelial activation.

Similar to the role played by AA metabolites in regulating vascular activity, cytokines and chemokines are proteins produced and secreted by a variety of cell types (activated lymphocytes, macrophages, dendritic cells; also, endothelial, epithelial, and connective tissue cells) to regulate immune and inflammatory activity. In acute inflammation, tumor necrosis factor alpha (TNF-α) and interleukin-1 beta (IL-1β) are essential for leukocyte recruitment by their promotion of endothelial adhesion and diapedesis. Given this activity, research on cytokine receptor blockade has produced therapeutic drug classes that have broad effects at modifying autoimmune disease outcomes. Beyond activating the endothelium and leukocytes, TNF-α, IL-1β, and IL-6 combine to induce the systemic acute phase response that is implicated in the development of sepsis (76–78). In comparison, chemokines serve to attract specific cells to the inflammatory site with individual chemokines of note being IL-8 from macrophages and endothelial cells that drive neutrophil recruitment (79), while monocyte chemoattractant protein (MCP-1) (80), macrophage inflammatory protein-1α (MIP-1α) (81), and regulated and normal T cell expressed and secreted (RANTES) (82), attract monocytes, eosinophils, basophils, and lymphocytes.

The elucidation of molecular mechanisms involved in leukocyte recruitment and migration during inflammation have led to major developments in the generation of therapeutic targets for a variety of inflammation-mediated diseases. Although first discovered to play a role in the pathogenesis of sepsis (83, 84), therapies to directly block TNF-α and IL-1β signaling have done more to change the progression and day-to-day symptomatology for patients with a variety of autoimmune (60, 85) and dermatological conditions (86). In contrast, a variety of clinical trials utilizing anti-TNF monoclonal antibodies (26)

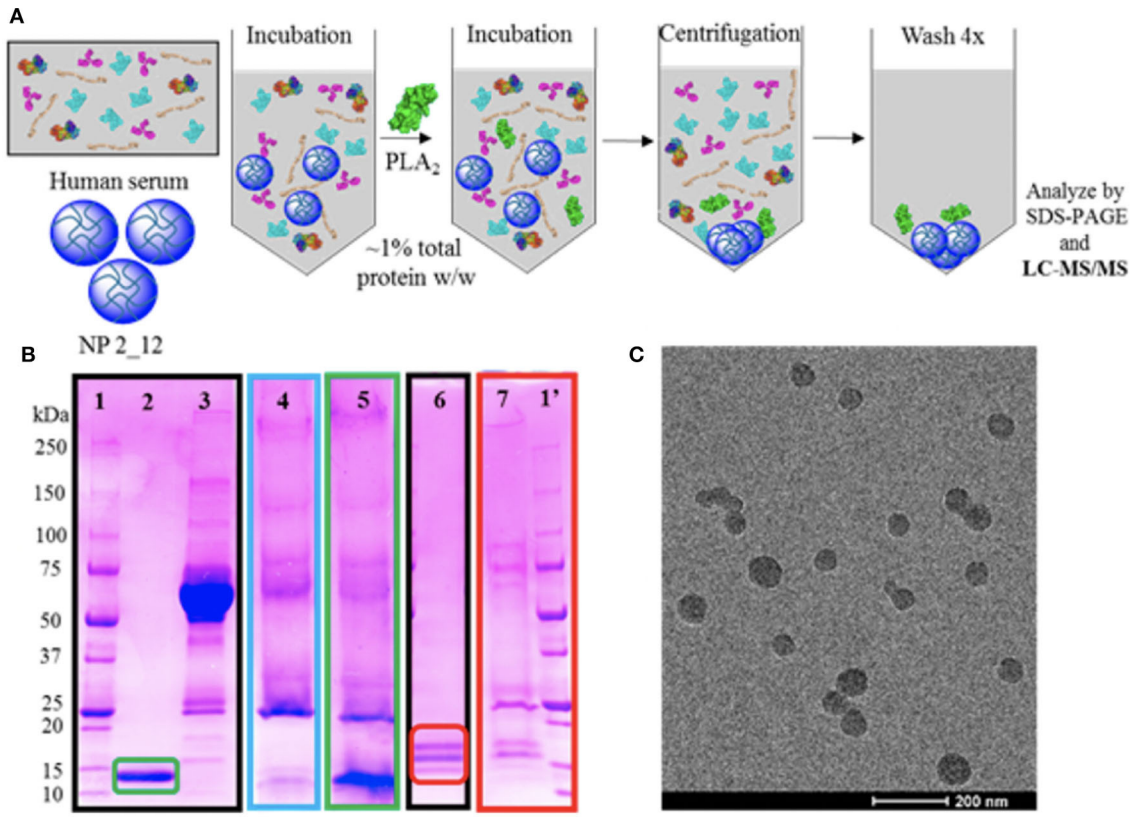

FIGURE 3 | Selectivity experiments and TEM characterization of nanoparticles for targeted sequestration of venom proteins. Polymer composition was optimized to enable specificity toward venom yet avoid serum protein binding. Strategy for assessing selectivity of nanoparticles to venom **(A)**. Selectivity assessment via SDS-PAGE visualization **(B)** of (1/1′) ladder; (2) purified PLA_2 from *Naja mossambica* venom; (3) serum control; (4) nanoparticle in serum only; (5) nanoparticle incubated in serum and PLA_2 from *N. mossambica* venom; (6) purified PLA_2 from honey-bee venom; (7) nanoparticle incubated in ovine plasma and PLA_2 from honey-bee venom. Unstained TEM image of nanoparticle for sequestration of venom **(C)**. Reprinted with permission from (74). Copyright (2016) American Chemical Society.

or even fusion proteins to neutralize TNF-α, like lenercept (87, 88), or etanercept (89), which is in common clinical usage today, have shown no benefit and even harm for patients with septic shock in the case of etanercept (89). This has also been shown with anakinra, an IL-1β decoy receptor, which failed to conclusively show a survival benefit for patients with sepsis or septic shock (90–92).

Interestingly, biomaterials have also been shown to have inherent capabilities to alter immune cells to downregulate key chemotactic molecules (**Figure 1** and **Table 2**) at play in recruiting leukocytes to inflammatory sites. As described above, key players of this process include the cytokines TNF-α and IL-1β. Inhibition of the innate immune cell's capability to secrete TNF-α and IL-1β serves to achieve a similar end as halting initiation of inflammatory signaling and shows the ability to act following activation of inflamed immune cells. Multiple groups have shown a capability to utilize biomaterials to affect this alteration in a variety of inflammation models and suggest a diversity of strategies to impart a similar net effect to modify the molecular regulators of immune activity during inflammation. Using poly(lactic acid) (PLA) and PLGA as nanoparticle cores with poly(ethylene-*alt*-maleic acid) (PEMA) and poly(vinyl alcohol) (PVA) as surfactants, Casey et al. (93), showed that polymer-based biomaterials, lacking any small molecule or biologic for therapeutic effect, have the inherent capability of suppressing cytokine secretion from bone marrow-derived macrophages and dendritic cells following LPS or CpG-DNA stimulation (**Figure 4**). This effect occurred in a surface charge-dependent manner and used polymeric particles in the 350–500 nm diameter range. Furthermore, these materials imparted a survival benefit in a murine LPS-induced endotoxemia model for sepsis. Remarkably, similar results were observed using completely different material composition. In another study, 2 nm gold core nanoparticles with a surface coating of hydroxylated tetraethylene glycol (TEGOH) (98)—again without any delivery of small molecules, peptides, or nucleic acid products—showed a survival benefit in a sepsis model. These nanoparticles were characterized as having an overall net neutral charge and the *in vitro* suppression of TNF-α production in monocytes appeared regardless of choice of surfactant (the TEGOH described above or the hydrophobic tetraethylene glycol coating, ZDiPen). Interestingly, using a

TABLE 2 | Methods to alter cytokine availability.

Biological effect	Physicochemical properties					Biological models		References
	Materials	Size	Zeta potential/ charge	Surface coating	Functionalization	Cell type	Animal models	
Decreased secretion of IL-6, TNF-α	Poly(lactic acid)	350–500 nm	−50 to −40 mV	Poly(ethylene-*alt*-maleic acid)		Bone marrow-derived macrophages	Mice (C57BL/6)	(93)
Partial decreased secretion of IL-6, TNF-α	Poly(lactic acid)	350–500 nm	−25 mV	Poly(vinyl alcohol)		Bone marrow-derived macrophages	Mice (C57BL/6)	(93)
Sequestration of IL-6, TNF-α, IFNɤ; decreased serum IL-6, TNF-α, IFNɤ	Poly(lactic-*co*-glycolic acid)	100–105 nm	−30 to −23 mV	Macrophage cell membrane		J774 macrophages, human umbilical vein endothelial cells	Mice (C57BL/6, BALB/c)	(54)
Decreased secretion of TNF-α, IL-6; increased serum IL-10; decreased serum IL-6	Poly(lactic-*co*-glycolic acid)	140–165 nm	0 to 0.5 mV		di(α2→ 8)*N*-acetylneuraminic acid	Peritoneal macrophages	Mice (C57BL/6)	(94)
Decreased secretion of IL-6, TNF-α	Poly(lactic-*co*-glycolic acid)	350–500 nm	−50 to −40 mV	Poly(ethylene-*alt*-maleic acid)		Bone marrow-derived macrophages	Mice (C57BL/6)	(93)
Partial decreased secretion of IL-6, TNF-α	Poly(lactic-*co*-glycolic acid)	350–500 nm	−25 mV	Poly(vinyl alcohol)		Bone marrow-derived macrophages	Mice (C57BL/6)	(93)
Increased CD206, IL-10, and arginase 1	Poly(lactic-*co*-glycolic acid)	350–500 nm	−50 to −40 mV	Poly(ethylene-*alt*-maleic acid)		Macrophages	Mice (C57BL/6)	(95)
Increased expression of *IL1RN*, *IL10*	Poly(phosphorHydrazone)				Acid azabisphosphorous	Monocytes	Human volunteers, cynomolgus monkeys	(96, 97)
Decreased TNF-α production *in vitro*; decreased serum TNF-α following LPS-induced endotoxemia	Gold	2 nm (core)	Neutral charge	Tetraethylene glycol with end hydroxyl group (TEGOH)		Monocytes	Mice	(98)
Decreased TNF-α production *in vitro*; increased serum TNF-α following LPS-induced endotoxemia	Gold	2 nm (core)	Neutral charge, hydrophobic	Tetraethylene glycol with hydrophobic end group (ZDiPen)		Monocytes	Mice	(98)
Decreased secretion of IL-1β, TNF-α, IL-6, IL-8	Gold	5 nm		Inner lipid: 1,2-dipalmitoyl-*sn*-glycero-3-phosphoethanolamine-N-[3-(2-pyridyldithio)propionate] (PDP PE 16:0) or 1,2-dioleoyl-*sn*-glycero-3-phosphoethanolamine-N-[3-(2-pyridyldithio)propionate (PDP PE 18:1) Outer lipid: 1,2-dipalmitoyl-*sn*-glycero-3-phsphocholine (DPPC), spingomyelin, cardiolipin, 1,2-dilinoleoyl-*sn*-glycero-3-phospho-(1′-rac-glycerol) (18:2 PG), 1,2-dimyristoyl-*sn*-glycer-3-phosphoethanolamine-N-(lissamine rhodamine B sulfonyl) (14:0 Liss Rhod PE)		Monocytes	Human	(99)

(Continued)

TABLE 2 | Continued

Biological effect		Physicochemical properties				Biological models		References
	Materials	Size	Zeta potential/ charge	Surface coating	Functionalization	Cell type	Animal models	
Decreased expression of *Il6*, *Il1b*, *Tnf*	Hydroxylated fullerene ($C_{60}[OH]_{44}$)					Peritoneal macrophages	Mice (C57BL/6)	(100)
Decreased TNF-α, IL-1β secretion and increased IL-10 secretion	Nanodiamond	5 nm	Negatively charged		Octadecylamine	Macrophages	Human	(101)
Decreased peritoneal IL-6 and IL-10 following CLP	Cell-derived nanoparticle (CDNPs)—composed of annexins, actin, histones, heat shock proteins, myosin, peroxiredoxines and vimentin and small traces of nucleic acids, with annexin A5 (AnxA5) being one of the most abundant components; [protein] = 150 μL/mL, [DNA] = 2 μg/mL, [RNA] = 4 μg/mL	50–200 nm				Source of CDNPs: MC3T3-E1 fibroblast cells, peritoneal lavage Takes up CDNPs: neutrophils, inflammatory monocytes, macrophages	Mice	(55)

murine LPS-induced endotoxemia model showed that only the TEGOH-coated gold nanoparticles showed the similar suppression of TNF-α production, whereas the hydrophobic ZDiPen failed to recapitulate the cytokine response. This further demonstrates the importance of designing nanoparticles with appropriate physicochemical properties followed by relevant *in vitro* and *in vivo* testing to obtain a comprehensive understanding of their effects on desired immunological outcomes.

Recruiting Leukocytes to Inflammatory Sites: Biomaterial-Driven Modification of Cellular Trafficking Patterns

A major role of lipid and peptide mediators for inflammation is to facilitate the recruitment of leukocytes to the sites of inflammation, which is necessary to eliminate the source of the infection and/or tissue damage. However, infiltration of these leukocytes can also further injure the inflamed tissue or nearby healthy tissue through the inherent activity of the neutrophils, inflammatory monocytes, macrophages, and other leukocytes. In order to limit their damage at the inflamed site beyond what is needed to control the infection or initial tissue damage, understanding how these sites are accessed from the vasculature and modification of the accessibility of these tissues can be of benefit in developing therapeutic strategies (**Figure 1** and **Table 3**).

Initiation of removal of the injury source requires dilation of the small blood vessels to allow for increased blood flow, increased permeability of the microvasculature, and emigration of the leukocytes from the microcirculation to accumulate in the inflamed tissue (109). Recruitment of leukocytes involves interactions between the vasculature and the immune response. Interjection at any of these steps through altered signaling and inhibition of chemical mediators or redirection and sequestration of leukocytes can alter the course of inflammation to limit the damage it inflicts.

Following sentinel cell recognition of breaches of normal tissue, the vascular mediators described above are mobilized to induce vasodilation while other chemical mediators trigger increased permeability of the postcapillary venules (110). This increased vessel diameter and loss of fluid slows blood flow and allows for concentration of blood cells at the site of tissue injury. As the stasis matures, it is accompanied by increasing amounts of immune mediators at the site to aid in exudation of leukocytes. Additionally, the vascular endothelium expresses increased levels of adhesion molecules that allow for leukocytes, particularly neutrophils, to accumulate along the endothelium and allow for emigration from the vasculature into the injured tissue.

Activation of the vascular endothelium results in selectin upregulation mediated by release of cytokines and chemokines by tissue macrophages, mast cells, and endothelial cells in response to injury. In particular, TNF-α and IL-1β act on endothelial cells of the postcapillary venules near the infection to trigger expression of E-selectin and ligands for L-selectin. Histamine and thrombin also play a role and stimulate P-selectin redistribution from endothelial cell granules (Weibel-Palade bodies) to the cell surface. In contrast, firm adhesion is mediated by integrins whose

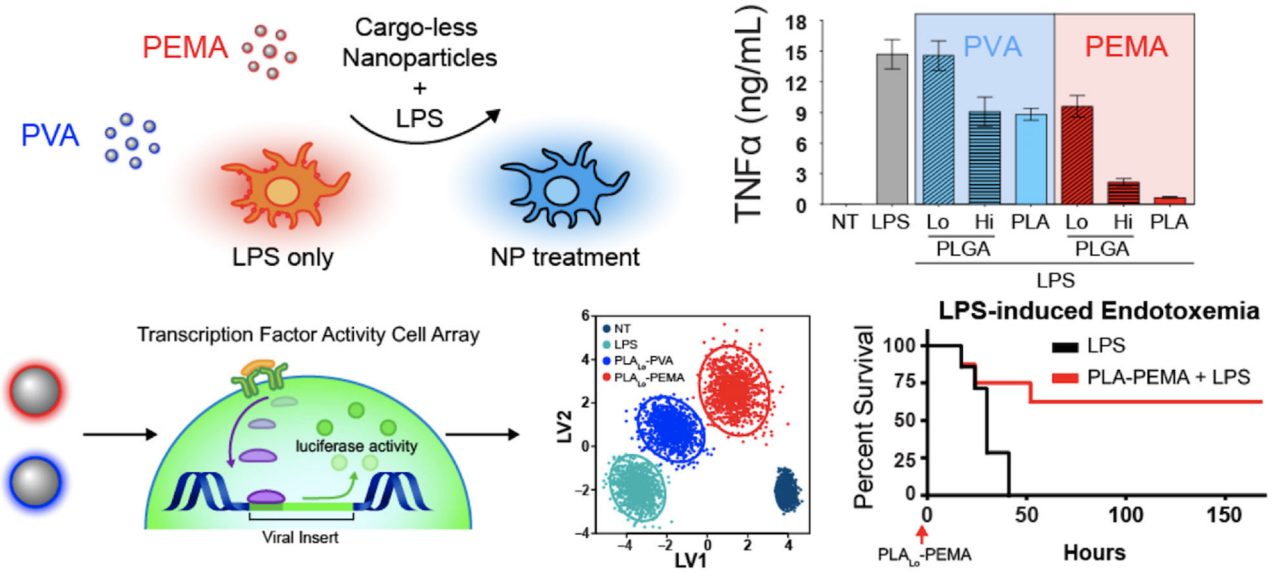

FIGURE 4 | Immunomodulatory effects of nanoparticles. Nanoparticle-dependent inflammatory cytokine suppression of innate immune cells when stimulated with LPS (top). Dynamic transcription factor activity of bone marrow-derived macrophages treated with particles followed by LPS stimulation and improved survival in lethal LPS-induced endotoxemia model. PVA, neutral charge. PEMA, negative charge. Adapted from (93). Copyright (2019) Elsevier.

expression are also under the influence of TNF-α and IL-1β. In the case of endothelium, these cytokines induce expression of vascular cell adhesion molecule 1 (VCAM-1, the ligand for β1 integrin VLA-4) and intercellular adhesion molecule 1 (ICAM-1, the ligand for the β2 integrins LFA-1 and Mac-1). Under normal conditions, the binding of the integrins to VCAM-1 and ICAM-1 are relatively low affinity, but under the influence of cytokines binding to the rolling leukocytes, VLA-4 and LFA-1 are converted to a high affinity state that allows for firm binding of the leukocytes to the endothelial surface (111).

Within the field of biomaterials, numerous groups have attempted to alter these vascular interactions to reduce inflammation [reviewed nicely in (112, 113)] but most have focused on delivery of therapeutics rather than investigation of physicochemical interactions that may modify endothelial behavior. In a few notable examples (102, 103), polystyrene in combination with denatured albumin modulated neutrophil adherence to the vasculature. This interaction aided in delivery of Syk inhibitors to prevent the inside-out signaling that increases leukocyte adhesion to the endothelium. By altering cellular trafficking through making the endothelium less sticky, these studies showed a protective effect against lung injury mediated through alterations in neutrophil activity. Similarly, direct delivery of NF-κB inhibitors to could be achieved through a biomimetic approach. Gao et al. (104) used myeloid cell-derived nanovesicles containing β2 integrins to bind directly to ICAM-1 on HUVECs. This showed a two-fold effect by firstly physically blocking further binding of other leukocytes while also delivering NF-κB inhibitors at the site to stop additional leukocyte diapedesis across the endothelium. Thus, developing a method to use inflammatory cell derivatives to block recruitment of leukocytes is a strategy similar in concept to that of cell membrane-coated nanoparticles described above by Thamphiwatana et al. (54).

Prevention of leukocyte binding is key to stopping cellular infiltration of the inflamed site and multiple mechanisms are simultaneously at play to encourage this process. In addition to the molecular regulators described above, chemokines are also simultaneously stimulating diapedesis through the interendothelial spaces along a concentration gradient toward the site of injury or infection where chemokines are actively being produced. Exogenous chemoattractants include bacterial products such as peptides with *N*-formylmethionine as the terminal amino acid and some bacteria-specific lipids while endogenous chemoattractants include a variety of chemokines (such as IL-8), proteins of the complement system (particularly C5a), and arachidonic acid (AA) metabolites (namely LTB_4). Again, biomaterial approaches have shown an ability to modify these chemokine responses without utilization of drug delivery. In the same Casey article from 2019 (93), in addition to modification of cytokine responses induced my nanoparticle uptake, similarly MCP-1 secretion was shown to be decreased suggesting a global reprogramming of functional responses upon uptake of PLA- and PLGA-based negatively charged particles (**Figure 4**). In parallel to Moyano et al. (98), modification of chemokines from monocytes can also be achieved with gold-based particles where affected chemokines are dependent on choice of surface coating with lipid-based substrates (99) to decrease chemokine release of IL-8, CCL5/RANTES, and CCL2/MCP-1 vs. decoration of gold particles with peptides containing aromatic and hydrophobic residues to impart a decrease in production of CCL2 and CCL4 (105, 106).

TABLE 3 | Modifiers of cellular trafficking patterns.

Biological effect	Physicochemical properties				Biological models		References
	Materials	Size	Zeta potential/ charge	Surface coating	Cell type	Animal models	
DIRECT MODIFICATIONS OF INTEGRIN AND SELECTIN AVAILABILITY							
Reduced neutrophil adhesion and migration across the endothelium to limit vascular inflammation modulated via adherent neutrophils; protective against lung injury with Syk inhibitor to prevent inside-out signaling	Polystyrene	100–117 nm		Denatured albumin	Neutrophils	Mice	(102, 103)
Binds ICAM-1 on HUVEC to deliver NF-κB inhibitors and stop diapedesis	Cell membrane-formed nanovesicles (cell disruption by nitrogen cavitation, centrifugation, and extrusion—contains integrin β2	200 nm	−20 to −12 mV		Source of nanovesicles: HL 60 myeloid cells		(104)
DECREASED CHEMOATTRACTANTS TO INFLAMED SITE							
Decreased secretion of MCP-1	Poly(lactic acid)	350–500 nm	−50 to −40 mV	Poly(ethylene-*alt*-maleic acid)	Bone marrow-derived macrophages	Mice (C57BL/6)	(93)
Partial decreased secretion of MCP-1	Poly[lactic acid)	350–500 nm	−25 mV	Poly(vinyl alcohol)	Bone marrow-derived macrophages	Mice (C57BL/6)	(93)
Decreased secretion of MCP-1	Poly(lactic-*co*-glycolic acid)	350–500 nm	−50 to −40 mV	Poly(ethylene-*alt*-maleic acid)	Bone marrow-derived macrophages	Mice (C57BL/6)	(93)
Partial decreased secretion of MCP-1	Poly(lactic-*co*-glycolic acid)	350–500 nm	−25 mV	Poly(vinyl alcohol)	Bone marrow-derived macrophages	Mice (C57BL/6)	(93)
Decreased secretion of IL-8, CCL5/RANTES, and CCL2/MCP-1	Gold	5 nm		Inner lipid: 1,2-dipalmitoyl-*sn*-glycero-3-phosphoethanolamine-N-[3-(2-pyridyldithio)propionate] (PDP PE 16:0) or 1,2-dioleoyl-*sn*-glycero-3-phosphoethanolamine-N-[3-(2-pyridyldithio)propionate (PDP PE 18:1) Outer lipid: 1,2-dipalmitoyl-*sn*-glycero-3-phsphocholine (DPPC), spingomyelin, cardiolipin, 1,2-dilinoleoyl-*sn*-glycero-3-phospho-(1′-rac-glycerol) (18:2 PG), 1,2-dimyristoyl-*sn*-glycer-3-phosphoethanolamine-N-(lissamine rhodamine B sulfonyl) (14:0 Liss Rhod PE)	Monocytes	Human	(99)
Decreased CCL2 and CCL4 production	Gold	13–20 nm	Negative charge	Peptides with hydrophobic and aromatic residues	Monocytes		(105, 106)
DIVERSION OF INFLAMMATORY CELLS AWAY FROM SITE OF INFLAMMATION							
Negligible sequestration of inflammatory monocytes and neutrophils away from sites of inflammation	Poly(lactic acid)	430–470 nm	−47 to −31 mV	Poly(ethylene-*alt*-maleic acid)	Inflammatory monocytes, neutrophils	Mice (SJL/J)	(107)

(Continued)

TABLE 3 | Continued

Biological effect	Physicochemical properties				Biological models		References
	Materials	Size	Zeta potential/ charge	Surface coating	Cell type	Animal models	
Negligible sequestration of inflammatory monocytes and neutrophils away from sites of inflammation	Poly(lactic-*co*-glycolic acid)—low molecular weight	330–510 nm	−56 to −40 mV	Poly(ethylene-*alt*-maleic acid)	Inflammatory monocytes, neutrophils	Mice (SJL/J)	(107)
Sequestration of inflammatory monocytes and neutrophils away from sites of inflammation	Poly(lactic-*co*-glycolic acid)—high molecular weight	510–590 nm	−43 to −36 mV	Poly(ethylene-*alt*-maleic acid)	Inflammatory monocytes, neutrophils	Mice (C57BL/6, SJL/J, BALB/c)	(107, 108)
Sequestration of inflammatory monocytes away from sites of inflammation	Polystyrene	500 nm	Negatively charged		Inflammatory monocytes	Mice (C57BL/6, SJL/J, BALB/c)	(108)

Uniquely, another approach in the literature by Getts et al. (108) bypasses the process of leukocyte migration. Rather than alter the cellular function of inflammatory cells, they showed that PLGA and polystyrene (PS) particles with negatively charged PEMA coating were actively taken up by $MARCO^+$ inflammatory monocytes to induce trafficking of these cells away from sites of tissue injury in multiple disease models (including West Nile virus-induced encephalitis, experimental autoimmune encephalomyelitis (EAE), and cardiac infarction). In each of these disease processes, excessive inflammation is implicated as a major source of disease pathogenesis. Whereby uptake of these particles targeted the offending inflammatory monocytes to be actively removed from the circulation and sequestered in the spleen for degradation. As a result of this redirection, this strategy aided in sparing of the end-organs in these disease models most at risk for damage and failure. Another study demonstrated that the composition of nanoparticles, PLGA (high or low molecular weight) vs. PLA, affected their interactions with neutrophils and monocytes *in vitro* and *in vivo*. Using the EAE mouse model, it was demonstrated that high molecular weight PLGA particles significantly improved disease scores compared to controls (107).

The same nanoparticle approach was taken by Park et al. (95) to abrogate paralysis-induced secondary to traumatic spinal cord injury (SCI). Using the same 500 nm diameter PLGA particles that had been shown to trigger sequestration of inflammatory macrophages and neutrophils away from the injury site (108), a non-invasive strategy was devised to alter the functional capacity of the immune cells at the SCI site and drive a predominantly regenerative phenotype at the SCI (**Figure 5**). Indeed, as seen with the preceding work, the nanoparticle-containing cells were predominantly sequestered and targeted for destruction at the spleen, but, in combination with spinal cord injury a protective population of M2-like macrophages expressing CD206 selectively homed at the site of injury in a way absent for sham injured mice. With this wound repair phenotype predominating at the SCI site, nanoparticle-mediated promotion of axonal regrowth and remyelination was shown, further emphasizing a therapeutic value to the presence of the materials themselves to engineer the dominant immune response at the site of injury.

Removing the Offending Microbes and Damaged Tissue: Developing Ways to Limit Collateral Damage

Once neutrophils and monocytes arrive at the injured tissue, recognition of microbes, or dead cells by TLRs and other PRRs drives leukocyte activation with phagocytosis and intracellular killing resulting in clearing of microbes and dead cells (114). As stated in the previous section, however, many of the mechanisms by which these cells clear microbes and dead cells are non-specific and can cause harm to healthy surrounding tissue. Because of this, strategies that can limit this collateral damage in combination with the methods described above can help to alleviate the most destructive organ damage seen with severe inflammation and sepsis.

Phagocytosis requires recognition and attachment by the leukocyte of the agent to be ingested, engulfment of the agent with a phagocytic vacuole, and killing or degradation of the extracellular products taken up by the cell. Recognition is often performed by mannose receptors, scavenger receptors, and a variety of opsonin receptors that can bind and ingest microbes. Of these the macrophage mannose receptor (MMR or CD206) from the lectin family binds terminal mannose and fucose residues of glycoproteins and glycolipids uniquely found on microbial cell walls to drive their phagocytosis (115). This parallels PRR-specific recognition of microbial PAMPs amid ignorance of molecular characteristics of mammalian cells. In a more generalized manner, scavenger receptors constantly sample the environment and can bind and mediate endocytosis of a variety of microbes in addition to oxidized or acetylated low-density lipoprotein (LDL) that fail to interact with the primary LDL receptor. Macrophage integrins, like Mac-1 introduced above (CD11b/CD18) can also bind microbes for phagocytosis. Coating of microbes by opsonins (particularly IgG antibodies,

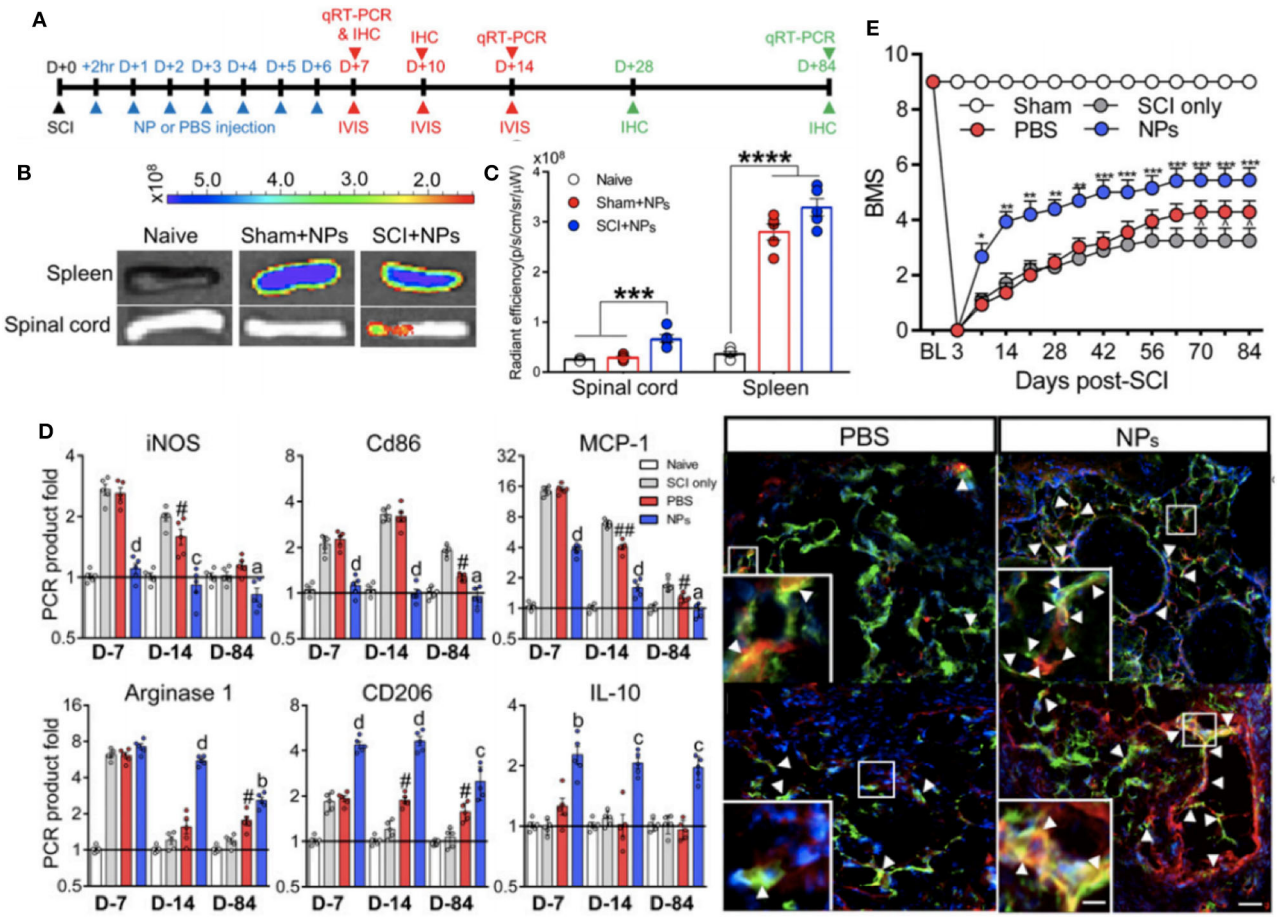

FIGURE 5 | Non-invasive strategy to alter immune cell responses to enhance spinal cord injury (SCI) recovery with *in vivo* biodistribution and analysis of nanoparticles. Experimental timeline for the study **(A)**. *In vivo* images from spinal cord and spleen at 1 day post-injection **(B)**. Fluorescence quantification of imaging in **(B)**, where $^{***}P < 0.001$ and $^{****}P < 0.0001$ **(C)**. Immunomodulation of macrophages as assessed with RT-qPCR data for pro-inflammatory and anti-inflammatory genes at multiple timepoints post-SCI and immunodetection of M2 macrophages (yellow color) within bridge following SCI ($^{a}P < 0.05$, $^{b}P < 0.01$, $^{c}P < 0.001$, and $^{d}P < 0.0001$ compared to the PBS group, and $^{\#}P < 0.05$ and $^{\#\#}P < 0.01$ relative to the SCI only group) **(D)**. Functional recovery of locomotor activity from SCI, where $^{*}P < 0.05$, $^{**}P < 0.01$, and $^{***}P < 0.001$ compared the the PBS group, and $^{\wedge}P < 0.05$ relative to the SCI only group **(E)**. Adapted from (95). Copyright (2019) National Academy of Sciences.

C3b from the complement system, and mannose-binding lectin) greatly increase the efficiency phagocytosis due to high-affinity receptors for opsonins on the cell surface of neutrophils and monocytes (116).

Alteration in CD206 is essential to the phagocytic capability of macrophages and is easily altered by nanoparticle formulations. As described above, Park et al. (95) showed increased levels of CD206, as well as other markers of M2-like macrophages such as IL-10 and arginase-1 at the site of spinal cord injury. In contrast, using peripheral blood monocytes from human volunteers and cynomolgus monkeys, Fruchon et al. (96, 97) show that another nanoparticle formulation using poly(phosphorHydrazone) functionalized with acid azabisphosphorous increased expression of MRC1 complemented with increased cell surface expression of the protein product, CD206.

Once microbes and necrotic debris have been engulfed, final killing and clearance by neutrophils and macrophages requires highly regulated microbicidal activity within phagocytic compartments driven by generation of reactive oxygen and nitrogen species (ROS and nitric oxide, NO, respectively) and lysosomal enzymes (117, 118). ROS production is dependent upon the rapid assembly and activation of NADPH oxidase on the phagosomal membrane. In neutrophils, evolution of superoxide ($O_2\cdot$) hydrogen peroxide (H_2O_2) is acted upon by myeloperoxidase (MPO) under the influence of halides like Cl^- to convert H_2O_2 to hypochlorite (OCl_2^-). These reactions in combination drive halogenation of microbial components or oxidation of microbial proteins and lipids. In addition to this efficient H_2O_2-MPO-halide system, H_2O_2 can also be converted to hydroxyl radicals ($^-OH\cdot$) to also drive modification of cellular lipids, proteins, and nucleic acids, thus destroying microbes. Similarly, NO is produced from arginine by inducible nitric oxide synthase (iNOS) in macrophages and neutrophils following activation by cytokines (e.g., IFNɤ) or microbial products. NO

can then react with O_2 to form the highly reactive free radical peroxynitrite ($ONOO^-$) to damage the lipids, proteins, and nucleic acids of microbes in a manner similar to ROS. Additional intracellular microbicidal activity is driven by lysosomal enzymes contained in lysosomal granules that contribute to microbial killing and vast amounts of tissue damage.

Although multiple groups have shown an ability to decrease ROS production *in vitro* (98, 100), Soh et al. (119) introduce an interesting twist in monocytes by using ceria-zirconia nanoparticles to actively scavenge ROS given the faster conversion of ceria-zirconia nanoparticles to convert between the Ce^{3+} and Ce^{4+} oxidation states of ceria nanoparticles alone. In LPS-induced endotoxemia rat models and CLP-induced bacteremia mouse models, this increase in ROS and NO scavenging had a net effect of increasing animal survival. At a tissue level, this increased survival is correlated to sparing of the liver and lungs from LPS-associated ROS and NO immune damage with intravenous LPS administration and the gastrointestinal tract of damage associated with similar bactericidal immune mechanisms in widespread polymicrobial bacteremia.

Additional mechanisms at play in microbial killing include neutrophil extracellular traps (NETs) that are composed of extracellular fibrillar networks with a high concentration of antimicrobial substances at the site of infection. These have the ability to trap microbes within the fibrils in response to bacteria and fungi and inflammatory mediators such as cytokines and chemokines, complement proteins, and ROS. NETs are viscous in nature due to neutrophil nuclei loss during NET formation leading to extracellular chromatin binding and concentrating granule proteins and these NETs have been shown in the literature to be particularly destructive during sepsis as they are broken down (120). Recent murine work has shown that antibody-mediated stabilization of NETs prevents release of their captured bacteria and additional toxic NET contents has shown to be protective during sepsis (121), suggesting further opportunities to design biomaterials to aid in minimizing in a controlled fashion the deleterious effects of this necessary microbicidal mechanism.

Resolution of Inflammation

Given the powerful host defense mechanisms at play during inflammation, resolution of the response needs to be tightly controlled to prevent deleterious consequences. Although complete resolution of inflammation is ideal, other consequences of inflammation include connective tissue replacement for healed tissues (scarring or fibrosis) and chronic inflammation.

Among endogenous modulators of inflammation, many are closely related to those driving the inflammatory response. Another AA metabolite class, lipoxins, serve to aid in resolution of inflammation by preventing leukocyte recruitment. LXA_4 and LXB_4 serve to prevent neutrophil chemotaxis and adhesion during the presence of both neutrophils and platelets at the site of inflammation. Among cytokines, transforming growth factor-beta (TGF-β) and IL-10 are generally regarded as having anti-inflammatory activity. With some nanoparticle strategies, direct induction of IL-10 production (55, 94, 96, 97, 101) has been possible with a variety of biomaterial composition approaches (**Table 4**). Additionally, the complement system contains a number of regulatory components with even more soluble protein mediators of resolving inflammation include resolvins, protectins, and maresins (129).

Because of the destructive nature of lysosomal enzymes, antiproteases are also present in the serum and tissue fluids to limit inflammation-associated lysosomal damage. Of these, α_1-antitrypsin is a major inhibitor of neutrophil elastase and α_2-macroglobulin is another found in serum and various secretions. Additionally, neutrophils themselves have very short lives and turnover of inflammatory cells and the produced mediators of inflammation following removal of the provoked injury are key to resolution. Of note, however, is that in cases of sepsis neutrophil apoptosis is delayed but their function is impaired. Under normal conditions circulating neutrophil have a short half-life (7–12 h *in vivo*) but this is increased downstream of LPS- and C5a-mediated neutrophil activation. This is attributed to a combination of pro-survival cell signaling, including decreased activation of caspase-8 (130) leading to an accumulation of nuclear factor myeloid nuclear differentiation antigen (MNDA) in parallel with accumulation of Mcl-1 (131), increased anti-apoptotic Bcl-xL (132), decreased pro-apoptotic Bim (133), and increased phosphorylation of Bad downstream of Akt activation (134–136). The net result of these combined molecular mediators is decreased neutrophil apoptosis. This long-lived neutrophil population in sepsis is also characteristic for its impaired transmigration to the site of inflammation. Rather than limiting the damaging effects of neutrophils solely to the site of tissue microbes and injury, neutrophils in sepsis are marked by aberrant neutrophil localization into remote organs where they can inflict damage and further augment the damage of inflammation (137–139).

Given the dramatic destruction inflicted by dysregulated trafficking of long-lived neutrophils during sepsis, it is of benefit to generate therapeutic strategies that can eliminate neutrophils while minimizing the collateral damage inflicted by these cells (behaving as they are expected to do) in aberrant tissue sites. As such, strategies in the literature that were originally intended as studies of the toxicity of nanoparticles provide hints of ways to normalize neutrophil behavior and limit organ dysfunction. With this in mind, **Table 4** reiterates the studies discussed above and summarized in **Tables 1–3** with an emphasis on cataloging features in biomaterial design. This allows for emphasizing the relationship between the physicochemical characteristics of the chosen materials and the resultant biological effects from the perspective of immune responses at the cellular and, when available, animal model level. As an example of how fine-tuning of physicochemical properties can be harnessed for desired biological effects, the Girard Lab provides an elegant series of studies that stresses this point. This group has shown (127, 128) with human neutrophils that silver nanoparticles in the range of 15–20 nm induced apoptosis and atypical cell death of neutrophils with the ability to inhibit *de novo* protein synthesis. In related studies, silver nanoparticles were further coated with

TABLE 4 | Empirical relationships determined between biomaterial physicochemical properties and immune cell activity.

Physicochemical properties				Immunological variables			References
Composition	**Size**	**Zeta potential/ charge**	**Surface coating/ functionalization**	**Cell type**	**Animal models**	**Biological effect**	
Polymers							
Poly(*N*-isopropylacrylamide)	80–300 nm	Neutral charge, hydrophobic		Erythrocytes	Human	Sequestration and neutralization of lipid-based toxins with erythrocyte sparing	(74, 75)
Poly(lactic acid)	350–500 nm	−50 to −40 mV	Poly(ethylene-*alt*-maleic acid)	Bone marrow-derived macrophages	Mice (C57BL/6)	Decreased secretion of IL-6, TNF-α, and MCP-1; decreased expression of MHC II, MARCO, CD80, CD86	(93)
Poly(lactic acid)	430–470 nm	−47 to −31 mV	Poly(ethylene-*alt*-maleic acid)	Inflammatory monocytes, neutrophils	Mice (SJL/J)	Negligible sequestration of inflammatory monocytes and neutrophils away from sites of inflammation	(107)
Poly(lactic acid)	350–500 nm	−25 mV	Poly(vinyl alcohol)	Bone marrow-derived macrophages	Mice (C57BL/6)	Partial decreased secretion of IL-6, TNF-α, and MCP-1	(93)
Poly(lactic-*co*-glycolic acid)	100–104 nm	−7 to −5 mV		Neutrophils	Human	Cationic surfactant leads to dramatic neutrophil death and LDH release	(122)
Poly(lactic-*co*-glycolic acid)	100–105 nm	−30 to −23 mV	Macrophage cell membrane	J774 macrophages, human umbilical vein endothelial cells	Mice (C57BL/6, BALB/c)	Sequestration of LPS; sequestration of IL-6, TNF-α, IFNɤ; decreased iNO production; decreased E-selectin expression; decreased serum IL-6, TNF-α, IFNɤ; survival benefit in *E. coli* bacteremia	(54)
Poly(lactic-*co*-glycolic acid)	140–165 nm	0 to 0.5 mV	di(α2→ 8)*N*-acetylneuraminic acid	Peritoneal macrophages	Mice (C57BL/6)	Decreased secretion of TNF-α, IL-6; increased Siglec-E expression; increased serum IL-10; decreased serum IL-6; increased survival benefit in LPS-induced endotoxemia	(94)
Poly(lactic-*co*-glycolic acid)	214–226 nm	35 to 43 mV	Soyaethyl morpholinium ethosulfate	Neutrophils	Human	Cationic surfactant leads to dramatic neutrophil death and LDH and elastase release, moderate increase in superoxide production	(122)
Poly(lactic-*co*-glycolic acid)	240–252 nm	24 to 34 mV	Cetyltrimethylammonium bromide	Neutrophils	Human	Cationic surfactant leads to dramatic neutrophil death and LDH and elastase release, dramatic increase in superoxide production	(122)
Poly(lactic-*co*-glycolic acid)	350–500 nm	−50 to −40 mV	Poly(ethylene-*alt*-maleic acid)	Bone marrow-derived macrophages	Mice (C57BL/6)	Decreased secretion of IL-6, TNF-α, and MCP-1; decreased expression of MHC II, MARCO, CD80, CD86; survival benefit in LPS-induced endotoxemia	(93)
Poly(lactic-*co*-glycolic acid)	350–500 nm	−25 mV	Poly(vinyl alcohol)	Bone marrow-derived macrophages	Mice (C57BL/6)	Partial decreased secretion of IL-6, TNF-α, and MCP-1	(93)
Poly(lactic-*co*-glycolic acid)—low molecular weight	330–510 nm	−56 to −40 mV	Poly(ethylene-*alt*-maleic acid)	Inflammatory monocytes, neutrophils	Mice (SJL/J)	Negligible sequestration of inflammatory monocytes and neutrophils away from sites of inflammation	(107)
Poly(lactic-*co*-glycolic acid)—high molecular weight	510–590 nm	−43 to −36 mV	Poly(ethylene-*alt*-maleic acid)	Inflammatory monocytes, neutrophils	Mice (C57BL/6, SJL/J, BALB/c)	Sequestration of inflammatory monocytes and neutrophils away from sites of inflammation	(107)

(Continued)

TABLE 4 | Continued

Physicochemical properties				Immunological variables			References
Composition	**Size**	**Zeta potential/ charge**	**Surface coating/ functionalization**	**Cell type**	**Animal models**	**Biological effect**	
Poly(lactic-*co*-glycolic acid)	500 nm	Negatively charged	Poly(ethylene-*alt*-maleic acid)	$MARCO^+$ macrophages	Mice (C57BL/6, SJL/J, BALB/c)	Sequestration of inflammatory monocytes away from sites of inflammation; functional reprogramming of macrophages from M1 to M2 at site of spinal cord injury	(95, 108)
Polystyrene	100–117 nm		Denatured albumin	Neutrophils	Mice	Albumin nanoparticles taken up by activated neutrophils through endocytosis mediated with FcγRIII to reduce neutrophil adhesion and migration across the endothelium to limit vascular inflammation modulated via adherent neutrophils; protective against lung injury with Syk inhibitor to prevent inside-out signaling	(102, 103)
Polystyrene	500 nm	Negatively charged	Poly[ethylene-*alt*-maleic acid)	$MARCO^+$ macrophages	Mice (C57BL/6, SJL/J, BALB/c)	Sequestration of inflammatory monocytes away from sites of inflammation	(108)
LIPIDS							
Liposomes—3.2% soybean phosphatidylcholine and 0.8% cholesterol	51–60 nm	37 to 55 mV	Cetyltrimethylammonium bromide	Neutrophils	Human	Dramatic neutrophil death, LDH release, high superoxide production, Ca^{2+} mobilization, promptly induces NET formation	(123)
Liposomes—3.2% soybean phosphatidylcholine and 0.8% cholesterol	73–81 nm	19 to 36 mV	Soyaethyl morpholinium ethosulfate	Neutrophils	Human	Increased neutrophil death at increasing concentrations, LDH release at high concentrations of surfactant	(123)
Liposomes—3.2% soybean phosphatidylcholine and 0.8% cholesterol	88–92 nm	−49 to 39 mV		Neutrophils	Human	Inert for neutrophils *in vitro*	(123)
Solid lipid nanoparticles (SLNs)—12% cetyl palmitate and 1% soybean phosphatidylcholine	192 nm	−41 mV		Neutrophils	Human	Inert for neutrophils *in vitro*	(124)
Solid lipid nanoparticles (SLNs)—12% cetyl palmitate and 1% soybean phosphatidylcholine	195 nm	44 mV	Cetyltrimethylammonium bromide	Neutrophils	Human	Dramatic neutrophil death, LDH release, superoxide production, elastase release, Ca^{2+} mobilization, p38 and JNK activation, and NET development	(124)
Nanostructured lipid carriers (NLCs)—composed of both solid and liquid lipids with a soft core matrix of 6% w/w soybean oil, 65% cetyl palmitate, 1% soybean phosphatidylcholine (SPC)	162–177 nm	51 to 53 mV	Cetyltrimethylammonium bromide	Neutrophils	Human	Dramatic neutrophil death and LDH and elastase release, moderate increase in superoxide production	(122)

(Continued)

TABLE 4 | Continued

Physicochemical properties				Immunological variables			References
Composition	**Size**	**Zeta potential/ charge**	**Surface coating/ functionalization**	**Cell type**	**Animal models**	**Biological effect**	
Nanostructured lipid carriers (NLCs)—composed of both solid and liquid lipids with a soft core matrix of 6% w/w soybean oil, 65% cetyl palmitate, 1% soybean phosphatidylcholine (SPC)	248–261 nm	−44 to −41 mV		Neutrophils	Human	Inert for neutrophils *in vitro*	(122)
Nanostructured lipid carriers (NLCs)—composed of both solid and liquid lipids with a soft core matrix of 6% w/w soybean oil, 65% cetyl palmitate, 1% soybean phosphatidylcholine (SPC)	257–261 nm	51 to 52 mV	Soyaethyl morpholinium ethosulfate	Neutrophils	Human	Cationic surfactant leads to dramatic neutrophil death and LDH release	(122)
DENDRIMER							
Poly(phosphorHydrazone)			Acid azabisphosphorous	Monocytes	Human volunteers, cynomolgus monkeys	Increased expression of *MRC1*, *IL1RN*, *IL10*, *CCL18*, *CD23*, *CCL5*; increased expression of cell surface CD206, decreased cell surface expression of CD64, CD13, HLA-DR, HLA-A/B/C, CD86	(96, 97)
METALS/METAL OXIDES							
Gold	2 nm (core)	Neutral charge	Tetraethylene glycol with end hydroxyl group	Monocytes	Mice	Decreased ROS production *in vitro*, decreased TNF-α production *in vitro*; decreased serum TNF-α following LPS-induced endotoxemia	(98)
Gold	2 nm (core)	Neutral charge, hydrophobic	Tetraethylene glycol with hydrophobic end group	Monocytes	Mice	Decreased ROS production *in vitro*, decreased TNF-α production *in vitro*; increased serum TNF-α following LPS-induced endotoxemia	(98)
Gold	2 nm (core)	Neutral charge, hydrophilic	Tetraethylene glycol with hydrophilic end group	Monocytes	Mice	No change over LPS treatment alone *in vitro* or *in vivo*	(98)
Gold	5 nm		Inner lipid: 1,2-dipalmitoyl-*sn*-glycero-3-phosphoethanolamine-N-[3-(2-pyridyldithio)propionate] (PDP PE 16:0) or 1,2-dioleoyl-*sn*-glycero-3-phosphoethanolamine-N-[3-(2-pyridyldithio)propionate (PDP PE 18:1)	Monocytes	Human	Decreased NF-κB activation; decreased expression of *Il1b*; decreased secretion of IL-1β, TNF-α, IL-6, IL-8, CCL5/RANTES, CCL2/MCP-1, GM-CSF	(99)

(Continued)

TABLE 4 | Continued

Physicochemical properties				Immunological variables			References
Composition	**Size**	**Zeta potential/ charge**	**Surface coating/ functionalization**	**Cell type**	**Animal models**	**Biological effect**	
			Outer lipid: 1,2-dipalmitoyl-*sn*-glycero-3-phsphocholine (DPPC), spingomyelin, cardiolipin, 1,2-dilinoleoyl-*sn*-glycero-3-phospho-(1'-rac-glycerol) (18:2 PG), 1,2-dimyristoyl-*sn*-glycer-3-phosphoethanolamine-N-(lissamine rhodamine B sulfonyl) (14:0 Liss Rhod PE)				
Gold	13–20 nm	Negative charge	Peptides with hydrophobic and aromatic residues	Monocytes		Decreased NF-κB and IRF3 activation following TLR agonist treatment, decreased CCL2 and CCL4 production; decreased lung damage and survival benefit in LPS-induced ALI; larger particles are more protective	(105, 106)
Silver	4 nm	−25 to −8 mV	Poly(vinyl alcohol)	Neutrophils	Human	Induces apoptosis and increases ROS generation at high concentrations (50 μM)	(125)
Silver	10 nm		Poly(vinyl pyrrolidone)	Neutrophils	Human	Increased cell death at greater concentrations (range of 25–100 μg/mL) with corresponding increases in neutrophil oxidative burst	(126)
Silver	15 nm	−9 to −7 mV		Neutrophils	Human	Atypical cell death at low concentrations (≤25 μg/mL) with no CD16 shedding, caspase-1 and caspase-4 dependent IL-1β activation, and caspase-1 and caspase-4 independent NET formation; necrosis at high concentrations (>50 μg/mL)	(127)
Silver	20 nm	−11 to −8 mV		Neutrophils	Human	High concentrations (100 μg/mL) induce apoptosis of neutrophils and inhibition of *de novo* protein synthesis	(128)
Silver	50 nm		Poly(vinyl pyrrolidone)	Neutrophils	Human	Limited cell death at greater concentrations (range of 25–100 μg/mL)	(126)
Ceria-zirconia ($Ce_{0.7}Zr_{0.3}O_2$)	2–4 nm			Monocytes	Rats, mice	Antioxidant activity (SOD, catalase, CAT, mimetic and hydroxyl radical antioxidant capacity, HORAC) decreased; decreased LDH; decreased $CD68^+$ monocytes at site of injury; survival benefit in LPS-induced endotoxemia and CLP	(119)

(Continued)

TABLE 4 | Continued

Physicochemical properties				Immunological variables			References
Composition	**Size**	**Zeta potential/ charge**	**Surface coating/ functionalization**	**Cell type**	**Animal models**	**Biological effect**	
CARBON-BASED							
Carbon nanotube	0.4–4.2 nm (length), 12–34 nm (diameter)		Carboxymethyl cellulose	Macrophages		Sequestration of complement proteins triggering opsonization	(57)
Carbon nanotube	0.4–4.2 nm (length), 12–34 nm (diameter)		RNA	Macrophages		Sequestration of complement proteins triggering opsonization	(57)
Hydroxylated fullerene ($C_{60}[OH]_{44}$)				Peritoneal macrophages	Mice (C57BL/6)	Decreased ROS production; decreased expression of *Il6*, *Il1b*, *Tnf*; decreased preterm birth	(100)
Nanodiamond	5 nm	Negatively charged	Octadecylamine	Macrophages	Human	Decreased TNF-α, IL-1β secretion and increased IL-10 secretion	(101)
BIOMIMETIC							
Cell-derived nanoparticle (CDNPs)—composed of annexins, actin, histones, heat shock proteins, myosin, peroxiredoxines and vimentin and small traces of nucleic acids, with annexin A5 (AnxA5) being one of the most abundant components; [protein] = 150 μL/mL, [DNA] = 2 μg/mL, [RNA] = 4 μg/mL	50–200 nm			Source of CDNPs: MC3T3-E1 fibroblast cells, peritoneal lavage Takes up CDNPs: neutrophils, inflammatory monocytes, macrophages	Mice	Decreased peritoneal IL-6 and IL-10 following CLP; decreased bacterial growth *in vitro*; increased expression of CD11b and MHCII on the cell surface of neutrophils, inflammatory monocytes, and macrophages	(55)
Cell membrane-formed nanovesicles (cell disruption by nitrogen cavitation, centrifugation, and extrusion—contains integrin β2	200 nm	−20 to −12 mV		Source of nanovesicles: HL 60 myeloid cells		Binds ICAM-1 on HUVEC to deliver NF-κB inhibitors and stop diapedesis	(104)

either PVA (125) or poly(vinyl pyrrolidone) (PVP) (126) to show a size-dependence to cell death induction. Indeed, smaller nanoparticles (4–10 nm) showed the most dramatic cell death in a manner dependent on neutrophil oxidative burst, while even small variations in nanoparticle size (50 nm) abrogated the neutrophil cell death. As this series of studies tell us, each element of material design, from the core material to size to even the choice of surfactant, can impart a dramatic change in the functional responses of innate immune cells further highlighting the importance of cataloging physicochemical characteristics to enable rational design strategies for immunomodulation.

POLYPHARMACOLOGICAL STRATEGIES FOR SEVERE INFLAMMATION AND SEPSIS

The dysregulation that develops due to sepsis affects cellular phenotypes and gene expression profiles in both transient and long-term manners. In humans, LPS administration resulted in

TABLE 5 | Nanoparticle physicochemical properties and desired immune responses to consider when designing biomaterials to fine tune inflammatory responses.

Tunable nanoparticle physicochemical properties	
Chemical composition	**Nanoparticle diameter**
• **Nanoparticle core** ◦ Polymer ◦ Lipid ◦ Metal/metal oxide ◦ Carbon-based ◦ Biomimetic • **Surfactant** ◦ Polymer-based ◦ Carbon-chain length ◦ Biomimetic source • **Functionalization** ◦ Core polymer conjugations ◦ Additional small molecules or biologics	• <200 nm • 200–800 nm • >800 nm **Surface properties** • **Zeta potential/charge** ◦ <-25 mV/negative ◦ −25 to 10 mV/neutral ◦ >10 mV/positive • **Surface chemistry** ◦ Hydrophilic ◦ Hydrophobic ◦ Zwitterionic

Desired nanoparticle-mediated immunological outcomes
Recognition of microbes/PAMPs/DAMPs
• Prevention of recognition by immune cells • Sequestration of insults away from immune site
Regulators of inflammation
• Alteration of transcription factor activity • Prevention of inflammatory gene activation • Prevention/delay of cytokine and chemokine release • Tuning of inflammatory mediators at immune site
Leukocyte recruitment
• Activation state of vascular endothelium • Sequestration of immune cell subsets away from immune site • Recruitment of immune cell subsets to immune site
Managing immune-mediated tissue damage
• Scavenging of ROS and RNS • Modification of NET stability
Resolution of inflammation
• Alteration of programmed apoptotic pathways • Alteration of phagocytic capacity • Increased clearance rate of pro-inflammatory regulators

3,714 genes being differentially expressed in blood leukocytes as early as 2 h post exposure with a near complete resolution of clinical perturbations within 24 h post challenge (140). Similar genomic studies in mice corroborate the vast genetic alterations and have identified over 1,900 differentially expressed genes following LPS challenge (141). Sepsis survivors generally suffer from additional morbidities including higher risk of readmission, cardiovascular disease, cognitive impairment, and death for years following sepsis. Epigenetic mechanisms such as DNA methylation, histone modifications, and non-coding RNAs are also perturbed in sepsis and are associated with increased mortality due to their contributions to long-term immunosuppression (142). Given that thousands of genes are differentially expressed during sepsis, the number of tractable therapeutic options that aim to augment or abrogate single molecular targets is out of the scope of practical and experimental possibilities.

Multiple target-based approaches should be considered to improve patient outcomes in sepsis. A single timepoint nor single cytokine/receptor intervention is unlikely to be successful on a broad range of patients with diverse conditions that have led to the state of sepsis (143). The complexity of disease states offers a range of potential molecular targets, as well as numerous other factors including the time of treatment administration and the combination of drugs. Providing further evidence for multi-target approaches, Cockrell and An developed computational algorithms and predicted the necessity for a multi-target therapy for the treatment of sepsis (144). The specificity to which small molecules and biologics modulate immune responses at a single-target level or through non-specific mechanisms limits their utility in treating the underlying dysfunction encoded in immune cells during and following sepsis. Due to the lack of conceivable small molecules or biologics, nanoparticles are uniquely positioned to achieve this goal due to their highly controllable physicochemical properties, targetability, and immune-modulating properties (7).

A polypharmacological strategy has the potential to address the redundant molecular, cellular, and tissue functions during inflammation but anti-inflammatory and anti-coagulants are neither innocuous nor without potential adverse effects in combination or alone. Of particular note is that morbidity and mortality associated with sepsis and septic shock tends to be most severe within the geriatric and pediatric population, two groups where polypharmacy can be especially deleterious in combination with existing comorbidities or developmental concerns (145–149). Given these concerns with a multi-drug approach, other strategies that can work with multimodal mechanisms of action and minimize adverse effects are ideal and ongoing research with biomaterials serves as an exciting area to deliver on some of these strategies. As such, biomaterials and what is known about the cellular and tissue effects of their physicochemical properties will serve as the focus of the remainder of this review.

There are advantages and disadvantages to each strategy in the management or cure of disease. However, particularly noteworthy in polypharmacology is the reduction in treatment complexity, reduced side effects, and reduced or altogether eliminated drug–drug interactions, in addition to improved patient compliance. Also, given that a single agent can simultaneously affect multiple targets in the same tissue (by default, both pharmacophores must co-localize), partial modulation of targets that are synergistically linked suggests that reduced doses may be sufficient to elicit full therapeutic efficacy, widening the therapeutic windows.

CONCLUSION AND FUTURE PROSPECTS FOR BIOMATERIAL-DRIVEN IMMUNE MODULATION

Developing strategies to control severe inflammation and sepsis remains a healthcare priority. Given the toll sepsis and septic shock plays in increasing healthcare costs and the continuing staggering rates of mortality and long-term morbidity for

those affected, it is essential that strategies to improve patient outcomes are informed by the pathophysiology of dysregulated inflammation. As laid out in the review, although sepsis can be triggered by one of numerous types of bacteria breeching initial defenses at a variety of tissue sites, the course of inflammation itself, although complex, has stereotypic physiological processes that provide opportunities for intervention (**Figure 1**). From the survey of studies included in this review, diverse strategies have been implemented that attempt to address each stage: (1) limiting initial activation of innate immune cells (**Figure 2** and **Table 1**), (2) regulating pro-inflammatory mediators (**Figures 3**, **4** and **Table 2**), (3) inhibiting further leukocyte recruitment (**Figures 1**, **4**, **5** and **Table 3**), (4) removing the initiating microbe and signals for inflammation, and (5) regulating mediators of resolution (**Figures 3**, **4** and **Table 2**). Among these works, the strategies with the most promise are those that attempt to affect multiple stages of this process. Indeed, the complex and parallel physiologic responses that have been thus far accounted for during sepsis show that effective management of sepsis requires a multi-targeted approach.

As we have put forth, biomaterials and the generation of nanotechnology-based approaches has the potential to allow for finely tuned engineering of immune responses based on experimentally determined rational design principles. Through elucidation of the principles at play in development of these biomaterials and nanoparticle platforms, the potential exists to generate multi-targeted therapeutics that meet our specific needs based on physicochemical properties deemed significant (e.g., composition, size, charge, and others) as summarized in **Table 5**. With the maturation of nanotechnology-based immune engineering, several outstanding questions remain to be addressed by all stakeholders in the field including development of biologically relevant animal models, standardization of GMP manufacturing procedures, standardization of formulations with potential implications for pharmacokinetics and pharmacodynamics, and further guidance from regulatory agencies in regard to the nanocarriers themselves. It is our hope that in the upcoming years, these design principles are further developed and adopted in the field as these questions for scalability of nanotechnology are addressed. Future biomaterial designs will be informed by the immunology it intends to assist and, vice versa, the immunology continues to provide new avenues of exploration for the application of biomaterials to improve human health. This interface promises to expand the development of nano-based therapeutics as well as to further the basic understanding of nano-bio interactions and their implications for therapeutic strategies.

AUTHOR CONTRIBUTIONS

JL and RP conceptualized the manuscript, wrote the text, drew and adapted figures and tables, and approved the manuscript. HK and MM assisted with gathering, reviewing references, and approved the manuscript. All authors contributed to the article and approved the submitted version.

FUNDING

This work was supported by startup funds by the University of Maryland School of Pharmacy, the University of Maryland Baltimore Institute for Clinical and Translational Research (ICTR) Accelerated Translational Incubator Pilot Grant (NIH #1UL1TR003098), and a New Investigator Award from the American Association of Colleges of Pharmacy (AACP) to RP. Additional support was provided by the NIAID-NIH Signaling Pathways in Innate Immunity Training Program (NIH #T32AI095190) and NHLBI-NIH Interdisciplinary Training Program in Cardiovascular Disease (NIH #T32HL007698) to JL.

REFERENCES

1. Heidland A, Klassen A, Rutkowski P, Bahner U. The contribution of rudolf virchow to the concept of inflammation: what is still of importance? *J Nephrol.* (2006) 19(Suppl.10):S102–9.
2. Gabay C, Kushner I. Acute-phase proteins and other systemic responses to inflammation. *N Engl J Med.* (1999) 340:448–54. doi: 10.1056/NEJM199902113400607
3. Venet F, Monneret G. Advances in the understanding and treatment of sepsis-induced immunosuppression. *Nat Rev Nephrol.* (2018) 14:121–37. doi: 10.1038/nrneph.2017.165
4. Lelubre C, Vincent JL. Mechanisms and treatment of organ failure in sepsis. *Nat Rev Nephrol.* (2018) 14:417–27. doi: 10.1038/s41581-018-0005-7
5. Mitchell MJ, Jain RK, Langer R. Engineering and physical sciences in oncology: challenges and opportunities. *Nat Rev Cancer.* (2017) 17:659–75. doi: 10.1038/nrc.2017.83
6. Riley RS, June CH, Langer R, Mitchell MJ. Delivery technologies for cancer immunotherapy. *Nat Rev Drug Discov.* (2019) 18:175–96. doi: 10.1038/s41573-018-0006-z
7. Pearson RM, Casey LM, Hughes KR, Miller SD, Shea LD. In vivo reprogramming of immune cells: Technologies for induction of antigen-specific tolerance. *Adv Drug Deliv Rev.* (2017) 114:240–55. doi: 10.1016/j.addr.2017.04.005
8. Pearson RM, Podojil JR, Shea LD, King NJC, Miller SD, Getts DR. Overcoming challenges in treating autoimmuntity: development of tolerogenic immune-modifying nanoparticles. *Nanomedicine.* (2019) 18:282–91. doi: 10.1016/j.nano.2018.10.001
9. Pearson RM, Hsu H-j, Bugno J, Hong S. Understanding nano-bio interactions to improve nanocarriers for drug delivery. *MRS Bulletin.* (2014) 39:227. doi: 10.1557/mrs.2014.9
10. Keshavan S, Calligari P, Stella L, Fusco L, Delogu LG, Fadeel B. Nano-bio interactions: a neutrophil-centric view. *Cell Death Dis.* (2019) 10:569. doi: 10.1038/s41419-019-1806-8
11. Kumar V, Abbas AK, Aster JC. *Robbins and Cotran pathologic basis of disease.* 9th ed. Philadelphia, PA: Elsevier/Saunders. (2015). p. 1391.
12. Rudd KE, Johnson SC, Agesa KM, Shackelford KA, Tsoi D, Kievlan DR, et al. Global, regional, and national sepsis incidence and mortality, 1990-2017: analysis for the global burden of disease study. *Lancet.* (2020) 395:200–11. doi: 10.1016/S0140-6736(19)32989-7
13. Fleischmann C, Scherag A, Adhikari NK, Hartog CS, Tsaganos T, Schlattmann P, et al. Assessment of global incidence and mortality of hospital-treated sepsis. Current Estimates and Limitations. *Am J Respir Crit Care Med.* (2016) 193:259–72. doi: 10.1164/rccm.201504-0781OC
14. Jensen IJ, Sjaastad FV, Griffith TS, Badovinac VP. Sepsis-induced T cell immunoparalysis: the ins and outs of impaired T cell immunity. *J Immunol.* (2018) 200:1543–53. doi: 10.4049/jimmunol.1701618

15. Hotchkiss RS, Moldawer LL, Opal SM, Reinhart K, Turnbull IR, Vincent JL. Sepsis and septic shock. *Nat Rev Dis Primers.* (2016) 2:16045. doi: 10.1038/nrdp.2016.45
16. Delano MJ, Ward PA. Sepsis-induced immune dysfunction: can immune therapies reduce mortality? *J Clin Invest.* (2016) 126:23–31. doi: 10.1172/JCI82224
17. Hotchkiss RS, Monneret G, Payen D. Immunosuppression in sepsis: a novel understanding of the disorder and a new therapeutic approach. *Lancet Infect Dis.* (2013) 13:260–8. doi: 10.1016/S1473-3099(13)70001-X
18. Cross D, Drury R, Hill J, Pollard AJ. Epigenetics in sepsis: understanding its role in endothelial dysfunction, immunosuppression, and potential therapeutics. *Front Immunol.* (2019) 10:1363. doi: 10.3389/fimmu.2019.01363
19. Sonego F, Castanheira FV, Ferreira RG, Kanashiro A, Leite CA, Nascimento DC, et al. Paradoxical roles of the neutrophil in sepsis: protective and deleterious. *Front Immunol.* (2016) 7:155. doi: 10.3389/fimmu.2016.00155
20. Paoli CJ, Reynolds MA, Sinha M, Gitlin M, Crouser E. Epidemiology and costs of sepsis in the united states-an analysis based on timing of diagnosis and severity level. *Crit Care Med.* (2018) 46:1889–97. doi: 10.1097/CCM.0000000000003342
21. Vincent JL, Marshall JC, Namendys-Silva SA, Francois B, Martin-Loeches I, Lipman J, et al. Assessment of the worldwide burden of critical illness: the intensive care over nations (ICON) audit. *Lancet Respir Med.* (2014) 2:380–6. doi: 10.1016/S2213-2600(14)70061-X
22. Iwashyna TJ, Ely EW, Smith DM, Langa KM. Long-term cognitive impairment and functional disability among survivors of severe sepsis. *JAMA.* (2010) 304:1787–94. doi: 10.1001/jama.2010.1553
23. Gotts JE, Matthay MA. Sepsis: pathophysiology and clinical management. *BMJ.* (2016) 353:i1585. doi: 10.1136/bmj.i1585
24. Fink MP, Warren HS. Strategies to improve drug development for sepsis. *Nat Rev Drug Discov.* (2014) 13:741–58. doi: 10.1038/nrd4368
25. Marshall JC. Why have clinical trials in sepsis failed? *Trends Mol Med.* (2014) 20:195–203. doi: 10.1016/j.molmed.2014.01.007
26. Fink MP. Animal models of sepsis. *Virulence.* (2014) 5:143–53. doi: 10.4161/viru.26083
27. Matthay MA. Severe sepsis–a new treatment with both anticoagulant and antiinflammatory properties. *N Engl J Med.* (2001) 344:759–62. doi: 10.1056/NEJM200103083441009
28. Bernard GR, Vincent JL, Laterre PF, LaRosa SP, Dhainaut JF, Lopez-Rodriguez A, et al. Efficacy and safety of recombinant human activated protein C for severe sepsis. *N Engl J Med.* (2001) 344:699–709. doi: 10.1056/NEJM200103083441001
29. Eichacker PQ, Natanson C, Danner RL. Surviving sepsis–practice guidelines, marketing campaigns, and eli lilly. *N Engl J Med.* (2006) 355:1640–2. doi: 10.1056/NEJMp068197
30. Ranieri VM, Thompson BT, Barie PS, Dhainaut JF, Douglas IS, Finfer S, et al. Drotrecogin alfa (activated) in adults with septic shock. *N Engl J Med.* (2012) 366:2055–64. doi: 10.1056/NEJMoa1202290
31. Marti-Carvajal AJ, Sola I, Gluud C, Lathyris D, Cardona AF. Human recombinant protein C for severe sepsis and septic shock in adult and paediatric patients. *Cochrane Database Syst Rev.* (2012) 12:CD004388. doi: 10.1002/14651858.CD004388.pub5
32. Lai PS, Thompson BT. Why activated protein C was not successful in severe sepsis and septic shock: are we still tilting at windmills? *Curr Infect Dis Rep.* (2013) 15:407–12. doi: 10.1007/s11908-013-0358-9
33. NAGMSC Working Group on Sepsis. *NAGMSC Working Group on Sepsis Final Report*. Bethesda, MD: National Institute of General Medical Sciences; National Institutes of Health. (2019).
34. Delano MJ, Ward PA. The immune system's role in sepsis progression, resolution, and long-term outcome. *Immunol Rev.* (2016) 274:330–53. doi: 10.1111/imr.12499
35. Fontana F, Figueiredo P, Bauleth-Ramos T, Correia A, Santos HA. Immunostimulation and immunosuppression: nanotechnology on the brink. *Small Methods.* (2018) 2:1700347. doi: 10.1002/smtd.201700347
36. Gammon JM, Jewell CM. Engineering immune tolerance with biomaterials. *Adv Healthc Mater.* (2019) 8:e1801419. doi: 10.1002/adhm.201801419
37. Akira S, Uematsu S, Takeuchi O. Pathogen recognition and innate immunity. *Cell.* (2006) 124:783–801. doi: 10.1016/j.cell.2006.02.015
38. Palm NW, Medzhitov R. Pattern recognition receptors and control of adaptive immunity. *Immunol Rev.* (2009) 227:221–33. doi: 10.1111/j.1600-065X.2008.00731.x
39. Brubaker SW, Bonham KS, Zanoni I, Kagan JC. Innate immune pattern recognition: a cell biological perspective. *Annu Rev Immunol.* (2015) 33:257–90. doi: 10.1146/annurev-immunol-032414-112240
40. Tang D, Kang R, Coyne CB, Zeh HJ, Lotze MT. PAMPs and DAMPs: signal 0s that spur autophagy and immunity. *Immunol Rev.* (2012) 249:158–75. doi: 10.1111/j.1600-065X.2012.01146.x
41. Yang H, Tracey KJ. Targeting HMGB1 in inflammation. *Biochim Biophys Acta.* (2010) 1799:149–56. doi: 10.1016/j.bbagrm.2009.11.019
42. Nesargikar PN, Spiller B, Chavez R. The complement system: history, pathways, cascade and inhibitors. *Eur J Microbiol Immunol.* (2012) 2:103–11. doi: 10.1556/EuJMI.2.2012.2.2
43. van de Wetering JK, van Golde LM, Batenburg JJ. Collectins: players of the innate immune system. *Eur J Biochem.* (2004) 271:1229–49. doi: 10.1111/j.1432-1033.2004.04040.x
44. Gupta G, Surolia A. Collectins: sentinels of innate immunity. *Bioessays.* (2007) 29:452–64. doi: 10.1002/bies.20573
45. Nayak A, Dodagatta-Marri E, Tsolaki AG, Kishore U. An insight into the diverse roles of surfactant proteins, SP-A and SP-D in innate and adaptive immunity. *Front Immunol.* (2012) 3:131. doi: 10.3389/fimmu.2012.00131
46. Ziegler EJ, McCutchan JA, Fierer J, Glauser MP, Sadoff JC, Douglas H, et al. Treatment of gram-negative bacteremia and shock with human antiserum to a mutant escherichia coli. *N Engl J Med.* (1982) 307:1225–30. doi: 10.1056/NEJM198211113072001
47. McCloskey RV, Straube RC, Sanders C, Smith SM, Smith CR. Treatment of septic shock with human monoclonal antibody HA-1A. A randomized, double-blind, placebo-controlled trial. CHESS trial study group. *Ann Intern Med.* (1994) 121:1–5. doi: 10.7326/0003-4819-121-1-199407010-00001
48. Greenman RL, Schein RM, Martin MA, Wenzel RP, MacIntyre NR, Emmanuel G, et al. A controlled clinical trial of E5 murine monoclonal IgM antibody to endotoxin in the treatment of gram-negative sepsis. The XOMA sepsis study group. *JAMA.* (1991) 266:1097–102. doi: 10.1001/jama.1991.03470080067031
49. Bone RC, Balk RA, Fein AM, Perl TM, Wenzel RP, Reines HD, et al. A second large controlled clinical study of E5, a monoclonal antibody to endotoxin: results of a prospective, multicenter, randomized, controlled trial. The E5 sepsis study group. *Crit Care Med.* (1995) 23:994–1006. doi: 10.1097/00003246-199506000-00003
50. Angus DC, Birmingham MC, Balk RA, Scannon PJ, Collins D, Kruse JA, et al. E5 murine monoclonal antiendotoxin antibody in gram-negative sepsis: a randomized controlled trial. E5 study investigators. *JAMA.* (2000) 283:1723–30. doi: 10.1001/jama.283.13.1723
51. Tidswell M, Tillis W, Larosa SP, Lynn M, Wittek AE, Kao R, et al. Phase 2 trial of eritoran tetrasodium (E5564), a toll-like receptor 4 antagonist, in patients with severe sepsis. *Crit Care Med.* (2010) 38:72–83. doi: 10.1097/CCM.0b013e3181b07b78
52. Opal SM, Laterre PF, Francois B, LaRosa SP, Angus DC, Mira JP, et al. Effect of eritoran, an antagonist of MD2-TLR4, on mortality in patients with severe sepsis: the ACCESS randomized trial. *JAMA.* (2013) 309:1154–62. doi: 10.1001/jama.2013.2194
53. Rice TW, Wheeler AP, Bernard GR, Vincent JL, Angus DC, Aikawa N, et al. A randomized, double-blind, placebo-controlled trial of TAK-242 for the treatment of severe sepsis. *Crit Care Med.* (2010) 38:1685–94. doi: 10.1097/CCM.0b013e3181e7c5c9
54. Thamphiwatana S, Angsantikul P, Escajadillo T, Zhang Q, Olson J, Luk BT, et al. Macrophage-like nanoparticles concurrently absorbing endotoxins and proinflammatory cytokines for sepsis management. *Proc Natl Acad Sci USA.* (2017) 114:11488–93. doi: 10.1073/pnas.1714267114
55. Kunz N, Xia BT, Kalies KU, Klinger M, Gemoll T, Habermann JK, et al. Cell-derived nanoparticles are endogenous modulators of sepsis with therapeutic potential. *Shock.* (2017) 48:346–54. doi: 10.1097/SHK.0000000000000855
56. Pannuzzo M, Esposito S, Wu LP, Key J, Aryal S, Celia C, et al. Overcoming nanoparticle-mediated complement activation by surface PEG pairing. *Nano Lett.* (2020) 20:4312–21. doi: 10.1021/acs.nanolett.0c01011
57. Pondman KM, Sobik M, Nayak A, Tsolaki AG, Jakel A, Flahaut E, et al. Complement activation by carbon nanotubes and its influence on the

phagocytosis and cytokine response by macrophages. *Nanomedicine.* (2014) 10:1287–99. doi: 10.1016/j.nano.2014.02.010
58. Meunier E, Coste A, Olagnier D, Authier H, Lefevre L, Dardenne C, et al. Double-walled carbon nanotubes trigger IL-1beta release in human monocytes through Nlrp3 inflammasome activation. *Nanomedicine.* (2012) 8:987–95. doi: 10.1016/j.nano.2011.11.004
59. Pondman KM, Salvador-Morales C, Paudyal B, Sim RB, Kishore U. Interactions of the innate immune system with carbon nanotubes. *Nanoscale Horiz.* (2017) 2:174–86. doi: 10.1039/C6NH00227G
60. Dinarello CA, Simon A, van der Meer JW. Treating inflammation by blocking interleukin-1 in a broad spectrum of diseases. *Nat Rev Drug Discov.* (2012) 11:633–52. doi: 10.1038/nrd3800
61. Kaufmann SHE, Dorhoi A, Hotchkiss RS, Bartenschlager R. Host-directed therapies for bacterial and viral infections. *Nat Rev Drug Discov.* (2018) 17:35–56. doi: 10.1038/nrd.2017.162
62. Du Buske LM. Clinical comparison of histamine H1-receptor antagonist drugs. *J Allergy Clin Immunol.* (1996) 98:S307–18. doi: 10.1016/S0091-6749(96)80116-3
63. Khanapure SP, Garvey DS, Janero DR, Letts LG. Eicosanoids in inflammation: biosynthesis, pharmacology, and therapeutic frontiers. *Curr Top Med Chem.* (2007) 7:311–40. doi: 10.2174/156802607779941314
64. Dennis EA, Norris PC. Eicosanoid storm in infection and inflammation. *Nat Rev Immunol.* (2015) 15:511–23. doi: 10.1038/nri3859
65. Annane D, Sebille V, Charpentier C, Bollaert PE, Francois B, Korach JM, et al. Effect of treatment with low doses of hydrocortisone and fludrocortisone on mortality in patients with septic shock. *JAMA.* (2002) 288:862–71. doi: 10.1001/jama.288.7.862
66. Bollaert PE, Charpentier C, Levy B, Debouverie M, Audibert G, Larcan A. Reversal of late septic shock with supraphysiologic doses of hydrocortisone. *Crit Care Med.* (1998) 26:645–50. doi: 10.1097/00003246-199804000-00010
67. Oppert M, Schindler R, Husung C, Offermann K, Graf KJ, Boenisch O, et al. Low-dose hydrocortisone improves shock reversal and reduces cytokine levels in early hyperdynamic septic shock. *Crit Care Med.* (2005) 33:2457–64. doi: 10.1097/01.CCM.0000186370.78639.23
68. Sprung CL, Annane D, Keh D, Moreno R, Singer M, Freivogel K, et al. Hydrocortisone therapy for patients with septic shock. *N Engl J Med.* (2008) 358:111–24. doi: 10.1056/NEJMoa071366
69. Arabi YM, Aljumah A, Dabbagh O, Tamim HM, Rishu AH, Al-Abdulkareem A, et al. Low-dose hydrocortisone in patients with cirrhosis and septic shock: a randomized controlled trial. *CMAJ.* (2010) 182:1971–7. doi: 10.1503/cmaj.090707
70. Briegel J, Forst H, Haller M, Schelling G, Kilger E, Kuprat G, et al. Stress doses of hydrocortisone reverse hyperdynamic septic shock: a prospective, randomized, double-blind, single-center study. *Crit Care Med.* (1999) 27:723–32. doi: 10.1097/00003246-199904000-00025
71. Sprung CL, Caralis PV, Marcial EH, Pierce M, Gelbard MA, Long WM, et al. The effects of high-dose corticosteroids in patients with septic shock. A prospective, controlled study. *N Engl J Med.* (1984) 311:1137–43. doi: 10.1056/NEJM198411013111801
72. Bone RC, Fisher CJ Jr, Clemmer TP, Slotman GJ, Metz CA, Balk RA. A controlled clinical trial of high-dose methylprednisolone in the treatment of severe sepsis and septic shock. *N Engl J Med.* (1987) 317:653–8. doi: 10.1056/NEJM198709103171101
73. Bernard GR, Wheeler AP, Russell JA, Schein R, Summer WR, Steinberg KP, et al. The effects of ibuprofen on the physiology and survival of patients with sepsis. The ibuprofen in sepsis study group. *N Engl J Med.* (1997) 336:912–8. doi: 10.1056/NEJM199703273361303
74. O'Brien J, Lee SH, Onogi S, Shea KJ. Engineering the protein corona of a synthetic polymer nanoparticle for broad-spectrum sequestration and neutralization of venomous biomacromolecules. *J Am Chem Soc.* (2016) 138:16604–7. doi: 10.1021/jacs.6b10950
75. O'Brien J, Shea KJ. Tuning the protein corona of hydrogel nanoparticles: the synthesis of abiotic protein and peptide affinity reagents. *Acc Chem Res.* (2016) 49:1200–10. doi: 10.1021/acs.accounts.6b00125
76. Dinarello CA. Proinflammatory cytokines. *Chest.* (2000) 118:503–8. doi: 10.1378/chest.118.2.503
77. Dinarello CA. Anti-cytokine therapies in response to systemic infection. *J Investig Dermatol Symp Proc.* (2001) 6:244–50. doi: 10.1046/j.0022-202x.2001.00046.x
78. Dinarello CA. The proinflammatory cytokines interleukin-1 and tumor necrosis factor and treatment of the septic shock syndrome. *J Infect Dis.* (1991) 163:1177–84. doi: 10.1093/infdis/163.6.1177
79. Harada A, Sekido N, Akahoshi T, Wada T, Mukaida N, Matsushima K. Essential involvement of interleukin-8 (IL-8) in acute inflammation. *J Leukoc Biol.* (1994) 56:559–64. doi: 10.1002/jlb.56.5.559
80. Leonard EJ, Skeel A, Yoshimura T. Biological aspects of monocyte chemoattractant protein-1 (MCP-1). *Adv Exp Med Biol.* (1991) 305:57–64. doi: 10.1007/978-1-4684-6009-4_7
81. Wolpe SD, Davatelis G, Sherry B, Beutler B, Hesse DG, Nguyen HT, et al. Macrophages secrete a novel heparin-binding protein with inflammatory and neutrophil chemokinetic properties. *J Exp Med.* (1988) 167:570–81. doi: 10.1084/jem.167.2.570
82. Lam HS, Ng PC. Biochemical markers of neonatal sepsis. *Pathology.* (2008) 40:141–8. doi: 10.1080/00313020701813735
83. Beutler B, Milsark IW, Cerami AC. Passive immunization against cachectin/tumor necrosis factor protects mice from lethal effect of endotoxin. *Science.* (1985) 229:869–71. doi: 10.1126/science.3895437
84. Vilcek J. First demonstration of the role of TNF in the pathogenesis of disease. *J Immunol.* (2008) 181:5–6. doi: 10.4049/jimmunol.181.1.5
85. Scallon B, Cai A, Solowski N, Rosenberg A, Song XY, Shealy D, et al. Binding and functional comparisons of two types of tumor necrosis factor antagonists. *J Pharmacol Exp Ther.* (2002) 301:418–26. doi: 10.1124/jpet.301.2.418
86. Scheinfeld N. A comprehensive review and evaluation of the side effects of the tumor necrosis factor alpha blockers etanercept, infliximab and adalimumab. *J Dermatolog Treat.* (2004) 15:280–94. doi: 10.1080/09546630410017275
87. Abraham E, Glauser MP, Butler T, Garbino J, Gelmont D, Laterre PF, et al. p55 tumor necrosis factor receptor fusion protein in the treatment of patients with severe sepsis and septic shock. A randomized controlled multicenter trial. Ro 45-2081 study group. *JAMA.* (1997) 277:1531–8. doi: 10.1001/jama.1997.03540430043031
88. Abraham E, Laterre PF, Garbino J, Pingleton S, Butler T, Dugernier T, et al. Lenercept (p55 tumor necrosis factor receptor fusion protein) in severe sepsis and early septic shock: a randomized, double-blind, placebo-controlled, multicenter phase III trial with 1,342 patients. *Crit Care Med.* (2001) 29:503–10. doi: 10.1097/00003246-200103000-00006
89. Fisher CJ Jr, Agosti JM, Opal SM, Lowry SF, Balk RA, Sadoff JC, et al. Treatment of septic shock with the tumor necrosis factor receptor:Fc fusion protein. The soluble TNF receptor sepsis study group. *N Engl J Med.* (1996) 334:1697–702. doi: 10.1056/NEJM199606273342603
90. Fisher CJ Jr, Dhainaut JF, Opal SM, Pribble JP, Balk RA, Slotman GJ, et al. Recombinant human interleukin 1 receptor antagonist in the treatment of patients with sepsis syndrome. Results from a randomized, double-blind, placebo-controlled trial. Phase III rhIL-1ra sepsis syndrome study group. *JAMA.* (1994) 271:1836–43. doi: 10.1001/jama.1994.03510470040032
91. Fisher CJ Jr, Marra MN, Palardy JE, Marchbanks CR, Scott RW, Opal SM. Human neutrophil bactericidal/permeability-increasing protein reduces mortality rate from endotoxin challenge: a placebo-controlled study. *Crit Care Med.* (1994) 22:553–8. doi: 10.1097/00003246-199404000-00008
92. Opal SM, Fisher CJ Jr, Dhainaut JF, Vincent JL, Brase R, Lowry SF, et al. Confirmatory interleukin-1 receptor antagonist trial in severe sepsis: a phase III, randomized, double-blind, placebo-controlled, multicenter trial. The interleukin-1 receptor antagonist sepsis investigator group. *Crit Care Med.* (1997) 25:1115–24. doi: 10.1097/00003246-199707000-00010
93. Casey LM, Kakade S, Decker JT, Rose JA, Deans K, Shea LD, et al. Cargo-less nanoparticles program innate immune cell responses to toll-like receptor activation. *Biomaterials.* (2019) 218:119333. doi: 10.1016/j.biomaterials.2019.119333
94. Spence S, Greene MK, Fay F, Hams E, Saunders SP, Hamid U, et al. Targeting Siglecs with a sialic acid-decorated nanoparticle abrogates inflammation. *Sci Transl Med.* (2015) 7:303ra140. doi: 10.1126/scitranslmed.aab3459
95. Park J, Zhang Y, Saito E, Gurczynski SJ, Moore BB, Cummings BJ, et al. Intravascular innate immune cells reprogrammed via intravenous

nanoparticles to promote functional recovery after spinal cord injury. *Proc Natl Acad Sci USA*. (2019) 116:14947–54. doi: 10.1073/pnas.1820276116
96. Fruchon S, Mouriot S, Thiollier T, Grandin C, Caminade AM, Turrin CO, et al. Repeated intravenous injections in non-human primates demonstrate preclinical safety of an anti-inflammatory phosphorus-based dendrimer. *Nanotoxicology*. (2015) 9:433–41. doi: 10.3109/17435390.2014.940406
97. Fruchon S, Poupot M, Martinet L, Turrin CO, Majoral JP, Fournie JJ, et al. Anti-inflammatory and immunosuppressive activation of human monocytes by a bioactive dendrimer. *J Leukoc Biol.* (2009) 85:553–62. doi: 10.1189/jlb.0608371
98. Moyano DF, Liu Y, Ayaz F, Hou S, Puangploy P, Duncan B, et al. Immunomodulatory effects of coated gold nanoparticles in LPS-stimulated *in vitro* and *in vivo* murine model systems. *Chem.* (2016) 1:320–7. doi: 10.1016/j.chempr.2016.07.007
99. Foit L, Thaxton CS. Synthetic high-density lipoprotein-like nanoparticles potently inhibit cell signaling and production of inflammatory mediators induced by lipopolysaccharide binding Toll-like receptor 4. *Biomaterials.* (2016) 100:67–75. doi: 10.1016/j.biomaterials.2016.05.021
100. Wakimoto T, Uchida K, Mimura K, Kanagawa T, Mehandjiev TR, Aoshima H, et al. Hydroxylated fullerene: a potential antiinflammatory and antioxidant agent for preventing mouse preterm birth. *Am J Obstet Gynecol.* (2015) 213:708 e1–9. doi: 10.1016/j.ajog.2015.07.017
101. Pentecost AE, Witherel CE, Gogotsi Y, Spiller KL. Anti-inflammatory effects of octadecylamine-functionalized nanodiamond on primary human macrophages. *Biomater Sci.* (2017) 5:2131–43. doi: 10.1039/C7BM00294G
102. Wang Z, Li J, Cho J, Malik AB. Prevention of vascular inflammation by nanoparticle targeting of adherent neutrophils. *Nat Nanotechnol.* (2014) 9:204–10. doi: 10.1038/nnano.2014.17
103. Chu D, Gao J, Wang Z. Neutrophil-mediated delivery of therapeutic nanoparticles across blood vessel barrier for treatment of inflammation and infection. *ACS Nano.* (2015) 9:11800–11. doi: 10.1021/acsnano.5b05583
104. Gao J, Chu D, Wang Z. Cell membrane-formed nanovesicles for disease-targeted delivery. *J Control Release.* (2016) 224:208–16. doi: 10.1016/j.jconrel.2016.01.024
105. Yang H, Fung SY, Xu S, Sutherland DP, Kollmann TR, Liu M, et al. Amino acid-dependent attenuation of toll-like receptor signaling by peptide-gold nanoparticle hybrids. *ACS Nano.* (2015) 9:6774–84. doi: 10.1021/nn505634h
106. Gao W, Wang Y, Xiong Y, Sun L, Wang L, Wang K, et al. Size-dependent anti-inflammatory activity of a peptide-gold nanoparticle hybrid *in vitro* and in a mouse model of acute lung injury. *Acta Biomater.* (2019) 85:203–17. doi: 10.1016/j.actbio.2018.12.046
107. Saito E, Kuo R, Pearson RM, Gohel N, Cheung B, King NJC, et al. Designing drug-free biodegradable nanoparticles to modulate inflammatory monocytes and neutrophils for ameliorating inflammation. *J Control Release.* (2019) 300:185–96. doi: 10.1016/j.jconrel.2019.02.025
108. Getts DR, Terry RL, Getts MT, Deffrasnes C, Muller M, van Vreden C, et al. Therapeutic inflammatory monocyte modulation using immune-modifying microparticles. *Sci Transl Med.* (2014) 6:219ra7. doi: 10.1126/scitranslmed.3007563
109. Leick M, Azcutia V, Newton G, Luscinskas FW. Leukocyte recruitment in inflammation: basic concepts and new mechanistic insights based on new models and microscopic imaging technologies. *Cell Tissue Res.* (2014) 355:647–56. doi: 10.1007/s00441-014-1809-9
110. Xiao L, Liu Y, Wang N. New paradigms in inflammatory signaling in vascular endothelial cells. *Am J Physiol Heart Circ Physiol.* (2014) 306:H317–25. doi: 10.1152/ajpheart.00182.2013
111. Liao JK. Linking endothelial dysfunction with endothelial cell activation. *J Clin Invest.* (2013) 123:540–1. doi: 10.1172/JCI66843
112. Kelley WJ, Safari H, Lopez-Cazares G, Eniola-Adefeso O. Vascular-targeted nanocarriers: design considerations and strategies for successful treatment of atherosclerosis and other vascular diseases. *Wiley Interdiscip Rev Nanomed Nanobiotechnol.* (2016) 8:909–26. doi: 10.1002/wnan.1414
113. Calin M, Manduteanu I. Emerging nanocarriers-based approaches to diagnose and red uce vascular inflammation in atherosclerosis. *Curr Med Chem.* (2017) 24:550–67. doi: 10.2174/0929867324666161123091627
114. Kieser KJ, Kagan JC. Multi-receptor detection of individual bacterial products by the innate immune system. *Nat Rev Immunol.* (2017) 17:376–90. doi: 10.1038/nri.2017.25
115. Azad AK, Rajaram MV, Schlesinger LS. Exploitation of the macrophage mannose receptor (CD206) in infectious disease diagnostics and therapeutics. *J Cytol Mol Biol.* (2014) 1:1000003. doi: 10.13188/2325-4653.1000003
116. Silva MT, Correia-Neves M. Neutrophils and macrophages: the main partners of phagocyte cell systems. *Front Immunol.* (2012) 3:174. doi: 10.3389/fimmu.2012.00174
117. Rosen H, Crowley JR, Heinecke JW. Human neutrophils use the myeloperoxidase-hydrogen peroxide-chloride system to chlorinate but not nitrate bacterial proteins during phagocytosis. *J Biol Chem.* (2002) 277:30463–8. doi: 10.1074/jbc.M202331200
118. Nauseef WM. Myeloperoxidase in human neutrophil host defence. *Cell Microbiol.* (2014) 16:1146–55. doi: 10.1111/cmi.12312
119. Soh M, Kang DW, Jeong HG, Kim D, Kim DY, Yang W, et al. Ceria-zirconia nanoparticles as an enhanced multi-antioxidant for sepsis treatment. *Angew Chem Int Ed Engl.* (2017) 56:11399–403. doi: 10.1002/anie.201704904
120. Yipp BG, Kubes P. NETosis: how vital is it? *Blood.* (2013) 122:2784–94. doi: 10.1182/blood-2013-04-457671
121. Gollomp K, Sarkar A, Harikumar S, Seeholzer SH, Arepally GM, Hudock K, et al. Fc-modified HIT-like monoclonal antibody as a novel treatment for sepsis. *Blood.* (2020) 135:743–54. doi: 10.1182/blood.2019002329
122. Hwang TL, Aljuffali IA, Lin CF, Chang YT, Fang JY. Cationic additives in nanosystems activate cytotoxicity and inflammatory response of human neutrophils: lipid nanoparticles versus polymeric nanoparticles. *Int J Nanomedicine.* (2015) 10:371–85. doi: 10.2147/IJN.S73017
123. Hwang TL, Hsu CY, Aljuffali IA, Chen CH, Chang YT, Fang JY. Cationic liposomes evoke proinflammatory mediator release and neutrophil extracellular traps (NETs) toward human neutrophils. *Colloids Surf B Biointerfaces.* (2015) 128:119–26. doi: 10.1016/j.colsurfb.2015.02.022
124. Hwang TL, Aljuffali IA, Hung CF, Chen CH, Fang JY. The impact of cationic solid lipid nanoparticles on human neutrophil activation and formation of neutrophil extracellular traps (NETs). *Chem Biol Interact.* (2015) 235:106–14. doi: 10.1016/j.cbi.2015.04.011
125. Paino IM, Zucolotto V. Poly(vinyl alcohol)-coated silver nanoparticles: activation of neutrophils and nanotoxicology effects in human hepatocarcinoma and mononuclear cells. *Environ Toxicol Pharmacol.* (2015) 39:614–21. doi: 10.1016/j.etap.2014.12.012
126. Soares T, Ribeiro D, Proenca C, Chiste RC, Fernandes E, Freitas M. Size-dependent cytotoxicity of silver nanoparticles in human neutrophils assessed by multiple analytical approaches. *Life Sci.* (2016) 145:247–54. doi: 10.1016/j.lfs.2015.12.046
127. Liz R, Simard JC, Leonardi LB, Girard D. Silver nanoparticles rapidly induce atypical human neutrophil cell death by a process involving inflammatory caspases and reactive oxygen species and induce neutrophil extracellular traps release upon cell adhesion. *Int Immunopharmacol.* (2015) 28:616–25. doi: 10.1016/j.intimp.2015.06.030
128. Poirier M, Simard JC, Antoine F, Girard D. Interaction between silver nanoparticles of 20 nm (AgNP20) and human neutrophils: induction of apoptosis and inhibition of *de novo* protein synthesis by AgNP20 aggregates. *J Appl Toxicol.* (2014) 34:404–12. doi: 10.1002/jat.2956
129. Serhan CN. Treating inflammation and infection in the 21st century: new hints from decoding resolution mediators and mechanisms. *FASEB J.* (2017) 31:1273–88. doi: 10.1096/fj.201601222R
130. Jia SH, Parodo J, Kapus A, Rotstein OD, Marshall JC. Dynamic regulation of neutrophil survival through tyrosine phosphorylation or dephosphorylation of caspase-8. *J Biol Chem.* (2008) 283:5402–13. doi: 10.1074/jbc.M706462200
131. Milot E, Fotouhi-Ardakani N, Filep JG. Myeloid nuclear differentiation antigen, neutrophil apoptosis and sepsis. *Front Immunol.* (2012) 3:397. doi: 10.3389/fimmu.2012.00397
132. Guo RF, Sun L, Gao H, Shi KX, Rittirsch D, Sarma VJ, et al. *In vivo* regulation of neutrophil apoptosis by C5a during sepsis. *J Leukoc Biol.* (2006) 80:1575–83. doi: 10.1189/jlb.0106065
133. Guo RF, Riedemann NC, Sun L, Gao H, Shi KX, Reuben JS, et al. Divergent signaling pathways in phagocytic cells during sepsis. *J Immunol.* (2006) 177:1306–13. doi: 10.4049/jimmunol.177.2.1306
134. Perianayagam MC, Balakrishnan VS, Pereira BJ, Jaber BL. C5a delays apoptosis of human neutrophils via an extracellular signal-regulated kinase

and bad-mediated signalling pathway. *Eur J Clin Invest.* (2004) 34:50–6. doi: 10.1111/j.1365-2362.2004.01273.x
135. Simon HU. Targeting apoptosis in the control of inflammation. *Eur Respir J Suppl.* (2003) 44:20s—1s. doi: 10.1183/09031936.03.00000603b
136. Simon HU. Neutrophil apoptosis pathways and their modifications in inflammation. *Immunol Rev.* (2003) 193:101–10. doi: 10.1034/j.1600-065X.2003.00038.x
137. Souto FO, Alves-Filho JC, Turato WM, Auxiliadora-Martins M, Basile-Filho A, Cunha FQ. Essential role of CCR2 in neutrophil tissue infiltration and multiple organ dysfunction in sepsis. *Am J Respir Crit Care Med.* (2011) 183:234–42. doi: 10.1164/rccm.201003-0416OC
138. Souto FO, Zarpelon AC, Staurengo-Ferrari L, Fattori V, Casagrande R, Fonseca MJ, et al. Quercetin reduces neutrophil recruitment induced by CXCL8, LTB4, and fMLP: inhibition of actin polymerization. *J Nat Prod.* (2011) 74:113–8. doi: 10.1021/np1003017
139. Speyer CL, Gao H, Rancilio NJ, Neff TA, Huffnagle GB, Sarma JV, et al. Novel chemokine responsiveness and mobilization of neutrophils during sepsis. *Am J Pathol.* (2004) 165:2187–96. doi: 10.1016/S0002-9440(10)63268-3
140. Calvano SE, Xiao W, Richards DR, Felciano RM, Baker HV, Cho RJ, et al. A network-based analysis of systemic inflammation in humans. *Nature.* (2005) 437:1032–7. doi: 10.1038/nature03985
141. Genster N, Ostrup O, Schjalm C, Eirik Mollnes T, Cowland JB, Garred P. Ficolins do not alter host immune responses to lipopolysaccharide-induced inflammation *in vivo*. *Sci Rep.* (2017) 7:3852. doi: 10.1038/s41598-017-04121-w
142. Carson WF, Cavassani KA, Dou Y, Kunkel SL. Epigenetic regulation of immune cell functions during post-septic immunosuppression. *Epigenetics.* (2011) 6:273–83. doi: 10.4161/epi.6.3.14017
143. Remick DG. Cytokine therapeutics for the treatment of sepsis: why has nothing worked? *Curr Pharm Des.* (2003) 9:75–82. doi: 10.2174/1381612033392567
144. Cockrell RC, An G. Examining the controllability of sepsis using genetic algorithms on an agent-based model of systemic inflammation. *PLoS Comput Biol.* (2018) 14:e1005876. doi: 10.1371/journal.pcbi.1005876
145. Golchin N, Frank SH, Vince A, Isham L, Meropol SB. Polypharmacy in the elderly. *J Res Pharm Pract.* (2015) 4:85–8. doi: 10.4103/2279-042X.155755
146. Maher RL, Hanlon J, Hajjar ER. Clinical consequences of polypharmacy in elderly. *Expert Opin Drug Saf.* (2014) 13:57–65. doi: 10.1517/14740338.2013.827660
147. Horace AE, Ahmed F. Polypharmacy in pediatric patients and opportunities for pharmacists' involvement. *Integr Pharm Res Pract.* (2015) 4:113–26. doi: 10.2147/IPRP.S64535
148. Morden NE, Goodman D. Pediatric polypharmacy: time to lock the medicine cabinet? *Arch Pediatr Adolesc Med.* (2012) 166:91–2. doi: 10.1001/archpediatrics.2011.162
149. Feudtner C, Dai D, Hexem KR, Luan X, Metjian TA. Prevalence of polypharmacy exposure among hospitalized children in the United States. *Arch Pediatr Adolesc Med.* (2012) 166:9–16. doi: 10.1001/archpediatrics.2011.161

Conflict of Interest: The authors declare that the research was conducted in the absence of any commercial or financial relationships that could be construed as a potential conflict of interest.

frontiers in Immunology

ORIGINAL RESEARCH
published: 06 August 2020
doi: 10.3389/fimmu.2020.01631

Developing an Unbiased Multiplex PCR System to Enrich the *TRB* Repertoire Toward Accurate Detection in Leukemia

Jinghua Wu[1,2†], Xie Wang[2†], Liya Lin[2†], Xuemei Li[2†], Sixi Liu[3], Wei Zhang[2,4], Lihua Luo[1,2], Ziyun Wan[2], Mingyan Fang[2], Yi Zhao[2], Xiaodong Wang[3], Huirong Mai[3], Xiuli Yuan[3], Feiqiu Wen[3], Changgang Li[3] and Xiao Liu[2,5*]*

[1] BGI Education Center, University of Chinese Academy of Sciences, Shenzhen, China, [2] BGI-Shenzhen, Shenzhen, China, [3] Hematology and Oncology Department, Shenzhen Children's Hospital, Shenzhen, China, [4] Department of Computer Science, City University of Hong Kong, Hong Kong, China, [5] Neoimmune, Shenzhen, China

OPEN ACCESS

Edited by:
Evan Alexander Scott,
Northwestern University, United States

Reviewed by:
Raffaele De Palma,
University of Genoa, Italy
Hongbo Hu,
Sichuan University, China

***Correspondence:**
Changgang Li
licg6336@sina.com
Xiao Liu
airson_LIU@163.com

[†] These authors have contributed equally to this work

Specialty section:
This article was submitted to T Cell Biology, a section of the journal Frontiers in Immunology

Received: 28 February 2020
Accepted: 18 June 2020
Published: 06 August 2020

Citation:
Wu J, Wang X, Lin L, Li X, Liu S, Zhang W, Luo L, Wan Z, Fang M, Zhao Y, Wang X, Mai H, Yuan X, Wen F, Li C and Liu X (2020) Developing an Unbiased Multiplex PCR System to Enrich the TRB Repertoire Toward Accurate Detection in Leukemia. Front. Immunol. 11:1631. doi: 10.3389/fimmu.2020.01631

Accurate T cell receptor repertoire profiling has provided novel biological and clinical insights in widespread immunological settings; however, there is a lack of reference materials in the community that can be used to calibrate and optimize the various experimental systems in different laboratories. In this study, we designed and synthesized 611 T cell receptor (TCR) beta chain (*TRB*) templates and used them as reference materials to optimize the multiplex PCR experimental system to enrich the *TRB* repertoire. We assessed the stability of the optimized system by repeating the experiments in different batches and by remixing the TRB templates in different ratios. These TRB reference materials could be used as independent positive controls to assess the accuracy of the experimental system, and they can also be used as spike-in materials to calibrate the residual biases of the experimental system. We then used the optimized system to detect the minimal residual disease of T cell acute lymphoblastic leukemia and showed a higher sensitivity compared with flow cytometry. We also interrogated how chemotherapy affected the TCR repertoire of patients with B-cell acute lymphoblastic leukemia. Our result shows that high-avidity T cells, such as those targeting known pathogens, are largely selected during chemotherapy, despite the global immunosuppression. These T cells were stimulated and emerged at the time of induction treatment and further expanded during consolidation treatment, possibly to fight against infections. These data demonstrate that accurate immune repertoire information can improve our understanding of the adaptive immunity in leukemia and lead to better treatment management of the patients.

Keywords: immune repertoire, *TRB*, multiplex PCR system optimization, minimal residual disease, leukemia

INTRODUCTION

The human T cell repertoire is generated by somatic rearrangement of the variable (V), diversity (D), and joining (J) segments on the T cell receptor (TCR) loci during T cell development, and a diverse TCR repertoire is pivotal to human health. Before the wide application of high throughput sequencing (HTS), spectratyping assays was the commonly used method for assessing the TCR

repertoire. However, TCR spectratyping is limited by its low resolution because it cannot provide precise information on the individual clonotype (1–3). The application of HTS in TCR repertoire analysis (TCR-seq) began 10 years ago (4–6) and has been widely used in basic and translational research (2, 7–9) due to its high resolution and throughput. The technology has been used in fields such as investigating the functional heterogeneity of the human T cell (10), comparing TCR repertoire of different tissues (11, 12), analyzing the effect of genetic background on TCR repertoire (13), identifying autoimmune-disease-related T cells (14–16), quantifying minimal residual disease in blood cancer (17), and predicting the responses of vaccination (18) or immunotherapy (19–21).

Single cell sequencing approach (e.g., 10X genomics) can provide information of α chain and β chain pairing, as well as transcription information of other genes in TCR repertoire study. However, it is still relatively expensive at present, and fresh specimens are usually required for living single cell isolation, which limit its broad application in disease and health research (22). In large cohort study, sequencing TCR repertoire from bulk cells is more commonly used because of its low cost, high throughput, and easy access to samples. For bulk TCR-seq, both genomic DNA and RNA can be used as the input material. The consistent copy number (only one productively rearranged alpha locus and beta locus per αβ T cell) and the accessibility make genomic DNA (gDNA) more convenient in future clinical applications.

Multiplex polymerase chain reaction (PCR) and rapid amplification of 5′ complementary DNA ends (5′RACE) are the two most commonly used library preparation methods. Although 5′RACE can control bias by refraining from the use of multiple primer sets, it works only for RNA (2, 22). Multiplex PCR was used as the most efficient and cost-effective method to enrich the completely rearranged TCR genes of both DNA and RNA samples. However, multiplex PCR can introduce biases due to differences in amplification efficiencies and cross-reactivities of multiple primers in the same reaction system, which can compromise the precision of the TCR repertoire data. For RNA sample, unique molecular identifiers (UMIs) can be incorporated by reverse transcription to adjust the bias (23, 24); however, it is challenging to bring in UMIs for gDNA sample. Therefore, it is critical to optimize the multiplex PCR experimental system to minimize the biases. In a previous effort, Carlson et al. (25) synthesized 56 TCR gamma chain *(TRG)* template sets to optimize the TRG repertoire amplification system; however, for the amplification system of other TCR chains, especially the most diverse β chain, few have been carefully refined in controlled systems or by reference standard materials.

Increased T cell infiltration has been widely reported to be associated with improved survival in patients with solid tumors (26–29). For blood cancer, the association between increased T cell infiltration with improved clinical outcome has been observed in diffuse large B-cell lymphoma (DLBCL) (30, 31). Beside the T cell infiltration level, Keane et al. (32) found that the clonality of intratumoral TCR repertoire is also associated with the clinical outcome of DLBCL (32). The T cells are dysfunctional in chronic lymphocytic leukemia (CLL), which is related with increased risk of infectious and autoimmune disease (33–35). Moreover, the TCR repertoire is skewed, which is reflected by restricted TRBV usage or increased clonality in CLL patients (36, 37). During ibrutinib therapy of CLL patients, large numbers of new T cell clonotypes emerged, and the TCR repertoire diversity increased, which may be related with decreased infection and improved clinical outcome (38). Chemotherapy is the mostly used treatment for acute lymphoblastic leukemia (ALL). Given the importance of T cells in fighting infections, the reconstruction of T cell immune repertoire during chemotherapy is very critical for the recovery from disease. In this study, we have designed a reference standard to develop an optimal reaction system for TCR beta chain (*TRB*) amplification, and then, we used this system to analyze the changes in *TRB* repertoire in acute ALL patients during chemotherapy.

Abbreviations: TCR, T cell receptor; TCR-seq, TCR repertoire sequencing; PCR, polymerase chain reaction; TRB, TCR beta chain; ALL, acute lymphoblastic leukemia; B-ALL, B-cell acute lymphoblastic leukemia; T-ALL, T-cell acute lymphoblastic leukemia; MRD, minimal residual disease; CDR3, complementarity determining region 3; PKPSC, proportion of known pathogen-specific *TRB* clonotypes; FC, flow cytometry.

METHODS

Synthesis of *TRB* Templates

We designed 611 *TRB* templates with known sequences, and then, those templates were synthesized and cloned into the pUC57-simple plasmid vector to produce a recombinant plasmid DNA. Then, the recombinant plasmid DNAs were transformed into *Escherichia coli* for sequencing and long-term storage. The concentration of each recombinant plasmid DNA containing synthetic *TRB* templates was determined using the Qubit 3.0 fluorometer (Life Technologies, Paisley, UK). Then, we pooled all the recombinant plasmid DNA at expected equimolar levels, and the pooling was repeated twice.

Quantifying the Composition of the Preamplified *TRB* Templates

To quantify the frequencies of each *TRB* template in the pool, the recombinant plasmid DNA pool was digested by restriction enzymes, and the synthetic *TRB* templates were purified and separated from the plasmid vector by gel extraction. Then, *TRB* templates were ligated with sequencing adapter and sequenced on BGISEQ-500 platform.

Enriching the Rearranged *TRB* Segments by Multiplex PCR

Two steps of PCR were used to enrich the complete rearranged *TRB* fragments. For the pooled recombinant plasmid DNAs, 100,000 templates were used, and for the natural human samples, 300–1,200 ng DNA was used. The first step PCR is a multiplex PCR, and it goes 30 cycles, which includes 28 forward primers located at the *TRBV* FR3 regions and 13 reverse primers located at the *TRBJ* regions (**Table S1**). The second step PCR is a simplex PCR using a universal primer and goes seven cycles, which brings

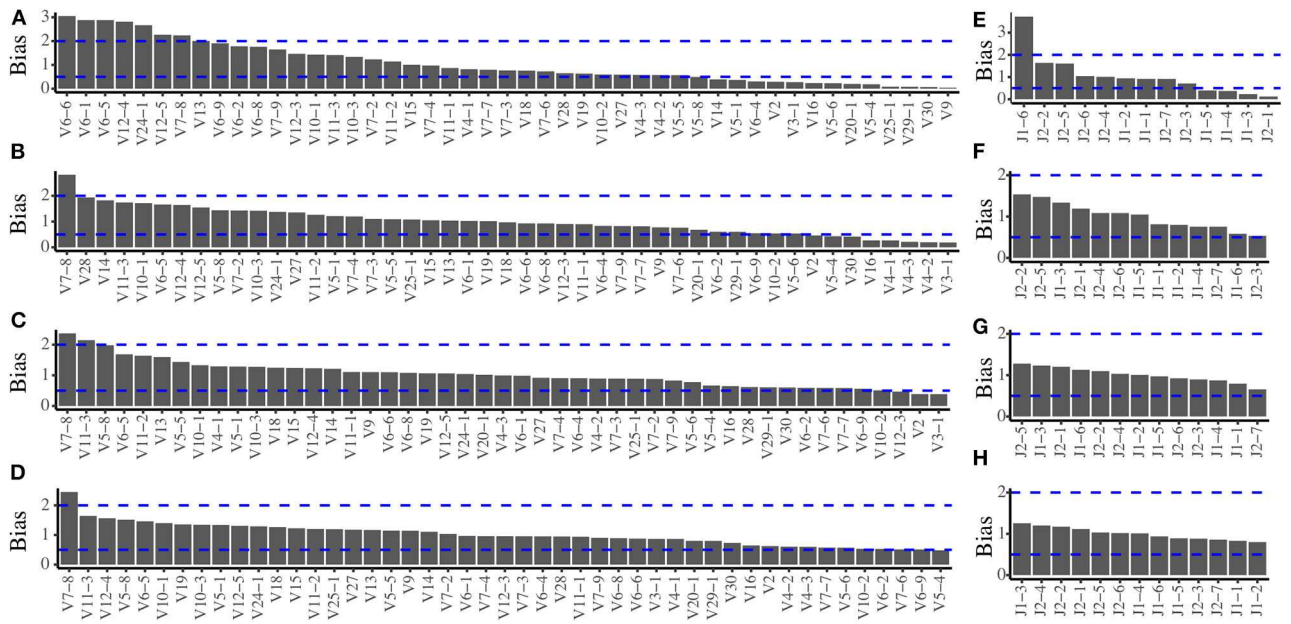

FIGURE 1 | Amplification bias of the multiplex PCR reaction system during primer mix optimization for pool 1. **(A)** The *TRBV* amplification bias before optimization. **(B,C)** The *TRBV* amplification bias during optimization. **(D)** The *TRBV* amplification bias after optimization. **(E)** The *TRBJ* amplification bias before optimization. **(F,G)** The *TRBJ* amplification bias during optimization. **(H)** The *TRBJ* amplification bias after optimization.

in the whole adaptor sequence for BGISEQ-500 platform to generate sequencing libraries.

Sequencing and Data Analyzing

The sequencing libraries were used to make the DNA nanoballs and then sequenced on BGISEQ-500 platform with a single-end 200-bp reads. The raw sequencing data of the pre- and post-amplified synthetic *TRB* templates were aligned to the 411 *TRB* references using Bowtie 2 with local mode. For the natural human samples, the raw sequencing reads were processed using *IMonitor* (39), and the CDR3s in a sample with the frequency of <3 in 1 million sequences were filtered to remove the CDR3s containing sequencing errors.

Optimizing Mixing Ratios of the Primers

Firstly, the V and J primers were mixed equimolarly, and the amplification bias of each V or J segment was calculated as the following formula:

Bias = (the V or J represent of postamplified templates)/(the V or J represent of preamplified templates).

For each V or J primer, if the amplification bias is >2 or <0.5, the proportion of the primer in the primer mixture will be adjusted until the amplification biases of most primers are in the range of 0.5–2.

Minimal Residual Disease Detection and the Repertoire Characteristics Analysis in ALL Samples

We enrolled 10 childhood patients with B-cell acute lymphoblastic leukemia (B-ALL) and two childhood patients with T cell acute lymphoblastic leukemia (T-ALL) in Shenzhen Children's Hospital. The study was carried out in accordance with the recommendations of Declaration of Helsinki. It was approved by BGI Institute of Review Board (BGI-IRB) and written informed consent was obtained from the parent(s) or guardian(s) of each patient. The clinical information of the patients is shown in **Table S2**. The bone marrow (BM) specimens were obtained at diagnosis and on day 33 and 64 during chemotherapy, and 30 BM samples were collected in total. The BM samples were stored at −80°C, and the genomic DNA was extracted using a DNA Blood Mini Kit (QIAGEN, Cat. no. 51106).

The minimal residual disease (MRD) detection in T-ALL patients was conducted following the method introduced in our previous paper (40). All the TRB clonotypes in this paper refer to the CDR3 sequences. Due to the effect of reads number on the repertoire diversity, only 0.5 million effective reads were used when calculating the Shannon index, Pielou's index, and top 100 clonotype frequency. The Shannon index was calculated using the formula described in a previous paper (39); Pielou's index was calculated using the following forum: Pielou's index = Shannon index/ln *S* (*S* is the unique clonotype number of a repertoire). The proportion of known pathogen-specific *TRB* clonotypes (PKPSC) was calculated using the method described before (41).

Statistics

Statistical analysis and data visualization were performed using R tools. The statistical significance of group comparison was tested using Wilcoxon rank sum test, and paired test was used where possible.

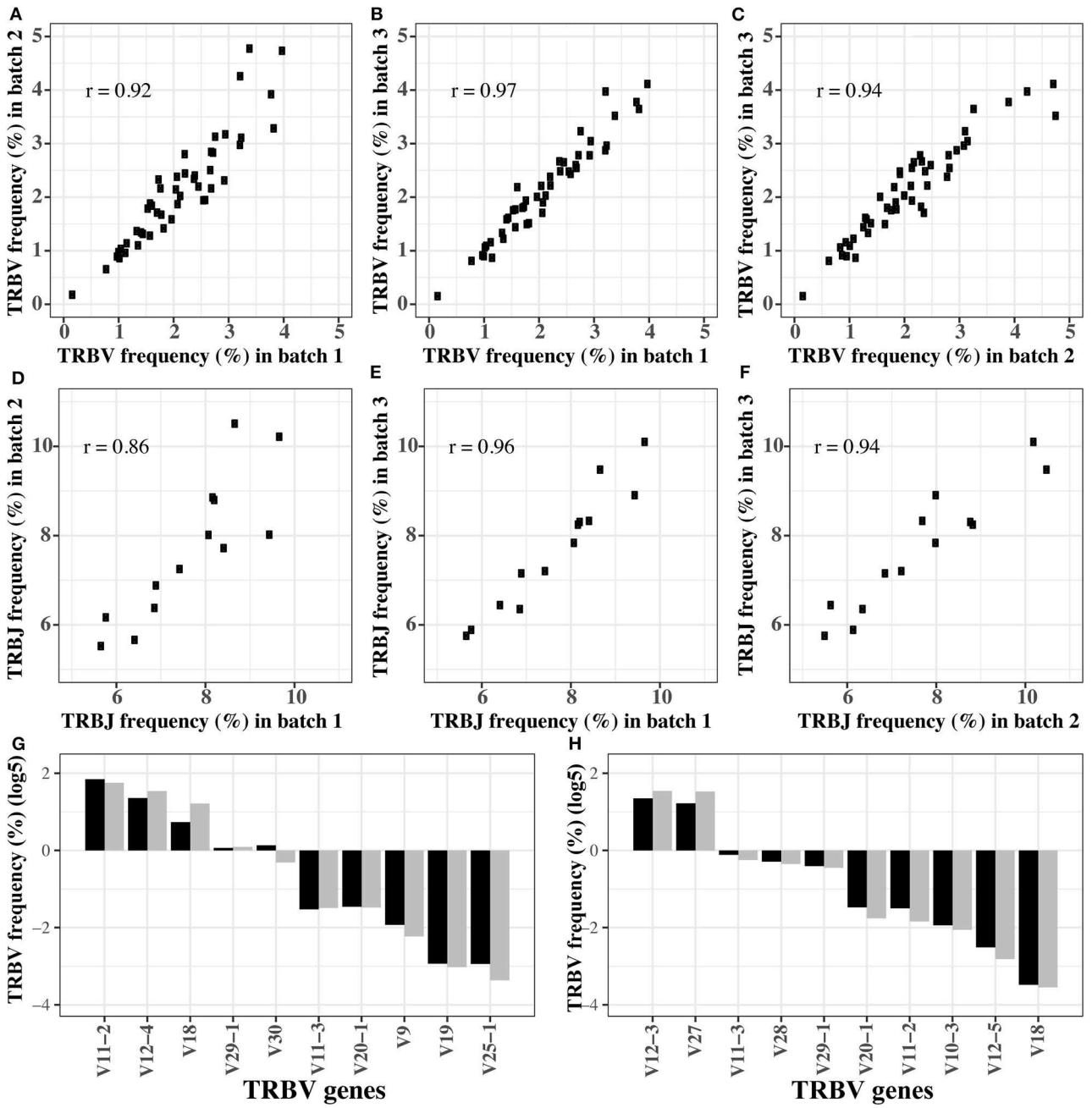

FIGURE 2 | The robustness of optimized multiplex PCR reaction system. **(A–C)** The *TRBV* usage frequency distributions in three batches of experiments. **(D–F)** The *TRBJ* usage frequency distributions in three batches of experiments. **(G,H)** The *TRBV* usage frequency before and after amplification for the first **(G)** and second **(H)** gradient mixture of the *TRB* templates. In **(G,H)**, the black bar is the TRBV usage before amplification, and gray bar is the TRBV usage after amplification.

RESULTS

Design of Reference Standard Materials to Minimize the Amplification Bias

The human *TRB* locus encodes 48 functional *TRBV* segments and 13 functional *TRBJ* segments in IMGT. However, due to the germline sequence of *TRBV6-2* and *TRBV6-3* being completely identical, there are 47 different functional *TRBV* segments. Therefore, we designed 611 (47 × 13) synthetic *TRB* templates in total to simulate all the possible random rearrangement pairs of *TRBV* and *TRBJ* segments. Those templates contain the germline sequence of the whole *TRBV* segments, a simulated complementarity determining region 3 (CDR3) with a length of 43 bp, the germline sequence of framework region 4 (part of J segments), and part of C segments.

In order to evaluate the amplification bias of the multiplex PCR system, we pooled all the *TRB* templates at expected

equimolar levels and two repeated pools (pools 1 and 2) were generated. The actual frequency of each of the 611 *TRB* templates of the two pools before amplification is quantified by sequencing (**Figure S1**), and the actual usage frequency of each *TRBV* segments and *TRBJ* segments before amplification are shown in **Figure S2**. After amplification by multiplex PCR, we calculated the *TRBV* and *TRBJ* segments usage frequencies using the same methods and compared them with the frequencies before amplification to assess the amplification bias. In pool 1, when the primers were mixed at equimolar, there are severe amplification biases for both the *TRBV* (**Figure 1A**) and *TRBJ* segment (**Figure 1E**) before any experimental optimizations. We then adjusted the ratio of each primer in the primer mixture, and the results showed a less difference between the pre- and postamplified templates (**Figures 1B,C,F,G**). After several rounds of adjustments, the amplification biases for most of the primers were in the range of 0.5–2 for both *TRBV* segments (**Figure 1D**) and *TRBJ* segments (**Figure 1H**). The result of pool 2 showed similar results with pool 1 (**Figure S3**).

The Stability of the Optimized Reaction System

In order to verify the stability of the optimized reaction system, we replicated the amplification of the pooled *TRB* templates (pool 1) in three different batches using the final primer mix. The Pearson coefficient of *TRBV* segment usage was 0.92, 0.94, and 0.97, respectively, between any two of the three batches (**Figures 2A–C**). For *TRBJ* segments usage, the Pearson coefficient was 0.86, 0.96, and 0.94, respectively, between any two of the three batches (**Figures 2D–F**). These results showed that the reaction system is stable and is minimally affected by experimental batches or operations.

Evaluating the Robustness of the Optimized Reaction System by Gradient Mixture

In order to test if the reaction system is robust when the templates are pooled in different concentrations, we remixed the 611 *TRB* templates at different concentrations to produce two new templates pools, and the expected concentration of each *TRB* template is shown in **Tables S3, S4**. Then, the preamplified pools were sequenced directly to determine the actual percentage of each template (the pre-amplification in **Tables S3, S4**). Afterwards, we amplified the pools using the optimized system, and the percentages of each *TRBV* segment are shown as the post-amplification in **Tables S3, S4**. The biases representing as the differences between the post- and pre-amplification concentrations were carefully evaluated. Although the expected concentration difference between some TRBV segments was several orders of magnitude, the frequency of these TRBV segments was similar before and after amplification (**Figures 2G,H**), and the biases were between 0.5 and 2 (**Figure S4**).

The Synthetic *TRB* Templates Can Serve as Spike-in Material to Calibrate the Residual Amplification Bias

We mixed 20,000 copies of *TRB* templates (pool 1) into the natural DNA samples to test if the *TRB* repertoire of natural samples would affect the amplification biases of the synthetic

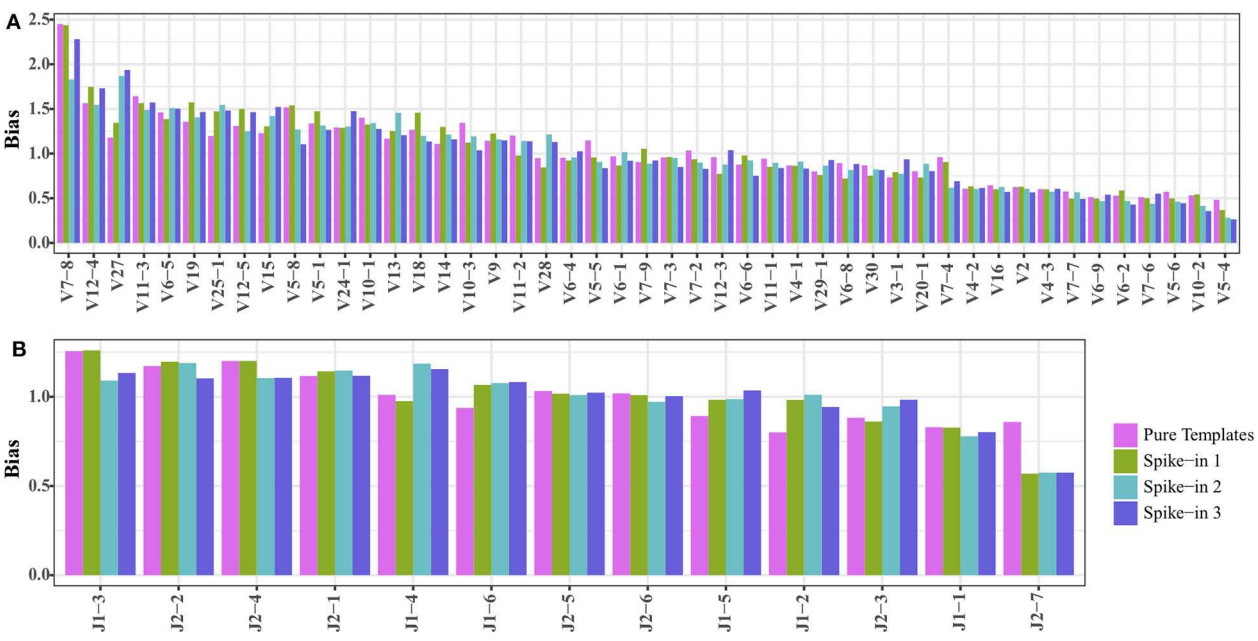

FIGURE 3 | Comparing the **(A)** *TRBV* and **(B)** *TRBJ* amplification bias of *TRB* templates as spike-in and pure templates. The spike-ins 1–3 indicated that 20,000 *TRB* templates were mixed with three natural DNA samples.

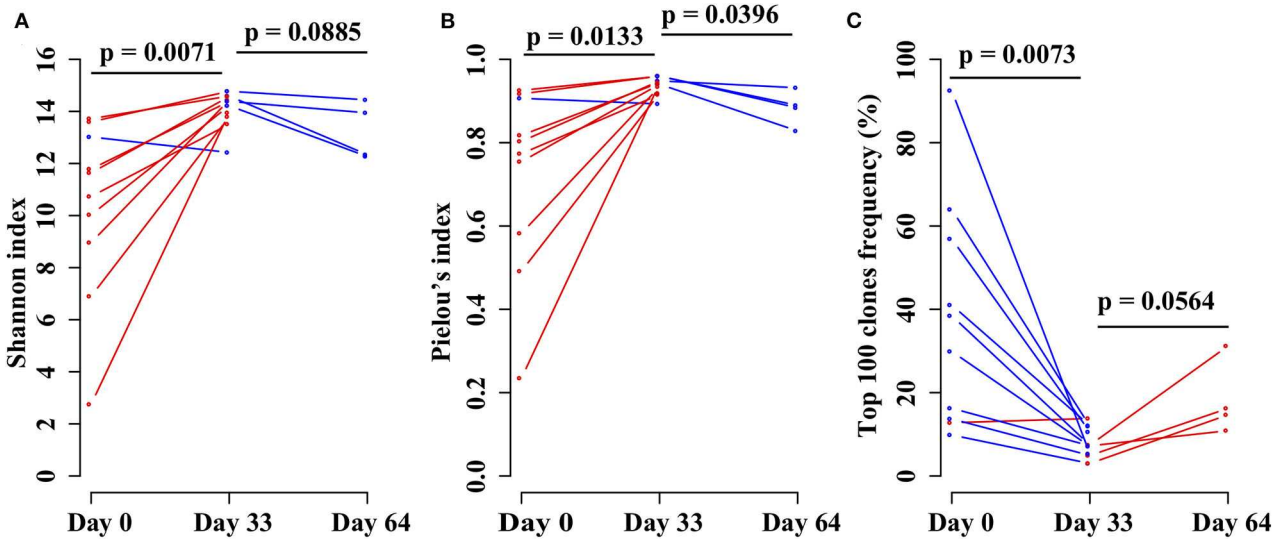

FIGURE 4 | Comparing the **(A)** Shannon index, **(B)** Pielou's index, and **(C)** percentage of top 100 maximal frequency clonotypes among three different time points of the same B-ALL patients. The three time points were before chemotherapy and 33 and 64 days after chemotherapy. *P*-value was calculated by two-sided paired *t*-test.

templates. The reads mapped to the synthetic *TRB* templates were split out after analysis using *IMonitor*, and the result showed that the amplification bias of the spike-in *TRB* templates was almost the same as that of the pure templates (**Figures 3A,B**). Therefore, the synthetic templates mixture can serve as a reference control to be spiked into natural samples, to evaluate or even calibrate the residual biases generated during the amplification.

MRD Detection in T-ALL

For two T-ALL patients, we detected MRD based on the *TRB* repertoire data and then compared it with the result detected by flow cytometry (FC). We calculated the percentage of T cells in total nucleated cells using the *TRB* repertoire data, and the result was similar to that detected by FC (**Table 1**). For MRD detection, when the MRD level is above 1%, the detection result of TCR-seq is comparable with that of FC; when MRD level is <0.5%, the FC gives a negative result. However, TCR-seq could detect the MRD with a higher sensitivity.

TABLE 1 | Comparing MRD detection results by TCR-seq and FC of T-ALL patients.

Patients	DAC	Cancer clonotype in TCR-seq data (%)	T cell percentage by FC (%)	T cell percentage by TCR-seq (%)	MRD by FC (%)	MRD by TCR-seq (%)
CYY	0	85.4	69	27.83	NA	NA
	33	24	12.18	14.36	3.8	3.45
	96	0.45	15.41	13.02	0	0.06
TDJ	8	63.96	ND	29.96	ND	19.16
	15	49.36	32.26	31.74	18.5	15.67
	33	2	15.16	15.30	0	0.31

The TRB CDR3 of cancer clonotype for patients CYY: TGCAGTGCCTCGCCTCCTCCTAGCGGGAGGGGGAATGAGCAGTTCTTC.
The TRB CDR3 of cancer clonotype for patients TDJ: TGCAGTGCTAGAGACCTGGGACAGGGGAGCAGGATTAGCTCCTACGAGCAGTACTTC.
DAC, day after beginning of chemotherapy; NA, not applicable; ND, not detection.

Dynamics of *TRB* Repertoire in Patients With B-ALL During Chemotherapy

In order to investigate the changes in the *TRB* repertoire in B-ALL patients during chemotherapy, the diversity, evenness, and clonality of the repertoire at different time points were compared. The diversity is represented by Shannon index, which reflects the richness of the repertoire and is a popular index used to measure the diversity of immune repertoire. The Shannon index increases from day 0 to 33 and then decreases from day 33 to 64 (**Figure 4A**). The evenness is assessed using the Pielou's index, and the same trend is identified as Shannon index (**Figure 4B**). The clonality is evaluated using the total frequency of top 100 *TRB* clonotypes, which can reflect the expansion of the clonotypes. In contrast to the diversity, the clonality decreases from day 0 to 33 and increases from day 33 to 64 (**Figure 4C**).

To further investigate the effect of chemotherapy on the dynamics of TCR clonotypes, we evaluated the frequencies and characteristics of the persistent clonotypes (overlapped clonotype between time points) from day 0 to 33 and from day 33 to 64 in the same patient. During induction treatment (days 0–33), most (95.94% on average) of the *TRB* clonotypes present on day 0 vanished on day 33, whereas a greater number (98.16% on average) of *TRB* clonotypes on day 33 were newly emerged (**Table S5**). For the persistent clonotypes from day 0 to 33, their frequencies in the repertoire were significantly higher than the private clonotypes (existing in only

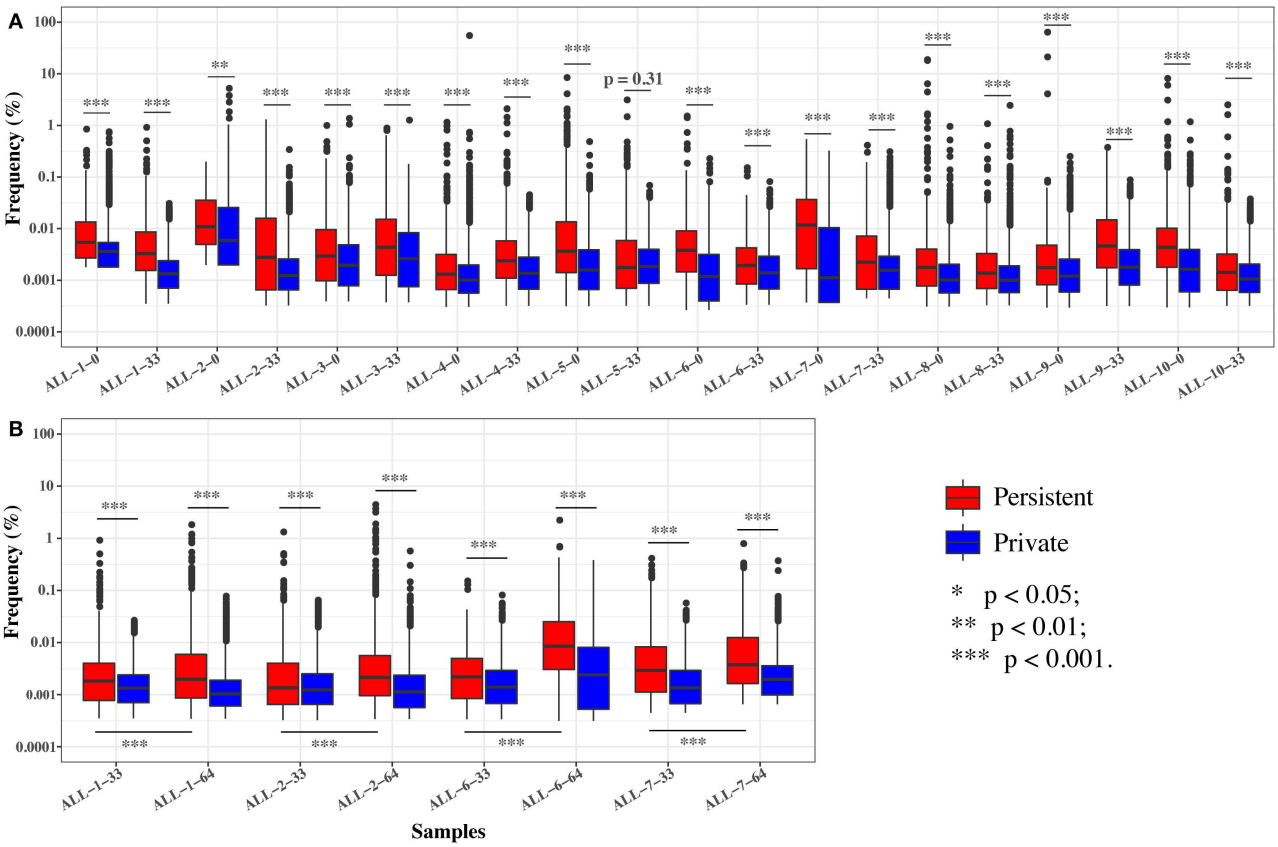

FIGURE 5 | The frequencies of the persistent and private clonotypes on two time points. **(A)** On days 0 and 33. **(B)** On days 33 and 64. ALL-1-0, ALL-1-33, and ALL-1-64 refer to frequencies on days 0, 33, and 64, respectively. Paired tests were performed on the frequencies of persistent clonotypes between day 33 and 64.

one time point) in all samples (**Figure 5A**). During consolidation chemotherapy treatment (days 33–64), the frequencies of the persistent clonotypes were also higher than the private ones in the repertoire and, to be noted, were significantly increased on day 64 compared to day 33 in all four patients (**Figure 5B**). To further explore the characteristics of the persistent clonotypes, we investigated the differences in PKPSC between the persistent and the private clonotypes. Notably, the PKPSC in persistent clonotypes was substantially higher than that in private clonotypes, indicating the enrichment of high-avidity T cells targeting known pathogens in the persistent clonotypes (**Figure 6**).

DISCUSSION

The immune system plays critical roles in human health, and a diverse TCR repertoire is necessary to warrant the potential of antigen recognition. In the future, if the antigen specificity of all the TCR CDR3s can be decoded, the T cell repertoire data will be of great help in disease diagnosis, treatment management, prognosis monitoring, and even risk evaluation. For future clinical applications, the most important thing is that we can accurately quantify the TCR repertoire. In order to evaluate the accuracy of the TCR-seq method, a TCR repertoire standard or reference with known compositions is particularly important (42); however, there are still no certified reference materials in this field. In this paper, we designed and synthesized 611 *TRB* templates, all of which have CDR3 that are out of frame to ensure that they do not exist in actual sample. We checked the *TRB* repertoire data of ∼6,000 human peripheral blood samples and did not find these templates appearing in any sample. Using these templates as reference materials, we optimized our *TRB* repertoire sequencing method and minimized the bias of multiplex PCR system.

The feasibility of immune repertoire sequencing technologies in MRD detection for blood cancer has been demonstrated in many studies (17, 40, 43, 44). Wood et al. (44) also reported that the patients with an MRD level of 0.01% by clonoSEQ, but negative by FC, had worse EFS compared with the patients who had a negative MRD by clonoSEQ (44). In fact, the clonoSEQ provided by Adaptive Biotechnologies has been cleared by the Food and Drug Administration (FDA) to detect the MRD for B-ALL and multiple myeloma. In this paper, we verified that TCR-seq MRD detection is more sensitive than FC for T-ALL patients.

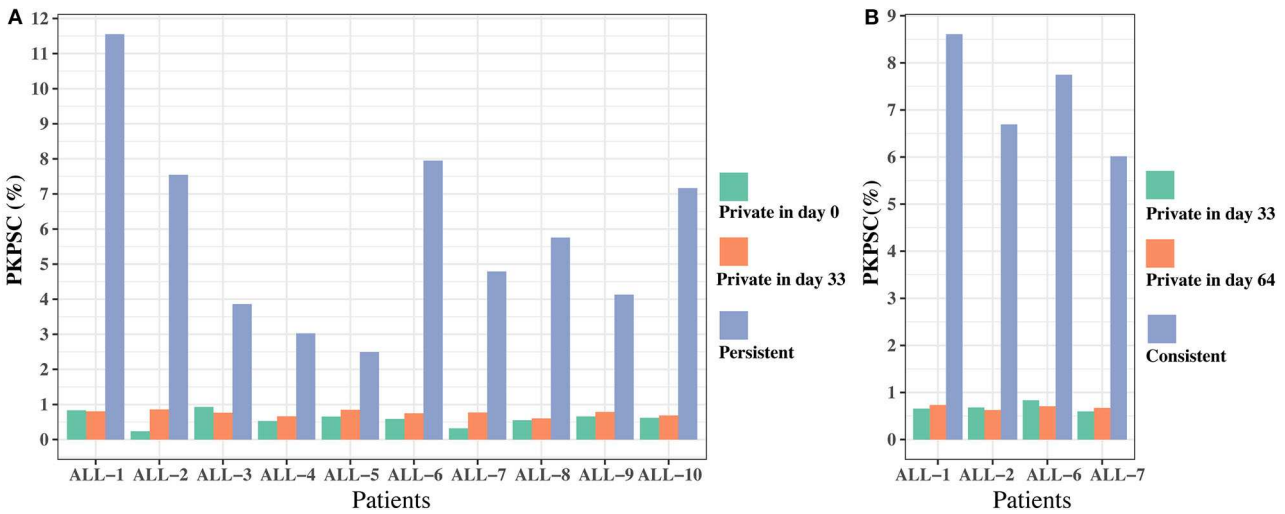

FIGURE 6 | The proportion of known pathogens specific *TRB* clonotypes (PKPSC) in persistent and private clonotypes on two time points. **(A)** On days 0 and 33. **(B)** On days 33 and 64.

Previous studies have demonstrated the immune reconstitution in leukemia patients after chemotherapy (45) and during chemotherapy (46) at the cellular subpopulation level. However, it is still unknown how chemotherapy affects the TCR repertoire of B-ALL patients. By analyzing the changes in *TRB* repertoire during chemotherapy, we showed that the diversity of *TRB* repertoire increases from day 0 to 33, which may relate with the recovery of the T cell number on day 33 at the end of the induction therapy (46). Consistently, the number of clonotypes on day 33 is 2–10 times that on day 0 from our data (**Table S5**). These may be rare preexisting naive T cells in the periphery or newly generated and recruited T cells, which is supported by T cell receptor excision circle (TREC) assay (46). We speculate that induction therapy could promote the recruitment and stimulation of a large number of pathogen-reactive naive T cells and diversify the repertoire. During the consolidation stage from day 33 to 64, these clonotypes experience further expansion, possibly driven by infection or external environment, which lower the repertoire diversity. Our data support that some relatively abundant TCR clonotypes, which are usually antigen experienced and target pathogens, are more likely to be selected under infection or other external environmental pressures and to be stably maintained during chemotherapy. In fact, a previous study showed that although chemotherapy reduced the naive T cell number, the memory T cells is least affected and preserved (47). However, it should be noted that it is difficult to analyze how much the repertoire is changed by infection, disease regression, or other prognosis factors, especially that we do not have these clinical data.

In summary, we have designed and synthesized some *TRB* reference templates to optimize the *TRB* multiplex reaction system. We then used this experimental system to detect the MRD in T-ALL patients. We also used it to investigate the dynamic change of TRB repertoire during the chemotherapy of B-ALL and found that the pathogen-specific memory T cells are selected and expanded during chemotherapy. Chemotherapy could suppress the immune system of cancer patients and put them at risk of infection; therefore, the recovery of the immune system during and after chemotherapy is very critical for cancer patients to resist infection and other immune related disease. Considering the importance of antigen recognition potential of immune system, in the future, combined with other omics technologies, it is possible that precise immune repertoire data could provide great help in evaluating an individual's immunity.

DATA AVAILABILITY STATEMENT

The data reported in this study are available in the CNGB Nucleotide Sequence Archive (CNSA: https://db.cngb.org/cnsa; accession number CNP0000882).

ETHICS STATEMENT

The studies involving human participants were reviewed and approved by BGI-IRB. Written informed consent to participate in this study was provided by the participants' legal guardian/next of kin.

AUTHOR CONTRIBUTIONS

SL, XiaW, HM, XY, and FW collected the samples and clinical information. JW, LLi, XieW, and MF performed the experiments. XuL, WZ, LLu, YZ, and ZW performed the data analysis and visualization. JW, CL, and XiL analyzed and interpreted the data. JW wrote the manuscript. CL and XiL supervised the

study. All authors contributed to the article and approved the submitted version.

FUNDING

This project has been funded by the National Natural Science Foundation of China under No. 31800765, the Science, Technology and Innovation Commission of Shenzhen Municipality under No. JCYJ20170817145404433, and Sanming Project of Medicine in Shenzhen (SZSM201512033).

SUPPLEMENTARY MATERIAL

The Supplementary Material for this article can be found online at: https://www.frontiersin.org/articles/10.3389/fimmu.2020.01631/full#supplementary-material

REFERENCES

1. Six A, Mariotti-Ferrandiz ME, Chaara W, Magadan S, Pham HP, Lefranc MP, et al. The past, present, and future of immune repertoire biology - the rise of next-generation repertoire analysis. *Front Immunol.* (2013) 4:413. doi: 10.3389/fimmu.2013.00413
2. Liu X, Wu J. History, applications, and challenges of immune repertoire research. *Cell Biol Toxicol.* (2018) 34:441–57. doi: 10.1007/s10565-018-9426-0
3. Woodsworth DJ, Castellarin M, Holt RA. Sequence analysis of T-cell repertoires in health and disease. *Genome Med.* (2013) 5:98. doi: 10.1186/gm502
4. Robins HS, Campregher PV, Srivastava SK, Wacher A, Turtle CJ, Kahsai O, et al. Comprehensive assessment of T-cell receptor beta-chain diversity in alphabeta T cells. *Blood.* (2009) 114:4099–107. doi: 10.1182/blood-2009-04-217604
5. Freeman JD, Warren RL, Webb JR, Nelson BH, Holt RA. Profiling the T-cell receptor beta-chain repertoire by massively parallel sequencing. *Genome Res.* (2009) 19:1817–24. doi: 10.1101/gr.092924.109
6. Wang C, Sanders CM, Yang Q, Schroeder HW, Wang E, Babrzadeh F, et al. High throughput sequencing reveals a complex pattern of dynamic interrelationships among human T cell subsets. *Proc Natl Acad Sci USA.* (2010) 107:1518–2. doi: 10.1073/pnas.0913939107
7. Robins H. Immunosequencing: applications of immune repertoire deep sequencing. *Curr Opin Immunol.* (2013) 25:646–52. doi: 10.1016/j.coi.2013.09.017
8. Hou D, Chen C, Seely EJ, Chen S, Song Y. High-throughput sequencing-based immune repertoire study during infectious disease. *Front Immunol.* (2016) 7:336. doi: 10.3389/fimmu.2016.00336
9. Liu X, Zhang W, Zeng X, Zhang R, Du Y, Hong X, et al. Systematic comparative evaluation of methods for investigating the TCRβ repertoire. *PLoS ONE.* (2016) 11:e0152464. doi: 10.1371/journal.pone.0152464
10. Becattini S, Latorre D, Mele F, Foglierini M, De Gregorio C, Cassotta A, et al. Functional heterogeneity of human memory CD4+ T cell clones primed by pathogens or vaccines. *Science.* (2015) 107:1518–23. doi: 10.1126/science.1260668
11. Shifrut E, Baruch K, Gal H, Ndifon W, Deczkowska A, Schwartz M, et al. CD4+ T cell-receptor repertoire diversity is compromised in the spleen but not in the bone marrow of aged mice due to private and sporadic clonal expansions. *Front Immunol.* (2013) 4:379. doi: 10.3389/fimmu.2013.00379
12. Wang T, Wang C, Wu J, He C, Zhang W, Liu J, et al. The different t-cell receptor repertoires in breast cancer tumors, draining lymph nodes, and adjacent tissues. *Cancer Immunol Res.* (2017) 5:148–56. doi: 10.1158/2326-6066.CIR-16-0107
13. Gao K, Chen L, Zhang Y, Zhao Y, Wan Z, Wu J, et al. Germline-encoded TCR-MHC contacts promote TCR V gene bias in umbilical cord blood T cell repertoire. *Front Immunol.* (2019) 10:2064. doi: 10.1101/621821
14. Gomez-Tourino I, Kamra Y, Baptista R, Lorenc A, Peakman M. T cell receptor β-chains display abnormal shortening and repertoire sharing in type 1 diabetes. *Nat Commun.* (2017) 8:1792. doi: 10.1038/s41467-017-01925-2
15. Liu X, Zhang W, Zhao M, Fu L, Liu L, Wu J, et al. T cell receptor β repertoires as novel diagnostic markers for systemic lupus erythematosus and rheumatoid arthritis. *Ann Rheum Dis.* (2019) 78:1070–8. doi: 10.1136/annrheumdis-2019-215442
16. Huang C, Li X, Wu J, Zhang W, Sun S, Lin L, et al. The landscape and diagnostic potential of T and B cell repertoire in immunoglobulin a nephropathy. *J Autoimmun.* (2019) 97:100–7. doi: 10.1016/j.jaut.2018.10.018
17. Wu D, Sherwood A, Fromm JR, Winter SS, Dunsmore KP, Loh ML, et al. High-throughput sequencing detects minimal residual disease in acute T lymphoblastic leukemia. *Sci Transl Med.* (2012) 4:134ra63. doi: 10.1016/j.clml.2013.07.066
18. Wang L, Zhang W, Lin L, Li X, Saksena NK, Wu J, et al. A comprehensive analysis of the t and b lymphocytes repertoire shaped by hiv vaccines. *Front Immunol.* (2018) 9:2194. doi: 10.3389/fimmu.2018.02194
19. Cha E, Klinger M, Hou Y, Cummings C, Ribas A, Faham M, et al. Improved survival with T cell clonotype stability after anti-CTLA-4 treatment in cancer patients. *Sci Transl Med.* (2014) 6:238ra70. doi: 10.1126/scitranslmed.3008211
20. Hopkins AC, Yarchoan M, Durham JN, Yusko EC, Rytlewski JA, Robins HS, et al. T cell receptor repertoire features associated with survival in immunotherapy-treated pancreatic ductal adenocarcinoma. *JCI Insight.* (2018) 3:e122092. doi: 10.1172/jci.insight.122092
21. Hogan SA, Courtier A, Cheng PF, Jaberg-Bentele NF, Goldinger SM, Manuel M, et al. Peripheral blood tcr repertoire profiling may facilitate patient stratification for immunotherapy against melanoma. *Cancer Immunol Res.* (2018) 7:canimm.0136.2018. doi: 10.1158/2326-6066.CIR-18-0136
22. Rosati E, Dowds CM, Liaskou E, Henriksen EKK, Karlsen TH, Franke A. Overview of methodologies for T-cell receptor repertoire analysis. *BMC Biotechnol.* (2017) 17:61. doi: 10.1186/s12896-017-0379-9
23. Qi Q, Liu Y, Cheng Y, Glanville J, Zhang D, Lee JY, et al. Diversity and clonal selection in the human T-cell repertoire. *Proc Natl Acad Sci USA.* (2014) 111:13139–44. doi: 10.1073/pnas.1409155111
24. Khan TA, Friedensohn S, De Vries ARG, Straszewski J, Ruscheweyh HJ, Reddy ST. Accurate and predictive antibody repertoire profiling by molecular amplification fingerprinting. *Sci Adv.* (2016) 2:e1501371. doi: 10.1126/sciadv.1501371
25. Carlson CS, Emerson RO, Sherwood AM, Desmarais C, Chung MW, Parsons JM, et al. Using synthetic templates to design an unbiased multiplex PCR assay. *Nat Commun.* (2013) 4:2680. doi: 10.1038/ncomms3680
26. Barnes TA, Amir E. HYPE or hope: the prognostic value of infiltrating immune cells in cancer. *Br J Cancer.* (2017) 117:451–60. doi: 10.1038/bjc.2017.220
27. Gentles AJ, Newman AM, Liu CL, Bratman S V., Feng W, Kim D, et al. The prognostic landscape of genes and infiltrating immune cells across human cancers. *Nat Med.* (2015) 21:938–94. doi: 10.1038/nm.3909
28. Li B, Severson E, Pignon JC, Zhao H, Li T, Novak J, et al. Comprehensive analyses of tumor immunity: Implications for cancer immunotherapy. *Genome Biol.* (2016) 17:174. doi: 10.1186/s13059-016-1028-7
29. Gooden MJM, De Bock GH, Leffers N, Daemen T, Nijman HW. The prognostic influence of tumour-infiltrating lymphocytes in cancer: a systematic review with meta-analysis. *Br J Cancer.* (2011) 105:93–103. doi: 10.1038/bjc.2011.189
30. Ansell SM, Stenson M, Habermann TM, Jelinek DF, Witzig TE. CD4+ T-cell immune response to large B-cell non-Hodgkin's lymphoma predicts patient outcome. *J Clin Oncol.* (2001) 19:720–6. doi: 10.1200/JCO.2001.19.3.720
31. Keane C, Gill D, Vari F, Cross D, Griffiths L, Gandhi M. CD4+ Tumor infiltrating lymphocytes are prognostic and independent of R-IPI in patients with DLBCL receiving R-CHOP chemo-immunotherapy. *Am J Hematol.* (2013) 88:273–6. doi: 10.1002/ajh.23398

32. Keane C, Gould C, Jones K, Hamm D, Talaulikar D, Ellis J, et al. The T-cell receptor repertoire influences the tumor microenvironment and is associated with survival in aggressive B-cell lymphoma. *Clin Cancer Res*. (2017) 23:1820–8. doi: 10.1158/1078-0432.CCR-16-1576
33. Ramsay AG, Clear AJ, Fatah R, Gribben JG. Multiple inhibitory ligands induce impaired T-cell immunologic synapse function in chronic lymphocytic leukemia that can be blocked with lenalidomide: establishing a reversible immune evasion mechanism in human cancer. *Blood*. (2012) 120:1412–21. doi: 10.1182/blood-2012-02-411678
34. Riches JC, Gribben JG. Understanding the immunodeficiency in chronic lymphocytic leukemia. potential clinical implications. *Hematol Oncol Clin North Am*. (2013) 27:207–35. doi: 10.1016/j.hoc.2013.01.003
35. Riches JC, Davies JK, McClanahan F, Fatah R, Iqbal S, Agrawal S, et al. T cells from CLLpatients exhibit features of T-cell exhaustion but retain capacity for cytokine production. *Blood*. (2013) 121:1612–21. doi: 10.1182/blood-2012-09-457531
36. Rezvany MR, Jeddi-Tehrani M, Wigzell H, Österborg A, Mellstedt H. Leukemia-associated monoclonal and oligoclonal TCR-BV use in patients with B-cell chronic lymphocytic leukemia. *Blood*. (2003) 101:1063–70. doi: 10.1182/blood-2002-03-0746
37. Vardi A, Agathangelidis A, Stalika E, Karypidou M, Siorenta A, Anagnostopoulos A, et al. Antigen selection shapes the T-cell repertoire in chronic lymphocytic leukemia. *Clin Cancer Res*. (2016) 22:167–74. doi: 10.1158/1078-0432.CCR-14-3017
38. Yin Q, Sivina M, Robins H, Yusko E, Vignali M, O'Brien S, et al. Ibrutinib therapy increases t cell repertoire diversity in patients with chronic lymphocytic leukemia. *J Immunol. (*2017) 198:1740–7. doi: 10.4049/jimmunol.1601190
39. Zhang W, Du Y, Su Z, Wang C, Zeng X, Zhang R, et al. IMonitor: a robust pipeline for TCR and BCR repertoire analysis. *Genetics*. (2015) 201:459–72. doi: 10.1534/genetics.115.176735
40. Wu J, Jia S, Wang C, Zhang W, Liu S, Zeng X, et al. Minimal residual disease detection and evolved IGH clones analysis in acute b lymphoblastic leukemia using IGH deep sequencing. *Front Immunol*. (2016) 7:403. doi: 10.3389/fimmu.2016.00403
41. Cao K, Wu J, Li X, Xie H, Tang C, Zhao X, et al. T-cell receptor repertoire data provides new evidence for hygiene hypothesis of allergic diseases. *Allergy Eur J Allergy Clin Immunol*. (2019) 75:681–3. doi: 10.1111/all.14014
42. Rubelt F, Busse CE, Bukhari SAC, Bürckert JP, Mariotti-Ferrandiz E, Cowell LG, et al. Adaptive immune receptor repertoire community recommendations for sharing immune-repertoire sequencing data. *Nat Immunol*. (2017) 18:1274–8. doi: 10.1038/ni.3873
43. Wu D, Emerson RO, Sherwood A, Loh ML, Angiolillo A, Howie B, et al. Detection of minimal residual disease in B lymphoblastic leukemia by high-throughput sequencing of IGH. *Clin Cancer Res*. (2014) 20:4540–8. doi: 10.1158/1078-0432.CCR-13-3231
44. Wood B, Wu D, Crossley B, Dai Y, Williamson D, Gawad C, et al. Measurable residual disease detection by high-throughput sequencing improves risk stratification for pediatric B-ALL. *Blood*. (2018) 131:1350–9. doi: 10.1182/blood-2017-09-806521
45. Van Tilburg CM, Van Gent R, Bierings MB, Otto SA, Sanders EAM, Nibbelke EE, et al. Immune reconstitution in children following chemotherapy for haematological malignancies: a long-term follow-up. *Br J Haematol*. (2011) 152:201–10. doi: 10.1111/j.1365-2141.2010.08478.x
46. Eyrich M, Wiegering V, Lim A, Schrauder A, Winkler B, Schlegel PG. Immune function in children under chemotherapy for standard risk acute lymphoblastic leukaemia - a prospective study of 20 paediatric patients. *Br J Haematol*. (2009) 147:360–70. doi: 10.1111/j.1365-2141.2009.07862.x
47. Haining WN, Neuberg DS, Keczkemethy HL, Evans JW, Rivoli S, Gelman R, et al. Antigen-specific T-cell memory is preserved in children treated for acute lymphoblastic leukemia. *Blood*. (2005) 106:1749–54. doi: 10.1182/blood-2005-03-1082

Conflict of Interest: JW, XieW, LLi, XuL, WZ, LLu, ZW, MF, YZ, and XiL were employed by BGI-Shenzhen.

The remaining authors declare that the research was conducted in the absence of any commercial or financial relationships that could be construed as a potential conflict of interest.

frontiers in Immunology

ORIGINAL RESEARCH
published: 18 August 2020
doi: 10.3389/fimmu.2020.01855

Multifactorial Design of a Supramolecular Peptide Anti-IL-17 Vaccine Toward the Treatment of Psoriasis

*Lucas S. Shores[1], Sean H. Kelly[1], Kelly M. Hainline[1], Jutamas Suwanpradid[2], Amanda S. MacLeod[2,3,4] and Joel H. Collier[1,3]**

[1] Department of Biomedical Engineering, Duke University, Durham, NC, United States, [2] Department of Dermatology, Duke University School of Medicine, Durham, NC, United States, [3] Department of Immunology, Duke University School of Medicine, Durham, NC, United States, [4] Department of Molecular Genetics and Microbiology, Duke University School of Medicine, Durham, NC, United States

Current treatments for chronic immune-mediated diseases such as psoriasis, rheumatoid arthritis, or Crohn's disease commonly rely on cytokine neutralization using monoclonal antibodies; however, such approaches have drawbacks. Frequent repeated dosing can lead to the formation of anti-drug antibodies and patient compliance issues, and it is difficult to identify a single antibody that is broadly efficacious across diverse patient populations. As an alternative to monoclonal antibody therapy, anti-cytokine immunization is a potential means for long-term therapeutic control of chronic inflammatory diseases. Here we report a supramolecular peptide-based approach for raising antibodies against IL-17 and demonstrate its efficacy in a murine model of psoriasis. B-cell epitopes from IL-17 were co-assembled with the universal T-cell epitope PADRE using the Q11 self-assembling peptide nanofiber system. These materials, with or without adjuvants, raised antibody responses against IL-17. Exploiting the modularity of the system, multifactorial experimental designs were used to select formulations maximizing titer and avidity. In a mouse model of psoriasis induced by imiquimod, unadjuvanted nanofibers had therapeutic efficacy, which could be enhanced with alum adjuvant but reversed with CpG adjuvant. Measurements of antibody subclass induced by adjuvanted and unadjuvanted formulations revealed strong correlations between therapeutic efficacy and titers of IgG1 (improved efficacy) or IgG2b (worsened efficacy). These findings have important implications for the development of anti-cytokine active immunotherapies and suggest that immune phenotype is an important metric for eliciting therapeutic anti-cytokine antibody responses.

Keywords: self-assembly, anti-cytokine, active immunotherapy, inflammatory diseases, immunoengineering

OPEN ACCESS

Edited by:
Evan Alexander Scott, Northwestern University, United States

Reviewed by:
Mustafa O. Guler, University of Chicago, United States
David Wilson, The Johns Hopkins Hospital, Johns Hopkins Medicine, United States

***Correspondence:**
Joel H. Collier
joel.collier@duke.edu

Specialty section:
This article was submitted to Immunological Tolerance and Regulation, a section of the journal Frontiers in Immunology

Received: *04 April 2020*
Accepted: *10 July 2020*
Published: *18 August 2020*

Citation:
Shores LS, Kelly SH, Hainline KM, Suwanpradid J, MacLeod AS and Collier JH (2020) Multifactorial Design of a Supramolecular Peptide Anti-IL-17 Vaccine Toward the Treatment of Psoriasis. Front. Immunol. 11:1855. doi: 10.3389/fimmu.2020.01855

INTRODUCTION

Anti-cytokine blockade with monoclonal antibodies (mAbs) has revolutionized the treatment of immune-mediated diseases by providing an efficacious treatment modality for multiple inflammatory conditions such as multiple sclerosis, rheumatoid arthritis, and plaque psoriasis (1). Despite incompletely understood etiologies (2), many chronic inflammatory conditions are fueled

by a limited set of cytokines which act in concert with immunological and non-immunological cells to induce symptoms of disease (3). In plaque psoriasis, for example, γδ T cells produce the cytokine IL-17, inducing both keratinocyte hyperplasia and the recruitment of neutrophils (4). Inhibition of IL-17 with the monoclonal antibody ixekizumab blocks this recruitment and has been shown to lead to the remission of symptoms in as many as 90% of plaque psoriasis patients receiving injections every 4 weeks. However, the effectiveness of mAbs can both be undercut by secondary resistance due to anti-drug antibodies and difficulties developing mAb subclasses that are most therapeutically effective. To counter these concerns, research has been undertaken to evaluate a new class of cytokine blockade therapies involving immunization against these inflammatory cytokines (5, 6). In some instances, biomaterial platforms are being investigated for this purpose. These therapies could provide an alternative to mAbs and could leverage the ability of biomaterials to induce tailored immune phenotypes in the context of long-term cytokine blockade therapy.

Monoclonal antibodies are manufactured with a uniform specificity (target and affinity for that target) and subclass (function) that dictates the phenotype of the response. While specificity has often been able to be optimized for neutralization, antibody subclass is generally selected for mAb half-life rather than optimal functionality for a specific disease (7, 8). Further, to maintain a therapeutic concentration of mAbs, patients must receive regularly scheduled injections, commonly for the duration of their lives. For example, the dosing of infliximab (anti-TNF) usually occurs once every 8 weeks intravenously, and adalimumab (anti-TNF) and ixekizumab (anti-IL17) are administered once every 2 weeks subcutaneously with adjustments made based on disease severity (9, 10). Anti-drug antibodies that develop against these frequently administered mAbs can lead to secondary resistance to therapy by rapidly clearing mAbs from circulation and can increase risk of adverse effects such as hypersensitivity reactions (11–13). In the case of bococizumab, a mAb designed to reduce LDL-cholesterol by targeting an endogenous kinase, the first long-term study in humans revealed anti-drug antibodies in more than 48% of patients, resulting in reduced outcomes and the cancellation of the drug's development (14).

As an alternative approach that could circumvent these challenges, anti-cytokine immunization has received attention (15). While both anti-cytokine immunization and mAb therapies can target the same inflammatory molecules, anti-cytokine immunization leads to the production of long-lived endogenous polyclonal antibodies and potentially allows for the tailoring of the immune response to elicit antibody subclasses that are most therapeutically effective. Although both approaches target a single epitope of the target cytokine, induced polyclonal antibody responses could have their affinity improved by repeated booster immunizations (16), can avoid any anti-antibody responses from foreign epitopes that vary by population (17), and provides a significantly longer half-life of serum antibody concentration (18, 19). Anti-cytokine immunizations that have been previously investigated have included endogenous cytokines conjugated to protein carriers such as keyhole limpet hemocyanin (KLH) (20) or virus-like particles (VLP) (21–23). In both cases, the carriers supply exogenous T cell epitopes to enable B cells to produce anti-cytokine antibodies in a T-dependent fashion (22, 24). Anti-IL-17A immunizations have previously been shown to induce antibodies when whole IL-17A was conjugated to ovalbumin protein (25), when conjugated to VLPs (26, 27), or when an IL-17 peptide epitope was conjugated to VLPs (28). A few of these approaches have reached clinical trials for various cytokines, but with limited success in terms of therapeutic efficacy (29–32).

While carrier proteins have offered one route for anti-cytokine immunotherapies, materials research has begun to redefine vaccine development by emphasizing how physical parameters such as size (33, 34), shape (35, 36), charge (37), and other materials properties can alter the immune response. Recently, our group has pursued anti-cytokine immunization via a supramolecular nanofiber platform based on the self-assembling peptide Q11 (Ac-QQKFQFQFEQQ-NH_2) (38). In contrast to carrier proteins, the use of supramolecular nanofibers facilitates the straightforward assembly of different immunological epitopes together in finely controlled ratios (37, 39–42). This modularity enables the application of multifactorial Design of Experiments (DoE) methodologies to investigate and optimize various co-assembled epitopes (43). In this context, previous work has shown that changing the T cell epitope content can alter both the T cell and B cell response of an anti-cytokine immunization (42). In an active immunotherapy raising antibodies against TNF, it was shown that prior immunization with Q11-based nanofibers bearing TNF B-cell epitopes and exogenous T-cell epitopes could partially protect mice in a model of acute inflammation (38).

Here we have expanded upon these previous observations to design peptide nanofibers raising antibodies against IL-17, a central cytokine in the pathophysiology of multiple diseases, particularly psoriasis (44–46). We investigated two anti-IL-17 peptide epitopes and demonstrated their ability to assemble into nanofibers and induce antibodies in an adjuvant-free context. Using a DoE approach, we elucidated that the B and T cell epitope density, as well as the ratio between these two components, strongly influenced the strength and quality of the anti-IL-17 antibody response. Finally, we evaluated optimized formulations in a murine model of psoriasis, finding that therapeutic efficacy is strongly correlated with the subclass of IgG antibodies raised.

METHODS

Epitope Selection

B-cell epitopes for investigation were selected using the Kolaskar Tongaonkar Antigenicity Test, which uses known antigenic sequences and amino acid neighbors to produce predictions with reported 75% accuracy (47). Scores from the murine sequence of IL-17 were then compared to known crystal structures from its human homolog. One previously reported epitope (28) also returned high scores using this tool and was evaluated for antigenicity within the Q11 platform. Two epitopes identified for this study were named IL17.1 and IL17.2 to avoid confusion with alternative IL17 isoforms (IL17A and IL17B). All peptide sequences studied are listed in **Supplementary Table 1**.

Solid Phase Peptide Synthesis

Peptides were synthesized as previously reported (48). Briefly, peptides were synthesized using microwave-assisted solid phase peptide synthesis on a Liberty Blue Peptide Synthesizer (CEM) with standard FMOC chemistry. Peptides were cleaved from the resin with trifluoroacetic acid and precipitated in diethyl ether prior to purification using reverse phase HPLC. Peptide identity was confirmed using MALDI mass spectrometry, and purity was assessed to be >80% by analytical HPLC.

Preparation of Immunization Formulations

Nanofibers were formed by mixing dry purified peptide for 10 min prior to adding sterile water to form an 8 mM peptide solution. This solution was incubated overnight at 4°C prior to adding 10x PBS (Corning 46-013-CM) and additional sterile water to form a 2 mM peptide solution in 1x PBS, which was incubated at room temperature for 3 h before being used for further studies. For immunizations containing CpG (ODN 1826, IAX-200-002-3001 Innaxon), CpG was added to peptide solutions at a concentration of 100 μg/mL, after overnight fibrillization (at the same time as the addition of 10x PBS), while for immunizations containing Alum (Invivogen Alhydrogel 2%), the adjuvant was mixed at a 1:1 concentration with previously formed nanofibers for 10 min.

Transmission Electron Microscopy

Peptide nanostructure was evaluated using Transmission Electron Microscopy (TEM) on an FEI Tecnai G^2 Twin. Peptides were fibrillized for 3 h, diluted to 0.2 mM in PBS as previously reported (37), applied to formvar copper grids (Electron Microscopy Sciences, EMS400-Cu), and negative-stained with uranyl acetate 1% (w/v) in distilled water (Electron Microscopy Sciences).

Thioflavin T Binding Assay

As a measure of fibrillization, the Thioflavin T (ThT) assay was utilized. For these measurements, 20 μL of 2 mM peptide solutions were mixed with 180 μL of a 50 μM solution of ThT (Alfa Aesar, J61043) in 1X PBS in a black 96-well plate and read using a Molecular Devices Spectramax M2 spectrophotometer (excitation at 440 nm, emission at 488 nm).

Immunizations

Female, wild-type C57BL/6 mice (Envigo) 8–12 weeks of age at the start of experimental protocols were used for all animal studies. Animal experiments were approved by the Institutional Animal Care and Use Committee of Duke University in compliance with the NIH Guide for the Care and Use of Laboratory Animals. Mice were anesthetized with isoflurane prior to subcutaneous immunization. For prime and boost immunizations, mice were injected subcutaneously with 50 μl of 2 mM peptide nanofiber solutions in PBS on their left and right shoulder. In all studies, mice were boosted with the same dose at week 2.5 and 5 after primary immunizations, with or without adjuvants indicated. For CpG, 10 μg per mouse per immunization was administered according to manufacturer guidelines. For alum, 500 μg per mouse per immunization of alum was administered according to manufacturer guidelines. Blood was collected for analysis at weeks 2, 4, and 7 unless otherwise indicated.

Enzyme-Linked Immunosorbent Assay (ELISA)

ELISA was conducted as previously described (38, 48). For total IgG ELISA, plates were coated with streptavidin overnight, and then either coated with biotinylated peptide solution (20 μg /ml) or PBS. A reported titer of 1 indicates no detectable signal above background. For measuring antibody responses against whole protein, murine IL-17A (R&D Systems #421-ML-025) was coated at 5 μg/mL overnight in sterile 4 mM HCl containing 0.1% w/v bovine serum albumin. Background wells were coated with the same solution lacking IL-17A. Plates were then blocked with a 2% (w/v) BSA solution. Serum was diluted and coated onto plates for 2 h prior to incubating with an antibody targeting the conserved Igκ fragment (Jackson ImmunoResearch #115-035-008). For the antibody avidity rank assay, 50 μl of 5M urea (Sigma) was added to half the wells and incubated for 5 min before washing and adding detection antibody. For antibody isotyping, isotype specific-antibodies (Southern Biotech #1010-05) were used in place of the total IgG detection antibody while all other steps were similar.

Enzyme-Linked Immune Absorbent Spot (ELISpot) Assay

T cell responses to immunizing peptides were measured by ELISpot assay. Mice were sacrificed 7 days after a booster vaccination to measure T cell responses (58 weeks after the initial immunization). Splenocytes purified from mice were plated at a density of 250,000 spots per well of a 96-well ELISpot plate (Millipore, MAIPSWU10) and stimulated with 5 μM soluble IL17.1 or PADRE peptide, left untreated, or stimulated with Concanavalin A (Con A) (Sigma, C5275) which non-specifically activates T cells. Biotinylated capture-detection antibody pairs for either IL-4 (BD Cat. 551878) or IFNγ (BD Cat. 551881) were used according to manufacturer's guidelines in conjunction with streptavidin-alkaline phosphatase (Mabtech, 3310-0) and Sigmafast BCIP/NBT (Sigma, B5655). After development, plates were evaluated for spot count by Zellnet Consulting using a Zeiss KS ELISpot reader.

Imiquimod-Induced Psoriasis

To induce psoriasis, hair was removed from the backs of mice by plucking, and 0.125 g 5% imiquimod cream [6.25 mg imiquimod (Perrigo)] was applied topically daily for 5 consecutive days. Twenty four hours after the last application, mice were sacrificed and skin was harvested for histology. Mice were immunized prophylactically at 8 weeks of age, with a boost 2.5 weeks afterwards, and imiquimod treatment was initiated 5 weeks after the primary immunization. Only one boost was administered to avoid the complication of barbering, a well-documented, age-dependent phenomenon in C57BL/6 mice (49) that interfered with the onset of IMQ-induced psoriasis in our hands. Anti IL-17 antibody was used as a control (Bio-X-Cell clone 17F3, #BE0173, 250 μg administered IP at 3 days before and again on

the same day as the initial imiquimod application). Body weight and spleen weight were recorded at the endpoint (immediately after euthanization).

Histology

Skin was harvested from the backs of mice and submerged in OCT solution prior to freezing with dry ice. Sections 18 μm thick were then collected (Thermo Scientific CryoStar NX50), stained with Toluidine Blue O (Harleco 364-12), and imaged with brightfield microscopy (EVOS FL Auto). Measurements of epidermal thickness in interfollicular regions were taken with ImageJ software at 4 locations *per section* from two different sections by an individual blinded to the experimental conditions. Follicles were not included in these measurements.

Statistical Analysis

For statistical analyses using multifactorial designs, JMP14 Pro software was used to determine statistical significance and power calculations. In multifactorial experiments, tests for main effect and interaction parameter were carried out using generalized linear regression models. For traditional one-factor at a time analyses involving one-way ANOVA, multiple comparisons, and individual *t*-tests, Graphpad prism software was used. Specific analyses are described in the figure legends.

RESULTS

Epitope Selection and Nanofiber Characterization

In order to develop an active immunotherapy capable of raising antibodies against a focused B cell epitope within IL-17A, we utilized Kolaskar Tongaonkar antigenicity predictions (47) and surveyed previously published B-cell epitopes (**Figure S1**). Two potential B cell epitopes were selected: IL17.1 was selected from a previous report employing virus-like particles (28) and IL17.2 was selected from antigenicity prediction and its apparent availability on the protein surface (**Figure 1A**). These epitopes were then synthesized in tandem with the Q11 self-assembling sequence.

Both IL17.1-Q11 and IL17.2-Q11 were found to assemble into nanofibers by TEM alone (**Figures 1B,D**) or when co-assembled with Q11 and PADRE-Q11 in a 1.0:0.05:0.95 molar ratio (**Figures 1C,E**). Interestingly, IL17.1-Q11 formed fibers that appeared more tape-like than Q11 nanofibers (**Figure 1A**), while IL17.2-Q11 formed assemblies more similar to Q11. Despite minor morphological dissimilarities, ThT binding indicated that both IL17.1-Q11 and IL17.2-Q11 formed structures with significant β-sheet character and maintained this character when co-assembled with Q11 (**Figure 1G**, **Figure S2**). The IL17.1 peptide lacking the Q11 assembly domain did not exhibit ThT fluorescence significantly above that of PBS (**Figure S2**), whereas, the soluble IL17.2 peptide did exhibit ThT fluorescence, potentially indicating that it had some capacity to assemble even without conjugation to Q11, yet this aspect was not explored further. In sum, owing to their capacity to form nanofibers both alone and when mixed with Q11 and PADRE-Q11, both IL17.1-Q11 and IL17.2-Q11 were carried forward into evaluations of immunogenicity.

IL-17 B-Cell Epitope Evaluation

Self-assembled formulations were subsequently tested for immunogenicity in mice. Mice were immunized with nanofibers containing IL17.1-Q11 or IL17.2-Q11 co-assembled with Q11 and PADRE-Q11, to provide nanofibers presenting both B cell epitopes from IL-17 and the universal T-helper epitope PADRE (50, 51). Mice were boosted at weeks 2.5 and 5, and antibody responses were measured at weeks 2, 4, and 7. For nanofibers containing IL17.1-Q11, all mice produced antibodies targeting the B-cell epitope peptide (**Figure 2A**, **Figure S3**). In contrast, only one of five mice produced antibodies against IL17.2-Q11 (**Figure 2B**). Further, when serum was tested against recombinant murine IL-17A, IL17.1 immunization produced a significantly higher response against the protein (**Figure 2C**). IL17.1 was accordingly chosen to advance into further study owing to its superior immunogenicity. Further characterization of the IL17.1 antibody response revealed that there was predominantly an IgG1-focused response with only 2 mice producing detectable titers of IgG2b at the lowest dilution tested. This potentially indicated a predominantly Th2 response, which corresponded with previous observations of Q11-based immunizations also raising predominant Th2 responses (38).

Q11-Based Vaccination Produced a Long-Lived Response Against IL17.1

Mice from the original IL17.1 trial were maintained for 1 year after the previous immunization schedule (**Figure 3A**). While as a group, mice at 57 weeks after immunization did not maintain statistically significant titers compared to unvaccinated mice, two of four mice maintained measurable titers, indicating that long-lived responses are possible. Moreover, the group responded to boosting with a recall response, with measurable, antigen-specific titers after 1 week in all four mice. This response did not cross-react with other peptide epitopes such as the OVA epitope from the model antigen ovalbumin (**Figure 3B**, **Figures S4, S5**). These kinetics are faster than observed for primary immunizations (**Figure 2**), suggesting a recall response. Though antibody titer measurement at week 58 was not significantly higher than the pre-boost (ns, $p = 0.1411$) it was significantly higher than antibody response at 2 weeks (**, $p = 0.0056$). Following this boost, spleens were harvested from mice at week 58, and the T cell responses to the IL17.1 peptide and the PADRE T cell epitope were analyzed. Strikingly, IL17.1 produced no detectable T cell responses, while PADRE stimulation indicated a significant population of responding T cells producing IL-4 but not IFN-γ (**Figures 3C,D**). This indicated a T cell response that was PADRE-specific but not IL17.1-specific, an important consideration for anti-cytokine immunization which aims to avoid breaking T cell tolerance (24).

Multifactorial Optimization

Multifactorial experimental designs are commonly employed in a broad range of technical fields to efficiently optimize a desired outcome while simultaneously gaining knowledge about how multiple factors may interact. Although traditionally underutilized in biological settings, such designs have been

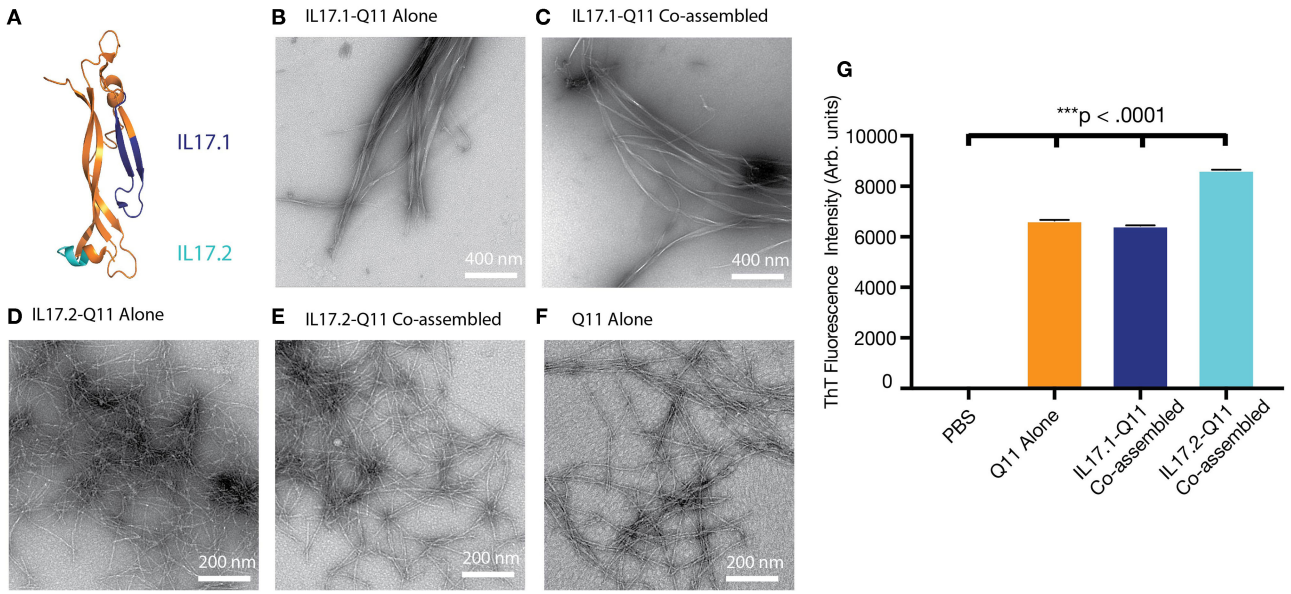

FIGURE 1 | Selection of IL-17 epitopes and characterization of IL17.1 and IL17.2 nanofibers. Two peptide epitopes, IL17.1 and IL17.2, were identified within mouse IL17A. **(A)** Homologous epitopes are shown within the crystal structure of human IL17A. **(B–F)** Both IL17.1-Q11 and IL17.2-Q11 peptides self-assembled into nanofibers (imaged using negative-stained TEM) alone or when co-assembled with Q11 and PADRE-Q11 (single peptides formulated at 2 mM; co-assembled peptides formulated at 1 mM IL17.1-Q11 or IL17.2-Q11/0.95 mM Q11/0.05 mM PADRE-Q11; all nanofibers diluted 10-fold before application to TEM grids). **(G)** All formulations had significant β-sheet character by ThT fluorescence (mean ± SD, $n = 3$, all groups significantly different from all other groups, $^{***}p < 0.001$ by one-way ANOVA and Tukey's Multiple Comparisons test).

receiving increasing attention recently (43, 52–54). We chose to employ this methodology to investigate how epitope content influenced overall titer and avidity, using a 2 × 2 full factorial design with a center point (**Figures 4A,D**). Based on previous research analyzing the impact of altering T cell epitope content alone (42), we chose three concentrations of T cell epitopes at different orders of magnitude and B cell epitopes over a linear range. All nanofibers were formed using a total peptide concentration of 2 mM, using unmodified Q11 peptide as a base material (**Figure 4A**). Based on previously published data comparing anti-cytokine responses at different T cell epitope ratios (38), we used JMP14 to select a sample size of 7 mice per group to provide an estimated 80% power for this experiment.

Analysis of these results by two-way ANOVA indicated that the B cell epitope content in nanofibers had a significant main effect influencing antibody titer ($p = 0.0242$) within the range tested. The T cell epitope content ($p = 0.4305$) and the interaction parameter ($p = 0.1940$). having a non-significant effect (**Figure 4B**). Antibody titer is a combined metric which is dependent on both antibody concentration in the serum and antibody avidity for the target. To better assess the antibody avidity, a urea assay was used on serum from the same 35 mice. Interestingly, avidity exhibited distinct differences compared with the response shown for antibody titers, with no significant main effect of either epitope density (B cell: $p = 0.9808$ and T cell: $p = 0.9188$) but a strongly significant effect for the interaction parameter ($p = 0.0054$) (**Figure 4C**). This suggested that neither the T cell nor B cell epitope alone were responsible for the changes in avidity noticed here, but rather the ratio of the T and B cell epitope density.

The predictive value of the model generated was tested by evaluating a new formulation not included in the original experimental design. A group of 5 mice was immunized with nanofibers containing a previously untested epitope ratio (shown schematically as an orange circle in **Figure 4B**, titer data shown in **Figure 4E**), and antibody titers were compared to the value predicted by the factorial design. The mean titer measured in this experiment closely matched the predicted antibody titer at week 7, supporting the validity of this model to predict responses not included in the original design. Fortuitously, the center of the design was selected as the formulation to advance into further studies with adjuvants and in a mouse model of psoriasis. All further experiments were conducted with this optimized nanofiber immunization formulation.

Adjuvants Enhanced Antibody Responses and Influenced Antibody Subclass

Although it is not yet clear what titers of anti-IL-17 antibodies will be most protective in the context of various inflammatory conditions, the antibody titers measured in the study thus far against optimized IL17.1-containing nanofibers were considered to be only moderate. To investigate the extent to which antibody titers could be augmented, we investigated formulations containing the adjuvants CpG (ODN 1826) or alum (Alhydrogel, Invivogen). Both adjuvants were able to

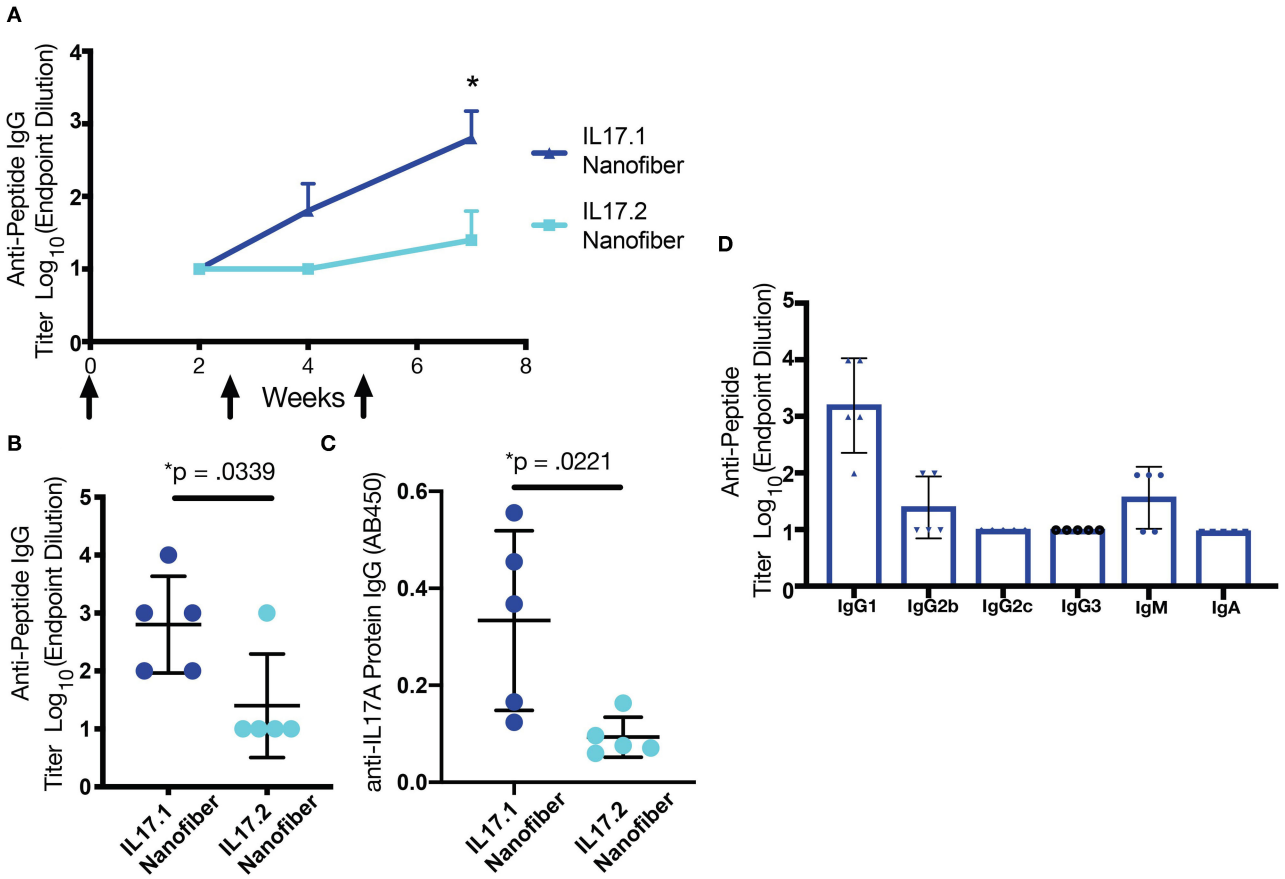

FIGURE 2 | B cell epitope screening in mice. **(A)** IL-17.1-Q11 and IL17.2-Q11 peptides were co-assembled into nanofibers with Q11 and PADRE-Q11 and injected subcutaneously without adjuvant at weeks 0, 2.5, and 5. Antibody titers were measured at weeks 2, 4, and 7. Mice immunized with IL17.1 raised significantly higher antibody titers against both immunizing peptide **(B)** and IL17A protein **(C)** compared to mice immunized with IL17.2. Analysis of the antibody isotype raised by IL17.1 demonstrated a bias toward IgG1 **(D)**. Statistical comparisons were conducted by Student's *t*-test ($n = 5$), $^*p < 0.05$. Data are presented as mean ± SD.

significantly increase ($p < 0.001$) the anti-IL17.1 IgG titer compared to the unadjuvanted formulation, but the two adjuvants also had distinct effects on IgG antibody subclasses elicited (**Figure 5**, **Figure S6**). Alum produced stronger total IgG and IgG1 responses but did not influence IgG2b, whereas CpG produced stronger IgG2b responses. These results were expected, as they corresponded with previous observations that alum-based adjuvants tend to skew the immune response toward an IgG1-dominated Th2 phenotype, while CpG skews toward an increased IgG2b phenotype associated with Th1 responses (55). These differences in IgG antibody subclass have been shown previously to influence cellular engagement with antibody-bound antigens. For example, mouse IgG1 interacts with activating receptor FcγRIII and inhibiting receptor FcγRIIB, which are found on all myeloid cells, while mouse IgG2b additionally binds the activating receptors FcγRI on monocyte-derived dendritic cells and FcγRIV on Ly6clo monocytes, macrophages, and neutrophils (56). While beneficial for the clearance of viral infections, the additional cellular recruitment and activation from IgG2b has not been thoroughly investigated for its role in anti-cytokine immunizations to our knowledge.

Reduction of Epidermal Thickening in a Model of Psoriasis

Mice immunized with variously adjuvanted nanofibers were then studied with a model of psoriasis in which the application of imiquimod leads to epidermal thickening (**Figure 6A**) mimicking plaque psoriasis in humans in addition to the increase of IL-17 and other inflammatory cytokines. Epidermal thickness, which correlates with the expression of these cytokines, was chosen for the sole metric of outcome. In this model, mice that had been previously immunized with unadjuvanted nanofibers showed an improvement compared to unvaccinated controls, exhibiting reduced epidermal thickening (**Figures 6B,D**, $p = 0.0315$). An even greater therapeutic effect was observed for alum-adjuvanted nanofibers, which significantly reduced epidermal thickening compared to unvaccinated ($p < 0.0001$), CpG-adjuvanted ($p < 0.0001$), and unadjuvanted ($p = 0.0109$) nanofiber formulations (**Figures 6E,G**). Strikingly, despite elevated IgG1 and total IgG titers compared to unadjuvanted controls, CpG-adjuvanted nanofibers exhibited the highest average epidermal thickness among all groups tested (**Figures 6C,G**),

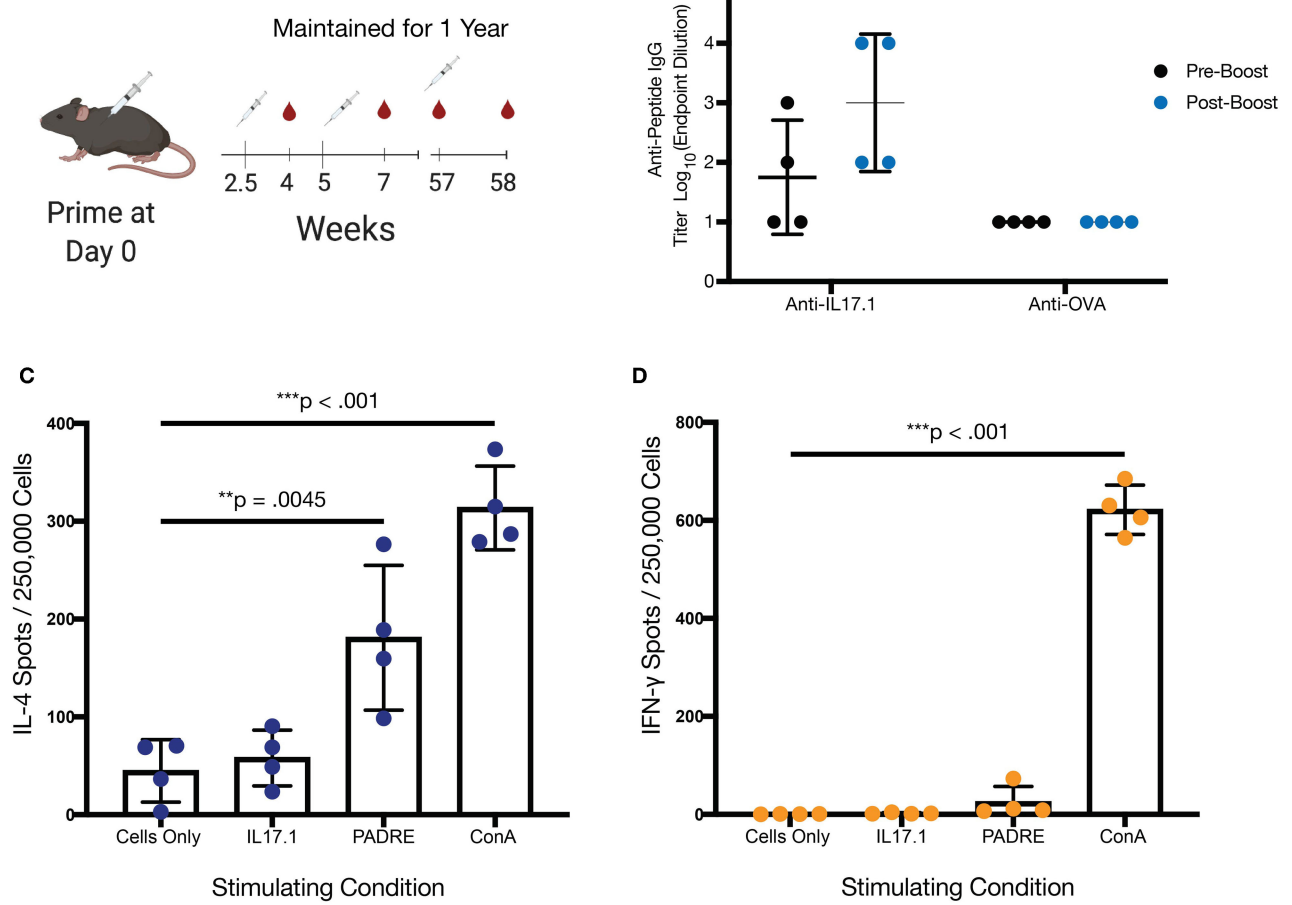

FIGURE 3 | Long-term immunization with IL-17.1 maintained immune memory without an autologous anti-IL17.1 T-cell response. **(A)** Mice were maintained for 1 year after the final immunization before blood collection and a subsequent boost, with the exception of one mouse that died of unrelated causes at 50 weeks. Final sera were collected at week 58 and mice were sacrificed for analysis of T cell response by ELISpot. **(B)** Anti-IL17.1 responses had declined by 1 year but rebounded after being recalled (unrelated antigen (OVA) responses included as a negative control). The difference was measurable although not statistically significantly different (ns, $p = 0.1411$) **(C)** Splenocytes were left unstimulated or stimulated with IL17.1 peptide, PADRE peptide, or Concanavalin A and demonstrated a significant IL-4 response against PADRE but no significant response against IL17.1. **(D)** Neither IL17.1 nor PADRE elicited a significant IFN-γ response. $n = 4$, statistical differences for antibody responses were calculated by paired *t*-test, while statistical differences for the ELISpot assay were calculated by one-way ANOVA and Tukey's test for multiple comparisons. $^{**}p < 0.01$, $^{***}p < 0.001$. Data are presented as Mean ± SD.

suggesting an exacerbation of psoriatic symptoms compared to unimmunized or immunized groups, although comparisons to unimmunized mice did not reach statistical significance. All imiquimod treated groups exhibited increased epidermal thickening compared to control mice that were not administered imiquimod (**Figure 6F**). A commercially available IL17 mAb was then compared to these samples in age-matched mice, with no significant differences observed between nanofiber immunization and anti-IL17 mAb treatment (**Figure S8**).

While the role of antibody subclass has been investigated thoroughly in the context of infectious disease, comparatively little work has been done to clarify the effects of subclass in anti-cytokine immunization. To further analyze the relationship between epidermal thickening and antibody subclass in this model, the absorbance of IgG2b at a dilution of 1:100 and IgG1 at a dilution of 1:1000 was compared. For unadjuvanted vs. alum-adjuvanted responses, where IgG2b titer was constant, IgG1 absorbance negatively correlated with epidermal thickening (**Figure 7A**, $R^2 = 0.50$, $p < 0.01$). That is, increased IgG1 was associated with reduction in the severity of psoriasis symptoms. In contrast, for alum- and CpG-adjuvanted groups where IgG1 titer was constant, IgG2b absorbance *positively* correlated with epidermal thickening (**Figure 7B,** $R^2 = 0.76$, $p < 0.01$). That is, IgG2b was associated with a *poorer* ability to reduce psoriasis symptoms and potentially an exacerbation of symptoms. Plotting this data as a heatmap of epidermal thickening, the optimal condition of low IgG2b and high IgG1 response becomes

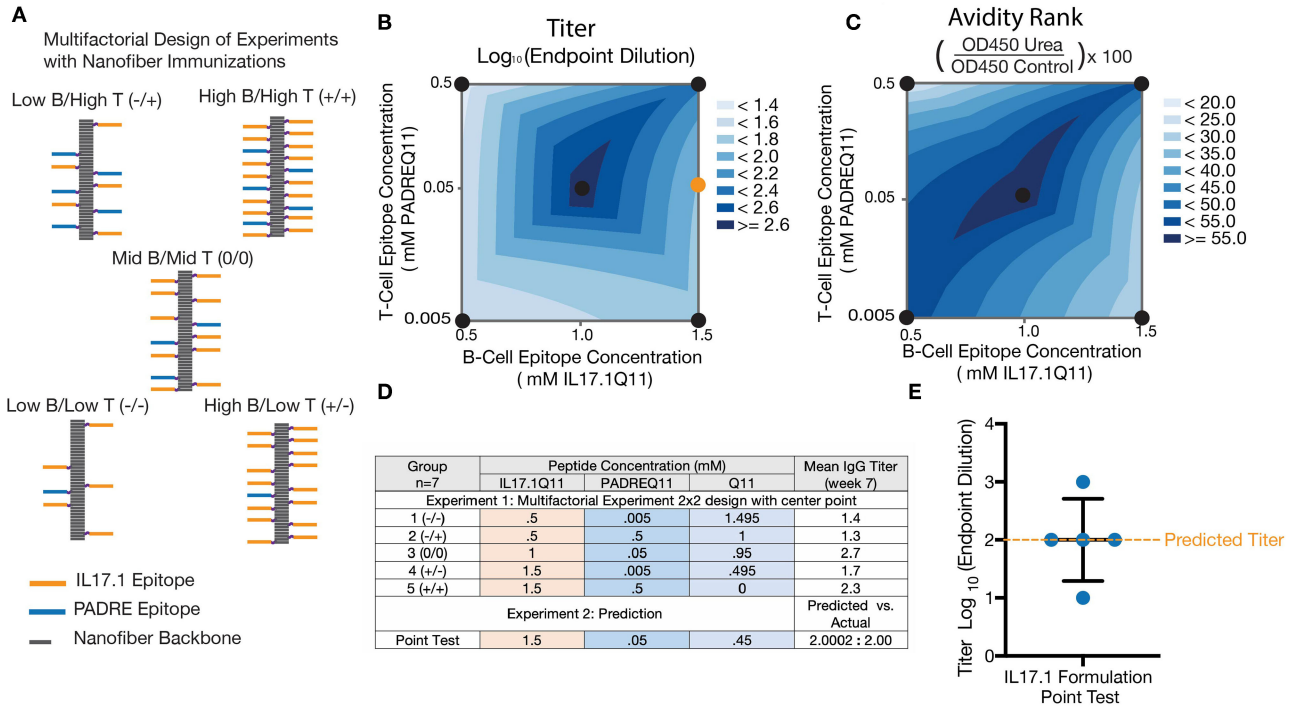

Group n=7	Peptide Concentration (mM)			Mean IgG Titer (week 7)
	IL17.1Q11	PADREQ11	Q11	
Experiment 1: Multifactorial Experiment 2x2 design with center point				
1 (-/-)	.5	.005	1.495	1.4
2 (-/+)	.5	.5	1	1.3
3 (0/0)	1	.05	.95	2.7
4 (+/-)	1.5	.005	.495	1.7
5 (+/+)	1.5	.5	0	2.3
Experiment 2: Prediction				Predicted vs. Actual
Point Test	1.5	.05	.45	2.0002 : 2.00

FIGURE 4 | Multifactorial optimization of nanofibers containing IL17.1 B-cell epitopes and PADRE T-cell epitopes. Design of Experiments (DoE) methodology **(A,D)** was employed to investigate how T-cell epitope and B-cell epitope content influenced anti-IL17 titers **(B)** and avidity **(C)**. A 2 × 2 multifactorial design with a center point was utilized, using nanofibers with stoichiometrically controlled amounts of B- and T-cell epitope indicated ($n = 7$). To test the predictive power of the DoE, a formulation not specifically tested in the original design was tested subsequently (Formulation shown by the orange dot in B). **(E)** Average titers generated by this formulation corresponded closely with the DoE prediction ($n = 5$, individual mice shown, with mean ± SD indicated).

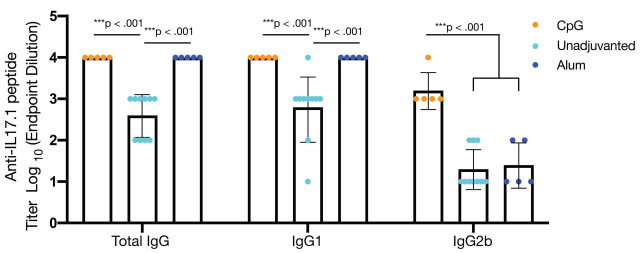

FIGURE 5 | Adjuvants impact antibody titer and alter IgG subclass. To enhance antibody titers, optimized nanofibers containing IL17.1 B cell epitopes and PADRE T cell epitopes were administered along with the adjuvants shown. CpG ($n = 5$) and alum ($n = 5$) enhanced total IgG and IgG1 anti-IL17.1 IgG titers compared to unadjuvanted controls ($n = 10$), but only CpG adjuvant significantly enhanced anti-IL17.1 IgG2b titers, indicating a more Th1-like phenotype. Data shown represent two separate experiments: Experiment 1: CpG $n = 5$ and unadjuvanted $n = 5$, Experiment 2: Alum $n = 5$ and unadjuvanted $n = 5$. ***$p < 0.001$ by one-way ANOVA and Tukey's test for multiple comparisons. Data are presented as means ± SD, with individual mice indicated.

clearly visible (**Figure 7C**). Of course, these data are correlative at present and are shown to suggest future mechanistic and immunologically controlled experiments clarifying causal relationships between IgG subclass and therapeutic efficacy of anti-cytokine vaccines.

DISCUSSION

Peptide nanofiber immunization against autologous targets offers a means to control both the magnitude and phenotype of therapeutic antibody responses for the long-term treatment of inflammatory diseases. While antibody responses have primarily been controlled by changing innate cell signaling, we demonstrate here how B- and T-cell epitope content can influence responses in a supramolecular peptide-based vaccine, utilizing DoE methodologies to demonstrate how both titer and avidity can be influenced by these inputs. We then demonstrate how phenotypes of the immune response can have a significant impact on the course of imiquimod-induced psoriasis. These results demonstrate how a peptide-based approach can allow for highly specific targeting of cytokines—both capitalizing on the strengths and buttressing the weaknesses of monoclonal antibody-based therapeutics.

Peptide immunization for anti-cytokine vaccination offers an opportunity to increase specificity of antibody responses, avoiding off-target effects which have hindered other anti-cytokine efforts such as non-neutralizing immunodominant epitopes and unwanted reactions against epitopes shared

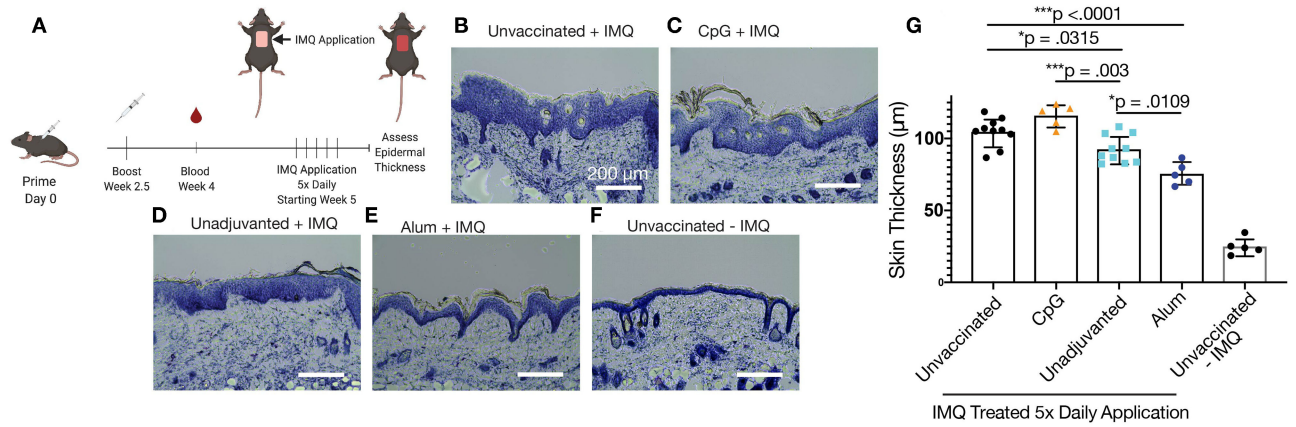

FIGURE 6 | IL17.1 nanofiber immunizations diminished imiquimod-induced psoriasis. Mice were immunized prophylactically at 8 weeks of age and boosted 2.5 weeks afterwards. Five weeks after primary immunization, imiquimod (IMQ) was applied daily for 5 days, and tissues were harvested on the sixth day **(A)**. Groups included unvaccinated mice **(B)**, mice vaccinated with CpG-adjuvanted nanofibers **(C)**, unadjuvanted nanofibers **(D)**, and alum-adjuvanted nanofibers **(E)**, plus mice that were neither vaccinated nor administered imiquimod **(F)**. Epidermal thickness was compared at 8 locations over two sections from each animal **(G)**. Statistical significance was measured by one-way ANOVA and Tukey's Multiple Comparisons *post-hoc* analysis. $*p < 0.05$, $***p < 0.001$. Data are presented as means ± SD. Data shown represent two separately conducted experiments: *Experiment 1:* unvaccinated + IMQ $n = 5$, CpG-adjuvanted nanofibers $n = 5$, unadjuvanted nanofibers $n = 5$, unvaccinated without IMQ $n = 5$; *Experiment 2:* unvaccinated + IMQ $n = 5$, alum-adjuvanted nanofibers $n = 5$, unadjuvanted nanofibers $n = 5$. See **Figure S7** for statistical justification for combining these experiments in the analysis shown in **(G)**.

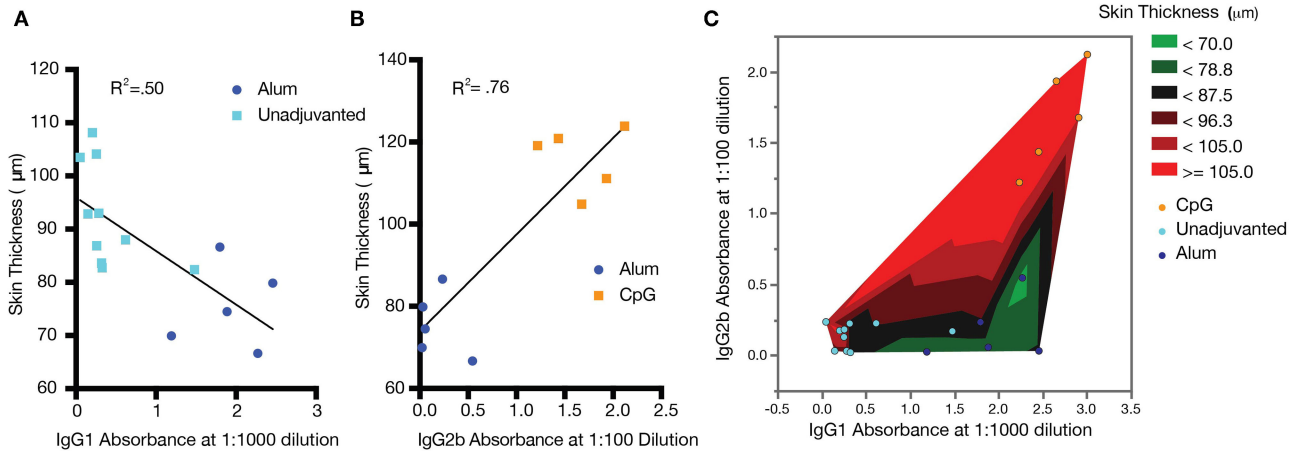

FIGURE 7 | Correlations between antibody titer, subclass, and psoriasis severity. Increased IgG1 correlates with improved psoriasis (decreased epidermal thickness) **(A)**, while increased IgG2b correlates with exacerbated psoriasis (increased epidermal thickness) **(B)**. A heatmap of epidermal thickness illustrates a target region (green) for reduced epidermal thickening **(C)**. Analysis was carried out by simple linear regression. Data shown represent a combination of two separately conducted experiments: Experiment 1: CpG $n = 5$ and unadjuvanted $n = 5$; Experiment 2: alum $n = 5$ and unadjuvanted $n = 5$.

between cytokines (6). However, the reduced immunogenicity of peptides has historically posed a challenge (57). Soluble peptides rarely elicit high-titer, long-lasting antibody responses without adjuvants, but biomaterials such as supramolecular nanofibers can be employed to produce long-lived, high-titer responses from these otherwise non-immunogenic peptides, in many cases without adjuvants (37, 40, 58–60). These nanofiber materials have also been demonstrated to be stable, maintaining immunogenicity *in vitro* under prolonged conditions which otherwise cause loss of immunogenicity for complex folded proteins (61). Nanofiber vaccine responses can be controlled by B-cell and T-cell epitope content, representing a modulation of adaptive immune signals as opposed to the more common approach of modulating antigen presenting cell signaling to change co-stimulation and cytokine production (62–65). Further, biomaterials with high modularity, such as supramolecular assemblies, are particularly amenable to engineering strategies such as Design of Experiments methodologies. These statistical constructs can be employed for optimization and can also provide insight into interactions between factors in a way that is more informative than simple presence/absence or one-factor-at-a-time experiments.

In addition to advantages offered by the modularity of Q11 with respect to changing epitope content, these materials can also be formulated with adjuvants to further shape the phenotypes of antibody responses (59). By themselves, Q11-based vaccines have been shown repeatedly to not induce pro-inflammatory cytokines, representing a relative "blank slate" that can be combined with additional adjuvants or immune modulators to further shape or augment responses (41, 58). In contrast to both Th1 and Th2 focused adjuvants that induce inflammation, Q11 nanofibers induce minimal inflammatory responses while still producing B-cell and T-cell responses (58), suggesting minimal direct interaction with TLRs or the adsorption of cytokines or other innate immune proteins that could trigger the inflammatory response. This suggests that Q11 adjuvanticity is independent of classical adjuvanting pathways which rely on inflammation for cellular recruitment, which may be one reason why antibody class switching was found here to be primarily driven by additional exogenous adjuvants and not by variations in the Q11 platform itself.

Although many anti-cytokine vaccines report total antibody titer for IgG, no publications to our knowledge report antibody subclass and isotype in the context of anti-cytokine immunization. This is in contrast to fields where vaccines are used to treat infectious disease. In these contexts, it is well-acknowledged that antibody subclass plays an active role in controlling viral infections (66–68). One posited role for this effect is the engagement of additional activating Fc Receptors in myeloid cell populations (56). In autoimmune conditions, where myeloid cell recruitment and complement activation are known to influence disease progression (69, 70), the same importance of antibody subclass is being actively explored with mAbs (71) but has yet to be shown *in vivo* with an anti-cytokine vaccination. Specifically for imiquimod-induced psoriasis, epidermal thickening via keratinocyte hyperproliferation is linked to both MyD88-dependent and MyD88-independent mechanisms and the recruitment of various myeloid populations (72). IgG2b, observed in the CpG vaccinated population, but not significantly in other adjuvanted conditions, also facilitates the recruitment of myeloid populations shown to be essential for IMQ psoriasis pathology (56).

Further, this study does not analyze the systemic effects of adjuvants such as CpG. CpG (ODN 1826) which acts as a TLR9 agonist (73), recruits many of the same cytokines that are essential for the IMQ-induced pathology (74). At sufficiently high doses systemic effects have been observed for as long as 8 days after administration (73, 75). Though this is significantly shorter than the 2.5 weeks between the final boost and beginning of IMQ application in this study it does not rule out at least some contribution of CpG systemic inflammation to the results reported here. Although the precise mechanism remains to be fully clarified, the replication of reduced therapeutic outcomes with CpG administration in both this and prior anti-cytokine therapies targeting TNF (38) suggests an important role for immune phenotype in the development of autologous antibody responses that will require further studies.

Additionally, the correlative nature of these conclusions highlights the limitations of our analysis of the IMQ-induced psoriasis model, which uses only epidermal thickening as the main metric for disease and does not examine different signaling pathways which may be responsible for the observed effects. The development and analysis of *in vitro* assays which are sensitive to both the specificity of induced-polyclonal antibodies for IL-17 protein in aqueous state and can account for effects induced by different Fc-receptor interactions will be necessary to characterize the mechanistic reason for the observed reductions in epidermal thickness. Assays not based on surface-bound antigen, which are subject to antigen denaturation or epitope occlusion, would also be able to more clearly measure the neutralizing characteristics of the antibodies raised against IL-17. Further investigation will also be required to determine if this is a phenomenon that is specific to the inhibition of inflammatory cytokines, or if the targeting of any endogenous protein will result in increased inflammation or pathology when the auto-antibody response has an IgG2b phenotype.

While tuning an anti-IL17 therapeutic in rodents has clear translational value in psoriasis, the role of this cytokine in other human disease appears to be less straightforward. Anti-IL-17 mAbs have not had the same success in rheumatoid arthritis, multiple sclerosis, or ankylosing spondylitis as has been seen in rodent models (3, 76, 77). While IL-17-dependent pathologies are seen in primary non-responders to other treatments such as anti-TNF therapy for rheumatoid arthritis (78), more commonly it is found that IL-17 synergistically promotes inflammation in several inflammatory diseases rather than acting as the primary driver of inflammation. This suggests that for future translation, a combination therapy or anti-cytokine immunization targeting multiple cytokines using a modular vaccine platform may provide an area of future exploration.

CONCLUSION

We show here that peptide self-assemblies displaying B-cell epitopes from IL-17A and exogenous T-cell epitopes can raise IL-17A-specific antibodies and diminish symptoms of imiquimod-induced psoriasis in mice. The modularity of the system enabled a Design-of-Experiments approach where the influence of T-cell and B-cell epitope content on antibody titer and avidity could be investigated. Unadjuvanted nanofibers and those adjuvanted with alum had therapeutic efficacy in a mouse model of psoriasis, whereas formulations adjuvanted with CpG showed the opposite effect. Therapeutic efficacy was correlated with IgG1 but inversely correlated with IgG2b, illustrating the importance of tuning immune phenotype in active immunotherapies against cytokine targets.

DATA AVAILABILITY STATEMENT

The original contributions presented in the study are included in the article/**Supplementary Material**. Further inquiries can be directed to the corresponding author/s.

ETHICS STATEMENT

The animal study was reviewed and approved by Duke Institutional Animal Care and Use Committee (IACUC).

AUTHOR CONTRIBUTIONS

LS designed experiments, conducted experiments, analyzed data, and wrote the manuscript. SK and KH designed experiments, conducted experiments, and analyzed data. JS designed experiments and conducted experiments. AM designed experiments and interpreted data. JC oversaw the project, designed experiments, analyzed data, and wrote the manuscript. All authors contributed to the article and approved the submitted version.

FUNDING

This research was supported by the United States National Institutes of Health (NIH/NIBIB, R01 EB009701). LS and SK were supported by the National Science Foundation Graduate Research Fellowship Program (DGE-1644868). AM was supported by the National Institute of Health (R01 AI39207) and the Duke Physician Scientists Strong Start Award and the Department of Dermatology. Any opinions, findings, and conclusions or recommendations expressed in this material are those of the authors and do not necessarily reflect the views of the National Science Foundation or the National Institutes of Health.

ACKNOWLEDGMENTS

We thank Peter Hoang for his help with the imiquimod-induced psoriasis model. Schematics in **Figures 3**, **6** were created with biorender.com.

SUPPLEMENTARY MATERIAL

The Supplementary Material for this article can be found online at: https://www.frontiersin.org/articles/10.3389/fimmu.2020.01855/full#supplementary-material

REFERENCES

1. Rodgers KR, Chou RC. Therapeutic monoclonal antibodies and derivatives: historical perspectives and future directions. *Biotechnol Adv.*(2016) 34:1149–58. doi: 10.1016/j.biotechadv.2016.07.004
2. Rosenblum MD, Remedios KA, Abbas AK. Mechanisms of human autoimmunity. *J Clin Investig.* (2015) 125:2228–33. doi: 10.1172/JCI78088
3. Siebert S, Tsoukas A, Robertson J, Mcinnes I. Cytokines as therapeutic targets in rheumatoid arthritis and other inflammatory diseases. *Pharmacol Rev.* (2015) 67:280–309. doi: 10.1124/pr.114.009639
4. Ha H-L, Wang H, Pisitkun P, Kim J-C, Tassi I, Tang W, et al. IL-17 drives psoriatic inflammation via distinct, target cell-specific mechanisms. *Proc Natl Acad Sci USA.* (2014) 111:E3422–31. doi: 10.1073/pnas.1400513111
5. Zagury D, Burny A, Gallo RC. Toward a new generation of vaccines: The anti-cytokine therapeutic vaccines. *Proc Natl Acad Sci USA.* (2001) 98:8024–9. doi: 10.1073/pnas.141224798
6. Assier E, Bessis N, Zagury JF, Boissier MC. IL-1 vaccination is suitable for treating inflammatory diseases. *Front Pharmacol.* 8:6. doi: 10.3389/fphar.2017.00006
7. Irani V, Guy AJ, Andrew D, Beeson JG, Ramsland PA, Richards JS. Molecular properties of human IgG subclasses and their implications for designing therapeutic monoclonal antibodies against infectious diseases. *Mol Immunol.* (2015) 67:171–82. doi: 10.1016/j.molimm.2015.03.255
8. Kang TH, Jung ST. Boosting therapeutic potency of antibodies by taming Fc domain functions. *Exp Mol Med.* (2019) 51:138. doi: 10.1038/s12276-019-0345-9
9. Bendtzen K, Geborek P, Svenson M, Larsson L, Kapetanovic MC, Saxne T. Individualized monitoring of drug bioavailability and immunogenicity in rheumatoid arthritis patients treated with the tumor necrosis factor alpha inhibitor infliximab. *Arthritis Rheum.* (2006) 54:3782–9. doi: 10.1002/art.22214
10. Maneiro JR, Salgado E, Gomez-Reino JJ. Immunogenicity of monoclonal antibodies against tumor necrosis factor used in chronic immune-mediated Inflammatory conditions: systematic review and meta-analysis. *JAMA Intern Med.* (2013) 173:1416–28. doi: 10.1001/jamainternmed.2013.7430
11. St Clair EW, Wagner CL, Fasanmade AA, Wang B, Schaible T, Kavanaugh A, et al. The relationship of serum infliximab concentrations to clinical improvement in rheumatoid arthritis: results from ATTRACT, a multicenter, randomized, double-blind, placebo-controlled trial. *Arthritis Rheum.* (2002) 46:1451–9. doi: 10.1002/art.10302
12. Radstake TR, Svenson M, Eijsbouts AM, Van Den Hoogen FH, Enevold C, Van Riel PL, et al. Formation of antibodies against infliximab and adalimumab strongly correlates with functional drug levels and clinical responses in rheumatoid arthritis. *Ann Rheum Dis.* (2009) 68:1739–45. doi: 10.1136/ard.2008.092833
13. Bartelds GM, Krieckaert CLM, Nurmohamed MT, Van Schouwenburg PA, Lems WF, Twisk JWR, et al. Development of antidrug antibodies against adalimumab and association with disease activity and treatment failure during long-term follow-up. *JAMA.* (2011) 305:1460–8. doi: 10.1001/jama.2011.406
14. Ridker PM, Tardif JC, Amarenco P, Duggan W, Glynn RJ, Jukema JW, et al. Lipid-reduction variability and antidrug-antibody formation with bococizumab. *N Engl J Med.* (2017) 376:1517–26. doi: 10.1056/NEJMoa1614062
15. Delavallee L, Duvallet E, Semerano L, Assier E, Boissier MC. Anti-cytokine vaccination in autoimmune diseases. *Swiss Med Week.* (2010) 140:28–32. doi: 10.4414/smw.2010.13108
16. Mesin L, Ersching J, Victora GD. Germinal center B cell dynamics. *Immunity.* (2016) 45:471–82. doi: 10.1016/j.immuni.2016.09.001
17. Pratt KP. Anti-drug antibodies: emerging approaches to predict, reduce or reverse biotherapeutic immunogenicity. *Antibodies.* (2018) 7:19. doi: 10.3390/antib7020019
18. Wraith DC. Anti-cytokine vaccines and the immunotherapy of autoimmune diseases. *Eur J Immunol.* (2006) 36:2844–8. doi: 10.1002/eji.200636760
19. Imamura CK. Therapeutic drug monitoring of monoclonal antibodies: Applicability based on their pharmacokinetic properties. *Drug Metab Pharmacokin.* (2019) 34:14–8. doi: 10.1016/j.dmpk.2018.11.003
20. Le Buanec H, Delavallee L, Bessis N, Paturance S, Bizzini B, Gallo R, et al. TNF alpha kinoid vaccination-induced neutralizing antibodies to TNF alpha protect mice from autologous TNF alpha-driven chronic and acute inflammation. *Proc Natl Acad Sci USA.* (2006) 103:19442–7. doi: 10.1073/pnas.0604827103
21. Chackerian B, Lowy DR, Schiller JT. Conjugation of a self-antigen to papillomavirus-like particles allows for efficient induction of protective autoantibodies. *J Clin Investig.* (2001) 108:415–23. doi: 10.1172/JCI11849
22. Jennings GT, Bachmann MF. Immunodrugs: therapeutic VLP-based vaccines for chronic diseases. *Ann Rev Pharmacol Toxicol.* (2009) 49:303–26. doi: 10.1146/annurev-pharmtox-061008-103129
23. Tissot AC, Spohn G, Jennings GT, Shamshiev A, Kurrer MO, Windak R, et al. A VLP-based vaccine against interleukin-1 alpha protects mice from atherosclerosis. *Eur J Immunol.* (2013) 43:716–22. doi: 10.1002/eji.201242687

24. Link A, Bachmann MF. Immunodrugs: breaking B- but not T-cell tolerance with therapeutic anticytokine vaccines. *Immunotherapy.* (2010) 2:561–74. doi: 10.2217/imt.10.30
25. Uyttenhove C, Van Snick J. Development of an anti-IL-17A auto-vaccine that prevents experimental auto-immune encephalomyelitis. *Eur J Immunol.* (2006) 36:2868–74. doi: 10.1002/eji.200636662
26. Foerster J, Bachman M. Beyond passive immunization: toward a nanoparticle-based IL-17 vaccine as first in class of future immune treatments. *Nanomedicine.* (2015) 10:1361–9. doi: 10.2217/nnm.14.215
27. Zeltins A, West J, Zabel F, El Turabi A, Balke I, Haas S, et al. Incorporation of tetanus-epitope into virus-like particles achieves vaccine responses even in older recipients in models of psoriasis, Alzheimer's and cat allergy. *NPJ Vaccines.* (2017) 2:13. doi: 10.1038/s41541-017-0030-8
28. Guan Q, Weiss CR, Qing G, Ma Y, Peng Z. An IL-17 peptide-based and virus-like particle vaccine enhances the bioactivity of IL-17 *in vitro* and *in vivo*. *Immunotherapy.* (2012) 4:1799–807. doi: 10.2217/imt.12.129
29. Lauwerys BR, Hachulla E, Spertini F, Lazaro E, Jorgensen C, Mariette X, et al. Down-regulation of interferon signature in systemic lupus erythematosus patients by active immunization with interferon α-kinoid. *Arthritis Rheuma.* (2013) 65:447–56. doi: 10.1002/art.37785
30. Durez P, Vandepapeliere P, Miranda P, Toncheva A, Berman A, Kehler T, et al. Therapeutic vaccination with TNF-kinoid in TNF antagonist-resistant rheumatoid arthritis: a phase II randomized, controlled clinical trial. *PLoS ONE.* (2014) 9:e113465. doi: 10.1371/journal.pone.0113465
31. Cavelti-Weder C, Timper K, Seelig E, Keller C, Osranek M, Lassing U, et al. Development of an interleukin-1 beta vaccine in patients with type 2 diabetes. *Mol Therapy.* (2016) 24:1003–12. doi: 10.1038/mt.2015.227
32. Ducreux J, Houssiau FA, Vandepapelière P, Jorgensen C, Lazaro E, Spertini F, et al. Interferon α kinoid induces neutralizing anti-interferon α antibodies that decrease the expression of interferon-induced and B cell activation associated transcripts: analysis of extended follow-up data from the interferon α kinoid phase I/II study. *Rheumatology.* (2016) 55:1901–5. doi: 10.1093/rheumatology/kew262
33. Rincon-Restrepo M, Mayer A, Hauert S, Bonner DK, Phelps EA, Hubbell JA, et al. Vaccine nanocarriers: coupling intracellular pathways and cellular biodistribution to control CD4 vs CD8 T cell responses. *Biomaterials.* (2017) 132:48–58. doi: 10.1016/j.biomaterials.2017.03.047
34. Rohner NA, Thomas SN. Flexible macromolecule versus rigid particle retention in the injected skin and accumulation in draining lymph nodes are differentially influenced by hydrodynamic size. *ACS Biomater Sci Eng.* (2017) 3:153–9. doi: 10.1021/acsbiomaterials.6b00438
35. Meyer RA, Sunshine JC, Perica K, Kosmides AK, Aje K, Schneck JP, et al. Biodegradable nanoellipsoidal artificial antigen presenting cells for antigen specific T-cell activation. *Small.* (2015) 11:1519–25. doi: 10.1002/smll.201402369
36. Frey M, Bobbala S, Karabin N, Scott E. Influences of nanocarrier morphology on therapeutic immunomodulation. *Nanomedicine.* (2018) 13:1795–811. doi: 10.2217/nnm-2018-0052
37. Wen Y, Waltman A, Han HF, Collier JH. Switching the immunogenicity of peptide assemblies using surface properties. *Acs Nano.* (2016) 10:9274–86. doi: 10.1021/acsnano.6b03409
38. Mora-Solano C, Wen Y, Han HF, Chen JJ, Chong AS, Miller ML, et al. Active immunotherapy for TNF-mediated inflammation using self-assembled peptide nanofibers. *Biomaterials.* (2017) 149:1–11. doi: 10.1016/j.biomaterials.2017.09.031
39. Rudra JS, Tian YF, Jung JP, Collier JH. A self-assembling peptide acting as an immune adjuvant. *Proc Natl Acad Sci USA.* (2010) 107:622–7. doi: 10.1073/pnas.0912124107
40. Rudra JS, Mishra S, Chong AS, Mitchell RA, Nardin EH, Nussenzweig V, et al. Self-assembled peptide nanofibers raising durable antibody responses against a malaria epitope. *Biomaterials.* (2012) 33:6476–84. doi: 10.1016/j.biomaterials.2012.05.041
41. Rudra JS, Sun T, Bird KC, Daniels MD, Gasiorowski JZ, Chong AS, et al. Modulating Adaptive Immune Responses to Peptide Self-Assemblies. *Acs Nano.* (2012) 6:1557–64. doi: 10.1021/nn204530r
42. Pompano RR, Chen JJ, Verbus EA, Han HF, Fridman A, Mcneely T, et al. Titrating T-cell epitopes within self-assembled vaccines optimizes CD4+helper T cell and antibody outputs. *Adv Healthcare Mater.* (2014) 3:1898–908. doi: 10.1002/adhm.201400137
43. Jung JP, Moyano JV, Collier JH. Multifactorial optimization of endothelial cell growth using modular synthetic extracellular matrices. *Integrative Biol.* (2011) 3:185–96. doi: 10.1039/c0ib00112k
44. Noack M, Miossec P. Th17 and regulatory T cell balance in autoimmune and inflammatory diseases. *Autoimmun Rev.* (2014) 13:668–77. doi: 10.1016/j.autrev.2013.12.004
45. Blauvelt A, Chiricozzi A. The immunologic role of IL-17 in psoriasis and psoriatic arthritis pathogenesis. *Clin Rev Allergy Immunol.* (2018) 55:379–90. doi: 10.1007/s12016-018-8702-3
46. Von Stebut E, Boehncke W-H, Ghoreschi K, Gori T, Kaya Z, Thaci D, et al. IL-17A in psoriasis and beyond: cardiovascular and metabolic implications. *Front Immunol.* (2019) 10:3096. doi: 10.3389/fimmu.2019.03096
47. Kolaskar AS, Tongaonkar PC. A semi-empirical method for prediction of antigenic determinants on protein antigens. *FEBS Lett.* (1990) 276:172–4. doi: 10.1016/0014-5793(90)80535-Q
48. Wu YY, Norberg PK, Reap EA, Congdon KL, Fries CN, Kelly SH, et al. A supramolecular vaccine platform based on alpha-helical peptide nanofibers. *Acs Biomater Sci Eng.* (2017) 3:3128–32. doi: 10.1021/acsbiomaterials.7b00561
49. Garner JP, Weisker SM, Dufour B, Mench JA. Barbering (Fur and whisker trimming) by laboratory mice as a model of human trichotillomania and obsessive-compulsive spectrum disorders. *Comp Med.* (2004) 54:216–24.
50. Alexander J, Sidney J, Southwood S, Ruppert J, Oseroff C, Maewal A, et al. Development of high potency universal Dr-restricted helper epitopes by modification of high-affinity Dr-blocking peptides. *Immunity.* (1994) 1:751–61. doi: 10.1016/S1074-7613(94)80017-0
51. Franke ED, Hoffman SL, Sacci JB, Wang R, Charoenvit Y, Appella E, et al. Pan DR binding sequence provides T-cell help for induction of protective antibodies against *Plasmodium yoelii* sporozoites. *Vaccine.* (1999) 17:1201–5. doi: 10.1016/S0264-410X(98)00341-7
52. Murphy KC, Whitehead J, Falahee PC, Zhou D, Simon SI, Leach JK. Multifactorial experimental design to optimize the anti-inflammatory and proangiogenic potential of mesenchymal stem cell spheroids. *Stem Cells.* (2017) 35:1493–504. doi: 10.1002/stem.2606
53. Kramer RM, Archer MC, Orr MT, Dubois Cauwelaert N, Beebe EA, Huang P-WD, et al. Development of a thermostable nanoemulsion adjuvanted vaccine against tuberculosis using a design-of-experiments approach. *Int J Nanomed.* (2018) 13:3689–711. doi: 10.2147/IJN.S159839
54. Patel A, Erb SM, Strange L, Shukla RS, Kumru OS, Smith L, et al. Combined semi-empirical screening and design of experiments (DOE) approach to identify candidate formulations of a lyophilized live attenuated tetravalent viral vaccine candidate. *Vaccine.* (2018) 36:3169–79. doi: 10.1016/j.vaccine.2017.04.086
55. Morgan MT, Bennett MT, Drohat AC. Kinetic analysis of the removal of halogenated uracil by human thymine DNA glycosylase. Effects of altering the CpG site context. *Faseb J.* (2007) 21:A291. doi: 10.1096/fasebj.21.5.A291-d
56. Bruhns P. Properties of mouse and human IgG receptors and their contribution to disease models. *Blood.* (2012) 119:5640–9. doi: 10.1182/blood-2012-01-380121
57. Li W, Joshi MD, Singhania S, Ramsey KH, Murthy AK. Peptide vaccine: progress and challenges. *Vaccines.* (2014) 2:515–36. doi: 10.3390/vaccines2030515
58. Chen JJ, Pompano RR, Santiago FW, Maillat L, Sciammas R, Sun T, et al. The use of self-adjuvanting nanofiber vaccines to elicit high-affinity B cell responses to peptide antigens without inflammation. *Biomaterials.* (2013) 34:8776–85. doi: 10.1016/j.biomaterials.2013.07.063
59. Kelly SH, Wu Y, Varadhan AK, Curvino EJ, Chong AS, Collier JH. Enabling sublingual peptide immunization with molecular self-assemblies. *Biomaterials.* (2020) 241:119903. doi: 10.1016/j.biomaterials.2020.119903
60. Wu Y, Kelly SH, Sanchez-Perez L, Sampson JH, Collier JH. Comparative study of α-helical and β-sheet self-assembled peptide nanofiber vaccine platforms: influence of integrated T-cell epitopes. *Biomater Sci.* (2020) 8:3522–35. doi: 10.1039/D0BM00521E
61. Sun T, Han H, Hudalla GA, Wen Y, Pompano RR, Collier JH. Thermal stability of self-assembled peptide vaccine materials. *Acta Biomater.* (2016) 30:62–71. doi: 10.1016/j.actbio.2015.11.019

62. Paul WE, Zhu JF. How are T(H)2-type immune responses initiated and amplified? *Nat Rev Immunol.* (2010) 10:225–35. doi: 10.1038/nri2735
63. Reed SG, Orr MT, Fox CB. Key roles of adjuvants in modern vaccines. *Nat Med.* (2013) 19:1597–608. doi: 10.1038/nm.3409
64. Smith DM, Simon JK, Baker JR. Applications of nanotechnology for immunology. *Nat Rev Immunol.* (2013) 13:592. doi: 10.1038/nri3488
65. Bonam SR, Partidos CD, Halmuthur SKM, Muller S. An overview of novel adjuvants designed for improving vaccine efficacy. *Trends Pharmacol Sci.* (2017) 38:771–93. doi: 10.1016/j.tips.2017.06.002
66. Huber VC, Mckeon RM, Brackin MN, Miller LA, Keating R, Brown SA, et al. Distinct contributions of vaccine-induced immunoglobulin G1 (IgG1) and IgG2a antibodies to protective immunity against influenza. *Clin Vaccine Immunol.* (2006) 13:981–90. doi: 10.1128/CVI.00156-06
67. Mehlhop E, Ansarah-Sobrinho C, Johnson S, Engle M, Fremont DH, Pierson TC, et al. Complement protein C1q inhibits antibody-dependent enhancement of flavivirus infection in an IgG subclass-specific manner. *Cell Host Microbe.* (2007) 2:417–26. doi: 10.1016/j.chom.2007.09.015
68. Su B, Dispinseri S, Iannone V, Zhang T, Wu H, Carapito R, et al. Update on Fc-mediated antibody functions against HIV-1 beyond neutralization. *Front Immunol.* (2019) 10:2968. doi: 10.3389/fimmu.2019.02968
69. Fairweather D, Cihakova D. Alternatively activated macrophages in infection and autoimmunity. *J Autoimmun.* (2009) 33:222–30. doi: 10.1016/j.jaut.2009.09.012
70. Chen M, Daha MR, Kallenberg CGM. The complement system in systemic autoimmune disease. *J Autoimmun.* (2010) 34:J276–86. doi: 10.1016/j.jaut.2009.11.014
71. Chan AC, Carter PJ. Therapeutic antibodies for autoimmunity and inflammation. *Nat Rev Immunol.* (2010) 10:301–16. doi: 10.1038/nri2761
72. Costa S, Marini O, Bevilacqua D, Defranco AL, Hou BD, Lonardi S, et al. Role of MyD88 signaling in the imiquimod-induced mouse model of psoriasis: focus on innate myeloid cells. *J Leukocyte Biol.* (2017) 102:791–803. doi: 10.1189/jlb.3MA0217-054RR
73. Liu H, Moynihan KD, Zheng Y, Szeto GL, Li AV, Huang B, et al. Structure-based programming of lymph-node targeting in molecular vaccines. *Nature.* (2014) 507:519–22. doi: 10.1038/nature12978
74. Lai C-Y, Su Y-W, Lin K-I, Hsu L-C, Chuang T-H. Natural modulators of endosomal toll-like receptor-mediated psoriatic skin inflammation. *J Immunol Res.* (2017) 2017:7807313. doi: 10.1155/2017/7807313
75. Von Beust BR, Johansen P, Smith KA, Bot A, Storni T, Kündig TM. Improving the therapeutic index of CpG oligodeoxynucleotides by intralymphatic administration. *Eur J Immunol.* (2005) 35:1869–76. doi: 10.1002/eji.200526124
76. Schett G, Elewaut D, Mcinnes IB, Dayer J-M, Neurath MF. How cytokine networks fuel inflammation: toward a cytokine-based disease taxonomy. *Nat Med.* (2013) 19:822–4. doi: 10.1038/nm.3260
77. Mcinnes IB, Buckley CD, Isaacs JD. Cytokines in rheumatoid arthritis - shaping the immunological landscape. *Nat Rev Rheumatol.* (2016) 12:63–8. doi: 10.1038/nrrheum.2015.171
78. Alzabin S, Abraham SM, Taher TE, Palfreeman A, Hull D, Mcnamee K, et al. Incomplete response of inflammatory arthritis to TNF alpha blockade is associated with the Th17 pathway. *Ann Rheumat Dis.* (2012) 71:1741–8. doi: 10.1136/annrheumdis-2011-201024

Conflict of Interest: JC is listed as an inventor on patents associated with the technology described. AM is a consultant for Silab and has previously received project funding from Silab, but Silab had no decision on the content or the publishing of any of the manuscripts' contents. AM also consults for the Leo Foundation and The Triangle Community Foundation and receives honoraria. AM's spouse is employed by Precision Biosciences and holds stock and stock options.

The remaining authors declare that the research was conducted in the absence of any commercial or financial relationships that could be construed as a potential conflict of interest.

frontiers in Immunology

ORIGINAL RESEARCH
published: 25 September 2020
doi: 10.3389/fimmu.2020.511513

Small Molecule NF-κB Inhibitors as Immune Potentiators for Enhancement of Vaccine Adjuvants

*Brittany A. Moser[1], Yoseline Escalante-Buendia[1], Rachel C. Steinhardt[1], Matthew G. Rosenberger[1], Britteny J. Cassaidy[1], Nihesh Naorem[1], Alfred C. Chon[1], Minh H. Nguyen[2], Ngoctran T. Tran[2] and Aaron P. Esser-Kahn[1]**

[1] Pritzker School of Molecular Engineering, The University of Chicago, Chicago, IL, United States, [2] Department of Chemistry, Chemical Engineering and Materials Science, Biomedical Engineering, University of California, Irvine, Irvine, CA, United States

Adjuvants are added to vaccines to enhance the immune response and provide increased protection against disease. In the last decade, hundreds of synthetic immune adjuvants have been created, but many induce undesirable levels of proinflammatory cytokines including TNF-α and IL-6. Here we present small molecule NF-κB inhibitors that can be used in combination with an immune adjuvant to both decrease markers associated with poor tolerability and improve the protective response of vaccination. Additionally, we synthesize a library of honokiol derivatives identifying several promising candidates for use in vaccine formulations.

Keywords: adjuvants, vaccines, NF-κB, honokiol, capsaicin

OPEN ACCESS

Edited by:
Evan Alexander Scott, Northwestern University, United States

Reviewed by:
Suraj Sable, Centers for Disease Control and Prevention (CDC), United States
John Tanner Wilson, Vanderbilt University, United States

****Correspondence:***
Aaron P. Esser-Kahn
aesserkahn@uchicago.edu

Specialty section:
This article was submitted to Molecular Innate Immunity, a section of the journal Frontiers in Immunology

Received: *11 November 2019*
Accepted: *25 August 2020*
Published: *25 September 2020*

Citation:
Moser BA, Escalante-Buendia Y, Steinhardt RC, Rosenberger MG, Cassaidy BJ, Naorem N, Chon AC, Nguyen MH, Tran NT and Esser-Kahn AP (2020) Small Molecule NF-κB Inhibitors as Immune Potentiators for Enhancement of Vaccine Adjuvants. Front. Immunol. 11:511513. doi: 10.3389/fimmu.2020.511513

INTRODUCTION

Vaccines remain one of the most effective ways of preventing disease. Despite their immense success in preventing diseases such as polio, tetanus, and small pox, diseases such as HIV and dengue present challenges that current clinical vaccine technologies cannot provide. To solve this problem, one strategy that has been explored is to include adjuvants, molecules that enhance the immune response (1). Although novel adjuvants generate higher quality immune responses that cannot be achieved with current approved adjuvants, to date, very few have been approved for use in human vaccines. This disconnect is due, in part, to the challenge of balancing the proinflammatory immune response with the protective, adaptive immune response (2–4). We recently reported that vaccines could be improved through the use of a peptide NF-κB inhibitor, SN50 in combination with an immune adjuvant (5). The addition of SN50 to adjuvanted vaccines led to increased safety of the adjuvant while enhancing protection against disease. Although this method proved both general across a wide range of adjuvants and effective against antigens of a variety of diseases, it still required a large amount of the peptide to enable optimal safety and protection. Scale-up of peptides present synthetic challenges and can result in expensive production costs, limiting their potential in a clinical setting (6, 7). Peptides might also induce an immune response against themselves leading to a potential for decreased enhancement in subsequent vaccinations. We chose to explore other small molecule NF-κB inhibitors as immune potentiators to overcome these challenges.

Here we demonstrate that select small molecule NF-κB inhibitors are effective at reducing adjuvant-induced inflammation while also increasing the adaptive humoral immune response. At the same time, we demonstrate that not all NF-κB inhibitors are effective immune potentiators.

Of the molecules we tested, honokiol and capsaicin proved to be effective at both limiting inflammation and potentiating the protective response. Through knockout studies, we demonstrate that the increase in antigen specific antibodies is independent from the anti-inflammatory activity, which is congruent with our previous studies (5). To determine if these small molecules could be improved by chemical synthesis, we explored derivatives of honokiol and found several promising candidates for potential use in vaccines.

RESULTS AND DISCUSSION

Exploration of Small Molecule NF-κB Inhibitors *in vitro*

To begin exploring alternative NF-κB inhibitors, we examined the literature for promising candidates. Due to the strong correlation between NF-κB activation and sepsis (8), cancer (9, 10) and autoimmune disorders (11), a large library of NF-κB inhibitors have been identified (12). Small molecule NF-κB inhibitors often do not act on the NF-κB subunits themselves, but rather inhibit particular proteins in the NF-κB pathway, upstream of NF-kB translocation to the nucleus (see **Supplementary Table S1**). We first wanted to analyze the potential of a variety small molecule NF-κB inhibitors to inhibit inflammation *in vitro* in combination with lipopolysaccharide (LPS), a TLR4 agonist. We chose several common commercially available NF-κB inhibitors and tested them in RAW macrophages. We chose to examine: Cardamonin (40 μM), Caffeic acid phenethyl ester (CAPE) (100 μM), Withaferin A (WA) (400 nM), Resveratrol (10 μM), Salicin (100 nM), 5Z-7-Oxozeaenol (5-z-O) (5 μM), Parthenolide (20 μM), Honokiol (20 μM), Capsaicin (200 μM), PDK1/Akt/Flt dual pathway inhibitor (PDK1) (1 μM), and GYY 4137 (GYY) (200 μM). To determine if immune potentiation was specific to NF-κB or general to all anti-inflammatory molecules, we included the most common FDA approved anti-inflammatory drugs, acetaminophen (10 mM) and ibuprofen (800 μM) (13, 14). We treated RAW macrophages with inhibitors and LPS and assayed the supernatant for IL-6 secretion (**Figure 1A**). CAPE, WA, 5-z-O, honokiol and capsaicin demonstrated the greatest reduction in IL-6 levels.

Exploration of Small Molecule NF-κB Inhibitors *in vivo*

We next wanted to examine how these inhibitors would alter safety and protection *in vivo*. To test this *in vivo*, we chose three of the small molecule inhibitors that were the most effective at inhibiting IL-6 expression *in vitro*, capsaicin, honokiol and withaferin A (WA) and ran them alongside acetaminophen and ibuprofen. We chose to vaccinate mice using CpG, a TLR9 agonist. For our *in vivo* vaccination, we used ovalbumin (OVA) as a model antigen to examine the changes in humoral response. We vaccinated mice with 100 μg OVA, 50 μg CpG, and inhibitor (800 μg ibuprofen, 2 mg acetaminophen, 400 μg honokiol, 20 μg capsaicin or 600 μg WA). Due to the difficulty in solubility of the inhibitors, all vaccines were formulated in Addavax, a squalene-based oil-in-water nano-emulsion, to enable effective vaccine suspensions. To enable comparison between groups PBS and CpG controls were also formulated in Addavax. We chose to analyze systemic levels of TNF-α and IL-6 because high levels of these cytokines are pyrogenic and have been correlated with undesirable vaccine-related side effects (15–17). We previously determined that CpG-induced TNF-α and IL-6 peak at 1 h post-vaccination (5). Mice vaccinated with CpG demonstrated high levels of TNF-α (1067 pg/mL) (**Figure 1B**). Addition of an NF-κB inhibitor decreased the level of TNF-α. Ibuprofen decreased to the mean level of TNF-α to 738 pg/mL (1.4 fold), acetaminophen 584 pg/mL (1.8 fold), honokiol 464 pg/mL (2.3 fold), capsaicin 38 pg/mL (28 fold, equivalent to background levels), and WA 580 pg/mL (1.8 fold). The systemic levels of IL-6 were also high with CpG vaccination (941 pg/mL). The groups that included an NF-κB inhibitor did not always decrease the level of IL-6 (**Figure 1C**). Ibuprofen, acetaminophen and WA did not alter the cytokine profile statistically significantly compared to CpG alone. Ibuprofen (1001 pg/mL) increased the level of IL-6 by 1.06 fold. Acetaminophen (866 pg/mL) decreased the level by 1.08 fold. WA increased the level of IL-6 to 967 pg/mL (1.02 fold increase). However, honokiol and capsaicin dramatically reduced the systemic levels of IL-6 to 206 pg/mL (3.5 fold) and 47 pg/mL (20 fold), respectively.

To broadly establish how the addition of these inhibitors impacts the antibody levels, we chose to analyze the total Ig (G+A+M) produced after 21 days (18). On day 21, we analyzed the anti-OVA antibody levels (**Figure 1D**). CpG was 1.6 fold (2312 U/mL) higher than PBS (1365 U/mL). Ibuprofen (708 U/mL) and acetaminophen (955 U/mL) were 3.2 and 2.4 fold lower that CpG alone. CpG + honokiol (12286 U/mL) was 5.3 fold more than CpG alone. CpG + capsaicin (8413 U/mL) was 3.6 fold higher than CpG alone. CpG + WA (3459 U/mL) was 1.5 fold higher than CpG alone.

These results demonstrate that honokiol and capsaicin are capable of both mitigating the systemic proinflammatory cytokines, TNF-α and IL-6, while also increasing the adaptive humoral response. WA demonstrated a decrease of systemic TNF-α while maintaining a similar antibody level as CpG alone. We were unable to formulate vaccines using CAPE and 5-z-O due to solubility issues; however, we believe they are worth exploring in future studies using alternative formulations.

Dose-Dependence of Capsaicin and Honokiol

Of the candidates, Capsaicin and honokiol demonstrated exceptional promise in these studies so we examined them further. To better understand how these molecules are altering the immune response over time, we vaccinated mice as described above and analyzed a larger variety of cytokines at various timepoints. We analyzed 13 cytokines: IL-1α, IL-1β, IL-6, IL-10, IL-12p70, IL-17A, IL-23, IL-27, MCP-1, IFN-β, IFN-γ, TNF-α, and GM-CSF. Of these, only six cytokines demonstrated detectable levels in our assay: TNF-α, IL-6, IL-10, IL-1α, MCP-1, and IFN-γ (**Figures 2A–F**). Consistent with our previous findings (5), CpG induced TNF-α and IL-6 expression peaked

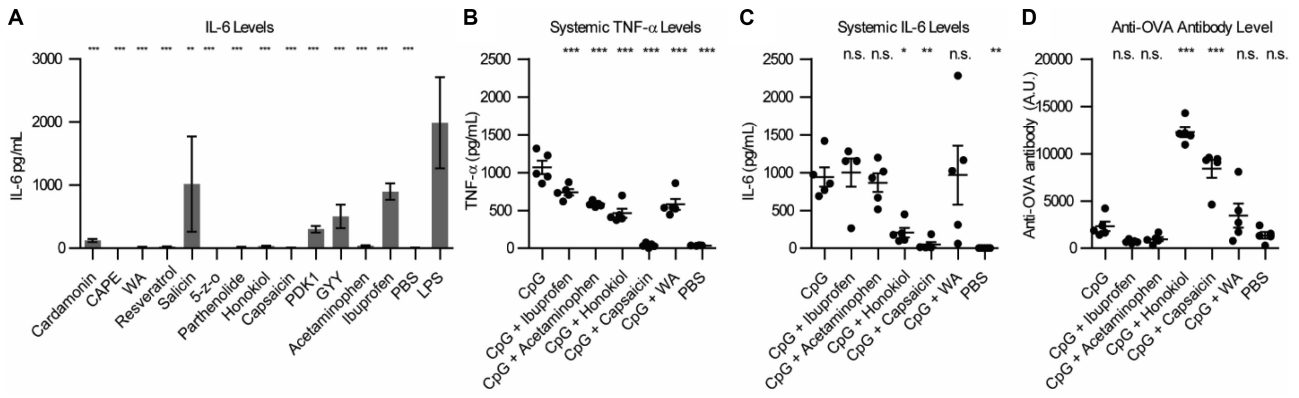

FIGURE 1 | Small molecule inhibitor screen *in vitro* and *in vivo*. **(A)** IL-6 levels from RAW macrophages 24 h post-stimulation with NF-κB inhibitor and LPS. Significance is compared to LPS alone, $n = 3$. **(B)** Systemic TNF-α expression 1 h post-vaccination, $n = 5$. **(C)** Systemic IL-6 expression 1 h post-vaccination, $n = 5$. **(D)** Anti-OVA antibody level 21 days post-vaccination, $n = 5$. Significance is compared to CpG vaccination. $^{*}p < 0.05$, $^{**}p < 0.01$, $^{***}p < 0.001$.

at 1 h. Interestingly, CpG combined with either capsaicin or honokiol had increased IFN-γ levels at 24 h compared to CpG alone (8 fold and 9 fold, respectively) and slightly elevated MCP-1 levels (2.5 and 2 fold, respectively), demonstrating that both capsaicin and honokiol are acting to potentiate the immune response and are not simply suppressing immune activation. We next wanted to understand how changing the dose would alter innate and adaptive humoral immune responses. For honokiol, we tested a concentration 2-fold higher (800 μg) and 2-fold lower (200 μg) than the original dose (400 μg). Mice vaccinated with our original dose of capsaicin (20 μg) appeared lethargic for 30 min post-injection, therefore we wanted to examine if we could lower the dose, but maintain adequate anti-inflammatory activity and antibody-boosting potential. We chose to test a dose 4-fold lower (5 μg) and 20-fold lower (1 μg) than the original dose (20 μg). Unfortunately, mice vaccinated with all doses of capsaicin appeared lethargic post-injection, however, mice vaccinated with the lowest dose of capsaicin (1 μg) only appeared lethargic for ten minutes. All doses of honokiol demonstrated a significant decrease in TNF-α expression compared to CpG alone, however, there was no significant difference between the different doses (**Figure 2G**). Capsaicin decreased TNF-α levels significantly across all doses compared to CpG alone. Capsaicin doses of 5 and 20 μg decreased levels of TNF-α significantly more than 1 μg (**Figure 2G**). The level of IL-6 was only decreased with 400 μg and 800 μg honokiol and 20 μg capsaicin (**Figure 2H**). Twenty-one days later, we analyzed differences in anti-OVA antibody level and found that all doses of honokiol increased levels of anti-OVA antibodies compared to CpG alone and the highest level was found with 400 μg honokiol (**Figure 2I**). 1 μg and 5 μg of capsaicin did not change level of anti-OVA antibodies in the serum compared to CpG alone, however, 20 μg significantly increased serum levels. These results indicate that honokiol can only limit TNF-α and IL-6 to a certain extent at which higher doses do not provide additional decreases in these systemic inflammatory cytokines. Additionally, the highest dose of honokiol decreased the antibody level, indicating that there is an optimal dose at which this inhibitor can function as an immune potentiator. Capsaicin demonstrated a dose-dependent response, where higher doses of capsaicin led to lower systemic TNF-α and IL-6 levels and higher antibody levels. This would point to a very promising candidate as an immune potentiator, however, these mice experienced other undesirable side effects (lethargy).

Determining the TRPV1-Mediated Effects of Capsaicin

The primary *in vivo* target for capsaicin is the transient receptor potential cation channel subfamily V member 1 (TRPV1). TRPV1 modulates the immune response in a variety of ways, and importantly, has been implicated in dampening systemic inflammation associated with sepsis (19–23). However, it has never been explored in a vaccine setting. To understand how activation of TRPV1 may be modulating the effects of the adjuvant, we compared the immediate inflammatory response of the vaccination in wild type mice (WT) and TRPV1 knockout mice. We vaccinated WT and TRPV1 KO mice with 100 μg OVA and: 50 μg CpG, 50 μg CpG + 20 μg capsaicin or PBS. We analyzed systemic levels of TNF-α and IL-6 1 h after vaccination. We found that CpG induced high levels of TNF-α and IL-6 in both WT and TRPV1 KO mice. Addition of capsaicin dramatically and significantly reduced both TNF-α levels and IL-6 levels in the WT mice (**Figures 3A,B** and **Supplementary Figure S1**). Although the mean was slightly lower for both TNF-α and IL-6 in the TRPV1 KO mice, these differences were not statistically significant. This demonstrated that TRPV1 activation is responsible for the capsaicin-induced decrease in systemic cytokine levels. As expected, the TRPV1 KO mice did not experience the lethargy experienced by the WT mice in response to capsaicin, indicating that activation of TRPV1 is responsible for this response. To examine if the increased antibody level was due to TRPV1 activation on day 21, we analyzed levels of anti-OVA antibodies in the serum (**Figure 3C** and **Supplementary Figure S1**). Interestingly, we found that anti-OVA antibody levels were increased in groups with Capsaicin + CpG in both WT

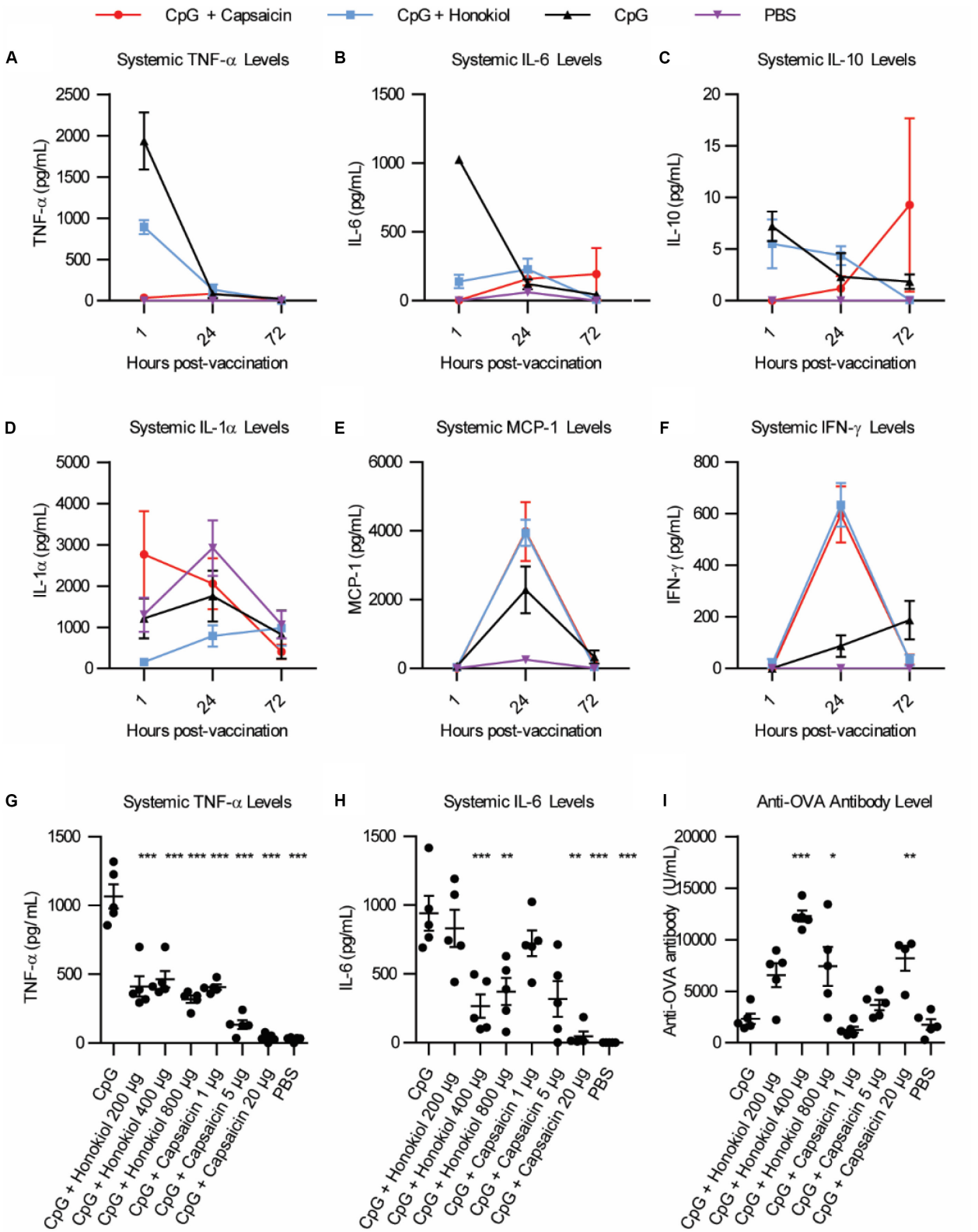

FIGURE 2 | Broader cytokine response and dose effects of honokiol and capsaicin. **(A–F)** Systemic cytokine levels at 1, 24, and 48 h post-vaccination, $n = 5$. CpG (black line), CpG + Capsaicin (red line), CpG + Honokiol (blue line), PBS (purple line) **(G)** Systemic TNF-α levels 1, 24, and 72 h post-vaccination with varying doses of honokiol and capsaicin, $n = 5$. **(H)** Systemic IL-6 levels 1 h post-vaccination, $n = 5$. **(I)** Anti-OVA antibody levels 21 days post-vaccination, $n = 5$. Significance is compared to CpG alone. $^{*}p < 0.05$, $^{**}p < 0.01$, $^{***}p < 0.001$.

and KO mice. This implies that the antibody-boosting activity of capsaicin is separate from TRPV1-dependent decrease in inflammatory cytokines. This result demonstrates both that the decrease in inflammation is not responsible for the antibody-boosting activity of the NF-κB inhibitor and also that the enhancement of the adaptive humoral response is independent of TRPV1 activation. These results, while not definitive, showed two separate, but correlated mechanisms for capsaicin that result in the reduction in cytokines and increase antibody levels. As such, capsaicin did not warrant further examination as a potential clinical immune potentiator. We will explore the mechanistic implications of this for immune potentiators more broadly in future publications.

Synthesis of Honokiol Derivative Library

With capsaicin possessing two parallel mechanisms and possessing well-established side effects (24), we wanted to explore honokiol for further development as a candidate. Oral intake of honokiol has been well studied in humans and has been established as safe with little to no side effects (25). However, it is subject to glucuronidation, leading to fast clearance (25). Additionally, vaccines for various diseases may require diverse potentiator activities. An important question for immune potentiators and honokiol was if standard SAR methods would yield alteration in potentiation activity. We wanted to investigate if compound libraries of promising immune potentiator candidates could be synthesized and provide alterations to activity. To further explore this idea, we synthesized a library of honokiol derivatives. Honokiol derivative libraries have been synthesized previously and examined for their effects on neuroprotection (26), antimicrobial agents (27) and anti-cancer (28) among others (29, 30). However, to date no such study has examined the effects of honokiol analogs on vaccines or a combination of anti-inflammatory activity and adaptive humoral immune response. Phenylphenols and biphenols were prepared using Pd-catalyzed Suzuki coupling using corresponding iodophenols and hydroxyphenylboronic acids as starting materials. These compounds were *O*-allylated using allylBr. Resulting compounds were subjected to Claisen rearrangement using diethyl aluminum chloride to yield a variety of ring substitutions (**Scheme 1** and **Figure 4A**).

We analyzed how the honokiol derivatives altered IL-6 production in RAW macrophages. We chose to analyze the

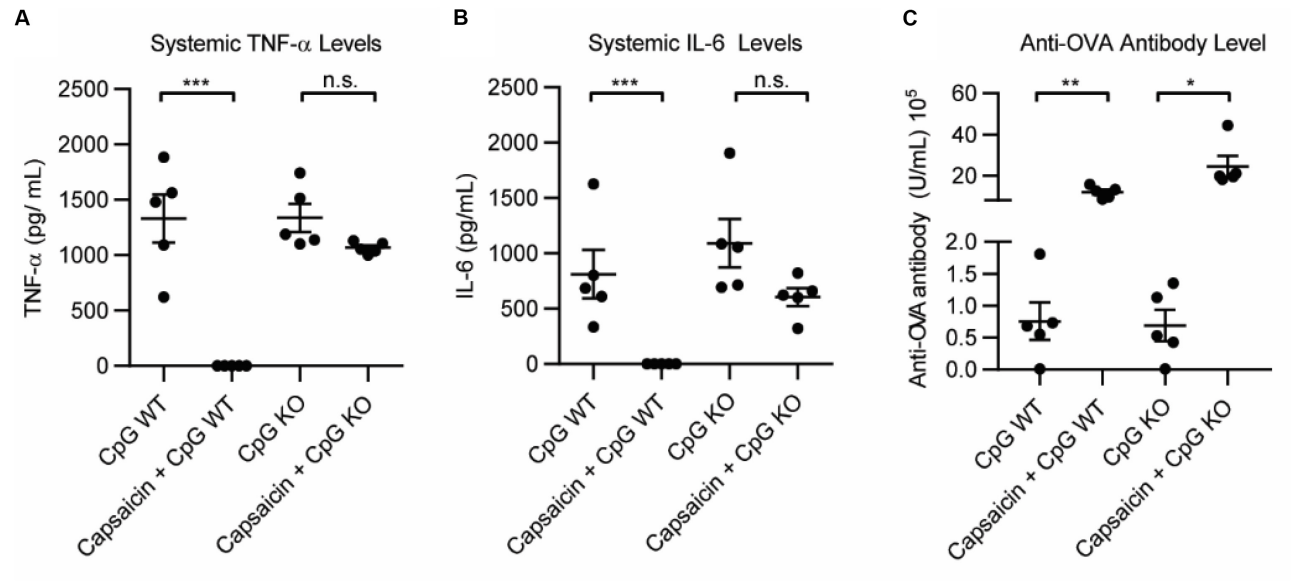

FIGURE 3 | Role of TRPV1 of capsaicin induced anti-inflammatory and immune potentiation. **(A)** Systemic TNF-α levels 1 h post vaccination in wild type (WT) mice and TRPV1 KO (KO), $n = 5$. **(B)** Systemic IL-6 levels 1 h post-vaccination, $n = 5$. **(C)** Anti-OVA antibody level 21 days post-vaccination, $n = 5$. $^{*}p < 0.05$, $^{**}p < 0.01$, $^{***}p < 0.001$.

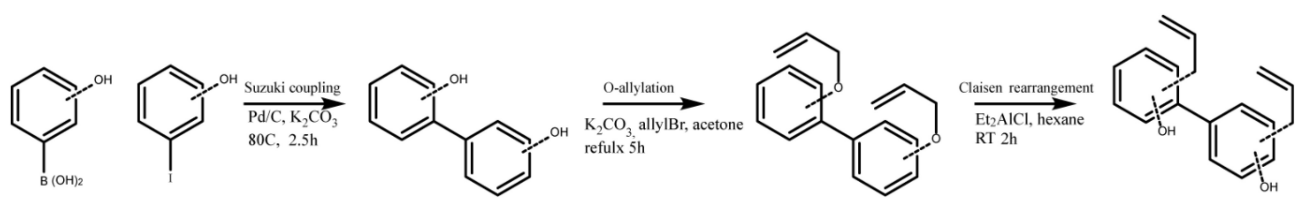

SCHEME 1 | Honokiol derivative synthesis.

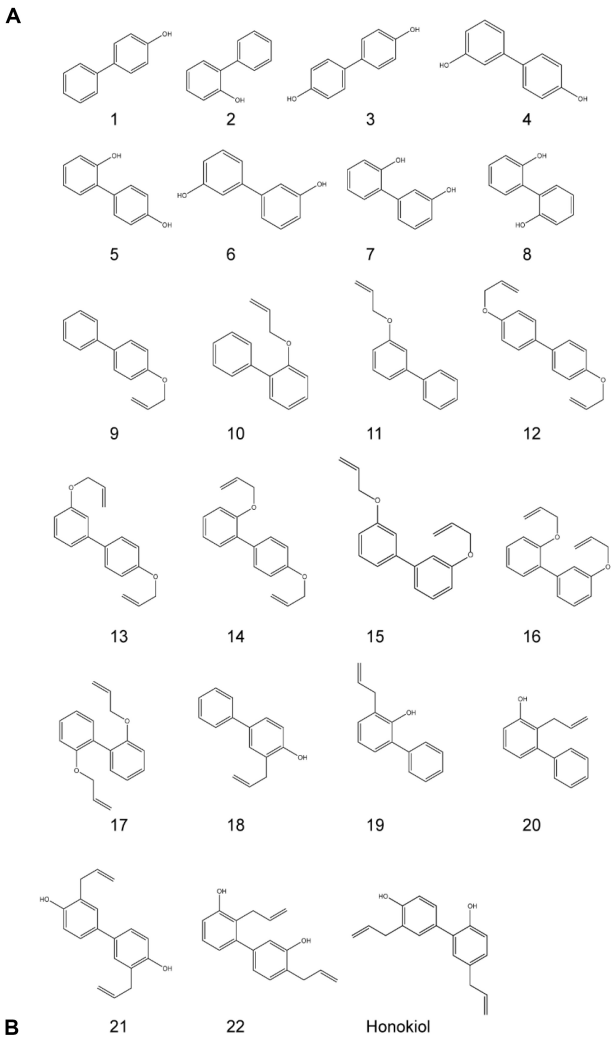

FIGURE 4 | Honokiol derivatives and their inhibitory activity on IL-6 expression. **(A)** Honokiol derivative library **(B)** IL-6 expression of RAW macrophages treated with honokiol derivatives and LPS, $n = 3$. Significance is compared to LPS alone. $^{**}p < 0.01$, $^{***}p < 0.001$.

hydroxybiphenyls and *O*-allylated derivatives in addition to the product from the Claisen rearrangement to understand how these functional groups play a role in the anti-inflammatory action or increase in adaptive immune response (**Figure 4B** and **Supplementary Figures S2, S3**). We treated RAW macrophages with honokiol derivatives and LPS and analyzed IL-6 expression. The addition of LPS alone without a honokiol derivative gave high levels of IL-6 expression (6848 pg/mL). The addition of honokiol decreased IL-6 levels to 260 pg/mL, a decrease of 26-fold. Several derivatives including compounds: **1**, **2**, **3**, **4**, **8**, and **11** demonstrated similar reductions in IL-6 expression *in vitro* making them promising candidates for *in vivo* analysis. As a small molecule, honokiol impacts multiple pathways aside from NF-κB such as: STAT3, EGFR, mTOR, and caspase-mediated common pathways (31). It is probable that alterations to the structure will impact which pathways are modulated, altering the downstream response. It is likely that different vaccine formulations will require potentiators with unique modulatory characteristics as well as pharmacokinetic/pharmacodynamic properties. Compounds lacking a free hydroxyl group (such as **11**) are unable to form glucuronide conjugates, potentially extending the half-life. Here we demonstrated that compound libraries can be synthesized and screened in vitro for immune activity and that alterations to the structure change the downstream response. Such libraries could be used for improving rational design of future immune potentiators through machine learning. In future studies we will explore the effects of these inhibitors *in vivo*.

CONCLUSION

In summary, we present that select small molecule inhibitors of NF-κB can decrease the inflammatory effects of adjuvanted vaccination – potentially enabling safer vaccination while also acting as immune potentiators and increasing the antibody level. We identified two such immune potentiators, honokiol and capsaicin that effectively decrease inflammation while increasing the adaptive humoral response. We additionally provide evidence that implies that the decrease in inflammation is separate from the increase in antibody response, potentially enabling distinct tunability of either response. This study also identifies that only select NF-κB inhibitors can be used as immune potentiators, this broadens the potential for further modulation of the immune response. We additionally synthesized and examined a library of honokiol derivatives and found that several honokiol derivatives are promising candidates for future testing *in vivo*. In the future, this information can be used in modern screening methods involving machine learning to identify better immune potentiators. The use of combining NF-kB inhibitors with vaccine adjuvants could find use in creating next-generation prophylactic vaccines and immunotherapy applications. In conclusion, we have demonstrated that using small molecule NF-κB inhibitors in combination with common immune adjuvants can decrease the production of pro-inflammatory cytokines TNF-α and IL-6 while boosting antibody levels.

MATERIALS AND METHODS

In vitro Assays

RAW Macrophage Cytokine Analysis

RAW 264.7 macrophages were passaged and plated in a cell culture treated 12- well plate at 0.5×10^6 cells/well in 1 mL DMEM containing 10% FBS. Cells were grown for 2 days.

Media was exchanged for 1 mL DMEM containing 10% HIFBS. Inhibitors were diluted in Addavax and then in PBS. Inhibitors were added at indicated concentrations and incubated for 45 min. After 45 min, LPS was added at 100 ng/mL and incubated at 37°C and 5% CO_2 for 24 h. Cell supernatant was removed and analyzed using BD Cytometric Bead Array Mouse Inflammation Kit.

Cell Viability Assay

RAW macrophages were plated at 100 k cells/well in 180 uL DMEM/10% HIFBS. Inhibitors were diluted as described above and added at indicated concentrations and incubated for 45 min. After 45 min, LPS was added to a final concentration of 100 ng/mL and incubated at 37°C and 5% CO_2 for 24 h. MTT reagent was made fresh at a concentration of 5 mg/mL in PBS and sterile filtered. 150 μL cell supernatant was removed and 150 μL PBS was added. 10 μL MTT reagent was added to each well and incubated at 37°C and 5% CO_2 for 2 h. 150 μL supernatant was removed from each well and replaced with 150 μL DMSO and incubated at 37°C and 5% CO_2 for 1 h or until purple crystals dissolved. Plate was analyzed using Multiskan FC plate reader (Thermo Fisher Scientific) and absorbance was measured at 450 nm. Data was analyzed using Graphpad Prism.

Flow Cytometry

RAW macrophages (2×10^6) were plated in a 12 well plate in DMEM/10% HIFBS. Inhibitors were diluted as described above and added at indicated concentrations and incubated for 45 min. After 45 min, LPS was added to a final concentration of 100 ng/mL and incubated at 37°C and 5% CO_2 for 24 h. Cells were stained for CD86 using BD cytofix/cytoperm fixation/permeabilization solution kit according to manufacturer's protocol. Cells were analyzed using NovoCyte flow cytometer (ACEA Biosciences, Inc).

In vivo Assays

All animal procedures were performed under a protocol approved by the University of Chicago Institutional Animal Care and Use Committee (IACUC). 6–8 week-old C57/B6 female mice were purchased from Jackson Laboratory (JAX). 6–8 week-old C57/B6 female $Trpv1^{tm1Ju}$ mice were purchased from JAX for TRPV1 KO experiment. All compounds were tested for endotoxin prior to use. All vaccinations were administered intramuscularly in the hind leg. Blood was collected from the submandibular vein at time points indicated.

Antigens were purchased from Invitrogen (VacciGrade Ovalbumin). VacciGrade CpG ODN 1826 was purchased from Adipogen. AddaVax™ was purchased from Invivogen.

Vaccination

Mice were lightly anesthetized with isoflurane and injected intramuscularly in the hind leg with 50 μL containing ovalbumin (100 μg), adjuvant, inhibitor and PBS. Adjuvant doses: CpG, 50 μg. Inhibitor concentrations: Honokiol (400 μg), Capsaicin (20 μg), Withaferin A (600 μg), acetaminophen (2 mg), ibuprofen (800 μg). All vaccines contained 25 μL AddaVax™ to enhance solubility.

Plasma Cytokine Analysis

Blood was collected from mice at time points indicated in 0.2 mL heparin coated collection tubes (VWR Scientific). Serum was isolated via centrifugation 2000 × *g* for 5 min. Supernatant was collected and stored at −80°C until use. Serum was analyzed using BD Cytometric Bead Array Mouse Inflammation cytokine kit or LEGENDplex™ Mouse Inflammation Panel (Biolegend) according to manufacturer's protocol.

Antibody Quantification

Mice were vaccinated with indicated formulations. Blood was collected at time points indicated in 0.2 mL heparin coated collection tubes (VWR Scientific) for plasma or uncoated tubes for serum. Plasma was isolated via centrifugation (2000 × *g*, 5 min). Serum was isolated by allowing blood to clot for 15–30 min RT and centrifuging (2000 × *g* for 10 min) at 4°C. Serum was analyzed using a quantitative anti-ovalbumin total Ig's ELISA kit (Alpha Diagnostic International) according to the specified protocol. Data was analyzed using Graphpad Prism.

Chemistry

Conditions for Suzuki Coupling

Hydroxyphenylboronic acid (20 mmol) was dissolved in 100 mL water. Appropriate iodophenol (10 mmol) and K_2CO_3 (40 mmol) was added followed by Pd/C (2 mol %). Solution heated to 80 C for 3 h. Solution was acidified with 1M HCl and extracted with EtOAc and washed with brine. Solvent evaporated in vacuo. Compound was purified by column chromatography.

Conditions for O-Allylations

Phenol (1 mmol) (Derivative **1**–**8**) was dissolved in dry acetone (5 mL) and K_2CO_3 (2 mmol) added. AllylBr was added dropwise and refluxed. Reaction was monitored by TLC until completion (5–12 h). Reaction mixture was cooled and volatiles were removed in vacuo. 10% NaOH was added to the mixture and extraction was performed using ethyl acetate, washed with brine and organic layers dried using $MgSO_4$. Solvent was removed in vacuo affording an oily material that was purified by column chromatography to yield the O-allylated derivative.

Conditions for Claisen Rearrangement

O-allylated derivatives (**9**–**17**) (1 mmol) were dissolved in dry hexane (10 mL). Et_2AlCl in dry hexane (4 mL) was added dropwise under argon. Mixture was stirred at room temperature for 2 h. The mixture was cooled on an ice bath and quenched using 2M HCl (20 mL). Extraction was performed with EtOAc, washed with brine and dried over MgSO4. Solvent was removed in vacuo affording an oily material that was purified by column chromatography to yield the C-allyl derivative.

Statistics and Replicates

Data is plotted and reported in the text as the mean ± s.e.m. Sample size is as indicated in biological replicates in all *in vivo* and *in vitro* experiments. The sample sizes were chosen based on

preliminary experiments or literature precedent indicating that the number would be sufficient to detect significant differences in mean values should they exist. *P*-values were calculated using a one-way ANOVA and Tukey *post hoc* test. All experiments have been repeated (sometimes with minor variations due to reagents and materials) and replication was successful.

AUTHOR'S NOTE

This manuscript has been released as a Pre-Print at ChemRxiv (32).

DATA AVAILABILITY STATEMENT

All datasets generated for this study are included in the article/**Supplementary Material**.

ETHICS STATEMENT

The animal study was reviewed and approved by the University of Chicago IACUC.

AUTHOR CONTRIBUTIONS

BM and AE-K conceived of and designed the project and experiments, and wrote the manuscript. BM, YE-B, RS, MR, BC, MN, and NT performed the experiments. BM synthesized the materials. BM, NN, and AC performed the compound characterization. All authors contributed to the article and approved the submitted version.

FUNDING

We would like to acknowledge support by the NIH (1U01Al124286-01 and 1DP2Al112194-01, GM099594). AE-K thanks the Pew Scholars Program and the Cottrell Scholars Program for generous support. BM thanks NSF-GRFP (DGE-1321846). BC thanks NSF-GRFP (DGE-1746045). We would also like to thank NSF instrumentation grant CHE-1048528. This work was supported, in part, by a grant from the Alfred P. Sloan Foundation.

SUPPLEMENTARY MATERIAL

The Supplementary Material for this article can be found online at: https://www.frontiersin.org/articles/10.3389/fimmu.2020.511513/full#supplementary-material

REFERENCES

1. Coffman RL, Sher A, Seder RA. Vaccine adjuvants: putting innate immunity to work. *Immunity*. (2010) 33:492–503. doi: 10.1016/j.immuni.2010.10.002
2. Audibert FM, Lise LD. Adjuvants: current status, clinical perspectives and future prospects. *Trends Pharmacol Sci*. (1993) 14:174–8. doi: 10.1016/0165-6147(93)90204-w
3. Bhardwaj N, Gnjatic S, Sawhney NB. TLR AGONISTS: are they good adjuvants? *Cancer J*. (2010) 16:382–91.
4. Tom JK, Albin TJ, Manna S, Moser BA, Steinhardt RC, Esser-Kahn AP. Applications of immunomodulatory immune synergies to adjuvant discovery and vaccine development. *Trends Biotechnol*. (2019) 37:373–88. doi: 10.1016/j.tibtech.2018.10.004
5. Moser B, Steinhardt R, Escalante-Buendia Y, Boltz D, Barker K, Yoo S, et al. Increased vaccine tolerability and protection via NF-kB modulation. *Sci. Adv*. (2020) 6:eaaz8700. doi: 10.1126/sciadv.aaz8700
6. Lau JL, Dunn MK. Therapeutic peptides: historical perspectives, current development trends, and future directions. *Bioorgan Med Chem*. (2018) 26:2700–7. doi: 10.1016/j.bmc.2017.06.052
7. Otvos L, Wade JD. Current challenges in peptide-based drug discovery. *Front Chem*. (2014) 2:62. doi: 10.3389/fchem.2014.00062
8. Shimaoka M, Park EJ. Advances in understanding sepsis. *Eur J Anaesthesiol*. (2008) 25:146–53. doi: 10.1017/s0265021507003389
9. Dolcet X, Llobet D, Pallares J, Matias-Guiu X. NF-kB in development and progression of human cancer. *Virchows Arch*. (2005) 446:475–82. doi: 10.1007/s00428-005-1264-9
10. Xia Y, Shen S, Verma IM. NF-κB, an active player in human cancers. *Cancer Immunol Res*. (2014) 2:823–30. doi: 10.1158/2326-6066.cir-14-0112
11. Bacher S, Schmitz ML. The NF-kB pathway as a potential target for autoimmune disease therapy. *Curr Pharm Des*. (2004) 10:2827–37. doi: 10.2174/1381612043383584
12. Gilmore TD, Herscovitch M. Inhibitors of NF-κ B signaling: 785 and counting. *Oncogene*. (2006) 25:6887–99. doi: 10.1038/sj.onc.1209982
13. Scheuren N, Bang H, Münster T, Brune K, Pahl A. Modulation of transcription factor NF-κB by enantiomers of the nonsteroidal drug ibuprofen. *Br J Pharmacol*. (1998) 123:645–52. doi: 10.1038/sj.bjp.0701652
14. Boulares AH, Giardina C, Inan MS, Khairallah EA, Cohen SD. Acetaminophen inhibits NF-kappaB activation by interfering with the oxidant signal in murine Hepa 1-6 cells. *Toxicol Sci*. (2000) 55:370–5. doi: 10.1093/toxsci/55.2.370
15. Christian LM, Porter K, Karlsson E, Schultz-Cherry S. Proinflammatory cytokine responses correspond with subjective side effects after influenza virus vaccination. *Vaccine*. (2015) 33:3360–6. doi: 10.1016/j.vaccine.2015.05.008
16. Simon WL, Salk HM, Ovsyannikova IG, Kennedy RB, Poland GA. Cytokine production associated with smallpox vaccine responses. *Immunotherapy*. (2014) 6:1097–112. doi: 10.2217/imt.14.72
17. Netea MG, Kullberg BJ, van der Meer JW. Circulating cytokines as mediators of fever. *Clin Infect Dis*. (2000) 31:S178–84.
18. Jung H, Kim D, Kang YY, Kim H, Lee JB, Mok H. CpG incorporated DNA microparticles for elevated immune stimulation for antigen presenting cells. *RSC Adv*. (2018) 8:6608–615. doi: 10.1039/C7RA13293J
19. Brito R, Sheth S, Mukherjea D, Rybak LP, Ramkumar V. TRPV1: a potential drug target for treating various diseases. *Cells*. (2014) 3:517–45. doi: 10.3390/cells3020517
20. Wang Y, Wang DH. TRPV1 ablation aggravates inflammatory responses and organ damage during endotoxic shock. *Clin Vaccine Immunol*. (2013) 20:1008–15. doi: 10.1128/cvi.00674-12
21. Toledo-Mauriño JJ, Furuzawa-Carballeda J, Villeda-Ramírez MA, Fonseca-Camarillo G, Meza-Guillen D, Barreto-Zúñiga R, et al. The transient receptor potential vanilloid 1 is associated with active inflammation in ulcerative colitis. *Mediat Inflamm*. (2018) 2018:6570371. doi: 10.1155/2018/6570371
22. Bodkin JV, Fernandes ES. TRPV1 and SP: key elements for sepsis outcome? *Br J Pharmacol*. (2013) 170:1279–92. doi: 10.1111/bph.12056
23. Fernandes ES, Liang L, Smillie S-J, Kaiser F, Purcell R, Rivett DW, et al. TRPV1 deletion enhances local inflammation and accelerates the onset of

systemic inflammatory response syndrome. *J Immunol*. (2012) 188:5741–51. doi: 10.4049/jimmunol.1102147

24. Winter JK, Bevan SA, Campbell EA. Capsaicin and pain mechanisms. *Br J Anaesth*. (1995) 75:157–68. doi: 10.1093/bja/75.2.157
25. Sarrica A, Kirika N, Romeo M, Salmona M, Diomede L. Safety and toxicology of magnolol and honokiol. *Planta Med*. (2018). 84:1151–164. doi: 10.1055/a-0642-1966
26. Tripathi S, Chan M-H, Chen C. An expedient synthesis of honokiol and its analogues as potential neuropreventive agents. *Bioorgan Med Chem Lett*. (2012) 22:216–21. doi: 10.1016/j.bmcl.2011.11.030
27. Kim Y-S, Lee J-Y, Park J, Hwang W, Lee J, Park D. Synthesis and microbiological evaluation of honokiol derivatives as new antimicrobial agents. *Arch Pharm Res*. (2010) 33:61–5. doi: 10.1007/s12272-010-2225-7
28. Sánchez-Peris M, Murga J, Falomir E, Carda M, Marco JA. Synthesis of honokiol analogues and evaluation of their modulating action on VEGF protein secretion and telomerase-related gene expressions. *Chem Biol Drug Des*. (2017) 89:577–84. doi: 10.1111/cbdd.12880
29. Shen J-L, Man K-M, Huang P-H, Chen W-C, Chen D-C, Cheng Y-W, et al. Honokiol and magnolol as multifunctional antioxidative molecules for dermatologic disorders. *Molecules*. (2010) 15:6452–65. doi: 10.3390/molecules15096452
30. Lee Y-J, Lee YM, Lee C-K, Jung JK, Han SB, Hong JT. Therapeutic applications of compounds in the Magnolia family. *Pharmacol Ther*. (2011) 130:157–76. doi: 10.1016/j.pharmthera.2011.01.010
31. Rauf A, Patel S, Imran M, Maalik A, Arshad MU, Saeed F. Honokiol: An anticancer lignan. *Biomed. Pharmacother*. (2018) 107:555–62. doi: 10.1016/j.biopha.2018.08.054
32. Moser B, Escalante-Buendia Y, Steinhardt RC, Rosenberger M, Cassaidy B, Naorem N, et al. Small molecule NF-kB inhibitors as immune potentiators for enhancement of vaccine adjuvants. *ChemRxiv* [Preprint] (2019). doi: 10.26434/chemrxiv.10043138.v1

Conflict of Interest: BM and AE-K are inventors on a pending patent related to this work filed by the University of Chicago (no. PCT/US19/64888, filed 16 December 2019).

The remaining authors declare that the research was conducted in the absence of any commercial or financial relationships that could be construed as a potential conflict of interest.

frontiers in Immunology

ORIGINAL RESEARCH
published: 09 December 2020
doi: 10.3389/fimmu.2020.571489

Neutrophil Inflammatory Response Is Downregulated by Uptake of Superparamagnetic Iron Oxide Nanoparticle Therapeutics

Gustavo Garcia[1], *Min-Ho Kim*[2], *Vasilios Aris Morikis*[1] *and Scott I. Simon*[1]*

[1] Department of Biomedical Engineering, University of California, Davis, Davis, CA, United States, [2] Department of Biological Sciences, Kent State University, Kent, OH, United States

Superparamagnetic iron oxide nanoparticles (SPION) are employed as diagnostics and therapeutics following intravenous delivery for the treatment of iron deficiency anemia (IDA) in adult patients with chronic kidney failure. Neutrophils are the first defense against blood borne foreign insult and recruit to vascular sites of inflammation *via* a sequential process that is characterized by adhesive capture, rolling, and shear resistant arrest. A primary chemotactic agonist presented on the glycocalyx of inflamed endothelium is IL-8, which upon binding to its cognate membrane receptor (CXCR1/2) activates a suite of responses in neutrophils. An early response is degranulation with accompanying upregulation of β2-integrin (CD11/CD18) and shedding of L-selectin (CD62L) receptors, which exert differential effects on the efficiency of endothelial recruitment. Feraheme is an FDA approved SPION treatment for IDA, but its effect on the innate immune response of neutrophils during inflammation has not been reported. Here, we studied the immunomodulatory effects of Feraheme on neutrophils freshly isolated from healthy human subjects and stimulated in suspension or on inflammatory mimetic substrates with IL-8. Cells treated with Feraheme exhibited reduced sensitivity to stimulation with IL-8, indicated by reduced upregulation of membrane CD11b/CD18 receptors, high affinity (HA) CD18, and shedding of CD62L. Feraheme also inhibited N-formyl-Met-Leu-Phe (fMLP) induced reactive oxygen species production. Neutrophil rolling, arrest, and migration was assessed in vascular mimetic microfluidic channels coated with E-selectin and ICAM-1 to simulate inflamed endothelium. Neutrophils exposed to Feraheme rolled faster on E-selectin and arrested less frequently on ICAM-1, in a manner dependent upon SPION concentration. Subsequent neutrophil shape change, and migration were also significantly inhibited in the presence of Feraheme. Lastly, Feraheme accelerated clearance of cytosolic calcium flux following IL-8 stimulation. We conclude that uptake of Feraheme by neutrophils inhibits chemotactic activation and downregulates normal rolling to arrest under shear flow. The mechanism involves increased calcium clearance following chemotactic activation, which may diminish the efficiency of recruitment from the circulation at vascular sites of inflammation.

Keywords: neutrophil recruitment, nanoparticle, iron oxide, inflammation, neutrophil degranulation, mechanosignaling, immunosupression, innate immunity

OPEN ACCESS

Edited by:
Ankur Singh,
Georgia Institute of Technology,
United States

Reviewed by:
Payel Sil,
National Institute of Environmental Health Sciences (NIEHS),
United States
Indira Neeli,
University of Tennessee Health Science Center (UTHSC),
United States

***Correspondence:**
Scott I. Simon
sisimon@ucdavis.edu

Specialty section:
This article was submitted to Molecular Innate Immunity, a section of the journal Frontiers in Immunology

Received: *11 June 2020*
Accepted: *19 October 2020*
Published: *09 December 2020*

Citation:
Garcia G, Kim M-H, Morikis VA and Simon SI (2020) Neutrophil Inflammatory Response Is Downregulated by Uptake of Superparamagnetic Iron Oxide Nanoparticle Therapeutics. Front. Immunol. 11:571489. doi: 10.3389/fimmu.2020.571489

INTRODUCTION

Superparamagnetic iron oxide nanoparticles (SPION) are used as contrast agents for magnetic resonance imaging (MRI) in the liver, central nervous system, gastrointestinal system, and in macrophages (1). SPION have also found clinical use as an FDA approved treatment of cancer (i.e., Nanotherm) and iron deficiency anemia (IDA) in patients with chronic kidney disease (CKD) (i.e., Feraheme) (1). While SPION have been used for various clinical applications, a primary consideration for any biomaterial based therapeutic is the host immune response elicited by the interaction of the biomaterial with blood cells. The increased use of SPION has raised concerns over their safety, with several formulations showing cytotoxic and immunotoxic effects (2). This motivated the current study to examine the systemic effects of Feraheme on neutrophils in human blood.

The innate immune system is by design able to recognize and eliminate foreign pathogens and particulate matter through pattern recognition receptors and opsonin receptors that sound the alarm upon detection of danger signals (3). Opsonization involves the binding of molecules such as antibodies or proteins of the complement system that enhances recognition and removal *via* endocytosis and phagocytosis of foreign matter by innate immune cells (4). As nanoparticles enter the blood stream, complement and other proteins immediately adsorb to the particle surface forming a corona (5). Physiochemical properties of nanoparticles have a direct influence on the composition and formation of the protein corona in such a manner to impact particle-cell interactions (6). Induction of immune hypersensitivity reaction in patients prompted FDA to cancel clinical use of the SPION Feridex and GastroMARK (7, 8). Further, studies have shown that SPION can induce oxidative stress and cell damage *in vitro* and in animal models (9, 10). Upon binding to the plasma membrane and endocytosis, nanoparticles can induce a variety of functional responses in neutrophils such as reactive oxygen species (ROS) and chemokine production that vary with different SPION formulations. While some SPION can induce these immune responses, others exert an inhibitory effect, thereby highlighting composition as a key factor when considering nanoparticle use as a therapeutic (2, 11). Conventional wisdom is that nanoparticle clearance is mediated by macrophages; however, recent studies indicate that neutrophils also play a key role in particle clearance and this process has been exploited to deliver therapeutic nanoparticles to tumors for cancer therapy (12, 13). Current literature on the immune effects of SPION have largely focused on monocytes and macrophages. This has resulted in an incomplete understanding of the full scope of SPION immune effects on neutrophil function (14).

Neutrophils are the most common leukocyte in blood circulation and are essential first responders during inflammation. Thus, intravenous administration of nanoparticles is likely to result in frequent neutrophil-particle interactions. Capture of SPION onto the plasma membrane and subsequent endocytosis can perturb the inflammatory response and recruitment of neutrophils to sites of inflammation. Dysregulation of neutrophil activation and recruitment is implicated in various autoimmune and inflammatory diseases (15). Failure of neutrophils to normally adhere to the endothelium and become activated can cause severe impairment of host defense against pathogens, while inappropriate levels of cell recruitment and activation leads to chronic inflammation and tissue damage (16, 17). There are reports of the capacity for coated (Polyacrylic acid) and non-coated iron oxide nanoparticles and metal oxide nanoparticles TiO2, CeO2, and ZnO, to induce ROS production and activate neutrophil degranulation (18, 19). Excessive release of neutrophil granules, which contain chemokine and integrin receptors, elastase, collagenase, and myeloperoxidase, along with overproduction of ROS can lead to inflammatory tissue injury (20, 21). Uptake of gold nanoparticles has been linked to endoplasmic reticulum stress and cleavage of cytoskeletal proteins in human neutrophils leading to apoptosis (22). Further, nano and micro particles have been reported to inhibit the recruitment of neutrophils from the circulation to sites of inflammation in mice and to cause a reduction in neutrophil attachment to endothelial monolayers in vascular mimetic flow channels (23, 24). The fine balance between the protective functions of neutrophils that maintain immune competence versus exuberant response that can result in tissue and organ damage has prompted the current studies on neutrophil activation and inflammatory recruitment in the presence of Feraheme. Intravenous infusion with Feraheme for delivery of complexed iron is FDA approved at a higher single dose than other products on the market (25). A typical treatment regime consists of two 510-mg doses separated by 5–8 days as compared to other products that require between 5 and 10 individual doses, thereby limiting the need for repeated infusion which typically lowers patient compliance. Feraheme also is approved for infusion at higher rates than other iron products with comparable safety (25, 26). The increased application of Feraheme in anemia patients who can receive frequent intravenous injections as a course of therapy highlight a need to understand the effects of SPION on neutrophils and their capacity to maintain normal immunosurveillance.

In the current study, we examined the effects of Feraheme on neutrophil degranulation and alterations in receptor expression and conformation on the plasma membrane. We hypothesized that neutrophil uptake of Feraheme in blood alters the normal process of adhesion receptor activation, shear stress resistant neutrophil rolling to arrest and subsequent shape change that precedes cell migration. Vascular mimetic flow channels were employed to assess the kinematics of neutrophil interactions on a substrate of recombinant E-selectin and ICAM-1 in an established model of endothelial inflammation. Feraheme in suspension inhibited neutrophil activation and degranulation induced by IL-8 stimulation, resulting in alteration in the expression of adhesion molecules necessary for the efficient recruitment on inflamed endothelium.

MATERIALS AND METHODS

Small Molecules, Antibodies, and Other Reagents

Monoclonal antibodies for flow cytometric detection of high affinity β2-integrin (mAb24), L-Selectin (Dreg-55, Dreg-56), CD11b (M170), CD18 (1B4), CD66b (G10F5) CD11a (HI111), PSGL-1 (PL-2, KPL-1), CXCR1(8F1/CXCR1), and CXCR2 (5E8/CXCR2)

along with antibodies that block CD11b function (Mac-1 blocking, M1/70), fixation buffer, and IL-8 were purchased from Biolegend (San Diego, CA). Recombinant human ICAM-1-IgG and E-Selectin-IgG produced as Fc chimeric constructs were purchased from R&D Systems (Minneapolis, MN). Adenosine A_{2A} receptor agonist CGS-21680, N-formyl-Met-Leu-Phe (fMLP), and ROS indicator Dihydrorhodamine 123 were purchased from Millipore Sigma (Burlington, MA). Adenosine A_{2A} receptor antagonist ZM 241385 was purchased from Tocris Bioscience (Minneapolis, MN). Feraheme (AMAG Pharmaceuticals, Waltham, MA) was purchased from the UC Davis Medical Center Pharmacy.

Human Neutrophil Isolation

Whole blood was obtained from healthy donors consented through a University of California, Davis institutional review board protocol #235586-9. Neutrophils were isolated from whole blood *via* negative enrichment using EasySep™ direct human neutrophil isolation kit purchased from StemCell Technologies as per manufacturers instruction (Cambridge, MA). Some studies employed a percoll gradient separation using Polymorphoprep® as per manufacturers instruction (Fresenius Kabi). Briefly, for gradient based isolation, whole blood is layered on an equal volume of Polymorphoprep solution and centrifuged at 760g for 30 min at 25°C. The neutrophil layer is collected and washed in Phosphate-buffered saline (PBS) before resuspension in HBSS buffer containing 0.1% human serum albumin (HSA) without Ca^{2+} and Mg^{2+} and kept at 1×10^7 cells/ml on ice after isolation and prior to experimentation. For EasySep neutrophil isolation, whole blood was diluted 1:1 with PBS then 100 µl of isolation cocktail and magnetic RapidSpheres each were added and incubated for 5 min. Cells were then placed in the EasySep magnet for 5 min. Cells were poured into a new tube and treated for an additional 5 min with 100 µl of magnetic RapidSpheres and placed on the EasySep magnet for 5 min twice more. Cells were then spun down and resuspended in HBSS containing 0.1% HSA without Ca^{2+} and Mg^{2+} and kept at 1×10 cells/mL on ice after isolation and prior to experimentation. Cell purity was >90% as determined by Beckman cell coulter counter. Cell viability was ~99% as determined by flow cytometry detection of zombie violet fluorescent dye staining (Biolegend).

Flow Cytometry Detection of Cell Surface Marker Expression

Neutrophils (1×10^6 cells/ml) in HBSS buffer containing Ca2+ and Mg2+ at 1 mM were treated with IL-8 at a dose range of concentrations (0.01–100 nM) and Feraheme (1–6 mg/ml) for 5 min at 37°C before addition of antibody (1.5–5 µg/ml). Cells were stained with antibodies for high affinity β2-integrin (mAb24), L-Selectin (Dreg-56), CD11b (M1/70), CD18 (1B4), CD11a (HI111), PSGL-1(KPL-1), CXCR1(8F1/CXCR1), and CXCR2 (5E8/CXCR2) for 20 min at 37°C before fixation with 4% paraformaldehyde at room temperature. After two washes with PBS cells were analyzed using the Attune NxT flow cytometer (Thermofisher). Neutrophils were gated by their characteristic forward scatter vs side scatter profile. Receptor expression in terms of sites/cell was determined by comparing the MFI of bound antibody to Quantum Simply Cellular beads (Bangs Laboratories, Inc., Fishers, IN) which contain five bead sets with increasing numbers of antibody binding sites on their surface. From this analysis, a linear relation between MFI and receptor expression was determined for each directly conjugated antibody bound to cells and the calibration bead set.

Microfluidic Shear Flow Assay

Vascular mimetic flow chambers were utilized to record neutrophil rolling and arrest behavior on substrates of endothelial ligands under physiological shear stresses. Devices were prepared as described previously (27). Briefly, polydimethylsiloxane (PDMS) microfluidic flow chambers with a minimum feature size of 5 µm were produced by curing Sylgard 184 prepolymer (Dow Corning, Midland, MI, USA) over a patterned silicon wafer. Holes were punched into the PDMS for flow channel and vacuum port access and the device was reversibly vacuum sealed on a glass coverslip coated with E-selectin (1 µg/ml) alone or with ICAM-1 (1 µg/ml) in PBS for 60 min at room temperature. To limit non-specific adhesion of neutrophils, coverslips were treated with 1% casein for 10 min before washing with PBS and assembly of the microfluidic device.

Isolated neutrophils were treated with Ca2+ indicators 1 Fluo-4 AM or Rhod-2 AM (1 µg/ml) for 20 min at room temperature in the dark. Cells were spun down and resuspended at 1×10^6 cells/ml and were treated with Mac-1 blocking antibody M1/70 and incubated with or without MNP in HBSS buffer containing Ca2+ and Mg2+ for 20 min at 37°C. Neutrophils were then treated with 0.5 nM IL-8 or vehicle control and immediately loaded into an open 100-µl reservoir and were drawn through the channel by negative pressure produced by a syringe pump at a shear of 2 dynes/cm^2.

Utilizing real time fluorescence microscopy, images of rolling neutrophils were acquired at 60 frames per minute for 4 min per field of view on an inverted microscope (Nikon) using a phase contrast 20× objective and recorded with 16-bit digital complementary metal oxide semiconductor (CMOS) camera (Andor ZYLA) connected to a PC (Dell) with NIS Elements imaging software (Nikon Instruments Inc.). Arrested neutrophils were defined as having a velocity less than 0.1 µm/s. Migrating neutrophils were identified by exhibition of a polarized shape defined as exceeding a length/width aspect ratio greater than 1.4 and phase dark contrast indicative of being outside the focal plane of rolling cells.

L-Selectin and PSGL-1 Clustering

Total internal reflection fluorescence (TIRF) microscopy and quantitative dynamic foot printing (qDF) were employed to record fluorescently tagged antibodies targeting L-selectin (non-blocking clone: DREG55) and PSGL-1(non-blocking clone: PL2). Cluster area and frequency during rolling of isolated neutrophils over E-selectin in the presence or absence of Feraheme was observed. A cluster was defined as an area of uniform fluorescence intensity two standard deviations above the mean fluorescence intensity of the cell. Additionally, a cluster was defined as having a surface area of 0.4 µm^2 or greater.

Measurement of Reactive Oxygen Species

Neutrophils (1×10^6 cells/ml) in HBSS buffer containing Ca2+ and Mg2+ at 1 mM were incubated with the ROS indicator Dihydrorhodamine 123 (2 µM) and treated with or without IL-8

(1 nM) and Feraheme (4 mg/ml) for 10 min at 37°C before addition of 1 μM fMLP. Cells were incubated with fMLP at 37°C for 5 min and then placed on ice to end reactions and ROS was then quantified through flow cytometry.

Measurement of Calcium Flux

Isolated neutrophils were treated with the Ca2+ indicator Fluo-4 AM (1 μg/ml) for 20 min at room temperature in the dark. Cells were spun down and resuspended at 1×10^6 cells/mL in HBSS buffer containing Ca2+ and Mg2+ at 1 mM and treated with or without the adenosine A_{2A} receptor antagonist ZM 241385 (2.5 μM) for 5 min at 37C. Feraheme (4 mg/ml) and or adenosine A2a receptor agonist CGS 21680 (1 μM) were then added to the cell solutions for 10 min at 37C. After incubation, IL-8 (1 nM) was added to cell solutions and calcium fluorescence time course was immediately read on the Facscan flow cytometer (BDbiosciences)

RESULTS

Feraheme Inhibits Neutrophil Activation and Degranulation Stimulated by IL-8

Stimulation with chemotactic factors activate within seconds neutrophil degranulation, which results from the fusion of granule membranes to the plasma membrane resulting in upregulation of additional CD11b/CD18 and CD66b receptors. Activation also results in a shift in the conformation of CD18 from a constitutive low affinity conformation at rest to high affinity upon CXCR ligation, as well as the shedding of L-selectin receptors through the action of the metalloprotease ADAM17 (28, 29). We first assessed the capacity of different concentrations of Feraheme in suspension to alter neutrophil responses to chemotactic activation *via* CXCR1/2 in cells stimulated at the K_D of IL-8 stimulation (~1 nM). Neutrophils were incubated at 37°C in the presence and absence of Feraheme and IL-8 for 5 min before the addition of fluorescent antibodies for 20 min followed by cell fixation. The presence of Feraheme led to significant alterations in expression of CD62L, CD11b, and high affinity (HA) CD18 at each dose applied (1–6 mg/ml) (**Figure 1**). A dose dependent increase in the inhibition of degranulation was observed, as well as diminished activation of integrin and proteolytic cleavage of L-selectin. Since the effect of Feraheme was observed to plateau at 4 mg/ml, subsequent studies were performed using this concentration.

We next evaluated the effect of Feraheme on adhesion receptor expression over a dose range of chemotactic stimulation with IL-8. A typical sigmoidal dose dependent decrease in L-selectin expression followed addition of IL-8 between 0.1 and 100 nM, which reached a maximum of ~90% loss at 5 nM IL-8 from baseline expression on quiescent neutrophils (**Figure 2A**). Upregulation in surface expression of CD11b and CD18 provided a sensitive measure of activation, increasing by 2-fold and 2.3-fold from baseline up to maximum expression at 10 nM IL-8 (**Figures 2B, C**). Another sensitive measure of neutrophil activation was provided by the increased binding of mAb24 that reports on the allosteric conversion of CD18 receptors from low to high affinity, which yielded a 3-fold increase in expression at maximum IL-8 stimulation (**Figures 2B, D**). It is noteworthy that the maximum extent of L-selectin shedding was lowered by Feraheme at 4 mg/ml compared with 0 mg/ml, as indicated by the elevated plateau at a dose of IL-8 > 5 nM from 10% up to 25% total receptor expression (**Figure 2A**). Moreover, the extent of upregulation of CD11b/CD18 and conversion of CD18 to the HA conformation was significantly inhibited, as indicated by a ~2-fold increase in the EC50 of IL-8 stimulation. This resulted in a reduced sensitivity to activation that was significant at IL-8 doses of 0.5 and 1 nM for CD11b, total CD18, and HA CD18 (**Figures 2B–D**). A marker of the release of secondary granules is the increase in membrane expression of CD66b, which is transported to the plasma membrane along with CD11b/CD18 (20). The presence of Feraheme elicited a significant inhibition in upregulation of CD66b, increasing the EC50 of IL-8 stimulation by ~30% (**Supplemental Figure 1**). In contrast, CD11a and PSGL-1 adhesion receptors that are constitutively expressed on circulating neutrophils and typically do not register a change in receptor number in response to chemotactic stimulation, remained constant over the dose range of IL-8 stimulation in the presence of Feraheme (**Supplemental Figure 1**).

Neutrophils are reported to endocytose CXCR1/2 following ligation and signaling by IL-8 (30). This motivated experiments to determine if Feraheme altered the expression of CXCR1/2, consequently accounting for the diminished capacity to induce changes in adhesion molecule expression following stimulation. Unexpectedly, incubating unstimulated neutrophils in suspension with Feraheme at 4 mg/ml elicited a ~26% increase in expression of CXCR1 and a ~15% increase in CXCR2 (**Figure 3**). A significant amount of CXCR1 endocytosis following IL-8 simulation was not observed in the presence or absence of Feraheme (**Figure 3A**). In contrast, the small amount of CXCR2 endocytosis in response to IL-8 stimulation was not altered in the presence of Feraheme (**Figure 3B**). These results indicate that CXCR1/2 expression either remains constant or increases in the presence of Feraheme and IL-8 stimulation as compared to controls. Thus, it is unlikely that the mechanism left-shifting the IL-8 dose response for activation is diminished expression of chemotactic receptors. Feraheme is also not altering the endocytosis of CXCR2 receptors in cells treated with 1 nM IL-8 indicating it is not interfering with IL-8 ligation of CXCR2. Thus, it is probable that Feraheme is leading to dramatically reduced responses to IL-8 stimulation by affecting intracellular signaling downstream of receptor ligation.

Feraheme Inhibits the Activation of ROS Production in Neutrophils

To further explore the influence of Feraheme on neutrophil function, ROS production was quantified using flow cytometry to detect intracellular Dihydrorhodamine 123 fluorescence. Production of ROS is a key antimicrobial mechanism of neutrophils and has also been implicated in recruitment to sites of inflammation by increasing vascular permeability (31). The bacterial tripeptide fMLP is a potent chemotactic factor that binds to G-protein coupled Formyl peptide receptors expressed on neutrophils and activates the respiratory burst and production of ROS. Feraheme led to a significant 30% reduction of ROS

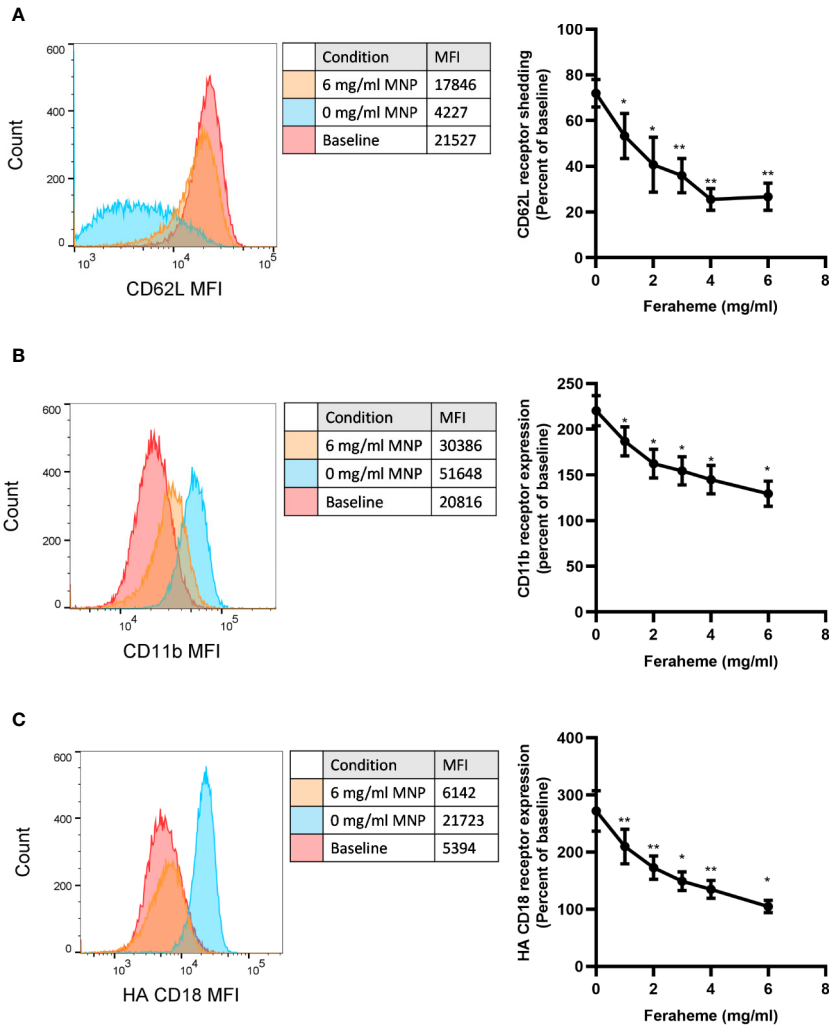

FIGURE 1 | Effect of Feraheme concentration on integrin and selectin expression following chemotactic stimulation of neutrophils. Isolated human neutrophils were incubated with 1 nM IL-8 and Feraheme magnetic nanoparticles (MNP) for 25 min and cell surface expression of **(A)** CD62L, **(B)** CD11b, and **(C)** HA CD18 was assessed by flow cytometry. Representative histograms depict fluorescent antibody detection for each adhesion receptor at baseline receptor expression and following IL-8 stimulation in presence and absence of MNP. Bivariate data are presented as the percent shedding from unstimulated baseline mean ± SEM for CD62L and percent of unstimulated baseline expression mean ± SEM for CD11b and HA CD18 (n ≥ 4 donors) with experimental replicates averaged for each donor. Paired T-test was performed comparing the average value at each concentration to the 0 mg/ml Feraheme condition of the same donor * and ** denote p value ≤.05 and ≤ 0.01, respectively.

production in neutrophils stimulated with 1 μM fMLP (**Figure 4**). Pre-treatment with IL-8 has previously been reported to prime neutrophils for enhanced fMLP induced ROS production through assembly of the NADPH oxidase components into lipid rafts on the plasma membrane (32). Feraheme significantly reduced ROS production by 48% in cells primed with low dose IL-8 and stimulated with fMLP. While uptake of SPION other than Feraheme have been reported to induce ROS production, the presence of Feraheme did not lead to detectable ROS production in unstimulated neutrophils. This data indicates that Feraheme inhibits formyl peptide receptor signaling of ROS production, including increased ROS induced by IL-8 priming.

Neutrophil Recruitment on Endothelial Adhesion Molecules Is Altered in the Presence of Feraheme

It has been reported that exposure to nanoparticles and microparticles reduced neutrophil recruitment to inflamed mesentery microvasculature in mice (23). Moreover, polystyrene nanoparticles have been shown to reduce adhesion of human neutrophils to inflamed human umbilical vein endothelial cells in parallel plate flow chamber studies (24). This motivated determination of the effect of Feraheme on the multistep process of recruitment *in vitro* using microfluidic flow channels (23, 24, 33). Fluorescence microscopy was employed to image the dynamics of

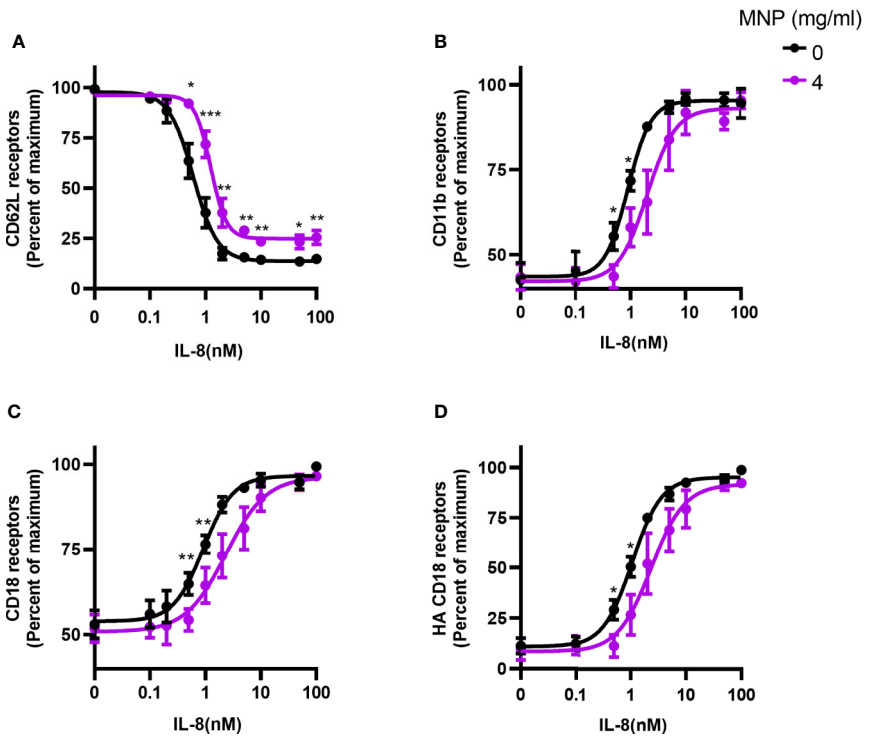

FIGURE 2 | Feraheme alters adhesion receptor expression over a dose range in stimulation with IL-8. Isolated human neutrophils were incubated with IL-8 and Feraheme MNP for 25 min and cell surface expression of **(A)** CD62L, **(B)** CD11b, **(C)** CD18, and **(D)** HA CD18 was assessed by flow cytometry. The data are presented as the percent of maximum receptor expression mean ± SEM (n ≥ 5 donors) with experimental replicates averaged for each donor. Paired T-tests were performed comparing the average of the 0 mg/ml to the 4 mg/ml conditions for the same donor *, **, and *** denote p value ≤.05, ≤ 0.01, and ≤ 0.001, respectively.

neutrophil rolling and arrest within vascular mimetic microfluidic channels containing substrates coated with E-selectin alone or in conjunction with ICAM-1. Neutrophil suspensions were incubated for 20 min with Feraheme at 1 mg/ml or 4 mg/ml and compared with vehicle control in response to stimulation with 0.5 nM IL-8 prior to perfusion through the flow channel. This dose of IL-8 corresponded with the lowest concentration of stimulus in which a significant inhibition of CD18 activation and L-selectin shedding was elicited by Feraheme. Capture and rolling on E-selectin is primarily mediated by recognition of sLe^x presenting ligands on L-selectin and PSGL-1 expressed on neutrophils. The velocity of neutrophil rolling on E-selectin at a venular shear stress of 2 dyne/cm^2 increased ~37% in the presence of Feraheme at 4 mg/ml compared to vehicle alone, whereas no alteration in rolling velocity was detected at 1 mg/ml (**Figures 5A, B**). This increased rolling velocity was accompanied by a 40% increase in the variance of the mean velocity, which is consistent with interruption of adhesive bond formation resulting in an unsteady trajectory of neutrophil rolling on the substrate under shear flow. Neutrophils require ICAM-1 on the substrate to provide an anchor for activated integrins to bind in order to achieve shear resistant cell arrest (28). Perfusion through flow channels derivatized with E-selectin and ICAM-1 were used to study Feraheme's effect on the kinematics of neutrophil arrest and transition to a migratory phenotype. In the absence of IL-8 chemotactic stimulation, Feraheme lead to a dose dependent increase in rolling velocity on E-selectin coated substrates, which increased by ~30% and ~60% when neutrophils were exposed to 1 and 4 mg/ml Feraheme, respectively (**Figures 5C, D**). Moreover, an ~80% increase in variance of mean velocity corresponded to treatment at 4 mg/ml Feraheme, while 1 mg/ml increased variance by 17%. Stimulation with IL-8 leads to the activation of HA CD18 that binds ICAM-1 and mediates deceleration to arrest (28). Consequently, stimulation with IL-8 on E-selectin/ICAM-1 coated substrates resulted in a 50% decrease in rolling velocity and within ~40 s most neutrophils exhibited a rapid transition to arrest (**Figures 5C, F**). Neutrophils treated with Feraheme at 4 mg/ml exhibited ~40% higher rolling velocity compared to the 1 mg/ml or vehicle control conditions (**Figure 5D**). In the absence of IL-8 stimulation, outside-in signaling *via* E-selectin binding and clustering of L-selectin is sufficient to activate ~40% of cells to convert from rolling to arrest that is supported by activation of HA CD18 to bind ICAM-1 (34). Feraheme at 1 and 4 mg/ml concentrations inhibited this L-selectin mediated signaling of arrest, as well as decreased transition to a migratory state from 12% of cells to <1% of cells assuming a polarized shape (**Figure 5E**). In contrast, in the presence of IL-8 stimulation, we did not detect significant inhibition in the frequency of neutrophils rolling to arrest in presence of Feraheme (**Figure 5E**). This is likely due to the fact that coupled with shear force mediated L-selectin signaling, even very low concentrations of IL-8 can lead to activation of HA CD18 receptors sufficient to mediate conversion from rolling to arrest (35). However, in the presence of Feraheme, a significant

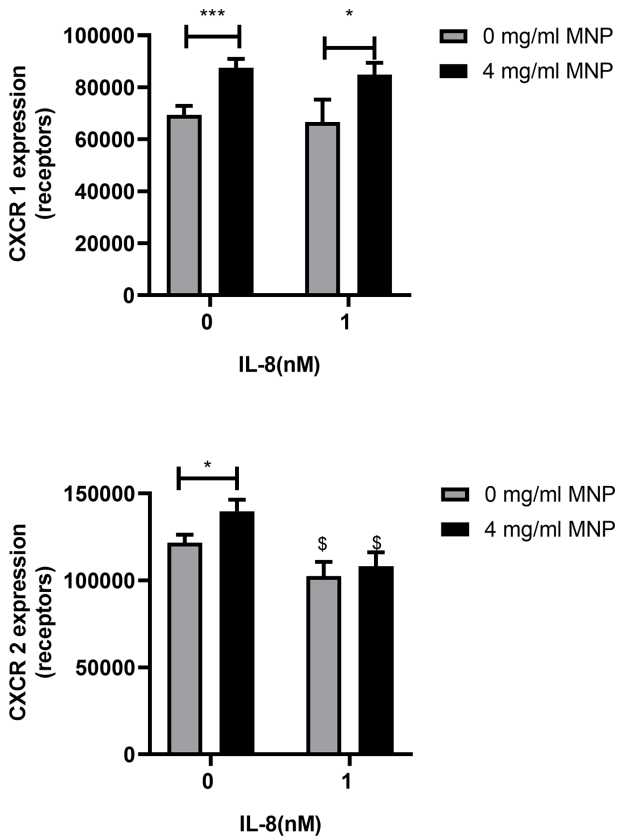

FIGURE 3 | Feraheme alters CXCR expression in neutrophils. Isolated human neutrophils were incubated with IL-8 or vehicle and Feraheme for 25 min and cell surface expression of **(A)** CXCR1 and **(B)** CXCR2 was assessed by flow cytometry. The data are presented as mean ± SEM (n ≥4 donors) with experimental duplicates averaged for each donor. Paired T-tests were performed comparing the average value for the 4 mg/ml to the 0 mg/ml Feraheme conditions of the same donor * and *** denote p value ≤.05 and ≤ 0.001, respectively. Paired T-tests were performed comparing the average value for a condition to the 0 nM IL-8 condition of the same donor $ denotes p value ≤.05.

increase was detected in the duration of rolling before the onset of cell arrest for both IL-8 stimulated and unstimulated neutrophil suspensions. In the absence of IL-8, rolling time to arrest increased from 42.1 seconds in the 0 mg/ml condition to 55.1 and 91.9 seconds in the 1 mg/ml and 4 mg/ml conditions, respectively (**Figure 5F**). In IL-8 treated cells only the 4 mg/ml condition resulted in significantly increasing the time to arrest compared to the 0 mg/ml condition, from 20.0 to 34.7 s. We conclude that Feraheme exerts a significant effect on the kinematics of rolling to arrest on E-selectin and ICAM-1 in terms of increasing the velocity and signaling associated with HA CD18 mediated arrest.

Feraheme Perturbs the Process of E-Selectin Ligand Clustering on Rolling Neutrophils

E-selectin recognition of L-selectin and PSGL-1 under shear flow leads to receptor co-clustering and mechanotransduction of signals leading to HA CD18 binding to ICAM-1 (34). To further examine how uptake of Feraheme effects the process of selectin mediated rolling and deceleration to arrest, total internal reflection fluorescence (TIRF) microscopy and quantitative dynamic footprinting (qDF) was performed to determine the L-selectin and PSGL-1 bond cluster formation during rolling on a substrate of E-selectin. Treatment with Feraheme resulted in an increase in L-selectin bond cluster area (i.e., lower density of L-selectin) and marginal changes in the frequency of cluster formation detected in the presence and absence of IL-8 stimulation (**Figures 6A, B**). Examining the average density of L-selectin receptors within clusters bound to E-selectin, a significant decrease was detected in the presence of IL-8 stimulation for 4 mg/ml compared to 0 mg/ml Feraheme (**Figure 6C**). In contrast, Feraheme did not affect E-selectin mediated formation of PSGL-1 cluster area and frequency nor PSGL-1 cluster density (**Figures 6D, E**). These data are consistent with the observed increase in rolling velocity and decreased outside-in signaling *via* E-selectin in the presence of Feraheme and indicate this effect may be a function of diminished L-selectin bond formation despite the observed higher frequency and area of L-selectin within sites of adhesive contact.

Feraheme Accelerates Clearance of Cytosolic Calcium After Flux

Calcium serves as a secondary messenger downstream of GPCR signaling that mediate neutrophil inflammatory responses including degranulation, integrin activation and adhesion, shape change, and ROS production (36). IL-8 ligation of CXCR leads to a release of endoplasmic reticulum (ER) stored calcium into the cytosolic space which is subsequently sequestered by the ER calciosomes to replenish stores. High concentrations of extracellular adenosine which binds to the adenosine A_{2A} receptor is known to dampen neutrophil inflammatory responses (37). The mechanism, as depicted in **Figure 7A**, is initiated by ligand binding to the adenosine A_{2A} receptor which induces disassociation and activation of the G_α subunit of the A_{2A} receptor linked heterotrimeric G protein which then activates adenylyl cyclase. Adenylyl cyclase activation leads to production of cyclic AMP (cAMP), which in turn activates cAMP-dependent protein kinase (PKA) and leads to accelerated sequestration of calcium through PKA-activated endo-membrane Ca^{2+}-ATPases. To determine if Feraheme's inhibitory effects on intracellular signaling are mediated through accelerated clearance of IL-8 induced calcium flux, the time course of cytosolic calcium stimulated by IL-8 in Feraheme treated neutrophils was compared in the presence and absence of adenosine A_{2A} receptor agonist CGS 21680 (CGS). Following IL-8 induced release of ER Ca^{2+}, Feraheme elicited an accelerated decrease in cytosolic calcium as compared to untreated cells. The level of accelerated Ca^{2+} clearance was equivalent and not additive with CGS (**Figure 7B**). The duration required for a decrease to 20% of the maximum Ca2+ flux elicited by IL-8 was 60 seconds in untreated cells compared to 36, 22, and 22 seconds for Feraheme, CGS, and Feraheme + CGS, respectively (**Figure 7C**). Neither Feraheme nor CGS alone reduced the maximal Ca^{2+} flux elicited by IL-8, while added together they resulted in a slight reduction (**Figure 7D**).

To determine if Feraheme mediated inhibition acts through release and binding of extracellular adenosine, the clearance of

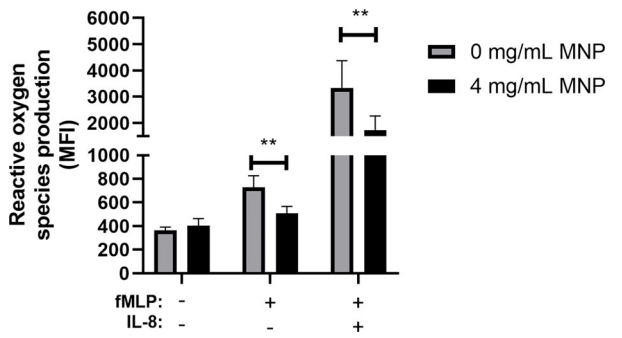

FIGURE 4 | Feraheme inhibits ROS production in fMLP stimulated neutrophils. Isolated human neutrophils stained with 2 μM DHR 123 and treated with or without Feraheme were preincubated with 1 nM IL-8 or vehicle control for 10 min before addition of 1 μM fMLP or vehicle control for 5 min. The data are presented as mean ± SEM (n ≥ 4 donors) with experimental duplicates averaged for each donor. Paired ratio T-test was performed comparing the average value for an experimental condition to the 0 mg/ml Feraheme condition of the same donor. ** denotes a p value ≤ 0.01.

calcium after IL-8 stimulated Ca^{2+} flux was compared to that activated by the adenosine A_{2A} receptor agonist CGS 21680 (CGS) while blocking signaling *via* the A_{2A} receptor with the adenosine A_{2A} receptor antagonist ZM 241385 (ZM) as depicted in **Figure 8A**. As expected, in neutrophils preincubated with ZM the sequestration effect of CGS was completely abrogated. In contrast, Feraheme treatment remained effective in accelerating the decrease in cytosolic Ca^{2+} following IL-8 stimulation (**Figure 8B**). In untreated cells the duration to 20% of maximum Ca^{2+} flux was 65 s compared to 46, 63, and 42 s for Feraheme, CGS, and Feraheme+ CGS, respectively (**Figure 8C**). All conditions registered the same maximal Ca^{2+} flux (**Figure 8D**).

DISCUSSION

Neutrophil recruitment and attachment to inflamed endothelium is mediated by a multistep process involving ligation and mechanosignaling from the outside-in through selectins and integrins following bond formation (38). CXCR ligation of IL-8 by neutrophils interacting with inflamed endothelium under shear flow induces degranulation and the activation of CD18 to a high affinity state, as well as the rapid shedding of L-selectin (20, 29). Here, we demonstrated that, treating neutrophils in suspension over a dose range with Feraheme elicited reduced responsiveness to stimulation with 1 nM IL-8 at each dose tested (1–6 mg/ml). This was manifest as increased inhibition of CD11b upregulation, HA CD18 activation, and L-selectin shedding with increasing particle concentration of Feraheme. Treating with a Feraheme dose of 4 mg/ml resulted in a consistent ~2-fold right shift in the EC50 of stimulation with IL-8 corresponding to diminished upregulation of CD11b/CD18, activation of HA CD18, and L-selectin shedding. Chemokine receptor expression in unstimulated cells was significantly elevated in the presence of Feraheme, but these changes in expression did not explain the inhibitory effects observed. Feraheme also did not alter endocytosis of CXCR2 in response to IL-8 signaling, suggesting that its mechanism of action is not through down regulation or interference with CXCR ligation. Feraheme also significantly reduced fMLP induced ROS production in the presence or absence of IL-8 priming. Taken together, we conclude that the inhibitory effects of Feraheme are not exclusive to CXCR1/2 signaling by IL-8, but include signaling through other GPCR namely, formyl peptide receptors.

Uptake of nanoscale poly(styrene) and liposomal particles by neutrophils was previously shown not to enhance apoptosis, activation, or cell death. Ingested nanoparticles were reported to reside in intracellular compartments that are retained during degranulation (39). Uncoated SPION are reported to aggregate and induce the formation of neutrophil extracellular traps (NETs) that are extracellular fibers consisting of expelled DNA. This pro-inflammatory host response is mitigated by coating SPION with layers of dextran or HSA (40). In our experiments, Feraheme did not reduce cell viability, which exceeded 99%. Although we did not specifically test for netosis in our studies of neutrophil arrest and migration, no visible changes in cell morphology that is characteristic of netosis was observed. In-vivo studies have demonstrated that uptake of nanoparticles can diminish the efficiency of neutrophil recruitment to inflamed endothelium within the lungs of mice. However, the mechanism that may involve cell-particle uptake and competitive binding to adhesion receptors, which could interfere with chemotactic or adhesive ligand binding during recruitment remained elusive (23, 24). Here, we report that following 20 min of exposure to Feraheme in suspension, we observed diminished efficiency of neutrophil arrest and migration as measured in an established model of endothelial inflammation in vascular mimetic shear flow channels. We have recently reported that deceleration of neutrophils within the vascular mimetic substrate in microfluidic flow channels is mediated by as few as 200 HA CD18 binding ICAM-1 in order to transition from rolling to arrest (34). In the absence of IL-8 stimulation and in the presence of Feraheme, a ~50% reduction was measured in the frequency of neutrophils rolling to arrest on E-selectin/ICAM-1 at both 1 and 4 mg/ml. Moreover, neutrophils rolled over twice the distance before activation and binding of HA CD18 integrin bonds formed stable arrest. Inhibition of neutrophil CD11b/CD18 mediated migration after arrest was also observed at 1 and 4 mg/ml Feraheme. Thus, Feraheme uptake in a concentration dependent manner alters both selectin and GPCR mediated signaling of HA CD18 necessary to transition from rolling on E-selectin to arrest on ICAM-1. It has been previously shown that L-selectin catch-bonds, characterized by a prolonged bond lifetime as tensile force is increased, is necessary and sufficient to signal CD18 transition to a HA state (34). We show that Feraheme reduced both L-selectin shedding in response to IL-8 and L-selectin clustering during rolling on E-selectin, but it had no effect on PSGL-1 expression. Noteworthy was the finding that cluster area of L-selectin bonds during rolling on E-selectin in the presence of

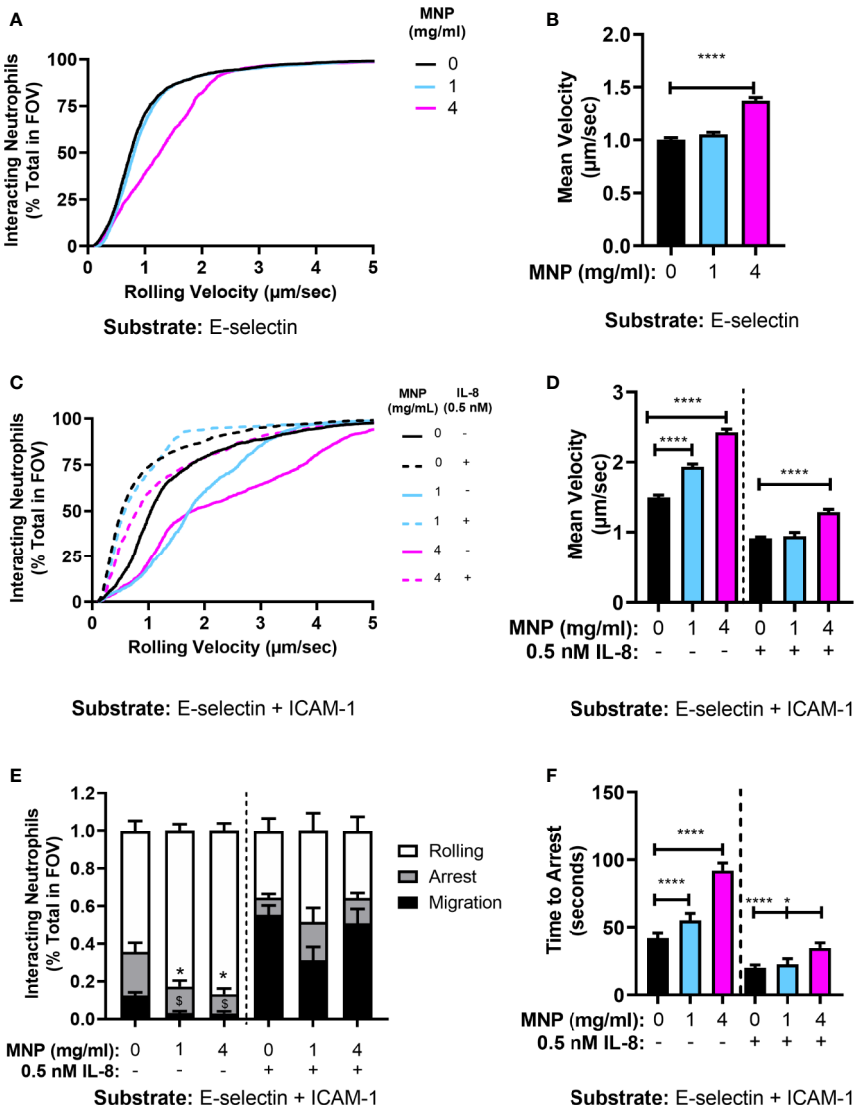

FIGURE 5 | Feraheme alters the kinetics of neutrophil rolling and arrest in microfluidic flow channels. **(A)** Neutrophil rolling velocity over an E-selectin substrate treated with vehicle or Feraheme (1 mg/ml, 4 mg/ml). **(B)** Cumulative rolling velocities of neutrophils over an E-selectin substrate treated with vehicle or Feraheme (1 mg/ml, 4 mg/ml). **(C)** Mean neutrophil rolling velocity over an E-selectin+ ICAM-1 substrate treated with Feraheme (1mg/ml, 4 mg/ml) and/or IL-8 (0.5 nM). **(D)** Cumulative rolling velocities of neutrophils over an E-selectin + ICAM-1 substrate treated with vehicle or Feraheme (1 mg/ml, 4 mg/ml) and/or IL-8 (0.5 nM). **(E)** Neutrophil rolling to arrest and migration over an E-selectin+ ICAM-1 substrate treated with Feraheme (1 mg/ml, 4 mg/ml) and/or IL-8 (0.5 nM). * and $ denote T-Test p-values of ≤.05 as compared to the 0 mg/ml MNP condition for arrest and migration, respectively. **(F)** Neutrophil time to arrest over an E-selectin+ ICAM-1 substrate treated with Feraheme (1 mg/ml, 4 mg/ml) and/or IL-8 (0.5 nM). For B, D, and F, * and **** denote T-Test p-values of ≤.05 and ≤ 0.0001, respectively. Data in B, D, E, and F are presented in mean ± SEM (n ≥ 4 donors) with at least 15 cells for each donor per condition.

shear stress and IL-8 stimulation was increased, while the density of bond formation within these clusters decreased. This indicates that Feraheme may alter L-selectin signaling, but not recognition by E-selectin on the surface of rolling neutrophils. This is consistent with the significant rise in the mean rolling velocity on E-selectin that was observed to increase with Feraheme concentration. This provides one potential explanation as to how Feraheme reduces the efficiency of the transition to cell arrest, in that it may alter the capacity of E-selectin/L-selectin to form catch-bonds. Increased availability of L-selectin to form bond clusters in the presence of Feraheme coincided with reduced density of bonds on E-selectin and also with a reduced frequency of cell arrest suggesting that the normal process of neutrophil deceleration at sites of inflammation may be perturbed. Reduced levels of L-selectin shedding may potentially contribute to the inhibition of arrest and polarization observed in Feraheme treated cells. Consistent with the latter observation are reports that L-selectin shedding

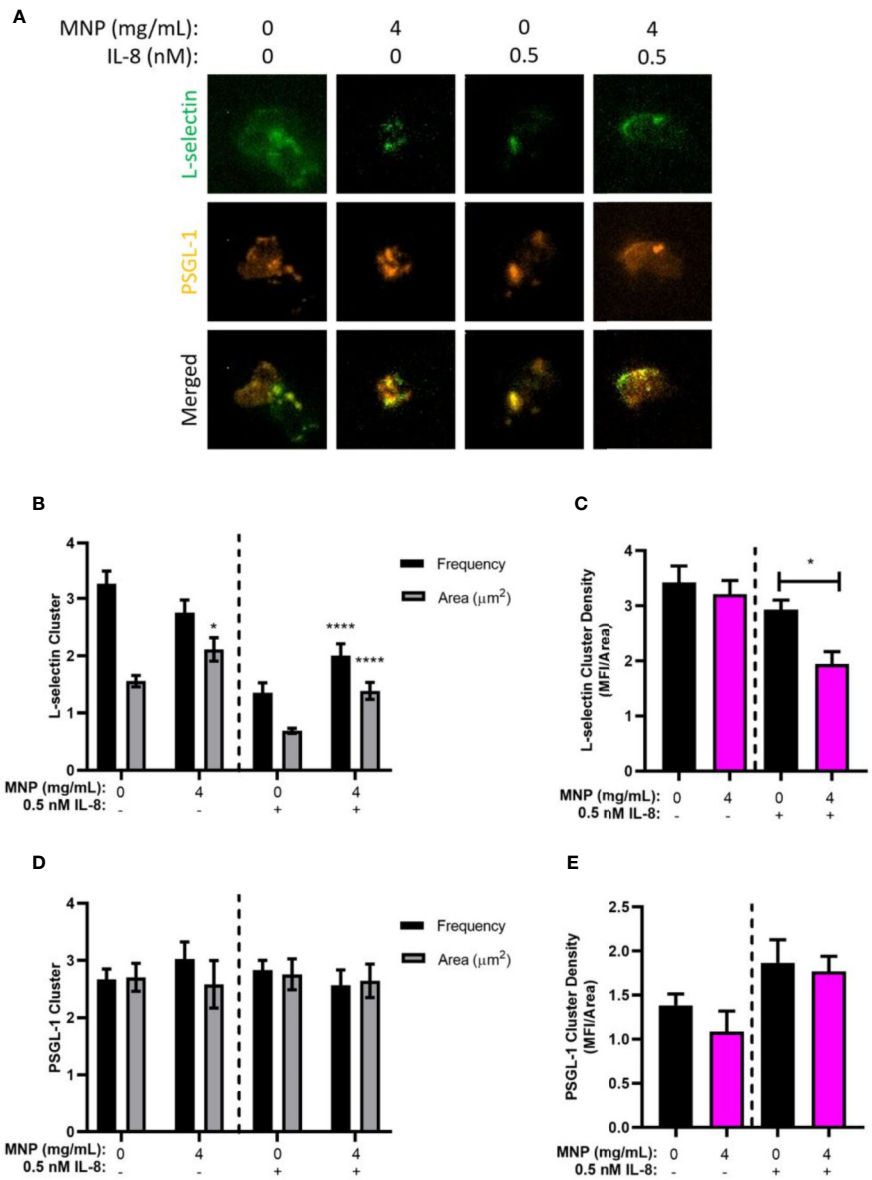

FIGURE 6 | Feraheme antagonism of E-selectin ligand bond formation. **(A)** Neutrophil rolling on a substrate of E-selectin in the presence of vehicle control or Feraheme MNP (4 mg/ml) was dynamically imaged using qDF to detect L-selectin (AF488 anti-human DREG55) and PSGL-1 (PE anti-human PL-1) engagement in the plane of adhesive contact. **(B)** L-selectin and **(C)** PSGL-1 receptor cluster area and frequency were determined. **(D)** L-selectin and **(E)** PSGL-1 receptor density was determined and reported as mean ± SEM (n = 3 donors) with at least 10 cells for each donor per condition. * and **** denote T-test p-values of ≤.05 and ≤ 0.0001, respectively, compared with the 0 mg/ml condition.

has been reported to amplify integrin-mediated outside-in signaling–dependent processes, including neutrophil migration, production of ROS, and phagocytosis (41). L-selectin shedding induces phosphorylation of phospholipase C (PLC)γ2, Akt, and Syk, critical regulators of intracellular calcium release that are important for E-selectin mediated slow rolling and CD18 integrin activation in neutrophils (41, 42). Thus, inhibition of L-selectin shedding may also interfere with normal activation of HA CD18 during rolling on E-selectin, despite the elevated expression of L-selectin on the surface. While it is likely that Feraheme is endocytosed by neutrophils in suspension, we cannot rule out that a fraction remain bound to the plasma membrane and sterically interfere with the recognition and mechanics of selectin bond formation. Due to optical limitations in real-time imaging of SPION bound to the plasma membrane at the nanoscale, we could not directly image whether Feraheme specifically bound to L-selectin receptors and sterically interfered with catch-bond formation

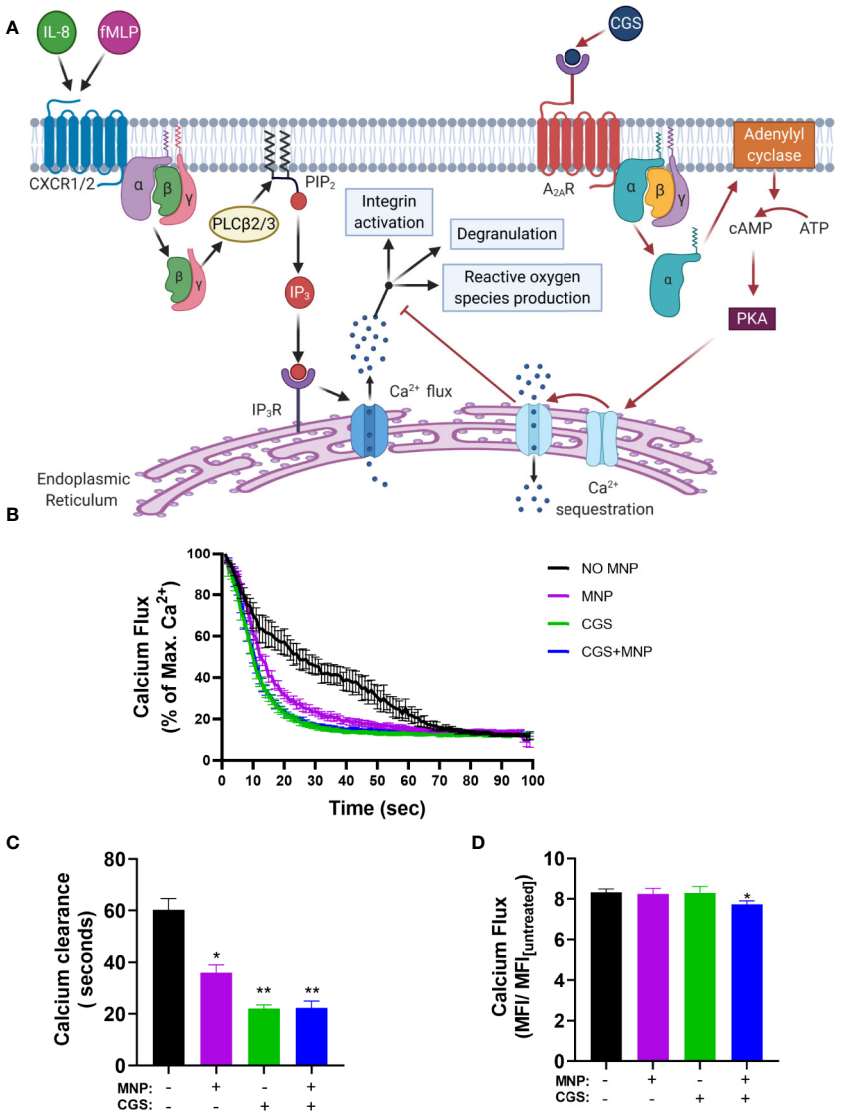

FIGURE 7 | Feraheme (4 mg/ml) accelerates clearance of cytosolic calcium following IL-8 stimulated calcium flux. **(A)** Diagram depicts the pathway of Ca2+ mediated neutrophil activation and antagonism by CGS 21680 via the Adenosine A_{2A} receptor. **(B)** Kinetics of cytosolic calcium clearance following maximal release due to 1 nM IL-8 at t = 0 s. **(C)** Duration for Ca2+ clearance to reach 20% of maximum value. **(D)** Fold change between maximal calcium flux and baseline level in untreated cells. Data are presented in mean ± SEM (n = 3 donors) with experimental replicates for each donor. Paired T-tests were performed comparing experimental conditions to the NO MNP condition of the same donor *, and ** denote p value ≤.05, and ≤ 0.01, respectively.

associated with mechanotransduction of CD18 activation. What is clear is that Feraheme altered the efficiency of L-selectin's capacity to mechanosignal activation of HA CD18, but not necessarily its ability to bind E-selectin and form focal clusters.

To elucidate a possible mechanism for Feraheme inhibition of GPCR signaling the effects of Feraheme on calcium flux after IL-8 stimulation was recorded. Feraheme significantly accelerated the clearance of calcium after flux and this response was comparable to that of the adenosine A_{2A} receptor agonist CGS 21680 known to inhibit degranulation and ROS production. The effect of Feraheme was not dependent on adenosine as treatment with the adenosine A_{2A} receptor antagonist ZM 241385 did not perturb the acceleration of calcium clearance in response to Feraheme. Calcium signaling plays a key role in GPCR mediated degranulation, L-selectin shedding, integrin activation, and ROS production which are all inhibited by Feraheme. Calcium is also necessary for selectin mechanosignaling induced activation of HA LFA-1 and for integrin signaling of shape change and polarization after arrest (38). Accelerated clearance of calcium could potentially result in the decreased arrest and polarization observed in Feraheme treated cells by inhibiting selectin mechanosignaling. These experiments highlight a consistent effect of Feraheme uptake on neutrophil intracellular signaling, but the mechanism which may involve Feraheme steric influence

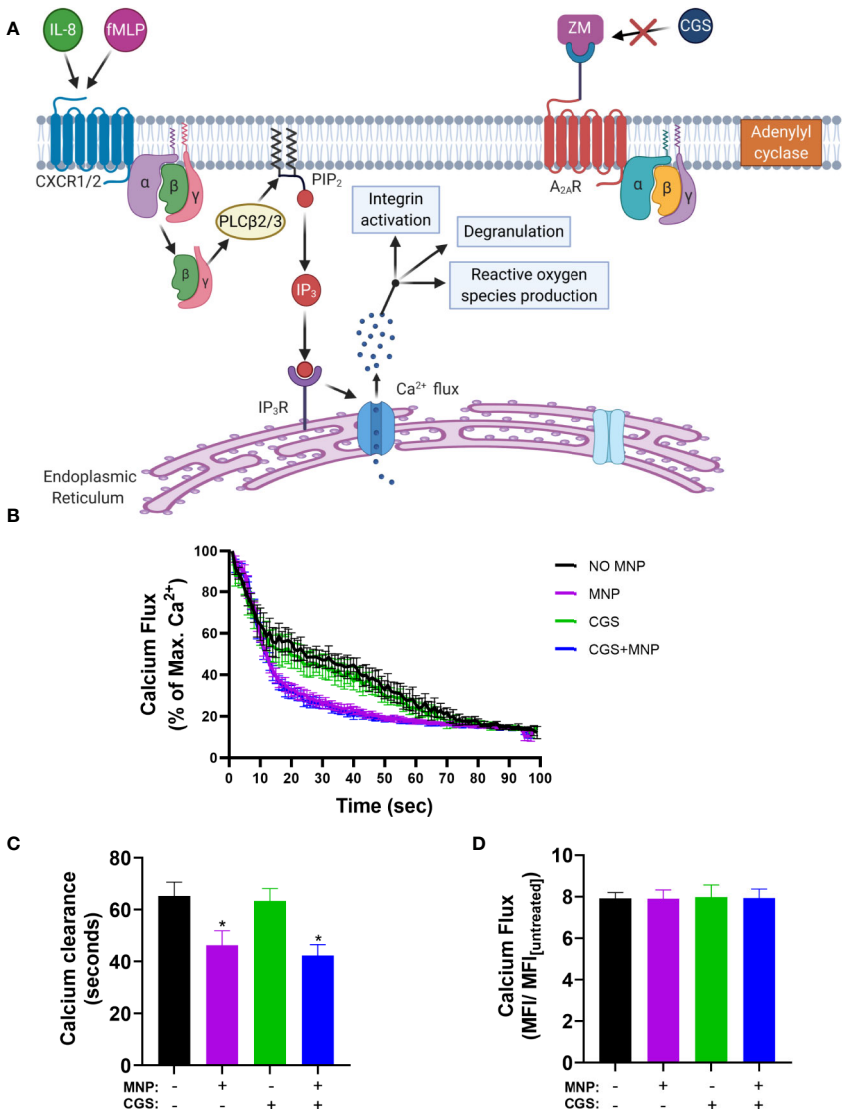

FIGURE 8 | Feraheme MNP (4 mg/ml) accelerated clearance of IL-8 stimulated cytosolic Ca2+ is independent of the Adenosine A_{2A} receptor. The Adenosine A_{2A} receptor antagonist ZM (2.5 μM) was applied for 5 min in calcium buffer. **(A)** Diagram depicts calcium flux in cells preincubated with ZM before treatment with the Adenosine A_{2A} receptor agonist CGS **(B)** Kinetics of cytosolic calcium resequestration from maximal flux induced by IL-8 (1 nM) at t=0 sec. **(C)** Time from maximal calcium flux until calcium levels reach 20 percent of max value. **(D)** Fold change between maximal calcium flux and untreated cells. Data are presented in mean ± SEM (n=3 donors) with experimental replicates for each donor. Paired T-tests were performed comparing experimental conditions to the NO MNP condition of the same donor. * denotes a p value ≤.05.

on normal cell surface receptor affinity or avidity in binding ligand needs to be confirmed in future studies. The non-additive inhibition in the presence of Feraheme and CGS could indicate a shared downstream mechanism for the accelerated clearance of Ca^{2+}. We propose that Feraheme may induce sequestration of calcium through activation of endo-membrane Ca^{2+}-ATPases rather than by efflux of calcium through activation of plasma membrane Ca^{2+}-pump, the proposed mechanism of action for CGS (**Figure 9**).

In summary, Feraheme exerted an immunosuppressive effect on neutrophil activation in response to IL-8 and fMLP, as well as outside-in signaling *via* E-selectin during neutrophil recruitment in shear flow. A potential mechanism may involve the observed Feraheme induced acceleration of calcium clearance resulting in a reduced capacity for cell signaling of immune responses. Further studies are warranted to elucidate the mechanism by which Feraheme induces accelerated calcium clearance, potentially though elevation of cAMP leading to downstream activation of endo-membrane Ca^{2+}-ATPases, and whether this is the primary mechanism for the inhibition of neutrophil inflammatory responses observed herein. Whether these effects are seen with other SPION formulations is also a relevant question to pursue.

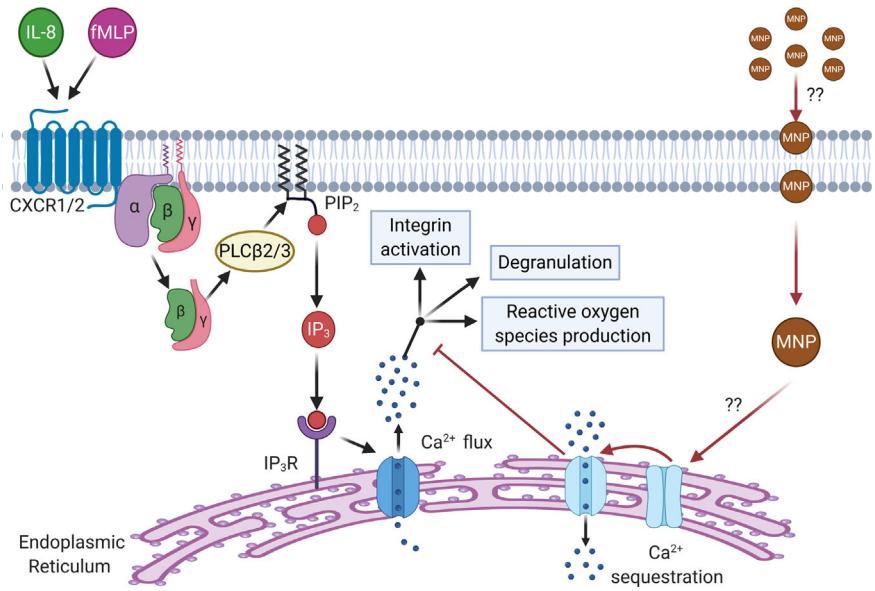

FIGURE 9 | Schematic depicting the proposed mechanism of Ca2+ sequestration and inhibition of downstream response by Feraheme. Feraheme may inhibit neutrophil function through activation of endo-membrane Ca2+-ATPases leading to accelerated clearance of cytosolic calcium inhibiting intracellular signaling. CXCR1/2 ligation by endogenous receptor ligands (IL-8, fMLP) leads to dissociation of Gα from Gβγ subunits of G proteins activating PLCβ2/3 which splits phosphatidylinositol 4,5 biphosphate (PIP_2). PIP_2 splits releasing inositol-1,4,5 triphosphate (IP_3) that binds to IP_3 receptor (IP_3R) on the surface of the endoplasmic reticulum inducing calcium flux which signals for downstream effector functions (integrin activation, degranulation, and reactive oxygen species production). We propose that Feraheme MNP are being endocytosed by neutrophils which through an unknown intermediary lead to activation of endo-membrane Ca2+-ATPases that sequester calcium and inhibit calcium signaling of functional responses down stream of GPCR.

These immunosuppressive effects could lead to impaired immune responses to infection or sterile tissue insult in patients treated with Feraheme. The current studies also point to the expanded use of SPION to downregulate the innate immune response as a therapy for ameliorating chronic inflammation and/or autoimmune diseases.

DATA AVAILABILITY STATEMENT

The raw data supporting the conclusions of this article will be made available by the authors, without undue reservation.

ETHICS STATEMENT

The studies involving human participants were reviewed and approved by UC Davis Institutional Review Board. The patients/participants provided their written informed consent to participate in this study.

AUTHOR CONTRIBUTIONS

GG designed the study and performed flow cytometry experiments. VM performed microfluidic experiments. GG and VM performed data analysis. GG wrote initial draft with aid of VM and SS. All authors contributed to the article and approved the submitted version.

FUNDING

This work was funded by the following grants from the National Institute of Health (NIH RO1 AI047294 to SS, NIH R01 NR015674 to MK, and NIH T32 HL086350).

ACKNOWLEDGMENTS

We would like to acknowledge former graduate student Leif Anderson for his help in initiating the project, collaborator Theodore Wun for assistance in supplying with Feraheme, and undergrad Tiffany Pan for assistance in performing experiments. Diagrams for **Figures 7A**, **8A**, and **9** were created with biorender.com

SUPPLEMENTARY MATERIAL

The Supplementary Material for this article can be found online at: https://www.frontiersin.org/articles/10.3389/fimmu.2020.571489/full#supplementary-material

REFERENCES

1. Dadfar SM, Roemhild K, Drude NI, von Stillfried S, Knuchel R, Kiessling F, et al. Iron oxide nanoparticles: Diagnostic, therapeutic and theranostic applications. *Adv Drug Deliver Rev* (2019) 138:302–25. doi: 10.1016/j.addr.2019.01.005
2. Valdiglesias V, Fernández-Bertólez N, Kiliç G, Costa C, Costa S, Fraga S, et al. Are iron oxide nanoparticles safe? Current knowledge and future perspectives. *J Trace Elem Med Biol* (2016) 38:53–63. doi: 10.1016/j.jtemb.2016.03.017
3. Gustafson HH, Holt-Casper D, Grainger DW, Ghandehari H, Grainger D. Nanoparticle Uptake: The Phagocyte Problem. *Nano Today* (2015) 10:487–510. doi: 10.1016/j.nantod.2015.06.006
4. Owens DEIII, Peppas NA. Opsonization, biodistribution, and pharmacokinetics of polymeric nanoparticles. *Int J Pharm* (2006) 307:93–102. doi: 10.1016/j.ijpharm.2005.10.010
5. Barbero F, Russo L, Vitali M, Piella J, Salvo I, Borrajo ML, et al. Formation of the Protein Corona: The Interface between Nanoparticles and the Immune System. *Semin Immunol* (2017) 34:52–60. doi: 10.1016/j.smim.2017.10.001
6. Szeto GL, Lavik EB. Materials Design at the Interface of Nanoparticles and Innate Immunity. *J Mater Chem B* (2016) 4:1610–8. doi: 10.1039/C5TB01825K
7. Bobo D, Robinson KJ, Islam J, Thurecht KJ, Corrie SR. Nanoparticle-Based Medicines: A Review of FDA-Approved Materials and Clinical Trials to Date. *Pharm Res* (2016) 33:2373–87. doi: 10.1007/s11095-016-1958-5
8. Wysowski DK, Swartz L, Borders-Hemphill BV, Goulding MR, Dormitzer C. Use of parenteral iron products and serious anaphylactic-type reactions. *Am J Hematol* (2010) 85:650–4. doi: 10.1002/ajh.21794
9. Wu X, Tan Y, Mao H, Zhang M. Toxic Effects of Iron Oxide Nanoparticles on Human Umbilical Vein Endothelial Cells. *Int J Nanomed* (2010) 5:385–99. doi: 10.2147/IJN.S10458
10. Gaharwar U,RP. Iron Oxide Nanoparticles Induced Oxidative Damage in Peripheral Blood Cells of Rat. *J Biomed Sci Eng* (2015) 8:274–86. doi: 10.4236/jbise.2015.84026
11. Soenen SJH, Himmelreich U, Nuytten N, De Cuyper M. Cytotoxic effects of iron oxide nanoparticles and implications for safety in cell labelling. *Biomaterials* (2011) 32:195–205. doi: 10.1016/j.biomaterials.2010.08.075
12. Jones SW, Roberts RA, Robbins GR, Perry JL, Kai MP, Chen K, et al. Nanoparticle Clearance Is Governed by Th1/Th2 Immunity and Strain Background. *J Clin Invest* (2013) 123:3061–73. doi: 10.1172/JCI66895
13. Naumenko V, Nikitin A, Garanina A, Melnikov P, Vodopyanov S, Kapitanova K, et al. Neutrophil-mediated transport is crucial for delivery of short-circulating magnetic nanoparticles to tumors. *Acta Biomaterialia* (2020) 104:176–87. doi: 10.1016/j.actbio.2020.01.011
14. Shah A, Dobrovolskaia MA. Immunological effects of iron oxide nanoparticles and iron-based complex drug formulations: Therapeutic benefits, toxicity, mechanistic insights, and translational considerations Nanomedicine: Nanotechnology. *Biol Med* (2018) 14:977–90. doi: 10.1016/j.nano.2018.01.014
15. Amulic B, Cazalet C, Hayes GL, Metzler KD, Zychlinsky A. Neutrophil function: from mechanisms to disease. *Annu Rev Immunol* (2012) 30:459–89. doi: 10.1146/annurev-immunol-020711-074942
16. Etzioni A, Frydman M, Pollack S, Avidor I, Phillips ML, Paulson JC, et al. Brief report: recurrent severe infections caused by a novel leukocyte adhesion deficiency. *N Engl J Med* (1992) 1327:1789–92. doi: 10.1056/NEJM199212173272505
17. Del Fresno C, Saz-Leal P, Enamorado M, Wculek SK, Martínez-Cano S, Blanco-Menéndez N, et al. DNGR-1 in dendritic cells limits tissue damage by dampening neutrophil recruitment. *Science* (2018) 362:351–6. doi: 10.1126/science.aan8423
18. Babin K, Antoine F, Goncalves DM, Girard D. TiO2, CeO2 and ZnO nanoparticles and modulation of the degranulation process in human neutrophils. *Toxicol Lett* (2013) 221:57–63. doi: 10.1016/j.toxlet.2013.05.010
19. Couto D, Freitas M, Vilas-Boas V, Dias I, Porto G, Lopez-Quintela MA, et al. Interaction of polyacrylic acid coated and non-coated iron oxide nanoparticles with human neutrophils. *Toxicol Lett* (2014) 225:57–65. doi: 10.1016/j.toxlet.2013.11.020
20. Lacy P. Mechanisms of Degranulation in Neutrophils. *All Asth Clin Immun* (2006) 2:98. doi: 10.1186/1710-1492-2-3-98
21. Winterbourn CC, Kettle AJ, Hampton MB. Reactive Oxygen Species and Neutrophil Function. *Annu Rev Biochem* (2016) 85:765–92. doi: 10.1146/annurev-biochem-060815-014442
22. Noël C, Simard JC, Girard D. Gold nanoparticles induce apoptosis, endoplasmic reticulum stress events and cleavage of cytoskeletal proteins in human neutrophils. *Toxicol In Vitro* (2016) 31:12–22. doi: 10.1016/j.tiv.2015.11.003
23. Fromen CA, Kelley WJ, Fish MB, Adili R, Nobl J, Hoenerhoff MJ, et al. Neutrophil–Particle Interactions in Blood Circulation Drive Particle Clearance and Alter Neutrophil Responses in Acute Inflammation. *ACS Nano* (2017) 11:10797–807. doi: 10.1021/acsnano.7b03190
24. Kelley WJ, Onyskiw PJ, Fromen CA, Eniola-Adefeso O. Model Particulate Drug Carriers Modulate Leukocyte Adhesion in Human Blood Flows. *ACS Biomater Sci Eng* (2019) 5:6530–40. doi: 10.1021/acsbiomaterials.9b01289
25. Macdougall I, Strauss W, McLaughlin J, Li Z, Dellana F, Hertel J. A randomized comparison of ferumoxytol and iron sucrose for treating iron deficiency anemia in patients with CKD. *Clin J Am Soc Nephrol* (2014) 4:705–12. doi: 10.2215/CJN.05320513
26. Coyne DW. Ferumoxytol for treatment of iron deficiency anemia in patients with chronic kidney disease. *Expert Opin Pharmacother* (2009) 10(15):2563–8. doi: 10.1517/14656560903224998
27. Foster GA, Gower RM, Stanhope KL, Havel PJ, Simon SI, Armstrong EJ. On-chip phenotypic analysis of inflammatory monocytes in atherogenesis and myocardial infarction. *Proc Natl Acad Sci USA* (2013) 110:13944–9. doi: 10.1073/pnas.1300651110
28. Lum AF, Green CE, Lee GR, Staunton DE, Simon SI. Dynamic regulation of LFA-1 activation and neutrophil arrest on intercellular adhesion molecule 1 (ICAM-1) in shear flow. *J Biol Chem* (2002) 277:20660–70. doi: 10.1074/jbc.M202223200
29. Miralda I, Uriarte SM, McLeish KR. Multiple phenotypic changes define neutrophil priming. *Front Cell Infect Microbiol* (2017) 7:217. doi: 10.3389/fcimb.2017.00217
30. Rose JJ, Foley JF, Murphy PM, Venkatesan S. On the mechanism and significance of ligand-induced internalization of human neutrophil chemokine receptors CXCR1 and CXCR2. *J Biol Chem* (2004) 279:24372–24386. doi: 10.1074/jbc.M401364200
31. Zhu L, He P. fMLP-stimulated release of reactive oxygen species from adherent leukocytes increases microvessel permeability. *Am J Physiol Heart Circ Physiol* (2006) 290:H365–72. doi: 10.1152/ajpheart.00812.2005
32. Guichard C, Pedruzzi E, Dewas C, Fay M, Pouzet C, Bens M, et al. Interleukin-8-induced priming of neutrophil oxidative burst requires sequential recruitment of NADPH oxidase components into lipid rafts. *J Biol Chem* (2005) 280:37021–32. doi: 10.1074/jbc.M506594200
33. Schaff UY, Xing MM, Lin KK, Pan N, Jeon NL, Simon SI. Vascular mimetics based on microfluidics for imaging the leukocyte–endothelial inflammatory response. *Lab Chip* (2007) 7:448–56. doi: 10.1039/b617915k
34. Morikis VA, Chase S, Wun T, Chaikof EL, Magnani JL. Simon SI; Selectin catch-bonds mechanotransduce integrin activation and neutrophil arrest on inflamed endothelium under shear flow. *Blood* (2017) 130:2101–10. doi: 10.1182/blood-2017-05-783027
35. Schaff UY, Yamayoshi I, Tse T, Griffin D, Kibathi L, Simon SI. Calcium flux in neutrophils synchronizes beta2 integrin adhesive and signaling events that guide inflammatory recruitment. *Ann BioMed Eng* (2008) 36:632–46. doi: 10.1007/s10439-008-9453-8
36. Immler R, Simon SI, Sperandio M. Calcium signalling and related ion channels in neutrophil recruitment and function. *Eur J Clin Invest* (2018) 48(Suppl. 2):e12964. doi: 10.1111/eci.12964
37. Anderson R, Visser SS, Ramafi G, Theron AJ. Accelerated resequestration of cytosolic calcium and suppression of the pro-inflammatory activities of human neutrophils by CGS 21680 in vitro. *Br J Pharmacol* (2000) 130:717–24. doi: 10.1038/sj.bjp.0703344
38. Morikis VA, Simon SI. Neutrophil mechanosignaling promotes integrin engagement with endothelial cells and motility within inflamed vessels. *Front Immunol* (2018) 9:2774. doi: 10.3389/fimmu.2018.02774
39. Simon SI, Hu Y, Vestweber D, Smith CW. Neutrophil tethering on E-selectin activates beta 2 integrin binding to ICAM-1 through a mitogen-activated protein kinase signal transduction pathway. *J Immunol* (2000) 164:4348–58. doi: 10.4049/jimmunol.164.8.4348
40. Bilyy R, Unterweger H, Weigel B, Dumych T, Paryzhak S, Vovk V, et al. Inert Coats of Magnetic Nanoparticles Prevent Formation of Occlusive Intravascular

Co-aggregates With Neutrophil Extracellular Traps. *Front Immunol* (2018) 9:2266. doi: 10.3389/fimmu.2018.02266

41. Cappenberg A, Margraf A, Thomas K, Bardel B, McCreedy DA, Van Marck V, et al. L-selectin shedding affects bacterial clearance in the lung: a new regulatory pathway for integrin outside-in signaling. *Blood* (2019) 134:1445–57. doi: 10.1182/blood.2019000685
42. Mueller H, Stadtmann A, Van Aken H, Hirsch E, Wang D, Ley K, et al. Tyrosine kinase Btk regulates E-selectin-mediated integrin activation and neutrophil recruitment by controlling phospholipase C (PLC) gamma2 and PI3Kgamma pathways. *Blood* (2010) 115:3118–27. doi: 10.1182/blood-2009-11-254185

Conflict of Interest: The authors declare that the research was conducted in the absence of any commercial or financial relationships that could be construed as a potential conflict of interest.

frontiers in Immunology

ORIGINAL RESEARCH
published: 06 January 2021
doi: 10.3389/fimmu.2020.613830

Altering Antigen Charge to Control Self-Assembly and Processing of Immune Signals During Cancer Vaccination

Shannon J. Tsai[1], *Allie Amerman*[1] *and Christopher M. Jewell*[1,2,3,4,5]*

[1] Fischell Department of Bioengineering, University of Maryland, College Park, MD, United States, [2] Robert E. Fischell Institute for Biomedical Devices, University of Maryland, College Park, MD, United States, [3] United States Department of Veterans Affairs, VA Maryland Health Care System, Baltimore, MD, United States, [4] Department of Microbiology and Immunology, University of Maryland Medical School, Baltimore, MD, United States, [5] Marlene and Stewart Greenebaum Cancer Center, Baltimore, MD, United States

Biomaterial delivery systems offer unique potential to improve cancer vaccines by offering targeted delivery and modularity to address disease heterogeneity. Here, we develop a simple platform using a conserved human melanoma peptide antigen (Trp2) modified with cationic arginine residues that condenses an anionic toll-like receptor agonist (TLRa), CpG, into polyplex-like nanoparticles. We reasoned that these structures could offer several useful features for immunotherapy – such as tunable loading, co-delivery of immune cues, and cargo protection – while eliminating the need for synthetic polymers or other complicating delivery systems. We demonstrate that Trp2/CpG polyplexes can readily form over a range of Trp2:CpG ratios and improve antigen uptake by primary antigen presenting cells. We show antigen loading can be tuned by interchanging Trp2 peptides with defined charges and numbers of arginine residues. Notably, these polyplexes with greater antigen loading enhance the functionality of Trp-2 specific T cells and in a mouse melanoma model, decrease tumor burden and improve survival. This work highlights opportunities to control the biophysical properties of nanostructured materials built from immune signals to enhance immunotherapy, without the added complexity or background immune effects often associated with synthetic carriers.

Keywords: immunotherapy, vaccine, cancer, immune, polyplex, nanoparticle, co-delivery, self-assembly

OPEN ACCESS

Edited by:
Li Tang,
École Polytechnique Fédérale de Lausanne, Switzerland

Reviewed by:
Jai Rudra,
Washington University in St. Louis, United States
Yiran Zheng,
Soochow University, China

***Correspondence:**
Christopher M. Jewell
cmjewell@umd.edu

Specialty section:
This article was submitted to Cancer Immunity and Immunotherapy, a section of the journal Frontiers in Immunology

Received: *03 October 2020*
Accepted: *19 November 2020*
Published: *06 January 2021*

Citation:
Tsai SJ, Amerman A and Jewell CM (2021) Altering Antigen Charge to Control Self-Assembly and Processing of Immune Signals During Cancer Vaccination. Front. Immunol. 11:613830. doi: 10.3389/fimmu.2020.613830

INTRODUCTION

Cancer vaccines present an exciting new strategy to harness the selective ability of the immune system to target tumor cells (1–3). Tumors evade normal immune function in part because they are self-derived cells, minimizing immunogenicity and the warning signals pathogens typically display (4). These innate immune signals are needed to activate dendritic cells (DCs) and other antigen presenting cells to support adaptive immune responses that can combat pathogen or tumors. Additionally, the tumor microenvironment is highly suppressive, hindering the ability of immune cells to maintain anti-tumor responses (5, 6). Improved understanding of the innate immune system

has allowed for the discovery and design of new immunomodulatory molecules that can target specific pathways to generate robust pro-immune responses and enhance tumor-specific T cell expansion (7, 8). Many candidate immunotherapeutic approaches are thus exploring agonists that target toll-like receptors (TLR), a family of pathways that recognize pathogen-associated molecular patterns that are expressed on bacteria, viruses, and peptides, or released from stressed or dying cells (9–11). These immunostimulatory molecules can induce potent T cell responses. Along these lines, several FDA-approved immunotherapies have emerged, such as Cervarix (cervical cancer) and Aldara (basal cell carcinoma) that trigger TLR4 and TLR7/8 (12). A number of candidate cancer vaccines are also exploring CpG – a DNA motif commonly found in bacteria – to promote an immunostimulatory cascade and potentiate an antigen-specific immune responses through TLR9 binding and activation (13–15).

Following immunization, DCs take up and present antigen, express co-stimulatory molecules, and produce distinct cytokines that activate and expand cytotoxic T cells (CTLs) able to attack tumors (16). Due to this requirement for dual-presentation of antigen and costimulatory markers, codelivery of antigens and adjuvants can significantly improve the effectiveness of antigen-specific immunotherapies. Thus, the mechanisms of delivery and route of administration remain important considerations (17, 18). As one example, adjuvants delivered alone do not generate durable responses, lack specificity, and can lead to off-target effects. Conversely, delivery of antigens in the absence of immunostimulatory signals can promote immune tolerance (19, 20).

Owing to the potential benefits of precision co-delivery, new molecular-scale and nano-scale delivery systems are being explored to improve immunotherapies (21–23). Nanoparticles as carriers for cancer vaccines, for example, offer a platform for enhancing immune responses through controlled release and targeting to sites such as lymph nodes – tissues that coordinate adaptive immunity. Co-adsorption or co-encapsulation of antigen and adjuvant particles onto polymer scaffolds or inorganic templates also provide co-delivery and control over the internalization of immune signals to generate more potent responses (24, 25). Despite these advantages, many challenges remain to fully realize the benefits of these system, including antigen loading efficiency, more complex manufacturing and regulatory characterization, and heterogenous formulations that can impact safety profiles.

Nanoparticles termed polyplexes have been studied for decades as simple carriers to condense or encapsulate biologic cargo using electrostatic interactions (26–28). Most prominently, synthetic cationic polymers have been developed as gene or protein delivery agents to condense anionic nucleic acid cargo into particulate form that are more readily endocytosed (29). Additionally, by altering polymer structure and function, molecules features can be installed to address barriers to intracellular delivery, such as endosomal escape. While useful, in the vaccine and immunotherapy fields, there are some unique considerations. For example, many polymeric carriers intrinsically activate (30), suppress (31), or alter immune signaling (32) even in the absence of other antigens or adjuvants. These intrinsic immune characteristics can be useful, but can also hinder rational vaccine design and translation because the carrier itself may change the immune response to the antigen or other vaccine components. Additionally, as mentioned above, high-density co-display of antigen and adjuvant is important to generate strong, specific immune responses; in this context polyplexes are particularly well-suited since they by definition juxtapose the condensed components comprising the polyplexes.

To address the issues just highlighted, we assembled polyplex-like structures comprised entirely of immune signals: tumor antigens and TLR ligand. In particular, we assembled CpG – an anionic TLR9 agonist, and a conserved human melanoma peptide (Trp2) modified with arginine residues to create a net cationic charge. This approach of building polyplexes from tumor immunotherapy components offers several attractive design features. First, in contrast to traditional polyplexes, these nanostructures are assembled entirely from immune signals; this unique approach simplifies the design by eliminating the complicating immunogenic effects often associated with carriers or excipients. Secondly, the lack of carriers ensures a high density of immune signals, as 100% of the formulation is cargo. Third, polyplexes maintain many of the attractive features of biomaterial carriers, including a particulate nature for improved uptake, cargo protection, and co-delivery of immune signals. As mentioned, the particulate nature of polyplexes can promote uptake and delivery to internal compartments within cells; these are features that can both be leveraged in immunotherapy design. For example, efficient internalization is critical for antigen processing and subsequent presentation by DCs. Further, many TLRs are located intracellularly within endosomes – including TLR9; agonists such as CpG must therefore be internalized by immune cells to be effective. Uniquely, in our approach, we demonstrate that anionic CpG and cationic Trp2 peptide electrostatically self-assemble to juxtapose antigen and adjuvant for co-delivery without need of synthetic polymers or other carriers. Using this platform, we show that Trp2/CpG polyplexes form over a range of Trp2:CpG ratios and improve antigen uptake by DCs. Treatment of primary DCs strongly activated these cells and promoted Trp2-specific T cell proliferation. Interestingly, polyplexes with higher Trp2:CpG ratios elicit increased inflammatory cytokine production. Leveraging the modularity of this platform, we demonstrate a role of antigen dose using Trp2 peptide modified with different numbers of arginine groups (i.e. 3, 6, and 9). Polyplexes with greater antigen loading enhance T cell functionality which correlates with reduced tumor burden and improved survival in a pre-clinical model of melanoma.

MATERIALS AND METHODS

Synthesis of Trp2:CpG Polyplexes

Trp2/CpG polyplexes were assembled by electrostatic condensation by mixing aqueous solutions of CpG DNA (5'-TCC ATG ACG TTC CTG ACG TT-3', IDT) and Trp2 peptide (SVYDFFVWL,

Genscript) modified with 3($Trp2R_3$), 6 ($Trp2R_6$) or 9 ($Trp2R_9$) arginine groups. CpG and Trp2R were combined at defined mass ratios ranging from 1:5 to 10:1 $Trp2R_x$: CpG (x=3, 6, 9) by fixing the CpG concentration at 10 μg/mL and varying the amount of $Trp2R_x$ under a fixed total volume. Thus, the amount of CpG in each polyplex formulation remained constant irrespective of mass ratio.

Characterization of Trp2/CpG Polyplexes

Polyplex formation was assessed by SYBR green exclusion assay. 10 μL SYBR Green I at 100X was added to 90 μL reaction mixture of complexes and incubated for 1h. Fluorescence was measured using an excitation wavelength of 497 nm and an emission wavelength of 520 nm. The resulting fluorescence was compared to the average fluorescence of free soluble CpG to determine the fraction of CpG that remained uncondensed. Formation and stability of polyplexes was evaluated by gel retardation assays. 10 μL (100 ng CpG) aliquots of polyplexes were loaded onto a 4% agarose gel with gel loading dye and SYBR Green I (Invitrogen). Electrophoresis was performed at 120V for 20 min in 1X Tris-Borate-EDTA (TBE) buffer. The gel was subsequently imaged using a UV illuminator. The hydrodynamic diameter and zeta potential of complexes were measured in triplicate using a Zetasizer Nano Z590.

Enzymatic Degradation Assay

CpG was labelled with Cy5 per manufacturer instructions (Mirus, Madison, WI). Polyplexes of varying $Trp2R_9$:CpG ratios were made using Cy5-CpG and $Trp2R_9$ in 100 uL 1X DNA I reaction buffer. Fluorescence was measured using an excitation wavelength of 640 nm and an emission wavelength of 670 nm to determine initial CpG levels. Fluorescent measurement was chosen to quantify CpG amount over spectrophotometry because peptides (i.e. $Trp2R_9$) exhibit absorbance overlap at 260 nm. The complexes were then incubated with 2 units of DNAse I (New England Biolabs) for 30 min at 37°C. Following incubation, the fluorescence was immediately measured again and the extent of degradation of Cy5-CpG in polyplexes was determined by comparing fluorescence intensities relative before and after the addition of DNAse I.

DC Uptake and Activation

Splenic $CD11c^+$ cells were isolated from 6-8 week old female C57BL/6J mice (Jackson Laboratories) through positive selection by magnetic isolation in accordance with manufacturer protocols (Miltenyi Biotech, Cambridge, MA). Cells were plated at 5 x 10^4 cells per well in 96-well plates with RPMI 1640 media (Lonza, Allendale, NJ) supplemented with 10% FBS, 2mM, L-glutamine, 1X non-essential amino acids, 10mM HEPES buffer (Fisher Scientific, Hampton, NH), 1% penicillin and streptomycin (Gibco), and 55 uM β-mercaptoethanol (Sigma-Aldrich). Cells were treated with either vehicle (water), 200ng of CpG complexed at increasing w/w ratio with $Trp2R_9$, or dose-matched soluble CpG and $Trp2R_9$. For uptake studies, CpG was labelled with Cy5 per manufacturer instructions (Mirus, Madison, WI) and Cy5 CpG was used to form complexes with FITC-$Trp2R_9$ (Genscript). DCs were incubated with treatments for 24h at 37°C, then washed and stained for DAPI, and analyzed by flow cytometry (BD Biosciences). Uptake was also confirmed by confocal microscopy. Splenic CD11c+ cells were isolated and 10^6 cells were plated onto glass-bottom dishes with No. 1.5 thickness (MatTek). Cells were incubated for 24 h, after which cells were fixed in 4% paraformaldehyde, stained for membrane (wheat germ agglutinin (WGA), Texas Red conjugate) and resuspended in Hoescht for imaging. Images were taken using a Leica SP5X Laser Scanning Confocal and analyzed by FIJI/ImageJ (National Health Institute). For activation studies, DCs were incubated with treatments for 24h, then washed and stained for DAPI and surface activation markers: CD40, CD80, CD86 (BD, San Jose, CA). Cells were then analyzed by flow cytometry.

DC/T Cell Co-culture

Splenic primary $CD11c^+$ cells were isolated as described above, plated at 5 x 10^4 cells, and treated with polyplexes. After incubation for 24 h, $CD8^+$ T cells were isolated from the spleens of Trp2-clone 37 mice (a gift from Dr. Giorgio Trinchieri, National Cancer Institute, NIH), a Trp2-specific transgenic strain, using negative selection *via* magnetic isolation in accordance with manufacturer instructions (StemCell Technologies, Vancouver, BC). Trp2-specific T cells were then labelled by incubating with 50 μM 5(6)Carboxyfluorescein diacetate N-succinimidyl ester (CFSE) (Sigma Aldrich) per mL of cells for 5 min at room temperature, followed by washing in media. 1.5 x 10^5 of CFSE labelled Trp2 T cells were then added to treated DC and cultured for an additional 72 h. Following incubation, cells were collected and stained for T cell specific surface markers (CD3e, CD8a), and resuspended in DAPI. T cell proliferation was determined by flow cytometry to measure CFSE dilution.

Enzyme-Linked Immunosorbent Assay (ELISA)

Supernatants from DC/T cell cultures were collected. Cytokine secretion levels were analyzed *via* ELISA for mouse interferon gamma (IFN-γ) secretion, following manufacturer instructions (BD). 96-well plates were coated with an IFN-γ capture antibody and incubated overnight. Supernatant samples were then added and allowed to bind for 2 hr, followed by an IFN-γ detection antibody and streptavidin-horseradish peroxidase conjugate mixture for 1 h. A tetramethylbenzidine and hydrogen peroxide mixture was added to each well; this reaction was stopped by the addition of 1 M phosphoric acid. Absorbance was read at 450 nm and IFN-γ concentrations were calculated from absorbance by comparing to a standard curve.

Murine Tumor Models

All studies involving mice (as a source of primary cells) were carried out in compliance with federal, state, and local laws and followed institutional guidelines, including the Guide for the Care and Use of Laboratory Animals and the Animal Welfare

Act. All experiments were reviewed and approved by the University of Maryland's Institutional Animal Care and Use Committee (IACUC). Mice were shaved and injected subcutaneously (s.c.) with $3x10^5$ B16-F10 cells in 50 µL of PBS, and weighed and monitored daily for tumor growth. Tumor size was determined as the product of two orthogonal diameters. Mice were treated s.c. with 50 µL of PBS or 25 µg $Trp2R_x$/CpG polyplex treatments when aggregate tumor burden reached 25 mm^2. Each group received additional doses every 3 days for up to four total treatments. Mice were euthanized according to the IACUC-approved humane endpoints when aggregate tumor burden reached 150 mm^2.

Statistics

One-way ANOVA was used to compare three or more groups, with Tukey post-test corrections for multiple comparisons. Log-rank tests were used in analyses of survival. All tests were two-sided analyses and were performed using GraphPad Prism. Error bars in all panels represent mean ± standard error of the mean and p values < 0.05 were considered significant.

RESULTS

$Trp2R_9$ and CpG Self-Assemble Into Polyplex Nanoparticles

We first tested if polyplexes could be electrostatically assembled from CpG and Trp2 modified with cationic arginine residues ($Trp2R_9$) (**Figure 1A**). In these studies, the mass of CpG was fixed while the mass of $Trp2R_9$ was varied over a range of 1:5-10:1 $Trp2R_9$:CpG (w/w). This weight ratio range corresponds to a cationic:anionic molecular charge ratio of 0.99-4.94 (**Table 1**). To determine the ratios at which polyplex formation occurred, we performed a SYBR green exclusion assay. SYBR green II binds secondary and tertiary structural features on single-stranded DNA by intercalating local regions of stacked base pairs. While unbound SYBR green displays low levels of fluorescence, when bound to DNA, the dye undergoes structural changes resulting in strong fluorescence that increases with nucleic acid concentration. In these studies, the fluorescent intensity of SYBR Green II was measured by UV-vis spectroscopy and normalized to soluble CpG to determine the amount of free CpG remaining. Soluble CpG controls incubated with SYBR Green II led

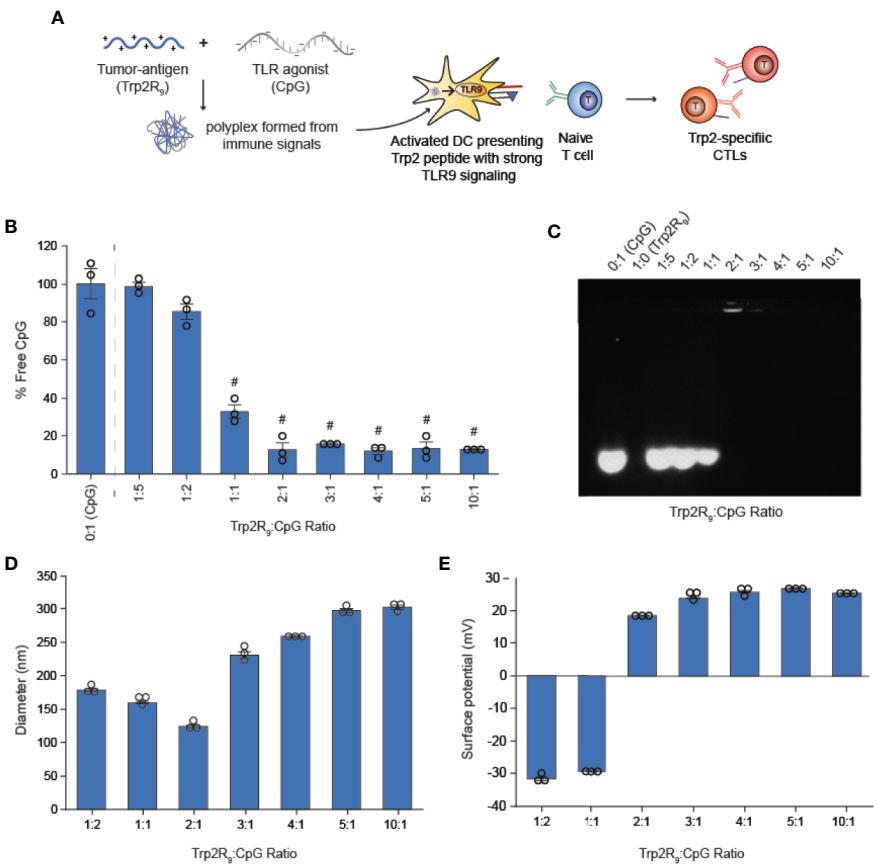

FIGURE 1 | $Trp2R_9$ and CpG self-assemble to form polyplexes **(A)** Schematic of polyplex assembly to activate cytotoxic T cells (CTLs) **(B)** SYBR Green exclusion assay confirms formation of polyplexes form at 1:1 $Trp2R_9$:CpG ratio **(C)** Gel retardation assay demonstrating the stability of polyplexes above 2:1 $Trp2R_9$:CpG ratio **(D)** Hydrodynamic diameter measurements of polyplexes confirming formation of polyplex nanoparticles. **(E)** Surface charge is readily tunable by altering the amount of $Trp2R_9$ during polyplex assembly. $^{\#}p < 0.0001$. Statistical comparisons are vs. 0:1 (CpG).

TABLE 1 | Physicochemical Properties of $Trp2R_x$/CpG polyplexes.

$Trp2R_x$: CpG (w/w)	$Trp2R_x$: CpGCharge Ratio			Diameter (nm)			Surface Charge (mV)			Composition (% Trp2)			Composition (% CpG)		
	x=3	x=6	x=9	x=3	x=6	x=9	x=3	x=6	x=9	x=3	x=6	x=9	x=3	x=6	x=9
1:1	0.39	0.76	0.99	*	145.83 ± 6.87	134.60 ± 2.12	*	-24.57 ± 0.21	-34.43 ± 0.69	64.6	60.1	55.0	35.4	39.9	45.0
2:1	0.78	1.51	1.98	81.34 ± 8.88	268.47 ± 19.23	120.77 ± 1.80	-26.10 ± 1.31	18.87 ± 0.50	-25.03 ± 0.41	72.5	59.2	59.0	27.5	40.8	41.0
3:1	1.17	2.26	2.96	199.7 ± 17.26	816.40 ± 60.73	128.63 ± 1.40	-11.53 ± .067	22.13 ± 0.21	21.63 ± 0.17	75.5	61.0	64.7	24.5	39.0	35.3
4:1	1.55	3.02	3.95	1765.6 ± 83.28	882.40 ± 37.08	159.87 ± 2.01	-.57 ± .13	24.73 ± 0.32	26.60 ± 0.35	75.3	65.1	66.1	24.7	34.9	33.9
5:1	1.94	3.77	4.94	1664.3 ± 160.73	686.07 ± 61.82	199.23 ± 2.76	5.96 ± .27	25.53 ± 0.55	26.4 ± 0.21	77.8	64.1	63.1	22.2	35.9	36.9

*particle concentration too dilute to measure.

to a high level of fluorescence (**Figure 1B**). We observed a significant reduction in fluorescence at 1:1 ratio of $Trp2R_9$:CpG and higher ratios, indicating condensation of CpG into polyplexes. To evaluate the stability of polyplexes, we performed gel migration assays. Electrophoresis of polyplexes loaded in agarose gels confirmed that polyplexes do not form below 1:1 $Trp2R_9$:CpG ratios (**Figure 1C**). This was indicated by the presence of free CpG under applied voltage. Disappearance of fluorescence above 1:1 $Trp2R_9$:CpG ratio indicated quenching of tightly bound nucleic acids and formation of larger complexes that did not migrate. Our studies revealed weak binding of $Trp2R_9$ and CpG at a 1:1 $Trp2R_9$:CpG weight ratio, as indicated by the presence of a CpG band under applied voltage. Disappearance of fluorescence at 2:1 or higher ratios – even though CpG was present at the same concentration in all wells – confirmed that CpG was fully condensed and $Trp2R_9$ and CpG formed stable polyplexes. These findings corresponded with the reduced fluorescence measured in the quantitative exclusion assays.

Dynamic light scattering confirmed the formation of nanoscale polyplexes with hydrodynamic diameters of 120.77 ± 1.80 nm to 280.8 ± 6.70 nm (**Figure 1D**). Following complete complexation of polyplexes (2:1 ratio), polyplex size increased with increasing $Trp2R_9$:CpG ratio. Size measurements could not be obtained below 1:2 $Trp2R_9$:CpG ratios, due to the low concentration of particles at this assembly ratio. Surface potential measurements revealed that at lower $Trp2R_9$:CpG ratios (i.e. 1:1), polyplexes exhibit negative surface charges, while at higher N:P ratios, the surface potential increased with the relative amount of $Trp2R_9$ in the polyplexes (**Figure 1E**). Charges ranged from -34.43 ± 0.69 mV to 25.4 ± .50mV, demonstrating the tunability of surface charge. As expected, reversal of zeta potential from negative to positive was found to occur between 1:1 and 2:1 $Trp2R_9$:CpG, corresponding to the ratio at which the positive and negative charges between $Trp2R_9$ and CpG are approximately balanced (i.e., a passing through a charge ratio of 1).

CpG Is Protected From Enzyme Degradation When Complexed With $Trp2R_9$

Nucleic acid TLR ligands delivered *in vivo* are exposed to nucleases in the extracellular environment or within endosomes that may degrade nucleic acids and inhibit TLR activation. Improving stability may not only increase half-life allowing for better bioavailability, but prolong adjuvant persistence which is important in the generation of more potent and longer-lasting immune responses. Thus, we next tested if condensation of $Trp2R_9$/CpG polyplexes could protect CpG from enzymatic degradation. Cy5-labelled CpG in soluble form or complexed with $Trp2R_9$ were incubated with DNAse and the fluorescent intensity was measured to quantify the amount of DNA present before and after degradation. These studies revealed that polyplexes significantly reduced CpG degradation across all charge ratios relative to free CpG, even at lower $Trp2R_9$:CpG ratios that only poorly or weakly condensed CpG (**Figure S1**). Thus, these wholly immunological polyplexes also maintain the cargo-protecting ability associated with conventional polyplexes that require synthetic polymers to condense cargo.

Polyplexes Colocalize Delivery of CpG and Trp2 and Increase Antigen Uptake by DCs

Because CpG is an agonist of TLR9, which is expressed intracellularly in endosomes, polyplexes must be internalized by DCs to initiate immunostimulatory signaling cascades. We hypothesized that the particulate nature of polyplexes would improve DC uptake compared to soluble controls. To test this, we next studied the immunological processing of complexes by measuring the level at which polyplexes were internalized by primary DCs. DCs were isolated from mouse spleens and incubated with polyplexes formed from fluorescently-labelled CpG and $Trp2R_9$ for 24 h. Corresponding dose-matched free CpG and $Trp2R_9$ were also included as controls. Flow cytometry analysis revealed that polyplexes generally provided a significant increase in both CpG (**Figures 2A, B**) and antigen (**Figures 2C, D**) relative to soluble forms of CpG and Trp2R9, respectively. This was indicated by increases in the mean fluorescence intensities of each signal. Antigen uptake was dose-dependent with the greatest $Trp2R_9$ uptake associated with the 5:1 $Trp2R_9$:CpG ratio; this ratio also contained the highest loading of $Trp2R_9$.

Initiation of immune responses requires simultaneous presentation of antigen and costimulatory signal. To assess whether polyplexes conferred co-delivery of immune signals within cells, DCs were also plated onto glass-bottom dishes, treated with polyplexes, and imaged by confocal microscopy. Internalized Trp2R9 and CpG signal was localized to similar regions within treated DCs, indicating intra-cellular co-localization of the cargo (**Figure 2E**). This ability to co-delivery signals is important to promote efficient adaptive immune responses, which require encounter of both antigen (e.g.Trp2) and stimulatory (e.g. CpG) signal. While flow cytometry

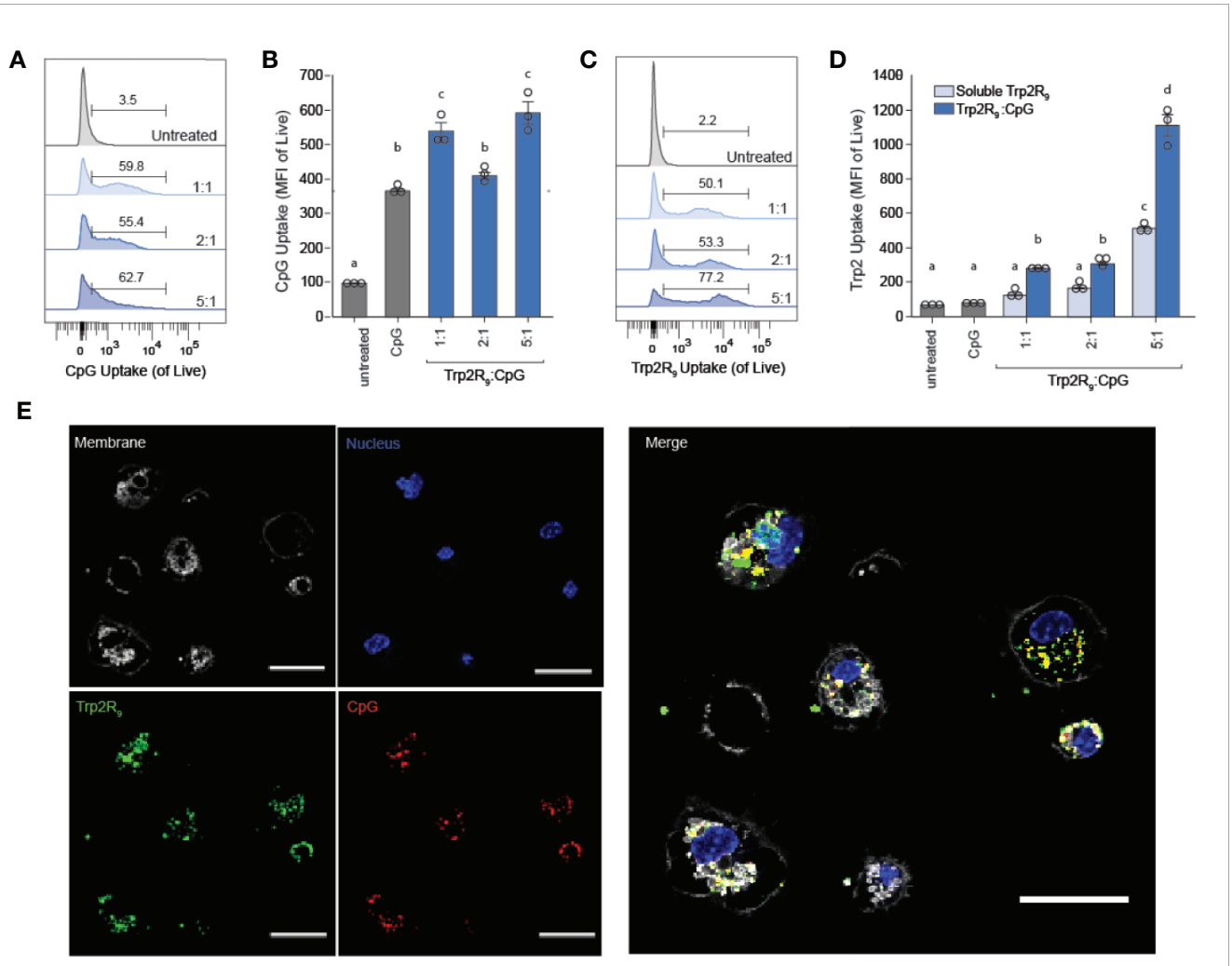

FIGURE 2 | $Trp2R_9$/CpG polyplexes improve immune signal uptake by DCs. **(A)** Representative gates and **(B)** quantification of CpG uptake by DCs following 24h incubation as measured by flow cytometry using Cy5-labelled CpG. **(C)** Representative gates and **(D)** quantification of $Trp2R_9$ uptake was measured using FITC-$Trp2R_9$. Quantitative analysis was performed to compare CpG uptake with soluble CpG controls or dose-matched $Trp2R_9$. **(E)** Confocal images of CpG and Trp2 uptake in DCs (scale bar = 30μm) demonstrate colocalization of immune signals within treated DCs. Different letters indicate statistical significance among means ($p < .05$).

provides quantitative data, these confocal microscopy studies provide spatial information. Thus, together, the data confirm polyplexes were taken up by DCs rather and the signals were co-localized, rather than a more general association with the extracellular surface of DCs.

Trp2R$_9$/CpG Polyplexes Activate DCs

To determine how polyplex uptake impacts DC activation, DCs were next treated with polyplexes ranging from 1:5 to 5:1 ratios. In these studies, polyplexes did not impact viability relative to other CpG-activated cells (**Figure 3A**). Compared to untreated cells and cells treated with soluble Trp2R$_9$, Trp2R$_9$/CpG polyplexes significantly increased expression of classical surface activation markers CD40, CD86, and CD80 (**Figures 3B–D**). Interestingly, at higher Trp2R$_9$:CpG ratios – which exhibited the most positive potentials (**Figure 1C**) and likely the strongest binding affinity between components, the polyplexes displayed reduced DC activation compared to soluble CpG; this was despite a constant fixed CpG dose across samples. In control studies, polyplexes formed with a non-immunostimulatory oligonucleotide in place of CpG did not cause any activation, suggesting that any activation activity observed with polyplexes is driven by the CpG component condensed in the polyplexes (**Figure S2**). Together, these results indicate that while the presence of CpG confers polyplex immunogenicity, the affinity and degree of condensation as a result of Trp2R$_9$ binding may influence the availability of CpG to stimulate TLR9.

Polyplexes Activate Trp2-Specific CD8$^+$ T Cells

The above results indicate that polyplexes differentially alter DC activation, a step that is critical in initiating and potentiating antigen-specific T cell responses. Antigen dose, however, can also play a critical role in shaping the magnitude and nature of adaptive immunity responses to cancer or infection. Thus, we next tested if different Trp2R$_9$:CpG ratios alter T the functional response of Trp2-specific T cells. In these experiments, splenic CD11c$^+$ DCs were isolated from mice and treated with polyplexes and cultured with CD8$^+$ T cells isolated from Trp2 transgenic mice (**Figure 4A**). CD8$^+$ T cells from these mice display T cell receptors specific for Trp2, and thus expand and secrete cytokines upon encountering antigen presentation with the appropriate co-stimulatory signals. Isolated T cells were labelled with fluorescent proliferation dye that becomes diluted with each generation of proliferation. Following co-culture for 72h, CD8$^+$ T cells were analyzed by flow cytometry to quantify proliferation. Interestingly, altering Trp2R$_9$:CpG ratios resulted in markedly different proliferation profiles (**Figure 4B**). Notably, lower ratios of Trp2R$_9$:CpG resulted in a heterogeneous population of T cells comprised of proliferated and unproliferated T cells that had undergone different levels of cell division, as indicated by the presence of several peaks across different intensities. Conversely, higher ratios of Trp2R$_9$:CpG resulted in a more uniform population of T cells undergoing similar levels of cell division, displaying only a few peaks over a narrow range of fluorescent intensity. While T cells treated with soluble CpG did not proliferate, all polyplex formulations resulted in T cells that strongly proliferated at similar levels to soluble CpG + Trp2 treated wells, as quantified by decreasing signal intensity of the proliferation dye (**Figure 4C**). This confirms the antigen-specific nature of this response. Further, at lower Trp2R$_9$:CpG ratios, combined delivery of CpG with Trp2R$_9$ in polyplexes significantly improved T cell expansion compared to soluble Trp2R$_9$ alone. However, these findings were not observed in polyplexes with higher Trp2R$_9$:CpG ratios, which expanded T cells at similar levels to soluble Trp2R$_9$. Notably, due to fixed CpG levels, lower Trp2R$_9$:CpG ratios contain less Trp2R$_9$, suggesting co-delivery with CpG

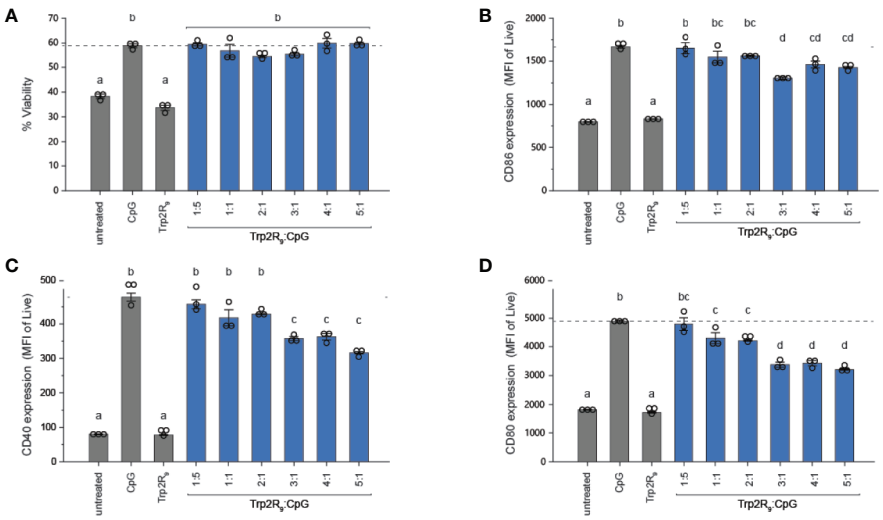

FIGURE 3 | Trp2R$_9$/CpG polyplexes are non-toxic and maintain ability to activate DCs. **(A)** Viability of treated DCs was measured by quantifying DAPI$^-$ cells. DC activation was measured by staining with fluorescent antibody conjugates for immunostimulatory markers **(B)** CD86, **(C)** CD40, and **(D)** CD80 and analyzed for expression levels by flow cytometry. Different letters indicate statistical significance among means ($p < .05$).

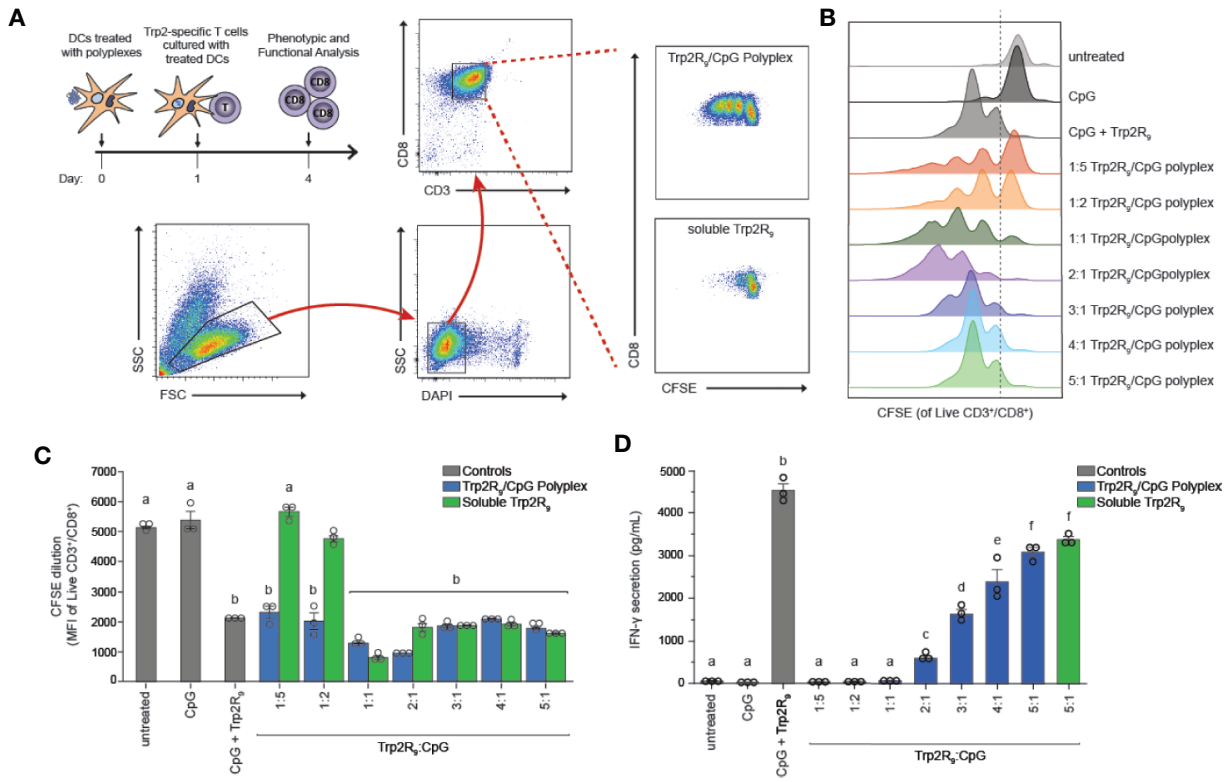

FIGURE 4 | Trp2R$_9$/CpG polyplexes promote antigen-specific T cell proliferation. DCs were treated with a library of Trp2R$_9$/CpG polyplex ratios, soluble CpG, or soluble Trp2R$_9$. After 24 h, T cells labeled with CFSE—a proliferation dye diluted with each generation of cell division—was added to culture. **(A)** Schematic of experimental set-up and representative gating schemes for flow cytometry analysis. Comparison is for proliferation of 1:5 Trp2R$_9$:CpG polyplexes and dose matched soluble Trp2 **(B)** Flow cytometry histograms for CFSE dilution illustrating distinct generations of T cell proliferation different proliferation profiles for each tested ratio of Trp2R$_9$:CpG **(C)** MFI of CFSE of CD3$^+$/CD8$^+$ cells following 72 h of DC/T-cell co-culture revealed that all complexes expanded Trp2-specific T cells with lower Trp2R$_9$:CpG ratios displaying increased levels of proliferation compared to dose-matched soluble Trp2 alone. **(D)** Higher ratios of Trp2R$_9$:CpG display increased levels of IFN-γ levels secreted in supernatants of DC/T cell co-cultures as measured by ELISA. Different letters indicate statistical significance among means ($p < .05$).

may be of particular importance at lower antigen doses to drive strong antigen-specific T cell proliferation.

To test if Trp2R$_9$:CpG polyplexes also altered T cell function, we measured interferon-gamma (IFN-γ) levels from culture supernatants by ELISA. IFN-γ is a key inflammatory cytokine and important for augmenting CD8$^+$ T cell cytotoxic function for enhancing anti-tumor and anti-viral effects (33). In these studies, IFN-γ secretion increased with increasing Trp2R$_9$:CpG ratio; the 5:1 Trp2R$_9$:CpG polyplexes displayed significantly higher levels of IFN-γ levels compared to all other tested ratios and similar levels to dose-matched soluble Trp2R$_9$ control (**Figure 4D**).

Polyplex Size, Charge, and Antigen Loading Can Be Tuned

The above results suggest that antigen dose plays an important role in T cell functionality. Thus, to further tune the dose of antigen and the relative number of epitopes – the number of copies of Trp2 delivered – we next used CpG to condense a series of alternate antigen designs in which Trp2 was modified with fewer arginine residues (i.e. Trp2R$_3$, Trp2R$_6$); this effectively increases the number of epitope copies at a fixed antigen dose. Using a fixed mass of CpG, polyplexes were formed by varying the mass ratio of Trp2R$_x$: CpG from 1:5-10:1. SYBR green exclusion assays revealed that Trp2R$_3$ and Trp2R$_6$ condensed CpG above 1:1 Trp2R$_x$: CpG ratios, as indicated by a significant reduction in fluorescence (**Figure 5A**). Dynamic light scattering revealed that condensation of CpG with Trp2R$_3$ resulted in smaller particles at 2:1 and 3:1 ratios (< 200nm), while polyplexes above 4:1 Trp2R$_3$:CpG ratio were much larger in size with particles ranging from 1664.33 ± 160.7 nm to 1791.03 ± 102.70 nm (**Figure 5B**). Sizes for ratios below 2:1 Trp2R$_3$:CpG could not be measured due to the low concentration of particles forming at this range or ratios. Surface charge ranged from -24.57 ± 0.21 mV to 25.53 ± 0.55 mV. As with Trp2R$_9$ complexes, surface charge increased with increasing Trp2R$_3$:CpG, however, charge inversion from negative to positive occurred at a higher Trp2R$_3$:CpG ratio of 2:1 (**Figure 5C**). This shift in zeta potential concurs with the ratio at which the Trp2R$_3$:CpG charge ratio is neutral (**Table 1**). Complexes formed using Trp2R$_6$ resulted in polyplexes that varied over a greater range of sizes compared to polyplexes formed using Trp2R$_9$, with hydrodynamic diameters of 145.83 ± 6.87 nm to 882.40 ± 37.08 nm (**Figure 5D**). Zeta potential measurements revealed that the surface charge

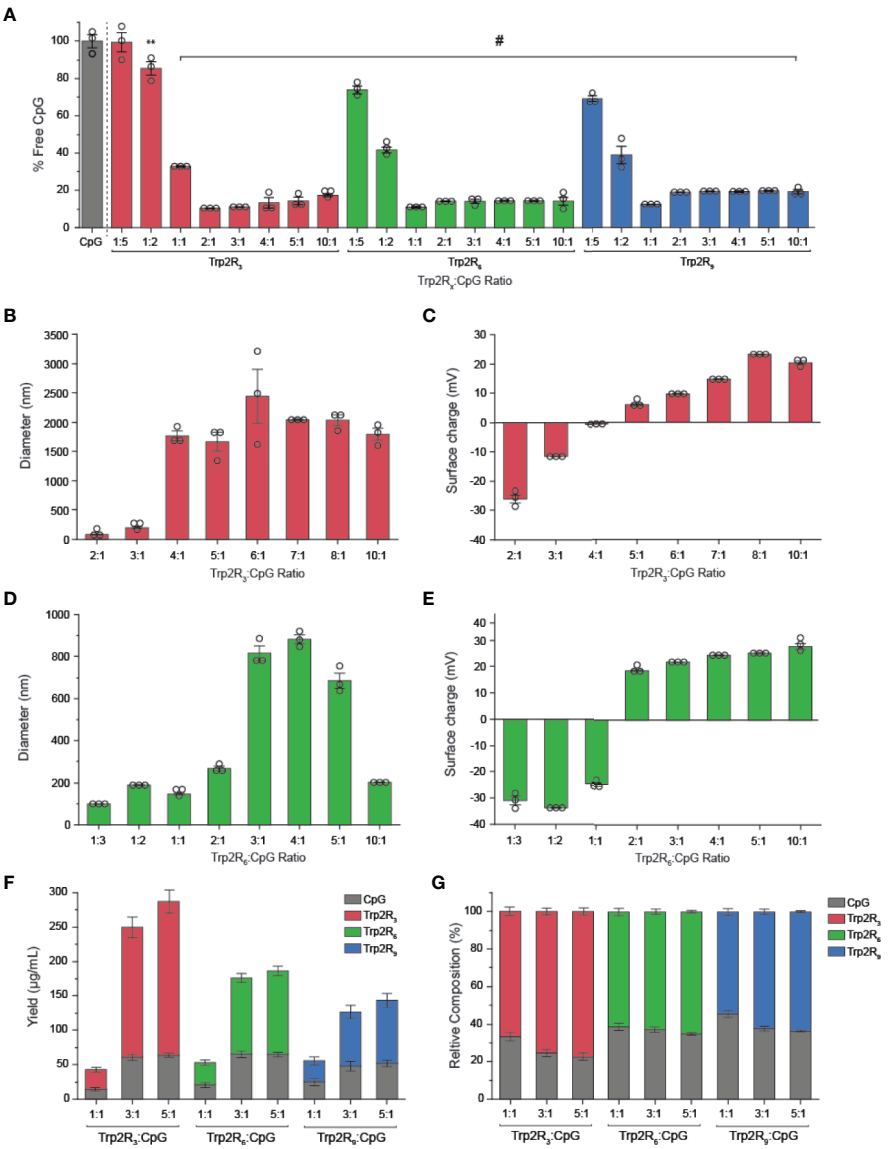

FIGURE 5 | Trp2/CpG polyplexes can be assembled with peptide modified with different numbers of arginine groups to form a diverse set of polyplexes with distinct size, charge, and loading characteristics. **(A)** SYBR Green exclusion assay demonstrate formation of polyplexes using Trp2 modified with R_3, R_6, and R_9. The hydrodynamic diameter **(B, D)** and **(C, E)** surface charge varied across $Trp2R_x$: CpG ratio for complexes formed with $Trp2R_3$ and $Trp2R_6$. Immune signal composition of assembled polyplexes was examined by analyzing **(F)** absolute and **(G)** relative loading. All significant comparisons are vs. soluble CpG and indicated, $^{**}p < 0.01$, $^{\#}p < 0.0001$.

for $Trp2R_6$/CpG polyplexes ranged from -24.57 ± 1.21 mV to 28.03 ± 1.93 mV (**Figure 5E**). Ratios below 1:1 exhibited negative surface charges, while at higher ratios, polyplexes were increasingly positively charged as a function of $Trp2R_6$:CpG ratios and as predicted by changes in charge ratio.

We next measured immune signal loading into complexes to assess how antigen composition was altered by using different levels of arginine modification and altering $Trp2R_x$: CpG ratios. In these studies, polyplexes formed using Trp2 with fewer arginine modifications (i.e. $Trp2R_3$) resulted in higher absolute yields of antigen within complexes (**Figure 5F**). 1:1 $Trp2R_x$: CpG ratios resulted in much lower yields of complexed immune signals. Similarly, the relative $Trp2R_x$ and CpG composition of polyplexes could be varied across different levels of arginine modifications and changes in $Trp2R_x$: CpG ratio, with 5:1 $Trp2R_3$:CpG polyplexes displaying the highest levels of antigen loading (**Figure 5G**). Comparisons of the polyplex diameter, charge, and loading between polyplexes formed by condensing CpG with $Trp2R_3$, $Trp2R_6$, and $Trp2R_9$ are provided in **Table 1**.

Polyplexes With Greater Amounts of Arginine Residues Drive Increased Antigen Uptake by DCs

The physicochemical properties of immune signal carriers play an important role in altering immune responses. For example, positive surface charges can improve carrier interactions with negatively charged cell membranes, and several studies demonstrate nanoparticles may allow for more efficient uptake compared to larger micron-sized particles. Due to the differences in size, charge and loading of polyplexes, we next compared polyplex uptake by DCs across varying ratios and number of arginine residues. In these studies, DC uptake of CpG was similar to soluble CpG across nearly all polyplexes tested, with the exception of 2:1 $Trp2R_9$, which showed increased CpG uptake (**Figure 6A**). In line with these findings, DC activation studies revealed that all polyplexes activated DCs on similar levels compared to soluble CpG controls (**Figure S3**). Notably, however, $Trp2R_9$ complexes displayed slightly lower levels of activation markers across CD86, CD40, and CD80. These findings may be attributed to tighter condensation of $Trp2R_9$ binding, which may influence the availability of CpG and Trp2 for DC activation and antigen presentation to T cells, respectively. To evaluate Trp2 uptake, soluble $Trp2R_3$, $Trp2R_6$, and $Trp2R_9$ were dose-matched to the highest level of $Trp2R_x$ given for each set of arginine modification (i.e. 5:1 $Trp2R_x$: CpG) (**Figure 6B**). At this dose of antigen, polyplexes increased $Trp2R_x$ uptake compared to their soluble $Trp2R_x$ counterparts. In this study, the most pronounced differences in increased antigen uptake was observed with increasing $TrpR_x$: CpG ratio. $Trp2R_x$ uptake, however, only modestly increased with increasing number of arginine residues (i.e $Trp2R_3$ vs. $Trp2R_6$ vs. $Trp2R_9$).

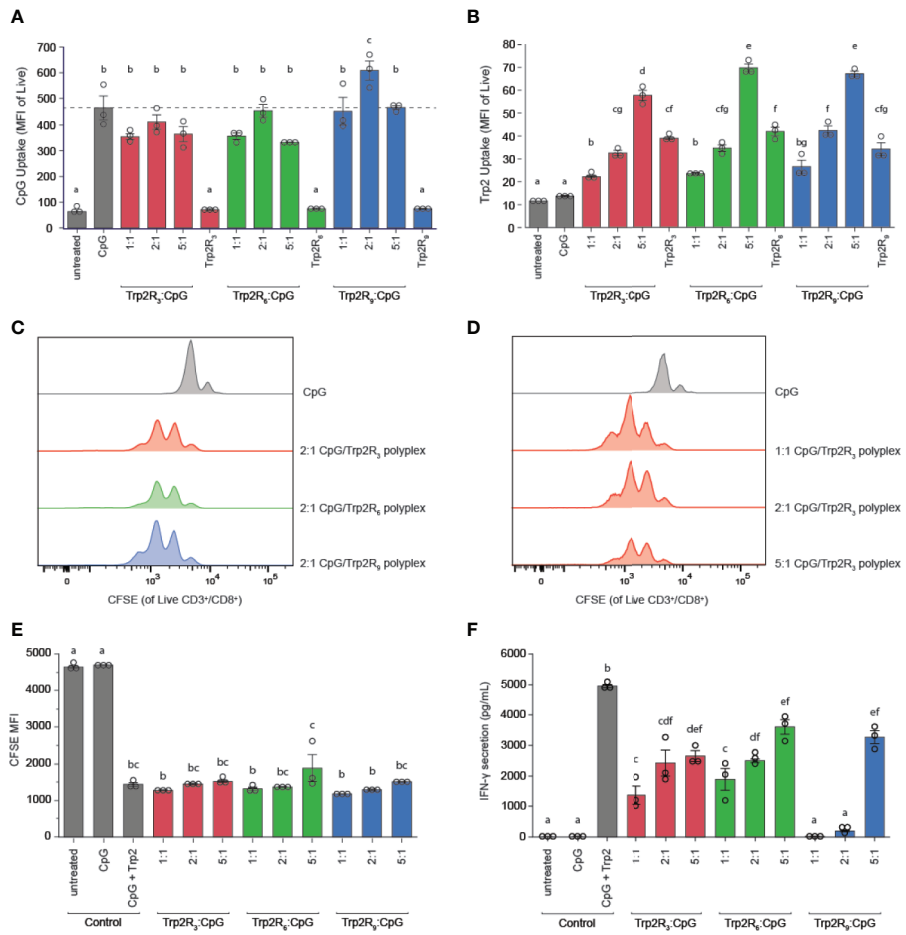

FIGURE 6 | Polyplexes with different arginine modifications on Trp2 retain ability to deliver immune signals and expand T cells, but Trp2 loading in polyplexes influences T cell functionality. Flow cytometry was used to measure **(A)** CpG uptake and **(B)** $Trp2R_x$ uptake following 24h incubation with $Trp2R_3$, $Trp2R_6$, or $Trp2R_9$ polyplexes. Representative histograms for T cells cultured with treated DCs demonstrate similar levels of T cell proliferation across different **(C)** numbers of arginine modification and **(D)** $Trp2R_x$: CpG ratio, with **(E)** quantification of proliferation by dilution of CFSE MFI. **(F)** ELISAs of supernatants from DC/T cell co-cultures reveal that IFN-γ secretion levels vary with number of arginine modifications and $Trp2R_x$: CpG ratio, with higher IFN-γ correlating with formulations with higher Trp2 loading. Different letters indicate statistical significance among means ($p < .05$).

Polyplexes With Different Arginine Modifications Retain Ability to Expand T Cells, With Higher Trp2 Loading Displaying Improved T Cell Functionality

Because polyplexes formed with different arginine modifications displayed different antigen compositions, we next tested if different levels of arginine modifications altered T cell proliferation and function. In these studies, $TrpR_x$: CpG polyplexes displayed similar levels of proliferation across both number of arginine modifications and $TrpR_x$: CpG ratio (**Figures 6C–E**). However, although CpG levels were fixed across ratios, we observed marked differences in IFN-γ levels, which increased with increasing $Trp2R_x$: CpG ratio (**Figure 6F**). Polyplexes formed using Trp2 modified with R_3 and R_6, which have improved Trp2 loading over $Trp2R_9$/CpG polyplexes, also promoted more IFN-γ secretion suggesting that Trp2 loading in polyplexes plays a role in promoting T cell functionality.

Trp2-CpG Polyplexes Slow Tumor Growth and Increase Survival Time in Mice

Having identified a link between antigen dose and activation of adaptive immune responses, we next tested if the relative amount of antigen in polyplexes impacted tumor progression in a mouse model of melanoma. For these studies, we leveraged different levels of arginine modifications to alter the number of epitopes delivered. Mice were inoculated with 3×10^5 B16-F10 cells in the right hind flank (**Figure 7A**). When tumors reached an aggregate tumor size of 0.25 cm^2 (~ 7 days following inoculation), mice were treated *s.c.* at the tail base on the tumor draining side with either PBS (sham) or polyplexes formed from $Trp2R_3$, $Trp2R_6$, or $Trp2R_9$ at 3:1 $Trp2R_x$: CpG ratio. Mice received three additional treatments at 3 day intervals. In these studies, the dose of CpG was constant in all groups containing oligonucleotide. Mice treated with sham exhibited mean survivals of 15 days, while polyplexes formed from $Trp2R_3$ significantly improved survival to 25.8 days (**Figures 7B, C**). Polyplexes formed from $Trp2R_6$

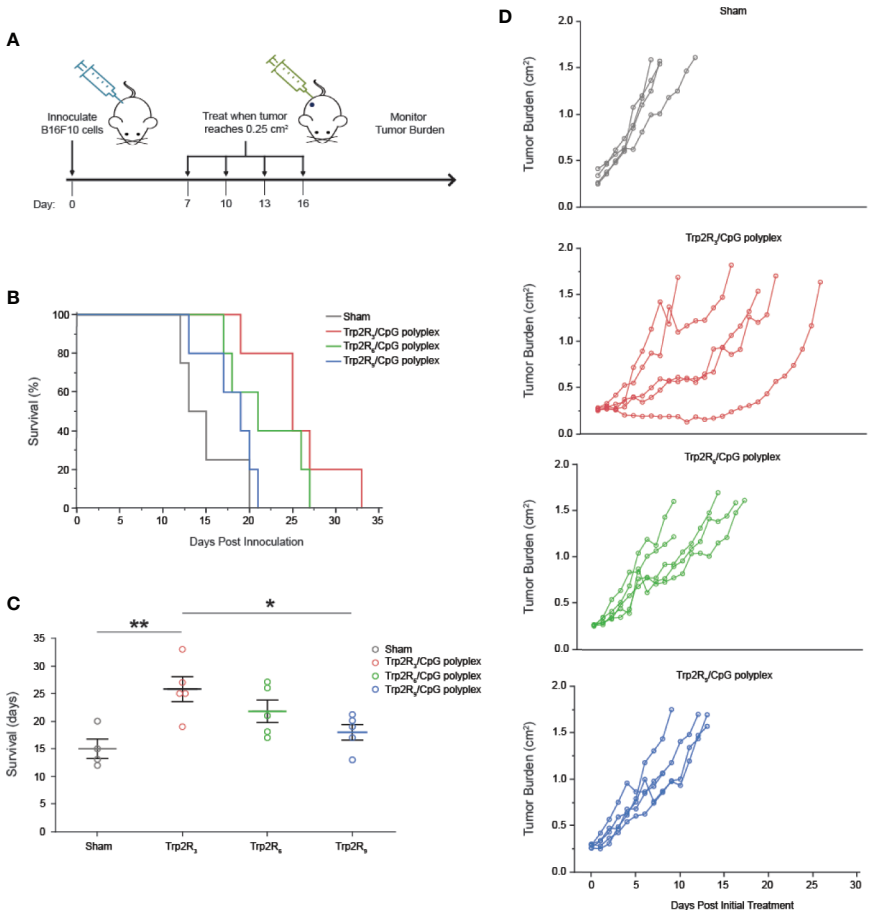

FIGURE 7 | Trp2/CpG polyplexes slow tumor growth and increase survival time in mouse melanoma model. **(A)** Schematic of treatment regimen. Mice were inoculated with tumors and treated with either: 1) PBS (Sham) and polyplexes comprised of CpG condense with Trp2 modified with 2) R_3 3) R_6 4) R_9. Mice were treated every 3 days for 4 treatments total. **(B)** Survival curves and **(C)** mean survival for each treatment. All significant comparisons are indicated *$p < 0.05$, **$p < 0.01$. Survival was measured as days post innoculation. **(D)** Tumor burden curves for each individual mouse in the study. All significant comparisons are indicated *$p < 0.05$, **$p < 0.01$.

and $Trp2R_9$ also showed a modest improvement in survival of 21.8 days and 18 days, however, these were not significant. The improvements in survival were also reflected in the relative rate of increase in tumor burden when assessing individual animals in each group (**Figure 7D**). In agreement with *in vitro* results, this study demonstrates that the ability of polyplexes to tune antigen dose and loading can be leveraged to promote significant improved outcomes during cancer vaccination.

DISCUSSION

Biomaterials offer many opportunities to improve upon current cancer therapies, many of which lack efficacy and fail to prevent relapse. We approached this challenge by harnessing the unique features of polyplexes to enable co-delivery of self-assembled melanoma antigen (Trp2) and a TLR agonist (CpG) in the absence of other carrier components. This approach can facilitate delivery of immune signals at high density to improve activation of potent immune responses. Designing simple, "carrier-free" vaccines provides an opportunity to develop insight into how each immune component impacts vaccine response to inform rational design of future vaccines. Additionally, we demonstrate that the modularity of this platform allows for incorporation of different antigen analogues to alter relative epitope concentration and physicochemical properties such as binding affinity, charge, and size. Importantly, we show that the underlying assembly processes are not impact by changes in the number of arginine modification, which is necessary to alter the amount of antigen in polyplexes. By assembling polyplexes with Trp2 and CpG, Trp2 was more efficiently internalized by DCs, colocalizing with CpG within cells. By tuning epitope concentration, we show that higher levels of antigen loading in polyplexes can promote improved antigen-specific T cell functionality *in vitro*, which translate to improved antitumor responses *in vivo*.

Polyplexes offer the opportunity to eliminate the presence of extraneous carrier materials in cancer vaccines while maintaining the features of traditional polymer platforms to leverage some of the physicochemical properties of biomaterial-based strategies. As one example, we found that polyplexes promoted improve antigen uptake compared to soluble antigen, which may be attributed to the particulate nature of complexes facilitating endocytosis. Additionally, modifying Trp2 with arginine residues results in a polyR tail, a motif commonly found in cell-penetrating peptides, which may drive transcytosis. This could be an interesting future direction to decipher the specific combination of internalization mechanisms, potentially as another level for controlling antigen and immune signal processing for self-assembled materials. Tunable surface charge can also influence uptake as cationic particles can improve material interactions with the negatively charged cell membranes. Surprisingly, in our studies, condensation of negatively charged CpG to form positively charged particles did not improve uptake compared to soluble CpG. One possibility is that surface charge may alter the mechanism of cellular uptake and subsequent intracellular trafficking, which can hinder uptake. Binding affinity may also affect the dissociation and subsequently the delivery and processing of immune signals within cells (34, 35).

Leveraging polyplex principles that require internalization in endosomes followed by escape into the cytosol for transcription and translation, our data demonstrates that polyplexes enable two distinct yet critical delivery routes. First, the ability of complexes to activate DCs suggests that polyplexes allow for the delivery and binding of CpG to receptors in endosomes to activate TLR pathways. Secondly, antigen delivered within cells can undergo endosomal escape into the cytosol for loading onto MHC-I, a critical step for activating $CD8^+$ T cells. Elucidating the precise trafficking mechanisms that facilitate polyplex processing through these pathways can offer valuable insight towards improving co-delivery of immune components.

We also observed some interesting differences in how CpG behaved in complexes versus soluble form. During DC activation studies with $Trp2R_9$ polyplexes, although $Trp2R_9$:CpG promoted high expression of activation markers, polyplex treated DCs were less activated compared to free CpG alone, and activation was further attenuated with increasing $Trp2R_9$:CpG (**Figures 3B–D**). One potential explanation is the strong binding between $Trp2R_9$ and CpG at higher ratios of $Trp2R_9$:CpG which could require a longer time for binding and processing or limit the availability of CpG to TLR9 receptors. Although the SYBR Green exclusion assay suggested similar binding levels (**Figure 1B**), more sensitive measurements of binding affinity such as surface plasmon resonance might provide additional insight into some of the different effects. Despite the less efficient activation of DCs by some $Trp2R_x$: CpG ratios, all polyplex formulations still promoted strong levels of activation and further, provide other benefits such as improved antigen uptake and protection from enzyme. Importantly in our studies, treatment of cells with free $Trp2R_x$ or $Trp2R_x$-ODN polyplexes generally did not activating cells, suggesting that CpG is the key driver of these observed effects.

Interestingly, polyplexes across all arginine modifications displayed similar levels of uptake, DC activation, and T cell expansion, despite changes in physicochemical properties for each library of Trp2 analogues. We instead observed that polyplexes formed from CpG and Trp2 modified with R_3 generally stronger T cell responses compared to complexes modified with R_6 or R_9. One possibility is that $Trp2R_3$ more closely resembles native Trp2 because it contains the fewest modifications and closest protein length, making it more easily processed by DCs and more readily identifiable by $CD8^+$ T cells specific to Trp2. Alternatively, at a given $Trp2R_x$: CpG ratio, $Trp2R_3$ complexes contained higher levels of Trp2, which may improve tumor-specific T cell activation. Many antigens expressed on tumors are also expressed on normal tissues; thus T cells specific to many tumor antigens are subject to thymic selection which deletes high avidity T-cells recognizing self-antigen (36). This leaves a repertoire of low avidity T cells that require high doses of antigen to become stimulated (37). This is

corroborated by our findings that increasing the antigen concentration by altering Trp2:CpG by was found to correlate with improved T cell functionality.

Our approach reveals several important questions for future studies. First, we prepared polyplexes using different analogues of the same tumor epitope. While T cells recognize specific epitopes, tumor antigens are larger proteins which present multiple peptide fragments, each with varying degrees of immunogenicity (38). Thus, additional studies are needed to investigate if the modularity of polyplexes can be extended to other tumor epitopes. Additionally, the polyplexes prepared in these studies contain a single antigen epitope. Recent studies, however, suggest that immunotherapies that target multiple epitopes allows for improved anti-tumor responses (39, 40). As one example, EMD640744, a multi-epitope vaccine for patients with advanced solid tumors, is currently undergoing phase I clinical trials (41). Targeting multiple epitopes allows for a wider spectrum of antigens that expanded T cells can recognize within heterogenous tumor cell populations. Further, potent anti-tumor responses arise from simultaneous induction of both humoral and cellular responses, requiring different epitopes to activate B cells and multiple subsets of T-cells (42–44). Thus, there is also motivation to test if multiple epitopes can be incorporated into polyplexes. Lastly, the finding that $Trp2R_3$ elicited the strongest functional T cell responses and subsequently improved tumor-burden raises some interesting implications surrounding the role of antigen in promoting anti-tumor immunity. Our results demonstrate that polyplex structures comprised of immune signals offer a tunable platform to co-deliver CpG and Trp2 peptide, while eliminating carrier components. As highlighted in our studies utilizing different Trp2 peptide modifications, the simple approach and modularity of this platform offers a unique opportunity to study the role of antigen dosing, structure, and co-delivery in stimulating effector T cell responses – this insight can contribute to new therapies to improve tumor-specific immune responses.

DATA AVAILABILITY STATEMENT

The datasets generated for this study are available on request to the corresponding author. Further inquiries can be directed to the corresponding author.

ETHICS STATEMENT

All studies involving animals were carried out in compliance with federal, state, and local laws and followed institutional guidelines, including the Guide for the Care and Use of Laboratory Animals and the Animal Welfare Act. All experiments were reviewed and approved by the University of Maryland's Institutional Animal Care and Use Committee (IACUC).

AUTHOR CONTRIBUTIONS

CJ, ST, and AA conceived the studies. ST and AA conducted the experiments and data analysis. All authors planned and wrote the manuscript. All authors contributed to the article and approved the submitted version.

FUNDING

This work was supported by in part by NIH # R01 EB027143 and United States Department of Veterans Affairs # I01 BX003690.

SUPPLEMENTARY MATERIAL

The Supplementary Material for this article can be found online at: https://www.frontiersin.org/articles/10.3389/fimmu.2020.613830/full#supplementary-material

REFERENCES

1. Mougel A, Terme M, Tanchot C. Therapeutic cancer vaccine and combinations with antiangiogenic therapies and immune checkpoint blockade. *Front Immunol* (2019) 10:467. doi: 10.3389/fimmu.2019.00467
2. Santos PM, Butterfield LH. Based Cancer Vaccines – Dendritic Cell Dendritic Cell–Based Cancer Vaccines. *J Immunol J Immunol Guest* (2018) 200:443–9. doi: 10.4049/jimmunol.1701024
3. Vermaelen K. Vaccine strategies to improve anticancer cellular immune responses. *Front Immunol* (2019) 10:8. doi: 10.3389/fimmu.2019.00008
4. Muenst S, Läubli H, Soysal SD, Zippelius A, Tzankov A, Hoeller S. The immune system and cancer evasion strategies: therapeutic concepts. *J Intern Med* (2016) 279:541–62. doi: 10.1111/joim.12470
5. Tormoen GW, Crittenden MR, Gough MJ. Role of the immunosuppressive microenvironment in immunotherapy. *Adv Radiat Oncol* (2018) 3:520–6. doi: 10.1016/j.adro.2018.08.018
6. Gu L, Mooney DJ. Biomaterials and emerging anticancer therapeutic: engineering the tumor microenvironment. *Nat Rev Cancer* (2016) 16:56–66. doi: 10.1038/nrc.2015.3.Biomaterials
7. Maisonneuve C, Bertholet S, Philpott DJ, De Gregorio E. Unleashing the potential of NOD- and Toll-like agonists as vaccine adjuvants. *Proc Natl Acad Sci* (2014) 111:12294–9. doi: 10.1073/pnas.1400478111
8. Latz E, Schoenemeyer A, Visintin A, Fitzgerald KA, Monks BG, Knetter CF, et al. TLR9 signals after translocating from the ER to CpG DNA in the lysosome. *Nat Immunol* (2004) 5:190–8. doi: 10.1038/ni1028
9. Huang L, Xu H, Peng G. TLR-mediated metabolic reprogramming in the tumor microenvironment: potential novel strategies for cancer immunotherapy. *Cell Mol Immunol* (2018) 15:428–37. doi: 10.1038/cmi.2018.4
10. Kuai R, Ochyl LJ, Bahjat KS, Schwendeman A, Moon JJ. Designer vaccine nanodiscs for personalized cancer immunotherapy. *Nat Mater* (2016) 16:489–96. doi: 10.1038/nmat4822
11. Lynn GM, Sedlik C, Baharom F, Zhu Y, Ramirez-Valdez RA, Coble VL, et al. Peptide–TLR-7/8a conjugate vaccines chemically programmed for nanoparticle self-assembly enhance CD8 T-cell immunity to tumor antigens. *Nat Biotechnol* (2020) 38:320–32. doi: 10.1038/s41587-019-0390-x
12. Karolinska C, Melero I, Gaudernack G, Gerritsen W, Huber C, Parmiani G, et al. Therapeutic vaccines for cancer: an overview of clinical trials. *Nat Publ Gr* (2014) 11:509–24. doi: 10.1038/nrclinonc.2014.111
13. Cai Z, Xin F, Wei Z, Wu M, Lin X, Du X, et al. Photodynamic Therapy Combined with Antihypoxic Signaling and CpG Adjuvant as an In Situ Tumor Vaccine Based on Metal–Organic Framework Nanoparticles to Boost Cancer Immunotherapy. *Adv Healthc Mater* (2020) 9:1900996. doi: 10.1002/adhm.201900996
14. Cano-Mejia J, Bookstaver ML, Sweeney EE, Jewell CM, Fernandes R. Prussian blue nanoparticle-based antigenicity and adjuvanticity trigger robust

antitumor immune responses against neuroblastoma. *Biomater Sci* (2019) 7:1875–87. doi: 10.1039/c8bm01553h
15. Cha BG, Jeong JH, Kim J. Extra-Large Pore Mesoporous Silica Nanoparticles Enabling Co-Delivery of High Amounts of Protein Antigen and Toll-like Receptor 9 Agonist for Enhanced Cancer Vaccine Efficacy. *ACS Cent Sci* (2018) 4:484–92. doi: 10.1021/acscentsci.8b00035
16. Le Gall CM, Weiden J, Eggermont LJ, Figdor CG. Dendritic cells in cancer immunotherapy. *Nat Mater* (2018) 17:474–5. doi: 10.1038/s41563-018-0093-6
17. Bookstaver ML, Hess KL, Jewell CM. Self-Assembly of Immune Signals Improves Codelivery to Antigen Presenting Cells and Accelerates Signal Internalization, Processing Kinetics, and Immune Activation. *Small* (2018) 14:1802202. doi: 10.1002/smll.201802202
18. Zhu M, Ding X, Zhao R, Liu X, Shen H, Cai C, et al. Co-delivery of tumor antigen and dual toll-like receptor ligands into dendritic cell by silicon microparticle enables efficient immunotherapy against melanoma. *J Control Release* (2018) 272:72–82. doi: 10.1016/j.jconrel.2018.01.004
19. Hess KL, Oh E, Tostanoski LH, Andorko JI, Susumu K, Deschamps JR, et al. Engineering Immunological Tolerance Using Quantum Dots to Tune the Density of Self-Antigen Display. *Adv Funct Mater* (2017) 27:1700290. doi: 10.1002/adfm.201700290
20. Zinzow-Kramer WM, Weiss A, Au-Yeung BB. Adaptation by naïve CD4+ T cells to self-antigen–dependent TCR signaling induces functional heterogeneity and tolerance. *Proc Natl Acad Sci USA* (2019) 116:15160–9. doi: 10.1073/pnas.1904096116
21. Irvine DJ, Hanson MC, Rakhra K, Tokatlian T. Synthetic Nanoparticles for Vaccines and Immunotherapy. *Chem Rev* (2015) 115:11109–46. doi: 10.1021/acs.chemrev.5b00109
22. Gammon JM, Dold NM, Jewell CM, Gammon JM, Dold NM, Jewell CM, et al. Improving the clinical impact of biomaterials in cancer immunotherapy. *Oncotarget* (2016) 7:15421–43. doi: 10.18632/oncotarget.7304
23. Bookstaver ML, Tsai SJ, Bromberg JS, Jewell CM. Improving Vaccine and Immunotherapy Design Using Biomaterials. *Trends Immunol* (2017) 39:135–50. doi: 10.1016/j.it.2017.10.002
24. Hess KL, Medintz IL, Jewell CM. Designing inorganic nanomaterials for vaccines and immunotherapies. *Nano Today* (2019) 27:73–98. doi: 10.1016/J.NANTOD.2019.04.005
25. Liu L, Ma P, Wang H, Zhang C, Sun H, Wang C, et al. Immune responses to vaccines delivered by encapsulation into and/or adsorption onto cationic lipid-PLGA hybrid nanoparticles. *J Control Release* (2016) 10:230–9. doi: 10.1016/j.jconrel.2016.01.050
26. Lu Y, Wu F, Duan W, Mu X, Fang S, Lu N, et al. Engineering a "PEG-g-PEI/DNA nanoparticle-in- PLGA microsphere" hybrid controlled release system to enhance immunogenicity of DNA vaccine. *Mater Sci Eng C* (2020) 106:110294. doi: 10.1016/j.msec.2019.110294
27. Wongrakpanich A, Adamcakova-Dodd A, Xie W, Joshi VB, Mapuskar KA, Geary SM, et al. The absence of CpG in plasmid DNA-chitosan polyplexes enhances transfection efficiencies and reduces inflammatory responses in murine lungs. *Mol Pharm* (2014) 11:1022–31. doi: 10.1021/mp400689r
28. Cui J, De Rose R, Best JP, Johnston APR, Alcantara S, Liang K, et al. Mechanically Tunable, Self-Adjuvanting Nanoengineered Polypeptide Particles. *Adv Mater* (2013) 25:3468–72. doi: 10.1002/adma.201300981
29. Zhang M, Weng Y, Cao Z, Guo S, Hu B, Lu M, et al. ROS Activatable siRNA-Engineered Polyplex for NIR-Triggered Synergistic Cancer Treatment. *ACS Appl Mater Interfaces* (2020) 12:32289–300. doi: 10.1021/acsami.0c06614
30. Andorko JI, Hess KL, Pineault KG, Jewell CM. Intrinsic immunogenicity of rapidly-degradable polymers evolves during degradation. *Acta Biomater* (2016) 32:24–34. doi: 10.1016/J.ACTBIO.2015.12.026
31. Saito E, Kuo R, Pearson RM, Gohel N, Cheung B, King NJC, et al. Designing drug-free biodegradable nanoparticles to modulate inflammatory monocytes and neutrophils for ameliorating inflammation. *J Control Release* (2019) 300:185–96. doi: 10.1016/J.JCONREL.2019.02.025
32. Zhu M, Du L, Zhao R, Wang HY, Zhao Y, Nie G, et al. Cell-Penetrating Nanoparticles Activate the Inflammasome to Enhance Antibody Production by Targeting Microtubule-Associated Protein 1-Light Chain 3 for Degradation. *ACS Nano* (2020). doi: 10.1021/acsnano.0c00962
33. Ivashkiv LB. IFNγ: signalling, epigenetics and roles in immunity, metabolism, disease and cancer immunotherapy. *Nat Rev Immunol* (2018) 18:545–58. doi: 10.1038/s41577-018-0029-z
34. Tsai SJ, Andorko JI, Zeng X, Gammon JM, Jewell CM. Polyplex interaction strength as a driver of potency during cancer immunotherapy. *Nano Res* (2018) 11:5642–56. doi: 10.1007/s12274-018-2181-y
35. You X, Gu Z, Huang J, Kang Y, Chu C-C, Wu J. Arginine-based poly(ester amide) nanoparticle platform: From structure–property relationship to nucleic acid delivery. *Acta Biomater* (2018) 74:180–91. doi: 10.1016/J.ACTBIO.2018.05.040
36. Kieback E, Hilgenberg E, Stervbo U, Lampropoulou V, Shen P, Bunse M, et al. Thymus-Derived Regulatory T Cells Are Positively Selected on Natural Self-Antigen through Cognate Interactions of High Functional Avidity. *Immunity* (2016) 44:1114–26. doi: 10.1016/j.immuni.2016.04.018
37. Carretero-Iglesia L, Couturaud B, Baumgaertner P, Schmidt J, Maby-El Hajjami H, Speiser DE, et al. High Peptide Dose Vaccination Promotes the Early Selection of Tumor Antigen-Specific CD8 T-Cells of Enhanced Functional Competence. *Front Immunol* (2020) 10:3016:3016. doi: 10.3389/fimmu.2019.03016
38. Zhang Y, Lin Z, Wan Y, Cai H, Deng L, Li R. The Immunogenicity and Anti-tumor Efficacy of a Rationally Designed Neoantigen Vaccine for B16F10 Mouse Melanoma. *Front Immunol* (2019) 10:2472. doi: 10.3389/fimmu.2019.02472
39. Alipour Talesh G, Ebrahimi Z, Badiee A, Mansourian M, Attar H, Arabi L, et al. Poly (I: C)-DOTAP cationic nanoliposome containing multi-epitope HER2-derived peptide promotes vaccine-elicited anti-tumor immunity in a murine model. *Immunol Lett* (2016) 176:57–64. doi: 10.1016/j.imlet.2016.05.016
40. Zhang L. Multi-epitope vaccines: A promising strategy against tumors and viral infections. *Cell Mol Immunol* (2018) 15:182–4. doi: 10.1038/cmi.2017.92
41. Lennerz V, Gross S, Gallerani E, Sessa C, Mach N, Boehm S, et al. Immunologic response to the survivin-derived multi-epitope vaccine EMD640744 in patients with advanced solid tumors. *Cancer Immunol Immunother* (2014) 63:381–94. doi: 10.1007/s00262-013-1516-5
42. Tsou P, Katayama H, Ostrin EJ, Hanash SM. The Emerging Role of B Cells in Tumor Immunity. *Cancer Res* (2016) 76:5597–601. doi: 10.1158/0008-5472.CAN-16-0431
43. Duong HTT, Thambi T, Yin Y, Kim SH, Nguyen TL, Phan VHG, et al. Degradation-regulated architecture of injectable smart hydrogels enhances humoral immune response and potentiates antitumor activity in human lung carcinoma. *Biomaterials* (2020) 230:119599. doi: 10.1016/j.biomaterials.2019.119599
44. Zhong X, Zhang Y, Tan L, Zheng T, Hou Y, Hong X, et al. An aluminum adjuvant-integrated nano-MOF as antigen delivery system to induce strong humoral and cellular immune responses. *J Control Release* (2019) 300:81–92. doi: 10.1016/j.jconrel.2019.02.035

Conflict of Interest: CJ is an employee of the VA Maryland Health Care System. The views reported in this paper do not reflect the views of the Department of Veterans Affairs or the United States Government. CJ has an equity position in Cellth Systems, LLC and Avidea Technologies.

The remaining authors declare that the research was conducted in the absence of any commercial or financial relationships that could be construed as a potential conflict of interest.

frontiers in Immunology

REVIEW
published: 24 February 2021
doi: 10.3389/fimmu.2021.566299

The Role of Extracellular Vesicles in the Pathogenesis and Treatment of Autoimmune Disorders

Mengrou Lu[1†], *Emma DiBernardo*[1,2†], *Emily Parks*[1], *Hannah Fox*[1], *Si-Yang Zheng*[1] *and Elizabeth Wayne*[1,2*]

[1] Department of Electrical and Computer Engineering, College of Engineering, Carnegie Mellon University, Pittsburgh, PA, United States, [2] Department of Chemical Engineering, College of Engineering, Carnegie Mellon University, Pittsburgh, PA, United States

OPEN ACCESS

Edited by:
Ankur Singh,
Georgia Institute of Technology,
United States

Reviewed by:
Bergithe Eikeland Oftedal,
University of Bergen, Norway
Wesley H. Brooks,
University of South Florida,
United States

***Correspondence:**
Elizabeth Wayne
ewayne@andrew.cmu.edu

[†]These authors have contributed equally to this work and share first authorship

Specialty section:
This article was submitted to Immunological Tolerance and Regulation, a section of the journal Frontiers in Immunology

Received: 27 May 2020
Accepted: 04 January 2021
Published: 24 February 2021

Citation:
Lu M, DiBernardo E, Parks E, Fox H, Zheng S-Y and Wayne E (2021) The Role of Extracellular Vesicles in the Pathogenesis and Treatment of Autoimmune Disorders. Front. Immunol. 12:566299. doi: 10.3389/fimmu.2021.566299

Extracellular vesicles (EVs) are important players in autoimmune diseases, both in disease pathogenesis and as potential treatments. EVs can transport autoimmune triggers throughout the body, facilitating the process of antigen presentation. Understanding the link between cellular stress and EV biogenesis and intercellular trafficking will advance our understanding of autoimmune diseases. In addition, EVs can also be effective treatments for autoimmune diseases. The diversity of cell types that produce EVs leads to a wide range of molecules to be present in EVs, and thus EVs have a wide range of physiological effects. EVs derived from dendritic cells or mesenchymal stem cells have been shown to reduce inflammation. Since many autoimmune treatments are focused only on symptom management, EVs present a promising avenue for potential treatments. This review looks at the different roles EVs can play in autoimmune diseases, from disease pathology to diagnosis and treatment. We also overview various methodologies in isolating or generating EVs and look to the future for possible applications of EVs in autoimmune diseases.

Keywords: extracellular vesicle, autoimmunity, antigen presentation, immune-related adverse events, therapeutic delivery

INTRODUCTION TO EXTRACELLULAR VESICLE (EV) BIOLOGY

Our understanding of the role of extracellular vesicles (EVs) in biological processes is rapidly evolving. There is substantial literature connecting cellular stress to autoimmunity, but surprisingly there are few that conceptualize EVs as the communication link (1–3). When EVs were first discovered, they were believed to be a final product, a mechanism for discarding unnecessary cellular materials (4). Subsequent studies showed that EVs could also function to transmit instructions for cell migration, proliferation, and differentiation (5). Later on, the role of EVs modulating immune responses through antigen presentation was uncovered (6). Immune cells secrete EVs and also receive cellular instructions from EVs that guide further immune reactions (7). We believe this is an emerging trend that should be evaluated when considering diagnostic and therapeutic applications.

EVs are produced by a variety of cells, and their content resembles their host cells—the lipid composition of the outer cell membrane makes up the outer membrane of the EV. In addition, EVs contain a mixture of bioactive molecules—i.e. proteins, nucleic acids, metabolites—derived from the cytoplasmic content of the host cell. Importantly, however, the concentration may not be similar, and studies have shown enrichment of proteins in EVs that was not apparent from the host cells (6, 8).

While exosome is the classical term, EV has become the more general term to encapsulate both the diversity and complexity of vesicles observed (9, 10). EVs range in size from 30 nm nanovesicles to ectosomes (100–1,000 nm) to 5 μm microparticles or microvesicles. Nanovesicles—the EV population most commonly thought of as exosomes—are thought to be derived from the fusion of specialized trafficking multi-vesicular endosomes within the cell membrane (11). In contrast, microvesicles are thought to be pinched or shed from the cell membrane (7). Microvesicles also include vesicles derived from apoptotic cells (ApoEVs) (12–14), which were formerly considered as debris rather than purposefully packaged compartments with immunoregulatory functions. The heterogeneity in nomenclature combined with historical EV isolation techniques that filtered out larger vesicles makes it difficult to compare studies (15). Moreover, some ApoEVs resemble nanovesicles in size, morphology, and surface markers (16). Nonetheless, these differences in biogenesis yield significant information about the host cells as well as the potential purpose of the resulting EVs.

Communication of EVs with immune cells occurs through a variety of mechanisms that are tightly paired with the intended downstream function. For example, EVs can be transmitted *via* direct cell-to-cell contact in the immune synapses, which are junctions between antigen-presenting cells (APCs) and T cells that mediate the antigen presentation process (17–19). EV membranes can include surface molecules that facilitate binding with the extracellular matrix (ECM) (20). The location of EVs within the ECM can also dictate certain physiological processes such as differentiation and angiogenesis (21). During skeletal regeneration, matrix-bound EVs guide macrophage differentiation and downstream myogenesis of skeletal muscle progenitor cells (22, 23). EVs can also be freely shed to travel through interstitial fluid to the lymph nodes or diffuse into the bloodstream (24). Each of these mechanisms becomes important for understanding the development of immune response leading to autoimmune diseases.

Proteomic, genomic, and metabolic data indicate that EVs from distressed cells differ in size, content, quantity, and biogenesis from healthy cells (12, 25). Healthy cells exposed to cellular stress show increases in EV production, content, and uptake. Bovine granulosa cells that were exposed to H_2O_2 oxidative stress released exosomes containing anti-oxidative molecules (26). Serum-starved mesenchymal stem cells (MSCs) produces exosomes that traffic to neurons 22-fold more efficently than non-serum deprived MSCs (27). While EV content and production were modulated when endothelial cells were exposed to hypoxic conditions, the properties were not reflected when exposed to high glucose (28). These suggest that EVs can modulate communication of stress signals, although not communicate all stresses equally.

EV PRODUCTION, CELLULAR STRESS, AND AUTOIMMUNITY

In the context of autoimmunity, the relationship between cellular stress and EV biogenesis is especially significant. Cellular stress is implicated in the initiation of many autoimmune diseases (3). While there are genetic factors that contribute to autoimmunity, genotype alone does not explain all the incidences. EV content varies widely based on cell type as well as the amount of cellular stress. It is unclear whether there is a consistent purpose for EV communication in autoimmunity. In some cases, EVs could function as a warning or protective signal to surrounding cells. On the other hand, it could simply be a disposal mechanism gone wrong. For example, ineffective clearing of ApoEVs can result in necrosis, causing the release of autoantigens with other pro-inflammatory signals, thereby contributing to autoimmune disease (12).

EV-mediated intercellular communication has garnered increasing attention and is thought to have a critical role in the development and progression of autoimmunity. In the same manner that tumor-derived EVs can condition bone marrow-derived cells to prepare distal organs for the arrival of metastatic cells, EVs from autoimmune organs can educate the immune system on how to react (24, 29). EVs can carry autoantigens, a "self" protein or protein complex that triggers an immune response, which then facilitates an autoimmune disease (**Table 1**).

The origin of autoimmunity is not known for many diseases, and clinical treatments frequently rely on addressing the symptoms rather than the root cause. For example, the standard treatment for Type 1 Diabetes is delivery of exogenously produced insulin, and rheumatoid arthritis is treated *via* delivery of systemic immunosuppressant drugs such as steroids. The growing literature about EVs' role in antigen presentation may bring the fields closer to not only explanations of disease initiation, but also methods to diagnose and treat autoimmunity.

Systemic Lupus Erythematosus (SLE)

One common autoimmune disorder associated with EVs is SLE. SLE is characterized with the hyperproduction of autoantibodies and the accumulation of immune-complexes (ICs), leading to inflammation and tissue damage (**Figure 1**) (31). ICs are formed when EVs containing surface antigens bind to circulating immunoglobulins or ECM proteins, thereby facilitating immune recognition (50, 51). These ICs induce complement-mediated immune responses (52). Apoptosis and immunogenic apoptotic bodies are commonly found in SLE, and may contain dsDNA or other nucleic acids (32, 36). These EVs may stimulate type-1 interferon (IFN) production, which is another major disease contributor in SLE (31). These EVs may also contain autoantigens such as galectin-3-binding protein (G3BP), which is strongly correlated with IC production and increased adherence to the endothelium and basement membrane (32–34).

Diabetes

Type 1 diabetes (T1D) is a tissue-specific autoimmune disease caused by the autoreactive T cell–mediated destruction of insulin-producing β-cells in the pancreas. EVs are thought to

TABLE 1 | Autoantigens found in EVs.

Disease	Autoantigens	Type of EVs	Cell type	Size	Reference
SLE/SS	RNPs Ro/SSA, La/SSB, SM G3BP, 14-3-3n, B6 tubulin	NV + MP	SGEC; non-neoplastic Peripheral Blood mononuclear cells	50–100 nm 100–1,000 nm	(30) (31–35) (36)
Diabetes (T1D)	GAD 65 IA-2 Proinsulin, ERV Gag, Env	NV	Rat/human islets, MSC insulinoma	100–150 nm	(37) (38, 39) (40)
Rheumatoid Arthritis	IL-1, Citrillinated Proteins, DEK	NV + MP	Platelets, FLS, leukocytes	30–1,000 nm	(41–45)
Vtiligo	tyrosinase, MART-1	ApoEV	Melanocytes	200+ nm	(46)
Pre-eclampsia	NEP, HLA-DR, HMGBI	MP	Synoytiotrophoblasts	200–1,000 nm	(47–49)

Disease type, autoanitgen found in or on EVs, classification of EVs, cell source, and size of EVs. NV, Nanovesicles; MP, Microparticles; RNP, Ribonucleoproteins; Ro/SSA; Ro protein/Sjögren's Syndrome related antigen A; La/SSB, La protein/Sjögren's Syndrome related antigen B; SM, Smith antigen; G3BP, Galectin 3-binding protein; GAD65, Glutamic Acid Decarboxylase- 65K; IA-2, Islet Antigen 2; ERV Gag, Endogenous retrovirus Gag antigen; IL-1, Interleukin 1; NEP, Neprilysin; HLA-DR, Human leukocyte antigen- DR; HMGBI, High Mobility Group Box 1.

contribute to T1D development in several ways. First, there is a working hypothesis that EVs containing autoantigens are released from stressed cells (**Figure 1**), leading to the activation of autoreactive T cells (40). Autoantigens (ZnT8, insulin, GAD65, and IA-2) have been found in EVs derived from pancreatic islet cells, in both human and rat models (37, 38, 53). These EVs are subsequently endocytosed by dendritic cells (DCs) followed with the activation of the APCs. Aside from the autoantigens, EVs derived from islets also contain immunostimulatory cytokines such as IFN-γ. These cytokines are able to stimulate monocytes, autoreactive B and T cells, which further contribute to the destruction of pancreatic cells (38, 54, 55). In this manner, EVs serve as an autoimmune trigger by facilitating the antigen presentation and activation of autoreactive immune cells (37).

EVs are also involved in the development of Type 2 Diabetes (T2D) by promoting insulin resistance *via* downregulation of glucose transporter type 4 (GLUT4) (56, 57). Microvesicles derived from pro-inflammatory macrophages have been shown to reduce insulin signal transduction and GLUT4 activity (57). Moreover, ApoEVs may induce pro-inflammatory macrophage polarization *via* secretion of mir-155, a potent circulating microRNA (miRNA) that is clinically elevated in T2D studies (58, 59).

Rheumatoid Arthritis (RA)

RA is a systemic autoimmune disease characterized by chronic inflammation of the synovial joints and the erosion of cartilage (60). EVs are also implicated in RA pathogenesis. Clinically, RA patients have increased EV concentration in synovial fluid and the joint space in comparison to healthy controls (41, 61, 62). The main sources of EVs in RA are platelets, leukocytes and fibroblast-like synoviocytes (FLS) (41–44). Platelet-derived EVs (PEVs) are of particular interest as their higher concentrations in patients with RA and are correlated with disease severity (61, 63). PEVs present interleukin-1 (IL-1) on their surface, which stimulate FLS to release pro-inflammatory IL-6 and IL-8 (44). Stimulated FLSs are also known to release a number of ECM-degrading enzymes that contribute to joint destruction (41). RA-associated EVs also frequently express citrullinated proteins including fibrinogen, fibrin, fibronectin and vimentin which can act as autoantigens (42, 45). EVs containing citrullinated proteins are of particular interest, given that anti-cyclic citrullinated peptide (anti-CCP) antibodies have a 96% specificity for the diagnosis of RA (63). These EVs can also form ICs which are pro-pro-inflammatory and stimulate neutrophils to release leukotrienes, which further perturbate the inflammation in the joint (42).

Vitiligo

Vitiligo is a disorder consisting of the destruction of melanocytes leading to the depigmentation of the skin (64). Oxidative stress *via* reactive oxygen species (ROS) causes damage to melanocytes which then release antigens through a number of pathways, including EVs (65). When exposed to ROS, melanocytes release EVs containing tyrosinase and Melan-A (MART-1), a melanosome antigen recognized by T cells, thus leading to activation of the autoimmune response (46, 66). Vitiligo also develops as an immune related adverse event (irAEs) following checkpoint inhibitor cancer immunotherapy (67, 68). Interestingly, in the case of melanoma, vitiligo is associated with successful treatment, and individuals with pre-existing vitiligo have lower frequencies of melanoma cancer development (69, 70). This suggests a dynamic relationship between T cell activation and melanocyte destruction.

Pre-Eclampsia (PE)

PE is a leading cause of maternal death, affecting 2–8% of pregnancies (71, 72). It manifests in two stages, the first being incomplete development of the placenta, while the second stage consists of the main pathology of the disease due to systemic inflammation in the mother (47). It is believed that EVs are directly involved in both stages of PE pathogenesis (73, 74).

During normal pregnancy, exosomes influence the spiral artery remodeling in the uterus, forming the blood vessels that allow for sufficient delivery of nutrients and oxygen from the mother to the fetus (75). Over the course of spiral artery remodeling, uterine arteries expand from 200 μm to 2 mm in diameter. This process occurs through the sequential steps of vessel dilation, vascular smooth muscle cell separation, endothelial cell swelling, extravillous trophoblast (EVT) cell invasion and fibrinoid deposition (75). In early-onset PE, poor placentation occurs due to insufficient spiral artery remodeling.

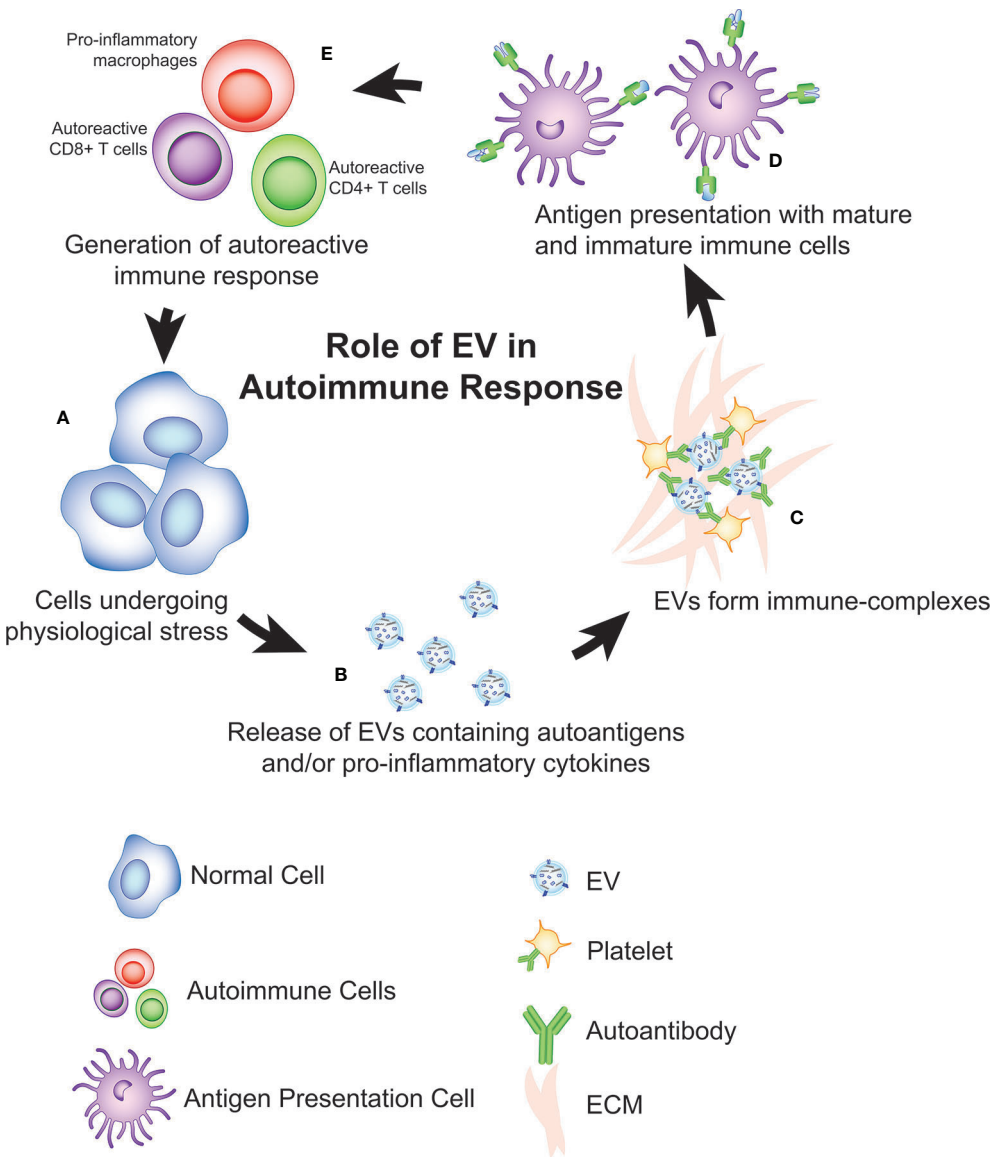

FIGURE 1 | Role of EVs in antigen presentation and initiation of autoimmune diseases. **(A)** a potential theory is that cells undergoing physiological stress initiation autoimmunity via release of **(B)** EVs containing autoantigens, pro-inflammatory cytokines, and/or genetic material (i.e. miRNA, DNA). **(C)** In some cases, these EVs can interact with ECM, antibodies, platelets to form immune-complexes (ICs) that can also facilitate presentation to **(D)** immature and mature antigen presenting cells. After antigen presentation, an adaptive autoimmune response is developed **(E)** as indicated by the expansion of autoreactive CD8+ T Cells, CD4+ T cells, autoreactive B cells, and the pro-inflammatory activation of innate immune cells (i.e. macrophages, neutrophils). This process produces a positive feedback loop, contributing to more cellular damage within the autoimmune microenvironment which leads to the production of more EVs.

The intrauterine oxygen tension in PE remains at hypoxic levels (1%-3%), leading to a 7-fold increase in exosome release (75, 76). In addition, bioactivity of the exosomes showed increased levels of hypoxia-induced factor 1-alpha (HIF-1α) and IL-8 (75).

The release of these exosomes is dependent upon the oxygen tension within the uterus. During the first trimester, intrauterine oxygen tension as low as 3%. The lower oxygen tension causes an increase in exosomal release and bioactivity, stimulating the invasion of the EVTs to perform proper placentation (75). Cytotrophoblast exosomes regulate this invasion in both a time and dose-dependent manner (75). After adequate spiral artery remodeling occurs, the oxygen tension increases to 8% (76). It has been hypothesized that the increase in exosomal release under hypoxia is an adaptive measure taken by the body to induce the proliferation and invasion of the EVTs to correct the poor placentation while sufficiently remodel the spiral arteries (77). However, the mechansims underlying why this process leads to normal pregnancy in some and PE in others is still unclear.

Much like in other autoimmune diseases summarized in this review, EVs generated *via* cellular stress contribute to PE. *In vitro* studies reveal that human placental cells (BeWo) undergoing endoplasmic reticulum stress (ER-stress) produce EVs that contain damage-associated molecular patterns (DAMPs) thought to contribute to the development of PE (78). EVs from the syncytiotrophoblast, the epithelial covering of the placenta interfacing with maternal blood, shed into the maternal blood carrying antigens (47, 74). EVs collected from patients with PE show significantly higher neprilysin and human leukocyte antigen (HLA-DR), with significantly lower synctin-2 compared to EVs from normal pregnancies (47, 79). Syncytiotropoblast-derived EVs stimulate monocytes, neutrophils, B and T lymphocytes which then release IL-6, IL-8 and tumor necrosis factor-α (TNF-α), leading to a pro-inflammatory response (74).

EV-FACILITATED THERAPIES TO TREAT AUTOIMMUNE DISEASE

MSC-Derived EVs as Autoimmune Diseases Therapies

Mesenchymal stem cells (MSCs) are key sources of immunosuppressive soluble factors that are critical to tissue repair and regeneration (80). Because of their unique function, MSCs or MSC-derived EVs (MSC-EVs) have been therapeutically administered to heal wounds and repair tissue after myocardial infarction (80, 81). Current autoimmune therapeutic strategies involving MSC-EVs have shown efficacy in reducing inflammation in several animal models including experimental autoimmune encephalomyelitis (EAE) mice, which can serve as a model for multiple sclerosis (MS). EAE mice treated with EVs from stimulated MSCs showed reduction in the clinical score, demyelination and neuroinflammation, with increased secretion of anti-inflammatory cytokines as well as upregulated regulatory T cells (82, 83). In a rat experimental autoimmune uveitis (EAU) model, MSC-EVs lead to a reduction of EAU in the eyes (84).

In addition to reducing inflammation, MSCs have been clinically explored to prevent tissue damage and promote regeneration. Tao et al., used human embryonic MSC-EVs to regenerate tissue following osteoarthritis-induced cartilage damage (85). The group found MSC-EVs improved histological scores and gross appearance of the cartilages over controls, with restoration of cartilage as well as subchondral bone by week 12. The characteristics of hyaline cartilage closely resembled the unoperated control. In addition to this, exosomes from human synovial MSC (SMSC) have been shown to promote cartilage regeneration with preventive effect in a rat osteoarthritis model (85). Bone marrow-derived MSC-EVs were shown to delay the inflammatory response in RA, measured through reduction in joint damage and pro-inflammatory gene expression (86). Interestingly, both MSC-EVs classified as exosomes and microvesicles can protect mice from joint damage (87).

Induced pluripotent MSC (iMSCs) are a valuable cell source for EV treatments due to their compatibility with autologous transplantation (88). Moreover, iMSCs pocesses the potential for scalability, which is vital due to the enourmous amounts of cells needed to produce therapeutic quantities of EVs and the limited population of source cells from which to derive. When tested for their ability to promote proliferation in a skin wound healing model, EVs derived from iMSCs performed similarly to EVs derived from native MSCs (89). Comparable studies show similar therapeutic results in osteoarthritis (90).

DC-Derived EVs as Autoimmune Diseases Therapies

DCs can regulate adaptive immunuity through antigen presentation to T cells and in this manner, DC derived EVs (DC-EVs) have also been explored for treatment of autoimmune diseases. DCs differ from MSCs slightly in that DCs can perform either pro-inflammatory or anti-inflammatory functions (91), thus DC-EVs must be harvested from DCs that have been conditioned to an immunosuppressive phenotype to illicit an anti-inflammatory effect. Nonetheless, DC-EVs have been assessed for their therapeutic potential to treat autoimmune diseases with cheerful efficacy across several animal models. DC-EVs delayed the onset of murine collagenase-induced arthritis (CIA) and dampened the severity of established arthritis (92). Mice that received EVs from engineered bone marrow DCs (BMDCs) even showed a reversal effect of established CIA, with the exosomes having a stronger immunosuppressing effect than the parental DCs (92). DC-EVs have also been studied for Irritable Bowel Disease (IBD), with showing a protective effective through induction of regulatory T cells (93).

EVs as A Drug Delivery Vehicle

Most of the current EV treatment strategies involve harvesting EVs from stimulated MSCs or DCs (**Table 2**). There are fewer studies that load harvested native EVs with therapeutic reagents for treatment in autoimmune disease, which could be a future growth opportunity. Various methods have been explored to utilize EVs to deliver drugs for septic shock, breast cancer, prostate cancer, hepatocarcinoma, and Parkinson's disease (94–99). EVs can be loaded externally, i.e. drugs are loaded *via* membrane manipluations. Sun et al. mixing the exosomes with curcumin and demonstrated an enhanced anti-inflammatory effect of curcumin in septic shock treatment (97). Loading EVs with aptamers through mechanical extrusion of breast cancer cells enhances breast cancer targeting effect of the EVs (94). Chemotherapy may also be improved with EVs, as co-incubated prostate cancer-derived EVs with paclitaxel showed a stronger therapeutic effect (98) than paclitaxel alone. EVs have also been loaded using internal mechanisms, i.e.loading cells and harvesting the drug-laden EVs from cell culture media. The Batrakova group has successfully used this strategy to delivery nucleic acids in Parkinson's Disease, cancer, and Batten's Disease (100–102). Other groups transfect cells with vectors encoding for nanobodies to enhance the EVs targeting capacity (103).

EV Isolation Methods

The manner in which EVs are isolated and characterized *via* size, morphology, and composition is well developed (8, 10, 104–107). However there is a missing connection between how the field characterizes EVs and their classifications *via* biogenesis. For

TABLE 2 | The use of extracellular vesicles (EVs) in clinical trials related to autoimmune disease.

Source	Type of EVs	Disease/Indication	Trial Number	Purpose
MSC	Exosome, conditioned media	GvHD		Treatment
Umbilical mesenchymal stem cells derived	Exosomes	Dry eye in patients with cGVHD	NCT04213248	Treatment
Umbilical mesenchymal Stem cells derived	Exosome, microvesicle	Type I diabetes	NCT02138331	Treatment
Plasma	Exosomes	Ulcer	NCT02565264	Treatment
Blood, urine	Exosomes	autoimmune thyroid heart disease	NCT03984006	Biomarker
Blood, urine	Exosomes	Adult-onset autoimmune diabetes	NCT03971955	Biomarker
Blood, urine	Exosomes	Type 1 diabetes	NCT04164966	Biomarker
Blood, urine	Exosomes	Relapsing multiple sclerosis (RMS)	NCT04121065	Biomarker
Blood, urine	Exosomes	Systemic autoimmune diseases (broad)	NCT02890121	Biomarker
Blood, urine	Microparticles	Systemic lupus erythematosus and systemic sclerosis	NCT03575156	Biomarker
Urine	Exosomes	Systemic lupus erythematosus	NCT04534647	Biomarker
Blood	Microparticles	Giant cell arteritis	NCT02333708	Biomarker
Blood; platelet	Microparticles	Type 1 diabetes	NCT01397513	Monitoring
Blood, urine	Microparticles	Type 1 diabetes	NCT00934336	Monitoring
Blood	Exosome	Type 1 diabetes	NCT03392441	Monitoring
Blood	EVs	Type 1 diabetes (T1DM), type 2 diabetes	NCT03106246	Biomarker
Blood, urine	Exosome	Connective tissue diseases (CTD) or systemic autoimmune diseases (SADs)	NCT02890147	Biomarker
Blood	Microparticles	Pregnancy related vascular complications	NCT00485784	Biomarker
Blood	Microparticles	Pregnancy related vascular complications	NCT01736826	Biomarker
Urine	Microparticles	Pre-eclampsia	NCT04520048	Monitoring
Blood, urine, and placental	Exosome	Pre-eclampsia	NCT04154332	Biomarker
Blood, umibilical cord mesenchymal stem cells (UCMSCs)	Exosome	Pre-eclampsia	NCT03562715	Biomarker

Results from the clinicaltrials.gov search of EVs for the diagnosis and/or treatment of autoimmune disease. This search included derivative terms such as exosomes, microvesicles, microparticles.

example, ApoEVs can be as large as 5 μm but also as small as 50 nm (12). In the context of autoimmune diseaases, the isolation and classification of EVs are particularly relevant, considering their diversed contribution to disease initiation and propagation. Various EV isolation methods have been used for autoimmune diseases, with each of them targeting specific EV populations.

Differential centrifugation is arguably the most commonly used technique for EV isolation (96, 108–110). This method usually involves a series of low-speed centrifugation steps to remove the cellular debris, followed by ultracentrifugation to pellet down the sub-micron size vesicles. Following differential centrifugation, density gradient centrifugation may further purify EVs (96, 108, 111). Tris/sucrose/D2O mixture is frequently used as a cushion, which is then topped with the partially isolated EVs. After centrifuging the combination at 100,000 x g for 75 min, the cushion is transferred into a new container and diluted, followed by another ultracentrifugation. For further characterization, ultrafiltration can be used. Ultrafiltration passes the EV suspension through one or a series of membrane filters with defined pore sizes, which separates EVs into subtypes based on sizes (110).

Chromatography is also used to isolate EVs. This includes size-exclusion chromatography where porous beads separate the particles based on the hydrodynamic radius. The fraction containing particles with the size of EVs are selectively collected (112–114). Alternatively, as EVs have negative charges, an anion exchange chromatography isolation protocol has been established. Culture medium containing EVs is passed through a solid-phase monolithic ion exchange column and then eluted with NaCl (115).

Precipitation methods are simple but with potentially compromised performance. Polymer precipitation with polyethylene glycol (PEG) is frequently adopted by the commercial kits to eliminate the usage of ultracentrifugation (116). Adding PEG or other super hydrophilic polymers into the EV-containing samples decreases the solubility of EVs, allowing pellet formation at 1,500 x g. Chemical precipitation includes organic solvents, sodium acetate, and protamine (117). Organic solvents precipitate EVs out of the solution through ion-pairing effect, while sodium acetate disturbs EV hydration and pellets by hydrophobic effect. Protamine, as a positively charged molecule, pellets the EVs in a similar manner, and is removed by gel filtration.

Affinity-based separation is another important approach, particularly because of the capacity to isolate EVs based on subpopulations. Here, antibody, aptamer or other affinity reagents are used to isolate EVs with a specific surface expression profile (118–121). Immunoprecipitation takes advantage of the markers commonly enriched on EV surface. The EV suspension is mixed with magnetic beads coupled with the corresponding antibodies, then isolated with a magnetic field. For total exosome isolation, tetraspanins CD63, CD9, and CD81 are normally used as surface antigen targets (96, 122).

Microfluidics are gaining interests in isolating EVs. Microfluidics isolate EVs from human sera or cell culture media in a lab-on-a-chip fashion (123). Chen et al. demonstrated the concept with herringbone groves in 50-μm-wide channels to increase surface area, while attached anti-CD63 antibodies to the surface *via* biotin-NeutrAvidin conjugation for EV capturing. As CD63 is not ubiquitously expressed in all EV population, Wan et al. first

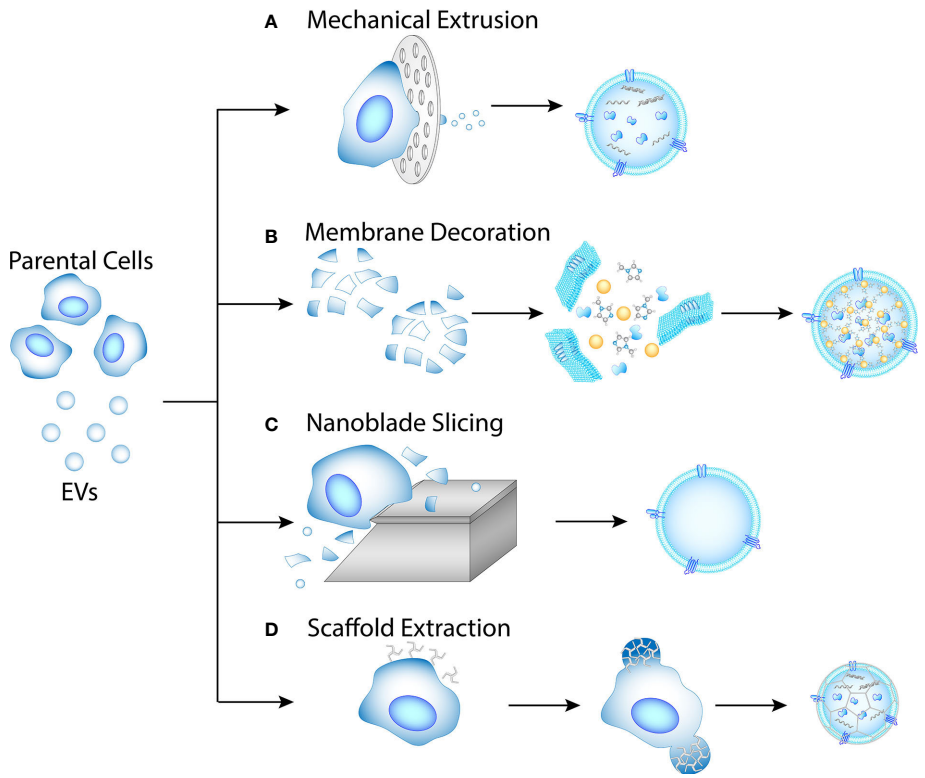

FIGURE 2 | Methods for artificial EV production. **(A)** Mechanical extrusion. Intracellular contents are pertained in the EVs. **(B)** Membrane decoration. Membrane fragments are obtained from lysed cell or EV, then mixed with nanoparticle or MOF cores. **(C)** Nanoblade slicing. Cellular membranes are sliced off the cells and allowed to self-assemble into EVs. **(D)** Scaffold extraction. Clathrin-like nanoparticles may extract EVs from cellular membrane by pinching.

designed a lipid nanoprobe that targets the EV membrane, then incorporated it onto a silica herringbone nanostructure microfluidic device for total EV isolation (124).

Artificial EV Generation Methods

The biocompatibility and functionality of EVs make them an advantageous drug delivery vehicle. However, cells secrete EV at a relatively low rate. Therefore, multiple approaches have been explored to generate EVs artificially (**Figure 2**), with a common method being mechanical extrusion (**Figure 2A**). Mechanical extrusion methods pass whole cells or membrane lysates through channels of 1–10 μm in diameter (94, 125–127). The channels can be created with tracked-etched membranes or microfluidic devices. Membrane decoration is an efficient method for EV drug loading, which encapsulates a core into lysed cellular or EV membranes (**Figure 2B**) (95, 128, 129). The core could be a metal-organic framework or nanoparticles.

Some other methods for artificial EV generation that have been investigated include nanoblade slicing (**Figure 2C**) and scaffold extraction (**Figure 2D**). Nanoblade slicing rolls cells over microfabricated 500 nm-thick silicon nitride blades (130). The cellular membrane is sliced into fragments during the process, which then self-assemble into nanovesicles with diameters of 100-300 nm. Substances such as nanobeads can be flowed simultaneously for encapsulation, with an efficiency around 30%. Scaffold extraction is potentially a method for extracting EVs directly from the cellular membrane (131). Using dissipative particle dynamics model, Li et al. simulated the extraction process with clathrin-like nanoparticles, and concluded that the size of the resulting vesicles depends on the concentration of the nanoparticles as wells as membrane surface tension.

Use of EVs in Clinical Trials for Auto-Immune Diseases

At the time of this writing there were 560 registered trials that involved EVs or derivative terms such as exosomes, microvesicles, and/or microparticles. Of these, 47 trials aligned with autoimmune diseases (**Table 2**). A subset of these clinical trials categorize the potential for EVs as autoimmune disease biomarkers. One such study is NCT04164966, an observational study to detect circulating beta-cell exosomes in early onset T1D in a pediatric population. Microparticles are also being studied as a prognostic indicator in SLE (NCT03575156) and arthritis (NCT02333708), highlighting the need for investigation of multiple EV populations. In addition, some trial studies measure EVs concentration as a monitoring tool to quantify the success of their drug intervention. An example of this is NCT01397513, a trial that correlates platelet microparticles to the effect of aspirin dosage on fibrin formation in T1D patients (132).

Of those, there were currently five clinical trials using EVs to treat autoimmune-related diseases. While this seems sparse, it should be noted that these numbers are likely due to the prevalence of cell-based treatments. Of the roughly 10,000 clinical trials related to autoimmune disease, ~300 trials are using MSCs or T cells as a treatment. As the scientific capacity to produce clinical-grade EVs increases, there will likely be an increase in EVs-based therapies for all diseases. As it stands, the results for EVs to treat autoimmune diseases is compelling but limited (**Table 2**). While not classified as such, the clinical manifestation and treatment strategies of graft-versus-host-disease (GvHD) are similar to textbook autoimmune disease (133). Kordelas et al. have demonstrated the feasibility of using the exosome to ameliorate GvHD in one patient that received allogeneic hematopoietic stem cell transplantation (134). Within two weeks, the cutaneous and mucosal GvHD syndromes were remarkably improved, which consequently reduced the dosage of steroid treatment from 125 mg/d to 30 mg/d after exosome therapy. Diarrhea volume of the patient was also objectively reduced.

Interestingly, another clinical trial used two distinct populations of MSC-EVs to treat T1D. The first dose included EVs that were 40–180 nm in size with CD63, CD9, Alix, TSG101 and HSP70 as markers. The second dose consisted of microvesicles of 180-1000 nm in size purified from same MSCs but characterized *via* with annexin V, flotillin-2, selectin, integrin, cd40 and metalloproteinase markers. Unfortunately, the publications listed by the study principal invesetigators do not include data on EVs but rather the delivery of MSCs, making it unclear whether either population of EVs would have had any promising effect (135, 136).

CONCLUSION: FUTURE GROWTH AREAS

There are many opportunities for EVs therapies in autoimmune disease. MSC and DC derived EVs are demonstrably efficacious for mounting anti-inflammatory response that promote regeneration, wound-healing, and ameliorating autoimmune disease. However, they are difficult to produce, they require large volumes of cells/media and their batch-to-batch variability lacks the consistency of traditional small molecule therapies. Artificial production of EVs can enable scalable solutions to production, purification, and modification challenges. Currently, the biomarker and diagnostics capabilities of EVs is more advanced than treatments used for autoimmune diseases. New techniques for producing and characterizing artificial EVs could facilitate treatment for autoimmune diseases.

While there has been a large amount of research done on the role of MSC-EVs and DC-EVs, there is comparatively little known about the role of EVs from other immune cells such as macrophages and B cells. Given their role in the pathogenesis of autoimmune disease, it is likely that the EVs from these cells play a significant part in the immune response and could be used in downstream treatment and diagnosis strategies.

Due to the increase of immunotherapy treatments (i.e. checkpoint inhibitors, CAR-T), there will likely be an increase in autoimmune disease events due to irAEs. One example is a treatment using checkpoint inhibitors designed to increase cytotoxic T cell activity in tumors gave rise to cases of vitiligo and hypo/hyper-thyroidism (67, 70). irAEs can range from mild skin reactions to life-long autoimmune-related diseases such as arthritis (137). This convergence in patient populations being treated for irAEs and autoimmune diseases creates an opportunity to gain insight into autoimmune pathology, which is still not universally understood. Investigating EVs in autoimmune disease also presents a unique opportunity to explore bidirectional relationships between diseases. A great example of this are findings that COVID-19 can initiate new-onset diabetes or enhance metabolic complications of pre-existing diabetes (138).

In conclusion, EVs play a significant role in autoimmune disease initiation and progression. Though the role of EVs vary throughout each autoimmune disease summarized, the common themes encourage further investigation of EVs as diagnostic and therapeutic tools. EVs facilitate autoimmune responses by presenting autoantigens from cellularly stressed cells to immune cells. In addition, the EVs can form immune complexes that trigger inflammatory responses. Deciphering the linkage between EVs biogenesis and trafficking may reveal insights into unanswered questions in autoimmune initiation and hold the key to effective treatment.

AUTHOR CONTRIBUTIONS

ML, ED, EP, HF, S-YZ, and EW wrote and edited the manuscript. EW conceived and oversaw the project. All authors contributed to the article and approved the submitted version.

FUNDING

ML was supported through NIH 7R01CA230339. ED was supported by the Molecular Biophysics and Structural Biology graduate program at the University of Pittsburgh and Carnegie Mellon University.

REFERENCES

1. Morito D, Nagata K. ER Stress Proteins in Autoimmune and Inflammatory Diseases. *Front Immunol* (2012) 3:48:48. doi: 10.3389/fimmu.2012.00048
2. Smallwood MJ, Nissim A, Knight AR, Whiteman M, Haigh R, Winyard PG. Oxidative stress in autoimmune rheumatic diseases. *Free Radic Biol Med* (2018) 125:3–14. doi: 10.1016/j.freeradbiomed.2018.05.086
3. Harris JE. Cellular stress and innate inflammation in organ-specific autoimmunity: lessons learned from vitiligo. *Immunol Rev* (2016) 269 (1):11–25. doi: 10.1111/imr.12369
4. Johnstone RM. Maturation of reticulocytes: formation of exosomes as a mechanism for shedding membrane proteins. *Biochem Cell Biol* (1992) 70 (3-4):179–90. doi: 10.1139/o92-028
5. Gangoda L, Boukouris S, Liem M, Kalra H, Mathivanan S. Extracellular vesicles including exosomes are mediators of signal transduction: are they

protective or pathogenic? *Proteomics* (2015) 15(2-3):260–71. doi: 10.1002/pmic.201400234
6. Robbins PD, Morelli AE. Regulation of immune responses by extracellular vesicles. *Nat Rev Immunol* (2014) 14(3):195–208. doi: 10.1038/nri3622
7. Lindenbergh MFS, Stoorvogel W. Antigen Presentation by Extracellular Vesicles from Professional Antigen-Presenting Cells. *Annu Rev Immunol* (2018) 36(1):435–59. doi: 10.1146/annurev-immunol-041015-055700
8. Xu R, Greening DW, Zhu HJ, Takahashi N, Simpson RJ. Extracellular vesicle isolation and characterization: toward clinical application. *J Clin Invest* (2016) 126(4):1152–62. doi: 10.1172/JCI81129
9. Witwer KW, Thery C. Extracellular vesicles or exosomes? On primacy, precision, and popularity influencing a choice of nomenclature. *J Extracell Vesicles* (2019) 8(1):1648167. doi: 10.1080/20013078.2019.1648167
10. Thery C, Witwer KW, Aikawa E, Alcaraz MJ, Anderson JD, Andriantsitohaina R, et al. Minimal information for studies of extracellular vesicles 2018 (MISEV2018): a position statement of the International Society for Extracellular Vesicles and update of the MISEV2014 guidelines. *J Extracell Vesicles* (2018) 7(1):1535750. doi: 10.1080/20013078.2018.1535750
11. Turchinovich A, Drapkina O, Tonevitsky A. Transcriptome of Extracellular Vesicles: State-of-the-Art. *Front Immunol* (2019) 10:202. doi: 10.3389/fimmu.2019.00202
12. Apoptotic Cell-Derived Extracellular Vesicles: More Than Just Debris. *Front Immunol* (2018) 9:1486:1486. doi: 10.3389/fimmu.2018.01486
13. Niessen A, Heyder P, Krienke S, Blank N, Tykocinski LO, Lorenz HM, et al. Apoptotic-cell-derived membrane microparticles and IFN-alpha induce an inflammatory immune response. *J Cell Sci* (2015) 128(14):2443–53. doi: 10.1242/jcs.162735
14. Kato Y, Park J, Takamatsu H, Konaka H, Aoki W, Aburaya S, et al. Apoptosis-derived membrane vesicles drive the cGAS-STING pathway and enhance type I IFN production in systemic lupus erythematosus. *Ann Rheum Dis* (2018) 77(10):1507–15. doi: 10.1136/annrheumdis-2018-212988
15. Tkach M, Kowal J, Thery C. Why the need and how to approach the functional diversity of extracellular vesicles. *Philos Trans R Soc Lond B Biol Sci* (2018) 373(1737):20160479. doi: 10.1098/rstb.2016.0479
16. Park SJ, Kim JM, Kim J, Hur J, Park S, Kim K, et al. Molecular mechanisms of biogenesis of apoptotic exosome-like vesicles and their roles as damage-associated molecular patterns. *Proc Natl Acad Sci U S A* (2018) 115(50):E11721–30. doi: 10.1073/pnas.1811432115
17. Mittelbrunn M, Gutierrez-Vazquez C, Villarroya-Beltri C, Gonzalez S, Sanchez-Cabo F, Gonzalez MA, et al. Unidirectional transfer of microRNA-loaded exosomes from T cells to antigen-presenting cells. *Nat Commun* (2011) 2:282. doi: 10.1038/ncomms1285
18. Gutiérrez-Vázquez C, Villarroya-Beltri C, Mittelbrunn M, Sánchez-Madrid F. Transfer of extracellular vesicles during immune cell-cell interactions. *Immunol Rev* (2013) 251(1):125–42. doi: 10.1111/imr.12013
19. Mittelbrunn M, Vicente Manzanares M, Sanchez-Madrid F. Organizing polarized delivery of exosomes at synapses. *Traffic* (2015) 16(4):327–37. doi: 10.1111/tra.12258
20. Németh A, Orgovan N, Sódar BW, Osteikoetxea X, Pálóczi K, Szabó-Taylor KÉ, et al. Antibiotic-induced release of small extracellular vesicles (exosomes) with surface-associated DNA. *Sci Rep* (2017) 7(1):8202. doi: 10.1038/s41598-017-08392-1
21. Todorova D, Simoncini S, Lacroix R, Sabatier F, Dignat-George F. Extracellular Vesicles in Angiogenesis. *Circ Res* (2017) 120(10):1658–73. doi: 10.1161/CIRCRESAHA.117.309681
22. Hussey GS, Dziki JL, Lee YC, Bartolacci JG, Behun M, Turnquist HR, et al. Matrix bound nanovesicle-associated IL-33 activates a pro-remodeling macrophage phenotype via a non-canonical, ST2-independent pathway. *J Immunol Regener Med* (2019) 3:26–35. doi: 10.1016/j.regen.2019.01.001
23. Huleihel L. HG, Naranjo JD, Zhang L, Dziki JL, Turner NJ, Stolz DB, et al. Matrix-bound nanovesicles within ECM bioscaffolds. *Sci Adv* (2016) 2(6):e1600502. doi: 10.1126/sciadv.1600502
24. Hood JL, San RS, Wickline SA. Exosomes released by melanoma cells prepare sentinel lymph nodes for tumor metastasis. *Cancer Res* (2011) 71(11):3792–801. doi: 10.1158/0008-5472.CAN-10-4455
25. Abramowicz A, Widlak P, Pietrowska M. Different Types of Cellular Stress Affect the Proteome Composition of Small Extracellular Vesicles: A Mini Review. *Proteomes* (2019) 7(2):23. doi: 10.3390/proteomes7020023
26. Saeed-Zidane M, Linden L, Salilew-Wondim D, Held E, Neuhoff C, Tholen E, et al. Cellular and exosome mediated molecular defense mechanism in bovine granulosa cells exposed to oxidative stress. *PloS One* (2017) 12(11):e0187569. doi: 10.1371/journal.pone.0187569
27. Haraszti RA, Miller R, Dubuke ML, Rockwell HE, Coles AH, Sapp E, et al. Serum Deprivation of Mesenchymal Stem Cells Improves Exosome Activity and Alters Lipid and Protein Composition. *iScience* (2019) 16:230–41. doi: 10.1016/j.isci.2019.05.029
28. de Jong OG, Verhaar MC, Chen Y, Vader P, Gremmels H, Posthuma G, et al. Cellular stress conditions are reflected in the protein and RNA content of endothelial cell-derived exosomes. *J Extracell Vesicles* (2012) 1:18396. doi: 10.3402/jev.v1i0.18396
29. Peinado H, Aleckovic M, Lavotshkin S, Matei I, Costa-Silva B, Moreno-Bueno G, et al. Melanoma exosomes educate bone marrow progenitor cells toward a pro-metastatic phenotype through MET. *Nat Med* (2012) 18(6):883–91. doi: 10.1038/nm.2753
30. Kapsogeorgou EK, Abu-Helu RF, Moutsopoulos HM, Manoussakis MN. Salivary gland epithelial cell exosomes: A source of autoantigenic ribonucleoproteins. *Arthritis Rheum* (2005) 52(5):1517–21. doi: 10.1002/art.21005
31. Rasmussen NS, Jacobsen S. Microparticles - culprits in the pathogenesis of systemic lupus erythematosus? *Expert Rev Clin Immunol* (2018) 14(6):443–5. doi: 10.1080/1744666X.2018.1474100
32. Rasmussen NS, Nielsen CT, Jacobsen S, Nielsen CH. Stimulation of Mononuclear Cells Through Toll-Like Receptor 9 Induces Release of Microvesicles Expressing Double-Stranded DNA and Galectin 3-Binding Protein in an Interferon-alpha-Dependent Manner. *Front Immunol* (2019) 10:2391:2391. doi: 10.3389/fimmu.2019.02391
33. Nielsen CT, Ostergaard O, Rasmussen NS, Jacobsen S, Heegaard NHH. A review of studies of the proteomes of circulating microparticles: key roles for galectin-3-binding protein-expressing microparticles in vascular diseases and systemic lupus erythematosus. *Clin Proteomics* (2017) 14:11. doi: 10.1186/s12014-017-9146-0
34. Ostergaard O, Nielsen CT, Tanassi JT, Iversen LV, Jacobsen S, Heegaard NHH. Distinct proteome pathology of circulating microparticles in systemic lupus erythematosus. *Clin Proteomics* (2017) 14:23. doi: 10.1186/s12014-017-9159-8
35. Ostergaard O, Nielsen CT, Iversen LV, Tanassi JT, Knudsen S, Jacobsen S, et al. Unique protein signature of circulating microparticles in systemic lupus erythematosus. *Arthritis Rheum* (2013) 65(10):2680–90. doi: 10.1002/art.38065
36. Mobarrez F, Fuzzi E, Gunnarsson I, Larsson A, Eketjall S, Pisetsky DS, et al. Microparticles in the blood of patients with SLE: Size, content of mitochondria and role in circulating immune complexes. *J Autoimmun* (2019) 102:142–9. doi: 10.1016/j.jaut.2019.05.003
37. Cianciaruso C, Phelps EA, Pasquier M, Hamelin R, Demurtas D, Alibashe Ahmed M, et al. Primary Human and Rat beta-Cells Release the Intracellular Autoantigens GAD65, IA-2, and Proinsulin in Exosomes Together With Cytokine-Induced Enhancers of Immunity. *Diabetes* (2017) 66(2):460–73. doi: 10.2337/db16-0671
38. Bashratyan R, Sheng H, Regn D, Rahman MJ, Dai YD. Insulinoma-released exosomes activate autoreactive marginal zone-like B cells that expand endogenously in prediabetic NOD mice. *Eur J Immunol* (2013) 43(10):2588–97. doi: 10.1002/eji.201343376
39. Bashratyan R, Regn D, Rahman MJ, Marquardt K, Fink E, Hu WY, et al. Type 1 diabetes pathogenesis is modulated by spontaneous autoimmune responses to endogenous retrovirus antigens in NOD mice. *Eur J Immunol* (2017) 47(3):575–84. doi: 10.1002/eji.201646755
40. Dai YD, Sheng H, Dias P, Jubayer Rahman M, Bashratyan R, Regn D, et al. Autoimmune Responses to Exosomes and Candidate Antigens Contribute to Type 1 Diabetes in Non-Obese Diabetic Mice. *Curr Diabetes Rep* (2017) 17(12):130. doi: 10.1007/s11892-017-0962-4
41. Fu H, Hu D, Zhang L, Tang P. Role of extracellular vesicles in rheumatoid arthritis. *Mol Immunol* (2018) 93:125–32. doi: 10.1016/j.molimm.2017.11.016
42. Cloutier N, Tan S, Boudreau LH, Cramb C, Subbaiah R, Lahey L, et al. The exposure of autoantigens by microparticles underlies the formation of potent inflammatory components: the microparticle-associated immune complexes. *EMBO Mol Med* (2013) 5(2):235–49. doi: 10.1002/emmm.201201846

43. Distler JH, Jungel A, Huber LC, Seemayer CA, Reich CF, Gay RE, et al. The induction of matrix metalloproteinase and cytokine expression in synovial fibroblasts stimulated with immune cell microparticles. *Proc Natl Acad Sci U S A* (2005) 102(8):2892–7. doi: 10.1073/pnas.0409781102
44. Boilard E, Nigrovic PA, Larabee K, Watts GF, Coblyn JS, Weinblatt ME, et al. Platelets amplify inflammation in arthritis via collagen-dependent microparticle production. *Science* (2010) 327(5965):580–3. doi: 10.1126/science.1181928
45. Skriner K, Adolph K, Jungblut PR, Burmester GR. Association of citrullinated proteins with synovial exosomes. *Arthritis Rheum* (2006) 54 (12):3809–14. doi: 10.1002/art.22276
46. van den Boorn JG, Picavet DI, van Swieten PF, van Veen HA, Konijnenberg D, van Veelen PA, et al. Skin-depigmenting agent monobenzone induces potent T-cell autoimmunity toward pigmented cells by tyrosinase haptenation and melanosome autophagy. *J Invest Dermatol* (2011) 131 (6):1240–51. doi: 10.1038/jid.2011.16
47. Tersigni C, Redman CW, Dragovic R, Tannetta D, Scambia G, Di Simone N, et al. HLA-DR is aberrantly expressed at feto-maternal interface in pre-eclampsia. *J Reprod Immunol* (2018) 129:48–52. doi: 10.1016/j.jri.2018.06.024
48. Xiao X, Xiao F, Zhao M, Tong M, Wise MR, Stone PR, et al. Treating normal early gestation placentae with preeclamptic sera produces extracellular micro and nano vesicles that activate endothelial cells. *J Reprod Immunol* (2017) 120:34–41. doi: 10.1016/j.jri.2017.04.004
49. Gill M, Motta-Mejia C, Kandzija N, Cooke W, Zhang W, Cerdeira AS, et al. Placental Syncytiotrophoblast-Derived Extracellular Vesicles Carry Active NEP (Neprilysin) and Are Increased in Preeclampsia. *Hypertension* (2019) 73(5):1112–9. doi: 10.1161/HYPERTENSIONAHA.119.12707
50. Fendl B, Eichhorn T, Weiss R, Tripisciano C, Spittler A, Fischer MB, et al. Differential Interaction of Platelet-Derived Extracellular Vesicles With Circulating Immune Cells: Roles of TAM Receptors, CD11b, and Phosphatidylserine. *Front Immunol* (2018) 9:2797:2797. doi: 10.3389/fimmu.2018.02797
51. Fortin PR, Cloutier N, Bissonnette V, Aghdassi E, Eder L, Simonyan D, et al. Distinct Subtypes of Microparticle-containing Immune Complexes Are Associated with Disease Activity, Damage, and Carotid Intima-media Thickness in Systemic Lupus Erythematosus. *J Rheumatol* (2016) 43 (11):2019–25. doi: 10.3899/jrheum.160050
52. Buzas EI, Toth EA, Sodar BW, Szabo-Taylor KE. Molecular interactions at the surface of extracellular vesicles. *Semin Immunopathol* (2018) 40(5):453–64. doi: 10.1007/s00281-018-0682-0
53. Nakayama M, Simmons KM, Michels AW. Molecular Interactions Governing Autoantigen Presentation in Type 1 Diabetes. *Curr Diabetes Rep* (2015) 15(12):113. doi: 10.1007/s11892-015-0689-z
54. Rahman MJ, Regn D, Bashratyan R, Dai YD. Exosomes Released by Islet-Derived Mesenchymal Stem Cells Trigger Autoimmune Responses in NOD Mice. *Diabetes* (2014) 63. doi: 10.2337/db13-0859
55. Rutman AK, Negi S, Gasparrini M, Hasilo CP, Tchervenkov J, Paraskevas S. Immune Response to Extracellular Vesicles From Human Islets of Langerhans in Patients With Type 1 Diabetes. *Endocrinology* (2018) 159 (11):3834–47. doi: 10.1210/en.2018-00649
56. Xiao Y, Zheng L, Zou X, Wang J, Zhong J, Zhong T. Extracellular vesicles in type 2 diabetes mellitus: key roles in pathogenesis, complications, and therapy. *J Extracell Vesicles* (2019) 8(1):1625677–1625677. doi: 10.1080/20013078.2019.1625677
57. Zhang Y, Shi L, Mei H, Zhang J, Zhu Y, Han X, et al. Inflamed macrophage microvesicles induce insulin resistance in human adipocytes. *Nutr Metab* (2015) 12:21–1. doi: 10.1186/s12986-015-0016-3
58. Polina ER, Oliveira FM, Sbruzzi RC, Crispim D, Canani LH, Santos KG. Gene polymorphism and plasma levels of miR-155 in diabetic retinopathy. *Endocr Connect* (2019) 8(12):1591–9. doi: 10.1530/EC-19-0446
59. Zhang Y, Mei H, Chang X, Chen F, Zhu Y, Han X. Adipocyte-derived microvesicles from obese mice induce M1 macrophage phenotype through secreted miR-155. *J Mol Cell Biol* (2016) 8(6):505–17. doi: 10.1093/jmcb/mjw040
60. Guo Q, Wang Y, Xu D, Nossent J, Pavlos NJ, Xu J. Rheumatoid arthritis: pathological mechanisms and modern pharmacologic therapies. *Bone Res* (2018) 6:15. doi: 10.1038/s41413-018-0016-9
61. Vinuela-Berni V, Doniz-Padilla L, Figueroa-Vega N, Portillo-Salazar H, Abud-Mendoza C, Baranda L, et al. Proportions of several types of plasma and urine microparticles are increased in patients with rheumatoid arthritis with active disease. *Clin Exp Immunol* (2015) 180(3):442–51. doi: 10.1111/cei.12598
62. Gyorgy B, Szabo TG, Turiak L, Wright M, Herczeg P, Ledeczi Z, et al. Improved flow cytometric assessment reveals distinct microvesicle (cell-derived microparticle) signatures in joint diseases. *PloS One* (2012) 7(11): e49726. doi: 10.1371/journal.pone.0049726
63. Withrow J, Murphy C, Liu Y, Hunter M, Fulzele S, Hamrick MW. Extracellular vesicles in the pathogenesis of rheumatoid arthritis and osteoarthritis. *Arthritis Res Ther* (2016) 18(1):286. doi: 10.1186/s13075-016-1178-8
64. Rashighi M, Harris JE. Vitiligo Pathogenesis and Emerging Treatments. *Dermatol Clin* (2017) 35(2):257–65. doi: 10.1016/j.det.2016.11.014
65. Xie H, Zhou F, Liu L, Zhu G, Li Q, Li C, et al. Vitiligo: How do oxidative stress-induced autoantigens trigger autoimmunity? *J Dermatol Sci* (2016) 81 (1):3–9. doi: 10.1016/j.jdermsci.2015.09.003
66. van den Boorn JG, Konijnenberg D, Dellemijn TA, van der Veen JP, Bos JD, Melief CJ, et al. Autoimmune destruction of skin melanocytes by perilesional T cells from vitiligo patients. *J Invest Dermatol* (2009) 129(9):2220–32. doi: 10.1038/jid.2009.32
67. Sibaud V. Dermatologic Reactions to Immune Checkpoint Inhibitors : Skin Toxicities and Immunotherapy. *Am J Clin Dermatol* (2018) 19(3):345–61. doi: 10.1007/s40257-017-0336-3
68. Sosa A, Lopez Cadena E, Simon Olive C, Karachaliou N, Rosell R. Clinical assessment of immune-related adverse events. *Ther Adv Med Oncol* (2018) 10:1758835918764628. doi: 10.1177/1758835918764628
69. Teulings H-E, Limpens J, Jansen SN, Zwinderman AH, Reitsma JB, Spuls PI, et al. Vitiligo-Like Depigmentation in Patients With Stage III-IV Melanoma Receiving Immunotherapy and Its Association With Survival: A Systematic Review and Meta-Analysis. *J Clin Oncol* (2015) 33(7):773–81. doi: 10.1200/jco.2014.57.4756
70. Freeman-Keller M, Kim Y, Cronin H, Richards A, Gibney G, Weber JS. Nivolumab in Resected and Unresectable Metastatic Melanoma: Characteristics of Immune-Related Adverse Events and Association with Outcomes. *Clin Cancer Res* (2016) 22(4):886–94. doi: 10.1158/1078-0432.CCR-15-1136
71. Duley L. The global impact of pre-eclampsia and eclampsia. *Semin Perinatol* (2009) 33(3):130–7. doi: 10.1053/j.semperi.2009.02.010
72. Al-Jameil N, Aziz Khan F, Fareed Khan M, Tabassum H. A brief overview of preeclampsia. *J Clin Med Res* (2014) 6(1):1–7. doi: 10.4021/jocmr1682w
73. Kohli S, Ranjan S, Hoffmann J, Kashif M, Daniel EA, Al-Dabet MM, et al. Maternal extracellular vesicles and platelets promote preeclampsia via inflammasome activation in trophoblasts. *Blood* (2016) 128(17):2153–64. doi: 10.1182/blood-2016-03-705434
74. Han C, Han L, Huang P, Chen Y, Wang Y, Xue F. Syncytiotrophoblast-Derived Extracellular Vesicles in Pathophysiology of Preeclampsia. *Front Physiol* (2019) 10:1236:1236. doi: 10.3389/fphys.2019.01236
75. Salomon C, Yee SW, Mitchell MD, Rice GE. The possible role of extravillous trophoblast-derived exosomes on the uterine spiral arterial remodeling under both normal and pathological conditions. *BioMed Res Int* (2014) 2014:693157–7. doi: 10.1155/2014/693157
76. Salomon C, Ryan J, Sobrevia L, Kobayashi M, Ashman K, Mitchell M, et al. Exosomal signaling during hypoxia mediates microvascular endothelial cell migration and vasculogenesis. *PloS One* (2013) 8(7):e68451. doi: 10.1371/journal.pone.0068451
77. Salomon C, Kobayashi M, Ashman K, Sobrevia L, Mitchell MD, Rice GE. Hypoxia-induced changes in the bioactivity of cytotrophoblast-derived exosomes. *PloS One* (2013) 8(11):e79636. doi: 10.1371/journal.pone.0079636
78. Collett GP RC, Sargent IL, Vatish M. Endoplasmic reticulum stress stimulates the release of extracellular vesicles carrying danger-associated molecular pattern (DAMP) molecules. *Oncotarget* (2018) 6:6707–17. doi: 10.18632/oncotarget.24158
79. O'Neill CP, Gilligan KE, Dwyer RM. Role of Extracellular Vesicles (EVs) in Cell Stress Response and Resistance to Cancer Therapy. *Cancers (Basel)* (2019) 11(2):136. doi: 10.3390/cancers11020136
80. Regulski MJ. Mesenchymal Stem Cells: "Guardians of Inflammation". *Wounds* (2017) 29(1):20–7.

81. Casado-Díaz A, Quesada-Gómez JM, Dorado G. Extracellular Vesicles Derived From Mesenchymal Stem Cells (MSC) in Regenerative Medicine: Applications in Skin Wound Healing. *Front Bioeng Biotechnol* (2020) 8:146:146. doi: 10.3389/fbioe.2020.00146
82. Mokarizadeh A, Delirezh N, Morshedi A, Mosayebi G, Farshid AA, Mardani K. Microvesicles derived from mesenchymal stem cells: potent organelles for induction of tolerogenic signaling. *Immunol Lett* (2012) 147(1-2):47–54. doi: 10.1016/j.imlet.2012.06.001
83. Riazifar M, Mohammadi MR, Pone EJ, Yeri A, Lasser C, Segaliny AI, et al. Stem Cell-Derived Exosomes as Nanotherapeutics for Autoimmune and Neurodegenerative Disorders. *ACS Nano* (2019) 13(6):6670–88. doi: 10.1021/acsnano.9b01004
84. Bai L, Shao H, Wang H, Zhang Z, Su C, Dong L, et al. Effects of Mesenchymal Stem Cell-Derived Exosomes on Experimental Autoimmune Uveitis. *Sci Rep* (2017) 7(1):4323. doi: 10.1038/s41598-017-04559-y
85. Tao SC, Yuan T, Zhang YL, Yin WJ, Guo SC, Zhang CQ. Exosomes derived from miR-140-5p-overexpressing human synovial mesenchymal stem cells enhance cartilage tissue regeneration and prevent osteoarthritis of the knee in a rat model. *Theranostics* (2017) 7(1):180–95. doi: 10.7150/thno.17133
86. Zheng J, Zhu L, Iok In I, Chen Y, Jia N, Zhu W. Bone marrow-derived mesenchymal stem cells-secreted exosomal microRNA-192-5p delays inflammatory response in rheumatoid arthritis. *Int Immunopharmacol* (2020) 78:105985. doi: 10.1016/j.intimp.2019.105985
87. Cosenza S, Ruiz M, Toupet K, Jorgensen C, Noel D. Mesenchymal stem cells derived exosomes and microparticles protect cartilage and bone from degradation in osteoarthritis. *Sci Rep* (2017) 7(1):16214. doi: 10.1038/s41598-017-15376-8
88. Diederichs S, Tuan RS. Functional comparison of human-induced pluripotent stem cell-derived mesenchymal cells and bone marrow-derived mesenchymal stromal cells from the same donor. *Stem Cells Dev* (2014) 23(14):1594–610. doi: 10.1089/scd.2013.0477
89. Kim S, Lee SK, Kim H, Kim TM. Exosomes Secreted from Induced Pluripotent Stem Cell-Derived Mesenchymal Stem Cells Accelerate Skin Cell Proliferation. *Int J Mol Sci* (2018) 19(10):3119. doi: 10.3390/ijms19103119
90. Zhu Y, Wang Y, Zhao B, Niu X, Hu B, Li Q, et al. Comparison of exosomes secreted by induced pluripotent stem cell-derived mesenchymal stem cells and synovial membrane-derived mesenchymal stem cells for the treatment of osteoarthritis. *Stem Cell Res Ther* (2017) 8(1):64. doi: 10.1186/s13287-017-0510-9
91. Sousa C, Pereira I, Santos AC, Carbone C, Kovačević AB, Silva AM, et al. Targeting dendritic cells for the treatment of autoimmune disorders. *Colloids Surf B Biointerfaces* (2017) 158:237–48. doi: 10.1016/j.colsurfb.2017.06.050
92. Kim K. KS, Choi S, Youn B, Kim H. Extracellular Vesicles as Drug Delivery Vehicles for Rheumatoid Arthritis. *Curr Stem Cell Res Ther* (2016) 11 (4):329–42. doi: 10.2174/1574888x11666151203223251
93. Cai Z, Zhang W, Yang F, Yu L, Yu Z, Pan J, et al. Immunosuppressive exosomes from TGF-beta1 gene-modified dendritic cells attenuate Th17-mediated inflammatory autoimmune disease by inducing regulatory T cells. *Cell Res* (2012) 22(3):607–10. doi: 10.1038/cr.2011.196
94. Wan Y, Wang L, Zhu C, Zheng Q, Wang G, Tong J, et al. Aptamer-conjugated extracellular nanovesicles for targeted drug delivery. *Cancer Res* (2017) 78(3):798–808. doi: 10.1158/0008-5472.CAN-17-2880
95. Fang RH, Hu C-MJ, Luk BT, Gao W, Copp JA, Tai Y, et al. Cancer Cell Membrane-Coated Nanoparticles for Anticancer Vaccination and Drug Delivery. *Nano Lett* (2014) 14(4):2181–8. doi: 10.1021/nl500618u
96. Tauro BJ, Greening DW, Mathias RA, Ji H, Mathivanan S, Scott AM, et al. Comparison of ultracentrifugation, density gradient separation, and immunoaffinity capture methods for isolating human colon cancer cell line LIM1863-derived exosomes. *Methods* (2012) 56(2):293–304. doi: 10.1016/j.ymeth.2012.01.002
97. Sun D, Zhuang X, Xiang X, Liu Y, Zhang S, Liu C, et al. A novel nanoparticle drug delivery system: the anti-inflammatory activity of curcumin is enhanced when encapsulated in exosomes. *Mol Ther* (2010) 18(9):1606–14. doi: 10.1038/mt.2010.105
98. Saari H, Lazaro-Ibanez E, Viitala T, Vuorimaa-Laukkanen E, Siljander P, Yliperttula M. Microvesicle- and exosome-mediated drug delivery enhances the cytotoxicity of Paclitaxel in autologous prostate cancer cells. *J Control Release* (2015) 220(Pt B):727–37. doi: 10.1016/j.jconrel.2015.09.031
99. O'Brien K, Lowry MC, Corcoran C, Martinez VG, Daly M, Rani S, et al. miR-134 in extracellular vesicles reduces triple-negative breast cancer aggression and increases drug sensitivity. *Oncotarget* (2015) 6(32):32774–89. doi: 10.18632/oncotarget.5192
100. Haney MJ, Zhao Y, Jin YS, Batrakova EV. Extracellular Vesicles as Drug Carriers for Enzyme Replacement Therapy to Treat CLN2 Batten Disease: Optimization of Drug Administration Routes. *Cells* (2020) 9(5):1273. doi: 10.3390/cells9051273
101. Haney MJ, Zhao Y, Fay J, Duhyeong H, Wang M, Wang H, et al. Genetically modified macrophages accomplish targeted gene delivery to the inflamed brain in transgenic Parkin Q311X(A) mice: importance of administration routes. *Sci Rep* (2020) 10(1):11818. doi: 10.1038/s41598-020-68874-7
102. Haney MJ, Zhao Y, Jin YS, Li SM, Bago JR, Klyachko NL, et al. Macrophage-Derived Extracellular Vesicles as Drug Delivery Systems for Triple Negative Breast Cancer (TNBC) Therapy. *J Neuroimmune Pharmacol* (2020) 15 (3):487–500. doi: 10.1007/s11481-019-09884-9
103. Kooijmans SA, Aleza CG, Roffler SR, van Solinge WW, Vader P, Schiffelers RM. Display of GPI-anchored anti-EGFR nanobodies on extracellular vesicles promotes tumour cell targeting. *J Extracell Vesicles* (2016) 5:31053. doi: 10.3402/jev.v5.31053
104. Li P, Kaslan M, Lee SH, Yao J, Gao Z. Progress in Exosome Isolation Techniques. *Theranostics* (2017) 7(3):789–804. doi: 10.7150/thno.18133
105. Coumans FAW, Brisson AR, Buzas EI, Dignat-George F, Drees EEE, El-Andaloussi S, et al. Methodological Guidelines to Study Extracellular Vesicles. *Circ Res* (2017) 120(10):1632. doi: 10.1161/CIRCRESAHA.117.309417
106. Szatanek R, Baran J, Siedlar M, Baj-Krzyworzeka M. Isolation of extracellular vesicles: Determining the correct approach (Review). *Int J Mol Med* (2015) 36(1):11–7. doi: 10.3892/ijmm.2015.2194
107. Liga A, Vliegenthart ADB, Oosthuyzen W, Dear JW, Kersaudy-Kerhoas M. Exosome isolation: a microfluidic road-map. *Lab Chip* (2015) 15(11):2388–94. doi: 10.1039/C5LC00240K
108. Momen-Heravi F. Isolation of Extracellular Vesicles by Ultracentrifugation. In: WP Kuo and S Jia, editors. *Extracellular Vesicles: Methods and Protocols*. New York, NY: Springer New York (2017). doi: 10.1007/978-1-4939-7253-1_3
109. Freitas D, Balmaña M, Poças J, Campos D, Osório H, Konstantinidi A, et al. Different isolation approaches lead to diverse glycosylated extracellular vesicle populations. *J Extracell Vesicles* (2019) 8(1):1621131. doi: 10.1080/20013078.2019.1621131
110. Lobb RJ, Becker M, Wen SW, Wong CSF, Wiegmans AP, Leimgruber A, et al. Optimized exosome isolation protocol for cell culture supernatant and human plasma. *J Extracell Vesicles* (2015) 4:27031–1. doi: 10.3402/jev.v4.27031
111. Kowal J, Arras G, Colombo M, Jouve M, Morath JP, Primdal-Bengtson B, et al. Proteomic comparison defines novel markers to characterize heterogeneous populations of extracellular vesicle subtypes. *Proc Natl Acad Sci* (2016) 113(8):E968–77. doi: 10.1073/pnas.1521230113
112. Ludwig N, Razzo BM, Yerneni SS, Whiteside TL. Optimization of cell culture conditions for exosome isolation using mini-size exclusion chromatography (mini-SEC). *Exp Cell Res* (2019) 378(2):149–57. doi: 10.1016/j.yexcr.2019.03.014
113. Corso G, Mäger I, Lee Y, Görgens A, Bultema J, Giebel B, et al. Reproducible and scalable purification of extracellular vesicles using combined bind-elute and size exclusion chromatography. *Sci Rep* (2017) 7(1):11561. doi: 10.1038/s41598-017-10646-x
114. Böing AN, van der Pol E, Grootemaat AE, Coumans FAW, Sturk A, Nieuwland R. Single-step isolation of extracellular vesicles by size-exclusion chromatography. *J Extracell Vesicles* (2014) 3(1):23430. doi: 10.3402/jev.v3.23430
115. Heath N, Grant L, De Oliveira TM, Rowlinson R, Osteikoetxea X, Dekker N, et al. Rapid isolation and enrichment of extracellular vesicle preparations using anion exchange chromatography. *Sci Rep* (2018) 8(1):5730. doi: 10.1038/s41598-018-24163-y
116. Weng Y, Sui Z, Shan Y, Hu Y, Chen Y, Zhang L, et al. Effective isolation of exosomes with polyethylene glycol from cell culture supernatant for in-depth proteome profiling. *Analyst* (2016) 141(15):4640–6. doi: 10.1039/C6AN00892E

117. Gallart-Palau X, Serra A, Wong ASW, Sandin S, Lai MKP, Chen CP, et al. Extracellular vesicles are rapidly purified from human plasma by PRotein Organic Solvent PRecipitation (PROSPR). *Sci Rep* (2015) 5:14664–4. doi: 10.1038/srep14664
118. Gao X, Ran N, Dong X, Zuo B, Yang R, Zhou Q, et al. Anchor peptide captures, targets, and loads exosomes of diverse origins for diagnostics and therapy. *Sci Trans Med* (2018) 10(444):eaat0195. doi: 10.1126/scitranslmed.aat0195
119. Carney RP, Hazari S, Rojalin T, Knudson A, Gao T, Tang Y, et al. Targeting Tumor-Associated Exosomes with Integrin-Binding Peptides. *Adv Biosyst* (2017) 1(5):1600038–n/a. doi: 10.1002/adbi.201600038
120. Nakai W, Yoshida T, Diez D, Miyatake Y, Nishibu T, Imawaka N, et al. A novel affinity-based method for the isolation of highly purified extracellular vesicles. *Sci Rep* (2016) 6:33935. doi: 10.1038/srep33935
121. Melo SA, Luecke LB, Kahlert C, Fernandez AF, Gammon ST, Kaye J, et al. Glypican-1 identifies cancer exosomes and detects early pancreatic cancer. *Nature* (2015) 523(7559):177–82. doi: 10.1038/nature14581
122. Tian Y, Gong M, Hu Y, Liu H, Zhang W, Zhang M, et al. Quality and efficiency assessment of six extracellular vesicle isolation methods by nano-flow cytometry. *J Extracell Vesicles* (2020) 9(1):1697028. doi: 10.1080/20013078.2019.1697028
123. Chen C, Skog J, Hsu C-H, Lessard RT, Balaj L, Wurdinger T, et al. Microfluidic isolation and transcriptome analysis of serum microvesicles. *Lab Chip* (2010) 10(4):505–11. doi: 10.1039/b916199f
124. Wan Y, Maurer M, He H-Z, Xia Y-Q, Hao S-J, Zhang W-L, et al. Enrichment of extracellular vesicles with lipid nanoprobe functionalized nanostructured silica. *Lab Chip* (2019) 19(14):2346–55. doi: 10.1039/C8LC01359D
125. Jo W, Kim J, Yoon J, Jeong D, Cho S, Jeong H, et al. Large-scale generation of cell-derived nanovesicles. *Nanoscale* (2014) 6(20):12056–64. doi: 10.1039/C4NR02391A
126. Jo W, Jeong D, Kim J, Cho S, Jang SC, Han C, et al. Microfluidic fabrication of cell-derived nanovesicles as endogenous RNA carriers. *Lab Chip* (2014) 14 (7):1261–9. doi: 10.1039/C3LC50993A
127. Jang SC, Kim OY, Yoon CM, Choi D-S, Roh T-Y, Park J, et al. Bioinspired Exosome-Mimetic Nanovesicles for Targeted Delivery of Chemotherapeutics to Malignant Tumors. *ACS Nano* (2013) 7(9):7698–710. doi: 10.1021/nn402232g
128. Cheng G, Li W, Ha L, Han X, Hao S, Wan Y, et al. Self-Assembly of Extracellular Vesicle-like Metal–Organic Framework Nanoparticles for Protection and Intracellular Delivery of Biofunctional Proteins. *J Am Chem Soc* (2018) 140(23):7282–91. doi: 10.1021/jacs.8b03584
129. Parodi A, Quattrocchi N, van de Ven AL, Chiappini C, Evangelopoulos M, Martinez JO, et al. Synthetic nanoparticles functionalized with biomimetic leukocyte membranes possess cell-like functions. *Nat Nanotechnol* (2013) 8 (1):61–8. doi: 10.1038/nnano.2012.212
130. Yoon J, Jo W, Jeong D, Kim J, Jeong H, Park J. Generation of nanovesicles with sliced cellular membrane fragments for exogenous material delivery. *Biomaterials* (2015) 59:12–20. doi: 10.1016/j.biomaterials.2015.04.028
131. Li Y, Zhang X, Lin J, Li R, Yue T. Extracting lipid vesicles from plasma membranes via self-assembly of clathrin-inspired scaffolding nanoparticles. *Colloids Surf B Biointerfaces* (2019) 176:239–48. doi: 10.1016/j.colsurfb.2019.01.008
132. Tehrani S, Antovic A, Mobarrez F, Mageed K, Lins PE, Adamson U, et al. High-dose aspirin is required to influence plasma fibrin network structure in patients with type 1 diabetes. *Diabetes Care* (2012) 35(2):404–8. doi: 10.2337/dc11-1302
133. Tyndall A, Dazzi F. Chronic GVHD as an autoimmune disease. *Best Pract Res Clin Haematol* (2008) 21(2):281–9. doi: 10.1016/j.beha.2008.03.003
134. Kordelas L, Rebmann V, Ludwig AK, Radtke S, Ruesing J, Doeppner TR, et al. MSC-derived exosomes: a novel tool to treat therapy-refractory graft-versus-host disease. *Leukemia* (2014) 28:970. doi: 10.1038/leu.2014.41
135. Zhao Y, Jiang Z, Zhao T, Ye M, Hu C, Yin Z, et al. Reversal of type 1 diabetes via islet β cell regeneration following immune modulation by cord blood-derived multipotent stem cells. *BMC Med* (2012) 10(1):3. doi: 10.1186/1741-7015-10-3
136. Ezquer F, Ezquer M, Contador D, Ricca M, Simon V, Conget P. The antidiabetic effect of mesenchymal stem cells is unrelated to their transdifferentiation potential but to their capability to restore Th1/Th2 balance and to modify the pancreatic microenvironment. *Stem Cells* (2012) 30(8):1664–74. doi: 10.1002/stem.1132
137. Smith MH, Bass AR. Arthritis After Cancer Immunotherapy: Symptom Duration and Treatment Response. *Arthritis Care Res (Hoboken)* (2019) 71 (3):362–6. doi: 10.1002/acr.23467
138. Rubino F, Amiel SA, Zimmet P, Alberti G, Bornstein S, Eckel RH, et al. New-Onset Diabetes in Covid-19. *N Engl J Med* (2020) 383(8):789–90. doi: 10.1056/NEJMc2018688

Conflict of Interest: The authors declare that the research was conducted in the absence of any commercial or financial relationships that could be construed as a potential conflict of interest.

frontiers in Oncology

METHODS
published: 17 May 2021
doi: 10.3389/fonc.2021.642144

Complement C1q (C1qA, C1qB, and C1qC) May Be a Potential Prognostic Factor and an Index of Tumor Microenvironment Remodeling in Osteosarcoma

*Long-hao Chen[1], Jin-Fu Liu[2], Yan- Lu[1], Xin-yu He[1], Chi- Zhang[2] and Hong-hai Zhou[1]**

[1] Faculty of Orthopedics and Traumatology, Guangxi University of Chinese Medicine, Nanning, China, [2] Graduate School, Guangxi University of Chinese Medicine, Nanning, China

OPEN ACCESS

Edited by:
Ankur Singh,
Georgia Institute of Technology,
United States

Reviewed by:
Qian-qian Liang,
Shanghai University of Chinese Medicine, China
Zhidao Xia,
Swansea University, United Kingdom

***Correspondence:**
Hong-hai Zhou
keguyixin@163.com

Specialty section:
This article was submitted to Cancer Immunity and Immunotherapy, a section of the journal Frontiers in Oncology

Received: 15 December 2020
Accepted: 20 April 2021
Published: 17 May 2021

Citation:
Chen L-h, Liu J-F, Lu Y-, He X-y, Zhang C- and Zhou H-h (2021) Complement C1q (C1qA, C1qB, and C1qC) May Be a Potential Prognostic Factor and an Index of Tumor Microenvironment Remodeling in Osteosarcoma. Front. Oncol. 11:642144. doi: 10.3389/fonc.2021.642144

The tumor microenvironment (TME) has important effects on the tumorigenesis and development of osteosarcoma (OS). However, the dynamic mechanism regulating TME immune and matrix components remains unclear. In this study, we collected quantitative data on the gene expression of 88 OS samples from The Cancer Genome Atlas (TCGA) database and downloaded relevant clinical cases of OS from the TARGET database. The proportions of tumor-infiltrating immune cells (TICs) and the numbers of immune and matrix components were determined by CIBERSORT and ESTIMATE calculation methods. Protein-protein interaction (PPI) network construction and Cox regression analysis were conducted to analyze differentially expressed genes (DEGs). The complement components C1qA, C1qB and C1qC were then determined to be predictive factors through univariate Cox analysis and PPI cross analysis. Further analysis found that the levels of C1qA, C1qB and C1qC expression were positively linked to OS patient survival time and negatively correlated with the clinicopathological feature percent necrosis at definitive surgery. The results of gene set enrichment analysis (GSEA) demonstrated that genes related to immune functions were significantly enriched in the high C1qA, C1qB and C1qC expression groups. Proportion analysis of TICs by CIBERSORT showed that the levels of C1qA, C1qB and C1qC expression were positively related to M1 and M2 macrophages and CD8+ cells and negatively correlated with M0 macrophages. These results further support the influence of the levels of C1qA, C1qB and C1qC expression on the immune activity of the TME. Therefore, C1qA, C1qB and C1qC may be potential indicators of remodeling in the OS TME, which is helpful to predict the prognosis of patients with OS and provide new ideas for immunotherapy for OS.

Keywords: C1q (A/B/C), tumor microenvironment, osteosarcoma, tumor-infiltrating immune cells, CIBERSORT, ESTIMATE

INTRODUCTION

Osteosarcoma (OS), which accounts for 9% of cancer deaths in children and adolescents aged 10-24 years, is the most common primary malignant bone tumor in children and adolescents. It has strong local invasiveness and early metastasis, with signs of metastasis indicating a poor prognosis in advanced osteosarcoma patients (1, 2). At present, chemotherapy combined with surgical resection is the most important method of OS treatment. The disease-free survival rate of OS patients is close to 70% (3). The prognosis of patients with OS recurrence or metastasis is still extremely poor, although great success has been achieved with multimodal combination therapies. The five-year overall survival rate is approximately 20%, which is still insufficient to a large extent (4, 5). Therefore, identifying new diagnostic biomarkers and developing more effective molecular targets for cancer treatment are still warranted.

In recent years, increasing attention has been given to the effects of the tumor microenvironment (TME) on tumorigenesis and development (6). Immune cells and stromal cells are the main structural components in the TME. They provide all the metabolites and factors that control the proliferation, spread, and drug resistance of OS cells. Tumors are inextricably linked to their local microenvironment (7). Studies have shown that stromal cells are involved in tumor angiogenesis and extracellular matrix remodeling (8). The interactions between host stromal cells and tumor cells play key roles in the growth and progression of tumors. However, different tumors have different matrix components. The mechanism of crosstalk between tumors is still poorly understood (9). Furthermore, the impacts of immune cells in the TME on the tumor have also attracted much attention. Many studies have tried to define the interactions between the immune system and tumors, and it is possible to conduct therapeutic interventions based on these interactions. Studies have shown that TICs in the TME are an important indicator for OS treatment decision-making, and the infiltration of lymphocytes and macrophages is remarkably linked to the prognosis of OS patients (10, 11). Immune-related risk models for OS have been established in some studies for the prediction of OS patient prognosis. The results indicated that a poor prognosis and immunosuppression were common in patients with a high risk score (12). The development of tumor-immune correlation studies has led to continuous improvements in tumor immunotherapy. Therefore, accurate genetic analysis that correctly reveals the dynamic mechanism regulating TME immune and matrix components is a research focus and a challenge.

In this paper, ESTIMATE and CIBERSORT calculation methods were applied to calculate the proportions of TICs and TME immune/interstitial components in OS patient samples collected from the TCGA database and ultimately identified the complement family members C1qA, C1qB and C1qC as predictive biomarkers. C1q is not only a key subcomponent of the classical complement activation pathway but also the main link between innate immunity driven by the classical pathway and acquired immunity mediated by IgG or IgM. C1q is synthesized in the tumor microenvironment and acts as an extracellular matrix protein that can promote tumor growth and metastasis (13, 14). Some studies have shown that C1q expression is present in the microenvironments of diverse types of human tumors, including prostate cancer, ovarian cancer, mesothelioma, and melanoma. In these microenvironments, C1q may perform promotive or inhibitory roles in cancer progression, but the majority of these results indicate that C1q expression in the tumor microenvironment is linked to a poor patient prognosis (15). In this paper, starting from the differentially expressed genes (DEGs) identified by comparing TME immune components and matrix components in OS patients, it is revealed that the complement family members C1qA, C1qB and C1qC may be potential indicators of TME remodeling in OS patients.

DATA COLLECTION AND PROCESSING

Materials and Methods

The quantified HTSeq-FPKM gene expression data for 88 OS samples were downloaded from the TCGA on August 9, 2020. At the same time, the latest clinical data for OS patients, including age, sex, race, overall survival time, survival status and other clinicopathological information, were downloaded from TARGET (https://ocg.cancer.gov/programs/target).

To screen the mRNA matrix data with genetic characteristics, we used PERL software (v5.30.2) (https://www.perl.org/) to annotate the human genome based on the expression profiles of the OS tumor samples downloaded from the TCGA database. Matrix data for the gene expression values of the OS tumor samples were obtained.

Establishment of the ImmuneScore, StromalScore, and ESTIMATEScore

Estimation of the levels of TME immune-stromal components in each sample was conducted using the ESTIMATE algorithm using R software (version 4.0.2) loaded with the estimate package (16). Three types of scores (ImmuneScore, StromalScore, and ESTIMATEScore) exhibited a positive association with 3 kinds of levels (immune, stromal, and the sum of both). The levels of the corresponding TME components were higher when the corresponding score was higher.

Survival Analysis

The combination of the TME score with the survival and survival status of OS patients was conducted using the Limma package of R software. According to the median immune score and matrix score, OS samples were divided into high- and low-score groups. Survival analyses were carried out using R software with the packages survival and survminer. Survival curves were plotted by the Kaplan-Meier method, and statistical significance was determined with the log-rank test; $p < 0.05$ was considered statistically significant.

Screening of DEGs Between the High and Low ImmuneScore or StromalScore Groups

The high and low ImmuneScore or StromalScore results for the 88 tumor samples were determined by comparing the results with the median score. Differential gene expression analyses were performed

using R with the limma package, and DEGs were identified by comparing the high- and low-score samples. An FDR<0.05 and a fold change after log2 transformation >1 (high-score group/low-score group) were used to select the significant DEGs.

GO and KEGG Enrichment Analyses

GO and KEGG enrichment analyses of 379 DEGs were conducted using R software with the packages clusterProfiler, enrichplot, and ggplot2. Terms were considered significantly enriched terms both the *p*- and *q*-values were <0.05.

Heatmaps

R software with the package pheatmap was applied for the production of DEG heatmaps.

Analysis of Score Differences in Clinicopathological Data

The clinicopathological data of patients with OS were statistically analyzed with R software, and comparisons of different clinical parameters were conducted with Wilcoxon or Kruskal-Wallis rank-sum tests to determine significance.

Construction of a PPI Network

The STRING database and Cytoscape (version 3.7.1) were applied for the construction and reconstruction of a PPI network, respectively. The network was built using the nodes with an interactive confidence value >0.7.

COX Regression Analysis

Univariate Cox regression analysis was conducted using R software with the survival package. The patients were divided into high and low expression groups based on the median gene expression value. The survival difference between the two groups was evaluated, and the Kaplan-Meier test was performed. The identified significant genes shown in the figures satisfied both univariate Cox $p < 0.05$ and Kaplan-Meier test $p < 0.05$.

Gene Set Enrichment Analysis

GSEA was conducted using gsea-4.1.0 software on the basis of the Molecular Signatures Database-derived HALLMARK and C7 target sets (v6.2). GSEA was conducted using the whole transcriptome of all tumor samples, and only gene sets with an FDR q < 0.06 and a NOM $p < 0.05$ were considered significant.

TIC Profile

Estimation of the TIC abundance profile among all tumor samples was carried out by the CIBERSORT computational method. The genes with low expression were removed, and a follow-up analysis was performed using only the tumor samples with $p < 0.05$.

RESULTS

Analysis Process of This Study

We downloaded data for 88 RNA-SEQ transcriptomes from the TCGA database and corresponding clinical data from the TARGET database. The proportions of tumor-infiltrating immune cells (TICs) and the numbers of immune and matrix components in the TME of OS patients were determined by CIBERSORT and ESTIMATE calculation methods. A protein-protein interaction (PPI) network was constructed using DEGs identified by both ImmuneScore and StromalScore, and then univariate Cox regression analysis was carried out. Intersection analyses were then applied to analyze the PPI core nodes and most significant factors identified by the Cox regression analysis. Seven key genes, ITGAM, C1qB, CD163, C1qA, C1qC, C3AR1 and CD14, were identified. We continued to screen the relationships between gene expression and survival and ultimately identified C1qA, C1qB and C1qC as the focus of a follow-up series of analyses, including gene set enrichment analysis (GSEA) and correlation analysis of clinicopathological features and TICs.

Scores Were Associated With OS Patient Survival

Kaplan-Meier survival analyses based on ImmuneScore, StromalScore and ESTIMATEScore results were performed to clarify the relationships between immune and matrix levels and survival rates. The number of immune cells or stromal cells in the TME is considered to be greater when the ImmuneScore or StromalScore result is higher. The combined result for the ImmuneScore and StromalScore for the TME is the ESTIMATEScore, which is calculated as the sum of the two scores. **Figures 1A, B** shows that the contents of immune cells and stromal cells were markedly linked to OS patient overall survival. The correlation between the ESTIMATEScore and overall survival was also significant (**Figure 1C**). It is suggested that the composition of TME can predict the prognosis of patients with OS.

Enriched DEGs Shared Between the ImmuneScore and StromalScore Were Mainly Immune-Related Genes

Analyses comparing samples with high and low scores were conducted to determine the exact gene profile alterations in immune and stromal components of the TME. In total, 1163 DEGs (609 upregulated and 554 downregulated genes) were acquired from the ImmuneScore (high- and low-score samples) compared to the median (**Figures 2A, C, D**). Similarly, 934 DEGs (379 upregulated and 555 downregulated) were acquired from the StromalScore (**Figures 2B–D**). In addition, 123 high-score upregulated genes and 32 low-score downregulated genes in the ImmuneScore and StromalScore were shown to intersect by Venn diagram analysis. These DEGs (155 genes in total) may be determinants of the TME status. Enrichment analysis of gene ontology (GO) results demonstrated that the DEGs generally mapped to terms linked to immunity, such as immunity mediated by B cells or immunoglobulin (**Figure 2E**). Kyoto Encyclopedia of Genes and Genomes (KEGG) enrichment analysis also showed DEG enrichment in the immune system-related disease spectrum (**Figure 2F**). Therefore, mapping of the DEGs to activities linked to immunity suggested that the key feature of the TME in OS is immune factor involvement.

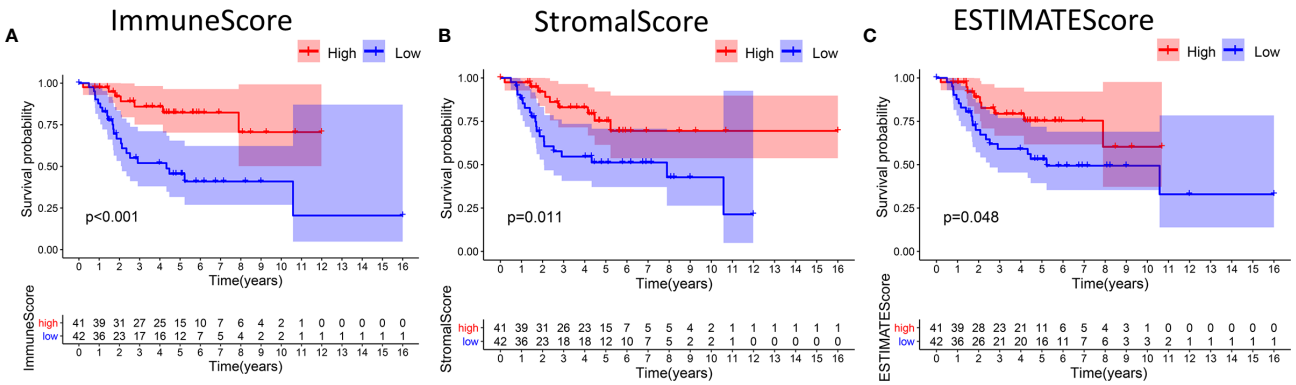

FIGURE 1 | Associations between the scores and survival of OS patients. **(A)** Kaplan-Meier survival analysis of OS patients in the high and low ImmuneScore subgroups, log-rank test $p < 0.001$. **(B)** Survival analysis of patients in the high and low StromalScore groups, $p = 0.011$. **(C)** Survival analysis of OS patients in the high and low ESTIMATEScore groups, $p = 0.048$.

Intersection Analysis of a PPI network and Univariate Cox Regression

The construction of a PPI network with the STRING database was performed using Cytoscape software to further reveal the underlying mechanism of the OS TME. **Figure 3A** shows the interactions among the 155 genes, and the top 30 genes were sorted based on the number of nodes (**Figure 3B**). Determination of significant prognostic factors for OS patients was conducted using univariate Cox regression analysis of the survival of the 155 patients (**Figure 3C**). Analyses of the intersections between the PPI core nodes and the top 15 Cox regression factors were then performed, identifying 7 overlapping factors, namely, C1qA, C1qB, C1qC, C3AR1, CD14, CD163, and ITGAM (**Figure 3D**).

Relationships Between DEG Expression and Survival Time in Patients With OS

In this study, high and low gene expression groups were established to divide all OS samples according to median gene expression levels. DEG survival analysis indicated that the survival rates of OS patients with high expression of C1qA, C1qB, C1qC, C3AR1, CD14 or ITGAM were higher than those of patients with corresponding low expression (**Figures 4A–F**). C1qA, C1qB and C1qC showed significant differences at the P<0.01 level. Therefore, we concluded that expression of C1qA, C1qB, C1qC, C3AR1, CD14 and ITGAM in the TME is positively correlated with the prognosis of OS patients, among which C1qA, C1qB and C1qC were more closely linked to the prognosis of OS patients. We identified C1qA, C1qB and C1qC as the main prognostic indicators in patients with OS.

Relationships Between the Levels of C1qA, C1qB, or C1qC Expression and Clinicopathological Characteristics in OS Patients

There are clear correlations between the levels of C1qA, C1qB, and C1qC expression and the survival time of OS patients. To further clarify the correlations between the expression levels of these factors and age, histologic response, percent necrosis at definitive surgery, primary site progression and primary tumor site in patients with OS, the relationships between the levels of C1qA, C1qB, or C1qC expression and these five clinical features of OS patients were analyzed. The results indicated that the levels of C1qA, C1qB and C1qC expression were significantly correlated with percent necrosis at definitive surgery in OS patients ($P < 0.05$) (**Figures 5C, H, M**), while age, histologic response, primary site progression and primary tumor site were not significantly correlated with C1qA, C1qB or C1qC gene expression ($P > 0.05$) (**Figures 5A, B, D–G, I–L, N, O**). We found that the C1qA, C1qB and C1qC gene expression levels in OS patients with a percent necrosis at definitive surgery less than 50% were higher than those in OS patients with a percent necrosis at definitive surgery higher than 50%.

C1qA, C1qB, and C1qC May Be Potential Indicators of TME Remodeling

In view of the fact that the levels of C1qA, C1qB, and C1qC expression are positively linked to OS patient survival, the high and low C1qA, C1qB, and C1qC expression groups were compared with the median group by GSEA. Both the Hallmark and C7 datasets showed that the groups with high C1qA, C1qB or C1qC expression levels were remarkably enriched in immune gene sets, indicating their immune functions, such as allograft rejection, the complement response, and the basic response, were more active than those in the low expression groups (**Figures 6A–F**). It is suggested that C1qA, C1qB and C1qC may be potential indexes that reflect the status of the TME.

Correlation Analysis of the Levels of C1qA, C1qB or C1qC Expression and TICs

The CIBERSORT algorithm was applied to analyze the proportions of tumor-infiltrating immune subsets to further confirm the correlations between the TME and C1qA, C1qB, and C1qC expression levels. Construction of 22 kinds of immune

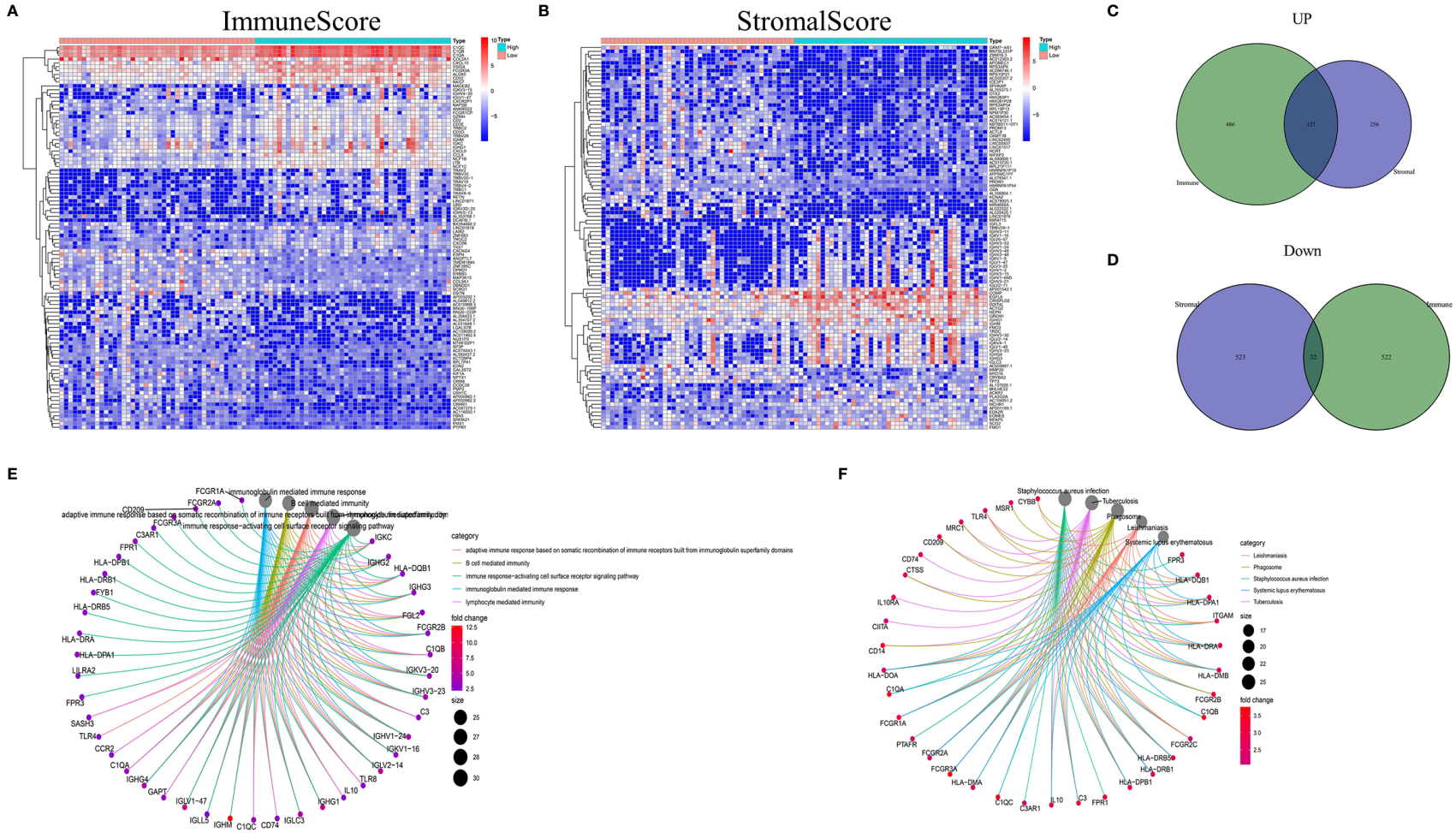

FIGURE 2 | DEG heatmaps, Venn diagrams, and GO and KEGG enrichment analyses. **(A)** Heatmaps for DEGs identified by comparing the high-score and low-score ImmuneScore groups. The gene name is shown in the row, and the sample ID (column name) is not shown. The Wilcoxon rank-sum test was used to identify differentially expressed genes, and the threshold of significance was set at q=0.05 and a fold change after log2 conversion >1. **(B)** DEG heatmaps, similar to **(A)**, produced by analysis related to the StromalScore. **(C, D)** The Venn diagrams displaying the shared up- or downregulated DEGs identified by the analyses using the ImmuneScore and StromalScore, with a filtering threshold of significance of q<0.05 and a fold change after log2 conversion >1. **(E, F)** GO and KEGG enrichment analyses were carried out for the 155 DEGs, with p and q < 0.05.

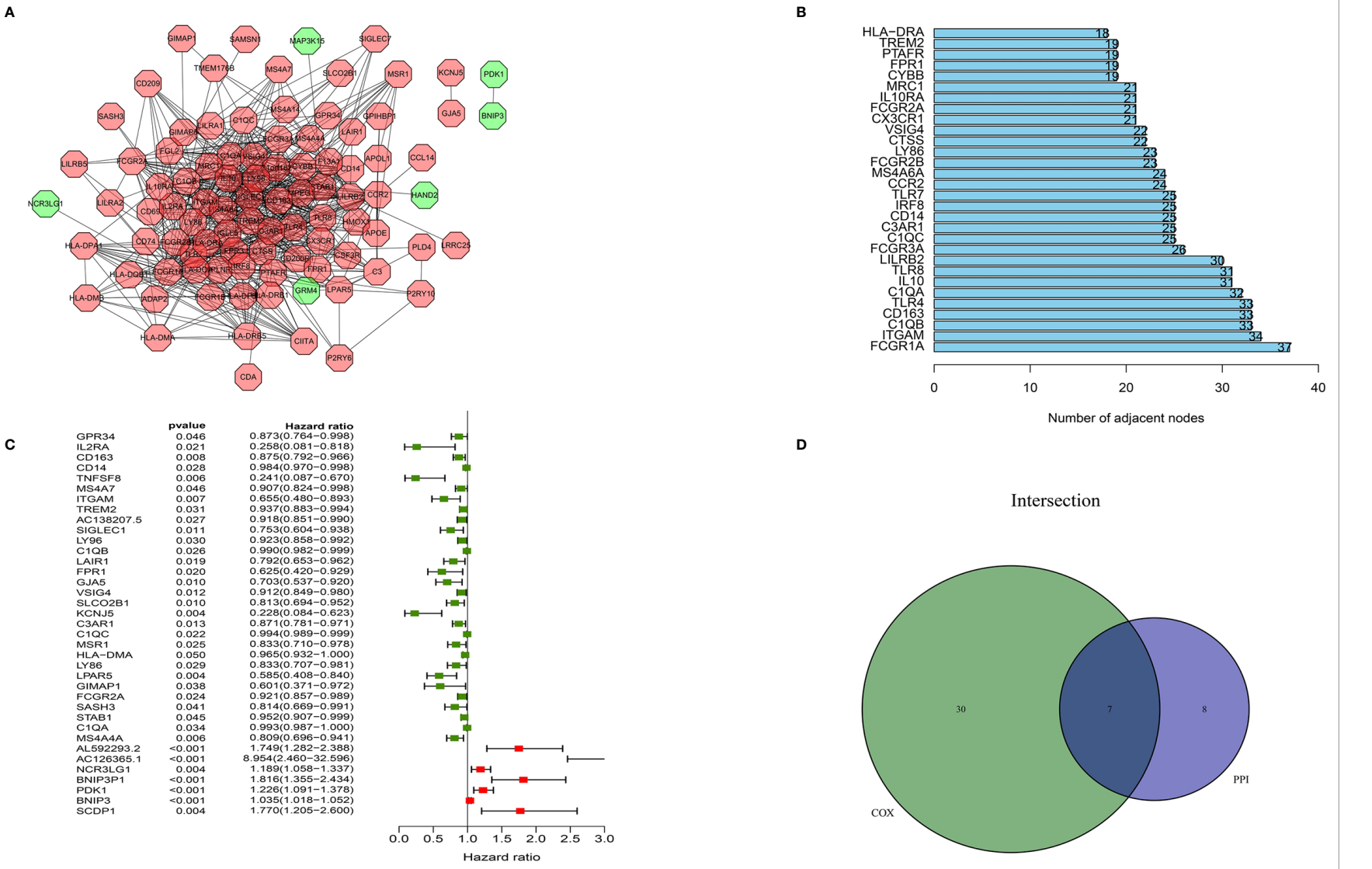

FIGURE 3 | Construction of a PPI network, univariate analysis by Cox regression analysis and intersection of the results. **(A)** Construction of the PPI network conducted using nodes with an interactive confidence value > 0.7. **(B)** Sorting of the top 30 genes on the basis of the number of PPI nodes. **(C)** The 155 DEGs were analyzed using univariate Cox regression analysis and the Kaplan-Meier test, and significant influencing factors with P < 0.05 are listed. **(D)** Venn diagram constructed to identify the factors shared by the top 30 PPI nodes and the top 15 univariate Cox regression factors.

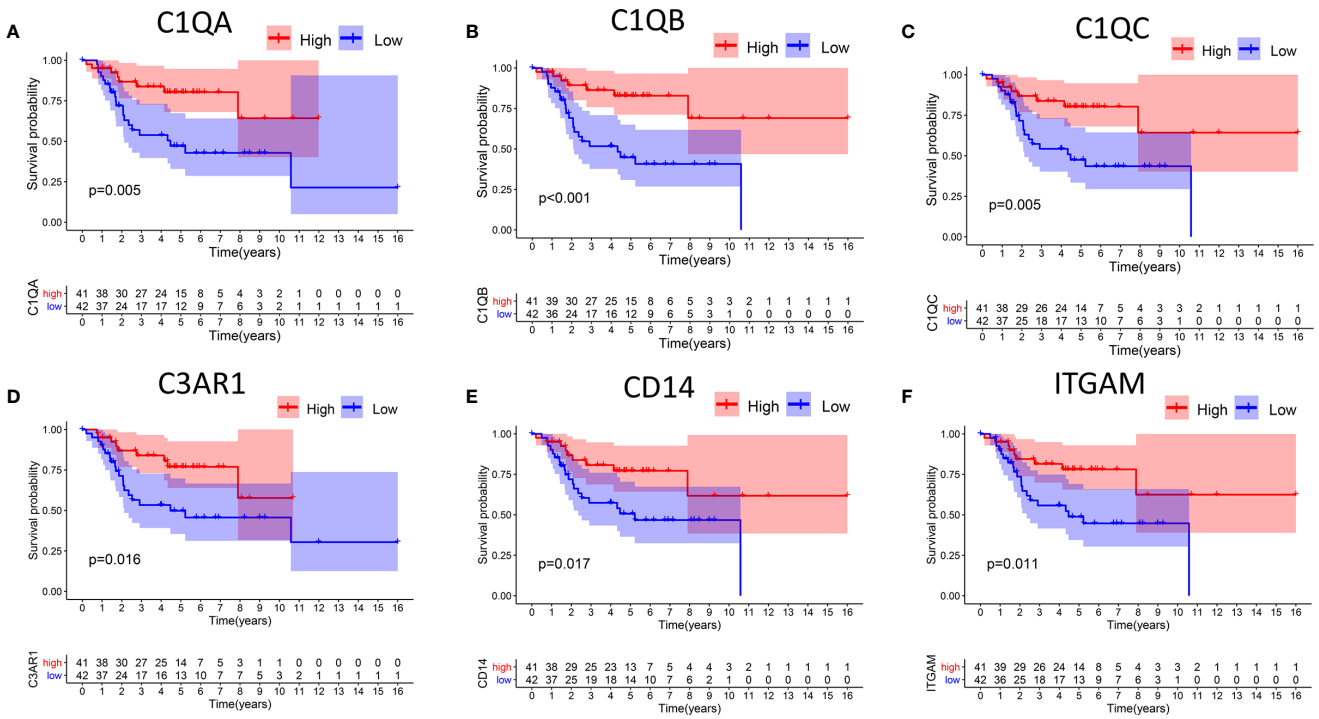

FIGURE 4 | Relationships between DEG expression and survival time in patients with OS. **(A–F)** Differences in survival between patients with high and low expression of DEGs. The high and low expression levels of DEGs in patients were defined according to the median expression level. $p < 0.05$ (log-rank test) for all these genes.

cell profiles in OS samples was performed (**Figure 7A**), and the correlations with TICs were calculated (**Figure 7B**). The differences and correlations between the C1qA, C1qB, and C1qC expression levels and the proportions of TICs were analyzed (**Figures 8** and **9**). The results showed that there were 8 kinds of C1qA expression-related TICs (**Figure 9A**). Among them, three kinds of TICs were positively associated with C1qA expression, including M1 macrophages, M2 macrophages, and CD8+ T cells. Five types of TICs, including M0 macrophages, resting NK cells, naive CD4+ T cells, and resting memory CD4 T cells, were negatively correlated with C1qA expression. Four types of TICs were linked to C1qB expression (**Figure 9B**); three kinds of TICs were positively associated with C1qB expression, including M1 macrophages, M2 macrophages, and CD8+ cells. A negative correlation between M0 macrophages and C1qB expression was found. Six types of TICs were linked to C1qC expression (**Figure 9C**). Among the types, 4 were positively associated with C1qC expression, including M1 macrophages, M2 macrophages, resting T cells, and CD8+ T cells. Two types of TICs were negatively correlated with C1qC expression, including M0 macrophages and resting memory CD4 T cells. However, the levels of M1 macrophages, M2 macrophages, and CD8+ T cells were positively associated with the expression levels of C1qA, C1qB and C1qC. These results further indicate the influence of C1qA, C1qB and C1qC expression levels on TME immunoactivities.

DISCUSSION

The TME has important effects on tumorigenesis and tumor development. Studies have shown that TME remodeling may promote the transformation of lung adenocarcinoma from a developmental status to an inhibitory status (17). In the TME literature related to OS, we found that scholars have explored the relationship between the immune score of TICs and the survival rate in OS patients, and PPARG, IGHG3 and PDK1 were used as prediction targets (12). The immune score has certain reference value for clinicians in evaluating the prognosis of OS patients and selecting appropriate immunotherapy targets. However, the associations between the targeted gene expression and clinicopathological characteristics of OS patients and TICs in the tumor microenvironment have not been reported. In our present study, a series of bioinformatic analyses using the TCGA and TARGET databases were performed to identify the genes related to the TME that can improve the prognosis of OS patients. Ultimately, C1qA, C1qB and C1qC were identified as the main indexes for predicting the prognosis of OS and remodeling of the TME. We will focus on the relationship between target gene expression and the TME to provide a new therapeutic target for OS immunotherapy.

According to the results of the study, we concluded that TME immune and matrix components contribute to OS patient prognosis. In particular, the proportions of TME immune

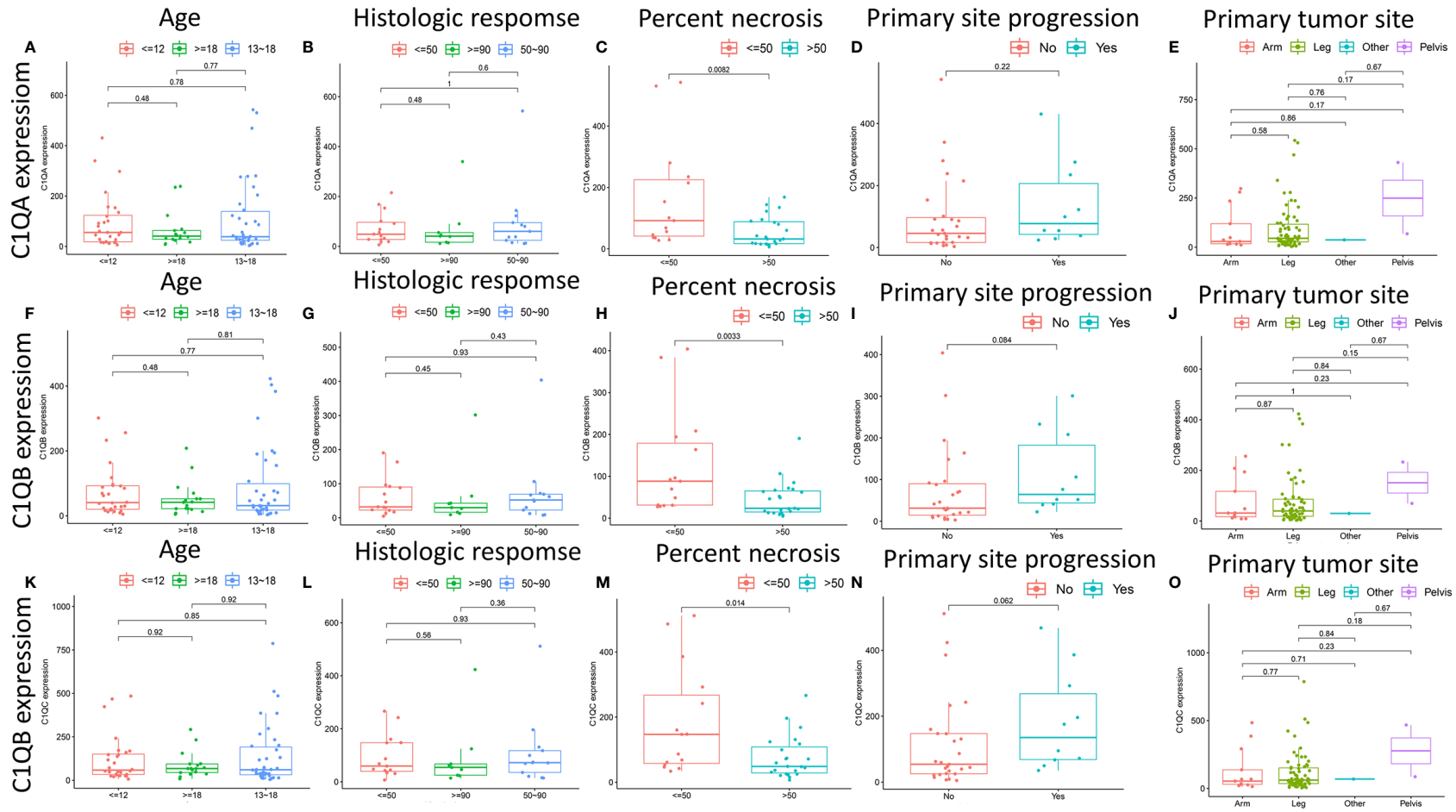

FIGURE 5 | **(A–O)** Relationships between the levels of C1qA, C1qB, or C1qC expression and clinicopathological features in OS patients. The Wilcoxon rank-sum test or Kruskal-Wallis rank-sum test was applied for statistical analysis.

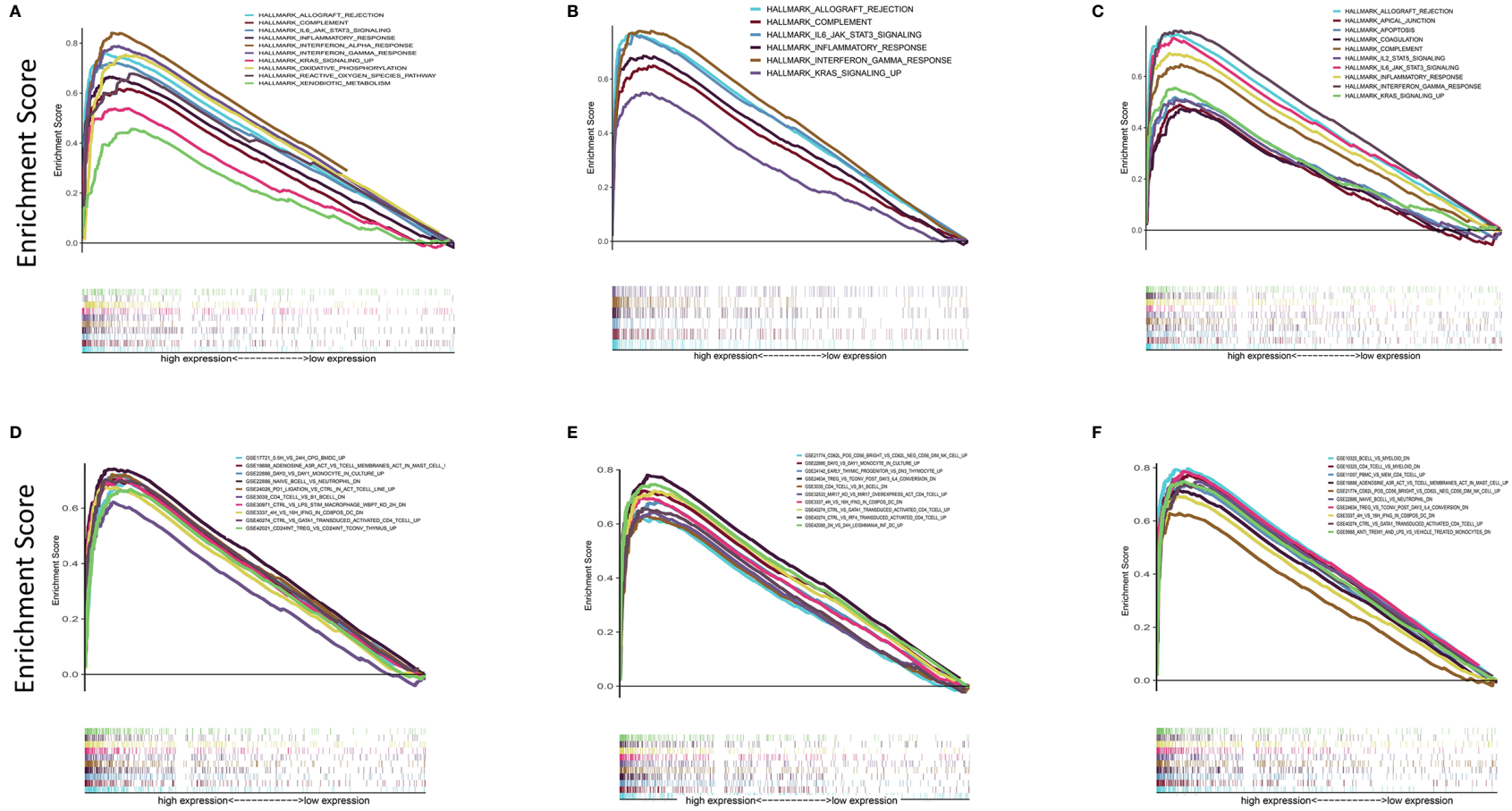

FIGURE 6 | GSEA of samples with high and low C1qA, C1qB and C1qC expression. **(A–C)** C1qA, C1qB and C1qC are associated with the gene set enriched in HALLMARK. Each line represents a specific set of genes, with the upregulated genes located at the origin near the coordinates on the left and the downregulated genes located on the right side of the x-axis. FDR $q < 0.05$ and NOM $p < 0.05$ were considered significant. Only a few leading gene sets are displayed in the figure panels. **(D–F)** Expression of genes in the C7 gene set (immunological gene set) in samples stratified by C1qA, C1qB or C1qC expression. Only a few gene sets with high NOM and FDR values are shown.

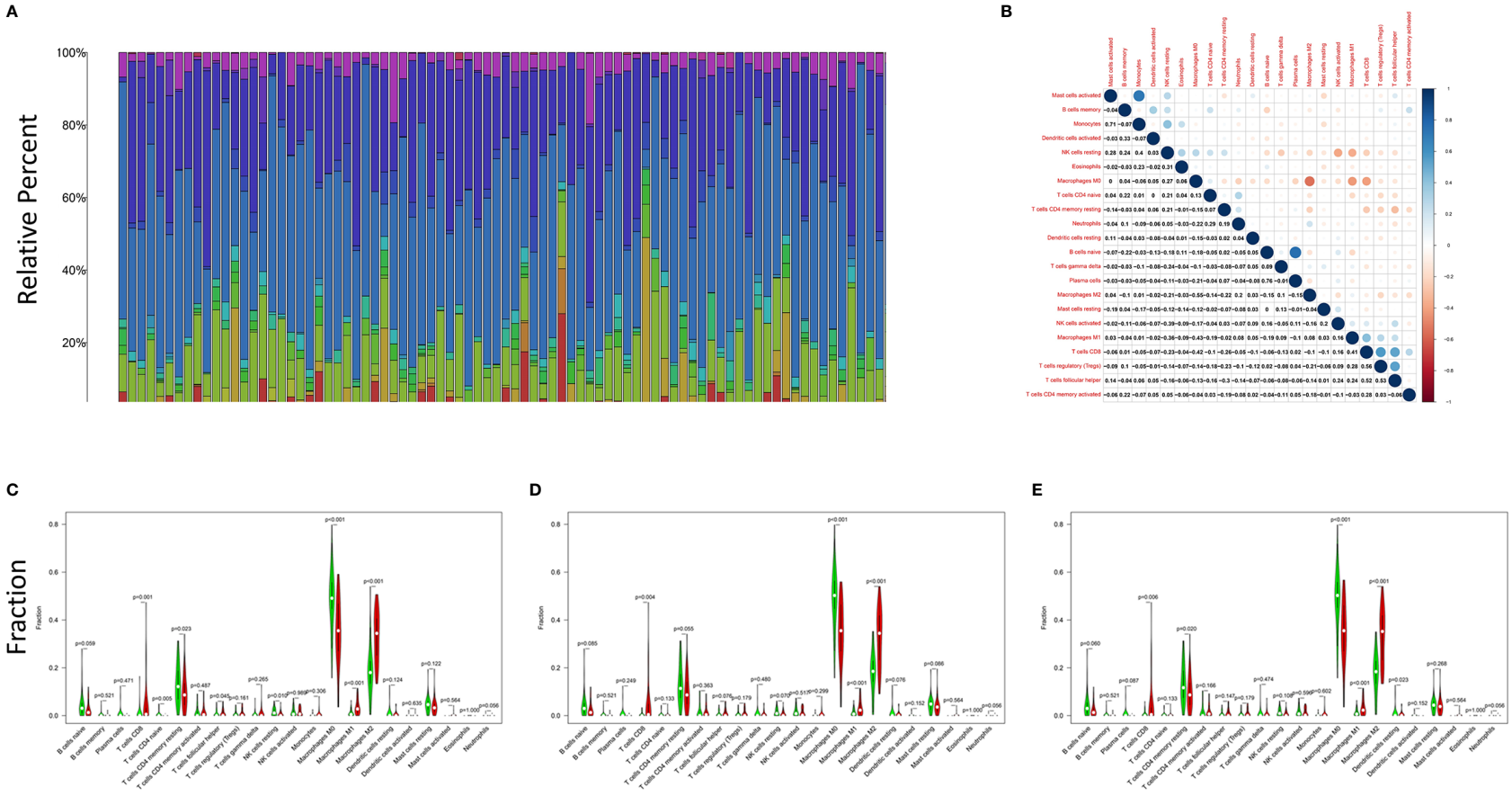

FIGURE 7 | TIC profiles of tumor samples from OS patients and correlation analyses. **(A)** The proportions of 22 types of TICs among the tumor samples from OS patients are shown in the bar chart. Sample IDs are used as the names of column. **(B)** The correlations among the 22 types of TICs in the different OS samples are indicated in the heatmap with the p values (number in each box) of the correlations between two cells shown. The corresponding correlation values (shade of each colored box) are displayed, and significance was evaluated using the Pearson correlation coefficient. **(C–E)** The differences in 22 kinds of TICs between the high and low C1qA, C1qB and C1qC expression groups are shown in the violin plot. The Wilcoxon rank-sum was applied to test significance. The TIC names are shown on the X-axis, and the contents are indicated on the Y-axis.

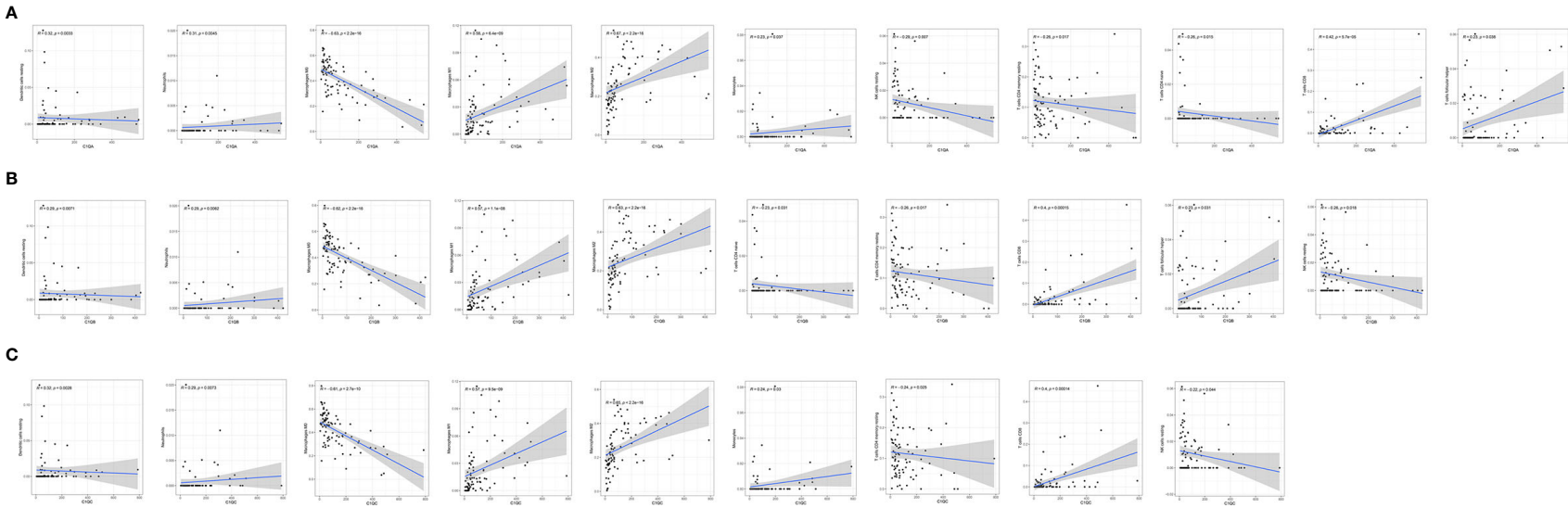

FIGURE 8 | Correlations between C1qA, C1qB, or C1qC expression levels and TIC proportions. **(A–C)** The scatter plots show the correlations between C1qA, C1qB or C1qC expression levels and TIC proportions ($p < 0.05$). The proportion tropism of the immune cells and C1qA, C1qB, and C1qC expression levels are indicated by a fitted linear model in each plot, as shown by the blue line. Significance was tested using the Pearson correlation coefficient.

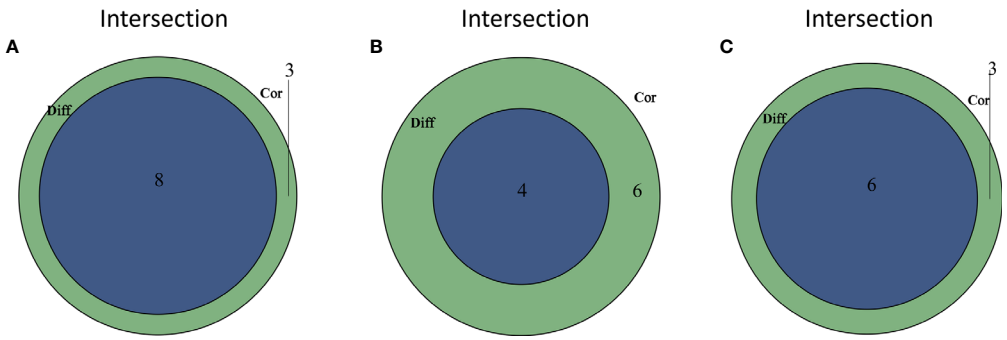

FIGURE 9 | TICs related to the expression of C1qA, C1qB or C1qC. **(A)** Venn diagram showing the 8 TICs related to C1qA expression. **(B)** Four TICs related to C1qB expression. **(C)** Six TICs related to C1qC expression. These TICs were determined jointly from the differences and correlation tests shown by the violin and scatter plots.

components are remarkably linked to invasion and metastasis in OS patients. The importance of uncovering the interaction between immune and tumor cells in OS is emphasized by these results. Studies have also confirmed that TICs are tightly associated with the progression and prognosis of OS (18). These associations provide a new theoretical basis for the development of more effective immunotherapy programs. Immunotherapy is a potentially valuable therapeutic strategy to treat human malignancies. In recent years, OS immunotherapy has made great progress (19). First, obvious clinical effects have been achieved with cytokines, including interleukin-2 (IL-2) and interferon (IFN), used for sarcoma immunotherapy. However, high-dose IL-2 treatment is likely to cause a series of adverse reactions, so its use is limited to some extent (20). Subsequently, immunotherapies such as vaccines, adoptive cell transfers and immunoassay blockers have been applied in clinical research, and certain research results have been achieved (21, 22). However, in recent years, there have been no major breakthroughs that improve the clinical therapeutic effect on OS. Therefore, actively exploring potential therapeutic targets involved in TME remodeling is of great significance to provide candidate regimens for OS immunotherapy.

First, we studied the correlations between TME immune and matrix components and the survival rate of OS patients. The results showed that the levels of immune cells and stromal cells were significantly linked to the overall survival rate of OS patients. High-score and low-score samples were compared and analyzed, and 155 DEGs were identified for determination of exact gene profile changes in TME immune and matrix components. Most of these genes were upregulated in the TME, and these DEGs might be important factors in the change in the TME state. Subsequently, these DEGs were found to generally map to immune-related terms or disease maps through GO and KEGG enrichment analyses. These studies indicate that immune factors are a major feature of the OS tumor microenvironment. To further uncover the underlying endogenous mechanism, the construction of a PPI network and univariate Cox regression analysis based on OS patient survival were carried out, and key genes that affect patient survival were identified. The relationships between the differential expression of key genes and OS patient survival were also analyzed, and the results indicated that C1qA, C1qB, and C1qC differential expression were positively linked to the overall survival of OS patients. The five-year survival rate of the high expression subgroup in each of these three groups was above 75%, which was markedly higher than that of the low expression subgroup. Bandini (23) also confirmed that C1qA, C1qB and C1qC expression levels were positively linked to a good prognosis in breast cancer patients using *in vivo* investigation of C1q-deficient mice.

The complement system is an important arsenal of the innate immune system against pathogens as well as cancer. The complement system is initiated in response to the tumor-associated antigens and leads to increased deposition of complement activation fragments on the surface of the tumor (24).The first recognition subcomponent C1q, belonging to the C1q/Tumor Necrosis Factor superfamily, is important in the classical pathway of the complement system. In a complement-dependent or complement-independent manner, C1q can perform various immune and nonimmune functions. Additionally, recognition of various ligands and pathogens for clearance *via* effector mechanisms such as opsonization and the inflammatory response can be performed by C1q through modulation of innate immunity (25). C1q is highly expressed in various human tumor microenvironments (26). For example, in prostate cancer cells, C1q induces apoptosis by activating the tumor inhibitor WOX1 (27). C1q has been shown to have protective effects that limit the progression of cancer in BALB-neuT mice with breast cancer (28). However, in malignant pleural mesothelioma, C1q promotes tumor cell proliferation and migration and aggravates tumor development (29). In addition, C1q can activate the classical complement pathway to aggravate disease progression in the later stage of inflammatory disease, but it plays a protective role in the early stage of inflammatory disease development (30). Therefore, C1q may play dual survival-promoting and apoptosis-inducing regulatory roles in tumors. The potential mechanism of this dual characteristic of C1q may be determined by various factors, such as the type of tumor cells, the expression of immune genes,

the nature of infiltrating immune cells, the degree of infiltration and the ability of infiltrating immune cells to synthesize C1q (and/or other complement components) locally. To clarify the roles of C1q in the occurrence and development of OS, the relationships between C1qA, C1qB, or C1qC expression levels and clinicopathological features (including age, histologic response, percent necrosis at definitive surgery, primary site progression, and primary tumor site) in OS patients was analyzed. The results demonstrated that the C1qA, C1qB and C1qC gene expression levels were higher in the OS patients with a percent necrosis at definitive surgery less than 50%. No significant correlations were found between the other clinical features and the expression of C1qA, C1qB or C1qC. Therefore, C1qA, C1qB and C1qC differential expression is closely related to the degree of tumor necrosis, plays a role in inhibiting tumor development to a certain extent. Some studies have found that human bone osteosarcoma epithelial cells (U2-OS) can activate the complement system by pooled normal human serum (31). This study presents a direct linkage of the complement system and angiogenesis in an *in vitro* cancer cell model, which could be useful in elucidating the relationship between the complement system and tumors necrosis and the underlying mechanisms.

To date, three "canonical" pathways of complement activation including the classical, alternative and lectin pathways have been identified. There is growing evidence that complement pathways can be activated in a variety of ways, depending on the triggering factors and the unique microenvironment or pathophysiological environment (32). Of course, complement may also play a tumor-promoting function that is unrelated to the activation of the canonical pathways. Based on previous GO and KEGG enrichment analysis results, we already knew that the overall function of DEGs seemed to map to immune-related activities, indicating that immune factors are a major feature of the TME. However, the immunomodulatory mechanism and actions of C1qA, C1qB and C1qC in osteosarcoma are not clear.

C1q receptors are expressed in a wide range of cells, including those that do not participate in the immune response. Nevertheless, the interaction of C1q with its receptor triggers various cellular responses, and these responses are suspected to involve certain signaling pathways (33). Therefore, we tried to further study the use of C1qA, C1qB, and C1qC through GSEA and evaluation of the correlations between immune regulation and differential expression. The results showed that the high C1qA, C1qB, and C1qC expression groups were all remarkably enriched in signaling pathways related to active immune functions, such as allograft rejection, the complement response, and the inflammatory response. However, with decreased differential expression of the C1qA, C1qB, and C1qC genes, the signaling pathway enrichment was significantly reduced. Obviously, the roles of the complement molecules C1qA, C1qB, and C1qC in inhibiting OS development are still related to antibody-mediated immunotherapy, which provides certain help for defining new treatment options.

Macrophages are reported to be the key effectors in the process of complement activation. Macrophages, the initial line of defense in the immune system, are specifically designed to initiate proper immune responses by responding to infectious microorganisms and normal or altered self-antigens. The CIBERSORT algorithm was applied to analyze the proportions of tumor-infiltrating immune types, and the construction of 22 immune cell profiles for OS samples was carried out. The results showed that the high expression groups for the three C1q chains (C1qA, C1qB, and C1qC) differed significantly from the corresponding low expression groups. In addition, M1 macrophages, M2 macrophages and T cells were positively correlated with the differential expression of the three C1q chains (C1qA, C1qB, and C1qC). M0 macrophages were negatively associated with the expression of the three C1q chains (C1qA, C1qB, and C1qC). These results suggest that the differential expression of the three C1q chains (C1qA, C1qB, and C1qC) is related to the levels of polarized M1 macrophages, polarized M2 macrophages and CD8+ T cells in the TME and is also a key indicator for improving the prognosis of OS. The polarization of macrophages is directed by the complement component C1q, and proresolution macrophages are generated, which can promote the clearance of apoptotic cells, diminish the production of proinflammatory cytokines, and increase anti-inflammatory cytokine production (34). Additionally, in response to tissue injury, macrophage-synthesized C1q may be an important effector driving the resolution of inflammation independent of other complement components. Numerous potentially beneficial interactions between C1q and phagocytes were identified *in vitro* in previous studies, including promotion of cellular and molecular debris phagocytosis and anti-inflammatory macrophage polarization. The prevention of autoimmunity may also be supported by these interactions (35). In addition, some studies have confirmed that C1q can regulate the mitochondrial metabolism of CD8+ T cells to inhibit responses to autoantigens, and there is a close relationship between C1q and CD8+ T cells (36). Moreover, CD8+ T cells can initiate autoimmunity and play a positive role in the prognosis of OS. The activation status (M1/M2) of macrophages may cause dual effects on tissue damage in neuroinflammatory diseases. M1 macrophages are reported to damage neurons, while M2 macrophages can regenerate and repair neurons (37). This conclusion contradicts our research. Therefore, the mechanism underlying the role of phagocytes in OS needs to be further confirmed by basic research.

In summary, we found for the first time through bioinformatics that the differential expression of the three C1q chains (C1qA, C1qB, and C1qC) is closely related to the survival prognosis, pathological features and TME of OS, which can provide some help for improving OS immunotherapy and clinical prognosis. Since the relationship between the complement system and tumors remains unclear, a complete theoretical framework has not emerged. Further research is needed to uncover the regulatory mechanism and develop new immunotherapeutic strategies.

DATA AVAILABILITY STATEMENT

The datasets presented in this study can be found in online repositories. The names of the repository/repositories and accession number(s) can be found below: https://portal.gdc.cancer.gov,

The Cancer Genome Atlas and https://ocg.cancer.gov/programs/target, TARGET database.

ETHICS STATEMENT

Written informed consent was obtained from the individual(s), and minor(s)' legal guardian/next of kin, for the publication of any potentially identifiable images or data included in this article.

AUTHOR CONTRIBUTIONS

L-hC, J-FL, and YL came up with the design and conception. The data analysis and visualization were conducted by L-hC, X-yH, and C-Z. The original writing of the draft and its editing were by L-hC and H-hZ. All authors contributed to the article and approved the submitted version.

SUPPLEMENTARY MATERIAL

The Supplementary Material for this article can be found online at: https://www.frontiersin.org/articles/10.3389/fonc.2021.642144/full#supplementary-material

Supplementary Figure 1 | Relationships between CD163 expression and survival time in patients with OS.

Supplementary Table 1 | TICs co-determined by difference test and correlation test.

REFERENCES

1. Kager L, Tamamyan G, Bielack S. Novel Insights and Therapeutic Interventions for Pediatric Osteosarcoma. *Future Oncol* (2017) 13(4):357–68. doi: 10.2217/fon-2016-0261
2. Biazzo A, De Paolis M. Multidisciplinary Approach to Osteosarcoma. *Acta Orthop Belg* (2016) 82(4):690–8.
3. Isakoff MS, Bielack SS, Meltzer P, Gorlick R. Osteosarcoma: Current Treatment and a Collaborative Pathway to Success. *J Clin Oncol* (2015) 33 (27):3029–35. doi: 10.1200/JCO.2014.59.4895
4. Kansara M, Teng MW, Smyth MJ, Thomas DM. Translational Biology of Osteosarcoma. *Nat Rev Cancer* (2014) 14:722–35. doi: 10.1038/nrc3838
5. Khanna C, Fan TM, Gorlick R, Helman LJ, Kleinerman ES, Adamson PC, et al. Toward a Drug Development Path That Targets Metastatic Progression in Osteosarcoma. *Clin Cancer Res* (2014) 20(16):4200–9. doi: 10.1158/1078-0432.CCR-13-2574
6. Arneth B. Tumor Microenvironment. *Med (Kaunas)* (2019) 56(1):15. doi: 10.3390/medicina56010015
7. Bi KW, Wei XG, Qin XX, Li B. Btk Has Potential to Be a Prognostic Factor for Lung Adenocarcinoma and an Indicator for Tumor Microenvironment Remodeling: A Study Based on TCGA Data Mining. *Front Oncol* (2020) 10:424. doi: 10.3389/fonc.2020.00424
8. Kidd S, Spaeth E, Watson K, Burks J, Lu H, Klopp A, et al. Origins of the Tumor Microenvironment: Quantitative Assessment of Adipose-Derived and Bone Marrow-Derived Stroma. *PloS One* (2012) 7(2):e30563. doi: 10.1371/journal.pone.0030563
9. Bussard KM, Mutkus L, Stumpf K, Gomez-Manzano C, Marini FC. Tumor-Associated Stromal Cells as Key Contributors to the Tumor Microenvironment. *Breast Cancer Res* (2016) 18(1):84. doi: 10.1186/s13058-016-0740-2
10. Deng C, Xu Y, Fu J, Zhu X, Chen H, Xu H, et al. Reprograming the Tumor Immunologic Microenvironment Using Neoadjuvant Chemotherapy in Osteosarcoma. *Cancer Sci* (2020) 111(6):1899–909. doi: 10.1111/cas.14398
11. Heymann MF, Lézot F, Heymann D. The Contribution of Immune Infiltrates and the Local Microenvironment in the Pathogenesis of Osteosarcoma. *Cell Immunol* (2019) 343:103711. doi: 10.1016/j.cellimm.2017.10.011
12. Zhang C, Zheng JH, Lin ZH, Lv HY, Ye ZM, Chen YP, et al. Profiles of Immune Cell Infiltration and Immune-Related Genes in the Tumor Microenvironment of Osteosarcoma. *Aging (Albany NY)* (2020) 12(4):3486–501. doi: 10.18632/aging.102824
13. Kishore U, Reid KB. C1q: Structure, Function, and Receptors. *Immunopharmacology* (2000) 49(1–2):159–70. doi: 10.1016/s0162-3109(00)80301-x
14. Bulla R, Tripodo C, Rami D, Ling GS, Agostinis C, Guarnotta C, et al. C1q Acts in the Tumour Microenvironment as a Cancer-Promoting Factor Independently of Complement Activation. *Nat Commun* (2016) 7:10346. doi: 10.1038/ncomms10346
15. Mangogna A, Belmonte B, Agostinis C, Zacchi P, Iacopino DG, Martorana A, et al. Prognostic Implications of the Complement Protein C1q in Gliomas. *Front Immunol* (2019) 10:2366. doi: 10.3389/fimmu.2019.02366
16. R Core Team. *R:a Language and Environment for Statistical Computing*. Vienna: R Foundation for Statistical Computing (2018). Available at: https://www.R-project.org/.
17. Wang W, Ren S, Wang Z, Zhang C, Huang J. Increased Expression of TTC21A in Lung Adenocarcinoma Infers Favorable Prognosis and High Immune Infiltrating Level. *Int Immunopharmacol* (2020) 78:106077. doi: 10.1016/j.intimp.2019.106077
18. Li X, Chen Y, Liu X, Zhang J, He X, Teng G, et al. Tim3/Gal9 Interactions Between T Cells and Monocytes Result in an Immunosuppressive Feedback Loop That Inhibits Th1 Responses in Osteosarcoma Patients. *Int Immunopharmacol* (2017) 44:153–59. doi: 10.1016/j.intimp.2017.01.006
19. Uehara T, Fujiwara T, Takeda K, Kunisada T, Ozaki T, Udono H. Immunotherapy for Bone and Soft Tissue Sarcomas. *BioMed Res Int* (2015) 2015:820813. doi: 10.1155/2015/820813
20. Schwinger W, Klass V, Benesch M, Lackner H, Dornbusch HJ, Sovinz P, et al. Feasibility of High-Dose Interleukin-2 in Heavily Pretreated Pediatric Cancer Patients. *Ann Oncol* (2005) 16(7):1199–206. doi: 10.1093/annonc/mdi226
21. Vergati M, Intrivici C, Huen NY, Schlom J, Tsang KY. Strategies for Cancer Vaccine Development. *J BioMed Biotechnol* (2010) 2010:596432. doi: 10.1155/2010/596432
22. Robbins PF, Morgan RA, Feldman SA, Yang JC, Sherry RM, Dudley ME, et al. Tumor Regression in Patients With Metastatic Synovial Cell Sarcoma and Melanoma Using Genetically Engineered Lymphocytes Reactive With NY-ESO-1. *J Clin Oncol* (2011) 29(7):917–24. doi: 10.1200/JCO.2010.32.2537
23. Bandini S, Macagno M, Hysi A, Lanzardo S, Conti L, Bello A, et al. The non-Inflammatory Role of C1q During Her2/neu-driven Mammary Carcinogenesis. *Oncoimmunology* (2016) 5(12):e1253653. doi: 10.1080/2162402X.2016.1253653
24. Mangogna A, Varghese PM, Agostinis C, Alrokayan SH, Khan HA, Stover CM, et al. Prognostic Value of Complement Properdin in Cancer. *Front Immunol* (2021) 11:614980. doi: 10.3389/fimmu.2020.614980
25. Mangogna A, Agostinis C, Bonazza D, Belmonte B, Zacchi P, Zito G, et al. Is the Complement Protein C1q a Pro- or Anti-tumorigenic Factor? Bioinformatics Analysis Involving Human Carcinomas. *Front Immunol* (2019) 10:865. doi: 10.3389/fimmu.2019.00865
26. Bulla R, Tripodo C, Rami D, Ling GS, Agostinis C, Guarnotta C, et al. C1q Acts in the Tumour Microenvironment as a Cancer-Promoting Factor Independently of Complement Activation. *Nat Commun* (2016) 7:10346. doi: 10.1038/ncomms10346
27. Hong Q, Sze CI, Lin SR, Lee MH, He RY, Schultz L, et al. Complement C1q Activates Tumor Suppressor WWOX to Induce Apoptosis in Prostate Cancer Cells. *PloS One* (2009) 4(6):e5755. doi: 10.1371/journal.pone.0005755
28. Bandini S, Macagno M, Hysi A, Lanzardo S, Conti L, Bello A, et al. The non-Inflammatory Role of C1q During Her2/neu-driven Mammary Carcinogenesis. *Oncoimmunology* (2016) 5(12):e1253653. doi: 10.1080/2162402X.2016.1253653
29. Agostinis C, Vidergar R, Belmonte B, Mangogna A, Amadio L, Geri P, et al. Complement Protein C1q Binds to Hyaluronic Acid in the Malignant Pleural

Mesothelioma Microenvironment and Promotes Tumor Growth. *Front Immunol* (2017) 8:1559. doi: 10.3389/fimmu.2017.01559
30. Espericueta V, Manughian-Peter AO, Bally I, Thielens NM, Fraser DA. Recombinant C1q Variants Modulate Macrophage Responses But do Not Activate the Classical Complement Pathway. *Mol Immunol* (2020) 117:65–72. doi: 10.1016/j.molimm.2019.10.008
31. Jeon H, Han SR, Lee S, Park SJ, Kim JH, Yoo S-M, et al. Activation of the Complement System in an Osteosarcoma Cell Line Promotes Angiogenesis Through Enhanced Production of Growth Factors. *Sci Rep* (2018) 8(1):5415. doi: 10.1038/s41598-018-23851-z
32. Ricklin D, Lambris JD. Complement in Immune and Inflammatory Disorders: Pathophysiological Mechanisms. *J Immunol* (2013) 190(8):3831–8. doi: 10.4049/jimmunol.1203487
33. Ghebrehiwet B, Peerschke EI. The C1q-R Participates in Immunoregulation and Signal Transduction. *Behring Inst Mitt* (1993) 93):236–40.
34. Bohlson SS, O'Conner SD, Hulsebus HJ, Ho MM, Fraser DA. Complement, c1q, and c1q-related Molecules Regulate Macrophage Polarization. *Front Immunol* (2014) 5:402. doi: 10.3389/fimmu.2014.00402
35. Espericueta V, Manughian-Peter AO, Bally I, Thielens NM, Fraser DA. Recombinant C1q Variants Modulate Macrophage Responses But do Not Activate the Classical Complement Pathway. *Mol Immunol* (2020) 117:65–72. doi: 10.1016/j.molimm.2019.10.008
36. Ling GS, Crawford G, Buang N, Bartok I, Tian K, Thielens NM, et al. C1q Restrains Autoimmunity and Viral Infection by Regulating CD8+ T Cell Metabolism. *Science* (2018) 360(6388):558–63. doi: 10.1126/science.aao4555
37. Vogel DY, Heijnen PD, Breur M, de Vries HE, Tool AT, Amor S, et al. Macrophages Migrate in an Activation-Dependent Manner to Chemokines Involved in Neuroinflammation. *J Neuroinflammation* (2014) 11:23. doi: 10.1186/1742-2094-11-23

Conflict of Interest: The authors declare that the research was conducted in the absence of any commercial or financial relationships that could be construed as a potential conflict of interest.

frontiers in Immunology

ORIGINAL RESEARCH
published: 16 July 2021
doi: 10.3389/fimmu.2021.631450

LncRNATUG1 Facilitates Th2 Cell Differentiation by Targeting the miR-29c/B7-H3 Axis on Macrophages

Huiming Sun†, Ting Wang†, Weili Zhang†, Heting Dong, Wenjing Gu, Li Huang, Yongdong Yan, Canhong Zhu and Zhengrong Chen**

Department of Respiratory Medicine, Children's Hospital of Soochow University, Suzhou, China

OPEN ACCESS

Edited by:
Evan Alexander Scott, Northwestern University, United States

Reviewed by:
Tomohide Takaya, Shinshu University, Japan
Feng Wang, Affiliated Hospital of Nantong University, China

***Correspondence:**
Zhengrong Chen
chenzhengrong@suda.edu.cn
Canhong Zhu
Canhongzhu@sina.com

†These authors have contributed equally to this work and share first authorship

Specialty section:
This article was submitted to Molecular Innate Immunity, a section of the journal Frontiers in Immunology

Received: *20 November 2020*
Accepted: *28 June 2021*
Published: *16 July 2021*

Citation:
Sun H, Wang T, Zhang W, Dong H, Gu W, Huang L, Yan Y, Zhu C and Chen Z (2021) LncRNATUG1 Facilitates Th2 Cell Differentiation by Targeting the miR-29c/B7-H3 Axis on Macrophages. Front. Immunol. 12:631450. doi: 10.3389/fimmu.2021.631450

The role of long non-coding RNAs (lncRNA) in asthma remains unclear. In this study, we examined the role of long non-coding RNA taurine upregulated 1 (lncRNA TUG1) in asthma. We found that lncRNA TUG1 is one of the differentially expressed lncRNAs in the monocytes of asthmatic children and is associated with Th cell differentiation. LncRNA TUG1 and miR-29c are mainly distributed in the cytoplasm of macrophages. Our data suggested that lncRNA TUG1 increased in macrophages stimulated by House Dust Mite in a dose-dependent manner. Using loss- and gain of function strategy, we found that miR-29c might regulate Th2 cell differentiation by directly targeting co-stimulatory molecule B7-H3. Furthermore, down-regulation of lncRNA TUG1 decreased the level of GATA3 in CD4+T cells and was associated with miR-29c/B7-H3 axis. Moreover, the dual-luciferase reporter assay confirmed that lncRNA TUG1 serves as a competing endogenous RNA to sponge miR-29c. According to the rescue experiment, lncRNA TUG1 regulated Th2 cell differentiation *via* miR-29c. These data suggest that lncRNA TUG1 in macrophages regulates Th2 cell differentiation *via* miR-29c/B7-H3 axis.

Keywords: bronchial asthma, long non-coding RNA taurine upregulated 1, miRNA-29c, B7-H3, T helper cell, macrophages

INTRODUCTION

Asthma is the most prevalent chronic respiratory disease worldwide. More than 300 million cases have been registered to date (1). Asthma is also the most common chronic respiratory disease in children. Over recent years, the prevalence of asthma symptoms has significantly increased in children and adolescents, particularly in developing countries, causing a consistent burden on the public health system (2).

Asthma is characterized by bronchial hyper-reactivity, mucus overproduction, airway inflammation, airway remodeling, and airway narrowing (3). T helper (Th) cells play a vital role in asthma. Th2 major cytokine (IL-4) production has been associated with allergic asthma and Th17 cytokine (IL-17) to neutrophilic asthma (4). Although many studies have focused on Th2 immune responses, there are still significant gaps in regulating Th2/Th17 cell differentiation and cytokine

secretion. In our previous study, we found that costimulatory molecule B7-H3, which is regulated by miRNA-29c (miR-29c), is highly expressed on macrophages and plays an important role in Th2 cell differentiation (5). However, the mechanism of regulation of miR-29c in macrophages is still not fully understood.

The increasing evidence supports that long non-coding RNA (lncRNAs) has an important role in Th cell differentiation (6). Zhu et al. found that LncGAS5 derived from allergic rhinitis epithelium is the key mediator in Th1/Th2 differentiation (7). In addition, Chen and colleagues found that lnc-M2 could control the process of M2 macrophage differentiation *via* the PKA/CREB pathway (8). A recent study demonstrated that lncRNA TUG1 promotes proliferation and invasion and suppresses apoptosis in melanoma cells by sponging miR-29c-3p (9). However, the role of lncRNA TUG1 in macrophage-Th cell communication remains unclear.

In the present study, we investigated the effect of lncRNA on the miR-29c/B7-H3 axis in macrophages and the role of Th cell differentiation. We also detected the expression of lncRNA, miR-29c, and B7-H3 in children with asthma exacerbation. Our data demonstrated that lncRNA-TUG1 could regulate B7-H3 expression in macrophages by sponging miR-29c, which then controls Th2 differentiation.

MATERIALS AND METHODS

Patients

Patients diagnosed with asthma according to the guidelines of the Global Initiative for Asthma (10) were enrolled from the department of pulmonary medicine at the Children's Hospital of Soochow University. In addition, non-atopic healthy subjects were included as a control group. Peripheral blood samples from 3 patients with asthma exacerbation and 3 healthy children were used for lncRNA sequencing. In addition, 10 children with asthma exacerbation were recruited, and peripheral blood samples of acute or convalescent phase were collected for subsequent qPCR detection. All the subjects were instructed to avoid the use of asthma medication (such as glucocorticoids) prior to testing.

The present study was approved by the local Ethics Committee of the Children's Hospital of Soochow University. All participants provided written informed consent.

Isolation of Monocytes From Peripheral Blood

Peripheral blood mononuclear cells (PBMCs) were isolated from 2 ml of heparin-anticoagulated venous blood using Ficoll Histopaque (Sigma-Aldrich, St Louis, MO, USA) according to the manufacturer's protocol. The monocytes were isolated from PBMCs using a negative selection kit (Miltenyi Biotec, Bergisch Gladbach, Germany). The procedure was described in a previous study (11).

LncRNA Sequencing and Analysis

PBMC samples from asthmatic children and healthy controls were used for RNA sequencing to obtain lncRNA expression profiles. After total RNA was isolated, rRNAs were removed usingRibo-Zero rRNA Removal Kits (Illumina, San Diego, CA, USA) following the manufacturer's instructions. RNA libraries were constructed by using rRNA-depleted RNAs with Tru-Seq Stranded Total RNA Library Prep Kit (Illumina, San Diego, CA, USA) according to the manufacturer's instructions. Libraries were controlled for quality and quantified using the BioAnalyzer 2100 system (Agilent Technologies, Inc., USA). A total of 10pM libraries were denatured as single-stranded DNA molecules, captured on Illumina flow cells, amplified *in situ* as clusters, and finally sequenced for 150 cycles on Illumina Hi-Seq Sequencer according to the manufacturer's instructions. Paired-end reads were harvested from Illumina HiSeq Sequencer after quality filtering. After 3' adaptor-trimming by cutadapt software (v1.9), the high-quality trimmed reads were aligned to the reference genome (UCSC hg19) guided by the Ensembl GFF gene annotation file with TopHat2 software. Then, cuffdiff software (part of cufflinks) was used to get the gene-level FPKM as the expression profiles of lncRNAs; fold change and q-value were calculated based on FPKM. Finally, differentially expressed lncRNAs (fold change ≥ 2, $P < 0.05$) were identified. GO enrichment analyses were performed based on the differentially expressed lncRNAs.

Culture of House Dust Mite (HDM)-Stimulated Macrophages

THP-1 cells (ATCC, Manassas, VA, USA) were seeded at 1×10^5 cells/dish. Cells were incubated with phorbol myristate acetate (PMA, 50 ng/ml) for 6h. After that, THP-1 was cultured with medium without PMA for another 72h to induce THP-1 differentiation into macrophages. HDM extract (Dermatophagoides pteronyssinus; Stallergenes Greer, Lenoir, USA) with different concentrations (0.2 μg/ml or 2 μg/ml) was used to stimulate the macrophages for another 48h. Consequently, cells were collected to detect B7-H3 mRNA and protein levels by quantitative polymerase chain reaction (qPCR) and Western blot, respectively.

Lentivirus Constructs

The over-expression and knockdown lentiviral vectors for miR-29c and B7-H3 were constructed by NOVOBIO Company (Shanghai, China). Empty vectors were used as a control. Recombinant plasmids were named LV210_pl-miR-29c (pLenti-miR-29c), LV289_pL6.3-GFP-TuDS-hsa-miR-29c (anti-miR-29c), VL1112-PDS159-B7H3 (pLenti-B7-H3), and VL1113-6_PDS019-B7H3-SH6 (anti-B7-H3). Lentiviral particles were produced in HEK293T cells as previously described (12). Briefly, lentiviral vectors encoding miR-29c or B7-H3 and packaging mix were co-infected into HEK293T cells. Then, the supernatant of HEK293Tcells were collected 48 hours after lentiviral vector transfection, and the concentration of the harvested virus was calculated by fluorescence ratio using flow cytometry.

Macrophages Transfection and Th Cells Co-culture

100 nM pLenti-miR-29c or anti-miR-29c with or without pLenti-B7-H3 or anti-B7-H3 was transfected into THP-1 (2×10^5/ml) for 48h. Then THP-1 cells (1×10^5/ml) were seeded in a six-well

plate, and cultured with RPMI 1640 medium (Life Technologies, Carlsbad, CA, USA) primed with 50 ng/ml PMA (Sigma, Louis, MO, USA) for 48h to induce macrophage differentiation. Meanwhile, naive CD4+ T cells (1×10^6) were isolated from peripheral blood of healthy persons (donate fromRed Cross, Suzhou, China), and then collected and cultured for another 24h. Then, the $CD4^+$ T cells were collected for further analysis.

RNA-Fluorescence *In Situ* Hybridization (FISH)

Cells were incubated with 0.2 mol/L HCl for 0.5 h after being fixed with 4% formaldehyde for 20 min and then incubated with 5 μg/mL proteinase K for 15 min. Acetylation was performed with a specific solution including miR-29c-3p probe2μl, lncRNA-TUG1 probe 5μl, Buffer E 70μl, and DEPC 23μl, hybridized with FITC labeled lncRNA TUG1 probe (5μg/mL) for 24 h. Subsequently, cells were washed twice with 2 × SSC detergent containing 0.01% Tween-20 at 55°C.

Dual-Luciferase Reporter Assay

The lncRNA TUG1 fragment containing miR-29c binding sites was synthesized to generate wild-type (lncRNA TUG1-WT) or mutant type (lncRNA TUG1-Mut). The lncRNA TUG1-WT and lncRNA TUG1-Mut fragments were subcloned into the firefly luciferase gene pGL3-Luciferase reporter vectors (Promega, USA) to generated pGL3-LncRNATUG1-WT and pGL3-LncRNA TUG1-MUT vectors, respectively. After that, the above vectors were co-transfected with miR-29c mimic or negative control into HEK293T cells for 24 h. Finally, firefly and renilla luciferase activities were sequentially measured using dual-luciferase assays (Promega) 24 h after the transfection and evaluated by the Bio Tek™ Microplate Reader.

Small Interfering lncRNA TUG1 Transfection

Three siRNAs targeting TUG1 were conducted and are presented in **Table S1**. In brief, siRNA oligo (GenePharma, Suzhou, China) were added into six-well plates with PMA-induced macrophages (2×105/well) and then treated by using GP-Transfect-Mate (GenePharma, Suzhou, China) according to the operation manual. After 24 or 48 h, macrophages were collected for further experiments. Then, qPCR analysis was applied to detect lncRNA TUG1 expression and to validate the transfected efficiencies. According to the interfering efficiencies, lncRNA TUG1 shRNA-1 was selected for the next experiment. In brief, lncRNA TUG1 shRNA-1 with or without miR-29c inhibitor (GenePharm, Suzhou, China) were added into macrophages for 6h and co-cultured with naive $CD4^+$ T cells described above for another 24 h. After that, the supernatant in the lower chamber and $CD4^+$ T cells in the upper chamber was collected.

RNA Extraction and Quantitative Polymerase Chain Reaction (qPCR)

Total RNA was extracted from experiment cells such as PBMCs, macrophages, and $CD4^+$ T cells using Trizol Reagent (Invitrogen, Carlsbad, USA) according to the manufacture's protocol. RNA was revere-transcribed into cDNA using PrimeScript TM RT reagent kit (Takara, Japan). Revere transcript qPCR Master Mix was purchased from (Takara, Japan). The primer sequences are shown in **Table S2**.

ELISA

The supernatants from cell cultures were collected, and all samples were preserved at −80°C for subsequent assay of soluble B7-H3 (sB7-H3) by ELISA as previously described (13). Meanwhile, IFN-γ, IL-4, and IL-17 were also detected by ELISA (R&D Systems, USA).

Statistical Analysis

All data were expressed using mean ± standard deviation (± SD). SPSS 21.0 software (SPSS Inc., IL, USA) was used to conduct statistical analysis. Student's t-test was used to analyze the differential expression of lncRNA TUG1, miR-29c, and B7-H3 mRNA between asthmatic children and controls. The comparisons among multiple groups were performed with a one-way analysis of variance followed by Dunnett's test. P-value of <0.05 was considered to have statistical significance.

RESULTS

Expression and Function Analysis of lncRNA TUG1 in Monocytes

A total of 23,709 lncRNAs were detected in the PBMCs collected from asthma and control patients. Compared to the control group, 163 lncRNAs were significantly up-regulated, and 226 lncRNAs were significantly down-regulated in patients with asthma (**Figures 1A, B**). Meanwhile, the mRNAs were also detected using RNA-seq (see the supplementary data).

Based on Gene Ontology (GO) analysis, the target mRNAs of this differentiated expressed lncRNA are involved in the T cell activation and T cell differentiation. According to the KEGG pathway analysis, the T cell receptor signaling pathway is one of the major pathways affecting T cell differentiation (**Figure 1C**).

The top 10 up-regulated and down-regulated lncRNAs are shown in **Figure 1D**. LncRNATUG1 was more than 5 fold higher in patients with asthma compared to the controls. The previous studies have demonstrated that lncRNATUG1 has an important role in promoting the development of pancreatic cancer and bladder cancer by sponging miR-29c (14, 15). However, no study has reported on the function of lncRNA TUG1 in macrophages and T cell differentiation. We examined the cellular location of lncRNA TUG1 and miR-29c in monocytes by RNA FISH analysis and found that both of them were mainly distributed in the cytoplasm of macrophages (**Figure 1E**), which suggested a potential role of the lncRNA TUG1/miR-29c axis in regulating the activation of the human macrophages.

LncRNA TUG1 Was Induced in the HDM-Stimulated Macrophages

As shown in **Figure 2A**, LncRNA TUG1 was increased in the macrophages stimulated by HDM in a dose-dependent manner. Meanwhile, the level of miR-29c significantly decreased even at

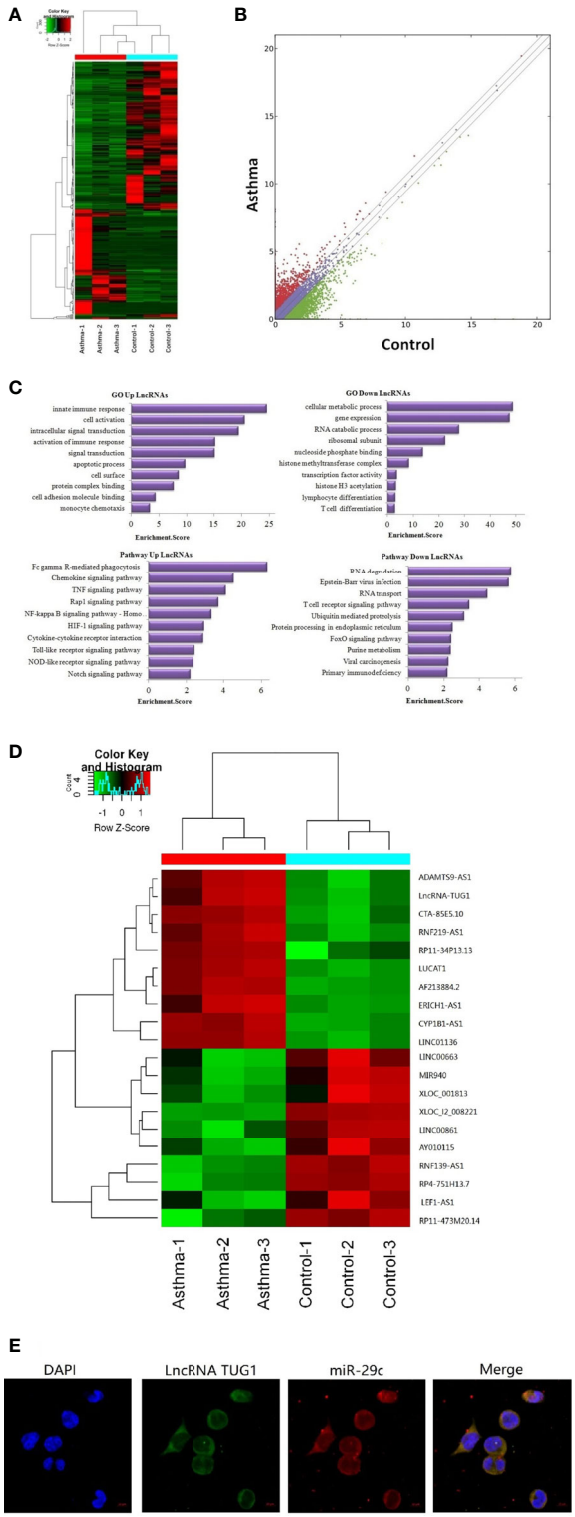

FIGURE 1 | Sequencing of lncRNAs in monocytes and co-location with miR-29c in macrophages. **(A)** The heat map depicts the hierarchical clustering of altered lncRNAs in monocytes between children with asthma exacerbation (n = 3) and the healthy control group (n = 3). **(B)** The scatter plot reveals that a significant difference existed in the distribution of lncRNAs between asthma exacerbation and the healthy control group. **(C)** GO and KEGG signaling pathways for lncRNAs that are differentially downregulated and target mRNAs. **(D)** The heat map depicts the hierarchical clustering of the top 10 up-regulated and down-regulated lncRNAs. **(E)** LncRNA TUG1 and miR-29c mainly distributed in the cytoplasm of macrophages using the FISH analysis from three independent experiments.

the low dose of HDM stimulation (**Figure 2B**). As for B7-H3, HDM could induce B7-H3 expression at mRNA and protein levels in a dose-dependent manner ($P < 0.05$) (**Figures 2C, D**). Taken together, our results suggest a negative correlation between lncRNA TUG1 and miR-29c, a previously described suppressor of B7-H3, during asthma progression.

Macrophages Regulate Th2 Cell Differentiation *via* miR-29c/B7-H3 Pathway

To confirm the possibility that miR-29c-mediated suppression of B7-H3 on macrophages leads to Th cell polarization, macrophages were co-cultured with naive $CD4^+$ T cells since the membrane B7-H3 and soluble B7-H3 have a different function on T cell activation and proliferation (16). Using loss- and gain-of-function strategy, pLenti-miR-29c or anti-miR-29c was transfected into macrophages. Then, pLenti-B7-H3 or anti-B7-H3 was added into the culture to evaluate the function of the miR-29c/B7-H3 axis in regulating Th cell differentiation. As shown in **Figure 3**, over-expression of miR-29c could decrease the level of GATA3 and RORγ-t and increase the T-bet in $CD4^+$T cells ($P < 0.05$). Meanwhile, down-regulation of miR-29c could increase GATA3 and RORγ-t and decrease the T-bet in $CD4^+$T cells ($P < 0.05$). The expression of GATA3, T-bet, and RORγ-t could be rescued by pLenti-B7-H3 or anti-B7-H3 ($P < 0.05$) (**Figure 3**). Meanwhile, the cytokines of IFN-γ, IL-4, and IL-17 were detected by ELISA. We found that over-expression of miR-29c could decrease IL-4 and IL-17 while down-regulation of miR-29c has the opposite effect (**Figure 3**). Taken together, these results suggested that miR-29c regulates Th2 cell differentiation by targeting co-stimulatory molecule B7-H3 in macrophages.

Knockdown of lncRNATUG1 Decreases the Level of GATA3 in $CD4^+$T Cells

To study the function of lncRNA TUG1 in the regulation of Th cell differentiation, we constructed 3 siRNAs of lncRNA TUG1. Compared to other siRNAs, siRNA-1 showed a better interfering effect at 24h and 48h ($P < 0.05$) (**Figure 4A**). To determine whether lncRNA TUG1 regulates Th cell differentiation through the miR-29c/B7-H3 axis, lncRNA TUG1-siRNA-1 was transfected into the macrophages and co-cultured with naive $CD4^+$ T cells. As shown in **Figure 4**, lncRNATUG1-siRNA-1 increased the expression of miR-29c and decreased the expression of B7-H3 mRNA and protein ($P < 0.05$) (**Figures 4B, C**). Simultaneously, the expression of GATA3 and RORγ-t in $CD4^+$ T cells decreased ($P < 0.05$) after lncRNATUG1-siRNA-1 transfection (**Figure 4D**). These results show that lncRNA TUG1 positively regulates Th cell differentiation by potentially targeting miR-29c/B7-H3 axis.

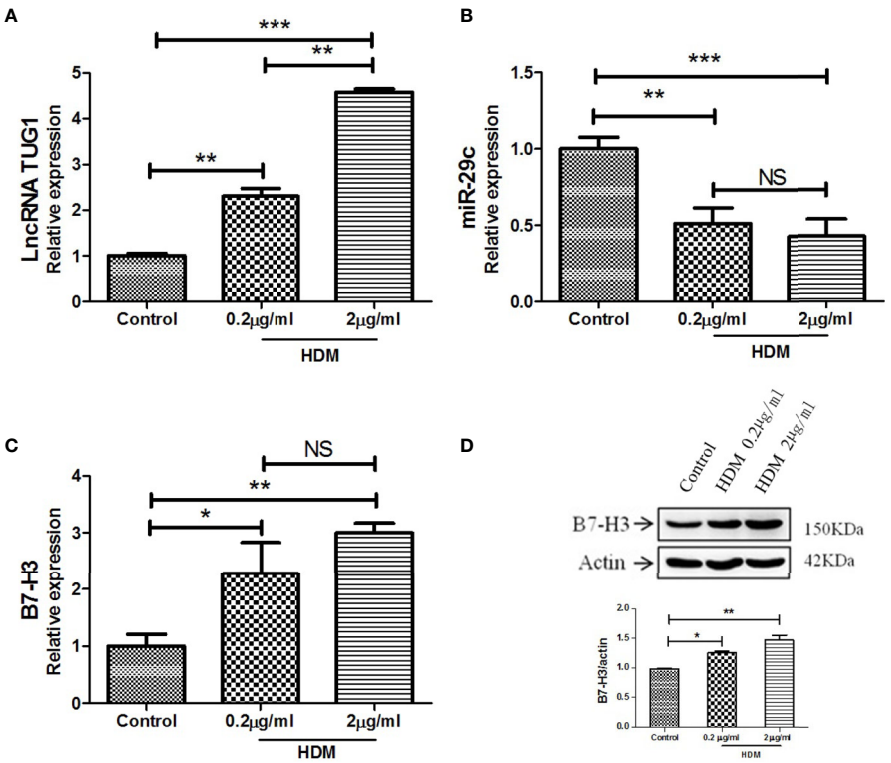

FIGURE 2 | LncRNA TUG1 induced by HDM in macrophages in a dose-dependent manner. **(A)** LncRNA TUG1 was increased in macrophages stimulated by HDM in a dose-dependent manner. **(B)** The level of miR-29c significantly decreased, but it was not dose-dependent. **(C, D)** HDM also could both induce B7-H3 expression at mRNA and protein levels in a dose-dependent manner. Data are shown as Mean ± SD and represent three independent experiments. *$p < 0.05$, **$p < 0.01$ and ***$p < 0.001$. NS, no significance.

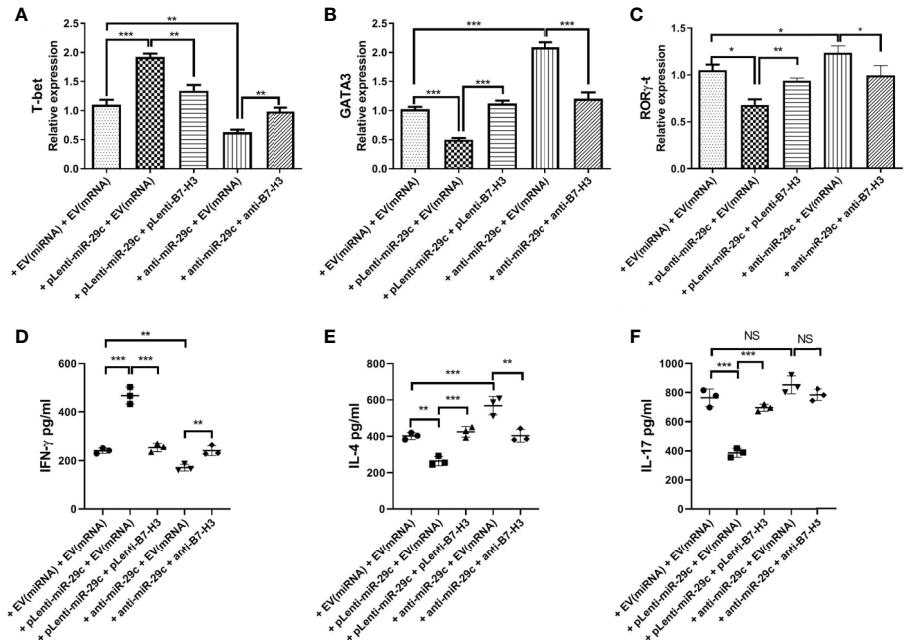

FIGURE 3 | Macrophages regulated Th2 cell differentiation *via* miR-29c/B7-H3 pathway. Using loss and gain of function strategy, 100 nMpLenti-miR-29c or anti-miR-29c was transfected into macrophages for 48h, and then pLenti-B7-H3 or anti-B7-H3 was added into the culture in the lower chambers of transwell for 24h. After that, RNA was extracted, and transcription factors were detected by qPCR and IFN-γ, IL-4 and IL-17 were detected by ELISA. **(A)** Relative expression of T-bet. **(B)** Relative expression of GATA3. **(C)** Relative expression of RORγ-t. **(D)** Levels of IFN-γ. **(E)** Levels of IL-4. **(F)** Levels of IL-17. Data shown as Mean ± SD and represent three independent experiments. *p < 0.05, **p < 0.01 and ***p < 0.001. NS, no significance.

LncRNA TUG1 Serves as a ceRNA to Sponge miR-29c

To investigate the interaction between lncRNA TUG1 and miR-29c, the starBase online website was employed to search the binding sites, and the binding sites are shown in **Figure 5A**. To further validate the interaction of lncRNA TUG1 and miR-29c, lncRNA TUG1-WT reporter containing predicted binding sites of miR-29c and lncRNA TUG1-Mut reporter with mutant binding sites of miR-29c were constructed. As shown in **Figure 5**, the luciferase activities were reduced after co-

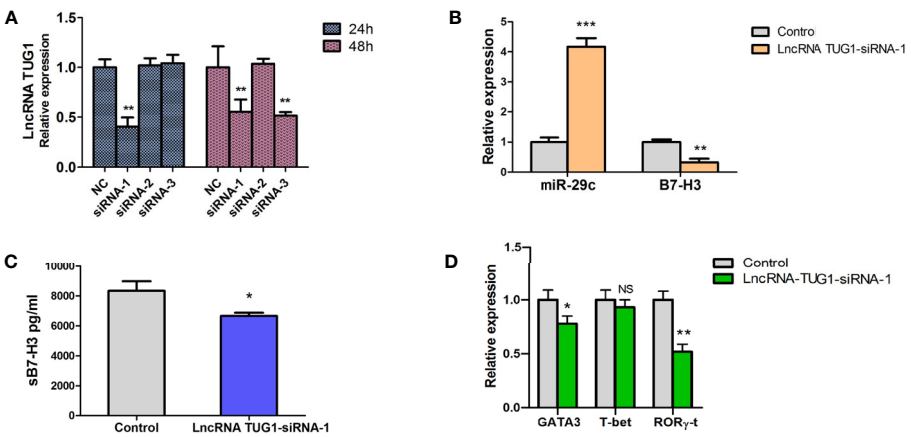

FIGURE 4 | Down-regulation of LncRNA TUG1 decreased the level of GATA3 in CD4+T cells and was associated with miR-29c/B7-H3 axis. **(A)** We constructed 3 siRNAs of LncRNA TUG1. Three siRNAs were added into macrophages and detected LncRNA TUG1 at 24h and 48h. **(B)** TUG1-siRNA-1 was added into co-culture of macrophages and naive CD4+ T cells, and miR-29c and B7-H3 in macrophages were detected by qPCR. **(C)** The supernatant was collected to detect sB7-H3 using ELISA. **(D)** CD4+T cells after co-culturing were collected, and the levels of GATA3 and RORγ-t in CD4+ T cells were detected by qPCR. Data were shown as Mean ± SD and represent three independent experiments. *p < 0.05, **p < 0.01 and ***p < 0.001. NS, no significance.

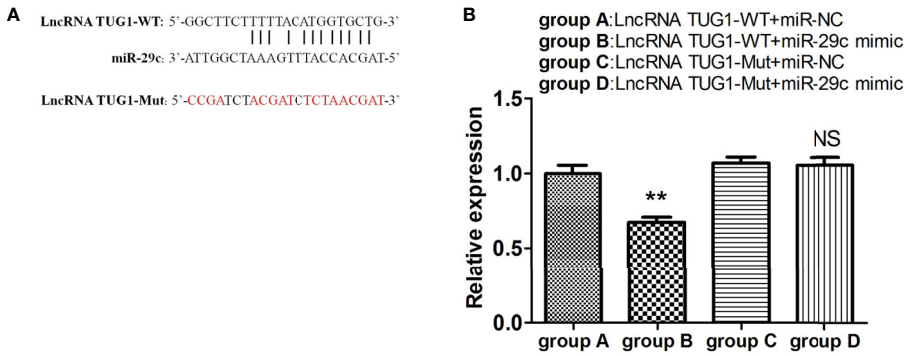

FIGURE 5 | LncRNA TUG1 serves as a ceRNA to sponge miR-29c. **(A)** The putative binding sites between LncRNA TUG1-WT and miR-29c. The sequence of LncRNA TUG1-Mut was also shown. **(B)** The LncRNA TUG1-WT and LncRNA TUG1-Mut fragments were subcloned into the Renilla luciferase gene pGL3-Luciferase reporter vectors (Promega, USA) to generated pGL3-LncRNATUG1-WT and pGL3-LncRNA TUG1-MUT vectors, respectively. After that, the above vectors were co-transfected with miR-29c mimic or negative control into 293T cells for 24 h, and then the luciferase activities were detected. Data are shown as Mean ± SD and represent three independent experiments. **p < 0.01. NS, no significance.

transfection of lncRNA TUG1-WT and miR-29c mimics into HEK293T cells (P < 0.01). However, no difference in luciferase activity was found between lncRNA TUG1-Mut groups (P > 0.05) (**Figure 5B**), suggesting that lncRNA TUG1 interacts with miR-29c using putative binding sites. A recent study confirmed that lncRNA TUG1 could sponge miR-29c directly in Sk-Hep-1 and HeP3B cells using an RNA-binding protein immunoprecipitation assay (17). Taken together, lncRNA TUG1 serves as a ceRNA to sponge endogenous miR-29c.

LncRNA TUG1 Facilitates Th2 Cell Differentiation by Inhibiting miR-29c

To confirm the mechanism of Th cell differentiation regulated by lncRNA TUG1, we performed rescue experiments. As shown in **Figure 6**, down-regulation of miR-29c could reverse the suppressive effect of sB7-H3 by lncRNA TUG1-siRNA-1 in macrophages and $CD4^+$ T cells co-culture (P < 0.05). Meanwhile, down-regulation of miR-29c in macrophages increased the expression of GATA3 and RORγ-t in $CD4^+$ T cells (P < 0.05) using the transwell co-culture system described above. These data suggest that lncRNA TUG1 may facilitate Th2 cell differentiation by inhibiting miR-29c.

Expression of lncRNA TUG1, miR-29c, and B7-H3 in Peripheral Blood in Children With Asthma Exacerbation

To further examine whether lncRNA TUG1, miR-29c, and B7-H3 participate in asthma exacerbation, we measured the expression of lncRNA TUG1, miR-29c, and B7-H3 in the peripheral blood collected from 10 children with asthma exacerbation and in the convalescent phase. As shown in **Figure 7**, lncRNA TUG1 and B7-H3 decreased in the convalescent phase compared to acute

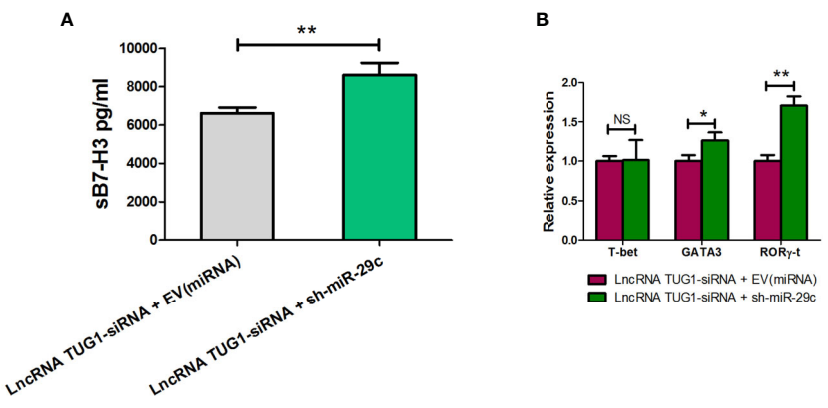

FIGURE 6 | LncRNA TUG1 regulated Th cell differentiation *via* miR-29c. **(A)** TUG1 siRNA-1 with or without miR-29c inhibitor (GenePharm, Suzhou, China) were transfected into macrophages for 6h and co-cultured with naive CD4+ T cells described above for another 24 h. After that, the supernatant in the lower chamber and CD4+ T cells in the upper chamber was collected for sB7-H3 detection. **(B)** CD4+T cells after co-culture were collected, and the levels of T-bet, GATA3, and RORγ-t in CD4+ T cells were detected by qPCR. Data are shown as mean ± SD and represent three independent experiments. *p < 0.05 and **p < 0.01. NS, no significance.

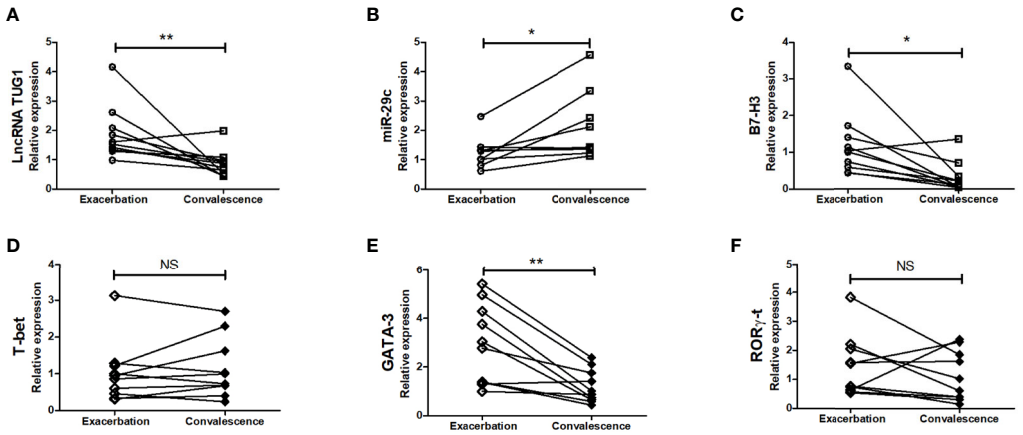

FIGURE 7 | Verification of the expression of LncRNA TUG1, miR-29c, and B7-H3 in asthmatic children. We determined the relative expression of LncRNA TUG1 (n = 10). **(A)**, miR-29c **(B)** and B7-H3 **(C)** T-bet **(D)**, GATA-3 **(E)**, RORγ-t **(F)** in peripheral blood in 10 children with asthma exacerbation and in convalescent-phase by qPCRs. *p < 0.05 and **p < 0.01. NS, no significance.

exacerbation, while miR-29c increased in the convalescent-phase (P < 0.05), which presumed that lncRNA TUG1/miR-29c/B7-H3 axis participates in the asthma exacerbation.

DISCUSSION

LncRNA is a type of non-coding RNA with 200 nucleotides (18). Recent studies have indicated that lncRNAs have the function of sponging miRNA and play an important role in lung diseases such as chronic obstructive pulmonary disease, cancer, and asthma (19). LncRNAs regulate epigenetic, transcriptional, and translational responses, and are critical regulators of immune cell differentiation, especially for type-2 immune responses (20, 21).

Previous studies have suggested that lncRNA TUG1 participates in the development of cancers (22, 23), hypoxic pulmonary hypertension (24), and Alzheimer's disease (25). Moreover, the experimental asthma model suggested that lncRNA TUG1 promotes airway smooth muscle cell proliferation and migration by sponging miR-590-5p/FGF1 (26). In this study, we further examined the role of lncRNA TUG1 in asthma pathogenesis, including Th2 and Th17 cell differentiation. We found that lncRNA TUG1 and B7-H3 were up-regulated in children with asthma exacerbation, and miR-29c was down-regulated compared to controls. Moreover, lncRNA TUG1 was increased in macrophages stimulated by HDM *in vitro* in a dose-dependent manner. Furthermore, our data indicated that lncRNA TUG1 interacted with miR-29c by putative binding sites in the cytoplasm. Moreover, we found that miR-29c might regulate Th2 cell differentiation by directly targeting co-stimulatory molecule B7-H3. Meanwhile, the down-regulation of lncRNA TUG1 decreased the level of GATA3 in CD4+T cells and was associated with miR-29c/B7-H3 axis.

LncRNA TUG1 has other miRNA targets, including miR-92a (27), miR-143-5p (28), miR-590-5p (29), et al., which suggests that lncRNAs could mediate sponge regulatory network of gene expression, which is confirmed in prostate cancer (30).

In summary, the present study found the novel mechanism of LncRNA TUG1 in the regulation of Th2 cell differentiation *via* the miR-29c/B7-H3 axis in macrophages. This study provides novel potential diagnostic biomarkers and therapeutic targets for asthma. However, further studies should be conducted to verify the effect of LncRNA TUG1 and miR-29c as therapeutic targets in terms of the experimental asthma model *in vivo*.

DATA AVAILABILITY STATEMENT

The original contributions presented in the study are included in the article/**Supplementary Material**. Further inquiries can be directed to the corresponding authors.

ETHICS STATEMENT

The present study was approved by the local Ethics Committee of Children's Hospital of Soochow University. Written informed consent to participate in this study was provided by the participants' legal guardian/next of kin. Written informed consent was obtained from the individual(s), and minor(s)' legal guardian/next of kin, for the publication of any potentially identifiable images or data included in this article.

AUTHOR CONTRIBUTIONS

HS, TW and WZ performed experiments, analyzed data, and wrote the manuscript. ZC and CZ designed the study, analyzed data, and revised the manuscript. HD and WG analyzed data. LH and YY collected the clinical data. All authors read and approved

the final manuscript. All authors contributed to the article and approved the submitted version.

FUNDING

This study was supported by the National Science Foundation of China (grant to ZC, no.81771676 and 81970027; grant to LH, no. 81971490; grant to Yongdong Yan, no. 81870006), the Social Development Projects of Jiangsu Province (grant to ZC, no. BE2019671), Jiangsu Provincial Medical Youth Talent (grant NO. QNRC2016766), Suzhou Medical Youth Talent (grant NO. GSWS2019047), and Suzhou Medical Technology Projects of Clinical Key Diseases (grant NO. LCZX201809).

SUPPLEMENTARY MATERIAL

The Supplementary Material for this article can be found online at: https://www.frontiersin.org/articles/10.3389/fimmu.2021.631450/full#supplementary-material

Supplementary Table 1 | The sequences of TUG1-siRNAs.

Supplementary Table 2 | The primers of PCRs.

REFERENCES

1. Collaborators GBDCRD. Global, Regional, and National Deaths, Prevalence, Disability-Adjusted Life Years, and Years Lived With Disability for Chronic Obstructive Pulmonary Disease and Asthma, 1990-2015: A Systematic Analysis for the Global Burden of Disease Study 2015. *Lancet Respir Med* (2017) 5(9):691–706. doi: 10.1016/S2213-2600(17)30293-X
2. Ferrante G, La Grutta S. The Burden of Pediatric Asthma. *Front Pediatr* (2018) 6:186. doi: 10.3389/fped.2018.00186
3. Lambrecht BN, Hammad H. The Immunology of Asthma. *Nat Immunol* (2015) 16(1):45–56. doi: 10.1038/ni.3049
4. Boonpiyathad T, Sozener ZC, Satitsuksanoa P, Akdis CA. Immunologic Mechanisms in Asthma. *Semin Immunol* (2019) 46:101333. doi: 10.1016/j.smim.2019.101333
5. Zhang X, Zhao X, Sun H, Yan Y, Huang L, Gu W, et al. The Role of miR-29c/B7-H3 Axis in Children With Allergic Asthma. *J Trans Med* (2018) 16(1):218. doi: 10.1186/s12967-018-1590-8
6. West KA, Lagos D. Long Non-Coding Rna Function in CD4(+) T Cells: What We Know and What Next? *Non-coding RNA* (2019) 5(3):43. doi: 10.3390/ncrna5030043
7. Zhu X, Wang X, Wang Y, Zhao Y. Exosomal Long non-Coding RNA GAS5 Suppresses Th1 Differentiation and Promotes Th2 Differentiation *Via* Downregulating EZH2 and T-bet in Allergic Rhinitis. *Mol Immunol* (2020) 118:30–9. doi: 10.1016/j.molimm.2019.11.009
8. Chen Y, Li H, Ding T, Li J, Zhang Y, Wang J, et al. Lnc-M2 Controls M2 Macrophage Differentiation *Via* the PKA/CREB Pathway. *Mol Immunol* (2020) 124:142–52. doi: 10.1016/j.molimm.2020.06.006
9. Wang Y, Liu G, Ren L, Wang K, Liu A. Long non-Coding RNA TUG1 Recruits miR29c3p From Its Target Gene RGS1 to Promote Proliferation and Metastasis of Melanoma Cells. *Int J Oncol* (2019) 54(4):1317–26. doi: 10.3892/ijo.2019.4699
10. Rajan S, Gogtay NJ, Konwar M, Thatte UM. The Global Initiative for Asthma Guidelines (2019): Change in the Recommendation for the Management of Mild Asthma Based on the SYGMA-2 Trial - a Critical Appraisal. *Lung India* (2020) 37(2):169–73. doi: 10.4103/lungindia.lungindia_308_19
11. Shi H, Chen L, Ridley A, Zaarour N, Brough I, Caucci C, et al. Gm-Csf Primes Proinflammatory Monocyte Responses in Ankylosing Spondylitis. *Front Immunol* (2020) 11:1520. doi: 10.3389/fimmu.2020.01520
12. Su Z, Wu F. Inflammatory Factors Induce Thrombosis Through the miR-146b-3p/p38MAPK/COX-2 Pathway. *BioMed Res Int* (2020) 2020:8718321. doi: 10.1155/2020/8718321
13. Zhang G, Hou J, Shi J, Yu G, Lu B, Zhang X. Soluble CD276 (B7-H3) Is Released From Monocytes, Dendritic Cells and Activated T Cells and Is Detectable in Normal Human Serum. *Immunology* (2008) 123(4):538–46. doi: 10.1111/j.1365-2567.2007.02723.x
14. Lu Y, Tang L, Zhang Z, Li S, Liang S, Ji L, et al. Long Noncoding Rna TUG1/miR-29c Axis Affects Cell Proliferation, Invasion, and Migration in Human Pancreatic Cancer. *Dis Markers* (2018) 2018:6857042. doi: 10.1155/2018/6857042
15. Guo P, Zhang G, Meng J, He Q, Li Z, Guan Y. Upregulation of Long Noncoding RNA Tug1 Promotes Bladder Cancer Cell Proliferation, Migration, and Invasion by Inhibiting Mir-29c. *Oncol Res* (2018) 26(7):1083–91. doi: 10.3727/096504018X15152085755247
16. Sun J, Fu F, Gu W, Yan R, Zhang G, Shen Z, et al. Origination of New Immunological Functions in the Costimulatory Molecule B7-H3: The Role of Exon Duplication in Evolution of the Immune System. *PLoS One* (2011) 6(9):e24751. doi: 10.1371/journal.pone.0024751
17. Zhao W, Jiang X, Yang S. Lncrna TUG1 Promotes Cell Proliferation, Migration, and Invasion in Hepatocellular Carcinoma *Via* Regulating miR-29c-3p/COL1A1 Axis. *Cancer Manag Res* (2020) 12:6837–47. doi: 10.2147/CMAR.S256624
18. Rinn JL, Chang HY. Genome Regulation by Long Noncoding Rnas. *Annu Rev Biochem* (2012) 81:145–66. doi: 10.1146/annurev-biochem-051410-092902
19. Li Y, Yin Z, Fan J, Zhang S, Yang W. The Roles of Exosomal miRNAs and lncRNAs in Lung Diseases. *Signal Transduct Target Ther* (2019) 4(1):47. doi: 10.1038/s41392-019-0080-7
20. Guidi R, Wedeles CJ, Wilson MS. ncRNAs in Type-2 Immunity. *Non-coding RNA* (2020) 6(1):10. doi: 10.3390/ncrna6010010
21. Xia L, Wang X, Liu L, Fu J, Xiao W, Liang Q, et al. lnc-BAZ2B Promotes M2 Macrophage Activation and Inflammation in Children With Asthma Through Stabilizing BAZ2B Pre-Mrna. *J Allergy Clin Immunol* (2020) 147(3):921–32. doi: 10.1016/j.jaci.2020.06.034
22. Shen X, Hu X, Mao J, Wu Y, Liu H, Shen J, et al. The Long Noncoding RNA TUG1 Is Required for TGF-beta/TWIST1/EMT-mediated Metastasis in Colorectal Cancer Cells. *Cell Death Dis* (2020) 11(1):65. doi: 10.1038/s41419-020-2254-1
23. El-Khazragy N, Mohammed HF, Yassin M, Elghoneimy KK, Bayoumy W, Hewety A, et al. Tissue-Based Long non-Coding RNAs "Pvt1, TUG1 and MEG3" Signature Predicts Cisplatin Resistance in Ovarian Cancer. *Genomics* (2020) 112(6):4640–6. doi: 10.1016/j.ygeno.2020.08.005
24. Yang L, Liang H, Shen L, Guan Z, Meng X. Lncrna Tug1 Involves in the Pulmonary Vascular Remodeling in Mice With Hypoxic Pulmonary Hypertension *Via* the microRNA-374c-mediated Foxc1. *Life Sci* (2019) 237:116769. doi: 10.1016/j.lfs.2019.116769
25. Li X, Wang SW, Li XL, Yu FY, Cong HM. Knockdown of Long non-Coding RNA TUG1 Depresses Apoptosis of Hippocampal Neurons in Alzheimer's Disease by Elevating microRNA-15a and Repressing ROCK1 Expression. *Inflammation Res* (2020) 69(9):897–910. doi: 10.1007/s00011-020-01364-8
26. Lin J, Feng X, Zhang J, Tong Z. Long Noncoding RNA TUG1 Promotes Airway Smooth Muscle Cells Proliferation and Migration *Via* Sponging miR-590-5p/FGF1 in Asthma. *Am J Trans Res* (2019) 11(5):3159–66. doi: 10.21203/rs.3.rs-15500/v1
27. Yang L, Li T. Lncrna TUG1 Regulates ApoM to Promote Atherosclerosis Progression Through miR-92a/FXR1 Axis. *J Cell Mol Med* (2020) 24(15):8836–48. doi: 10.1111/jcmm.15521
28. Yu X, Hu L, Li S, Shen J, Wang D, Xu R, et al. Long Non-Coding RNA Taurine Upregulated Gene 1 Promotes Osteosarcoma Cell Metastasis by Mediating HIF-1alpha *Via* Mir-143-5p. *Cell Death Dis* (2019) 10(4):280. doi: 10.1038/s41419-019-1509-1
29. Ai Y, Chen M, Liu J, Ren L, Yan X, Feng Y. Lncrna TUG1 Promotes Endometrial Fibrosis and Inflammation by Sponging miR-590-5p to Regulate Fasl in Intrauterine Adhesions. *Int Immunopharmacol* (2020) 86:106703. doi: 10.1016/j.intimp.2020.106703

30. Du Z, Sun T, Hacisuleyman E, Fei T, Wang X, Brown M, et al. Integrative Analyses Reveal a Long Noncoding RNA-Mediated Sponge Regulatory Network in Prostate Cancer. *Nat Commun* (2016) 7:10982. doi: 10.1038/ncomms10982

Conflict of Interest: The authors declare that the research was conducted in the absence of any commercial or financial relationships that could be construed as a potential conflict of interest.

frontiers in Immunology

ORIGINAL RESEARCH
published: 02 August 2021
doi: 10.3389/fimmu.2021.686846

Mannose Receptor Mediates the Activation of Chitooligosaccharides on Blunt Snout Bream (*Megalobrama amblycephala*) Macrophages

Aotian Ouyang[1], *Huabing Wang*[1], *Jianguo Su*[1,2,3] *and Xiaoling Liu*[1,2*]

[1] *Department of Aquatic Animal Medicine, College of Fisheries, Huazhong Agricultural University, Wuhan, China,* [2] *Hubei Provincial Engineering Laboratory for Pond Aquaculture, Hubei Engineering Technology Research Center for Aquatic Animal Disease Control and Prevention, Wuhan, China,* [3] *Engineering Research Center of Green Development for Conventional Aquatic Biological Industry in the Yangtze River Economic Belt, Ministry of Education, Wuhan, China*

Chitooligosaccharide (COS) is an important immune enhancer and has been proven to have a variety of biological activities. Our previous research has established an M1 polarization mode by COS in blunt snout bream (*Megalobrama amblycephala*) macrophages, but the mechanism of COS activation of blunt snout bream macrophages remains unclear. In this study, we further explored the internalization mechanism and signal transduction pathway of chitooligosaccharide hexamer (COS6) in blunt snout bream macrophages. The results showed that mannose receptor C-type lectin-like domain 4-8 of *M. amblycephala* (MaMR CTLD4-8) could recognize and bind to COS6 and mediate COS6 into macrophages by both clathrin-dependent and caveolin-dependent pathways. In the inflammatory response of macrophages activated by COS6, the gene expression of tumor necrosis factor (TNF)-α, interleukin (IL)-1β, and nitric oxide synthase 2 (NOS2) was significantly inhibited after MaMR CTLD4-8-specific antibody blockade. However, even if it was blocked, the expression of these inflammation-related genes was still relatively upregulated, which suggested that there are other receptors involved in immune regulation. Further studies indicated that MaMR CTLD4-8 and Toll-like receptor 4 (TLR4) cooperated to regulate the pro-inflammatory response of macrophages caused by COS6. Taken together, these results revealed that mannose receptor (MR) CTLD4-8 is indispensable in the process of recognition, binding, internalization, and immunoregulation of COS in macrophages of blunt snout bream.

Keywords: chitooligosaccharide, mannose receptor, toll-like receptor, macrophages, *Megalobrama amblycephala*

OPEN ACCESS

Edited by:
Lonnie Shea,
University of Michigan, United States

Reviewed by:
Shuming Zou,
Shanghai Ocean University, China
Hong Zhou,
Zunyi Medical University, China

***Correspondence:**
Xiaoling Liu
liuxl@mail.hzau.edu.cn

Specialty section:
This article was submitted to Molecular Innate Immunity, a section of the journal Frontiers in Immunology

Received: *28 March 2021*
Accepted: *16 July 2021*
Published: *02 August 2021*

Citation:
Ouyang A, Wang H, Su J and Liu X (2021) Mannose Receptor Mediates the Activation of Chitooligosaccharides on Blunt Snout Bream (Megalobrama amblycephala) Macrophages. Front. Immunol. 12:686846. doi: 10.3389/fimmu.2021.686846

HIGHLIGHTS

1. MaMR CTLD4-8 can recognize and bind to COS.
2. MaMR CTLD4-8 mediates COS internalization into macrophages.
3. COS is internalized by clathrin- and caveolin-dependent pathways.
4. TLR4 and MaMR CTLD4-8 coordinately regulated the pro-inflammatory response.

INTRODUCTION

Chitooligosaccharide (COS) is used as an important immune enhancer. It is a linear oligomer of N-acetylglucosamine or glucosamine linked by β-1,4 glycosidic bonds (1, 2). Essentially, COS is the degraded products of chitin/chitosan by acid hydrolysis, enzymatic degradation, or both. Its degree of deacetylation (DD) is >90%, degree of polymerization (DP) is <20, and molecular weight (MW) is <3,900 Da (3, 4). It is easily soluble in water and has the advantages of non-toxicity, non-sensitization, and excellent biocompatibility. In recent years, studies have shown that COS has a variety of biological effects, which can enhance immune effects and antimicrobial and antitumor activities (5–7).

As one of the most important components of innate immunity, macrophages play a key role in inflammation and host defense. The resting macrophages can be induced to activate M1-type macrophages under the stimulation of interferon (IFN)-γ and lipopolysaccharide (LPS), secreting a large number of pro-inflammatory factors (8), including interleukin (IL)-1, IL-6, and tumor necrosis factor (TNF)-α, and upregulate the messenger RNA (mRNA) level of inducible nitric oxide synthase (iNOS) [also called nitric oxide synthase 2 (NOS2)]. It has been reported that COS can activate the immune activity of macrophages; the recognition of COS by macrophages and the regulation of their functions are some of the important ways to exert immunomodulatory effects (9, 10). The immune regulation function of COS mainly reflects its activation and inhibition of different signal pathways, thereby regulating the production of NO and cytokines or mediators and finally acting on the innate immune system and the adaptive immune system (11–13). In mammals, COS has a specific signal pathway that regulates the activation of macrophages. It has been previously reported that the use of low-molecular weight chitohexaose (chitooligosaccharide hexamer, COS6) or COS with a degree of polymerization of only 1-6 can activate the nuclear factor (NF)-κB pathway of mouse macrophages and induce the production of nitric oxide (NO) and TNF-α (14, 15). There are also reports showing that COS or sulfurized COS modulates immune effects in mouse macrophages by regulating the mitogen-activated protein kinase (MAPK) and phosphoinositide 3-kinase (PI3K)/Akt signaling pathways (16, 17).

The mannose receptor (MR) is a type I transmembrane protein, which is an important member of the C-type lectin family and can realize rapid endocytosis through the cell membrane. From N-terminal to C-terminal of MR, there are cysteine-rich domain (CR), fibronectin type II domain (FNII), eight tandemly arranged C-type lectin-like domains (CTLDs), transmembrane domain, and short cytoplasmic tail. As the main carbohydrate recognition domain of MR, the CTLDs can mediate MR recognition of carbohydrate or carbohydrate complexes with D-mannose, L-fucose, and N-acetylglucosamine as terminal (18, 19). Combined with ligands, MR can initiate intracellular signaling cascades that promote or inhibit the production of NO and the expression of cytokines. The intracytoplasmic domain of MR is very short and does not contain signal transduction motif. Therefore, the involvement of MR in signal transduction requires the participation of other receptors for the expression of target genes.

Although there have been reports on the mechanism of COS to activate macrophages in mammals, there are still controversies. Previous studies have shown that the immunostimulatory effect of COS on macrophages depends on Toll-like receptor 4 (TLR4) (11), MR (20), CD14, or complement receptor 3 (CR3) (15). COS is an important immune enhancer in the field of aquaculture. However, the mechanism by which COS activates macrophages in aquatic animals is still unclear. In previous studies, we established a COS-activated blunt snout bream macrophage M1 polarization model and successfully expressed mannose receptor C-type lectin-like domain 4-8 of *M. amblycephala* recombinant protein (rMaMR CTLD4-8); the anti-MaMR CTLD4-8 polyclonal antibody has also been prepared. In order to further prove the mechanism of COS in activating blunt snout bream macrophages, in this study, we selected the kind of COS (COS6, molecular weight about 1,300 Da) that has the best inflammation activation effect as the experimental material. The results showed that the internalization of COS6 in the macrophages of blunt snout bream was mediated by MR CTLD4-8, and it was found that the immune stimulation of COS6 on macrophages was coordinated by MR CTLD4-8 and TLR4.

MATERIALS AND METHODS

Fish Sampling

Blunt snout bream (*M. amblycephala*), ranging from 400 to 500 g in weight, were obtained from a fish farm located in Hubei Province, China, and kept in a recirculating freshwater system at 25°C–26°C with a natural photoperiod. The animals were fed twice per day with a commercial pellet diet (Haida, Hubei, China) amounting to 3% of body weight. The study was approved by the Institutional Animal Care and Use Ethics Committee of Huazhong Agricultural University (ID Number: HZAUFI-2021-0007).

Isolation of Head Kidney Macrophages

Blunt snout bream head kidney macrophages were isolated as described previously with slight modifications (21). Briefly, fish were anesthetized with MS222 (Syndel Laboratories, Ltd., Canada), and the head kidney was removed aseptically and passed through a 100-μm mesh (Falcon, Becton Dickinson) in Leibovitz medium (L-15) (Invitrogen, USA) containing 2% fetal bovine serum (FBS) (Gibco, USA) and 200 IU/ml penicillin plus streptomycin (Amresco, USA). The resulting cell suspension was layered onto a 34%/51% Percoll (Pharmacia, Uppsala, Sweden) density gradient and centrifuged at 400 g for 30 min at 4°C. The interface was collected, and the cells were washed twice with L-15 at 400 g for 10 min at 4°C before being resuspended to 1×10^7 cells/ml in L-15 containing 10% FBS.

Indirect Immunofluorescence Assay

Indirect immunofluorescence was used to observe the binding of COS6 to MR CTLD4-8 in the head kidney macrophages from blunt snout bream. The macrophage (1×10^7cells/ml in L-15) suspension is evenly cultured on the cell slide in 24-well plates.

Cells were incubated with 0.05 mM fluorescein isothiocyanate (FITC)-labeled COS6 (Xianqiyue, China) at 28°C for 30 min. Cells were fixed with 4% paraformaldehyde for 10 min. Blocking solution 5% normal goat serum (Guge Biology, China) was added to minimize nonspecific fluorescence, and then anti-MaMR-CTLD4-8 immunoglobulin G (IgG) (9.6 μg/ml in blocking solution) was incubated at 28°C for 2 h, followed by incubation with Cy3-conjugated goat anti-mouse IgG (Abclonal, China) for 40 min. Nuclei were stained with 4′,6-diamidino-2-phenylindole (DAPI; Sigma, Germany) for 10 min. The membrane was stained by 1,1-dioctadecyl-3,3,3,3-tetramethylindodicarbocyanine (DiD; Beyotime, China) for 15 min. Anti-fluorescence quencher mounted and fixed cell slides. The slide is imaged by a confocal microscope (Leica TCS SP8, Germany).

Direct Binding Assay of MaMR CTLD4-8 to Carbohydrates

The binding activity of MaMR CTLD4-8 to COS6 was performed by enzyme-linked immunosorbent assay (ELISA) according to the previous method with a little modification (22). COS6 and D-mannose (Man) at 80 μg/ml (100 μl) were used to coat a 96-well microtiter plate (Corning, USA). The plates were air-dried at 37°C and then blocked with 100 μl/well of 5% bovine serum albumin (BSA) in phosphate buffered saline with Tween 20 (PBST) for 2 h at 37°C. Wells were washed three times with PBST. Then, 100 μl rMaMR CTLD4-8 of different concentrations were added to the wells. After incubation at 37°C for 2 h, the plate was washed three times with PBST. After that, 100 μl mouse anti-glutathione-S-transferase (GST)-tag IgG (Abclonal, China) diluted 1:2,000 in 5% BSA were added to each well at 37°C for 1 h. Then, the plate was rewashed and incubated with 100 μl of goat anti-mouse IgG–horseradish peroxidase (HRP) conjugate (Biosharp, China) diluted 1:5,000 in 5% BSA at 37°C for 1 h. After washing with PBST three times, 100 μl of 3,3′,5,5′-tetramethylbenzidine (TMB) solution (Solarbio, China) was added to each well and incubated at 37°C for 10 min in the dark. The reaction was stopped by adding 100 μl of 2 M sulfuric acid per well. The absorbance was measured with an automatic ELISA reader (Tecan, Switzerland) at 450 nm. Mannose (Man) as a positive control; GST tag protein was employed as a negative control. The assay was repeated three times.

Distribution of FITC-COS6 in Macrophages

The macrophage (1×10^7cells/ml in L-15) suspension is evenly cultured on the cell slide in 24-well plates. Cells and 0.05 mM FITC-COS6 were incubated for 0, 2, 4, 6, 8, and 10 min at 4°C or 28°C. As above, the cells were fixed, DAPI and 1,1'-dioctadecyl-3,3,3',3'-tetramethylindocarbocyanine perchlorate (DiI; Beyotime, China) stained, and observed by confocal microscope.

Effect of Endocytosis Inhibitors on FITC-COS6 Internalization of Macrophages

The macrophage (1×10^7cells/ml in L-15) suspension is evenly cultured on the cell slide in 24-well plates. The cells in each well were pretreated with chlorpromazine (CPZ, 40 μM), sucrose (300 mM), nystatin (100 μM), methyl-β-cyclodextrin (M-β-CD, 1 mM), 1,1'-dithiodi-2-naphthtol (IPA-3, 40 μM), and NSC23766 (hydrochloride, 40 μM) for 2 h at 28°C; according to the previous test method, it has been appropriately modified (23). The above inhibitors were purchased from MCE (China). Then, cells were incubated with 0.05 mM FITC-COS6 for 30 min. The final result was shown by the fluorescence images. After the cells were washed with PBS, lysed (Beyotime, China), add 100μ L supernatant to each well of 96-well plate, for fluorescence intensity was measured by fluorescence microplate at 488 nm. WCIF ImageJ software was used to analyze the co-localization of FITC-COS6 and DAPI-stained nucleus in macrophages.

Effect of Anti-MaMR CTLD4-8 Antibody on FITC-COS6 Internalization of Macrophages

The macrophage (1×10^7cells/ml in L-15) suspension is evenly cultured on the cell slide in six-well plates. Macrophages were preincubated with anti-MaMR CTLD4-8 IgG (4.8 μg/ml) for 2 h at 28°C. As a positive control, D-mannose (2 mg/ml) can effectively bind to MaMR CTLD4-8, and normal mouse IgG (4.8 μg/ml) is used as a negative control. Then, cells were incubated with 0.05 mM FITC-COS6 for 30 min at 28°C. The adherent macrophages were digested with trypsin containing 0.05% ethylenediaminetetraacetic acid (EDTA; Gibco, USA), and the digestion was terminated with serum after the cells were completely suspended. The cells were washed with PBS, centrifuged and resuspended to 1×10^6 cells, and the fluorescence intensity at 488 nm was measured by flow cytometry (Berkam, USA). Or through the same processing method as above, the cells were incubated, washed, lysed, and mixed uniformly. Fluorescence intensity was measured by fluorescence microplate at 488 nm. The mean fluorescence intensity (MFI) of internalization from FITC-COS6 in macrophages was recorded. The percentage of FITC-COS6 intake under different pretreatments, which is the ratio of the MFI values measured from the blocked cells to those measured from the untreated cells, was plotted to reflect the efficiency of receptor endocytosis. Flow cytometry graphs shown in the *Results* section were representative data from at least three independent experiments.

Western Blotting

Macrophages (1×10^7 cells) were seeded into a six-well plate and cultured for 24 h. After 2 h preincubation with or without anti-MaMR CTLD4-8 IgG (4.8 μg/ml), COS6 (50 μg/ml) was added, giving a final volume of 1 ml. Incubated for 30 min, the cells were collected and lysed with a radioimmunoprecipitation assay (RIPA) lysis buffer (Beyotime, China) containing proteinase inhibitors on ice. The protein concentration was determined by a bicinchoninic acid (BCA) protein assay kit (Beyotime, China). Equal amounts of total protein were separated by 8%–12% sodium dodecyl sulfate–polyacrylamide gel electrophoresis (SDS-PAGE) gels and transferred onto nitrocellulose membranes (Millipore, Germany). The membranes were

blocked in fresh 5% BSA dissolved in Tris-buffered saline with Tween 20 (TBST) buffer at room temperature for 1 h, then incubated with antibody TLR4 (1:500 dilution; HuaBio, China), TLR2 (1:500; HuaBio, China), and β-tubulin (1:4,000; Abclonal, China) overnight at 4°C. They were then washed three times with TBST buffer and incubated with HRP-conjugated goat anti-rabbit IgG (Abclonal, China) for 1 h at room temperature. Immunodetection was performed using enhanced chemiluminescence (ECL) reagents (GE Healthcare, USA).

Quantitative Real-Time PCR Assay

Quantitative real-time PCR (qRT-PCR) was used to investigate the target gene expression patterns in different groups and different time points of macrophages after COS6 stimulation. Macrophages (1×10^7 cells) were seeded into a six-well plate and cultured for 24 h.

To investigate the effect of MaMR CTLD4-8 after COS6 stimulated macrophages, cells were preincubated with anti-MaMR CTLD4-8 antibody and then cell samples were collected after stimulation with COS6 for 0, 3, 6, and 12 h. In order to investigate the effect of resatorvid (TAK 242; MCE, China) on COS6-stimulated macrophages, the cells were blocked with TAK242 and anti-MaMR CTLD4-8 antibody, and cell samples were collected after COS6 stimulation for 3 h. After the above method, the total RNA was extracted and cDNA was synthesized, and the following assay was prepared after uniform concentration.

Primers used for qRT-PCR of this experiment are given in **Table 1**. The qRT-PCR mixture reaction volume was 20 μl, containing 10 μl LightCycler® 480 SYBR Green I Master, 7.4 μl ddH_2O, 0.8 μl of each primer (10 mM), and 1 μl cDNA template. The reactions were performed using LightCycler® 480 II (Roche Diagnostics GmbH, USA) according to the procedure as follows: preincubation at 95°C for 5 min, then 40 cycles at 95°C for 5 s, 55°C for 20 s, and 72°C for 20 s. Each sample was tested in triplicate. Specificity of the amplified target gene was assessed using dissociation curve analysis. The target gene relative expression levels *vs.* the β-actin gene (selected as the reference gene) were calculated according to the $2^{-\Delta\Delta CT}$ method. To determine the relative fold change of the target gene at different time points, the expression value was normalized using the corresponding control group.

Statistical Analysis

In the present study, statistical analysis and presentation graphics were carried out by the GraphPad Prism 8.0 software. Results were shown as mean ± SD from at least three independent experiments, and statistical significance was determined with ANOVA, followed by two-tailed Student's t-test. The p–values <0.05 are considered statistically significant differences and p-values <0.01 as extreme difference.

RESULTS

COS6-Induced Pro-Inflammatory Response of Macrophages Involves MaMR CTLD4-8

The M1 polarization model of COS-activated blunt snout bream macrophages has been successfully established in previous studies (24). On this basis, we first investigated the concentration gradient and time gradient of COS6-stimulated bream macrophages based on previous studies. After stimulation, these genes were significantly upregulated relative to the control group, and the expression levels of MR, TNF-α, and IL-1β were most significant at a COS6 concentration of 50 μg/ml (**Figure 1A**), and the expression levels of each gene were significantly upregulated at 3 h after stimulation (**Figure 1B**). After preblocking with anti-MaMR CTLD4-8 antibody, the gene expression after COS6 stimulation was quantitatively detected. Compared with the COS6 group, in the early stage of stimulation (12 h), MR (**Figure 1C**), TNF-α (**Figure 1D**), and IL-1β (**Figure 1E**) were most significantly blocked by antibody at 6 h, while NOS2 (**Figure 1F**) was most significantly blocked at 3 h. However, it is worth noting that the expression of inflammation-related genes and MR is still significantly upregulated compared to the 0 h control group. There may be other receptors or pathways involved in the regulation of COS6-

TABLE 1 | Primers used in this study.

Primer name	Primer direction	Sequence (5'–3')	GenBank	Application
MR	Forward	GATGGCAGTGGAGCAATGGA	KC495437.1	qRT-PCR
MR	Reverse	CTGGTGGAATGGTAGGAACAGA		
TNF-α	Forward	CCGCTGCTGTCTGCTTCA	HQ696609.1	qRT-PCR
TNF-α	Reverse	GCCTGGTCCTGGTTCACTCT		
IL-1β	Forward	GTGCCAGGTGCCAAGTAGC	KF245425.1	qRT-PCR
IL-1β	Reverse	AAGCCCAAGATATGCAGGAGT		
NOS2	Forward	ATTCAAGGGCAGCTTCCAGG	KJ668755.1	qRT-PCR
NOS2	Reverse	CAGGGGCAAAGTTTAAGGGC		
TLR4	Forward	CTGTCGTATGGTAGAGGTC	KR013051	qRT-PCR
TLR4	Reverse	TTCAGGTTTGAGTGGGTAA		
MyD88	Forward	GACAACAGGGATTAGACG	KP192128.1	qRT-PCR
MyD88	Reverse	TGGAACAGACTGAATACAAC		
β-Actin	Forward	ACCCACACCGTGCCCATCTA	ADV57164.1	qRT-PCR
β-Actin	Reverse	CGGACAATTTCTCTTTCGGCTG		

IL, interleukin; MR, mannose receptor; NOS, nitric oxide synthase; TLR, Toll-like receptor; TNF, tumor necrosis factor.

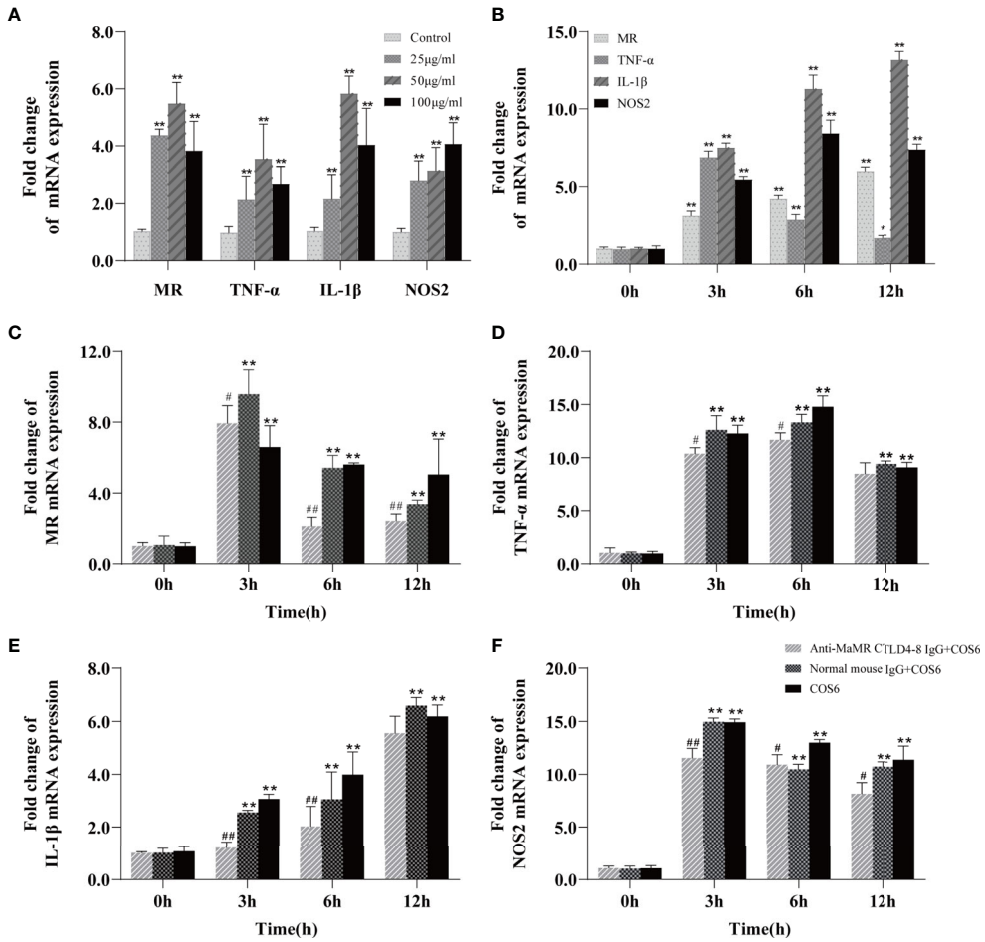

FIGURE 1 | qRT-PCR analysis of the expression of mannose receptor (MR) and inflammation-related genes induced by chitooligosaccharide hexamer (COS6) in macrophages. **(A)** Gene expression in macrophages stimulated by COS6 for 6 h in 25, 50, and 100 μg/ml. **(B)** The macrophage gene expression was stimulated with 50 μg/ml COS6 at 0, 3, 6, and 12 h. Pre-blocking cells with or without anti-mannose receptor C-type lectin-like domain 4-8 of *Megalobrama amblycephala* (MaMR CTLD4-8) antibody, and the expression patterns of MR **(C)**, tumor necrosis factor (TNF)-α **(D)**, interleukin (IL)-1β **(E)**, and nitric oxide synthase (NOS)2 **(F)** were determined. The samples were analyzed at 0, 3, 6, and 12 h after 50 μg/ml COS6 stimulation. β-Tubulin was used as an internal reference. Each experiment was executed in triplicate. Data were shown as means ± SD (n = 3), with (*) $p < 0.05$ and (**) $p < 0.01$ *vs.* the 0 μg/ml or 0 h, ($^{\#}$) $p < 0.05$ and ($^{\#\#}$) $p < 0.01$ *vs.* the COS6 group (set as 1).

induced macrophages. In conclusion, the blocking of MaMR CTLD4-8 antibody downregulated the expression of macrophage inflammation-related genes after COS6 stimulation, indicating that MR CTLD4-8 is indeed related to the COS6-induced inflammation of macrophages.

Mannone Receptor Bound COS6 Through CTLD4-8

To illustrate COS6 as a recognized ligand of MR, the molecular level assay was performed by ELISA, and the cell level assay was demonstrated by indirect immunofluorescence. In the molecular level assay, OD450 values reflecting the binding ability of rMaMR CTLD4-8 with COS6 or D-mannose increased with the elevation of the concentration of rMaMR4-8, indicating that MaMR CTLD4-8 can bind to COS6 and D-mannose in a dose-dependent manner. GST-tag protein was used as a negative control, and its OD450 was maintained at about 0.3 without significant change, which indicates that GST-tag protein could not bind COS6 or D-mannose (**Figure 2A**). In the cell level assay, immunofluorescence microscopy was performed to examine the locations of MaMR CTLD4-8 and COS6 in macrophages. The results indicate that COS6 and MaMR CTLD4-8 co-localized in macrophages (**Figure 2B**).

COS6 Was Internalized Into Macrophages

The kinetics of FITC-COS6 internalization in macrophages was visualized by confocal microscopy. The internalization of FITC-COS6 in blunt snout bream macrophages was temperature-dependent. Internalization at 4°C (**Figure 3A**) was a relatively slow uptake process compared to that at 28°C (**Figure 3B**). The internalization of FITC-COS6 by blunt snout bream macrophages was time-dependent. FITC-COS6 bound to the cell membrane first, then gradually internalized into the cell, and

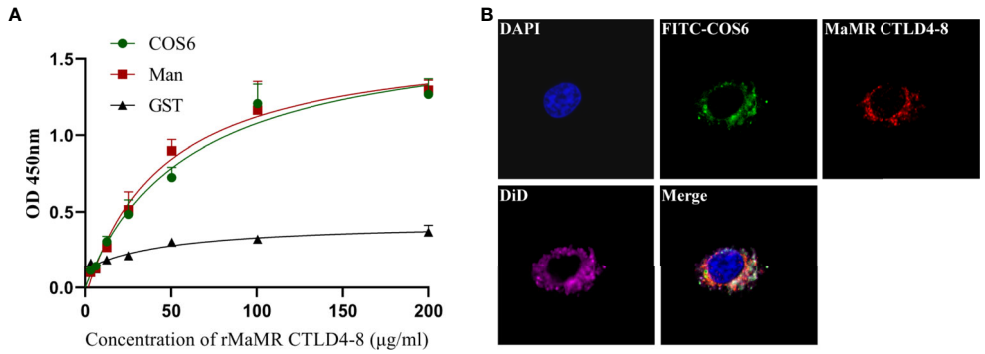

FIGURE 2 | Interaction of chitooligosaccharide hexamer (COS6) to mannose receptor C-type lectin-like domain 4-8 of *Megalobrama amblycephala* (MaMR CTLD4-8). **(A)** ELISA analysis of the interaction between rMaMR CTLD4-8 and COS6. The microtiter plates were coated with carbohydrates (Man as a positive control) and incubated with the recombinant protein [glutathione-S-transferase (GST)-tag protein as a negative control]. After incubation with anti-MaMR CTLD4-8 antibody, the interaction was detected with goat anti-mouse immunoglobulin G (IgG)–horseradish peroxidase (HRP) conjugate at 450 nm. **(B)** Co-localization of COS6 and MaMR CTLD4-8 by indirect immunofluorescent assay. Primary macrophages were incubated with fluorescein isothiocyanate (FITC)-labeled COS6 for 30 min, 4% (v/v) paraformaldehyde-fixed, anti-MaMR CTLD4-8 incubated, labeled with Cy3, 4′,6-diamidino-2-phenylindole (DAPI), and 1,1-dioctadecyl-3,3,3,3-tetramethylindodicarbocyanine (DiD) staining, and the results were presented *via* confocal microscopy. Data were shown as means ± SD (n = 3). Scale bar:10 μm.

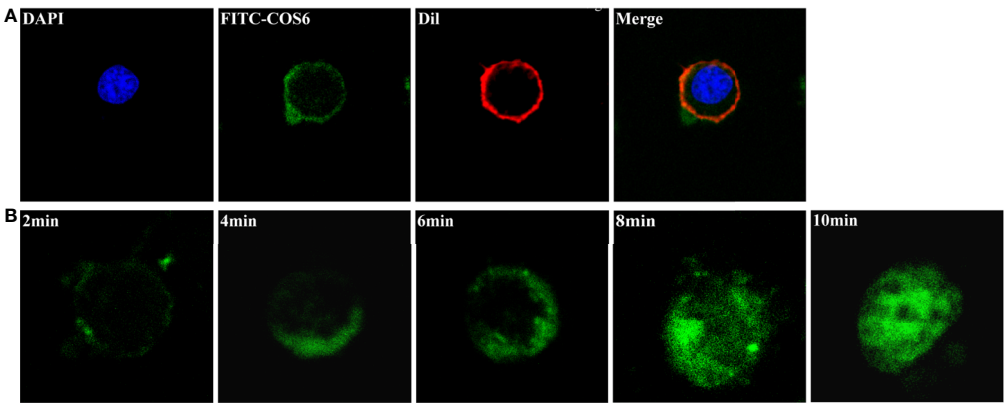

FIGURE 3 | Internalization of chitooligosaccharide hexamer (COS6) in macrophages. **(A)** Here, 0.05 mM fluorescein isothiocyanate (FITC)-COS6 is internalized into macrophages by incubating for 10 min at 4°C, then the cell membrane was stained with 1,1'-dioctadecyl-3,3,3',3'-tetramethylindocarbocyanine perchlorate (DiI) and the cell nucleus was stained with 4′,6-diamidino-2-phenylindole (DAPI). **(B)** The internalization of FITC-COS6 at different times (2, 4, 6, 8, and 10 min). Cells (1×10^6–1×10^7) were incubated with 0.05 mM FITC-COS6 at 28°C and examined by a confocal microscope. All the experiments were repeated at least three times. Scale bar:5 μm.

finally spread to the cytoplasm, and the fluorescence intensity also increased with time (**Figure 2B**).

The Internalization of COS6 by Macrophages Was Mediated by Mannose Receptor CTLD4-8

To determine the effect of MR CTLD4-8 in internalizing COS6 in the macrophages of blunt snout bream, we used anti-MaMR CTLD4-8 antibody to block the cells. The final result was presented by flow cytometry and fluorescence microplate reader. The internalization results of FITC-COS6 showed that compared with the blank group, the internalization rate of FITC-COS6 by macrophages that were not blocked reached 57.51%, and the internalization rate of the negative control group also reached 53.69%. As a positive control group, D-mannose reduced the internalization rate of FITC-COS6 to 11.08%, but the antibody pretreatment group also significantly reduced the internalization of FITC-COS6 by macrophages to 10.37% (**Figure 4A**). The fluorescence intensity measured by the fluorescence microplate reader was consistent with the trend of flow cytometry results (**Figure 4B**). These results confirmed that MaMR CTLD4-8 mediates the internalization of COS6 in blunt snout bream macrophages.

The Internalization of COS6 in Macrophages Depends on Clathrin- and Caveolin-Mediated Pathways

To investigate the endocytosis of COS6 in the macrophages of blunt snout bream, we used endocytosis inhibitors to block clathrin-dependent (CPZ and sucrose), caveolin-dependent (M-β-CD and nystatin), and micropinocytosis (NSC23766 and

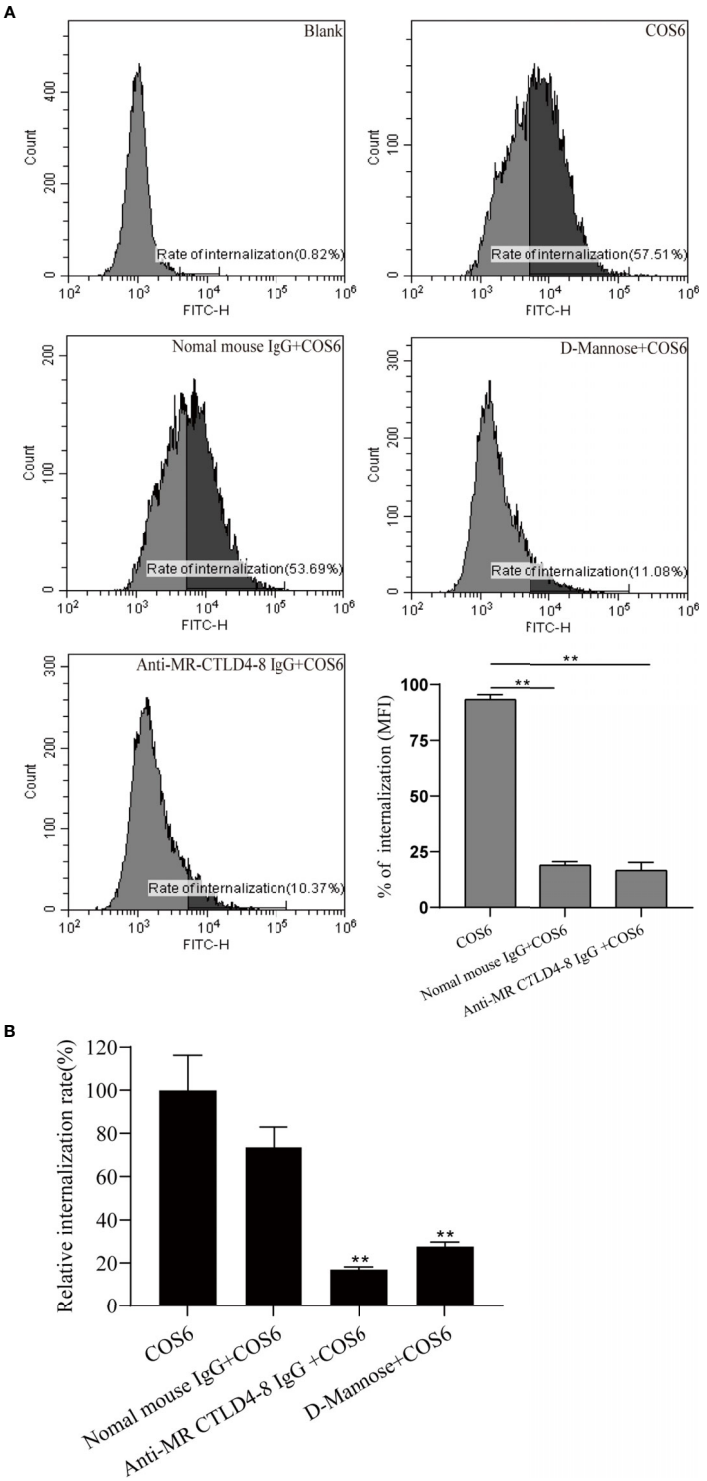

FIGURE 4 | Internalization of fluorescein isothiocyanate (FITC)-chitooligosaccharide hexamer (COS6) by macrophages with or without blocking mannose receptor (MR) CTLD4-8. Anti-MR CTLD4-8 (4 μg/ml) and D-mannose (2 mg/ml) blockade of the cells for 2 h, and the macrophages were incubated with FITC-COS in a six-well plate at 28°C for 30 min. **(A)** The internalization rate of FITC-COS6 by flow cytometry. The mean fluorescence intensity (MFI) of internalization in macrophages was recorded. **(B)** Inhibitors of MR binding and function block the association of COS with primary macrophage. Cells were preincubated with 2 mg/ml D-mannose, mannose receptor C-type lectin-like domain 4-8 of *Megalobrama amblycephala* (MaMR-CTLD4-8) specific antibody, negative IgG, or medium alone. Then, 0.05 mM FITC-COS6 was added, and cells were incubated, washed, lysed, and mixed uniformly. Fluorescence intensity was measured. Data were shown as means ± SD and collected from three independent experiments, with (*) $p < 0.05$ and (**) $p < 0.01$ *vs.* the COS6 group (set as 100).

IPA-3) pathways. Relative to the control group, confocal image showed that CPZ, sucrose, nystatin, and M-β-CD can effectively block the uptake of COS6 by macrophages, and NSC23766 and IPA-3 have no significant effect on the uptake of COS6 by macrophages (**Figure 5A**). By measuring the fluorescence intensity of ingested FITC-labeled COS6, the internalization rate relative to the control group was significantly reduced by clathrin and caveolin pathway inhibitors, reducing to 57.80% (sucrose), 40.90% (CPZ), and 47.27% (nystatin). Similarly, macropinocytosis pathway inhibitor had no significant effect (**Figure 5B**). It indicated that COS6 is internalized into macrophages through clathrin- and caveolin-dependent pathways.

Toll-Like Receptor 4 and Mannose Receptor CTLD4-8 Coordinately Regulated the Pro-Inflammatory Response of Macrophages by COS6

Since the intracytoplasmic domain of MR is very short and does not contain signal transduction motifs (25) and previous results also indicated that MR CTLD4-8 is involved in the immune regulation of COS6-stimulated macrophages (**Figure 1**), other receptors are needed to explore the signal transduction involved in MR. Therefore, we investigated whether TLR2 or TLR4 were also involved in COS6-activated signal transduction pathway in blunt snout bream macrophages. In our results, compared with the PBS group, the gene expression of TLR4 was significantly upregulated after the MaMR CTLD4-8 antibody blocked the recognition of COS6 (**Figure 6A**), while the gene expression of TLR2 was not significantly changed (**Figure 6B**). The expression of MyD88, a downstream linker molecule of TLRs, was also significantly upregulated with TLR4 (**Figure 6C**). Normal mouse IgG was used as a negative control in the experiment. Similarly, at the level of protein expression, the expression of TLR4 was significantly upregulated after antibody blocking, while TLR2 did not change significantly (**Figure 6D**). To further investigate the signal transduction through TLR4-mediated signal pathway after COS6 activation in blunt snout bream macrophages, we used the TLR4 inhibitor TAK242 to block the intracellular TIR domain of TLR4 and block signal transmission. As shown in the figure,

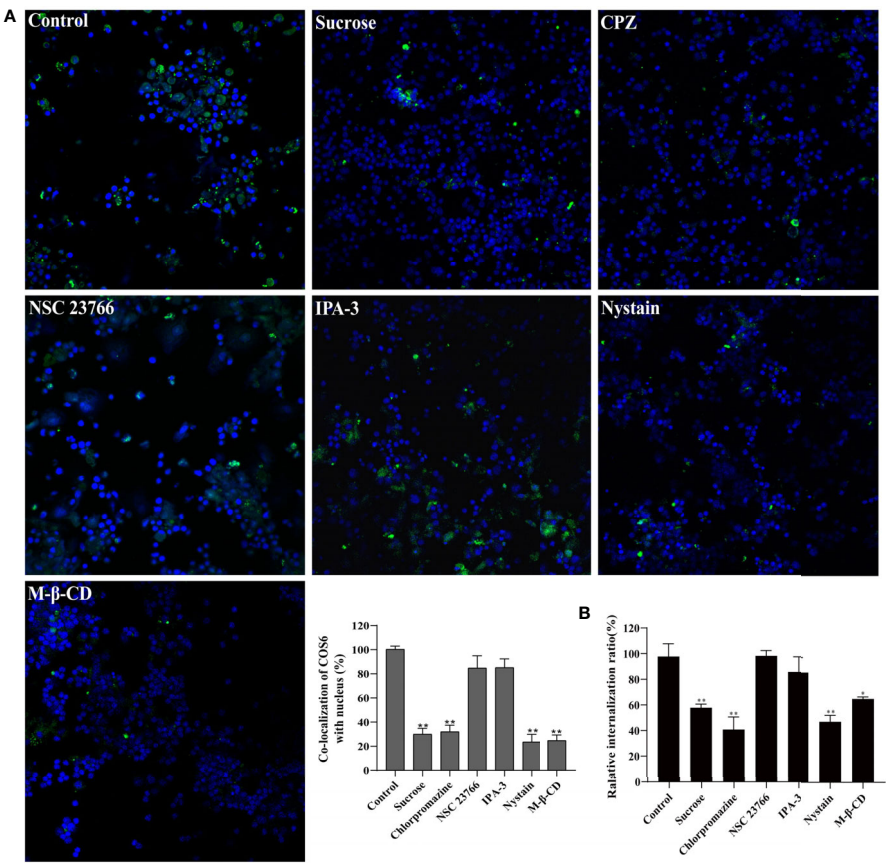

FIGURE 5 | Effect of endocytic pathway inhibitors on chitooligosaccharide hexamer (COS6) uptake by macrophages. **(A)** Pretreat cells with endocytosis inhibitors or absence (control) and observe the uptake of fluorescein isothiocyanate (FITC)-COS6 by macrophages under a confocal microscope. The co-localization percentage of FITC-COS6 and nucleus was analyzed using WCIF ImageJ software. **(B)** Cells were treated with endocytosis inhibitors and incubated with FITC-labeled COS6, washed, lysed, and mixed uniformly. Fluorescence intensity was measured. Data were shown as means ± SD (n = 3), with (*) $p < 0.05$ and (**) $p < 0.01$ *vs.* the control group (set as 100). Scale bar: 250 μm.

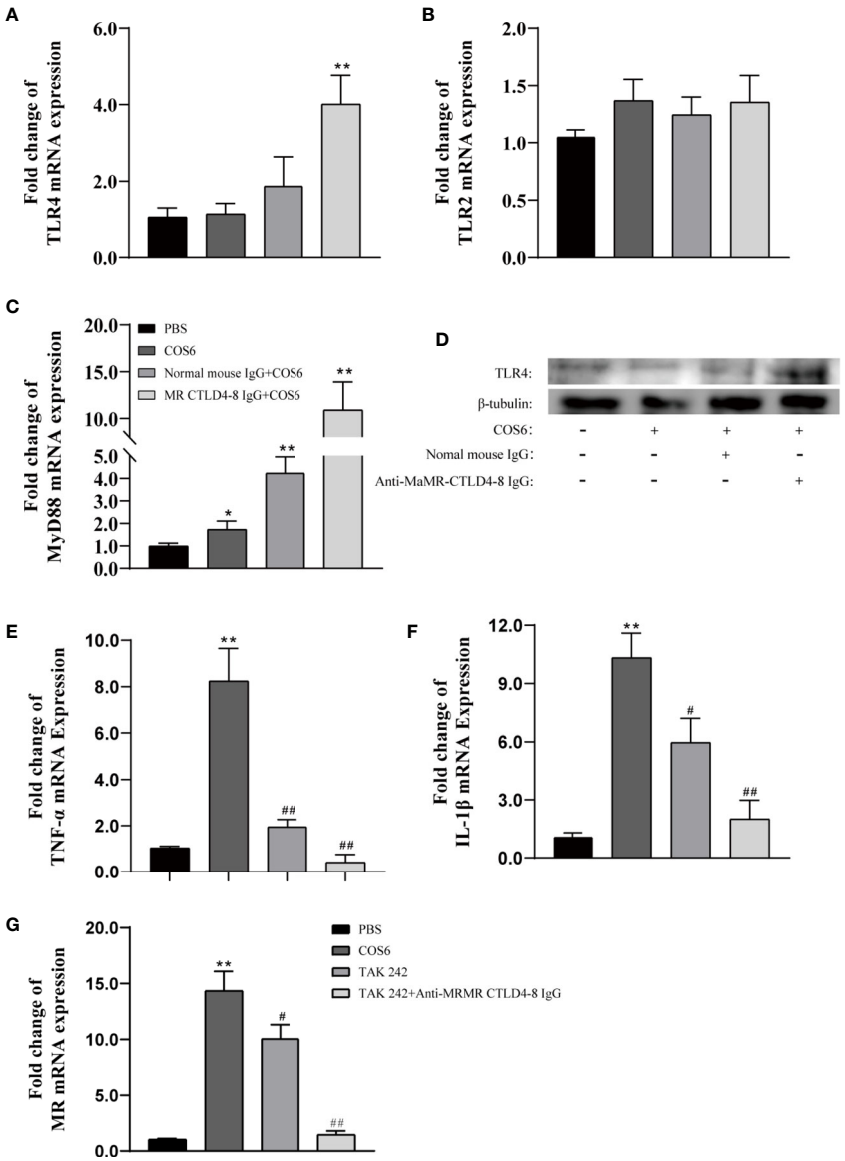

FIGURE 6 | The expression of Toll-like receptor (TLR)2/4, mannose receptor (MR), and inflammation-related genes in chitooligosaccharide hexamer (COS6)-stimulated macrophages with or without blocking. **(A)** TLR4, **(B)** TLR2, **(C)** MyD88, **(D)** Western blot analysis of TLR4 and TLR2, **(E)** tumor necrosis factor (TNF)-α, **(F)** interleukin (IL)-1β, **(G)** MR. Western blot analysis using anti-TLR4, anti-TLR2 antibodies, and anti-β-tubulin antibody was used to evaluate the quantity of proteins in each lane. TLR2 has no significant difference; the data are not shown. Each experiment was executed in triplicate. Data were shown as means ± SD (n = 3), with (*) $p < 0.05$ and (**) $p < 0.01$ *vs.* the phosphate buffered saline (PBS) group, ($^{\#}$) $p < 0.05$ and ($^{\#\#}$) $p < 0.01$ *vs.* the COS6 group (set as 1).

TAK242 significantly inhibited the inflammatory activation effect of COS6 on macrophages, and under the combined action of anti-MaMR CTLD4-8 and TAK242, the expression of TNF-α (**Figure 6E**) and IL-1β (**Figure 6F**) was significantly inhibited, and the expression level was reduced to the same level as that of the PBS group. Moreover, the expression of MR was also significantly inhibited by TAK242, and the expression level of MR was consistent with that of resting macrophages after both extracellular and intracellular signal recognition and transduction pathways were blocked (**Figure 6G**). These results indicated that MR and TLR4 were inseparable in COS6 activation of macrophages. Collectively, MR-mediated COS6-induced macrophage inflammation is regulated by the intracellular signal transduction pathway of TLR4. Previous studies have shown that COS6 activates macrophages through the MAPK/NF-κB pathway (24), suggesting that COS6 activates macrophages through the TLR4–MyD88–NF-κB signaling pathway, and is co-mediated by MR CTLD4-8 and TLR4.

DISCUSSION

Chitosan has become a popular adjuvant widely studied in aquaculture in recent years due to its nontoxic, biodegradable, good viscosity, and antimicrobial biological properties (26). In previous studies, we have confirmed that chitosan combined with IFN-γ can effectively activate grass carp (*Ctenopharyngodon idella*) macrophages (27) and is an aquatic adjuvant with excellent immune protection (28, 29). COS is an oligomer of chitosan. Compared with chitosan, it also has the characteristics of good water solubility and easy absorption. In mammals, COS is widely known to activate resting macrophages and has good immune effects in both pro-inflammatory and anti-inflammatory aspects (10, 15, 30). In previous studies, we have a certain understanding of the effect of COS on the immune activity of fish macrophages (24, 31), but the mechanism of COS on fish macrophages is still blank. As an important immune effector cell, macrophages can not only eliminate pathogens and presenting antigens but also release a large number of inflammation-related genes to participate in host defense and maintain tissue homeostasis (32). In recent years, the immunostimulating activity of COS *in vitro* has also been focused on macrophages. In this study, we used the head kidney macrophages of blunt snout bream as the experimental subject to demonstrate the important role of MR in COS6 activation of macrophages. We explored the recognition and binding ability of COS6 and MaMR CTLD4-8 at the molecular and cellular levels respectively and explored the internalization properties of COS6 in macrophages. Last but not least, the signal transduction pathway that COS6 activates macrophages has also been explained.

The most notable feature of MR is that a single peptide chain contains multiple CTLD domains. Among them, the CTLD4 domain can recognize specific carbohydrate components (mannose, fucose, N-acetylglucosamine, and other specific sugar residues), thereby binding to the carbohydrates containing these sugar residues mediates cellular immune regulation, for example, sugars on the surface of some pathogenic microorganisms (33, 34), allergens (35, 36), or polysaccharides of traditional Chinese medicine (TCM) (37, 38). However, CTLD4 requires two Ca^{2+} to be involved in the binding sugar ligand, and Ca^{2+} is related to the release of ligands from CTLD4 in the endosome. Although CTLD4 can bind monosaccharides alone, the binding of the entire receptor and ligand requires the participation of CTLD4-8 (39). N-acetylglucosamine is the smallest unit of COS, and CTLD4 of MR can specifically recognize and bind to the glucose residues of N-acetylglucosamine. However, N-acetylglucosamine has been shown to be unable to activate blunt snout bream macrophages in our previous studies (24). Our results showed that COS6 not only could activate the macrophages but also was specifically recognized and bound by MR CTLD4-8. The binding curve showed that the binding activity of COS6 and MR CTLD4-8 is almost the same as mannose, which was previously considered the best ligand. The binding of Ca^{2+} between MR and ligand in mammals is essential, and we have previously reported that MaMR CTLD4-8-mediated phagocytosis of bacteria is also Ca^{2+}-dependent (40). We think that MaMR CTLD4-8 also requires the participation of Ca^{2+} in the recognition and binding of COS6. In addition, as same as macrophages MR-targeted nanocarriers or vaccines in recent years (41), COS6 is a ligand that can specifically bind to MR and is an excellent immune enhancer. Nanocarriers or vaccines targeting macrophage MR with COS as the material are worthy of further development.

MR is a highly effective endocytic receptor, which mediates the macrophages to uptake a variety of pathogenic microorganisms or ligands. MR is targeted into cells expressing MR by interacting with specific ligands (42). There have been many reports on MR-mediated internalization of soluble antigens, and they are often complexes or nanoparticles that have been glycosylated or modified by MR-specific ligands (43–45). MR recycles constantly between the plasma membrane and the early endosome (46). It relies on an aromatic amino acid motif in the cytoplasmic tail to guide the ligand-bound MR from the endosome to the plasma membrane (47). And MR-ligand is thought to circulate between the cell membranes through the clathrin pathway (48). In our results, it showed that COS6 could be internalized by macrophages of blunt snout bream in a time- and temperature-dependent manner. This is similar to the situation in mammals, except that accumulation of COS6 at the nucleolus has not yet been observed (20). And in the flow cytometry analysis, the internalization of FITC-labeled COS6 in macrophages was significantly inhibited after antibody blocking, proving that MaMR CTLD4-8 plays a key role in the internalization of COS6 by macrophages. Different from the mammalian MR-mediated endocytosis that is dependent only on clathrin, the MaMR CTLD4-8-mediated COS6 internalization is dependent both on clathrin and caveolin. The caveolin in the plasma membrane is often used as a marker protein molecule for lipid rafts (49). It not only participates in the transport of materials across the membrane but also contains a variety of key signal molecules that participate in cell signal transduction (50). This also suggests that the immune regulation of COS6 on macrophages is closely related to lipid rafts. After COS6 is internalized with MR CTLD4-8, it may be sent to the lysosome (51) or through the endosome to the Golgi apparatus (52), and the ligand is degraded after separation, to fully exert the immune regulatory effect of COS6.

Most immunostimulants bind specifically to receptors on the cell surface to activate cellular immunity. MR (12, 20), TLR4 (11, 53), and CR3 (15) are thought to mediate the immunostimulatory effect of COS on macrophages. In addition, TLR2 is also believed to be involved in the immune regulation of chitin (COS is its oligomeric derivative) on macrophages (54). Our results showed that the activation of COS6 on macrophages of blunt snout bream was closely related to MaMR CTLD4-8, which could mediate the expression of inflammation-related genes in macrophages. However, the expression of inflammation-related genes was not completely suppressed under the blocking of antibodies. It suggested that other receptors may also be involved in mediating the immune activation of COS6 on macrophages. The cytoplasmic tail of MR is extremely short and has no signal transduction motif (55). Therefore, it participates in signal transduction for immune

regulation and requires the cooperation of other receptors. There have been many reports confirming that MR can coordinate with TLR2 or TLR4 to regulate the immune effect of cells in response to the stimulation of pathogenic microorganisms (25, 56, 57) or immune enhancers (38). Our results show that TLR4 is also involved in the MR-mediated immune response of macrophages to COS6. Combined with previous results (11), it is shown that the inflammatory response of COS-activated blunt snout bream macrophages involves MR and TLR4 and is regulated by the TLR4–MyD88–NF-κB signaling pathway. Although previously studied in human alveolar macrophages, *Pneumocystis* can promote the direct interaction of MR and TLR2, which leads to the release of IL-8 (56). However, we are still unclear about the interaction mechanism between the MR and TLR4. Lipid rafts serve as a platform for a variety of signal molecular interactions (58), and both pattern recognition receptors and lectin receptors in mammals are related to lipid rafts (59–61). Combining the previous results, lipid rafts may be the interaction and signal transduction platform for MR CTLD4-8 and TLR4.

In conclusion, this study explored the internalization mechanism and signal transduction pathway during the activation of blunt snout bream macrophages stimulated by COS6. The results showed that MaMR CTLD4-8 could specifically recognize and bind to COS6 and mediate COS6 into macrophages by both clathrin- and caveolin-dependent pathways, and MaMR coordinated with TLR4 to regulate the pro-inflammatory response of blunt snout bream macrophages. However, the interaction mechanism between MR and TLR4 remains elusive and needs to be further explored.

DATA AVAILABILITY STATEMENT

The original contributions presented in the study are included in the article/**Supplementary Material**. Further inquiries can be directed to the corresponding author.

ETHICS STATEMENT

The animal study was reviewed and approved by Ethics Committee of Huazhong Agricultural University.

AUTHOR CONTRIBUTIONS

XL and AO conceived and designed the experiments. AO and HW performed the experiments and analyzed the data. AO, XL, and JS wrote the manuscript. All authors contributed to the article and approved the submitted version.

FUNDING

This work was supported by the National Natural Science Foundation of China (31772879).

ACKNOWLEDGMENTS

The author would like to thank Mr. Yanqi Zhang, Ms. Jia Zeng, Mr. Huanxuan Li, and Ms. Huijie Chen for their technical support to the experiment and helpful discussion. We also thank Mr. Zhe Hu (State Key Laboratory of Agricultural Microbiology, Huazhong Agricultural University) for confocal microscopy.

SUPPLEMENTARY MATERIAL

The Supplementary Material for this article can be found online at: https://www.frontiersin.org/articles/10.3389/fimmu.2021.686846/full#supplementary-material

REFERENCES

1. Xia WS, Liu P, Zhang JL, Chen J. Biological Activities of Chitosan and Chitooligosaccharides. *Food Hydrocoll* (2011) 25:170–9. doi: 10.1016/j.foodhyd.2010.03.003
2. Zou P, Yang X, Wang J, Li YF, Yu HL, Zhang YX, et al. Advances in Characterisation and Biological Activities of Chitosan and Chitosan Oligosaccharides. *Food Chem* (2016) 190:1174–81. doi: 10.1016/j.foodchem.2015.06.076
3. Shun-Hsien C, Yi-Yung L, Guan-James W, Chung-Hsiung H, Guo Jane T. Effect of Chitosan Molecular Weight on Anti-Inflammatory Activity in the RAW 264.7 Macrophage Model. *Int J Biol Macromol* (2019) 131:167–75. doi: 10.1016/j.ijbiomac.2019.02.066
4. Naveed M, Phil L, Sohail M, Hasnat M, Baig M, Ihsan AU, et al. Chitosan Oligosaccharide (COS): An Overview. *Int J Biol Macromol* (2019) 129:827–43. doi: 10.1016/j.ijbiomac.2019.01.192
5. Pae HO, Seo WG, Kim NY, Oh GS, Kim GE, Kim YH, et al. Induction of Granulocytic Differentiation in Acute Promyelocytic Leukemia Cells (HL-60) by Water-Soluble Chitosan Oligomer. *Leukemia Res* (2001) 25:339–46. doi: 10.1016/s0145-2126(00)00138-7
6. Rahman MH, Hjeljord LG, Aam BB, Sorlie M, Tronsmo A. Antifungal Effect of Chito-Oligosaccharides With Different Degrees of Polymerization. *Eur J Plant Pathol* (2015) 141:147–58. doi: 10.1007/s10658-014-0533-3
7. Jeon YJ, Kim SK. Antitumor Activity of Chitosan Oligosaccharides Produced in Ultrafiltration Membrane Reactor System. *J Microbiol Biotechn* (2002) 12:503–7. doi: 10.1103/PhysRevB.56.2387
8. Seo WG, Pae HO, Kim NY, Oh GS, Park IS, Kim YH, et al. Synergistic Cooperation Between Water-Soluble Chitosan Oligomers and Interferon-Gamma for Induction of Nitric Oxide Synthesis and Tumoricidal Activity in Murine Peritoneal Macrophages. *Cancer Lett* (2000) 159:189–95. doi: 10.1016/s0304-3835(00)00551-6
9. Jeong HJ, Koo HN, Oh EY, Chae HJ, Kim HR, Suh SB, et al. Nitric Oxide Production by High Molecular Weight Water-Soluble Chitosan *via* Nuclear Factor-κb Activation. *Int J Immunopharmacol* (2000) 22:923–33. doi: 10.1016/s0192-0561(00)00055-2
10. Vasconcelos DP, Fonseca AC, Costa M, Amaral IF, Barbosa MA, Aguas AP, et al. Macrophage Polarization Following Chitosan Implantation. *Biomaterials* (2013) 34:9952–9. doi: 10.1016/j.biomaterials.2013.09.012
11. Zhang P, Liu WZ, Peng YF, Han BQ, Yang Y. Toll Like Receptor 4 (TLR4) Mediates the Stimulating Activities of Chitosan Oligosaccharide on Macrophages. *Int Immunopharmacol* (2014) 23:254–61. doi: 10.1016/j.intimp.2014.09.007
12. Feng J, Zhao LH, Yu QQ. Receptor-Mediated Stimulatory Effect of Oligochitosan in Macrophages. *Biochem Biophys Res Commun* (2004) 317:414–20. doi: 10.1016/j.bbrc.2004.03.048
13. Sanchez A, Mengibar M, Fernandez M, Alemany S, Heras A, Acosta N. Influence of Preparation Methods of Chitooligosaccharides on Their

Physicochemical Properties and Their Anti-Inflammatory Effects in Mice and in RAW264.7 Macrophages. *Mar Drugs* (2018) 16:13. doi: 10.3390/md16110430
14. Yu ZJ, Zhao LH, Ke HP. Potential Role of Nuclear Factor-κb in the Induction of Nitric Oxide Nd Tumor Necrosis Factor-α by Oligochitosan in Macrophages. *Int Immunopharmacol* (2004) 4:193–200. doi: 10.1016/j.intimp.2003.12.001
15. Wu GJ, Tsai GJ. Chitooligosaccharides in Combination With Interferon-γ Increase Nitric Oxide Production *via* Nuclear Factor-κb Activation in Murine RAW264.7 Macrophages. *Food Chem Toxicol* (2007) 45:250–8. doi: 10.1016/j.fct.2006.07.025
16. Yang Y, Xing RG, Liu S, Qin YK, Li KC, Yu HH, et al. Immunostimulatory Effects of Chitooligosaccharides on RAW 264.7 Mouse Macrophages *via* Regulation of the MAPK and PI3K/Akt Signaling Pathways. *Mar Drugs* (2019) 17:12. doi: 10.3390/md17010036
17. Yang Y, Xing RG, Liu S, Qin YK, Li KC, Yu HH, et al. Immunostimulatory Effects of Sulfated Chitosans on RAW 264.7 Mouse Macrophages *via* the Activation of PI3K/Akt Signaling Pathway. *Int J Biol Macromol* (2018) 108:1310–21. doi: 10.1016/j.ijbiomac.2017.11.042
18. Martinez-Pomares L. The Mannose Receptor. *J Leukoc Biol* (2012) 92:1177–86. doi: 10.1189/jlb.0512231
19. East L, Isacke CM. The Mannose Receptor Family. *Biochim Biophys Acta-Gen Subj* (2002) 1572:364–86. doi: 10.1016/s0304-4165(02)00319-7
20. Han YP, Zhao LH, Yu ZJ, Feng J, Yu QQ. Role of Mannose Receptor in Oligochitosan-Mediated Stimulation of Macrophage Function. *Int Immunopharmacol* (2005) 5:1533–42. doi: 10.1016/j.intimp.2005.04.015
21. Braunnesje R, Bertheussen K, Kaplan G, Seljelid R. Salmonid Macrophages: Separation, *In Vitro* Culture and Characterization. *J Fish Dis* (1981) 4:141–51. doi: 10.1111/j.1365-2761.1981.tb01118.x
22. Yu Y, Yu Y, Huang H, Feng K, Pan M, Yuan S, et al. A Short-Form C-Type Lectin From Amphioxus Acts as a Direct Microbial Killing Protein *via* Interaction With Peptidoglycan and Glucan. *J Immunol* (2007) 179:8425–34. doi: 10.4049/jimmunol.179.12.8425
23. Sui Z-h, Xu H, Wang H, Jiang S, Chi H, Sun L. Intracellular Trafficking Pathways of *Edwardsiella Tarda*: From Clathrin- and Caveolin-Mediated Endocytosis to Endosome and Lysosome. *Front Cell Infect Microbiol* (2017) 7:400. doi: 10.3389/fcimb.2017.00400
24. Wu CS, Dai YS, Yuan GL, Su JG, Liu XL. Immunomodulatory Effects and Induction of Apoptosis by Different Molecular Weight Chitosan Oligosaccharides in Head Kidney Macrophages From Blunt Snout Bream (*Megalobrama Amblycephala*). *Front Immunol* (2019) 10:869. doi: 10.3389/fimmu.2019.00869
25. Nakaira-Takahagi E, Golim MA, Bannwart CF, Puccia R, Peracoli MTS. Interactions Between TLR2, TLR4, and Mannose Receptors With Gp43 From *Paracoccidioides Brasiliensis* Induce Cytokine Production by Human Monocytes. *Med Mycol* (2011) 49:694–703. doi: 10.3109/13693786.2011.565485
26. Vinsova J, Vavrikova E. Chitosan Derivatives With Antimicrobial, Antitumour and Antioxidant Activities - a Review. *Curr Pharm Design* (2011) 17:3596–607. doi: 10.2174/138161211798194468
27. Chen T, Hu YZ, Zhou JC, Hu SB, Xiao X, Liu XL, et al. Chitosan Reduces the Protective Effects of IFN-γ 2 on Grass Carp (*Ctenopharyngodon Idella*) Against Flavobacterium Columnare Infection Due to Excessive Inflammation. *Fish Shellfish Immunol* (2019) 95:305–13. doi: 10.1016/j.fsi.2019.10.034
28. Zhang JC, Fu XZ, Zhang YQ, Zhu WT, Zhou Y, Yuan GL, et al. Chitosan and Anisodamine Improve the Immune Efficacy of Inactivated Infectious Spleen and Kidney Necrosis Virus Vaccine in Siniperca Chuatsi. *Fish Shellfish Immunol* (2019) 89:52–60. doi: 10.1016/j.fsi.2019.03.040
29. Zhu WT, Zhang YQ, Zhang JC, Yuan GL, Liu XL, Ai TS, et al. Astragalus Polysaccharides, Chitosan and Poly(I:C) Obviously Enhance Inactivated *Edwardsiella Ictaluri* Vaccine Potency in Yellow Catfish Pelteobagrus Fulvidraco. *Fish Shellfish Immunol* (2019) 87:379–85. doi: 10.1016/j.fsi.2019.01.033
30. Fernandes JC, Spindola H, de Sousa V, Santos-Silva A, Pintado ME, Malcata FX, et al. Anti-Inflammatory Activity of Chitooligosaccharides. *Vivo Mar Drugs* (2010) 8:1763–8. doi: 10.3390/md8061763
31. Liu L, Zhou Y, Zhao X, Wang H, Wang L, Yuan G, et al. Oligochitosan Stimulated Phagocytic Activity of Macrophages From Blunt Snout Bream (*Megalobrama Amblycephala*) Associated With Respiratory Burst Coupled With Nitric Oxide Production. *Dev Comp Immunol* (2014) 47:17–24. doi: 10.1016/j.dci.2014.06.005
32. Okabe Y, Medzhitov R. Tissue Biology Perspective on Macrophages. *Nat Immunol* (2016) 17:9–17. doi: 10.1038/ni.3320
33. Paveley RA, Aynsley SA, Turner JD, Bourke CD, Jenkins SJ, Cook PC, et al. The Mannose Receptor (CD206) is an Important Pattern Recognition Receptor (PRR) in the Detection of the Infective Stage of the Helminth *Schistosoma Mansoni* and Modulates Ifnγ Production. *Int J Parasitol* (2011) 41:1335–45. doi: 10.1016/j.ijpara.2011.08.005
34. Kang PB, Azad AK, Torrelles JB, Kaufman TM, Beharka A, Tibesar E, et al. The Human Macrophage Mannose Receptor Directs *Mycobacterium Tuberculosis* Lipoarabinomannan-Mediated Phagosome Biogenesis. *J Exp Med* (2005) 202:987–99. doi: 10.1084/jem.20051239
35. Emara M, Royer P-J, Abbas Z, Sewell HF, Mohamed GG, Singh S, et al. Recognition of the Major Cat Allergen Fel D 1 Through the Cysteine-Rich Domain of the Mannose Receptor Determines its Allergenicity. *J Biol Chem* (2011) 286:13033–40. doi: 10.1074/jbc.M111.220657
36. Royer P-J, Emara M, Yang C, Al-Ghouleh A, Tighe P, Jones N, et al. The Mannose Receptor Mediates the Uptake of Diverse Native Allergens by Dendritic Cells and Determines Allergen-Induced T Cell Polarization Through Modulation of IDO Activity. *J Immunol* (2010) 185:1522–31. doi: 10.4049/jimmunol.1000774
37. Liu L, Guo ZJ, Lv ZG, Sun Y, Cao W, Zhang R, et al. The Beneficial Effect of *Rheum Tanguticum* Polysaccharide on Protecting Against Diarrhea, Colonic Inflammation and Ulceration in Rats With TNBS-Induced Colitis: The Role of Macrophage Mannose Receptor in Inflammation and Immune Response. *Int Immunopharmacol* (2008) 8:1481–92. doi: 10.1016/j.intimp.2008.04.013
38. Li WJ, Tang XF, Shuai XX, Jiang CJ, Liu X, Wang LF, et al. Mannose Receptor Mediates the Immune Response to *Ganoderma Atrum* Polysaccharides in Macrophages. *J Agric Food Chem* (2017) 65:348–57. doi: 10.1021/acs.jafc.6b04888
39. Taylor ME, Bezouska K, Drickamer K. Contribution to Ligand Binding by Multiple Carbohydrate-Recognition Domains in the Macrophage Mannose Receptor. *J Biol Chem* (1992) 267:1719–26. doi: 10.1016/0014-5793(92)80312-5
40. Zhao X, Liu L, Hegazy AM, Wang H, Li J, Zheng F, et al. Mannose Receptor Mediated Phagocytosis of Bacteria in Macrophages of Blunt Snout Bream (*Megalobrama Amblycephala*) in a Ca^{2+}-Dependent Manner. *Fish Shellfish Immunol* (2015) 43:357–63. doi: 10.1016/j.fsi.2015.01.002
41. Irache JM, Salman HH, Gamazo C, Espuelas S. Mannose-Targeted Systems for the Delivery of Therapeutics. *Expert Opin Drug Del* (2008) 5:703–24. doi: 10.1517/17425247.5.6.703
42. Taylor PR, Gordon S, Martinez-Pomares L. The Mannose Receptor: Linking Homeostasis and Immunity Through Sugar Recognition. *Trends Immunol* (2005) 26:104–10. doi: 10.1016/j.it.2004.12.001
43. Burgdorf S, Lukacs-Kornek V, Kurts C. The Mannose Receptor Mediates Uptake of Soluble But Not of Cell-Associated Antigen for Cross-Presentation. *J Immunol* (2006) 176:6770–6. doi: 10.4049/jimmunol.176.11.6770
44. Gage E, Hernandez MO, O'Hara JM, McCarthy EA, Mantis NJ. Role of the Mannose Receptor (CD206) in Innate Immunity to Ricin Toxin. *Toxins* (2011) 3:1131–45. doi: 10.3390/toxins3091131
45. Shibaguchi K, Tamura A, Terauchi M, Matsumura M, Miura H, Yui N. Mannosylated Polyrotaxanes for Increasing Cellular Uptake Efficiency in Macrophages Through Receptor-Mediated Endocytosis. *Molecules* (2019) 24:439. doi: 10.3390/molecules24030439
46. Gazi U, Martinez-Pomares L. Influence of the Mannose Receptor in Host Immune Responses. *Immunobiology* (2009) 214:554–61. doi: 10.1016/j.imbio.2008.11.004
47. Schweizer A, Stahl PD, Rohrer J. A Di-Aromatic Motif in the Cytosolic Tail of the Mannose Receptor Mediates Endosomal Sorting. *J Biol Chem* (2000) 275:29694–700. doi: 10.1074/jbc.M000571200
48. Shrivastava R, Shukla N. Attributes of Alternatively Activated (M2) Macrophages. *Life Sci* (2019) 224:222–31. doi: 10.1016/j.lfs.2019.03.062
49. Anderson RG. The Caveolae Membrane System. *Annu Rev Biochem* (1998) 67:199–225. doi: 10.1146/annurev.biochem.67.1.199
50. Head BP, Patel HH, Insel PA. Interaction of Membrane/Lipid Rafts With the Cytoskeleton: Impact on Signaling and Function: Membrane/Lipid Rafts,

Mediators of Cytoskeletal Arrangement and Cell Signaling. *Biochim Biophys Acta* (2014) 1838:532–45. doi: 10.1016/j.bbamem.2013.07.018
51. Bourbouze R, Raffi F, Dameron G, Halimiraftab H, Loko F, Vilde JL. N-Acetyl-β-D-Glucosaminidase (NAG) Isoenzymes Release From Human Monocyte-Derived Macrophages in Response to Zymosan and Human Recombinant Interferon-γ. *Clin Chim Acta* (1991) 199:185–94. doi: 10.1016/0009-8981(91)90110-x
52. Ozment TR, Goldman MP, Kalbfleisch JH, Williams DL. Soluble Glucan is Internalized and Trafficked to the Golgi Apparatus in Macrophages *via* a Clathrin-Mediated, Lipid Raft-Regulated Mechanism. *J Pharmacol Exp Ther* (2012) 342:808–15. doi: 10.1124/jpet.112.196329
53. Dang Y, Li S, Wang W, Wang S, Zou M, Guo Y, et al. The Effects of Chitosan Oligosaccharide on the Activation of Murine Spleen $CD11c^+$ Dendritic Cells *via* Toll-Like Receptor 4. *Carbohydr Polym* (2011) 83:1075–81. doi: 10.1016/j.carbpol.2010.08.071
54. Da Silva CA, Chalouni C, Williams A, Hartl D, Lee CG, Elias JA. Chitin is a Size-Dependent Regulator of Macrophage TNF and IL-10 Production. *J Immunol* (2009) 182:3573–82. doi: 10.4049/jimmunol.0802113
55. Liu XL, Tang XC, Wang L, Li J, Wang H, Wei S, et al. Molecular Cloning and Expression Analysis of Mannose Receptor in Blunt Snout Bream (*Megalobrama Amblycephala*). *Mol Biol Rep* (2014) 41:4601–11. doi: 10.1007/s11033-014-3331-2
56. Tachado SD, Zhang J, Zhu J, Patel N, Cushion M, Koziel H. Pneumocystis-Mediated IL-8 Release by Macrophages Requires Coexpression of Mannose Receptors and TLR2. *J Leukoc Biol* (2007) 81:205–11. doi: 10.1189/jlb.1005580
57. Xaplanteri P, Lagoumintzis G, Dimitracopoulos G, Paliogianni F. Synergistic Regulation of *Pseudomonas Aeruginosa*-Induced Cytokine Production in Human Monocytes by Mannose Receptor and TLR2. *Eur J Immunol* (2009) 39:730–40. doi: 10.1002/eji.200838872
58. Li CL, Lu N, Qi Q, Li FN, Ling Y, Chen Y, et al. Gambogic Acid Inhibits Tumor Cell Adhesion by Suppressing Integrin β1 and Membrane Lipid Rafts-Associated Integrin Signaling Pathway. *Biochem Pharmacol* (2011) 82:1873–83. doi: 10.1016/j.bcp.2011.09.013
59. Kim S, Watarai M, Suzuki H, Makino S, Kodama T, Shirahata T. Lipid Raft Microdomains Mediate Class A Scavenger Receptor-Dependent Infection of *Brucella Abortus*. *Microb Pathog* (2004) 37:11–9. doi: 10.1016/j.micpath.2004.04.002
60. Li Y, Guan J, Wang W, Hou C, Zhou L, Ma J, et al. TRAF3-Interacting JNK-Activating Modulator Promotes Inflammation by Stimulating Translocation of Toll-Like Receptor 4 to Lipid Rafts. *J Biol Chem* (2019) 294:2744–56. doi: 10.1074/jbc.RA118.003137
61. Szöor A, Szöllosi J, Vereb G. Rafts and the Battleships of Defense: The Multifaceted Microdomains for Positive and Negative Signals in Immune Cells. *Immunol Lett* (2010) 130:2–12. doi: 10.1016/j.imlet.2009.12.016

Conflict of Interest: The authors declare that the research was conducted in the absence of any commercial or financial relationships that could be construed as a potential conflict of interest.

Publisher's Note: All claims expressed in this article are solely those of the authors and do not necessarily represent those of their affiliated organizations, or those of the publisher, the editors and the reviewers. Any product that may be evaluated in this article, or claim that may be made by its manufacturer, is not guaranteed or endorsed by the publisher.

frontiers in Immunology

ORIGINAL RESEARCH
published: 17 August 2021
doi: 10.3389/fimmu.2021.729820

Targeting the Microtubule-Network Rescues CTL Killing Efficiency in Dense 3D Matrices

*Renping Zhao[1], Xiangda Zhou[1], Essak S. Khan[2], Dalia Alansary[3], Kim S. Friedmann[1], Wenjuan Yang[1], Eva C. Schwarz[1], Aránzazu del Campo[2], Markus Hoth[1] and Bin Qu[1,2]**

[1] Biophysics, Center for Integrative Physiology and Molecular Medicine (CIPMM), School of Medicine, Saarland University, Homburg, Germany, [2] INM-Leibniz Institute for New Materials, Saarbrücken, Germany, [3] Molecular Biophysics, CIPMM, School of Medicine, Saarland University, Homburg, Germany

Efficacy of cytotoxic T lymphocyte (CTL)-based immunotherapy is still unsatisfactory against solid tumors, which are frequently characterized by condensed extracellular matrix. Here, using a unique 3D killing assay, we identify that the killing efficiency of primary human CTLs is substantially impaired in dense collagen matrices. Although the expression of cytotoxic proteins in CTLs remained intact in dense collagen, CTL motility was largely compromised. Using light-sheet microscopy, we found that persistence and velocity of CTL migration was influenced by the stiffness and porosity of the 3D matrix. Notably, 3D CTL velocity was strongly correlated with their nuclear deformability, which was enhanced by disruption of the microtubule network especially in dense matrices. Concomitantly, CTL migration, search efficiency, and killing efficiency in dense collagen were significantly increased in microtubule-perturbed CTLs. In addition, the chemotherapeutically used microtubule inhibitor vinblastine drastically enhanced CTL killing efficiency in dense collagen. Together, our findings suggest targeting the microtubule network as a promising strategy to enhance efficacy of CTL-based immunotherapy against solid tumors, especially stiff solid tumors.

Keywords: CTLs, collagen, dense matrices, microtubules, migration, nuclear deformation, 3D killing

OPEN ACCESS

Edited by:
Li Tang,
École Polytechnique Fédérale de Lausanne, Switzerland

Reviewed by:
Shi Jiao,
Fudan University, China
Yugang Guo,
École Polytechnique Fédérale de Lausanne, Switzerland

***Correspondence:**
Bin Qu
bin.qu@uks.eu

Specialty section:
This article was submitted to T Cell Biology, a section of the journal Frontiers in Immunology

Received: *23 June 2021*
Accepted: *31 July 2021*
Published: *17 August 2021*

Citation:
Zhao R, Zhou X, Khan ES, Alansary D, Friedmann KS, Yang W, Schwarz EC, del Campo A, Hoth M and Qu B (2021) Targeting the Microtubule-Network Rescues CTL Killing Efficiency in Dense 3D Matrices. Front. Immunol. 12:729820. doi: 10.3389/fimmu.2021.729820

INTRODUCTION

Cytotoxic T lymphocytes (CTLs), which are activated $CD8^+$ T cells, compose an essential arm of the immune system to fight aberrant cells like tumorigenic and pathogen-infected cells (1, 2). CTLs recognize their targets *via* engagement of T cell receptors (TCRs) with the cognate antigens presented on the surface of target cells (3–5). Once the matching antigens are identified, activation of TCRs triggers the downstream signaling cascades to re-orientate the CTL killing machinery towards the contact site, termed immunological synapse (IS) (6–8). The major killing mechanisms employed by CTLs are lytic granules (LGs) and Fas/FasL pathway (9). LGs contain cytotoxic proteins such as pore-forming protein perforin and serine-protease granzymes (10). Upon target recognition, LGs are enriched at the IS and are eventually released into the synaptic cleft to induce destruction of target cells (11, 12). In order to locate their targets, CTLs need to migrate through peripheral tissues across the three-dimensional (3D) extracellular matrix (ECM).

The ECM is a 3D network of fibrous structural proteins, collagen being the major constituent (13). The ECM of solid tumors is often densified, creating a physical hindrance that impairs infiltration of CTLs, accompanied with diminished killing efficiency (14, 15). Proliferation of T cells is also reduced in a high-density matrix (16). Using an elegant 2.5 D engineered platforms with grooves, a recent study shows that the dynamics of microtubule plays an important role in migration of primary human $CD4^+$ T cells, and this tendency is verified with mouse $CD8^+$ T cells (17). However, the impact of dense ECM on killing efficiency of CTLs *per se* still remains largely uncharacterized.

The cytoskeleton, including actin and the microtubule network, plays a pivotal role in regulating migration of $CD8^+$ T cells (18, 19). During migration, T cells generate protrusions at the leading edge, which are mainly driven by polymerization of actin (20). The myosin-mediated contraction of F-actin generates force to retract the uropod, the rear part of the cell, and enables T cells to move forward (21). In T cells, myosin IIA is the predominantly expressed member of the myosin family (20). Blockage of myosin IIA activity results in deficiency of uropod retraction and therefore significantly impairs T cell migration (21). During T cell migration, the microtubule-organizing center (MTOC) is located at the uropod (22). Abrogation of microtubule polymerization does not hinder T cell migration (23).

Nuclear deformability serves as a rate limiting factor of cell migration through physical restricted 3D spaces (24, 25). To pass the restricted space between pillars, or narrow channel, the nucleus has to be deformed by force from cytoskeleton to fit the size of space (24, 26, 27), which also facilitates cell migration along the path of least resistance in a complex environment (25). Further reports showed that the nucleus shape and its shape changes are correlated with the velocity of cell migration (28, 29).

In this work, we investigated CTL-mediated cytotoxicity against tumor cells in collagen matrices of different densities that mimic physiological and pathological microenvironments. We confirmed that CTL killing efficiency was substantially reduced in dense collagen matrices. Although the killing machinery *per se* remained intact, migration of CTLs was significantly impaired. Migrating CTLs in dense matrices exhibit deformed nuclei, the extent of which correlated with migration velocity, indicating that flexibility of CTL nuclei is pivotal to CTL migration in 3D. We found that nuclei flexibility is regulated by the microtubule networks. Importantly, disruption of microtubule but not actin polymerization can rescue the impaired migration as well as the reduced cytotoxic efficiency of CTLs in dense collagen matrices.

MATERIALS AND METHODS

Antibodies and Reagents

All chemicals not specifically mentioned are from Sigma-Aldrich (highest grade). All inhibitors not specifically mentioned are from Cayman Chemical. The following antibodies were used: Alexa Fluor 647 anti-human CD3 antibody (UCHT1, BioLegend), Alexa Fluor 488 anti-human Granzyme A antibody (CB9, BioLegend), Alexa Fluor 647 or Brilliant Violet (BV) 510 anti-human perforin antibody (dG9, BioLegend), Alexa Fluor 647 anti-human granzyme B antibody (GB11, BioLegend), Brilliant Violet (BV) 421 anti-human CD178 (Fas-L), anti α-Tubulin mAb antibody (DM1A, Cell Signaling Technology), and Alexa Fluor 405 conjugated goat anti-mouse IgG (H+L) cross-absorbed secondary antibody (ThermoFisher Scientific). All isotype controls of fluorescence conjugated primary antibodies are from BioLegend. The following reagents were used: Hoechst 33342 (ThermoFisher Scientific), Alexa Fluor 488 or Alexa Fluor 568 phalloidin (ThermoFisher Scientific), Atto 488 NHS ester ((ThermoFisher Scientific), collagenase type I (ThermoFisher Scientific), FibriCol® type I collagen Solution (Bovine, Advanced Biomatrix).

DNA Constructs

For pGK-puro-pCasper-pMax (referred to as pCasper-pMax in the manuscript), the vector backbone used for generation of this plasmid is a kind gift from Ulrich Wissenbach (Saarland University) who previously modified the AMAXA vector (Lonza) by replacing the sequence encoding GFP with a linker sequence encoding a multiple cloning site (pMAX). In a first step, the sequence encoding pCasper was amplified from pCasper3-GR (evrogen #FP971) with the following primers introducing an XhoI recognition site at both ends of the amplicon. Forward primer: 5'-CTCGAGGCCACCATGGTG AGCGAG -3', reverse primer: rev 5'-GACGAGCTGTACCG CTGACTCGAG-3'. The amplicon was subcloned into the XhoI site of pMAX. In a second step, the sequence encoding puromycin resistance was introduced into the intermediate plasmid under the control of 3-phosphoglycerate kinase promoter (PGK-1). The PGK-1-Puromycin sequence was amplified out of pGK-Puro-MO70 vector backbone (Alansary et al., BBA 2015) using the following primers introducing SacI recognition sites at both ends of the amplicon to insert it into the Sac-I site of the intermediate plasmid. Forward primer: 5'-GAGCTCAATTCTACCGGGTAGGGGA-3', reverse primer 5'-GCAAGCCCGGTGCCTGAGAGCTC-3'. The final plasmid is named pGK-puro-pCasper-pMAX. Final and intermediate plasmids were controlled by endonuclease digestion patterns and sequencing. As a gift from William Bement (Addgene plasmid # 26741). Histone 2B-GFP was a gift from Geoff Wahl (Addgene plasmid # 11680). LifeAct-mRuby was a kind gift from Roland Wedlich-Söldner (University of Muenster). pmEGFP_a_tubulin_C1 was a gift from Daniel Gerlich (Addgene plasmid # 21039). pmCherry-C1 mCherry-NLS was a gift from Dyche Mullins (Addgene plasmid # 58476).

CTL Preparation, Cell Culture, and Nucleofection

Peripheral blood mononuclear cells (PBMCs) were obtained from healthy donors as described before (30). Briefly, leukocyte reduction chambers were flushed with Hank's Balanced Salt Solution and loaded on a standard density gradient Leukocyte separation medium (LSM 1077, PAA). PBMCs were isolated by a

density gradient centrifugation (450 g, 30 min), and remaining red blood cells were removed by the lysis buffer (155 mM NH_4Cl, 10 mM $KHCO_3$, 0.1 mM EDTA, pH=7.3). Human primary $CD8^+$ T Cells were negatively isolated from PBMCs using Dynabeads™ Untouched™ Human CD8 T Cells Kit (ThermoFisher Scientific) or Human $CD8^+$ T Cell Isolation Kit (Miltenyi Biotec), stimulated with Dynabeads™ Human T-Activator CD3/CD28 (ThermoFisher Scientific) with 17 ng/ml of recombinant human IL-2 (ThermoFisher Scientific). MART-1-specific $CD8^+$ T-cell clones were generated by Friedmann et al. (31). All $CD8^+$ T cells were cultured in AIM V medium (ThermoFisher Scientific) containing 10% fetal calf serum (FCS) and 1% Penicillin-Streptomycin. For nucleofection, CD3/CD28 beads were removed 48 hours after stimulation and 5×10^6 CTLs were electroporated with 2 µg plasmid using 4D-Nucleofector (Lonza). Medium was changed 6 hours after nucleofection and transfected cells were used 24-36 hours after electroporation.

Raji and NALM-6 cells were cultured in RPMI-1640 medium (ThermoFisher Scientific) containing 10% FCS and 1% Penicillin-Streptomycin. NALM-6 pCasper cells were generated by Knörck et al. (32) and were cultured in RPMI-1640 in the presence of puromycin (0.2 µg/ml). SK-Mel-5 cells were transfected with pCasper-pMax using jetOPTIMUS® DNA Transfection Reagent (Polyplus-transfection) following the manufacturer's instructions and then cultured in MEM medium (ThermoFisher Scientific) containing 10% FCS and 1% penicillin-streptomycin. All cells were cultured at 37°C with 5% CO_2.

Preparation of Collagen Matrix and Cell Embedding

Collagen hydrogels were prepared following previous protocols (33). Briefly, bovine collagen type I stock solution (10 mg/ml) was neutralized with 0.1 N NaOH solution on ice to reach pH 7.0-7.4. 10×PBS was added into the neutralized collagen to a dilution factor of 1:10. The collagen solution was further diluted with PBS to the final concentrations. Cells were resuspended in the collagen solution and the mixture was left for 1 hour at 37°C with 5% CO_2 (if not mentioned otherwise) for fibrillation in 96-well plates. In order to increase the stiffness of the collagen matrix, the collagen stock solution was first diluted to a concentration of 3 mg/ml with 0.1% acetic acid with 100 mM ribose (34). These collagen solutions were kept at 4°C for 5 days, and then used for cell encapsulation as described before.

Killing Assay in 3D With the High-Content Imaging Setup

For killing assays, we used either NALM-6 cells stably expressing apoptosis reporter pCasper-pMax or SK-Mel-5 cells transiently transfected with pCasper-pMax (referred to as NALM-6-pCasper or SK-Mel-5-pCasper, respectively) as target cells. NALM-6-pCasper were pulsed with staphylococcal enterotoxin A (SEA, 0.1 µg/ml) and SEB (0.1 µg/ml) at 37°C with 5% CO_2 for 40 min prior to killing assays. Target cells were resuspended in chilled collagen solution, and transferred in 96-well plates. After centrifugation at 4°C (200 g, 7.5 min), collagen was solidified in the incubator for 1 hour. CTLs were then added from the top if not mentioned otherwise. For the inhibitor-treatment, CTLs were added on top of solidified collagen in medium containing the corresponding inhibitor or vehicle. The effector to target (E:T) ratio for pre-mixed condition is 1:1. For the condition that CTLs were added on top of the collagen, the E:T ratio is 5:1 or 1:1 for CTL : NALM-6-pCasper and MART1 specific CTLs: SK-Mel-5-pCasper, respectively.

Images were acquired by ImageXpress (Molecular Devices) with Spectra X LED illumination (Lumencor) at 37°C with 5% CO_2 for 12 to 24 hours. As described previously (35), fluorescence of pCasper-pMax was acquired using LEDs 470/24 for excitation and the following filter sets (Semrock): Ex 472/30 nm, Em 520/35 nm for GFP and Em 641/75 nm for RFP/FRET. A 20× S Fluor 0.75 numerical aperture objective (Nikon) was used. The killing efficiency was calculated as $(1\text{-}N_{exp}(t)/(N_{exp}(t_0)\times N_{live}(t)/N_{live}(t_0))\times 100\%$.

(N_{live}: number of live target cells in the control wells without CTLs; N_{exp}: number of live target cells in the experimental wells; t_0: the first time point of the measurement; t: end time point of the measurement).

Immunostaining and Flow Cytometry

CTLs were fixed with pre-chilled 4% paraformaldehyde (PFA) after recovery from collagen degraded with collagenase. Then cells were washed twice with PBS/0.5% BSA, permeabilized and blocked with 0.1% saponin in PBS containing 5% FCS and 0.5% BSA, and then stained with the indicated primary antibody or Alexa Fluor 488 Phalloidin for 30 min at room temperature followed by staining of Alexa Fluor 405 labeled secondary antibody if the primary antibody was not fluorophore-conjugated. Flow cytometry data were acquired using a FACSVerse™ flow cytometer (BD Biosciences) and were analyzed with FlowJo v10 (FLOWJO, LLC).

3D Live-Cell Imaging Using Light-Sheet Microscopy

As described previously (33), collagen with 10×10^6 CTLs/ml polymerized in the capillary at 37°C with 5% CO_2 for 2 hours. Afterwards, the samples were scanned with light-sheet microscopy Z1 (Zeiss) at 37°C for 30 min with an interval of 30 sec and a z-step size of 1 µm. A 20× objective (W Plan-Apochromat, N.A. 1.0) was used. Excitation was realized by two lasers, 488 and 561 nm. Emission was filtered *via* Em525/40nm and Em 585 LP filters. The images were acquired with ZEN 2014 SP1 Hotfix 2 software. Trajectories of CTLs and nuclear irregularity index (NII) were determined and analyzed with Imaris 8.1.2 (containing Imaris, ImarisTrack, ImarisMeasurementPro, ImarisVantage from Bitplane AG). The nuclei or the cell bodies were detected automatically by ImageJ/Fiji based on the corresponding fluorescence, and parameters (circularity and Feret's diameter) were analyzed with ImageJ/Fiji. Nucleus deformability is the average of nucleus sphericity change between two neighbor time points.

Visualization of CTL Migration in a Planar 3D Collagen Matrix With Zeiss Observer Z.1

CTLs (5×10^6 cells/ml) were resuspended in collagen solution with or without Calcein labeled target cells (5×10^6 cells/ml). Cell/collagen mixture (3 µl) was pipetted as a droplet onto the center of an Ibidi µ-dish (Ibidi GmbH). Then a Sigmacote® (Merck) coated glass coverslip (5 mm, Orsatec GmbH) was carefully placed on top to flatten the droplet (calculated thickness around 150 µm). The Ibidi µ-dish was closed with the lid and incubated at 37°C with 5% CO_2 for 1 hour. After collagen polymerization, the glass coverslip was removed from collagen matrix. For migration assay, CTLs were either non-fluorescent (in presence with target cells) or stained with 1 µg/ml Hoechst 33342 in AIMV (10% FCS) medium for 30 min (without target cells), and then were incubated in fresh AIMV (10% FCS) medium for another 30 min in presence of inhibitors or vehicles as indicated in the figure legends. Raji cells and unlabeled CTLs were mixed. The images were acquired with Zeiss Observer Z.1 for 30 min or 3 hours at 37°C with 5% CO_2 with a Zeiss Colibri LED illumination system and 20× objectives (Fluar 20×/0.75 M27 Air). Images were taken using an AxioCamM1 CCD camera and AxioVision 4.1.8. The images of cell migration and nuclear irregularity index (NII, measured as nuclear circularity) were analyzed using Imaris 8.1.2. Migration trajectories in presence of target cells were analyzed by Fiji. Nuclear deformationability is defined as standard deviation of NII. To quantify CTL search efficiency, CTLs were randomly selected from the CTLs that were observed for the whole period. The probability for CTLs finding at least one target within 3 hours was quantified. From these CTLs, the time of CTL contacting the first target cells was quantified, if this CTL could find at least one target cell within 3 hours. Nucleus deformability is the average of nucleus circularity change between two neighbor time points.

Confocal Microscopy and Determination of Nuclear Deformation

For the fixed sample, CTLs were fixed at indicated time points with 4% PFA and permeabilized with 0.3% Triton-100 with 5% FCS in PBS, followed by staining with indicated antibodies or fluorescent dyes according to the manufacturers' instructions. Images were acquired by confocal microscopy LSM 710 with a 63× objective (N.A. 1.4) and a Nikon E600 camera using ZEN software. The nuclear irregularity index (NII, measured as nuclear circularity from maximum intensity projection) was analyzed with ImageJ. The distance between nucleus and MTOC was analyzed with Imaris 9.6.

Visualization of Collagen Structure and Determination of Porosity

After collagen polymerization in the capillary, collagen was stained with Atto 488 NHS ester in PBS (50 µM) at room temperature for 15 min. Afterwards, the collagen matrix was washed by PBS twice. Matrix structure of collagen was visualized by light-sheet microscopy with a 20× objective (W Plan-Apochromat, N.A. 1.0). Collagen pore size was measured in the middle slice of the z-stack by Fiji (BIOP version) with Max Inscribed Circles plugin as described elsewhere (36).

Shear Rheology Stiffness Measurement

Rheology measurements with different concentrations of bovine collagen were performed using DHRIII Rheometer (TA Instruments). 50 µl of the neutralized collagen solution (pH 7.0-7.4) was placed between two parallel plates of 12 mm diameter pre-heated to either 25°C or 37°C. The shear moduli were measured at frequency ω – 3 rad/s at 37°C as described previously (37). All experiments were performed in triplicates.

Viability Assay

CTLs were embedded in 5 mg/ml collagen in a 96-well plate. After collagen polymerization, 100 µl AIMV medium with 10% FCS, 1 µg/ml propidium iodide, and nocodazole or DMSO was added. Images were acquired by ImageXpress with Spectra X LED illumination (Lumencor) using LEDs 542/27 for excitation. The filter set was Ex 542/27 nm and Em 641/75 nm. A 20× S Fluor 0.75 numerical aperture objective (Nikon) was used. The images were acquired at 37°C with 5% CO_2 every 1 h for 12 h.

Ethical Considerations

Research carried out for this study with healthy donor material (leukocyte reduction system chambers from human blood donors) is authorized by the local ethic committee [declaration from 16.4.2015 (84/15; Prof. Dr. Rettig-Stürmer)].

Statistical Analysis

Data are presented as mean ± SD. GraphPad Prism 6 Software (San Diego, CA, USA) was used for statistical analysis. If the number of data points is smaller than 8, the differences between two columns were analyzed by the Student's t-test. Otherwise, the data were first examined for Gaussian distribution. If the dataset fit Gaussian distribution, the differences between two columns ware analyzed with the Student's t-test, otherwise with the Mann-Whitney test.

RESULTS

CTL Killing Efficiency and Motility Is Substantially Impaired in Dense Collagen

To investigate the impact of collagen density on the killing efficiency of CTLs, we used collagen matrices prepared at three different collagen concentrations (2, 4, and 5 mg/ml). Primary human $CD8^+$ T cells were stimulated with anti-CD3/anti-CD28 antibody-coated beads to obtain CTLs. Target cells (NALM-6-pCasper) were embedded in the collagen matrices and CTLs were settled on top of the gels, as depicted in **Figure 1A** (schematic diagram). Target cells stably expressing apoptosis reporter pCasper-pMax, a GFP-RFP FRET pair linked by a sequence containing caspase recognition site (DEVD), allowing the detection of cell death (32). Apoptotic target cells switches the fluorescence to green as the linker between the GFP-RFP FRET pair is cleaved and necrotic target cells show a complete loss of

fluorescence (35) (**Supplementary Figure 1A**). Using a high-content imaging setup (ImageXpress), we observed that 85.4 ± 10.9% of target cells in 2 mg/ml collagen were killed by either apoptosis or necrosis after 24 hours. The fraction of apoptotic and necrotic target cells eliminated by CTLs dropped to 42.1 ± 8.8% and 7.3 ± 6.3% in collagen matrices in 4 and 5 mg/ml collagen matrices, respectively. (**Figures 1A, B**). The same trend was observed at earlier time points (12 hours, **Supplementary Figure 1B**).

To exclude a possible influence of the CTL infiltration step from the gel surface into the gel interior, similar experiments were performed by embedding the CTLs with the target cells in the collagen gel. The cytotoxic efficiency of CTLs was similar to

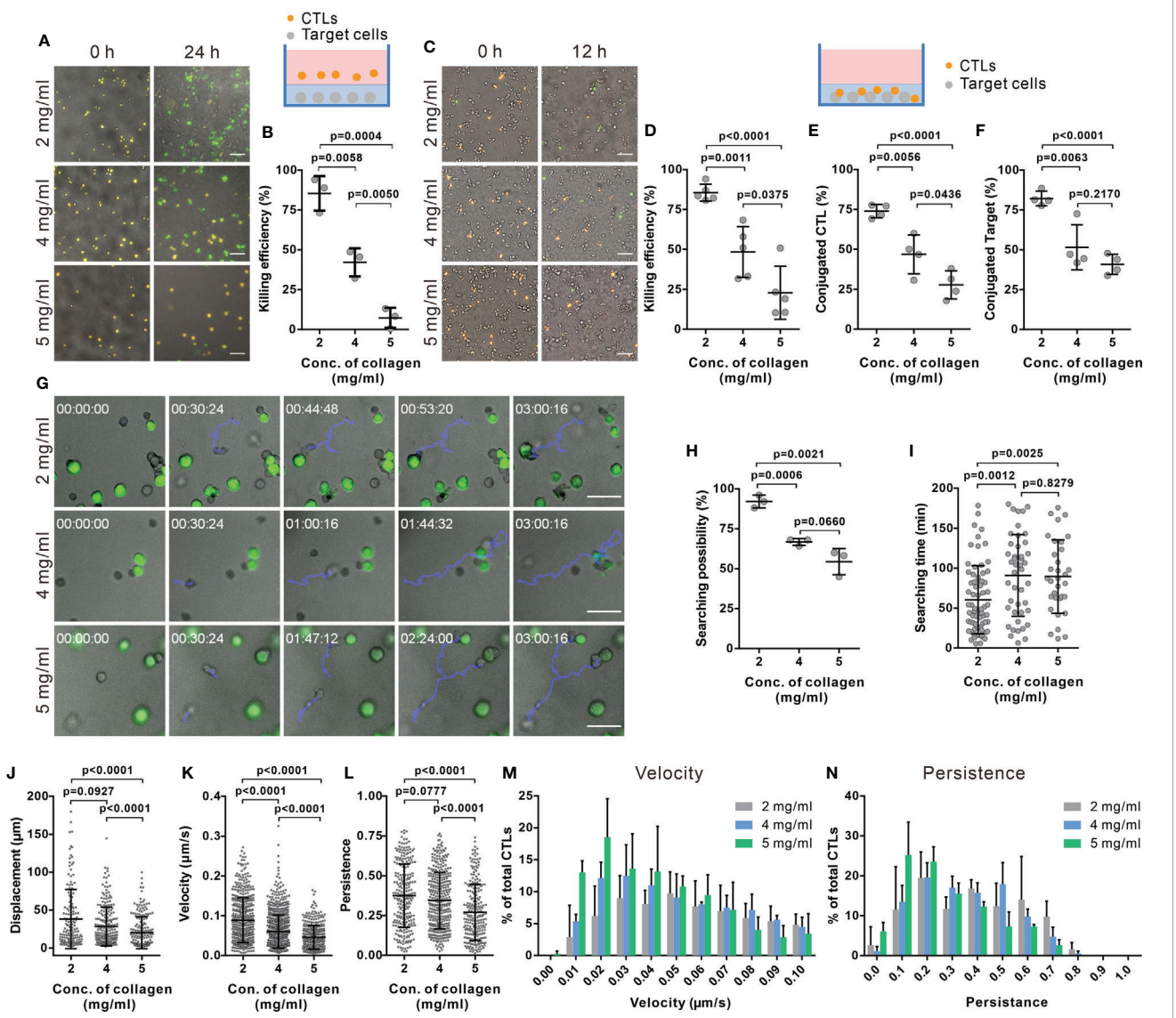

FIGURE 1 | The killing efficiency of CTLs is substantially decreased in dense collagen matrices. **(A, B)** CTL killing efficiency is impaired in dense collagen matrices. Target cells (SEA/SEB pulsed NALM-6-pCasper) were embedded in collagen in absence (**A, B,** 3 donors, E (effector cells): T (Target cells) = 5:1) or presence of CTLs (**C, D,** 5 donors, E:T=1:1). Images were acquired using ImageXpress with Spectra X LED illumination (Lumencor) for 24 hours **(A, B)** or 12 hours **(C, D)**. Orange and green color indicates live and apoptotic target cells, respectively. **(E, F)** Fraction of CTLs in conjugation with target cells **(E)** or target cells in conjugation with CTLs **(F)** was analyzed at 1 hour after polymerization (4 donors). **(G–I)** Searching efficiency of CTLs is reduced in dense collagen. Target cells (SEA/SEB pulsed Raji) were loaded with calcein (green) and embedded in planar collagen with CTLs. Migration was visualized using Cell Observer (20× objective) at 37°C for 3 hours. Representative tracks are shown in **(G)** (blue lines). The likelihood to find a target within 3 hours is shown in **(H)** (3 donors). Time required for CTLs to find their first target (if the cell found at least one target cell) is shown in **(I)**. **(J–N)** Characterization of CTL migration in collagen matrices. CTLs were transfected with histone 2B-GFP and LifeAct-mRuby, and then embedded in 3D collagen. Migration was visualized using light-sheet microscopy (20× objective) every 30 sec for 30 min. The nuclei positions were identified with Imaris to analyze displacement **(J)**, velocity **(K)**, and persistence of CTLs **(L)** (3 donors). The distribution of CTL velocity and persistence is shown in **(M, N)**, respectively. One dot represents either one donor (in **B, D–F, H**) or one cell (in **I–L**). Results are presented as Mean ± SD. The unpaired Student's t-test was used for statistical significance, except **(I–L)** (the Mann-Whitney test was used). Scale bars are 50 μm.

the experiment that included infiltration (**Figures 1A–D**). These results indicate that CTL killing efficiency was solely diminished by the dense collagen network.

To unravel the underlying mechanisms for a reduced CTL killing efficiency in dense collagen matrices, we first examined lytic granule and FAS/FASL pathways. To test the expression of cytotoxic proteins, we recovered CTLs from collagen matrices using collagenase. Control experiments showed that the collagenase treatment does not alter the protein level on T cells, e.g. CD3 expression (**Supplementary Figure 2A**). No significant differences in the expression of cytotoxic proteins (perforin, granzyme A and granzyme B) were observed in CTLs extracted from the collagen hydrogels of the three different concentrations (**Supplementary Figure 2B**). FasL expression was also examined, which was at very low levels for all three concentrations (**Supplementary Figure 2C**). Interestingly, in dense collagen, the fraction of CTLs conjugated with targets (**Figure 1E**) and the fraction of target cells conjugated with CTLs (**Figure 1F**) were significantly reduced. These results indicate that the impaired CTL killing efficiency in dense collagen is not owed to changes in the main components of the killing machinery but rather to a reduced search efficiency.

We next investigated the search efficiency of CTLs in collagen in detail using live-cell imaging. **Figure 1G** shows that a migrating CTL (highlighted by the blue track) in a 2 mg/ml collagen needs around 45 min to find the first target, whereas CTLs in 4 and 5 mg/ml ECM need about 100 min (lower panels of **Figure 1G**). In 2 mg/ml collagen matrices, most CTLs (92.0 ± 4.0%) found at least one target cell within 3 hours; whereas this likelihood was reduced to 66.8 ± 2.1% or 54.4 ± 8.2% in 4 and 5 mg/ml matrices (**Figure 1H**). Analyzing only the CTLs that found target cells, in 4 and 5 mg/ml collagen matrices, these needed about 90 min to find the first target but only about 60 min in 2 mg/ml collagen (**Figure 1I**). These results suggest that the probability of CTLs to find their targets is decreased in dense collagen matrices.

The mobility of CTLs in the matrix is a key factor for optimal search efficiency. To quantify motility, we analyzed displacement, migration velocity, and persistence (indicating how directed the migration is) of CTLs inside the collagen matrices using light-sheet microscopy. In dense collagen matrices (4 and 5 mg/ml), the displacement of CTLs (distance between the starting point and the end point) was reduced (**Figure 1J**, **Supplementary Figure 3, Supplementary Movies 1–3**). Analysis of trajectories in 3D collagen shows that velocity and persistence of migrating CTLs decreased with increasing collagen concentration (**Figures 1K, L**, **Supplementary Figure 3**). It was also observed that CTL migration was impaired in the high concentration of collagen when target cells are present (**Supplementary Figures 4A–C**). Analysis of velocity and persistence distributions reveals a higher fraction of CTLs with low velocity and low persistence in dense collagen (5 mg/ml, **Figures 1M, N**). Moreover, migration velocity is negatively correlated with the time of CTL searching target cells (**Supplementary Figure 4D**). In summary, our findings suggest that in a dense matrix, CTL migration is hindered, and this is likely the reason for longer search time and reduced cytotoxic efficiency.

CTL Migration in 3D Collagen Matrices Is Regulated by the Matrix Stiffness and Porosity

We examined the correlation between CTL killing efficiency and the physical properties of collagen matrix, including pore size and the stiffness. We fluorescently labeled collagen to visualize its structure (**Figure 2A**) to determine pore size (**Supplementary Figure 5**) and found the pore size was decreased with increasing density (**Figures 2A, B**). Collagen stiffness was determined with the storage modulus G' measured by rheology, which increased from 0.81 kPa to 3.64 kPa with collagen density between 2 and 5 mg/ml (**Figure 2C**). To study which of these two features contributes to the impaired CTL migration in collagen matrix, we modified the collagen matrix. To widen the range of stiffness keeping the pore size constant, we also prepared collagen matrices with 100 mM ribose (34), which showed increased storage modulus up to 1.24 kPa (**Figure 2D**), without affecting the pore size (**Figure 2E**). We observed no changes in CTL velocity with increasing stiffness (**Figure 2F**), while the persistence was reduced (**Figure 2G**). In line with this result, the cytotoxic efficiency of CTLs was reduced in collagen matrices prepared in the presence of ribose (**Figure 2H**). These results indicate that stiffness is involved in regulating CTL migration persistence, which could influence CTL killing efficiency.

To increase the pore size of the matrix maintaining a constant collagen concentration, the fibrillation step was performed at room temperature [instead of 37°C (38)]. Noticeably, collagen matrices obtained at 2 mg/ml collagen concentration showed similar shear moduli, while 4 mg/mL matrices with larger pores showed an increased stiffness (**Figure 2I**). This could be attributed to slower fibrillation kinetics of collagen at RT (39, 40). Nevertheless, in matrices with larger pore sizes (**Figures 2J, K**) the cytotoxic efficiency of CTLs was enhanced (**Figure 2L**). Together, these results suggest that smaller pore size and higher stiffness in dense collagen matrices lead to impaired CTL killing efficiency as a result of hindered migration, whereby CTL migration persistence is mainly determined by matrix stiffness while the velocity is likely determined by the pore size of the matrix.

Deformability of Nucleus Is a Limiting Factor for CTL Migration in Dense ECM

As the stiffest organelle in cells, the nucleus is essential for decision making of migration direction for immune cells migrating through restricted space (24, 26, 27). Therefore, we examined the morphology of the nucleus in impaired CTL migration in dense matrices. First, we noticed that the nuclear morphology was deformed to an hour-glass shape in migrating CTLs (**Figure 3A**, **Supplementary Movies 4–6**). To quantify the extent of this nuclear deformation, we analyzed the diameter of cross-sections (the shortest intersection of the hour-glass shape), as well as the sphericity (how closely an object resembles a sphere). The cross-section diameter was decreased in matrices

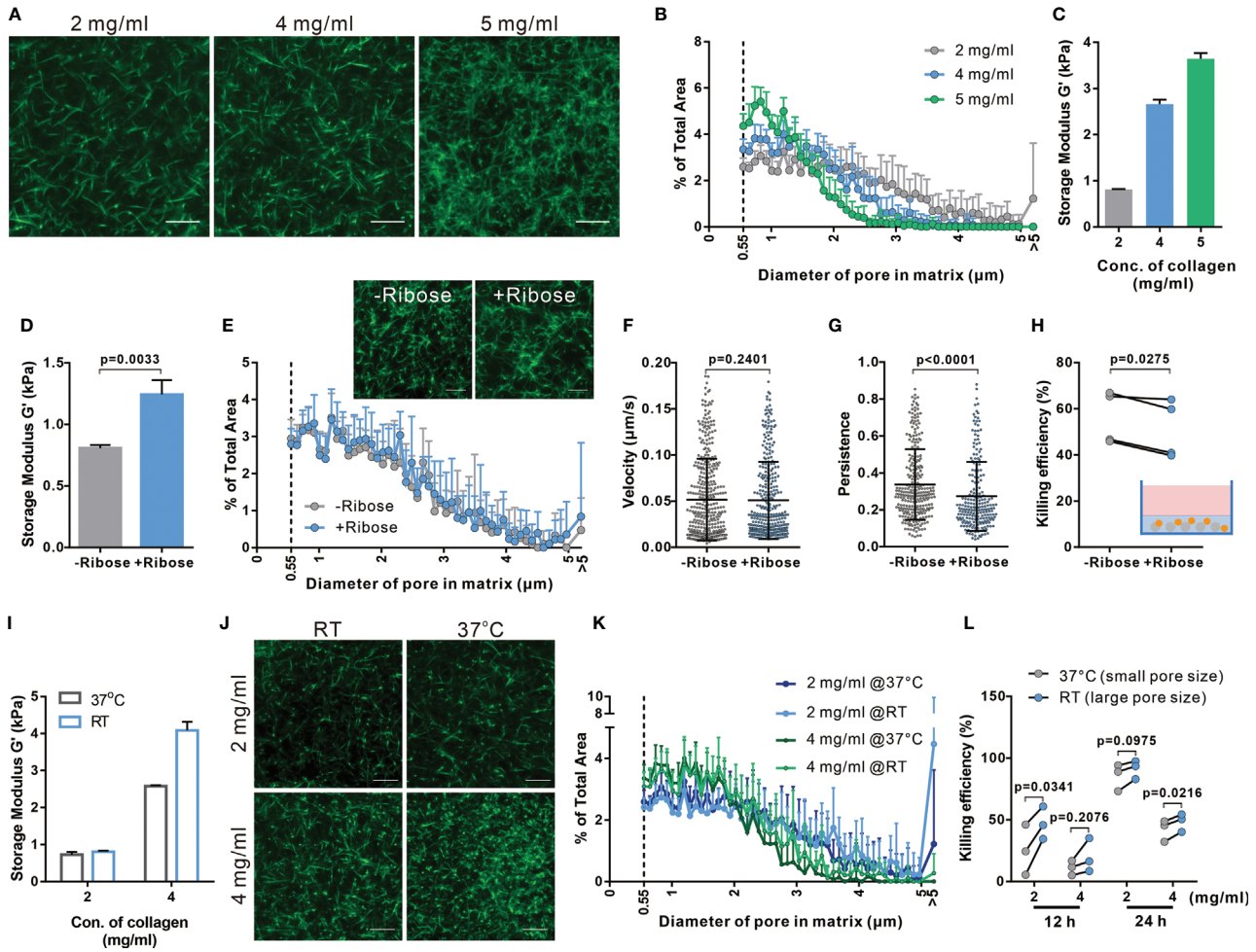

FIGURE 2 | Both enhanced stiffness and reduced pore size contribute to impaired CTL killing efficiency in dense matrices. **(A, B)** Characterization of porosity in collagen matrices with different densities. Structure of collagen stained with Atto 488 NHS ester was visualized using light-sheet microscopy with a 20× objective **(A)**. The distribution of pore size in these matrices is shown in **(B)**. **(C)** Stiffness of collagen matrices was determined by the storage modulus using rheometer. **(D–H)** Adding ribose increases stiffness of collagen (2 mg/ml) without affecting the pore size. Stiffness and pore size of the respective conditions is shown in **(D, E)**, respectively. **(F–H)** Stiffening collagen leads to reduced CTL killing efficiency in 3D. Hoechst 33342-stained CTLs were embedded in a planar 3D collagen matrix. Migration was visualized using Cell Observer (20× objective) for 30 min **(F, G)**. Migration velocity and persistence are shown in **(F, G)**, respectively. To determine killing efficiency, CTLs were embedded with NALM-6-pCasper (E:T=1:1) for 4 hours **(H)**. **(I–K)** Pore size is increased by polymerizing collagen at RT. Stiffness of collagen matrices was determined by the storage modulus using rheometer **(I)**. The structure was visualized using light-sheet microscopy (20× objective) **(J)**. The pore size at each condition is shown in **(K)**. **(L)** Enlarged pore size improves CTL killing in 3D. NALM-6-pCasper cells were embedded in the matrices and CTLs were added from the top (E:T=5:1). Results are presented as Mean ± SD from 2 **(A, B, E, J, K)** or 3 independent experiments (for **F–H**, **L**, results are from 3 donors). One dot stands for either one cell (in **F**, **G**) or one donor (in **H**, **L**). For statistical significance, the unpaired Student's t-test **(D)**, the Mann-Whitney test **(F, G)** or the paired Student's t-test **(H, K)** was used. Scale bars are 10 µm.

with higher collagen density (**Figures 3B, C**). Furthermore, the nuclei of migrating CTLs in dense collagen matrices were more frequently deformed to an hour-glass shape than their counterparts in low-density collagen (**Figure 3D**). Nuclear irregularity index decreased in dense collagen (4 and 5 mg/ml) (**Figure 3E**). It is reported that in dendritic cells, the nucleus is drastically deformed when migrating through spatially restricted areas (25). Together, our results suggest that the extent of nuclear deformation is increased in dense collagen likely due to its decreased porosity.

We next examined whether nuclear deformation correlated with CTL migration in 3D. As shown in the exemplary cells, at the time points when the nucleus was deformed, the real-time velocity was high. This phenomenon was observed for all three concentrations (**Figure 3F**, **Supplementary Movies 4–6**). The respective analyses show that the migration velocity of CTLs is positively correlated to nuclear deformability as determined by the change in nuclear irregularity index (sphericity) in each density (**Figure 3G**). This observation is in good agreement with a recent report, showing that cell migration velocity positively correlated to

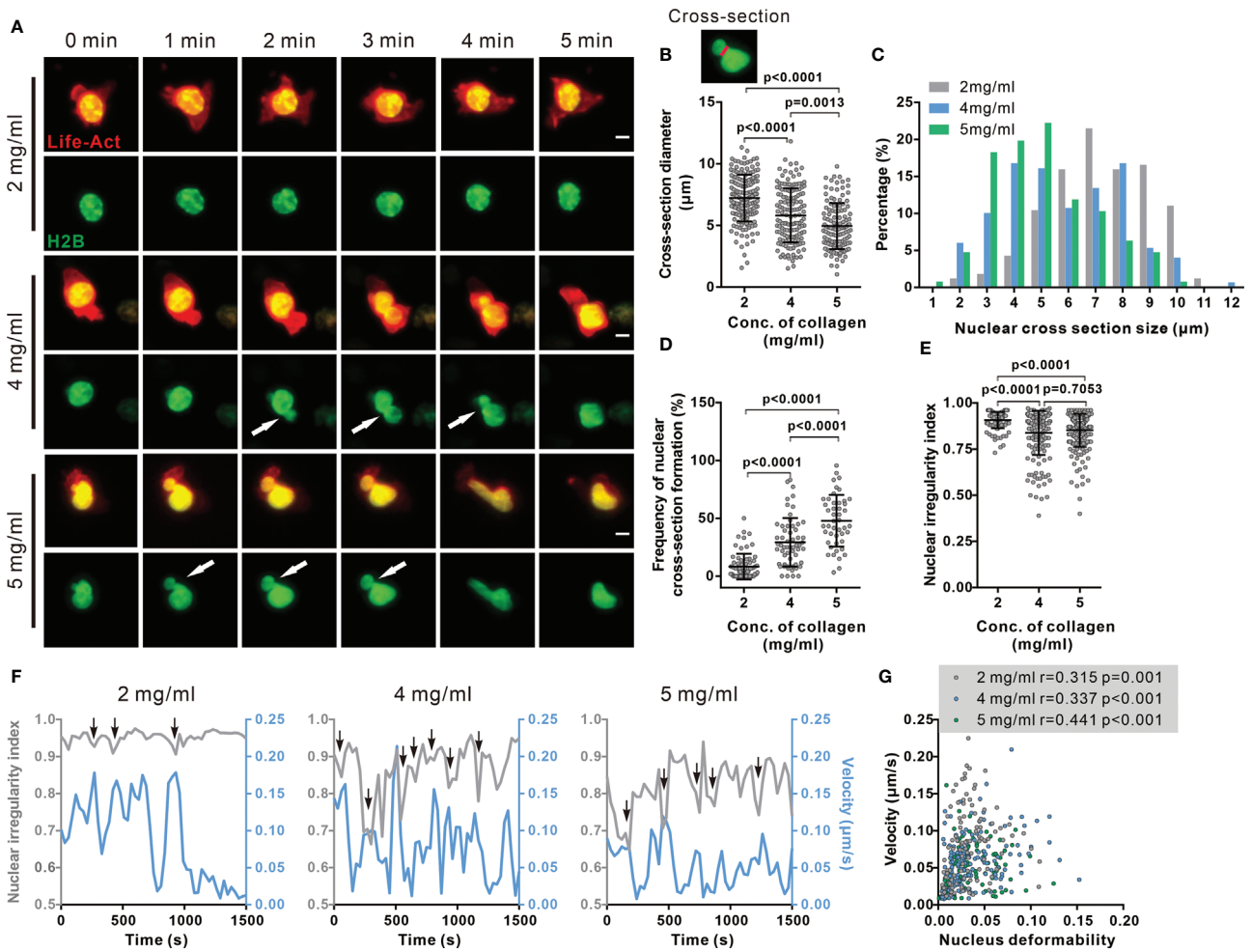

FIGURE 3 | Nuclear deformation is correlated with migration velocity in dense collagen matrices. **(A–E)** Nuclear deformation in CTLs is enhanced upon the increase in matrix density. CTLs transfected with Histone 2B-GFP (green) and LifeAct-mRuby (red) were embedded in collagen. Migration was visualized using light-sheet microscopy (20× objective) at 37°C every 30 sec for 30 min. Exemplary cells are shown in **(A)**. Cross-sections are pointed by the arrowheads. Scale bars are 5 µm. Quantification of cross-section diameter, their distribution and duration is shown in **(B)** (indicated as red-line in the inset), **(C**, **D)**. The nuclear irregularity index of the cells in **(A–D)** is shown in **(E)**. Results are presented as Mean ± SD for **(B**, **D**, **E)**. All results are from 3 donors. The Mann-Whitney test was used for statistical significance. **(F**, **G)** Migration velocity of CTLs is positively correlated with nuclear deformation. NII (sphericity) and velocity as function of time in exemplary cells are shown in **(F)**. Correlation between velocity and nuclear deformability is shown in **(G)**. One dot represents one cell. Correlation coefficient r is analyzed with Spearman's correlation. All results are from 3 donors.

the change in nucleus shape in 2D (28). Together, these findings suggest that deformability of the nucleus is a key factor to determine CTL migration in 3D.

Nuclear Deformability Is Regulated by the Microtubule Network

Cytoskeleton is an essential regulator for nuclear deformation induced by mechanical forces (41, 42) as well as for cell migration (43). Therefore, we examined the contribution of key cytoskeletal components to the regulation of nuclear deformation and CTL migration in 3D. The expression of F-actin (**Figure 4A**) and microtubules (**Figure 4B**) in collagen-embedded CTLs was modestly upregulated in the dense matrices (4 mg/ml and 5 mg/ml). We analyzed the intracellular distribution of F-actin and microtubules using immuno-staining. Confocal images and live-cell imaging show that F-actin was mainly located in the CTL cortex, whereas the microtubule network was enriched around the microtubule-organizing center (MTOC) at the uropod and nucleus-surrounding areas (**Figure 4C**, **Supplementary Movie 7**) as reported by the others (44). Noticeably, the average distance of microtubule network and the nucleus was decreased upon the increase in collagen density (**Figures 4D, E**, **Supplementary Figures 6A, B**). Moreover, short distance between microtubule network and the nucleus benefits to keep the nucleus volume and sphericity in dense collagen (**Supplementary Figures 6C–G**). As it has been reported that the volume of the nucleus is limited by the microtubule network (42), we hypothesized that the microtubule network is involved in regulating CTL nuclear deformability.

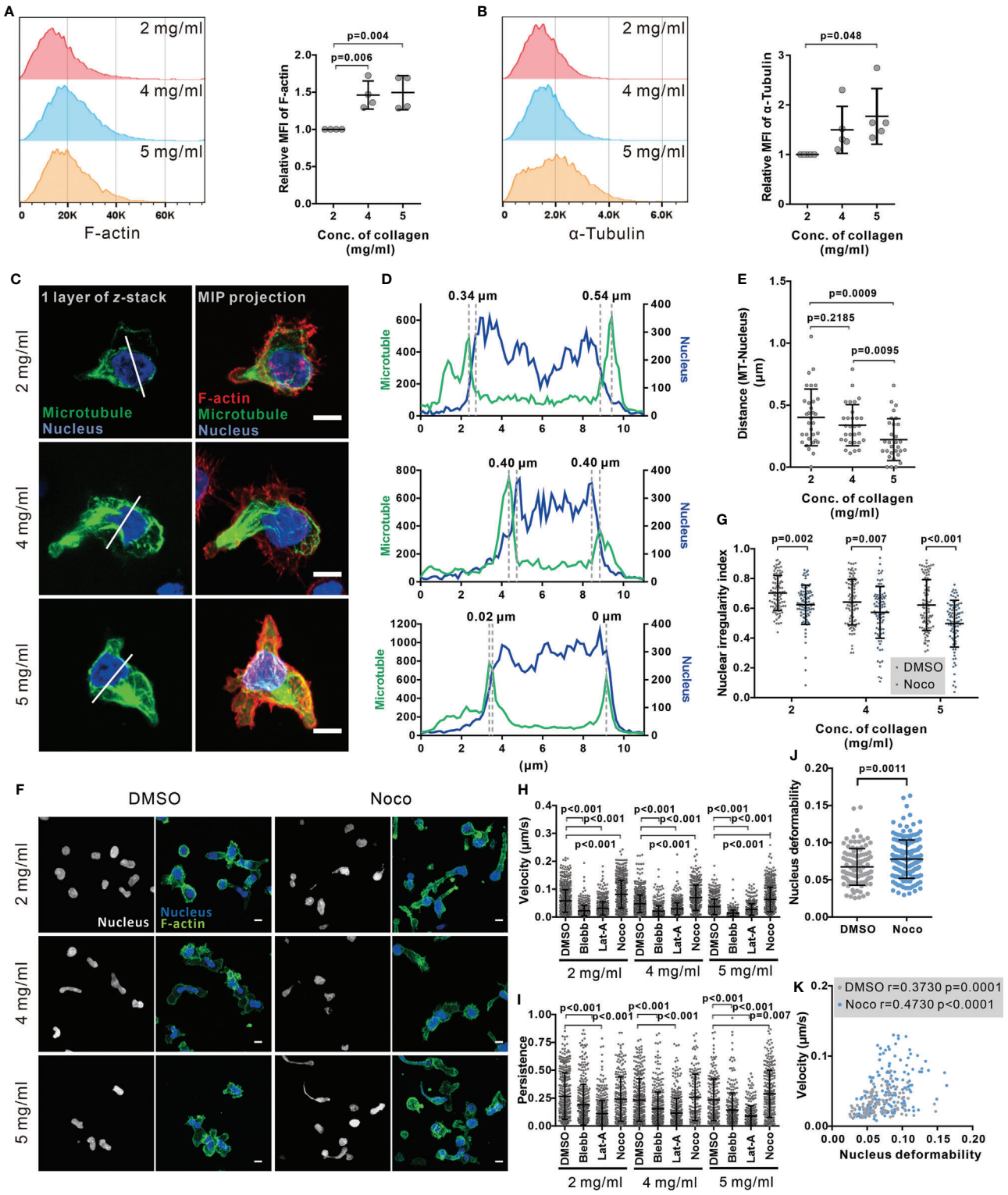

FIGURE 4 | Continued

FIGURE 4 | Disruption of microtubule network enhances CTL nuclear deformation and migration in dense collagen matrices. **(A, B)** Dense matrices slightly up-regulates expression of F-actin and α-tubulin. CTLs were embedded in the collagen matrix for 5 hours after polymerization and then recovered from collagen. The F-actin and α-tubulin were stained with Alexa 488-Phalloidin and anti α-Tubulin mAb antibody. The samples were analyzed with flow cytometry. Presentative donors are shown in the left panels and the quantifications are shown in the right panels. One dot represents one donor. **(C–E)** The microtubule network is located at the nucleus-surrounding region. CTLs were transfected with EMTP-3×GFP (green). 24 hours post-transfection CTLs were fixed and stained with Hoechst 33342 (blue), and Alexa 568-phalloidin (F-actin, red). Images were acquired with confocal microscopy (63× objective). MIP: maximum intensity projection. Scale bars are 5 μm. The fluorescence intensity along the random line cross nucleus depicted in **(C)** is shown in **(D)**. Distance between microtubules and nucleus is defined as the distance between two maxima as indicated in **(D)** and quantified in **(E)**. **(F, G)** Disruption of the microtubule network increases the level of nuclear deformation in CTLs. Collagen-embedded CTLs were treated with nocodazole (Noco, 10 μM) or DMSO for 5 hours prior to fixation. Then CTLs were stained with Hoechst 33342 (blue) and Alexa 488-phalloidin (F-actin, green). Images were acquired with confocal microscopy (63× objective). Exemplary images are shown in **(F)**. Quantification of the nuclear irregularity index in maximum intensity projection is shown in **(G)**. **(H, I)** Impact of cytoskeletal components on CTL migration in 3D. Hoechst 33342-stained CTLs were embedded in planar collagen and treated with DMSO, blebbstatin (Blebb, 50 μM), latrunculin-A (Lat-A, 50 nM), or nocodazole (Noco, 10 μM). Migration was visualized with cell observer (20× objective) at 37°C for 30 min. Migration velocity and persistence are shown in **(H, I)**, respectively. **(J, K)** Disruption of the microtubule network enhances nuclear deformability. CTLs were embedded in collagen (5 mg/ml) and then treated as in **(H, I)**. Average deformability of CTLs is shown in **(J)**. Correlation between migration velocity and nuclear deformability is shown in **(K)**. The correlation coefficient r is analyzed with Spearman's correlation. One dot represents one cell. Scale bars are 5 μm. Results are presented as Mean ± SD from 3 donors. For statistical significance, the unpaired Student's t-test (in **A**, **B**, **E**) or the Mann-Whitney test **(G–J)** was used.

To investigate this hypothesis, we used nocodazole, an inhibitor of tubulin polymerization, to abrogate the functionality of the microtubule network. We found that nuclear circularity was significantly decreased by nocodazole treatment as illustrated in the exemplary cells (**Figure 4F**) and the quantitative analysis (**Figure 4G**), indicating that with microtubules depolymerized, the nucleus is more deformable.

Combined with the finding that nuclear deformation is correlated with CTL migration, we postulated that disruption of the microtubule network should impact CTL migration, especially in dense ECM. Analysis of migration of CTLs in collagen matrices shows that in CTLs treated with nocodazole migration velocity was enhanced at all matrix densities (**Figure 4H**); whereas persistence was only increased in collagen with 5 mg/ml (**Figure 4I**). In comparison, disruption of the actin network by latrunculin-A or abrogation of myosin IIA by blebbstatin almost abolished CTL velocity and persistency for all three collagen densities (**Figures 4H**, **5I**). Inhibition of a myosin IIA-upstream kinase Rock, or focal adhesion kinase also drastically impaired CTL velocity (**Supplementary Figure 7A**) but did not drastically change 3D migration persistence (**Supplementary Figure 7B**). Furthermore, live-cell imaging shows that the nucleus in the nocodazole-treated CTLs was more deformable than their DMSO-treated counterparts (**Figure 4J**). For CTLs, despite nocodazole-, vehicle-, or other inhibitors-treated, the migration velocity was positively correlated with the extent of nuclear deformation (**Figure 4K**, **Supplementary Figure 8**). In summary, we conclude that disruption of the microtubule network enhances CTL migration especially in dense collagen matrices, which is correlated with enhanced deformability of nucleus in CTLs.

Disruption of Microtubules Ameliorate Impaired CTL Killing in Dense ECM

Considering the dependence of CTL migration velocity and persistence on the microtubule-network, we hypothesized that interference with microtubules should improve the impaired killing efficiency in dense ECM. Results of 3D killing assay show that indeed in dense matrix (4 mg/ml and 5 mg/ml), disruption of the microtubule network ameliorated CTL killing (**Figures 5A–C**). Moreover, to further confirm this phenomenon, we used primary human CTL clones specific for MART1 (also known as Melan-A) (31). A melanoma cell line SK-Mel-5, which endogenously, present MART1 on their surface (45), was used as target cells. The time lapse shows that in good agreement with previous results, nocodazole-treatment significantly enhanced killing efficiency of CTL clones to remove SK-Mel-5 (**Figures 5D, E**). Together, our findings suggest that the microtubule network is as a promising target to improve CTL killing against tumor cells in dense ECM.

We further confirmed that also in presence of target cells, disruption of the microtubule-network with nocodazole treatment (10 μM) promoted 3D CTL migration (**Figure 5F**), but not reduced cytotoxic protein secretion and expression (**Supplementary Figure 9**). Concomitantly, the likelihood for microtubule-disrupted CTLs showed increased velocity (**Figure 5G**) and had a higher probability to find their target cells (**Figure 5H**). Only analyzing CTL which were successful to find at least one target, nocodazole-treated CTLs needed similar times to locate their first targets compared to DMSO-treated CTLs (**Figure 5I**), there was only a slight but insignificant reduction of search time for the first target. However, on average, the number of target cells found by nocodazole-treated CTLs was significantly higher than by control CTLs (**Figure 5J**). In addition, we examined CTL viability after 12 hour-nocodazole treatment, which is the condition we used to examine killing efficiency. We found that under this condition, CTL viability in 5 mg/ml collagen was slightly reduced (**Supplementary Figure 10**). Together, we conclude that enhancement of CTL killing efficiency in dense collagen by nocodazole-treatment is due to the amelioration of CTL migration and infiltration, not due to improvement of CTL survival.

Finally, we tested vinblastine, a microtubule-inhibitor applied as a chemotherapeutic to disrupt tumor cell mitosis (46). We treated CTLs with vinblastine to determine CTL killing efficiency in dense collagen. We found that vinblastine increases both killing efficiency of primary CTLs (**Figure 5K**) and human MART1-specific CTL clones (**Figure 5L**). In summary, we conclude that disruption of the microtubule network significantly enhances CTL migration and killing efficiency in dense collagen.

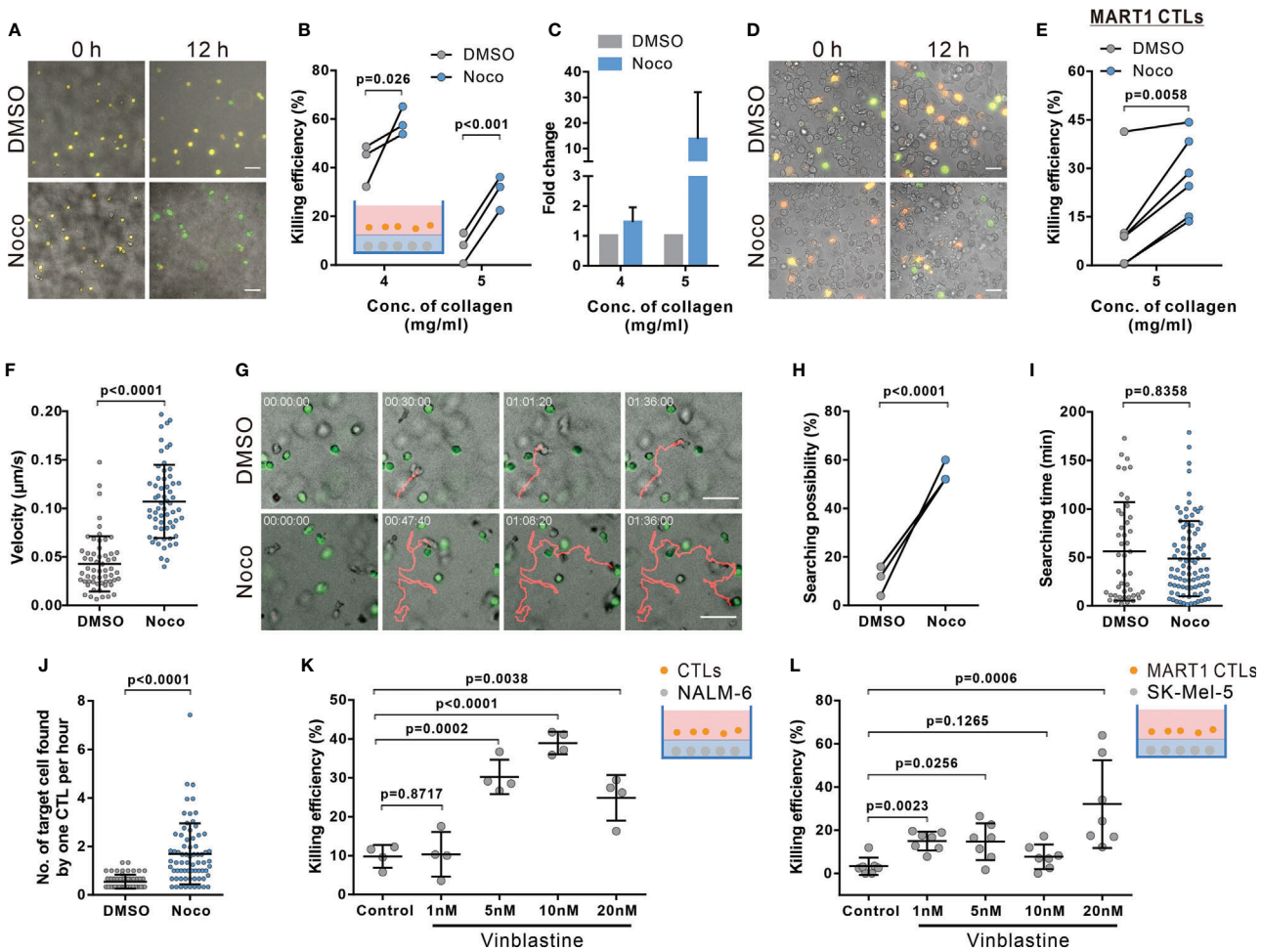

FIGURE 5 | Disruption of microtubules ameliorates impaired CTL killing in dense collagen matrices. **(A–E)** Inhibition of microtubule polymerization improves CTL killing in dense collagen. Nocodazole (Noco, 10 μM) was used to disrupt the microtubule network. Images were acquired using ImageXpress (20× objective) at 0 and 12 hours. NALM-6-pCasper and bead-stimulated CTLs **(A–C)**, or SK-Mel-5 pCasper and MART1-specific CTLs **(D, E)** were used as target and killer cells. Representative experiments from 5 mg/ml are shown in **(A, D)**. **(F–J)** Nocodazole treatment elevates migration and searching efficiency in dense collagen. CTLs and calcein-loaded target cells (green) were embedded in planer collagen matrix (5 mg/ml) and visualized with cell observer. Migration velocity within the duration of 30 min before conjugating with target cells is shown in **(F)**. Representative migration trajectories are shown in **(G)**. The likelihood for CTLs to find target cells and the time required for CTL to find their first target cell are shown in **(H, I)**. Number of target cells found by one CTL per hour is shown in **(J)**. **(K, L)** Vinblastin enhances killing efficiency of CTLs in dense matrices. Respective target cells as indicated were embedded in collagen (5 mg/ml). Killing efficiency was determined at 24 hours **(K)** or 12h **(L)** after adding CTLs using ImageXpress (20× objective). The ratio between effector cells and targets is 5:1 in **(A–C, K)**. The ratio between effector cells and targets is 1:1 in **(D, E, L)**. One dot represents one donor (**B**, **H**, **K**, n = 3 donors), one independent experiment (**E**, n = 6 and **L**, n = 7 experiments), or one cell (**F**, **I**, **J**, n = 4 donors). Scale bars are 50 μm. Results are presented as Mean ± SD. Scale bars are 50 μm. For statistical significance, the paired Student's t-test **(B, E, H)** or the Mann-Whitney test **(F, I–L)** were used.

DISCUSSION

The motility of CTLs in 3D environments, especially when moving through dense tissue matrices, is key for their search efficacy and consequent killing efficiency. In this work, we used bovine collagen matrices with three concentrations (2, 4, and 5 mg/ml) to mimic healthy tissue, soft and stiff solid tumor, mainly based on the stiffness. The storage moduli of 2 mg/ml, 4 mg/ml, and 5 mg/ml of bovine collage is 0.811 ± 0.009 kPa, 2.661 ± 0.098 kPa, and 3.640 ± 0.127 kPa, respectively (**Figure 2C**), which are in a comparable range of human healthy tissue (e.g. colon ~0.9 kPa, mammary gland ~1 kPa) and tumors (e.g. liver tumors ~2.4 kPa, breast cancer ~2.5 kPa and colon tumors ~5 kPa) (47–49). We found that two physical properties of matrices are decisive for T cell migration: pore size and stiffness (or elasticity) of the fibrils. As concentration of collagen increases, pore size gets smaller and stiffness increases, which is in line with other reports (24, 50). Our work shows that human CTLs migrate spontaneously in 3D collagen matrix. Both the speed and the persistence of their 3D migration diminish with increasing collagen concentration. The concentration-dependent correlation of porosity and stiffness can be decoupled in

reconstituted collagen matrices. Keeping the concentration of collagen constant, lowering polymerization temperature increases the pore size of the fibrillar matrix, whereas pretreatment of collagen with ribose enhances the stiffness of collagen fibrils. We show that speed and persistence of human CTL migration in 3D are distinctively regulated: the speed strongly correlated with the pore size, in good agreement with previous reports (51, 52); while the persistence is mainly determined by the stiffness, in good agreement with a recent report for ovarian cancer cells (53).

For migrating human CTLs, a positive correlation between nuclear deformation and cell speed in 3D collagen matrices was observed. The nuclei of cells displayed an hourglass-like deformation in migrating CTLs, very likely through confined spaces. The diameters of the neck of hourglass (cross-section) decreases with enhanced density of collagen. The nucleus is the most rigid intracellular organelle, which provides protection of the chromatin content (54, 55). As reported in many cell types, severe deformation or even rupture of nuclei leads to DNA damage and ultimately cell death (26). In dense ECM, the enhanced nuclear deformation could therefore also lead to an elevated level of CTL apoptosis, which could eventually also contribute to dense ECM-impaired CTL killing efficiency.

Interestingly, we observed that the microtubule network is located in vicinity to the envelope of nucleus and that disruption of microtubule polymerization further enhances nuclear deformation/rupture consequently resulting in more CTL apoptosis, suggesting a protective role of the microtubule network on nuclear morphology and integrity of chromatins. Compelling evidence shows that the nuclear envelope protein lamin-A/C acts is a critical structural element required for nuclear membrane organization and stability (56). The nucleus morphology is associated with the microtubule network (**Supplementary Figure 6**) and the microtubule network could protect nucleus in coordination with lamin A/C (57). It is reported that lamin A/C is induced upon activation of T cells (58). Notably, microtubules are 300 fold more rigid than actin filaments (59). Thus, the microtubule network could provide a mechanistically stable structure surrounding the nucleus to protect the integrity of chromatins, in collaboration with lamin A/C and/or other nuclear envelope proteins.

Our live-cell imaging shows that when CTL migrate through a physical restriction, actin-driven protrusions leads the way through the confinement followed by translocation of the microtubule network along with the nucleus through the confined space. It is reported that in cells, deficiency in actomyosin-based contractility by myosin IIA depletion or inhibition of ROCK impedes contraction of the cell rear and fails to propel the nucleus through a restricted space (24, 60, 61), and profilin-1 is involved in protrusion formation in CTLs (62). The nucleus serves as a mechano-limiting factor, which determines the possibility of cells to go through physical confinement (25, 51). In our work, we found that abrogation of myosin IIA or ROCK significantly limited CTL migration in 3D collagen matrices ranging from low to intermediate-density. This is very likely due to the absence of actomyosin contraction resulting in failing translocation of nucleus through the physical restriction. Unexpectedly, disruption of microtubule polymerization with nocodazole promotes both nuclear deformation and CTL migration in low, intermediate and high density. This indicates that the microtubule network serves as an additional mechano-limiting factor in addition to the nucleus to control CTL migration in 3D, especially through restricted space (27). In comparison, in large pores/channels, the microtubule network is not the rate-limiting factors as one recent report shows that nocodazole has no effect on T cell migration through micro-channels with width equals to or beyond 6 μm (63), which already exceeds physical constrains in low-density collagen, porosity of which ranges from 2-5 μm (24). In addition, several recent studies have reported the impact of microtubule integrity on infiltration or migration of T cells *in vivo* or *ex vivo*. More specifically, inhibition of microtubule polymerization using combretastatin A-4 increases the number of infiltrating $CD8^+$ T lymphocytes in tumors in a mouse model (64). Moreover, nocodazole-treatment increases mouse CTL migration velocity in tumor slices ex *vivo* (17). These results strongly suggest that microtubule disruption improves CTL migration also *in vivo*.

Integrity of both actin-cytoskeleton and the microtubule network is pivotal to execute CTL killing processes. Actin-cytoskeleton has two compensatory roles. On one hand, functionality of cortical actin is essential for TCR triggered release of lytic granules to induce destruction of target cells (65). On the other hand, recovery of cortical actin in CTLs at the contact site with the target cell terminates release of lytic granules (66). In addition, latrunculin-A treatment for target cells could also reduce target lysis-induced by perforin (67). In our work, we show that disassembly of F-actin significantly diminishes CTL motility and killing efficiency in 3D matrices. The concentration of latrunculin-A we used was 50 nM, which should only partially disassemble F-actin as CTLs could still migrate and kill under this condition. The impairment of CTL motility and the consequent reduction in searching efficiency is the primary factor for the reduced killing by disassembly of F-actin. The effect of latrunculin-A on target cells might contribute to reduced killing to some extent, but if so only as a secondary factor.

In terms of the microtubule network, re-orientation of MTOC to the IS is a hallmark for CTL activation upon recognition of target cells, which plays a key role in enriching lytic granules towards the IS (66, 68). Perturbation of the microtubule architecture in CTLs results in reduced killing efficiency but does not affect degranulation (46). In our work, although the microtubule network was disrupted by nocodazole (10 μM) to a large extent, the remaining network was sufficient to support LG release as shown in **Supplementary Figure 9A**. The role of microtubule in human CTL migration in 3D is also strongly supported by the recent study showing that perturbation of microbutules enhances migration of human $CD4^+$ T cells and mouse $CD8^+$ T cells in 3D (17). More importantly, the enhancement in migration of nocodazole-treated CTLs in dense collagen leads to more conjugation and a consequently elevated efficiency of target destruction. Therefore, we conclude that in dense collagen

matrices, CTL motility serves as a rate-limiting factor for killing. Several microtubule inhibitors are applied as chemotherapeutic reagents, such as vinblastine and vincristine. Interestingly, we found that vinblastine indeed enhances CTL-mediated elimination of tumor cells in dense ECM. Our findings suggest that microtubule-inhibiting chemotherapeutic reagents do not only have a direct effect on abrogation of tumor cell proliferation, but also have the potential to enhance CTL killing efficiency against tumor cells in densely packed tumor microenvironment.

DATA AVAILABILITY STATEMENT

The datasets presented in this study can be found in online repositories. The names of the repository/repositories and accession number(s) can be found below: https://cloud.hiz-saarland.de/s/g3cR3BSfbs42reD.

AUTHOR CONTRIBUTIONS

RZ designed and performed most experiments and all the corresponding analyses if not mentioned otherwise. XZ stained collagen matrices and imaged the structure. EK carried out rheology experiments and AC helped interpret the results. WY helped with flow cytometry. KF and ES established MART1-specific T cells clones. ES established NALM-6-pCasper cell lines. DA provided expertise in pCasper-pMax and the corresponding analysis. MH helped with data interpretation and provided critical feedback on all aspects of the project. BQ and RZ generated concepts, designed experiments, and BQ wrote the manuscript. All authors contributed to the article and approved the submitted version.

FUNDING

This project was funded by the Deutsche Forschungsgemeinschaft (SFB 1027; Forschungsgroßgeräte (GZ: INST 256/419-1 FUGG for the light-sheet microscope, GZ: INST 256/423-1 FUGG for the flow cytometer, and GZ: INST 256/429-1 FUGB for ImageXpress), Bundesministerium für Bildung und Forschung (BMBF, 031L0133 to MH), University of Saarland HOMFORexzellent grant (to RZ), and by the Leibniz-Gemeinschaft (INM Fellow to BQ).

ACKNOWLEDGMENTS

We thank the Institute for Clinical Hemostaseology and Transfusion Medicine for providing donor blood; Carmen Hässig, Cora Hoxha, Gertrud Schwär and Susanne Renno for excellent technical help; Sylvia Zöphel for helping with MART1-specific T cell clones; Carsten Kummerow for technical help in ImageXpress and light-sheet microscopy; Sonderforschungsbereich 894 platform P1 for the use of confocal microscopy.

SUPPLEMENTARY MATERIAL

The Supplementary Material for this article can be found online at: https://www.frontiersin.org/articles/10.3389/fimmu.2021.729820/full#supplementary-material

REFERENCES

1. Halle S, Halle O, Forster R. Mechanisms and Dynamics of T Cell-Mediated Cytotoxicity *In Vivo*. *Trends Immunol* (2017) 38:432–43. doi: 10.1016/j.it.2017.04.002
2. Zhang N, Bevan MJ. CD8(+) T Cells: Foot Soldiers of the Immune System. *Immunity* (2011) 35:161–8. doi: 10.1016/j.immuni.2011.07.010
3. Artyomov MN, Lis M, Devadas S, Davis MM, Chakraborty AK. CD4 and CD8 Binding to MHC Molecules Primarily Acts to Enhance Lck Delivery. *Proc Natl Acad Sci USA* (2010) 107:16916–21. doi: 10.1073/pnas.1010568107
4. Li Y, Yin Y, Mariuzza RA. Structural and Biophysical Insights Into the Role of CD4 and CD8 in T Cell Activation. *Front Immunol* (2013) 4:206. doi: 10.3389/fimmu.2013.00206
5. Huang J, Edwards LJ, Evavold BD, Zhu C. Kinetics of MHC-CD8 Interaction at the T Cell Membrane. *J Immunol* (2007) 179:7653–62. doi: 10.4049/jimmunol.179.11.7653
6. Bromley SK, Burack WR, Johnson KG, Somersalo K, Sims TN, Sumen C, et al. The Immunological Synapse. *Annu Rev Immunol* (2001) 19:375–96. doi: 10.1146/annurev.immunol.19.1.375
7. Dieckmann NM, Frazer GL, Asano Y, Stinchcombe JC, Griffiths GM. The Cytotoxic T Lymphocyte Immune Synapse at a Glance. *J Cell Sci* (2016) 129:2881–6. doi: 10.1242/jcs.186205
8. Dustin ML, Chakraborty AK, Shaw AS. Understanding the Structure and Function of the Immunological Synapse. *Cold Spring Harb Perspect Biol* (2010) 2:a002311. doi: 10.1101/cshperspect.a002311
9. Barry M, Bleackley RC. Cytotoxic T Lymphocytes: All Roads Lead to Death. *Nat Rev Immunol* (2002) 2:401–9. doi: 10.1038/nri819
10. Peters PJ, Borst J, Oorschot V, Fukuda M, Krahenbuhl O, Tschopp J, et al. Cytotoxic T Lymphocyte Granules Are Secretory Lysosomes, Containing Both Perforin and Granzymes. *J Exp Med* (1991) 173:1099–109. doi: 10.1084/jem.173.5.1099
11. Stinchcombe JC, Bossi G, Booth S, Griffiths GM. The Immunological Synapse of CTL Contains a Secretory Domain and Membrane Bridges. *Immunity* (2001) 15:751–61. doi: 10.1016/s1074-7613(01)00234-5
12. Qu B, Pattu V, Junker C, Schwarz EC, Bhat SS, Kummerow C, et al. Docking of Lytic Granules at the Immunological Synapse in Human CTL Requires Vti1b-Dependent Pairing With CD3 Endosomes. *J Immunol* (2011) 186:6894–904. doi: 10.4049/jimmunol.1003471
13. Yue B. Biology of the Extracellular Matrix: An Overview. *J Glaucoma* (2014) 23:S20–23. doi: 10.1097/ijg.0000000000000108
14. Salmon H, Franciszkiewicz K, Damotte D, Dieu-Nosjean MC, Validire P, Trautmann A, et al. Matrix Architecture Defines the Preferential Localization and Migration of T Cells Into the Stroma of Human Lung Tumors. *J Clin Invest* (2012) 122:899–910. doi: 10.1172/jci45817
15. Peng DH, Rodriguez BL, Diao L, Chen L, Wang J, Byers LA, et al. Collagen Promotes Anti-PD-1/PD-L1 Resistance in Cancer Through LAIR1-Dependent CD8+ T Cell Exhaustion. *Nat Commun* (2020) 11:4520. doi: 10.1038/s41467-020-18298-8
16. Kuczek DE, Larsen AMH, Thorseth ML, Carretta M, Kalvisa A, Siersbaek MS, et al. Collagen Density Regulates the Activity of Tumor-Infiltrating T Cells. *J Immunother Cancer* (2019) 7:68. doi: 10.1186/s40425-019-0556-6
17. Tabdanov ED, Rodríguez-Merced NJ, Cartagena-Rivera AX, Puram VV, Callaway MK, Ensminger EA, et al. Engineering T Cells to Enhance 3D Migration Through Structurally and Mechanically Complex Tumor

Microenvironments. *Nat Commun* (2021) 12:2815. doi: 10.1038/s41467-021-22985-5
18. Acuto O, Cantrell D. T Cell Activation and the Cytoskeleton. *Annu Rev Immunol* (2000) 18:165–84. doi: 10.1146/annurev.immunol.18.1.165
19. Dupre L, Houmadi R, Tang C, Rey-Barroso J. T Lymphocyte Migration: An Action Movie Starring the Actin and Associated Actors. *Front Immunol* (2015) 6:586. doi: 10.3389/fimmu.2015.00586
20. Krummel MF, Bartumeus F, Gerard A. T Cell Migration, Search Strategies and Mechanisms. *Nat Rev Immunol* (2016) 16:193–201. doi: 10.1038/nri.2015.16
21. Jacobelli J, Friedman RS, Conti MA, Lennon-Dumenil AM, Piel M, Sorensen CM, et al. Confinement-Optimized Three-Dimensional T Cell Amoeboid Motility Is Modulated *via* Myosin IIA-Regulated Adhesions. *Nat Immunol* (2010) 11:953–61. doi: 10.1038/ni.1936
22. Ratner S, Sherrod WS, Lichlyter D. Microtubule Retraction Into the Uropod and Its Role in T Cell Polarization and Motility. *J Immunol* (1997) 159:1063–7.
23. Billadeau DD, Nolz JC, Gomez TS. Regulation of T-Cell Activation by the Cytoskeleton. *Nat Rev Immunol* (2007) 7:131–43. doi: 10.1038/nri2021
24. Wolf K, Te Lindert M, Krause M, Alexander S, Te Riet J, Willis AL, et al. Physical Limits of Cell Migration: Control by ECM Space and Nuclear Deformation and Tuning by Proteolysis and Traction Force. *J Cell Biol* (2013) 201:1069–84. doi: 10.1083/jcb.201210152
25. Renkawitz J, Kopf A, Stopp J, de Vries I, Driscoll MK, Merrin J, et al. Nuclear Positioning Facilitates Amoeboid Migration Along the Path of Least Resistance. *Nature* (2019) 568:546–50. doi: 10.1038/s41586-019-1087-5
26. Denais CM, Gilbert RM, Isermann P, McGregor AL, te Lindert M, Weigelin B, et al. Nuclear Envelope Rupture and Repair During Cancer Cell Migration. *Science* (2016) 352:353–8. doi: 10.1126/science.aad7297
27. Thiam HR, Vargas P, Carpi N, Crespo CL, Raab M, Terriac E, et al. Perinuclear Arp2/3-Driven Actin Polymerization Enables Nuclear Deformation to Facilitate Cell Migration Through Complex Environments. *Nat Commun* (2016) 7:10997. doi: 10.1038/ncomms10997
28. Krause M, Yang FW, te Lindert M, Isermann P, Schepens J, Maas RJA, et al. Cell Migration Through Three-Dimensional Confining Pores: Speed Accelerations by Deformation and Recoil of the Nucleus. *Philos Trans R Soc B Biological Sci* (2019) 374:20180225. doi: 10.1098/rstb.2018.0225
29. Kim DH, Cho S, Wirtz D. Tight Coupling Between Nucleus and Cell Migration Through the Perinuclear Actin Cap. *J Cell Sci* (2014) 127:2528–41. doi: 10.1242/jcs.144345
30. Kummerow C, Schwarz EC, Bufe B, Zufall F, Hoth M, Qu B. A Simple, Economic, Time-Resolved Killing Assay. *Eur J Immunol* (2014) 44:1870–2. doi: 10.1002/eji.201444518
31. Friedmann KS, Knörck A, Cappello S, Hoxha C, Schwär G, Iden S, et al. Combined CTL and NK Cell Cytotoxicity Against Cancer Cells. *bioRxiv* (2020) 2020.2006.2014.150672. doi: 10.1101/2020.06.14.150672
32. Knörck A, Schwär G, Alansary D, Thurner L, Hoth M, Schwarz EC. Cytotoxic Efficiency of Human $CD8^+$ T Cell Memory Subtypes. *bioRxiv* (2021) 2021.2003.2015.435339. doi: 10.1101/2021.03.15.435339
33. Schoppmeyer R, Zhao R, Hoth M, Qu B. Light-Sheet Microscopy for Three-Dimensional Visualization of Human Immune Cells. *J Vis Exp* (2018) 136: e57651. doi: 10.3791/57651
34. Mason BN, Starchenko A, Williams RM, Bonassar LJ, Reinhart-King CA. Tuning Three-Dimensional Collagen Matrix Stiffness Independently of Collagen Concentration Modulates Endothelial Cell Behavior. *Acta Biomater* (2013) 9:4635–44. doi: 10.1016/j.actbio.2012.08.007
35. Backes CS, Friedmann KS, Mang S, Knorck A, Hoth M, Kummerow C. Natural Killer Cells Induce Distinct Modes of Cancer Cell Death: Discrimination, Quantification, and Modulation of Apoptosis, Necrosis, and Mixed Forms. *J Biol Chem* (2018) 293:16348–63. doi: 10.1074/jbc.RA118.004549
36. Acton SE, Farrugia AJ, Astarita JL, Mourao-Sa D, Jenkins RP, Nye E, et al. Dendritic Cells Control Fibroblastic Reticular Network Tension and Lymph Node Expansion. *Nature* (2014) 514:498–502. doi: 10.1038/nature13814
37. Madsen CD, Cox TR. Relative Stiffness Measurements of Tumour Tissues by Shear Rheology. *Bio-Protocol* (2017) 7:Artn E2265. doi: 10.21769/Bioprotoc.2265
38. Shannon GS, Novak T, Mousoulis C, Voytik-Harbin SL, Neu CP. Temperature and Concentration Dependent Fibrillogenesis for Improved Magnetic Alignment of Collagen Gels. *Rsc Adv* (2015) 5:2113–21. doi: 10.1039/c4ra11480a
39. Leikina E, Mertts MV, Kuznetsova N, Leikin S. Type I Collagen Is Thermally Unstable at Body Temperature. *Proc Natl Acad Sci USA* (2002) 99:1314–8. doi: 10.1073/pnas.032307099
40. Zhu J, Kaufman LJ. Collagen I Self-Assembly: Revealing the Developing Structures That Generate Turbidity. *Biophys J* (2014) 106:1822–31. doi: 10.1016/j.bpj.2014.03.011
41. Alisafaei F, Jokhun DS, Shivashankar GV, Shenoy VB. Regulation of Nuclear Architecture, Mechanics, and Nucleocytoplasmic Shuttling of Epigenetic Factors by Cell Geometric Constraints. *Proc Natl Acad Sci USA* (2019) 116:13200–9. doi: 10.1073/pnas.1902035116
42. Kim DH, Li B, Si FW, Phillip JM, Wirtz D, Sun SX. Volume Regulation and Shape Bifurcation in the Cell Nucleus. *J Cell Sci* (2015) 128:3375–85. doi: 10.1242/jcs.166330
43. Serrador JM, Nieto M, Sanchez-Madrid F. Cytoskeletal Rearrangement During Migration and Activation of T Lymphocytes. *Trends Cell Biol* (1999) 9:228–33. doi: 10.1016/s0962-8924(99)01553-6
44. Kopf A, Renkawitz J, Hauschild R, Girkontaite I, Tedford K, Merrin J, et al. Microtubules Control Cellular Shape and Coherence in Amoeboid Migrating Cells. *J Cell Biol* (2020) 219(6):e201907154. doi: 10.1083/jcb.201907154
45. Sugita S, Sagawa K, Mochizuki M, Shichijo S, Itoh K. Melanocyte Lysis by Cytotoxic T Lymphocytes Recognizing the MART-1 Melanoma Antigen in HLA-A2 Patients With Vogt-Koyanagi-Harada Disease. *Int Immunol* (1996) 8:799–803. doi: 10.1093/intimm/8.5.799
46. Tamzali Y, Kemp-Symonds J. *Clinical Equine Oncology, Chapter 9: Principles of Oncological Therapy*. (Elsevier). (2015).
47. Garteiser P, Doblas S, Daire J-L, Wagner M, Leitao H, Vilgrain V, et al. MR Elastography of Liver Tumours: Value of Viscoelastic Properties for Tumour Characterisation. *Eur Radiol* (2012) 22:2169–77. doi: 10.1007/s00330-012-2474-6
48. Deptula P, Lysik D, Pogoda K, Ciesluk M, Namiot A, Mystkowska J, et al. Tissue Rheology as a Possible Complementary Procedure to Advance Histological Diagnosis of Colon Cancer. *ACS Biomaterials Sci Eng* (2020) 6:5620–31. doi: 10.1021/acsbiomaterials.0c00975
49. Sinkus R, Siegmann K, Xydeas T, Tanter M, Claussen C, Fink M. MR Elastography of Breast Lesions: Understanding the Solid/Liquid Duality can Improve the Specificity of Contrast-Enhanced MR Mammography. *Magnetic Resonance Med* (2007) 58:1135–44. doi: 10.1002/mrm.21404
50. Lang NR, Skodzek K, Hurst S, Mainka A, Steinwachs J, Schneider J, et al. Biphasic Response of Cell Invasion to Matrix Stiffness in Three-Dimensional Biopolymer Networks. *Acta Biomater* (2015) 13:61–7. doi: 10.1016/j.actbio.2014.11.003
51. Hons M, Kopf A, Hauschild R, Leithner A, Gaertner F, Abe J, et al. Chemokines and Integrins Independently Tune Actin Flow and Substrate Friction During Intranodal Migration of T Cells. *Nat Immunol* (2018) 19:606–16. doi: 10.1038/s41590-018-0109-z
52. Sadjadi Z, Zhao RP, Hoth M, Qu B, Rieger H. Migration of Cytotoxic T Lymphocytes in 3D Collagen Matrices. *Biophys J* (2020) 119:2141–52. doi: 10.1016/j.bpj.2020.10.020
53. Hetmanski JHR, de Belly H, Busnelli I, Waring T, Nair RV, Sokleva V, et al. Membrane Tension Orchestrates Rear Retraction in Matrix-Directed Cell Migration. *Dev Cell* (2019) 51:460–75.e410. doi: 10.1016/j.devcel.2019.09.006
54. Feng Q, Kornmann B. Mechanical Forces on Cellular Organelles. *J Cell Sci* (2018) 131(21):jcs218479. doi: 10.1242/jcs.218479
55. Lammerding J. Mechanics of the Nucleus. *Compr Physiol* (2011) 1:783–807. doi: 10.1002/cphy.c100038
56. Goldberg MW, Huttenlauch I, Hutchison CJ, Stick R. Filaments Made From A- and B-Type Lamins Differ in Structure and Organization. *J Cell Sci* (2008) 121:215–25. doi: 10.1242/jcs.022020
57. Tariq Z, Zhang H, Chia-Liu A, Shen Y, Gete Y, Xiong ZM, et al. Lamin A and Microtubules Collaborate to Maintain Nuclear Morphology. *Nucleus* (2017) 8:433–46. doi: 10.1080/19491034.2017.1320460
58. Rocha-Perugini V, Gonzalez-Granado JM. Nuclear Envelope Lamin-A as a Coordinator of T Cell Activation. *Nucleus* (2014) 5:396–401. doi: 10.4161/nucl.36361

59. Gittes F, Mickey B, Nettleton J, Howard J. Flexural Rigidity of Microtubules and Actin Filaments Measured From Thermal Fluctuations in Shape. *J Cell Biol* (1993) 120:923–34. doi: 10.1083/jcb.120.4.923
60. Ren XD, Wang RX, Li QY, Kahek LAF, Kaibuchi K, Clark RAF. Disruption of Rho Signal Transduction Upon Cell Detachment. *J Cell Sci* (2004) 117:3511–8. doi: 10.1242/jcs.01205
61. Lammermann T, Bader BL, Monkley SJ, Worbs T, Wedlich-Soldner R, Hirsch K, et al. Rapid Leukocyte Migration by Integrin-Independent Flowing and Squeezing. *Nature* (2008) 453:51–5. doi: 10.1038/nature06887
62. Schoppmeyer R, Zhao R, Cheng H, Hamed M, Liu C, Zhou X, et al. Human Profilin 1 Is a Negative Regulator of CTL Mediated Cell-Killing and Migration. *Eur J Immunol* (2017) 47:1562–72. doi: 10.1002/eji.201747124
63. Park H, Doh J. Study on the Role of Microtubules on T Cell Migration Under Confined Environments. *Biomed Eng Lett* (2015) 5:188–93. doi: 10.1007/s13534-015-0197-8
64. Hua S, Chen F, Wang X, Gou S. Dual-Functional Conjugates Improving Cancer Immunochemotherapy by Inhibiting Tubulin Polymerization and Indoleamine-2,3-Dioxygenase. *Eur J Medicinal Chem* (2020) 189. doi: 10.1016/j.ejmech.2020.112041
65. Lyubchenko TA, Wurth GA, Zweifach A. The Actin Cytoskeleton and Cytotoxic T Lymphocytes: Evidence for Multiple Roles That Could Affect Granule Exocytosis-Dependent Target Cell Killing. *J Physiol* (2003) 547:835–47. doi: 10.1113/jphysiol.2002.033522
66. Ritter AT, Kapnick SM, Murugesan S, Schwartzberg PL, Griffiths GM, Lippincott-Schwartz J. Cortical Actin Recovery at the Immunological Synapse Leads to Termination of Lytic Granule Secretion in Cytotoxic T Lymphocytes. *Proc Natl Acad Sci USA* (2017) 114:E6585–94. doi: 10.1073/pnas.1710751114
67. Basu R, Whitlock BM, Husson J, Le Floc'h A, Jin WY, Oyler-Yaniv A, et al. Cytotoxic T Cells Use Mechanical Force to Potentiate Target Cell Killing. *Cell* (2016) 165:100–10. doi: 10.1016/j.cell.2016.01.021
68. Yi JS, Wu XF, Chung AH, Chen JK, Kapoor TM, Hammer JA. Centrosome Repositioning in T Cells Is Biphasic and Driven by Microtubule End-on Capture-Shrinkage. *J Cell Biol* (2013) 202:779–92. doi: 10.1083/jcb.201301004

Conflict of Interest: The authors declare that the research was conducted in the absence of any commercial or financial relationships that could be construed as a potential conflict of interest.

Publisher's Note: All claims expressed in this article are solely those of the authors and do not necessarily represent those of their affiliated organizations, or those of the publisher, the editors and the reviewers. Any product that may be evaluated in this article, or claim that may be made by its manufacturer, is not guaranteed or endorsed by the publisher.

frontiers in Oncology

ORIGINAL RESEARCH
published: 25 November 2021
doi: 10.3389/fonc.2021.713853

Immune Checkpoints OX40 and OX40L in Small-Cell Lung Cancer: Predict Prognosis and Modulate Immune Microenvironment

*Peixin Chen[1,2], Hao Wang[1,2], Lishu Zhao[1,2], Haoyue Guo[1,2], Liping Zhang[3], Wei Zhang[3], Chenglong Sun[1,4], Sha Zhao[1,2], Wei Li[1,2], Jun Zhu[1,2], Jia Yu[1,2], Chunyan Wu[3] and Yayi He[1,2]**

[1] School of Medicine, Tongji University, Shanghai, China, [2] Department of Medical Oncology, Shanghai Pulmonary Hospital, School of Medicine, Tongji University, Shanghai, China, [3] Department of Pathology, Shanghai Pulmonary Hospital, Tongji University School of Medicine, Shanghai, China, [4] Anhui No. 2 Provincial People's Hospital, Hefei, China

OPEN ACCESS

Edited by:
Ankur Singh, Georgia Institute of Technology, United States

Reviewed by:
Chengzhi Zhou, National Respiratory Medical Center, China
Pierpaolo Correale, Azienda ospedaliera "Bianchi-Melacrino-Morelli", Italy

***Correspondence:**
Yayi He
yayi.he@tongji.edu.cn

Specialty section:
This article was submitted to Cancer Immunity and Immunotherapy, a section of the journal Frontiers in Oncology

Received: *24 May 2021*
Accepted: *04 August 2021*
Published: *25 November 2021*

Citation:
Chen P, Wang H, Zhao L, Guo H, Zhang L, Zhang W, Sun C, Zhao S, Li W, Zhu J, Yu J, Wu C and He Y (2021) Immune Checkpoints OX40 and OX40L in Small-Cell Lung Cancer: Predict Prognosis and Modulate Immune Microenvironment. Front. Oncol. 11:713853. doi: 10.3389/fonc.2021.713853

Background: OX40 and OX40 ligand (OX40L), as essential immune checkpoint (IC) modulators, are highly correlated with cancer immunity regulation as well as tumor microenvironment (TME). Immunotherapy showed outstanding advantages in small-cell lung cancer (SCLC) therapy. However, functions and clinical significance of OX40 and OX40L in SCLC were not clear yet.

Materials and Methods: SCLC samples of 143 patients were collected for immunohistochemistry (IHC) or whole-exome sequencing (WES). We comprehensively explored the expression and mutation of OX40/OX40L in SCLC, and systematically linked OX40/OX40L with TME.

Results: The expression of OX40/OX40L on tumor cells and tumor-infiltrating lymphocytes (TILs) was found in the IHC cohort and verified in other cohorts with SCLC tissues and cell lines. The results showed co-expression patterns among OX40/OX40L, other ICs, and T-cell markers. The WES data suggested that OX40/OX40L mutation is rare in SCLC (<5%). Patients with positive OX40 protein expression on TILs showed substantially higher recurrence-free survival than those with negative expression (p=0.009). The external dataset also indicated that high OX40/OX40L expression was correlated with better prognosis [overall survival: OX40, p<0.001; OX40L, p=0.019]. Importantly, activation of immunity and high infiltration of CD4(+) and CD8(+) T cells were observed in the high OX40/OX40L expression group.

Conclusions: Collectively, this work highlighted the significance of OX40 and OX40L in prognosis and TME cell infiltration characterization of SCLC. Evaluating the OX40/OX40L-expression levels of individual patients with SCLC might contribute to guiding more precise therapy.

Keywords: small cell lung cancer, OX40 (CD134), OX40 ligand, tumor immune microenvironment, prognosis

INTRODUCTION

According to the latest cancer statistics, lung cancer remained the primary causes of death of oncology patients all over the world (1–3). There is a growing trend in the incidence of non-small-cell lung cancer (NSCLC) and small-cell lung cancer (SCLC) in recent years (1–3). SCLC, which comprised between 10 and 15% of total lung cancer, is a rapidly proliferating and highly aggressive tumor (1–4). For extensive disease SCLC (ED-SCLC), platinum-based doublet chemotherapy was the standard therapy. Despite the initially high response rate (approximately 60%), a large proportion of patients with SCLC would relapse within 2 years (5–8). Drug resistance severely affected the prognosis of SCLC patients. Immunotherapy, such as programmed cell death ligands-1 (PD-L1) inhibitor and programmed cell death-1 (PD-1) inhibitor, was considered as a major breakthrough in tumor treatment. The clinical benefits of immune checkpoint (IC) inhibitors in SCLC were revealed by several clinical trials (9–13). Clinical data suggested that the response rate of immunotherapy was higher than that of chemotherapy alone (9–13). Both CASPIAN and IMPOWER 133, two randomized phase 3 trials, highlighted the application prospect of PD-L1 inhibitor in first-line treatment of ED-SCLC (9, 10). However, the first-line immunotherapy plus platinum–etoposide merely extended overall survival (OS) to 12.3–13 months from a previous 10.3 months of the chemotherapy group (9, 10). These clinical studies also found the unsatisfying predictive performance of PD-L1 expression in immunotherapy efficacy and prognosis (9, 10). CheckMate 311, another phase 3 trial of immunotherapy *versus* standard chemotherapy in SCLC, failed in achieving statistically significant difference in OS (14). Thus, exploring the clinical values of other immune-related markers in SCLC might be an effective method to introduce novel combined immunotherapy and develop useful prognostic biomarkers.

OX40 and OX40 ligand (OX40L), serving as promising target of tumor immunotherapy, were expressed on various types of cancers and immune cells (15–22). The interaction of OX40 and OX40L promoted the stimulation and accumulation of T cells, resulting in the antitumor effect (15, 16). The conflicting prognostic implications of OX40/OX40L was found in different types of cancers. In NSCLC, melanoma, and colorectal cancer, OX40/OX40L indicated improved prognosis (17–19). The high proportion of OX40(+) cells inhibited distant metastasis in malignant melanoma (19). However, in another cohort with early-stage NSCLC, high OX40 expression was correlated with early recurrence and shorter OS (20). Similar negative roles of OX40/OX40L in prognosis were also found in liver cancer and leukemia (21, 22). In SCLC, the amplification of OX40, also known as tumor necrosis factor receptor superfamily member 4 (TNFRSF4), was found (23). For SCLC cases, the expression profile of OX40 and OX40L and their roles in clinical outcome and tumor microenvironment (TME) remained unclear. The limited clinical benefits of immunotherapy in SCLC might ascribe to the finite cognition of tumor immune microenvironment (24–26). For these reasons, we identified the OX40/OX40L protein expression and gene mutation in SCLC by immunohistochemistry (IHC) and whole-exome sequencing (WES). Then, the relationship among OX40, OX40L, PD-1, PD-L1, CD3, CD4, CD8, FOXP3, tumor mutation burden (TMB), OS, recurrence-free survival (RFS), and other clinicopathological characteristics was fully explored. We determined the signal pathways and immune cell infiltration features of patients with SCLC on the basis of OX40/OX40L expression. Above clinical findings were verified in addition cohorts.

PATIENTS AND METHODS

Patients' Enrollment and Sample Collection

From 2014 to 2019, a total of 143 eligible patients with SCLC were enrolled in the study. We gathered tumor tissues and blood samples of patients with SCLC before any clinical therapy. We collected and reviewed complete electronic records of all enrolled cases. The SCLC staging were determined by the tumor-node-metastasis (TNM) system. With the approval of the ethics committee of Shanghai Pulmonary Hospital, China (ethical numbers: K20-022), we conducted the study. All participants signed informed consents at the start of study.

IHC and Cutoff Value for OX40/OX40L

We measured the expression of OX40 and OX40L in 102 SCLC specimens by means of IHC. Under the strict asepsis procedure, samples were acquired and diagnosed as SCLC by pathology. After formalin fixation and paraffin embedment, pathology slides were made and prepared for further staining. We used the routine method of dewaxing. Then, specimens were soaked in citrate buffer for antigen recovery. The usage of 3% hydrogen peroxide helped block the activity of endogenous peroxidase. Later, fetal bovine serum was used as blocking reagent. Primary antibodies (OX40, 61637, Rabbit mAb, Cell Signaling Technology; OX40L, ab211287, Rabbit mAb, Abcam) and secondary antibody were applied standardly. In the end, the commonly used diaminobenzidine colorimetry and digital microscope (IX73, OLYMPUS) were applied to quantify protein expression levels of OX40 and OX40L. Three microscope fields at 20× magnification was selected randomly for expression evaluation. The expression of OX40 and OX40L on cancer cells and tumor-infiltrating lymphocytes (TILs) was scored by two pathologists independently.

The survival analysis was the approach to determine the best cutoff point of OX40 and OX40L (27). According to survival analysis results, the p value of the best cutoff value was the minimum. For OX40, more than 20% staining on cancer cells was defined as positive expression, while any staining on TILs was deemed positive expression. The scope of positive OX40L expression on tumor cells (TCs) and TILs was more than 80% staining and 10% staining, respectively.

DNA Extraction and Sequencing

We performed WES on 41 SCLC cases. After the standard process of sample collection, the DNA characteristics of SCLC

tissues and blood samples were analyzed by WES. For DNA extraction and quantification, we used QIAamp DNA Tissue Kit (Qiagen, Valencia, USA), RelaxGene Blood DNA system (Tiangen, Beijing, China), Fluorometer (Qubit 2.0), and the Qubit dsDNA HS assay kit (Thermo Fisher Scientific, CA, USA). Once we obtained fragmented genomic DNA by particular instrument and reagents (28, 29), we constructed DNA library by Kapa Biossystems (MA, USA). Then, fragments with poor quality were excluded, while remaining reads were amplified by a certain circulation of polymerase chain reaction. The Illumina Novaseq 6000 platform was used for DNA sequencing.

With the help of Genome Analysis ToolKit (V 4.1) and Mutect2, DNA fragments were aligned to hg19 reference genome (GRch37), thus detecting somatic mutation, single nucleotide variants, and insertion-deletion mutations. Eventually, according to conventional formula for TMB calculation (28), the somatic TMB value of each case was obtained.

Public Datasets Acquisition and Processing

We aimed at further investigating the clinical significance of OX40 and OX40L in the SCLC public cohorts. We queried the Cancer Genome Atlas (TCGA) Database (https://portal.gdc.cancer.gov) and the Gene Expression Omnibus (GEO) Database (https://www.ncbi.nlm.nih.gov/geo/) to get datasets that match the inclusive criteria. All enrolled datasets must own complete RNA sequencing (RNA-seq) and clinicopathologic data for human SCLC specimens. In addition, we surfed a website, named the Cancer Cell Line Encyclopedia (CCLE, https://portals.broadinstitute.org/ccle) Database (30) to verify the expression of OX40 and OX40L in SCLC cell lines. R Studio software (V4.0.1) and several R packages were installed for exporting data from public databases and conducting subsequent bioinformatics analysis, such as differently expressed genes (DEGs) identification, functional analysis, etc.

Gene Biological Role and Function Analysis

The biological functions and pathway enrichment of DEGs between two groups were explored by the Gene Ontology (GO) analysis (http://www.geneontology.org/) and the Kyoto Encyclopedia of Genes and Genomes (KEGG) pathway analysis (https://www.kegg.jp/). The GO bar charts consisted of three sections, namely, cellular components, biological processes, and molecular functions. The KEGG plot demonstrated significantly DEGs-related pathways.

Estimation of TME Characterization in SCLC

In the current study, we conducted the Estimation of STromal and Immune cells in MAlignant Tumours using Expression data (ESTIMATE) algorithm and CIBERSORTx algorithm on the global gene expression profiles of SCLC patients. The ESTIMATE algorithm provided the overall abundance of immune cells and stromal cells of each clinical sample (31). Apart from the immune score and the stromal score, the tumor purity of each SCLC case was also deduced by the ESTIMATE algorithm (31). As one of deep deconvolution and machine-learning tools, the CIBERSORTx used the linear support vector regression and a set of leukocyte genes called LM22 (32, 33). For CIBERSORTx algorithm, it can statistically infer the particular infiltration percentage of 22 kinds of TILs in SCCL TME, such as subgroups of T cells, B cells, natural killer (NK) cells, etc.

Statistical Analysis

The chi-square tests and Pearson correlation tests were used for detecting relationship among OX40/OX40L, PD-1, PD-L1, other biomarkers, and clinical factors. In addition, the Mann-Whitney U test was applied to compare continuous variables between two groups. For survival analysis, the Kaplan-Meier approach and the log-rank test were utilized. By means of univariate and multivariate logistic regression method, factors that affected the expression status of OX40 and OX40L were found. Through univariate and multivariate Cox regression method, independent prognostic factors in SCLC were also identified. Two-sided p value less than 0.05 was deemed to be statistically significant. Two statistical tools were used in the research, namely, the SPSS software (V 22.0) and the RStudio software (V4.0.1).

RESULTS

Clinical and Tumor Features of Patients

Totally, the whole cohort contained 143 patients with SCLC (**Table 1** and **Table S1**). The age of participants ranged from 38 to 84 years old. A high percentage of patients were males (121/143, 84.6%) and smokers (77/143, 53.8%). The baseline characteristics of the IHC group and the WES group were separately detailed in **Tables S2** and **S3**. The sample size of the IHC cohort and the WES cohort was 102 and 41, respectively.

Expression Characteristics of OX40 and OX40L in SCLC

Through IHC, the protein expressions of OX40 and OX40L were found on both TCs and TILs (**Figure 1**). For OX40, the positive

TABLE 1 | Clinical and tumor characteristics of the whole cohort (n=143).

Variables	No. (%)	Variables	No. (%)
Sex		T stage	
Female	22 (15.4)	T1–2	97 (67.9)
Male	121 (84.6)	T3–4	46 (32.1)
Age, median, years	65	N stage	
<70	110 (76.9)	N0–1	71 (49.7)
≥70	33 (23.1)	N2–3	72 (50.3)
Smoking history		Metastasis	
Non-smoker	66 (46.2)	No	120 (83.9)
Smoker	77 (53.8)	Yes	23 (16.1)
SCLC TNM staging			
I–II	61 (42.7)		
III–IV	82 (57.3)		

N, lymph node; SCLC, small-cell lung cancer; T, tumor, TNM, tumor-node-metastasis.

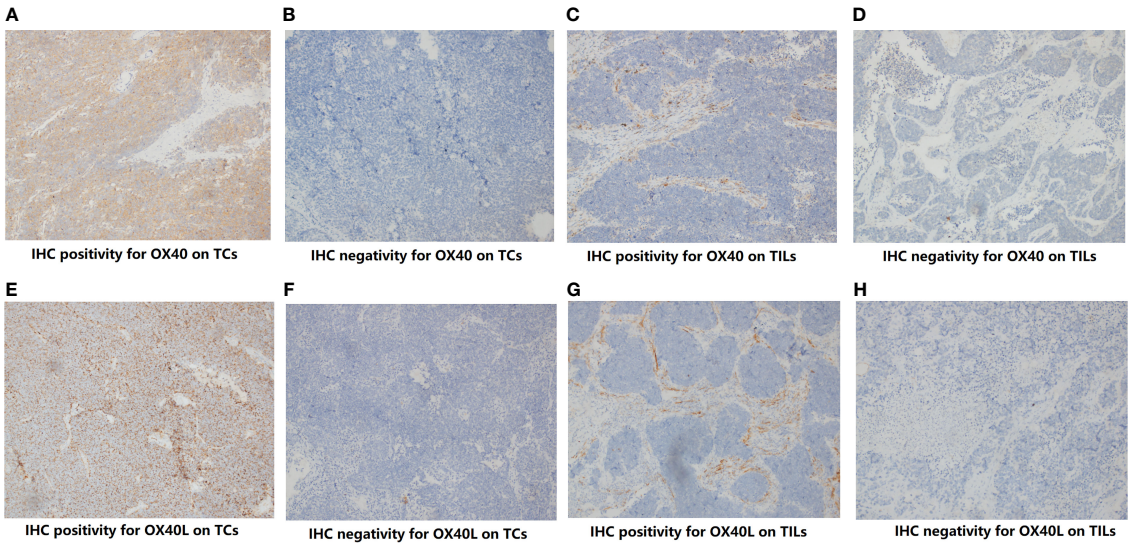

FIGURE 1 | The protein expression of OX40 and OX40 ligand (OX40L) on tumor cells (TCs) and Infiltrating lypmphocytes (TILs). **(A)** IHC positivity for OX40 on TCs. **(B)** IHC negativity for OX40 on TCs. **(C)** IHC positivity for OX40 on TILs. **(D)** IHC negativity for OX40 on TILs. **(E)** IHC positivity for OX40L on TCs. **(F)** IHC negativity for OX40L on TCs. **(G)** IHC positivity for OX40L on TILs. **(H)** IHC negativity for OX40L on TILs.

rate on cancer cells and TILs was 7.8% (8/102) and 72.5% (74/102), respectively. Of these 102 tissues, 22 samples exhibited positive OX40L staining on TILs (21.6%), while only two samples showed positive OX40L staining on TCs (2.0%). We then explored the correlation among OX40, OX40L, clinical factors, and eight conventional IHC markers (**Table S4**). The OX40 protein expression status on TILs had contacts with TNM staging (p=0.044), synaptophysin (p=0.009), and P40 (p=0.013). However, no significant relationship was found between TCs' OX40 expression and clinical factors. On TILs, the expression degree of OX40 was not significantly linked to enrolled binary markers.

In the study, we also investigated relevance between OX40/OX40L and immune markers (**Figure S1A** and **Table S5**). The expression level of OX40 on TILs was significantly correlated with OX40L expression on TILs (p=0.048), PD-1 expression on TILs (p=0.003), PD-L1 on TILs (p=0.019), CD3 (p<0.001), CD4 (p=0.001), and CD8 (p=0.023). OX40L on TILs also had widespread connection with PD-1, PD-L1, and several major markers of T cells (both p<0.05). There was a distinct correlation between OX40 and OX40L expression on TCs (p=0.001). Except for OX40L on TCs, the negative correlation between malignant cells' OX40 expression and other markers was indicated.

The genetic expressions of OX40 and OX40L in SCLC were verified in 22 SCLC human samples that were extracted from GSE43346 and 54 cell lines that were collected in the public CCLE Database (**Figure S1**). As shown in **Figure S1B**, mRNA expressions of OX40 and OX40L in SCLC samples were higher than them in normal tissues. When compared with NSCLC cell lines, the relative low expression levels of OX40 and OX40L in SCLC cell lines were displayed (**Figure S1C**).

Logistic Regression Analysis of OX40 and OX40L Expression

The logistic regression analysis was used to study factors predicting expression of OX40 and OX40L in SCLC. Regarding the limited number of cases that showed positive OX40 or OX40L expression on TCs, we separately developed the logistic regression models for OX40 and OX40L on TILs (**Tables S6**, **S7**). We calculated odds ratio (OR) and 95% confidence interval (CI) of each factor for quantitative analysis. On TILs, eight variables were identified as underlying predictors in OX40 expression status by univariate logistic regression analysis, while none of these was deemed to be significantly predictive factor by multivariate logistic regression analysis (**Table S6**). Similar negative results were found in OX40L expression (**Table S7**).

Survival Analysis for OX40 and OX40L in SCLC

RFS data of 102 patients with SCLC was collected in the IHC cohort. Higher recurrence rate was found in patients with smoking history (31/44, 70.5%) when compared with non-smokers (33/58, 56.9%). The Kaplan-Meier curves reflected prognostic differences between different expression status groups (**Figure 2**). On TCs, OX40 expression status had no marked relation with RFS (p=0.333, **Figure 2A**). The overexpression of OX40 on TILs significantly elevated clinical profits in SCLC (vs low OX40 expression: RFS 34.7 months, 95% CI 27.8-41.5 vs 16.3 months, 95% CI 11.5-21.1, p=0.009; **Figure 2B**). Regretfully, there was no statistical significance in the survival analysis of OX40L in SCLC (**Figures 2C, D**).

On the basis of OX40 and OX40L expression in SCLC, we conducted the subgroup analysis in the primary cohort (**Figure S2**).

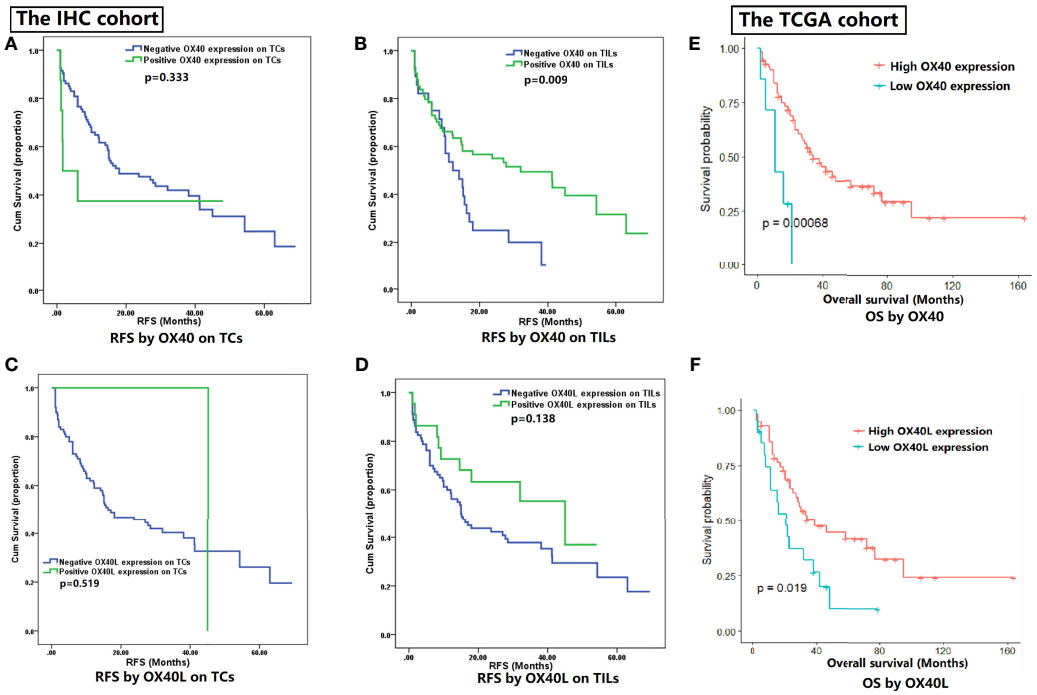

FIGURE 2 | Survival analysis for OX40 and OX40 ligand (OX40L) expression. **(A)** RFS by OX40 on TCs. **(B)** RFS by OX40 on TILs. **(C)** RFS by OX40L on TCs. **(D)** RFS by OX40L on TILs. **(E)** OS by OX40. **(F)** OS by OX40L.

We combined OX40 and OX40L with each other and tested their influences on outcomes (**Figure S2**). TILs' OX40 in combination with TCs' OX40L (p=0.015) or TILs' OX40L (p=0.012) could effectively distinguish patients with different prognosis.

Given the meaningful findings in the IHC cohort, we further verified the clinical values of OX40 and OX40L in the public TCGA cohort (**Figures 2E, F**). The OS data of 77 SCLC patients in the TCGA cohort were downloaded online (34). The survival analysis demonstrated OS was better in SCLC patients with higher expression levels of OX40 (p<0.001) and OX40L (p=0.019), which had high consistency with our IHC results.

Cox Regression for Survival Analysis

Sixteen clinicopathological traits were enrolled in the univariate and multivariate Cox regression analyses for RFS (**Table 2**). All cox regression outcomes were analyzed by using hazard ratio (HR) and 95% CI. By means of univariate Cox regression analysis, nine potential prognostic indicators were found, including age (HR=1.744, p=0.045), smoking status (HR=1.612, p=0.064), TNM staging (HR=1.854, p=0.014), OX40 on TILs (HR=0.502, p=0.011), PD-L1 on TILs (HR=0.604, p=0.068), CD3 (HR=0.613, p=0.052), CD4 (HR=0.627, p=0.089), FOXP3 (HR=0.564, p=0.049) and CD8 (HR=0.577, p=0.058). Then, we performed multivariable regression analysis on the above nine factors. After adjustment of confounding characteristics, multivariate results suggested that smoking status (HR=1.915, p=0.029) and OX40 on TILs (HR=0.523, p=0.032) were significant prediction factors in patients with SCLC.

Mutational Status of OX40/OX40L and Their Associations With Prognosis

The statistics analysis implied that the mutation frequency of OX40 was 4.9% (2/41), while OX40L did not show any mutation in SCLC tissues. Concurrent mutations were found in OX40 and 14 genes, including ADGRB3, BBX, FRMPD3, LAMA5, MUC16, MUC5B, OR5L2, OTOG, PCDH10, PGP, TAAR8, THSD4, and TP53. Then, the somatic TMB values of 41 SCLC samples were calculated for further analysis. As shown in **Figure S3A**, the OX40 mutation group represented higher TMB values (*vs.* the OX40 wild-type group: TMB 7.545 *vs.* 7.214), but the difference was not significant (p>0.05).

In the whole WES cohort, the progression-free survival (PFS) information was collected in 36 patients (87.8%). In addition, the OS data were obtained in 31 subjects (75.6%). In both PFS and OS, instead of having a perfect separation between two survival curves, the Kaplan-Meier curve of OX40 mutation cases met the curve of OX40 wild-type cases, indicating few influences of OX40 mutation status on prognoses of patients with SCLC (**Figures S3B, C**).

GO and KEGG Enrichment Analyses for OX40 and OX40L in SCLC

In order to explore the biological behaviors between different OX40 and OX40L expression patterns, we performed GO and

TABLE 2 | Cox regression analysis for recurrence-free survival in the whole IHC cohort*.

Variables	Univariate			Multivariate		
	HR	95% CI	p	HR	95% CI	p
Gender (Female *vs.* Male)	1.373	0.678–2.280	0.379			
Age (<70 *vs.* ≥70)	1.744	1.014–3.000	**0.045**	1.448	0.816–2.571	0.206
Smoking status (Non-smoker *vs.* Smoker)	1.612	0.973–2.669	**0.064**	1.915	1.070–3.430	**0.029**
SCLC staging (I–II *vs.* III)	1.854	1.130–3.040	**0.014**	1.488	0.898–2.467	0.123
OX40 on TCs (negative *vs.* positive)	1.560	0.624–3.903	0.342			
OX40 on TILs (negative *vs.* positive)	0.502	0.296–0.851	**0.011**	0.523	0.290–0.944	**0.032**
OX40L on TCs (negative *vs.* positive)	0.529	0.073–3.828	0.528			
OX40L on TILs (negative *vs.* positive)	0.604	0.307–1.190	0.145			
PD-1 on TILs (negative *vs.* positive)	0.799	0.479–1.332	0.390			
PD-L1 on TCs (negative *vs.* positive)	1.373	0.430–4.388	0.593			
PD-L1 on TILs (negative *vs.* positive)	0.604	0.352–1.037	**0.068**	0.958	0.424–2.161	0.917
CD3 (negative *vs.* positive)	0.613	0.374–1.005	**0.052**	0.742	0.357–1.540	0.423
CD4 (negative *vs.* positive)	0.627	0.366–1.073	**0.089**	1.095	0.514–2.333	0.815
CD8 (negative *vs.* positive)	0.577	0.327–1.018	**0.058**	1.076	0.4712–2.457	0.863
FOXP3 (negative *vs.* positive)	0.564	0.319–0.997	**0.049**	0.688	0.262–1.705	0.399

*HR, hazard ratio; SCLC, small-cell lung cancer; TCs, tumor cells; TILs, tumor-infiltrating lymphocytes; PD-1, program death-1; PD-L1, program death-ligand 1; FOXP3, forkhead box protein P3; OX40L, OX40 ligand; P, P value for whole; 95% CI, 95% confidence interval. Statistically significant data were marked with bold and underline. *Recurrence-free survival data was updated in May, 2021.*

KEGG enrichment analyses on the TCGA dataset. For OX40, the high-expression group contained 41 subjects, while the rest of the subjects were allocated to the low-expression group (n=40). Of all DEGs between the two groups, a large proportion of DEGs downregulated in the high-OX40-expression group (2,719/4,405, 61.7%; **Figure 3A**). As shown in **Figures 3B, C**, high OX40 expression was markedly enriched in activation pathways of immune cells, such as neutrophil activation (GO:0042119,

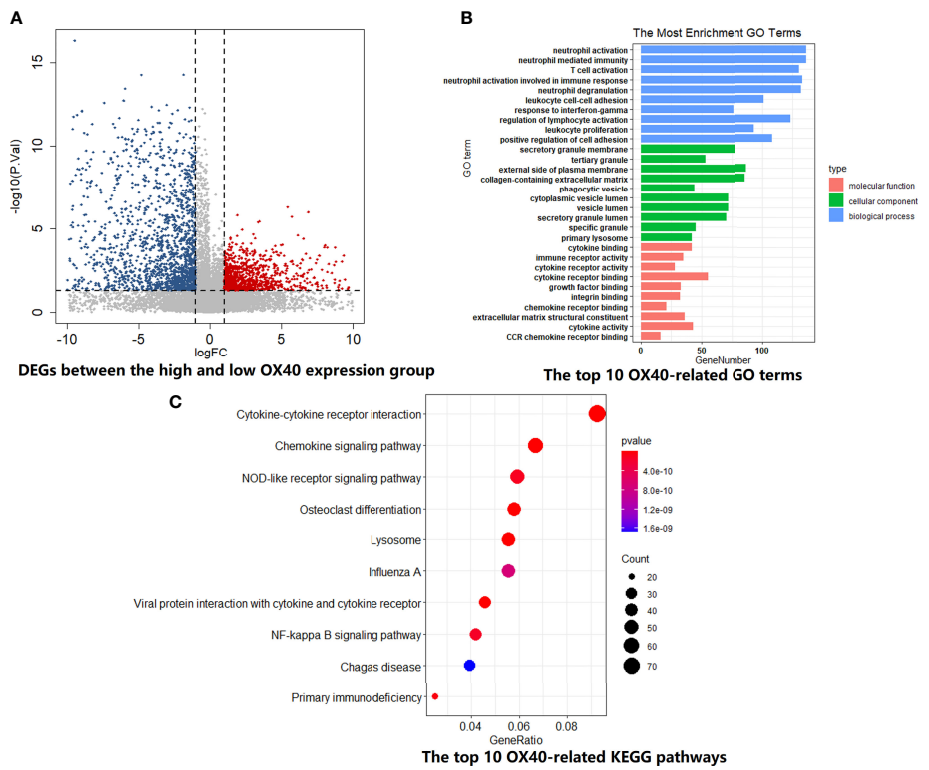

FIGURE 3 | GO and KEGG enrichment analysis for OX40 in SCLC. **(A)** Differentially expressed genes (DEGs) between the high and low OX40 expression groups were visualized in the volcano plot. **(B)** The top l0 OX40-relatd GO terms in the field of cellular component, biological process, and molecular function. **(C)** The top l0 OX40-relatd KEGG pathways. GO, Gene Ontology; KEGG, Kyoto Encyclopedia of Genes and Genomes; SCLC, small cell lung cancer.

p=2.16E-39), T cell activation (GO:0042110, p=5.92E-39), leukocyte proliferation (GO:0070661, p=4.50E-32), and cytokine–cytokine receptor interaction (hsa04060, p=5.66E-15). Concrete top 10 OX40-related functions, biological processes, and pathways are summarized (**Tables S8**, **S9**).

For OX40L, similar grouping method was adopted. The volcano plot demonstrated the enrichment or depletion of 3,048 DEGs in SCLC patients with high OX40L expression level (**Figure 4A**). Specifically, the ratio of downregulated genes to upregulated genes was closed to 2:1 (1,941:1,107). As the ligand of OX40, OX40L also principally related to immune-related functions and pathways. There was a huge overlap between the GO and KEGG enrichment analyses results of OX40 and OX40L in SCLC (**Figures 4B, C** and **Tables S10**, **S11**). Therefore, we hypothesized that OX40 along with OX40L might have important functions in antitumor immunity of SCLC.

TME Features Mediated by OX40/OX40L in SCLC

To test the hypothesis, we compared the TME landscapes between the high- and low-expression groups by the ESTIMATE and CIBERSORTx methods (**Figures 5–7**). The overall abundance of immune cells and stromal cells was higher in the high-OX40- or high-OX40L-expression group (**Figure 5**). Relative low tumor purity was found in tissues with high OX40 or OX40L expression. Moreover, the CIBERSORTx results were consistent with above findings and further confirmed our hypothesis (**Figures 6**, **7**). The TME with high OX40 expression significantly existed increased immune infiltration of various types of immune cells, including memory B cells (p=0.0018), resting dendritic cells (p=4.3e-05), M1 macrophages (p=1.6e-05), activated memory CD4+ T cells (p=0.0024), and CD8+ T cells (p=0.014; **Figure 6**). For the high-OX40L-expression group, the enrichment of TME resting dendritic cells (p=0.00018) and activated memory CD4+ T cells (p=0.0018) infiltration was also found (**Figure 7**). To sum up, OX40 and OX40L acted as vital immunoregulators in SCLC.

Development of the OX40/OX40L-Based Immune Interaction Network

For the sake of illustrating distinct expression patterns among OX40, OX40L, and immune genes (IGs), we developed the OX40/OX40L-based immune network. The gene set of 2,518 IGs was available in the ImmPort Database (35). The correlation analysis was firstly implemented to quantify the relationship between OX40/OX40L and 1,347 IGs, which were tested in the

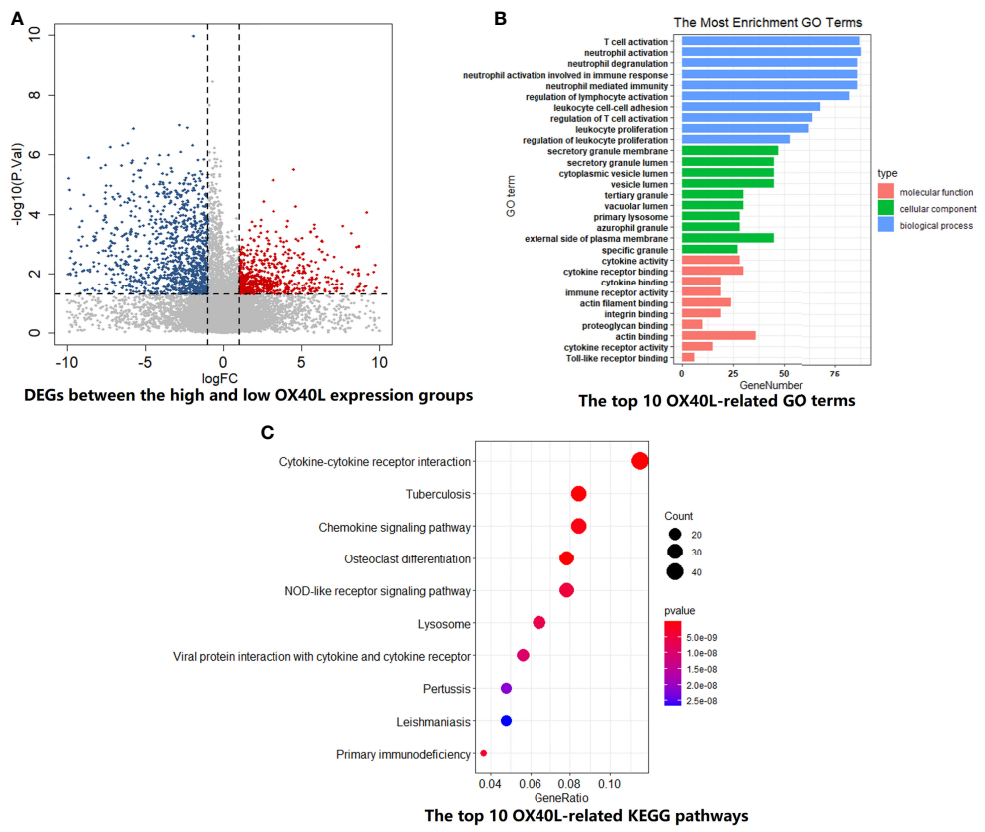

FIGURE 4 | The biological functions and pathway enrichment of OX40L-related DEGs in SCLC. **(A)** A total of 3048 DEGs were identified between the high and low OX40L expression group. **(B)** The GO enrichment results of OX40L-related DEGs in SCLC. Go terms were divided into three types, including cellular component, biological process, and molecular function. **(C)** The KEGG enrichment results of OX40L-related DEGs in SCLC. DEGs, differentially expressed genes; GO, Gene Ontology; KEGG, Kyoto Encyclopedia of Genes and Genomes; SCLC, small cell lung cancer; OX40L, OX40 ligand.

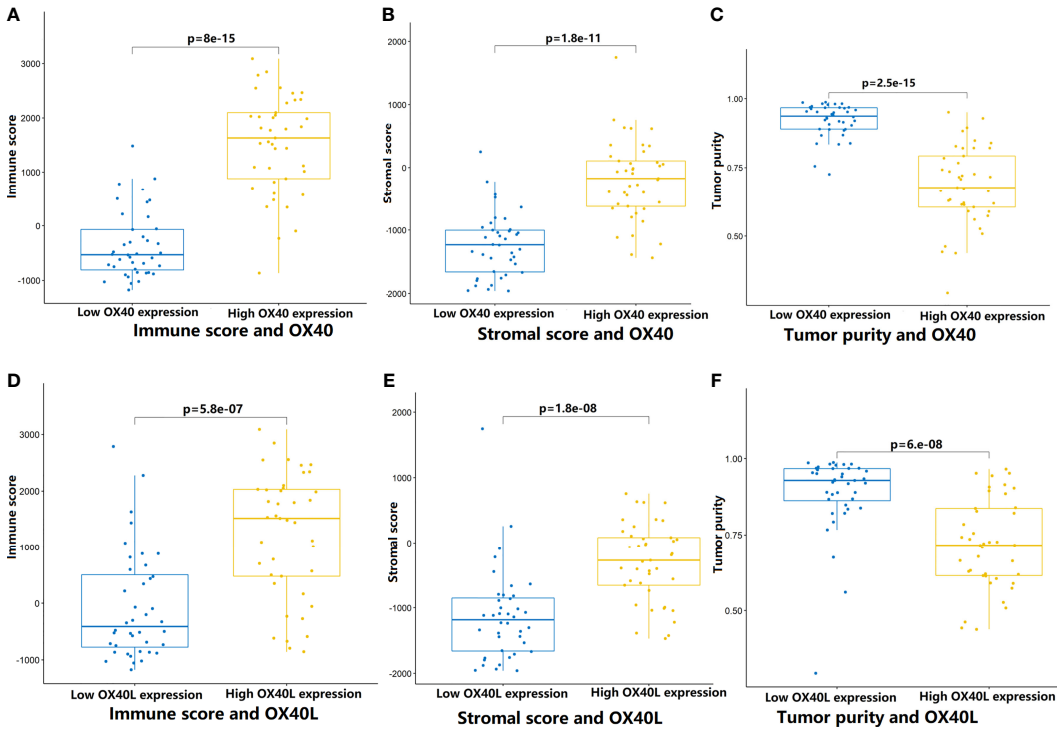

FIGURE 5 | Comparison of tumor microenvironment features that mediated by OX40/0X40L in SCLC. **(A–C)** By the ESTIMATE algorithm, the differences of immune score, stromal score, and tumor purity between the high and low OX40 expression groups. **(D–F)** Comparison of immune score, stromal score, and tumor purity between the high and low OX40L expression groups. SCLC, small cell lung cancer; OX40L, OX40 ligand.

public TCGA cohort. Correlation coefficients and p value were calculated. The number of significantly OX40-related IGs and OX40L-related IGs was 471 and 360, respectively. A small portion of gene expression levels were inversely associated with OX40 expression (25/471, 5.3%). Then, 50 significantly OX40/OX40L-related IGs with correlation coefficient more than 0.70 were selected for subsequently analysis. For survival analysis, subjects of the TCGA cohort were split evenly on the basis of expression level of target gene. Eventually, eight IGs with the p value equal to or less than 0.1 in the survival analysis were chosen for the construction of the OX40/OX40L-based immune interaction network (**Figure S4**). The interactions among OX40, OX40L, NCR3, CSF1, TGFB1, RELB, TNFRSF8, HCST, TNFRSF1B, and CARD11 were extensive (**Figure S5**).

DISCUSSION

The whole analysis of the current study centered on the exploration of roles of OX40 and OX40L in SCLC. We comprehensively investigated the expression levels and mutation frequencies of OX40 and OX40L in patients with SCLC. Our statistical analysis indicated that OX40 and OX40L were closely associated with clinical characteristics, prognosis, TMB, immune-related genes and pathways, and TME immune cell infiltration characterization. Although the functions of OX40 and OX40L were reported in various cancers, including NSCLC, this is, to our knowledge, the first study to fully investigate the clinical and biological significances of OX40 and OX40L in SCLC.

OX40 is a type 1 glycoprotein, while OX40L is a type II glycoprotein (36). The expressions of OX40 and OX40L were detected in various kinds of tumor tissues, such as NSCLC and oral carcinoma (17, 20, 37, 38). In SCLC, we found that TILs' OX40 expression was associated with TNM staging, and TCs' OX40L expression was related to age, indicating different expression patterns of OX40 and OX40L in different cancer types. The mutation of TNFRSF4, encoding OX40, led to the deficiency of T cells, thus inducing Kaposi sarcoma, an endothelial malignancy (39, 40). Additionally, for TNFSF4, which encode OX40L, its mutation downregulated the risk of atherosclerosis and myocardial infarction (41). TNFRSF4 and TNFSF4 mutations in cancers were rarely reported. Similarly, our current research also revealed that most SCLC samples failed to find TNFRSF4 or TNFSF4 mutation.

As crucial ICs, OX40 and OX40L exhibited giant prospects in clinical application. High OX40/OX40L expression was correlated to better clinical prognosis in patients with NSCLC, melanoma, and colorectal cancer (17–19, 42, 43). Nevertheless, high OX40/OX40L also suggested poor prognosis in hepatocellular carcinoma, acute leukemia, as well as head and neck squamous cell carcinoma (21, 22, 44, 45). Given the contradictory results of prognostic effect of OX40/OX40L in

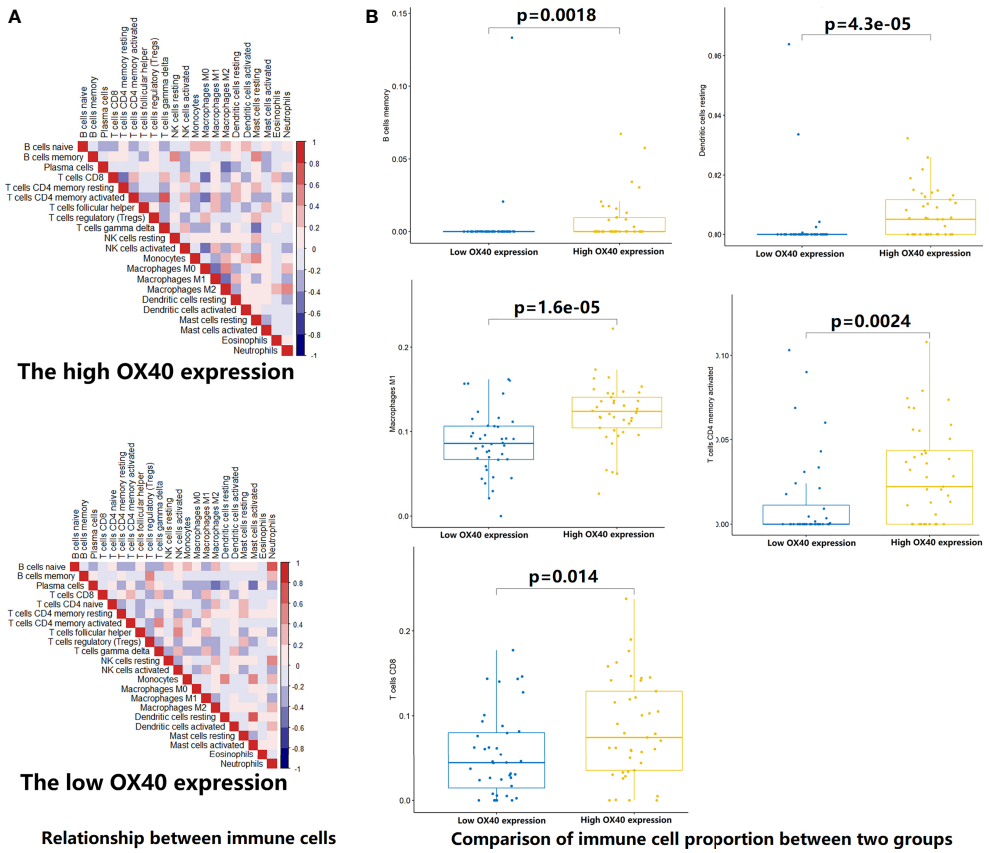

FIGURE 6 | Estimation of relative infiltration proportions of 22 kinds of immune cells in the high and low OX40 expression group. **(A)** By the CIBERSORTx algorithm, relationship matrixes of 22 immune cells in small cell lung cancer patients wit h high and low OX40 expression. **(B)** The high OX40 expression group presented increased infiltration of 5 kinds of immune cells.

cancers, it is worth evaluating the influences of OX40 and OX40L on prognosis of SCLC patients. By survival analysis in the local and public cohorts, we found that SCLC patients with high OX40L expression showed superior prognosis than those with low OX40L expression. Moreover, SCLC patients with positive OX40 expression on TILs significantly relapsed later and lived longer. Similar meaningful result of OX40 in prognosis was obtained by bioinformatics analysis. In glioblastoma, Ichiyo Shibahara et al. revealed that the immunoregulation effect of OX40 principally changed with the TME (46). This might explain why OX40/OX40L showed different influences on prognosis in various cancers.

Mounting evidence displayed that OX40-OX40L signals have an indispensable role in immune cell activation and antitumor immunity. In NSCLC, there was a robust correlation between OX40 expression on TILs and FOXP3 (17), which was consistent with our findings in the SCLC cohort. By IHC, we found that FOXP3 could predict OX40 expression status on TILs. The mechanisms of OX40/OX40L in regulating FOXP3 expression and Treg expansion were complex. Several studies showed that the dynamic equilibrium of Treg cells partly rely on OX40/OX40L axis (47–51). Accumulating researches highlighted the immunomodulation effects of OX40 and OX40L in T cells (52–54). OX40/OX40L mediated the differentiation of helper T cell (Th) through NF-kappa B pathway (55). OX40/OX40L axis also enhanced activity and effects in T cell subsets through PI3K/PKB, MAPK, and NFA T pathways (52–54). In SCLC, the top 10 OX40/OX40L-related biological processes and pathways were also enriched in the activation, maturation, and proliferation of T cells, such as cytokine–cytokine receptor interaction, chemokine signaling pathway, NF-kappa B signaling pathway, etc. Positive correlation was found between the expression of OX40/OX40L and T-cell markers, such as CD3, CD4, and CD8 expression (17, 52–54). Consistent with these results, the extensive connection between OX40/OX40L and immune markers was also found in our cohort and the public cohort. Interestingly, CD3, CD4, and CD8 were identified as predictive markers for OX40L expression status on TILs. Following ESTIMATE and CIBERSORTx analyses further demonstrated higher infiltration abundance of immune cells, especially CD4(+) and CD8(+) T cells, in the high OX40/OX40L expression group. SCLC patients with high OX40/OX40L expression showed improved outcomes might be owing to augment of CD4(+) and CD8(+) T cells, which play essential roles in antitumor effect. Tumor immune heterogeneity was

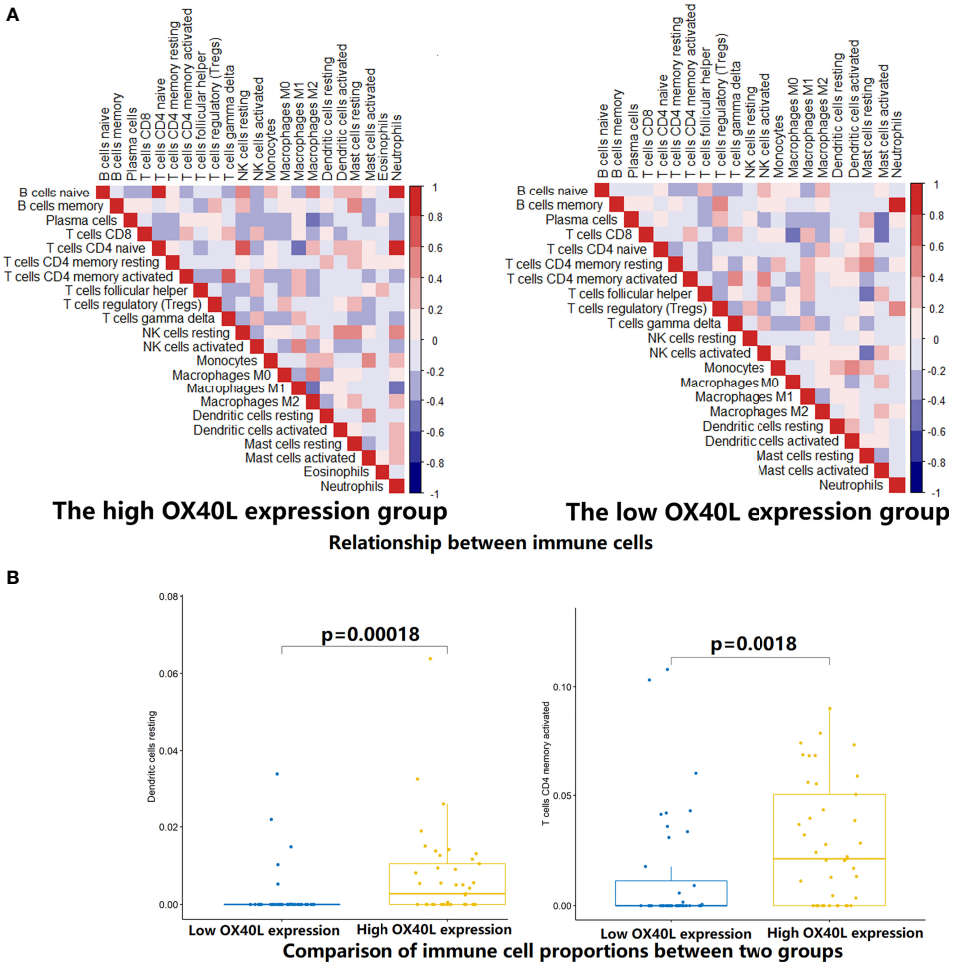

FIGURE 7 | Estimation of relative infiltration proportions of 22 kinds of immune cells in the high and low OX40 ligand (OX40L) expression group. **(A)** By the CIBERSORTx algorithm, relationship matrixes of 22 immune cells in small cell lung cancer patients with high and low OX40L expression. **(B)** The infiltration of resting dendritic cells (p=O.OOO18) and activated memory CD4+ T cells (p=0.0018) was elevated in the hi OX40L group.

found between high and low OX40/OX40L expression SCLC patients.

Some limitations in the current research should be admitted. Firstly, IHC and WES data are limited. Only 102 and 41 SCLC samples separately obtained IHC and WES data. Secondly, it is a retrospective study with limited prognostic data. And different postoperative treatment might affect our study results. In addition, we did not find the relationship between metastasis that considered by clinical imaging before surgery and prognosis in previous studies (24, 27, 56). Future study with metastatic patients is warranted to further estimate the predictive efficacy of the OX40/OX40L protein expression in SCLC.

CONCLUSIONS

In summary, we elucidated the crucial roles of OX40 and OX40L in many respects of SCLC. The OX40-OX40L axle induced immune activation and promoted immune cell infiltration in SCLC. The expression levels of OX40 and OX40L were correlated with clinical outcomes in patients with SCLC. It is worthwhile to conduct translational and clinical researches to further validate our findings in SCLC.

DATA AVAILABILITY STATEMENT

The data presented in the study are deposited in the **Supplemental Table 1** and the China National Genebank (CNGB, https://db.cngb.org/cnsa/), accession number CNP0002096.

ETHICS STATEMENT

The studies involving human participants were reviewed and approved by the ethics committee of Shanghai Pulmonary

Hospital, Tongji University. The patients/participants provided their written informed consent to participate in this study.

AUTHOR CONTRIBUTIONS

Conception and design: PC and YH. Administrative support: YH. Provision of study materials or patients: YH. Collection and assembly of data: PC, LPZ, WZ, CS, and CW. Data analysis and interpretation: PC. Manuscript writing: All authors. All authors contributed to the article and approved the submitted version.

FUNDING

This study was supported in part by a grant of National Natural Science Foundation of China (81802255), Clinical research project of Shanghai Pulmonary Hospital (FKLY20010), Young Talents in Shanghai (2019 QNBJ), "Dream Tutor" Outstanding Young Talents Program (fkyq1901), Clinical Research Project of Shanghai Pulmonary Hospital (fk18005), Key Discipline in 2019 (oncology), Project of Shanghai Municipal Science and Technology Commission (Project of Municipal Science and Technology Commission), Scientific research project of Shanghai Pulmonary Hospital (fkcx1903), Shanghai Municipal Commission of Health and Family Planning (2017YQ050), Innovation Training Project of SITP of Tongji University, and key projects of leading talent (19411950300). Youth project of hospital management research fund of Shanghai Hospital Association (Q1902037).

SUPPLEMENTARY MATERIAL

The Supplementary Material for this article can be found online at: https://www.frontiersin.org/articles/10.3389/fonc.2021.713853/full#supplementary-material

REFERENCES

1. Sung H, Ferlay J, Siegel RL, Laversanne M, Soerjomataram I, Jemal A, et al. Global Cancer Statistics 2020: GLOBOCAN Estimates of Incidence and Mortality Worldwide for 36 Cancers in 185 Countries. *CA: Cancer J Clin* (2021) 71(3):209–49. doi: 10.3322/caac.21660
2. Zhang Y, Luo G, Etxeberria J, Hao Y. Global Patterns and Trends in Lung Cancer Incidence: A Population-Based Study. *J Thoracic Oncol* (2021) 16 (6):933–44. doi: 10.1016/j.jtho.2021.01.1626
3. Siegel RL, Miller KD, Jemal A. Cancer Statistics, 2020. *CA: Cancer J Clin* (2020) 70(1):7–30. doi: 10.3322/caac.21590
4. Byers L, Rudin C. Small Cell Lung Cancer: Where Do We Go From Here? *Cancer* (2015) 121(5):664–72. doi: 10.1002/cncr.29098
5. Jett JR, Schild SE, Kesler KA, Kalemkerian GP. Treatment of Small Cell Lung Cancer: Diagnosis and Management of Lung Cancer, 3rd Ed: American College of Chest Physicians Evidence-Based Clinical Practice Guidelines. *Chest* (2013) 143(5 Suppl):e400S–19S. doi: 10.1378/chest.12-2363
6. Fruh M, De Ruysscher D, Popat S, Crino L, Peters S, Felip E. Small-Cell Lung Cancer (SCLC): ESMO Clinical Practice Guidelines for Diagnosis, Treatment and Follow-Up. *Ann Oncol* (2013) 24(Suppl 6):vi99–105. doi: 10.1093/annonc/mdt178
7. Hanna N, Bunn PA Jr, Langer C, Einhorn L, Guthrie T Jr., Beck T, et al. Randomized Phase III Trial Comparing Irinotecan/Cisplatin With Etoposide/Cisplatin in Patients With Previously Untreated Extensive-Stage Disease Small-Cell Lung Cancer. *J Clin Oncol* (2006) 24(13):2038–43. doi: 10.1200/JCO.2005.04.8595
8. Kuang P, Chen P, Wang L, Li W, Chen B, Liu Y, et al. RNA Sequencing Analysis of Small Cell Lung Cancer Reveals Candidate Chemotherapy Insensitivity Long Noncoding Rnas and Micrornas. *Ann Trans Med* (2020) 8(4):121. doi: 10.21037/atm.2020.01.75
9. Paz-Ares L DM, Chen Y, Reinmuth N, Hotta K, Trukhin D, Statsenko G, et al. Durvalumab Plus Platinum-Etoposide Versus Platinum-Etoposide in First-Line Treatment of Extensive-Stage Small-Cell Lung Cancer (CASPIAN): A Randomised, Controlled, Open-Label, Phase 3 Trial. *Lancet (London England)* (2019) 394(10212):1929–39. doi: 10.1016/S0140-6736(19)32222-6
10. Horn L MA, Szczęsna A, Havel L, Krzakowski M, Hochmair MJ, Huemer F, et al. First-Line Atezolizumab Plus Chemotherapy in Extensive-Stage Small-Cell Lung Cancer. *New Engl J Med* (2018) 379(23):2220–9. doi: 10.1056/NEJMoa1809064
11. Hellmann MD, Ott PA, Zugazagoitia J, Ready NE, Hann CL, Braud FGD, et al. Nivolumab (Nivo) ± Ipilimumab (Ipi) in Advanced Small-Cell Lung Cancer (SCLC): First Report of a Randomized Expansion Cohort From Checkmate 032. *J Clin Oncol* (2017) 35(15_suppl):8503. doi: 10.1200/JCO.2017.35.15_suppl.8503
12. Ott PA, Elez E, Hiret S, Kim DW, Morosky A, Saraf S, et al. Pembrolizumab in Patients With Extensive-Stage Small-Cell Lung Cancer: Results From the Phase Ib KEYNOTE-028 Study. *J Clin Oncol Off J Am Soc Clin Oncol* (2017) 35:3823–9. doi: 10.1200/JCO.2017.72.5069
13. Gelsomino F, Leonetti A, Rihawi K, Sperandi F, Casolari L, Melotti B, et al. Immune Checkpoint Inhibition in Small Cell Lung Cancer: A Key to Reach an Unmet Need? *Trans Cancer Res* (2017) 6:S1484–8. doi: 10.21037/tcr.2017.11.25
14. Spigel DR, Vicente D, Ciuleanu TE, Gettinger S, Peters S, Horn L, et al. Second-Line Nivolumab in Relapsed Small-Cell Lung Cancer: Checkmate 331. *Ann Oncol* (2021) 32(5):631–41. doi: 10.1016/j.annonc.2021.01.071
15. Soroosh P, Ine S, Sugamura K, Ishii N. OX40-OX40 Ligand Interaction Through T Cell-T Cell Contact Contributes to CD4 T Cell Longevity. *J Immunol (Baltimore Md: 1950)* (2006) 176(10):5975–87. doi: 10.4049/jimmunol.176.10.5975
16. Sugamura K, Ishii N, Weinberg AD. Therapeutic Targeting of the Effector T-Cell Co-Stimulatory Molecule OX40. *Nat Rev Immunol* (2004) 4(6):420–31. doi: 10.1038/nri1371
17. Massarelli E, Lam VK, Parra ER, Rodriguez-Canales J, Behrens C, Diao L, et al. High OX-40 Expression in the Tumor Immune Infiltrate Is a Favorable Prognostic Factor of Overall Survival in Non-Small Cell Lung Cancer. *J Immunother Cancer* (2019) 7(1):351. doi: 10.1186/s40425-019-0827-2
18. Weixler B, Cremonesi E, Sorge R, Muraro MG, Delko T, Nebiker CA, et al. OX40 Expression Enhances the Prognostic Significance of CD8 Positive Lymphocyte Infiltration in Colorectal Cancer. *Oncotarget* (2015) 6 (35):37588–99. doi: 10.18632/oncotarget.5940
19. Ladányi A, Somlai B, Gilde K, Fejös Z, Gaudi I, Tímár J. T-Cell Activation Marker Expression on Tumor-Infiltrating Lymphocytes as Prognostic Factor in Cutaneous Malignant Melanoma. *Clin Cancer Research: An Off J Am Assoc Cancer Res* (2004) 10(2):521–30. doi: 10.1158/1078-0432.CCR-1161-03
20. He Y, Zhang X, Jia K, Dziadziuszko R, Zhao S, Deng J, et al. OX40 and OX40L Protein Expression of Tumor Infiltrating Lymphocytes in Non-Small Cell Lung Cancer and Its Role in Clinical Outcome and Relationships With Other Immune Biomarkers. *Trans Lung Cancer Res* (2019) 8(4):352–66. doi: 10.21037/tlcr.2019.08.15
21. Rothfelder K, Hagelstein I, Roerden M, Blumenstock G, Hofmann M, Nuebling T, et al. Expression of the Immune Checkpoint Modulator OX40 in Acute Lymphoblastic Leukemia Is Associated With BCR-ABL Positivity. *Neoplasia (New York NY)* (2018) 20(11):1150–60. doi: 10.1016/j.neo.2018.09.005
22. Xie K, Xu L, Wu H, Liao H, Luo L, Liao M, et al. OX40 Expression in Hepatocellular Carcinoma Is Associated With a Distinct Immune Microenvironment, Specific Mutation Signature, and Poor Prognosis. *Oncoimmunology* (2018) 7(4):e1404214. doi: 10.1080/2162402X.2017.1404214

23. Kim YH, Girard L, Giacomini CP, Wang P, Hernandez-Boussard T, Tibshirani R, et al. Combined Microarray Analysis of Small Cell Lung Cancer Reveals Altered Apoptotic Balance and Distinct Expression Signatures of MYC Family Gene Amplification. *Oncogene* (2006) 25 (1):130–8. doi: 10.1038/sj.onc.1208997
24. Chen P, Zhang L, Zhang W, Sun C, Wu C, He Y, et al. Galectin-9-Based Immune Risk Score Model Helps to Predict Relapse in Stage I-III Small Cell Lung Cancer. *J Immunother Cancer* (2020) 8(2):e001391. doi: 10.1136/jitc-2020-001391
25. Chen S, Wu S, Zhang L, Zhang W, Liu Y, Chen B, et al. CD39: The Potential Target in Small Cell Lung Cancer. *Trans Lung Cancer Res* (2020) 9(4):1483–95. doi: 10.21037/tlcr-20-798
26. Sun C, Zhang L, Zhang W, Liu Y, Chen B, Zhao S, et al. Expression of PD-1 and PD-L1 on Tumor-Infiltrating Lymphocytes Predicts Prognosis in Patients With Small-Cell Lung Cancer. *OncoTargets Ther* (2020) 13:6475–83. doi: 10.2147/OTT.S252031
27. Chen P, Zhao L, Wang H, Zhang L, Zhang W, Zhu J, et al. Human Leukocyte Antigen Class II-Based Immune Risk Model for Recurrence Evaluation in Stage I-III Small Cell Lung Cancer. *J Immuno Cancer* (2021) 9(8):e002554. doi: 10.1136/jitc-2021-002554
28. He Y, Song L, Wang H, Chen P, Liu Y, Sun H, et al. Mutational Profile Evaluates Response and Survival to First-Line Chemotherapy in Lung Cancer. *Advanced Sci (Weinheim Baden-Wurttemberg Germany)* (2021) 8(4):2003263. doi: 10.1002/advs.202003263
29. He Y, Chen L, Zhao L, Dang S, Liu G, Sasada S, et al. Genomic and Transcriptional Alterations in First-Line Chemotherapy Exert a Potentially Unfavorable Influence on Subsequent Immunotherapy in NSCLC. *Theranostics* (2021) 11(14):7092–109. doi: 10.7150/thno.58039
30. Ghandi M, Huang FW, Jané-Valbuena J, Kryukov GV, Lo CC, McDonald ER3rd, et al. Next-Generation Characterization of the Cancer Cell Line Encyclopedia. *Nature* (2019) 569(7757):503–8. doi: 10.1038/s41586-019-1186-3
31. Yoshihara K, Shahmoradgoli M, Martínez E, Vegesna R, Kim H, Torres-Garcia W, et al. Inferring Tumour Purity and Stromal and Immune Cell Admixture From Expression Data. *Nat Commun* (2013) 4:2612. doi: 10.1038/ncomms3612
32. Scholkopf B, Smola AJ, Williamson RC, Bartlett PL. New Support Vector Algorithms. *Neural Comput* (2000) 12(5):1207–45. doi: 10.1162/089976600300015565
33. Newman AM, Liu CL, Green MR, Gentles AJ, Feng W, Xu Y, et al. Robust Enumeration of Cell Subsets From Tissue Expression Profiles. *Nat Methods* (2015) 12(5):453–7. doi: 10.1038/nmeth.3337
34. George J, Lim JS, Jang SJ, Cun Y, Ozretić L, Kong G, et al. Comprehensive Genomic Profiles of Small Cell Lung Cancer. *Nature* (2015) 524(7563):47–53. doi: 10.1038/nature14664
35. Bhattacharya S, Andorf S, Gomes L, Dunn P, Schaefer H, Pontius J, et al. Immport: Disseminating Data to the Public for the Future of Immunology. *Immunologic Res* (2014) 58(2-3):234–9. doi: 10.1007/s12026-014-8516-1
36. Croft M. Control of Immunity by the TNFR-Related Molecule OX40 (CD134). *Annu Rev Immunol* (2010) 28:57–78. doi: 10.1146/annurev-immunol-030409-101243
37. Liu Y, Chen P, Wang H, Wu S, Zhao S, He Y, et al. The Landscape of Immune Checkpoints Expression in Non-Small Cell Lung Cancer: A Narrative Review. *Trans Lung Cancer Res* (2021) 10(2):1029–38. doi: 10.21037/tlcr-20-1019
38. Maroun CA, Zhu G, Fakhry C, Gourin CG, Seiwert TY, Vosler PS, et al. An Immunogenomic Investigation of Oral Cavity Squamous Cell Carcinoma in Patients Aged 45 Years and Younger. *Laryngoscope* (2021) 131(2):304–11. doi: 10.1002/lary.28674
39. Jackson CC, Dickson MA, Sadjadi M, Gessain A, Abel L, Jouanguy E, et al. Kaposi Sarcoma of Childhood: Inborn or Acquired Immunodeficiency to Oncogenic HHV-8. *Pediatr Blood Cancer* (2016) 63(3):392–7. doi: 10.1002/pbc.25779
40. Byun M, Ma CS, Akçay A, Pedergnana V, Palendira U, Myoung J, et al. Inherited Human OX40 Deficiency Underlying Classic Kaposi Sarcoma of Childhood. *J Exp Med* (2013) 210(9):1743–59. doi: 10.1084/jem.20130592
41. Wang X, Ria M, Kelmenson PM, Eriksson P, Higgins DC, Samnegård A, et al. Positional Identification of TNFSF4, Encoding OX40 Ligand, as a Gene That Influences Atherosclerosis Susceptibility. *Nat Genet* (2005) 37(4):365–72. doi: 10.1038/ng1524
42. Kashima J, Okuma Y, Hosomi Y, Hishima T. High Serum OX40 and OX40 Ligand (OX40L) Levels Correlate With Reduced Survival in Patients With Advanced Lung Adenocarcinoma. *Oncology* (2020) 98(5):303–10. doi: 10.1159/000505975
43. Roszik J, Markovits E, Dobosz P, Layani A, Slabodnik-Kaner K, Baruch EN, et al. TNFSF4 (OX40L) Expression and Survival in Locally Advanced and Metastatic Melanoma. *Cancer Immunol Immunother: CII* (2019) 68(9):1493–500. doi: 10.1007/s00262-019-02382-0
44. Gu S, Zi J, Han Q, Song C, Ge Z. Elevated TNFRSF4 Gene Expression Is a Predictor of Poor Prognosis in Non-M3 Acute Myeloid Leukemia. *Cancer Cell Int* (2020) 20:146. doi: 10.1186/s12935-020-01213-y
45. Lecerf C, Kamal M, Vacher S, Chemlali W, Schnitzler A, Morel C, et al. Immune Gene Expression in Head and Neck Squamous Cell Carcinoma Patients. *Eur J Cancer (Oxford England: 1990)* (2019) 121:210–23. doi: 10.1016/j.ejca.2019.08.028
46. Shibahara I, Saito R, Zhang R, Chonan M, Shoji T, Kanamori M, et al. OX40 Ligand Expressed in Glioblastoma Modulates Adaptive Immunity Depending on the Microenvironment: A Clue for Successful Immunotherapy. *Mol Cancer* (2015) 14:41. doi: 10.1186/s12943-015-0307-3
47. Webb GJ, Hirschfield GM, Lane PJ. OX40, OX40L and Autoimmunity: A Comprehensive Review. *Clin Rev Allergy Immunol* (2016) 50(3):312–32. doi: 10.1007/s12016-015-8498-3
48. Zhang X, Xiao X, Lan P, Li J, Dou Y, Chen W, et al. OX40 Costimulation Inhibits Foxp3 Expression and Treg Induction *via* BATF3-Dependent and Independent Mechanisms. *Cell Rep* (2018) 24(3):607–18. doi: 10.1016/j.celrep.2018.06.052
49. Duan W, So T, Croft M. Antagonism of Airway Tolerance by Endotoxin/Lipopolysaccharide Through Promoting OX40L and Suppressing Antigen-Specific Foxp3+ T Regulatory Cells. *J Immunol (Baltimore Md: 1950)* (2008) 181(12):8650–9. doi: 10.4049/jimmunol.181.12.8650
50. Gavin MA, Clarke SR, Negrou E, Gallegos A, Rudensky A. Homeostasis and Anergy of CD4(+)CD25(+) Suppressor T Cells *In Vivo*. *Nat Immunol* (2002) 3 (1):33–41. doi: 10.1038/ni743
51. Griseri T, Asquith M, Thompson C, Powrie F. OX40 Is Required for Regulatory T Cell-Mediated Control of Colitis. *J Exp Med* (2010) 207 (4):699–709. doi: 10.1084/jem.20091618
52. Watts TH. TNF/TNFR Family Members in Costimulation of T Cell Responses. *Annu Rev Immunol* (2005) 23:23–68. doi: 10.1146/annurev.immunol.23.021704.115839
53. Croft M, So T, Duan W, Soroosh P. The Significance of OX40 and OX40L to T-Cell Biology and Immune Disease. *Immunological Rev* (2009) 229(1):173–91. doi: 10.1111/j.1600-065X.2009.00766.x
54. Croft M. The Role of TNF Superfamily Members in T-Cell Function and Diseases. *Nat Rev Immunol* (2009) 9(4):271–85. doi: 10.1038/nri2526
55. Xiao G, Harhaj EW, Sun SC. NF-KappaB-Inducing Kinase Regulates the Processing of NF-Kappab2 P100. *Mol Cell* (2001) 7(2):401–9. doi: 10.1016/S1097-2765(01)00187-3
56. Jiang M, Wu C, Zhang L, Sun C, Wang H, Xu Y, et al. FOXP3-Based Immune Risk Model for Recurrence Prediction in Small-Cell Lung Cancer at Stages I-III. *J Immuno Cancer* (2021) 9(5):e002339. doi: 10.1136/jitc-2021-002339

Conflict of Interest: The authors declare that the research was conducted in the absence of any commercial or financial relationships that could be construed as a potential conflict of interest.

Advantages of publishing in Frontiers

OPEN ACCESS
Articles are free to read for greatest visibility and readership

FAST PUBLICATION
Around 90 days from submission to decision

HIGH QUALITY PEER-REVIEW
Rigorous, collaborative, and constructive peer-review

TRANSPARENT PEER-REVIEW
Editors and reviewers acknowledged by name on published articles

Frontiers
Avenue du Tribunal-Fédéral 34
1005 Lausanne | Switzerland

Visit us: www.frontiersin.org
Contact us: frontiersin.org/about/contact

REPRODUCIBILITY OF RESEARCH
Support open data and methods to enhance research reproducibility

DIGITAL PUBLISHING
Articles designed for optimal readership across devices

FOLLOW US
@frontiersin

IMPACT METRICS
Advanced article metrics track visibility across digital media

EXTENSIVE PROMOTION
Marketing and promotion of impactful research

LOOP RESEARCH NETWORK
Our network increases your article's readership